

Fiscal Year 2022: Fourth Quarter

Progress Reports:  
**Advanced Battery Materials Research  
(BMR) Program  
&  
Battery500 Consortium**

Released January 2023  
for the period of July – September 2022

*Approved by*

Tien Q. Duong

Manager, Advanced Battery Materials Research Program & Battery500 Consortium

Batteries & Electrification R&D

Office of Energy Efficiency and Renewable Energy – Vehicle Technologies Office

U.S. Department of Energy

## **ACKNOWLEDGMENTS**

**This report has been edited by the following team members:**

- **T. A. Zachry**, Energy & Environmental Resources Group
- **Patricia H. Smith**, Naval Sea Systems Command – Carderock Division

## TABLE OF CONTENTS

### A Message from the Managers:

**Advanced Battery Materials Research and Battery500 Consortium.....xxvii**

### Advanced Battery Materials Research Program

<b>Task 1 –Solid-State Electrolytes .....</b>	<b>1</b>
Task 1.1 – Multifunctional Gradient Coatings for Scalable, High-Energy-Density Sulfide-Based Solid-State Batteries (Justin Connell, Argonne National Laboratory).....	4
Task 1.2 – Electrolytes for High-Energy, All-Solid-State, Lithium-Metal Batteries (Guiliang Xu, Argonne National Laboratory) .....	8
Task 1.3 – Thioborate Solid-State Electrolytes for Practical All-Solid-State Batteries (Yi Cui, Stanford University) .....	12
Task 1.4 – Substituted Argyrodite Solid Electrolytes and High-Capacity Conversion Cathodes for All-Solid-State Batteries (Jagjit Nanda, SLAC Stanford Battery Research Center) .....	15
Task 1.5 – Stable Solid-State Electrolyte and Interface for High-Energy, All-Solid-State, Lithium-Sulfur Battery (Dongping Lu, Pacific Northwest National Laboratory) .....	18
Task 1.6 – Development of Thin, Robust, Lithium-Impenetrable, High-Conductivity, Electrochemically Stable, Scalable, and Low-Cost Glassy Solid Electrolytes for Solid-State Lithium Batteries (Steve Martin, Iowa State University of Science and Technology) .....	21
Task 1.7 – All-Solid-State Batteries Enabled by Multifunctional Electrolyte Materials (Pu Zhang, Solid Power Inc.).....	26
Task 1.8 – Developing Materials for High-Energy-Density Solid-State Lithium-Sulfur Batteries (Donghai Wang, Pennsylvania State University).....	29
Task 1.9 – Hot Pressing of Reinforced Lithium-NMC All-Solid-State Batteries with Sulfide Glass Electrolyte (Thomas Yersak, General Motors, LLC) .....	32
Task 1.10 – Three-Dimensional Printing of All-Solid-State Lithium Batteries (Jianchao Ye, Lawrence Livermore National Laboratory) .....	36
Task 1.11 – Physical and Mechano-Electrochemical Phenomena of Thin-Film Lithium-Ceramic Electrolyte Constructs (Jeff Sakamoto, University of Michigan).....	40
Task 1.12 – Low Impedance Cathode/Electrolyte Interfaces for High-Energy-Density Solid-State Batteries (Eric Wachsman and Yifei Mo, University of Maryland).....	43
Task 1.13 – Development of All-Solid-State Battery Using Anti-Perovskite Electrolytes (Zonghai Chen and Tao Li, Argonne National Laboratory) .....	47

Task 1.14 – Lithium Halide-Based Superionic Solid Electrolytes and High-Voltage Cathode Interface (Robert Sacci, Oak Ridge National Laboratory) .....	51
Task 1.15 – Developing an <i>In Situ</i> Formed Dynamic Protection Layer to Mitigate Lithium Interface Shifting: Preventing Dendrite Formation on Metallic Lithium Surface to Facilitate Long Cycle Life of Lithium Solid-State Batteries (Deyang Qu, University of Wisconsin, Milwaukee).....	55
Task 1.16 – Polyester-Based Block Copolymer Electrolytes for Lithium-Metal Batteries (Nitash Balsara, University of California, Berkeley) .....	58
Task 1.17 – Advanced Polymer Materials for Batteries (Zhenan Bao and Yi Cui, Stanford University).....	61
Task 1.18 – Molecular Ionic Composites: A New Class of Polymer Electrolytes to Enable All-Solid-State and High-Voltage Lithium Batteries (Louis A. Madsen, Virginia Polytechnic Institute and State University).....	65
Task 1.19 – Synthesis of Composite Electrolytes with Integrated Interface Design (Sanja Tepavcevic, Argonne National Laboratory).....	69
Task 1.20 – Polymer Electrolytes for Stable, Low-Impedance, Solid-State Battery Interfaces (X. Chelsea Chen, Oak Ridge National Laboratory) .....	73
Task 1.21 – Ion Conductive High Li <sup>+</sup> Transference Number Polymer Composites for Solid-State Batteries (Bryan McCloskey, University of California, Berkeley) .....	78
Task 1.22 – Inorganic-Polymer-Composite Electrolyte with Architecture Design for Lithium-Metal Solid-State Batteries (Enyuan Hu, Brookhaven National Laboratory).....	81
Task 1.23 – Solid-State Batteries with Long Cycle Life and High Energy Density through Materials Design and Integration (Gerbrand Ceder, University of California, Berkeley).....	84
Task 1.24 – Low-Pressure All-Solid-State Cells (Anthony Burrell, National Renewable Energy Laboratory).....	92
Task 1.25 – Precision Control of the Lithium Surface for Solid-State Batteries (Andrew Westover, Oak Ridge National Laboratory) .....	100
<b>Task 2 – Advanced Diagnostics .....</b>	<b>104</b>
Task 2.1 – Characterization and Modeling of Lithium-Metal Batteries: Model-System Synthesis and Advanced Characterization (Guoying Chen, Lawrence Berkeley National Laboratory).....	106
Task 2.2 – Interfacial Processes – Diagnostics (Robert Kostecski, Lawrence Berkeley National Laboratory) .....	110
Task 2.3 – Advanced <i>In Situ</i> Diagnostic Techniques for Battery Materials (Xiao-Qing Yang and Enyuan Hu, Brookhaven National Laboratory).....	113
Task 2.4 – Probing Interfacial Processes Controlled Electrode Stability in Rechargeable Batteries (Chongmin Wang, Pacific Northwest National Laboratory) .....	116

Task 2.5 – Integrated Atomic-, Meso-, and Micro-Scale Diagnostics of Solid-State Batteries (Yi Cui, William Chueh, and Michael Toney; Stanford University/SLAC National Accelerator Laboratory).....	121
Task 2.6 – Fundamental Understanding of Interfacial Phenomena in Solid-State Batteries (Xingcheng Xiao, General Motors) .....	124
Task 2.7 – Multidimensional Diagnostics of the Interface Evolutions in Solid-State Lithium Batteries (Yan Yao, University of Houston) .....	127
<b>Task 3 – Modeling.....</b>	<b>130</b>
Task 3.1 – Characterization and Modeling of Lithium-Metal Batteries: First-Principles Modeling and Machine Learning (Kristin Persson, Lawrence Berkeley National Laboratory).....	131
Task 3.2 – Electrode Materials Design and Failure Prediction (Venkat Srinivasan, Argonne National Laboratory) .....	135
Task 3.3 – Modeling of Amorphous Solid-State Conductors (Gerbrand Ceder, University of California, Berkeley) .....	138
Task 3.4 – <i>In Situ</i> and <i>Operando</i> Thermal Diagnostics of Buried Interfaces in Beyond Lithium-Ion Cells (Ravi Prasher, Lawrence Berkeley National Laboratory).....	140
Task 3.5 – Multiscale Modeling of Solid-State Electrolytes for Next-Generation Lithium Batteries (Anh Ngo, Larry A. Curtiss, and Venkat Srinivasan, Argonne National Laboratory).....	143
Task 3.6 – First-Principles Modeling of Cluster-Based Solid Electrolytes (Puru Jena, Virginia Commonwealth University).....	146
Task 3.7 – Predictive Engineering of Interfaces and Cathodes for High-Performance All-Solid-State Lithium-Sulfur Batteries (Badri Narayanan, University of Louisville) .....	149
Task 3.8 – Predicting the Nucleation and Evolution of Interphases in All-Solid-State Lithium Batteries (Sabrina (Liwen) Wan, Lawrence Livermore National Laboratory).....	155
Task 3.9 – Design of Strain Free Cathode – Solid-State Electrolyte Interfaces Using Chemistry-Informed Deep Learning (Hakim Iddir, Argonne National Laboratory).....	158
Task 3.10 – Tackling Solid-State Electrochemical Interfaces from Structure to Function Utilizing High-Performance Computing and Machine-Learning Tools (Shinjae Yoo, Feng Wang, and Deyu Lu, Brookhaven National Laboratory; Nongnuch Artrith and Alexander Urban, Columbia University).....	164
Task 3.11 – Integrated Multiscale Model for Design of Robust, Three-Dimensional, Solid-State Lithium Batteries (Brandon Wood, Lawrence Livermore National Laboratory).....	169

<b>Task 4 – Metallic Lithium</b> .....	<b>173</b>
Task 4.1 – Lithium Dendrite Prevention for Lithium Batteries (Wu Xu, Pacific Northwest National Laboratory).....	174
Task 4.2 – Prelithiation for High-Energy Lithium-Ion Batteries (Yi Cui, Stanford University).....	177
Task 4.3 – Anode-Free Lithium Batteries (Ji-Guang Zhang and Xia Cao, Pacific Northwest National Laboratory) .....	180
<b>Task 5 – Lithium-Sulfur Batteries</b> .....	<b>183</b>
Task 5.1 – Novel Chemistry: Lithium Selenium and Selenium Sulfur Couple (Khalil Amine, Argonne National Laboratory).....	186
Task 5.2 – Development of High-Energy Lithium-Sulfur Batteries (Dongping Lu and Jun Liu, Pacific Northwest National Laboratory) .....	190
Task 5.3 – Nanostructured Design of Sulfur Cathodes for High-Energy Lithium-Sulfur Batteries (Yi Cui, Stanford University).....	194
Task 5.4 – Investigation of Sulfur Reaction Mechanisms (Enyuan Hu, Brookhaven National Laboratory; Deyang Qu, University of Wisconsin, Milwaukee).....	196
Task 5.5 – New Electrolytes for Lithium-Sulfur Battery (Gao Liu, Lawrence Berkeley National Laboratory) .....	199
Task 5.6 – Strategies to Enable Lean Electrolytes for High Loading and Stable Lithium- Sulfur Batteries (Y. Shirley Meng, University of California, San Diego).....	202
Task 5.7 – New Engineering Concepts to High-Energy-Density Lithium-Sulfur Batteries (Prashant N. Kumta, University of Pittsburgh) .....	213
Task 5.8 – Development of Lithium-Sulfur Battery Cells with High Energy Density and Long Cycle Life (Donghai Wang, Pennsylvania State University).....	218
<b>Task 6 – Lithium-Air Batteries</b> .....	<b>221</b>
Task 6.1 – Lithium-Air Batteries (Khalil Amine and Larry A. Curtiss, Argonne National Laboratory).....	222
Task 6.2 – Lithium Oxygen Battery Design and Predictions (Larry A. Curtiss/Anh Ngo, Argonne National Laboratory; Amin Salehi-Khojin, University of Illinois, Chicago).....	225
Task 6.3 – Development of a High-Rate Lithium-Air Battery Using a Gaseous CO <sub>2</sub> Reactant (Amin Salehi-Khojin, University of Illinois, Chicago).....	228
<b>Task 7 – Sodium-Ion Batteries</b> .....	<b>231</b>
Task 7.1 – Exploratory Studies of Novel Sodium-Ion Battery Systems (Xiao-Qing Yang and Enyuan Hu, Brookhaven National Laboratory).....	232
Task 7.2 – Development of a High-Energy Sodium-Ion Battery with Long Life (Chris Johnson and Khalil Amine, Argonne National Laboratory).....	235

Task 7.3 – Tailoring High-Capacity, Reversible Anodes for Sodium-Ion Batteries  
(Marca M. Doeff, Lawrence Berkeley National Laboratory) ..... 239

Task 7.4 – Electrolytes and Interfaces for Stable High-Energy Sodium-Ion Batteries  
(Phung M. L. Le, Pacific Northwest National Laboratory)..... 242

**Battery500 Consortium Program**

**Innovation Center for Battery500**  
(Jun Liu, Pacific Northwest National Laboratory; Yi Cui, Stanford University)..... 245

**Appendix – Acronym Guide..... 275**

## TABLE OF FIGURES

Figure 1. Calculated density of states (DOS) for LPSCI solid-state electrolyte with varying concentrations of oxygen at generalized gradient approximation (top row) and hybrid functional (bottom row) levels of theory.....	5
Figure 2. Computed structures of (a) argyrodite (001) surface (top view), and (b) amorphous alumina (side view) were used to determine work functions from (c-d) potential profiles normal to these surfaces, respectively. The Fermi levels are shown with dashed lines.....	6
Figure 3. Calculated barriers for lithium hopping in several products of reaction of alumina with LPSCI indicate feasibility of lithium ionic transport through the interfacial layers.....	6
Figure 4. Contour plot of <i>in situ</i> X-ray diffraction (XRD) pattern during synthesis of $\text{Li}_{5.5}\text{PS}_{4.5}\text{Br}_{1.5}$ from 25°C to 600°C. The heating rate is 5°C/min, and the time interval between two successive XRD patterns is 30 seconds. The colors represent intensity, with blue and red representing low and high, respectively. ....	9
Figure 5. Contour plot of <i>in situ</i> X-ray diffraction (XRD) pattern during synthesis of $\text{Li}_{5.5}\text{PS}_{4.4}\text{O}_{0.1}\text{Br}_{1.5}$ from 25°C to 600°C. The heating rate is 5°C/min, and the time interval between two successive XRD patterns is 30 seconds. The colors represent intensity, with blue and red representing low and high, respectively. ....	10
Figure 6. Comparison on the lattice parameter and percentage of site disorder of $\text{Li}_6\text{PS}_5\text{Br}$ , $\text{Li}_6\text{PS}_{4.8}\text{O}_{0.2}\text{Br}$ , $\text{Li}_{5.5}\text{PS}_{4.5}\text{Br}_{1.5}$ , and $\text{Li}_{5.5}\text{PS}_{4.4}\text{O}_{0.1}\text{Br}_{1.5}$ .....	10
Figure 7. Effect of holding time on the crystal structures of final products during rapid cooling: (a) 0.5 hours, and (b) 12 hours. ....	11
Figure 8. (a) Nyquist plots of Li- $\text{Li}_{10}\text{B}_{10}\text{S}_{20}$ -Li cells after rest from 1-15 days. (b) Ionic conductivity extrapolated from the Nyquist plots of the Li- $\text{Li}_{10}\text{B}_{10}\text{S}_{20}$ -Li cells.....	13
Figure 9. (a-c) X-ray photoelectron spectroscopy (XPS) of $\text{Li}_{10}\text{B}_{10}\text{S}_{20}$ powder: (a) lithium 1s, (b) boron 1s, and (c) sulfur 2p. (d-f) XPS of $\text{Li}_{10}\text{B}_{10}\text{S}_{20}$ powder after reaction with lithium metal: (d) lithium 1s, (e) boron 1s, and (f) sulfur 2p.....	14
Figure 10. Electrochemical performance of solid-state batteries containing NMC-811 composite cathodes and $\text{Li}_x\text{In}$ anodes. (a-b) Schematics of the cell designs. Voltage profiles for cells containing (c) single-layer $\text{Li}_6\text{PS}_5\text{Cl}$ and (d) bilayer $\text{Li}_6\text{PS}_5\text{Cl}/\text{Li}_3\text{InCl}_6$ separators. (e) Discharge capacity over 40 cycles. Cells were cycled by polarizing the cathode between 2.6 V – 4.3 V versus $\text{Li}/\text{Li}^+$ at a constant current of $\pm 66 \mu\text{A}/\text{cm}^2$ (cycle 1) and $\pm 127 \mu\text{A}/\text{cm}^2$ (cycles 2-40). Due to the use of $\text{Li}_x\text{In}$ anodes, potentials were referenced against $\text{Li}/\text{Li}^+$ by adding 0.622 V to the measured cell potential. ....	16
Figure 11. Nyquist plots of (a) $\text{Li}/\text{Li}_7\text{P}_2\text{S}_8\text{Br}/\text{Li}$ , (b) $\text{Li}/\text{Li}_7\text{P}_2\text{S}_8\text{Br}_{0.5}\text{I}_{0.5}/\text{Li}$ , and (c) $\text{Li}/\text{Li}_7\text{P}_2\text{S}_8\text{I}/\text{Li}$ cells with equivalent circuit fitting at 20°C. (d) Evolution of areal interfacial resistance of each cell with time at 20°C.....	19

Figure 12. (a-c) Long-term cycling of a Li/Li <sub>7</sub> P <sub>2</sub> S <sub>8</sub> Br <sub>0.5</sub> I <sub>0.5</sub> /Li cell at (a) 0.5 mA/cm <sup>2</sup> with a charge/discharge capacity of 0.25 mAh cm <sup>-2</sup> at 20°C, (b) 1 mA/cm <sup>2</sup> with a charge/discharge capacity of 0.5 mA cm <sup>-2</sup> at 60°C, and (c) 2 mA/cm <sup>2</sup> with a charge/discharge capacity of 1 mAh cm <sup>-2</sup> at 100°C. ....	19
Figure 13. Compositional analysis of bulk and drawn thin film ISU-6 via X-ray photoelectron spectroscopy (XPS) and nuclear magnetic resonance (NMR). NMR values were determined through fitting of the NMR spectra and charge compensation. XPS values were determined through survey scans after argon etching. Error bars for XPS are the standard deviation of two depth scans, while they are 10% of the value for the NMR. ....	22
Figure 14. Image of 60-μm thin film in a micrometer. ....	23
Figure 15. Galvanostatic cycling of a Li   ISU-6   composite cathode film full cell at C/50. ....	23
Figure 16. Pre- and post-mortem Raman spectroscopy of cycled cell components, the (a) ISU-6 glassy solid electrolyte and (b) composite cathode film. ....	24
Figure 17. The sulfide solid-state electrolyte materials enabling a flexible platform that incorporates a variety of anode and cathode materials for a high-energy and low-cost all-solid-state-battery cell. ....	27
Figure 18. Cycle life of an NMC/Li-metal solid-state pouch cell with the multifunctional solid-state electrolyte at 45°C. ....	28
Figure 19. Cycling performance of the all-solid-state Li-S batteries using the new sulfur cathode developed this quarter. The cell was tested at 0.1 C with high sulfur loading content under room temperature. Discharge capacities are based on the weight of sulfur in the cathodes. ....	30
Figure 20. Cycling performance of the all-solid-state Li-S batteries using the as-synthesized alloy anodes. The cells were tested at 0.1 C under 60°C, and the specific capacity is based on the weight of sulfur ....	31
Figure 21. (a) Picture of the retrofitted glovebox. The glovebox is equipped with a custom system to maintain a dry-room environment within a predetermined moisture setpoint range. (b) Schematic of the glovebox moisture control system. It consists of a moisture probe, a microcontroller, a solid-state relay, and a cartridge-based desiccant system. ....	33
Figure 22. (a) Micro – computed tomography (CT) image of a cold-pressed separator after a critical current density (CCD) experiment. Red arrows point to Li-metal deposit. (b) Micro-CT image of a hot-pressed separator after a CCD experiment. A red arrow points to a lithium deposit that has expanded an incipient micro-crack. For both images, the vertical direction corresponds to the thru plane, transverse direction of the separator. Large speckles in both images are attributed to the Kevlar® reinforcing fibers.....	33
Figure 23. (a) 70Li <sub>2</sub> S·(30-x)P <sub>2</sub> S <sub>5</sub> ·xA solid-state electrolyte (SSE) solids mass loss after soaking in a variety of liquid electrolyte (LE) formulations. All SSEs soaked in Li(G3)TFSI solvate ionic liquid are stable. (b) UV-Vis molecular absorption spectroscopy results for 70Li <sub>2</sub> S·(30-x)P <sub>2</sub> S <sub>5</sub> ·xA SSE samples soaked in Li(G3)TFSI solvate ionic LE and (c) Li(G3) <sub>4</sub> TFSI LE. ....	34

Figure 24. (b-c) Backscattered scanning electron microscopy cross-sections of composite cathodes coated on pre-sintered LLZTO pellets and co-sintered at 900°C for 2 hours in argon; (a) optical image before sintering. (d) Optical images of the back side of the LLZTO pellets after co-sintering at different temperatures and in different environments (air versus argon). Electrochemical measurements using lithium as the anode: (e) electrochemical impedance spectroscopy comparison before cycling. (f) Voltage profiles for the 1 <sup>st</sup> charge/discharge cycle at C/20. ....	37
Figure 25. Representative voltage versus capacity profiles for cathode materials sintered at 750°C and 900°C for 2 hours in argon before electrode preparation. Half cells were cycled at C/10 charge/discharge using liquid electrolyte (1.2 M LiPF <sub>6</sub> in 3:7 wt% EC/EMC) and lithium as the anode. (a) Comparison of LCO cells. (b) Comparison of NMC-622 cells. ....	38
Figure 26. 75 wt% LCO / 25 wt% LLZTO pellets laser co-sintered at 26 W for 90 seconds using a laser diode array. (a) Standard and backscattered scanning electron microscopy images of cross-sections after co-sintering. (b) X-ray diffraction (XRD) comparison of laser and furnace co-sintered samples. ....	39
Figure 27. Cycling at 108 $\mu\text{A}/\text{cm}^2$ at room temperature with carbon paper. A Li-LLZO-DOL/DME/S hybrid battery can be discharged to 1,300 mAh/g and be cycled with minimal capacity loss. ....	41
Figure 28. Nyquist plots and distribution of relaxation times analysis of electrochemical impedance spectroscopy of (a) Li <sub>2</sub> ZrO <sub>3</sub> -NMC-622, (b) LiAlO <sub>2</sub> -NMC-622, and (c) Li <sub>2</sub> SiO <sub>3</sub> -NMC-622 co-sintered in a 1:1 wt ratio with Li <sub>6.75</sub> La <sub>3</sub> Zr <sub>1.75</sub> Ta <sub>0.25</sub> O <sub>12</sub> onto LLZTO trilayers at 1000°C in O <sub>2</sub> . ....	44
Figure 29. Nyquist plots (inset) and distribution of relaxation times analysis of the electrochemical impedance spectroscopy of (a) LiAlO <sub>2</sub> -NMC-622, and (b) Li <sub>2</sub> SiO <sub>3</sub> -NMC-622 co-sintered in 1:1 wt ratio with Li <sub>6.75</sub> La <sub>3</sub> Zr <sub>1.75</sub> Ta <sub>0.25</sub> O <sub>12</sub> (LLZTO) onto LLZTO trilayers at 1000°C in O <sub>2</sub> . ....	45
Figure 30. Rietveld refinement results of X-ray diffraction of (a) LiAlO <sub>2</sub> -NMC-622, and (b) Li <sub>2</sub> SiO <sub>3</sub> -NMC-622 co-sintered in a 1:1 wt ratio with Li <sub>6.75</sub> La <sub>3</sub> Zr <sub>1.75</sub> Ta <sub>0.25</sub> O <sub>12</sub> (LLZTO) onto LLZTO trilayers at 900°C in argon. ....	45
Figure 31. Scanning electron microscopy images of cold-pressed electrolyte pellets from (a) Li <sub>2</sub> HOCl and (b) Li <sub>2</sub> HO <sub>10.75</sub> Br <sub>0.25</sub> , showing the presence of big voids, which can significantly reduce the nominal Li-ion conductivity of the electrolyte pellets. ....	48
Figure 32. Measured Li-ion conductivity of hot-pressed anti-perovskite electrolyte pellets. The pellets were prepared at 200°C and 1000 MPa to reduce their porosity. ....	49
Figure 33. Differential scanning calorimetry of Li <sub>2</sub> HOC <sub>10.75</sub> Br <sub>0.25</sub> showing the extra phase transformation before the melting of the electrolyte (at ~ 250°C). ....	49
Figure 34. Initial voltage profile of all-solid-state cell using LiNi <sub>0.6</sub> MN <sub>0.2</sub> Co <sub>0.2</sub> O <sub>2</sub> (NMC-622) as the cathode, and Li <sub>2</sub> HOC <sub>10.75</sub> Br <sub>0.25</sub> as both the electrolyte and the catholyte. ....	49
Figure 35. Optical micrographs of Dreamweaver Gold porous membranes before and after Li <sub>3</sub> InCl <sub>3</sub> infiltration from ethanol solution precursor. ....	52
Figure 36. <i>In situ</i> neutron diffraction of Li <sub>3</sub> InCl <sub>6</sub> being synthesized from ethanol solution. ....	53

Figure 37. Scanning electron micrograph cross-sections of a Li-In alloy/LiNi <sub>0.85</sub> Mn <sub>0.1</sub> Co <sub>0.05</sub> O <sub>2</sub> full cell that uses ethanol-derived Li <sub>3</sub> InCl <sub>6</sub> as the bulk solid electrolyte and the electrolyte within the cathode. After 50 cycles, the team observes extensive delamination in both the cathode-Li <sub>3</sub> InCl <sub>6</sub> composite and the bulk Li <sub>3</sub> InCl <sub>6</sub> itself. ....	53
Figure 38. (a) The voltage profiles of $\mu$ -Li <sub>x</sub> Si   SSE   LTO cell (top) along with correlated evolution of stress (middle) and stress change (bottom). (b) Schematic of pressure-monitoring cell. (c) Corresponding dQ/dV curves. (d) Voltage and stress change plotted as a function of the molar amount of lithium extracted from or inserted into the $\mu$ -Li <sub>x</sub> Si phase. Prolonged cycling of (e) the $\mu$ -Li <sub>x</sub> Si   SSE   $\mu$ -Li <sub>x</sub> Si symmetric cell and (g) the Li-In   SSE   Li-In symmetric cell at 25°C. ....	56
Figure 39. (left) All-solid-state pouch cell (full cell, 2 × 3 inch), and (right) cell under test in a pressure fixture. ....	56
Figure 40. Concentration cell open-circuit potential ( <i>U</i> ) as a function of natural log molality (ln[ <i>m</i> ]) at 90°C. The fit is shown in dashed line. Three data points at each salt concentration represent reproducibility of the data.....	59
Figure 41. Linear sweep voltammetry (3-6 V versus Li <sup>+</sup> /Li) of PPM and PEO electrolytes at 90°C. The scanning rate is 1 mV/s. ....	60
Figure 42. Chronopotentiometry curve of a sodium/polymer/sodium symmetric cell with a PPM/NaTFSI electrolyte at <i>r</i> = 0.06, under a current density of 0.125 mA/cm <sup>2</sup> at 80°C. The inset is the normalized Nyquist plot before and after polarization.....	60
Figure 43. Cycling of SP <sup>2</sup> -coated lithium anode in Li   NMC cells: (a) rate capabilities, (b) cycle life and capacity, and (c) Coulombic efficiency of each cycle. (d) Comparison of cycle life (80% capacity retention) plotted against excess lithium amount of the SP <sup>2</sup> coating with other coatings / electrolyte strategies. The x axis locations of 4, 5, 7, 11, and 12 are 10 mAh cm <sup>-2</sup> ; they are adjusted slightly to dodge. ....	62
Figure 44. Temperature dependence of the cation (Pyr <sub>14</sub> <sup>+</sup> ) and anion (TFSI <sup>-</sup> ) diffusion coefficients in the cycled/charged molecular ionic composite (MIC) films. The solid data points represent the cation diffusion coefficients and the open data points represent the anion diffusion coefficients. The red triangles are the diffusion coefficients of the uncycled MIC film before assembly into a battery, and the diffusion coefficients agree with the uncycled MIC film reported in the <i>Advanced Energy Materials</i> paper (black squares). The blue circular data points are of the MIC film charged to 4.4 V in a Li/MIC/NMC-811 cell, and the green diamonds are of the MIC film after 20 cycles in a Li/MIC/LFP cell. Both MIC membranes collected after cell assembly, and then charging, and/or cycling have similar diffusion coefficients, which are half as high as the uncycled MIC material, possibly due to some mobile ions pushed into the porous cathode during cell assembly. These data provide critical information for further optimizing MIC composition, casting process, and cell assembly. ....	66
Figure 45. Constant current charging step of Li / molecular ionic composite / NMC-811 cell, run at 60°C with a 0.1C charging rate and an upper cut off voltage of 4.4 V.....	67
Figure 46. Charge/discharge profile of Li / molecular ionic composite / LiFePO <sub>4</sub> cell at room temperature. The cell was run at each constant current density for 5 cycles before increasing current density, for a total of 20 cycles. ....	67

Figure 47. Specific capacity of Li / molecular ionic composite (MIC) / NMC-811 cells with (a) previous MIC composition and (b) modified MIC with mixed ion composition measured at 60°C when cycled between 2.5 V and 4.4 V. ....	68
Figure 48. Demonstration of computationally predicted percolation thresholds experienced by polymer/ceramic composites. (a) Geometrical approximation of an elongated fiber as an ellipsoid. Aspect ratio of the fiber is defined as the ratio between the length over the diameter of the fibrous inclusions. (b) Percolation threshold experienced by the fiber reinforced composites as a function of the aspect ratio of the fibers. Fiber content within the matrix is demonstrated as volume percentage. (c) Conversion of the percolation threshold from volume percentage to weight percentage. Given that the density of LLZO fibers is larger than that of the PEO matrix, the weight percentage of fibers needed for percolation is much larger than the volume percentage. ....	70
Figure 49. (a) Ionic conductivity of composite polymer electrolytes with 0, 2, 5, 10, and 50 wt% LLZO nanofibers. 50 wt% corresponds to 20 vol% of the LLZO filler in the polymer matrix. (b) Scanning electron micrograph of the as-prepared composite electrolyte, showing that nanofibers are coated with thin layers of polymer and are likely not in direct contact with each other. ....	71
Figure 50. Morphology of dry xPEO/PFPE electrolytes. (a) Scanning electron microscopy image showing the surface morphology of 60PFPE electrolyte membranes at the micrometer scale. Inset: photo of the membrane. (b) Scanning probe microscopy phase image showing the surface morphology of 60PFPE electrolyte membranes at the nanometer scale. (c) Small-angle X-ray scattering (SAXS) profiles of PFPE, xPEO, 40PFPE, and 60PFPE in the pristine form and with LiTFSI salt. (d) Wide-angle X-ray scattering (WAXS) profiles of PFPE, xPEO, 40PFPE, and 60PFPE in the pristine form and with LiTFSI salt. SAXS and WAXS measurements were taken at room temperature. ....	74
Figure 51. Differential scanning calorimetry (DSC) of dry xPEO/PFPE electrolytes. (a) DSC thermogram (2 <sup>nd</sup> heating) of pristine xPEO, PFPE, 60PFPE and 40PFPE. (b) DSC thermogram (2 <sup>nd</sup> heating) of xPEO, PFPE, 60PFPE, and 40PFPE infused with LiTFSI salt. (c) Glass transition temperature ( $T_g$ ) of the hydrocarbon and fluorocarbon phases of the membranes as a function of PFPE wt%. The values used in this plot are from samples without LiTFSI salt. ....	76
Figure 52. (a) Chronoamperometry measurement of xPEO-LiTFSI and 60PFPE-LiTFSI electrolytes at 70°C. (b) Interfacial impedance between lithium and xPEO-LiTFSI at 70°C. (c) Interfacial impedance between lithium and 60PFPE-LiTFSI at 70°C. ....	76
Figure 53. Nuclear magnetic resonance data for GCMA polymerization with AIBN in DMSO (top) and ACPA in acetonitrile (bottom). The peaks at 5.7 and 6.0 correspond to the monomer, while the double-humped peak from 0.6-1.0 represents the polymer. ....	79
Figure 54. Soft X-ray absorption spectroscopy (sXAS) and pair distribution function (PDF) characterization of the polymer electrolytes (PEs). (a) Carbon, (b) oxygen, (c) fluorine K-edge sXAS of PVDF mixed with NMP and vacuum dried. (d) PDF results of polymer, salts, and PEs. ....	82

Figure 55. (a) Computed density functional theory formation energy for ground-state structures predicted by cluster expansion in BCC (red triangle), FCC (green dot), and $\gamma$ -brass (magenta cross) lattice types. The convex hull of formation energy is marked with dashed line, under which single-phase regions are shaded with light red (BCC), light green (FCC), and light magenta ( $\gamma$ ). The composition range $0.4 < xLi < 0.6$ is enlarged in the middle. Phonon energy and entropy contributions are not included. (b) Predicted ground-state structures as marked with arrows in (a).....	85
Figure 56. Charge-discharge voltage profiles of Li/Li <sub>6</sub> PS <sub>5</sub> Cl/ABL cells. Active buffer layers are Ag-C, Sn-C, and Mg-C composites at 0.17 mA cm <sup>-2</sup> . All the tests were conducted at 25°C.....	86
Figure 57. (a-c) X-ray diffraction patterns and (c-e) Nyquist plots of Li <sub>3-x</sub> Y <sub>1+x</sub> Cl <sub>6</sub> ( $0 \leq x \leq 0.13$ ) samples prepared from solid state (a/d), co-melting (b/e), and mechanochemical synthesis (c/f).....	87
Figure 58. Comparison of normalized unit cell volumes (a) and room-temperature ionic conductivities (b) of Li <sub>3-x</sub> Y <sub>1+x</sub> Cl <sub>6</sub> ( $0 \leq x \leq 0.13$ ) samples prepared by different synthesis methods. ▲ indicates trigonal phase and □ indicates orthorhombic phase.....	87
Figure 59. Schematic view of sintering condition (top) and effect of dead weight on the flatness of the sintered thin LLZO film (bottom).....	88
Figure 60. Picture of LLZO films after sintering at different temperatures. ....	88
Figure 61. Property testing of different mol% of LiTFSI in succinonitrile. (a) Nyquist plot. (b) Direct current polarization. (c) Linear sweep voltammetry. ....	89
Figure 62. Scanning electron microscopy images of LPSCI-PEO composites with the polymer content of 2 wt%, 8 wt%, and 12 wt% (from left to right).....	90
Figure 63. Chemical and mechanical evaluations of LPSCI-PEO composite. (a-b) Elemental mappings of oxygen, phosphorus, sulfur, and chlorine in LPSCI-PEO composites with 2 wt% polymer content. Note that the composites are prepared by two methods: (a) dispersion mix and (b) solution-precipitation methods.....	91
Figure 64. Powder X-ray diffraction patterns of borohydride-substituted argyrodites. ....	93
Figure 65. Nyquist plot of phase pure substituted argyrodite, ionic conductivity = $8 \times 10^{-3}$ S/cm.....	93
Figure 66. Powder X-ray diffraction of Li <sub>6.5</sub> Sb <sub>0.5</sub> Ge <sub>0.5</sub> S <sub>5</sub> I synthesized with a salt flux method. Peaks with (*) come from the salt flux while (#) is an unidentified phase.....	94
Figure 67. Powder X-ray diffraction of different synthetic preparations of Li <sub>4</sub> SiS <sub>4</sub> (blue, red) compared with the calculated pattern (black).....	94
Figure 68. Subset of curve-fitted spectra acquired during virtual-electrode X-ray photoelectron spectroscopy (VE-XPS) experiment on baseline argyrodite LPSCI+S-based polymer composite / lithium foil sample. These XPS core-level spectra reveal formation and passivation of the SEI (primarily comprised of Li <sub>2</sub> S, Li <sub>3</sub> P, Li <sub>3</sub> PO <sub>4</sub> , and Li <sub>2</sub> O) followed by plating of metallic lithium on the free surface that occurs beginning at approximately cycle 46. ....	95

Figure 69. (a) Plot of peak areas and (b) binding energy shifts for the LPSCI and Li <sub>2</sub> S during the virtual-electrode X-ray photoelectron spectroscopy experiment on an LPSCI/S-polymer composite. In these experiments, binding energy shifts can be interpreted in terms of changes in doping levels in materials, as well as changes to interface defect populations that affect the interfacial dipole, and thus reveal changes in interfacial energy band alignments.....	96
Figure 70. (a) Potential map on the interface of the solid-state electrolyte and lithium metal. (b) Potential profile averaged along the vertical in (a); (b) inside, showing two electrical double layers that raise the two sides of the potential peak.....	97
Figure 71. Illustration showing electrode and electrolyte stack. ....	98
Figure 72. Cycling data for the NMA versus silicon cell cycled at room temperature and C/20. Erratic voltage profiles for the 1 <sup>st</sup> charge/discharge can be caused by a loss of physical contact between active particles and the electrolyte.....	98
Figure 73. Li/PEO-LiTFSI/Li symmetric cycling. All cells were cycled under the same conditions at 0.1 mA/cm <sup>2</sup> for 10 hours at 70°C. (a) Commercial Supplier #1. (b) Commercial Supplier #2. (c) Commercial Supplier #3. (d) Commercial Supplier #4. (e) Evaporated lithium. (f) Plot of the thickness of the estimated interface including the surface layer and distinct Li <sub>2</sub> O layers (excluding the mixed Li <sub>2</sub> O / lithium metal layer) versus the resistance determined from the plating overpotential.....	101
Figure 74. Li/LiPSCI argyrodite (NEI) / lithium test under 5 MPa of pressure at room temperature at a current density of 0.1 mA/cm <sup>2</sup> for 10 hours. Blue: Commercial Supplier #2. Purple: Evaporated lithium. ....	102
Figure 75. Electrochemical performance (a-b) and Nyquist plots (c-d) collected at 3.67 V during the 4 <sup>th</sup> discharge of the all-solid-state batteries with polycrystalline – NMC-811 (a/c) and single crystalline – NMC-811 (b/d) cathode active material. (e) Equivalent circuit model for fitting the electrochemical impedance spectroscopy data. The colored lines in (c) and (d) are shown to guide the placement of the various semi-circle components on the Nyquist plots. ....	107
Figure 76. Nyquist plots obtained at 3.67 V during the discharge of polycrystalline – NMC-811 (a) and single crystalline – NMC-811 (b) all-solid-state battery cells at the indicated cycle numbers. (c-e) Resistance values obtained from fitting the corresponding Nyquist plots in (a) and (b).....	108
Figure 77. Nanoscale “white light” imaging of SEI layer on Li-metal surface under various electrochemical conditions: (top left) Li-metal electrode after oxidation under galvanostatic conditions. (top right) Nickel electrode after plating lithium under galvanostatic conditions. (bottom left) Li-metal electrode after an oxidation-reduction cycle under galvanostatic conditions. (bottom right) Nickel electrode after a cycle of plating and stripping of lithium. ....	111
Figure 78. Nano – Fourier transform infrared (FTIR) spectroscopy of SEI layer under various electrochemical conditions. Plated lithium on nickel (red trace), oxidized lithium surface (blue trace), plated and stripped lithium “dead lithium” (orange trace), and reduced lithium surface after oxidation cycle (green trace). Attenuated total reflectance FTIR spectrum of dried GEN 2 electrolyte (gray trace).....	111

- Figure 79. (a) Schematic of conceptualized *in situ* solid-state electrochemical cell to be prepared. (b) Atomic force microscopy topography data of a pristine LAGP surface. Colored diamonds indicate locations where nano – Fourier transform infrared (nano-FTIR) data were collected. (c) Spatially dependent nano-FTIR absorption data that show sub-diffraction-limit chemical heterogeneity across the LAGP surface; traces are color matched to the corresponding spatial locations shown in (b). ..... 112
- Figure 80. Carbon K-edge X-ray absorption spectroscopy both in total electron yield (TEY, left panel) and partial fluorescence yield (PFY, right panel) of *ex situ* SPAN electrodes cycled in various electrolytes. .... 115
- Figure 81. Transmission electron microscopy and scanning transmission electron microscopy images of deposited lithium from Li||Cu and Cu||NMC coin cells in the localized high-concentration electrolyte (LHCE) without and with nickel impurities. (a-d) Morphology and microstructure of deposited lithium and SEI from Li||Cu in the LHCE without nickel. (e-h) Morphology and microstructure of deposited lithium and SEI from Li||Cu in the LHCE with nickel. (i-l) Morphology and microstructure of deposited lithium and SEI from Cu||NMC in the LHCE without nickel. (m-p) Morphology and microstructure of deposited lithium and SEI from Cu||NMC in the LHCE with nickel. .... 118
- Figure 82. Elemental composition of lithium deposits and their SEIs formed in different electrolyte in a coin cell. (a) Cryogenic scanning transmission electron microscopy – high-angle annular dark-field-(cryo-STEM-HAADF) image reveals the SEI layer on the lithium particle formed in Li||Cu coin cell using localized high-concentration electrolyte (LHCE) without nickel. (b) Corresponding electron energy loss spectroscopy (EELS) elemental maps show the elemental distribution of SEI. (c) Cryo-STEM-HAADF image reveals the SEI layer on the lithium particle formed in Li||Cu coin cell using LHCE with nickel. (d) Corresponding EELS elemental maps show the elemental distribution of SEI. (e) Cryo-STEM-HAADF image reveals the SEI layer on the lithium particle formed in Cu||NMC coin cell using LHCE without nickel. (f) Corresponding EELS elemental maps show the elemental distribution of SEI. (g) Cryo-STEM-HAADF image reveals the SEI layer on the lithium particle formed in Cu||NMC coin cell using LHCE with nickel. (h) Corresponding EELS elemental maps show the elemental distribution of SEI. .... 119
- Figure 83. *Operando* microprobe scanning electron microscopy (SEM) setup on LLZO cantilever. .... 122
- Figure 84. *Operando* LLZO cantilever bending experiments revealing a strong mechanical strain effect on regulating the intrusion propagation behavior. Colorized scanning electron microscopy images showing intrusions at (a) 0% strain (free end of the cantilever), (b) 0.033% strain (center of the cantilever), and (c-e) 0.070% strain (base of the cantilever). The intrusion propagates in random directions at 0% strain and becomes gradually more aligned along the longitudinal direction of the cantilever with increasing compressive strain. (d-e) Intrusion propagation at 0.070% with the cantilever rotated by 20° and 45° relative to the microprobe. The intrusion propagation direction remains along the cantilever. (f) Schematic showing the crack closure effect of external compressive strain to the pre-existing cracks normal to the strain direction. .... 123

Figure 85. (a) Photos of lithium foil as it is cleaned and polished. (b) X-ray photoelectron spectroscopy at the K-edge of lithium, oxygen, and carbon, respectively, as its surface layer is slowly removed by the Ar-ion milling process. ....	125
Figure 86. (a) Electrochemical impedance spectroscopy (EIS) spectra taken on DTL-coated lithium symmetric pouch cell. (b) Bare lithium symmetric pouch cell EIS data. ....	125
Figure 87. <i>Operando</i> time-of-flight secondary ion mass spectrometry mapping of $\text{Li}^+$ and $\text{Ag}^+$ at the electrolyte – silver-carbon interface. The x-axis and y-axis represent the spatial coordinates in $\mu\text{m}$ . The brightness in color represents the ion count. (Left column) Structure of the solid-state Li-metal cell used in the observation; the observation area is marked with a black square. (Top row) Mapping of $\text{Li}^+$ ; the strong $\text{Li}^+$ signal in the top region ( $40 < y < 75$ ) originates from the solid electrolyte. (Bottom row) Mapping of $\text{Ag}^+$ ; $\text{Ag}^+$ signal is only present within the silver-carbon layer ( $y < 40$ ). ....	128
Figure 88. Evolution of spatial distribution of $\text{Ag}^+$ and $\text{Li}^+$ during charging. Curves processed from time-of-flight secondary ion mass spectrometry spectra such as those displayed in Figure 87. ....	128
Figure 89. (a) Distribution of the reduction and oxidation limits for each category that passes thermodynamic stability descriptor. (b) Distribution of the reaction energy with $\text{LiNiO}_2$ , $\text{LiCoO}_2$ , $\text{LiMn}_2\text{O}_4$ , and $\text{LiFePO}_4$ cathodes for each category that passes electrochemical stability descriptor. The horizontal dash lines represent the limits of the descriptors. The histograms in (a) and (b) illustrate the numbers of compounds for each category that passes the descriptors. ....	132
Figure 90. Distribution of the reaction energy $\Delta E_{\text{rxt}}$ with $\text{Li}_3\text{PS}_4$ (a) and HF (b) for each category that passes chemical stability with the cathodes descriptor. The horizontal dash lines represent the limits of the descriptors. The histograms in (a) and (b) illustrate the numbers of compounds for each category that passes the descriptors. ....	133
Figure 91. (a) Lithium/solid-electrolyte mesh used in the present analysis. The grain interior and grain boundaries (GBs) are denoted by the blue and black regions, respectively. Butler-Volmer reaction current is implemented at the lithium/solid-electrolyte interface. (b) Distribution of reaction current at the electrode/electrolyte interface (black line) after 1 second for GB conductivity and shear modulus being 50% and 10% of the grain interior, respectively. (c) Increase in reaction current density at the GB region with time, which demonstrates an increasing trend. In (b) and (c), the blue dashed line indicates the applied current density. ....	136
Figure 92. (a) Current focusing at the grain boundary (GB) region after 1 second as a function of the shear modulus of the GBs. Decreasing the GB modulus enhances the current focusing. (b) Phase map between conductivity and shear modulus of the GBs indicating regions where current focusing should occur at the GBs (yellow domain). Homogeneous distribution of reaction current can be achieved by adopting stiff GBs. ....	137

- Figure 93. (a) The structure schematic of the assembled lithium aluminum germanium phosphate (LAGP) symmetric cell and insulation setup. (b) The temperature rises in 2 minutes under different frequency  $\pm 2V$  sin wave. (c) The example of fitting result between COMSOL simulation and experiments..... 142
- Figure 94. Exchange current density (black squares along left axis) and jumping frequencies (red circles along right axis) for different energy barriers, which is demonstrated along the x-axis. *Ab initio* molecular dynamics calculations reveal smaller energy barriers ( $\sim 0.48$  eV), which lead to larger exchange current densities ( $\sim 10^3$  mA/cm<sup>2</sup>). Climbing image nudged elastic band (cNEB) calculations provide relatively higher energy barrier,  $\sim 0.58$  eV for CNT+S cathode and 0.905 eV for graphene+S cathodes. The exchange current densities follow a similar trend with higher energy barrier providing a smaller magnitude of the exchange current density. The experimentally observed exchange current density between Li<sub>7</sub>P<sub>3</sub>S<sub>11</sub> and C-S cathode is  $\sim 3.8$  mA/cm<sup>2</sup>, which is shown by the black dashed line. The average energy barrier ( $\sim 0.655$  eV) leads to the best correlation with experimental results. Jumping frequencies increase with increasing energy barrier, but their magnitude is similar..... 144
- Figure 95. (a) Model structure of the Li<sub>6</sub>PS<sub>5</sub>(SCN)-Li interface from the simulation at 300 K. (b) Bond completeness for the clusters against the simulation time..... 147
- Figure 96. (a) Li-uptake plot of Li<sub>2</sub>S against the voltage. (b) Modeled structures at the Li<sub>6</sub>PS<sub>5</sub>(SCN)-Li<sub>2</sub>S interface before and after the simulation run. (c) Analysis on cluster completeness of the interfacial models with different terminal groups..... 148
- Figure 97. Solvent-based synthesis of I- and F- doped argyrodite electrolytes. (a) X-ray diffraction patterns for as-synthesized Li<sub>6</sub>PS<sub>5</sub>I, Li<sub>6</sub>PS<sub>5</sub>F<sub>0.25</sub>I<sub>0.75</sub>, Li<sub>6</sub>PS<sub>5</sub>F<sub>0.5</sub>I<sub>0.5</sub>, and Li<sub>6</sub>PS<sub>5</sub>F<sub>0.75</sub>I<sub>0.25</sub> indicating high phase purity of the argyrodites. (b) Arrhenius plots of solvent synthesized Li<sub>6</sub>PS<sub>5</sub>I after two different heating treatment temperatures (200°C and 290°C). Transmission electron microscopy elemental mapping of synthesized Li<sub>6</sub>PS<sub>5</sub>I argyrodite after heating treatment at (c) 200°C and (d) 290°C. Note: sulfur in yellow; iodine in red; and oxygen in pink. .... 150
- Figure 98. Anion-disorder in dual-doped argyrodite solid electrolytes and the impact on Li-ion conduction. Atomic-scale structures of (a) Li<sub>6</sub>PS<sub>5</sub>I and (b) Li<sub>6</sub>PS<sub>5</sub>F<sub>0.25</sub>I<sub>0.75</sub> optimized by density functional theory. In each panel, the energy change associated with swapping a sulfur atom at 4*d* site (cage-center) with a halogen [iodine in panel (a), and fluorine in panel b)] are indicated. The lithium, phosphorus, sulfur, fluorine, and iodine atoms are depicted as blue, purple, yellow, red, and green spheres, respectively. (c) Arrhenius plots (30-90°C) of Li<sub>6</sub>PS<sub>5</sub>I and hybrid-doped argyrodites obtained from electrochemical impedance spectroscopy measurements..... 151
- Figure 99. Electrochemical stability of Li<sub>6</sub>PS<sub>5</sub>F<sub>0.75</sub>I<sub>0.25</sub> sulfide electrolyte against Li-metal obtained from cycling performance of Li-symmetric cell. (a) Voltage profiles of Li<sub>6</sub>PS<sub>5</sub>F<sub>0.25</sub>I<sub>0.25</sub>·0.5 LiF-based symmetric cell cycling up to 1100 hours (0.05 mA cm<sup>-2</sup>). X-ray photoelectron spectra of cycled symmetric cell with Li<sub>6</sub>PS<sub>5</sub>F<sub>0.25</sub>I<sub>0.25</sub>·0.5 LiF sulfide electrolyte: (b) iodine 3d, (c) sulfur 2p, and (d) lithium 1s. .... 152

Figure 100. Effect of amount of functionalizing ionic liquid (IL) on the discharge profiles for batteries consisting of lithium anode, SP-S cathode with 4.0 mg/cm <sup>2</sup> loading and 30% sulfide electrolyte, and Li <sub>6</sub> PS <sub>5</sub> F <sub>0.5</sub> Cl <sub>2</sub> electrolyte. Discharge profiles at selected cycles are shown for different amounts of functionalizing IL (LiTFSI in Pyr:DOL(1:3) at 3M) at the cathode-SSE interface at 30°C, namely, (a) 40 μL, (b) 10 μL, and (c) 5 μL. As the amount of IL decreases, the discharge profile changes from a two-plateau (at 40 μL) indicative of a quasi-solid-state behavior, to a single slope (at 5 μL) akin to an all-solid-state Li-S battery.....	153
Figure 101. Electrochemical cycling performance of batteries consisting of lithium anode, SP-S cathode with 4.0 mg/cm <sup>2</sup> loading pressed with 25% sulfide electrolyte, Li <sub>6</sub> PS <sub>5</sub> F <sub>0.5</sub> Cl <sub>2</sub> sulfide electrolyte with 5 μL of ionic liquid [LiTFSI in Pyr:DOL(1:3) at 3M] at the cathode – solid-state-electrolyte interface. (a) Capacity variation, and Coulombic efficiency as a function of cycles at 60°C at C/20. (b) Discharge profiles at selected cycles. ....	153
Figure 102. Electrochemical cycling performance of batteries consisting of lithium anode, SP-S cathode with 4.0 mg/cm <sup>2</sup> loading pressed with 25% sulfide electrolyte, Li <sub>6</sub> PS <sub>5</sub> F <sub>0.5</sub> Cl <sub>2</sub> sulfide electrolyte with 5 μL of ionic liquid [LiTFSI in Pyr:DOL(1:3) at 3M] at the cathode – solid-state electrolyte interface under applied pressure. (left) Picture of the specialized cell being tested inside the glovebox under applied pressure. (right) Initial discharge curve at 0.05 C for batteries tested under 0, 5, 10, and 20 bar. ....	154
Figure 103. Snapshot of LLZO(001) LCO(104) interface after 10 ns of large-scale molecular dynamic simulation at 1500 K using the team’s recently developed machine-learning force field. The atomic model shows two distinct interfacial regions with different initial chemical compositions. The blue, green, magenta, red, and yellow spheres represent lithium, lanthanum, zirconium, oxygen, and cobalt atoms, respectively.....	156
Figure 104. Comparison of a proton defect in O1-NiO <sub>2</sub> (left) and O3-NiO <sub>2</sub> (right).....	161
Figure 105. A trajectory for proton motion in NiO <sub>2</sub> .....	161
Figure 106. X-ray diffraction of La-doped NMC-811 material.....	162
Figure 107. Clustering of simulated sulfur XANES spectra in the LPS dataset. The left column (a-f) plots the spectra in all six clusters, as well as experimental spectra measured on pristine LPS and LPS after the first and second delithiation. The right column (g-i) plots the extracted structure descriptors. The markers show the mean values of the descriptors within each cluster, with error bars representing the standard deviation. (j) Experimentally measured pristine and slightly delithiated LPS spectra. ....	166

Figure 108. Experimentally measured X-ray absorption near-edge spectroscopy (XANES) spectra of (a) phosphorus, (b) sulfur, and (c) chlorine K-edges on LPSCI sample cycled to different stages with cyclic voltammetry (CV). XANES data were measured in fluorescence mode at the TES beamline of NSS-II. (d) Electrochemistry profile of CV measurement, with current and voltage represented by solid and dashed lines, respectively. CV measurements were conducted at 0.1 mV/s over 0 – 5 V versus Li <sup>+</sup> /Li voltage range. The markers in (d) indicate the states in which the batteries were disassembled and the electrodes were collected for X-ray absorption measurements. ....	167
Figure 109. (a) $\Sigma 5(130)/[001]$ and (b) $\Sigma 13(230)/[001]$ symmetric tilt grain boundaries of LLZO. Lithium, lanthanum, zirconium, and oxygen atoms are shown in blue, green, magenta, and red, respectively. ....	170
Figure 110. Microstructure-aware mesoscale modeling and calculation of the mechanical properties of LLZO. (a) Calculated effective elastic properties of polycrystalline (PC) LLZO based on different models. <b>C11</b> , <b>C12</b> , <b>C44</b> : elastic stiffness tensor components, <b>K</b> : Bulk modulus, <b>A</b> : asymmetric factor. (b) Calculated von Mises stress $\sigma_{VM}$ distribution within a 3D polycrystalline microstructure of LLZO generated by phase-field grain growth simulations. The color corresponds to the value of $\sigma_{VM}$ , and a threshold of $\sigma_{VM}^{thres} = 1.0$ Gpa is applied to the half of the 3D structure to illustrate the mechanical hotspots. (c) Histograms of $\sigma_{VM}$ in the PC models with and without considering the grain boundary phase to be disordered. (d) Volume fraction of hotspots as a function of applied longitudinal strain $\epsilon_{xxapp}$ along $x$ . ....	171
Figure 111. Scanning electron microscopy images and X-ray energy dispersive spectroscopy mapping images for copper distribution on Cu@PI mat of (a) top-view and (b) cross-sectional view. ....	175
Figure 112. Scanning electron microscopy images of deposited lithium morphologies on (a/c) bare copper foil and (b/d) Cu@PI mat. ....	175
Figure 113. Room-temperature cycling performance of Li  NMC-622 coin cells using Cu@PI and bare copper current collectors. ....	176
Figure 114. Kinetics studies of the lithium diffusion in the prelithiation process. (a) The <i>in situ</i> optical cell used to visualize the lithium diffusion process within silicon electrodes; left: schematic, and right: photo of the device. (b) The optical microscopy image of the area of interest before shorting (time = 0 min) with labeled components and scales. (c) <i>In situ</i> dark-field optical microscopy image displaying the prelithiation process within electrodes, scale bar = 100 $\mu\text{m}$ . ....	178
Figure 115. (a) Average lithium Coulombic efficiency (CE) of Cu  Li cells using the standard CE protocol. (b-d) Cycling performance of Cu  NMC-811 cell cycled between 3.5 V – 4.4 V with the commercial 2032 coin-cell set. ....	181

- Figure 116. (a) Voltage profile of Li||NMC-811 baseline cell charged to 4.5 V. (b) Digital photograph of copper electrode after the first lithium deposition to 4.5 V. (c) Scanning electron microscopy images with X-ray energy dispersive spectroscopy data (insets) for the top (left) and cross-sectional (right) views of the center (upper) and edge (lower) regions of the copper electrode after the first lithium deposition to 4.5 V. (d) Digital photographs displaying the non-uniform thickness of the stainless-steel spacer with a schematic illustration of the non-uniform lithium deposition leading to a porous/brittle SEI layer by non-uniform pressure/current distribution on copper electrode. (e) Cycling performance of Cu||NMC-811 cell cycled between 3.5 V – 4.4 V with the commercial 2032 coin-cell set..... 182
- Figure 117. Structure and composition analysis of cathode material. (a) Scanning electron microscopy image of OMSH host material. (b-c) Transmission electron microscopy and corresponding X-ray energy dispersive spectroscopy chemical mapping of OMSH-Se/S (interesting elements are sulfur, zinc, selenium, and cobalt). (d-e) High-resolution X-ray photoelectron spectra of (d) sulfur 2p and (e) selenium 3d of OMSH-SeS cathode material. (f) Thermal gravimetric analysis curve of OMSH-SeS cathode material under argon atmosphere from room temperature to 450°C..... 187
- Figure 118. Electrochemical characterizations of OMSH-Se/S cathode material. (a) Cycling performance of OMSH-Se/S cathode in HFE-based electrolyte at 160 mA g<sup>-1</sup> with an areal Se/S loading of 2 mg cm<sup>-2</sup>. (b) Cycling performance of OMSH-Se/S cathode with higher areal Se/S loading conditions (3.0 mg cm<sup>-2</sup> and 5.8 mg cm<sup>-2</sup>) in HFE-based electrolyte at 200 mA g<sup>-1</sup>. (c) Voltage profiles of various cycles of OMSH-Se/S cathode under high areal Se/S loading (5.8 mg cm<sup>-2</sup>) condition in HFE-based electrolyte. (d-e) Voltage profiles of OMSH-Se/S cathode (~ 6.5 mg cm<sup>-2</sup>) that rested for one week after two initial cycles in (d) DME-based and (e) HFE-based electrolytes. (f) Cycling performance of OMSH-Se/S cathode after resting for one week in HFE-based electrolyte. Hollow and solid symbols in (a), (b), and (f) represent Coulombic efficiency and discharge capacity, respectively. .... 188
- Figure 119. X-ray nano-computed tomography images of sulfur concentration distribution in (a) NKB11, (b) NKB12, and (c) NKB15, respectively. The scale bar is 6 μm. (d) Discharge/charge curves of different NKB/S electrodes in the 1<sup>st</sup> cycle. (e) Discharge/charge curves of different NKB/S electrodes after 40 cycles. (f) Cycling performance of different NKB/S electrodes in 40 cycles at low E/S ratio..... 191
- Figure 120. (a) Discharge/charge curves of 5 mg/cm<sup>2</sup> NKB11/S electrode at different cycles. (b) Cycling performance of the 5 mg/cm<sup>2</sup> NKB11/S electrode. (c) Discharge/charge curves of NKB11/S-Polymer electrodes at different cycles. (d) Cycling performance of NKB11/S-Polymer cathodes. .... 192
- Figure 121. Electrochemical performance of Li<sub>2</sub>S cathodes with AQT redox mediator in all-solid-state Li-S batteries. (a) Voltage profile at the 2<sup>nd</sup> cycle of the Li<sub>2</sub>S@AQT cell with a high mass-loading (3.7 mg cm<sup>-2</sup>) at a current density of 0.25 mA cm<sup>-2</sup>. (b) Cycling performance of the high loading cell. (c) Specific capacity of Li<sub>2</sub>S@AQT cathodes cycled from 0.06 C to 0.48 C. All cells are operated at 60°C..... 195

Figure 122. Li-S pouch cell.....	197
Figure 123. (a) Charge and discharge curves for an S/NC800 pouch cell with E/S ratio of 10 $\mu\text{L}$ . (b) Charge and discharge curves for the S/NC800 pouch cell with E/S ratio of 20 $\mu\text{L}$ . (c) Comparison of the 1 <sup>st</sup> 100 cycles for the pouch cells made with S/NC800 with E/S ratio of 10 $\mu\text{L}$ and 20 $\mu\text{L}$ . The cells were tested under 0.2 C rate. ....	198
Figure 124. CD plots of the as-prepared electrolytes-based S/C//electrolyte//Li half-cell at 0.1 C rate. (a) Specific discharge capacity plots of the cells as a function of CD cycles at 0.1 C. (b) Coulombic efficiency of the Li-S batteries with as-prepared electrolytes as a function of CD cycles. Note: For acronym meanings, see Table 7.....	200
Figure 125. (a) The organic synthetic setup installed at Ampcera with on-site visiting by University of California, San Diego (UCSD). (b) Photos of the HATN monomer synthesized by Ampcera and UCSD. (c-d) The hydrogen – nuclear magnetic resonance spectrum of the synthesis precursor of diamino-benzonitrile with its physical appearance (insets) used at Ampcera (c) and UCSD (d). ....	204
Figure 126. (a-b) The potential scaling-up setup design for the synthesis of HATN monomer. (c) The designated glovebox for materials storage at Ampcera. ....	205
Figure 127. (a) Cycling behavior of the nanostructured C-S and the bulk C-S cathode in baseline electrolyte with E/S ratio of 10 ml $\text{mg}_{\text{sulfur}}^{-1}$ and 100 mm lithium. The sulfur loading of is 3.8 $\text{mg}_{\text{sulfur}} \text{cm}^{-2}$ of the nano C-S and 2.52 $\text{mg}_{\text{sulfur}} \text{cm}^{-2}$ of the bulk C-S. (b) high performance liquid chromatography – ultraviolet (HPLC-UV) spectra of the fresh electrolyte, DOL/DME solvent, $\text{LiNO}_3$ and LiTFSI in DOL/DME solvent, and the cycled electrolyte of the nano C-S cathode. (c) HPLC-UV spectra of the pristine electrolyte and cycled electrolyte for bulk C-S cathode. ....	206
Figure 128. Schematic of the electrochemical infusion of sulfur species in the HATN/CNT-S cathode. ....	207
Figure 129. (a) The voltage profile of HATN/CNT-S cathode without sulfur melt infusion in baseline electrolyte of 1 M LiTFSI in a DOL/DME mixture (1:1, v/v) with 2 wt% $\text{LiNO}_3$ , using 100 $\mu\text{m}$ lithium and E/S ratio of 6 $\mu\text{l}$ $\text{mg}_{\text{sulfur}}^{-1}$ . (b) The cryogenic focused ion beam scanning emission microscopy (cryo-FIB SEM) image of the cross-section of the University of California, San Diego, nano C-S cathode with highly porous structure. (c) The cryo-FIB SEM image of the cross-section of the HATN/CNT-S cathode via electrochemical infusion, which is highlighted with a low average 2D tortuosity ( $\tau$ ) of 1.22 and a bulk particle size of > 10 $\mu\text{m}$ . (d) X-ray energy dispersive spectrum of the selected area (red rectangle in Figure 129c), showing the successful electrochemical sulfur infusion.....	208

- Figure 130. (a) The summary of the 1<sup>st</sup> discharge curves and scanning emission microscopy (SEM) images (inset) of the cathodes of GM C-S, University of California, San Diego (UCSD) C-S, and HATN/CNT-S with/without sulfur melt infusion with a similar sulfur loading of  $\sim 5 \text{ mg cm}^{-2}$ . The cells were assembled by pairing against 100- $\mu\text{m}$  lithium anodes in baseline electrolyte with E/S ratios of  $10 \mu\text{l mg}_{\text{sulfur}}^{-1}$  for C-S and  $6 \mu\text{l mg}_{\text{sulfur}}^{-1}$  for HATN/CNT-S. (b) The photos of the discharged cathodes of GM C-S and the optimized HATN/CNT-S, washed by DOL/DME solvent. (c-d) The cryogenic focused ion beam SEM images of the cross-sections of the HATN/CNT-Li<sub>2</sub>S cathode and the GM C-S cathode (discharged, 1<sup>st</sup> cycle). The particles are highlighted in (c), while the pores are identified in (d)..... 209
- Figure 131. The top-view of scanning electron microscopy images of the pristine GM C-S cathode using the secondary-particle technology and the pristine HATN/CNT-S cathode (a/c) and after 1<sup>st</sup> discharge in Figure 130a (b/d) with a similar sulfur loading of  $\sim 5 \text{ mg cm}^{-2}$  under a small magnification. .... 210
- Figure 132. Voltage profiles of (a) the HATN/CNT-S cathode with  $6.30 \text{ mg}_{\text{sulfur}} \text{ cm}^{-2}$  and (c) the GM C-S cathode with  $5.36 \text{ mg}_{\text{sulfur}} \text{ cm}^{-2}$  in baseline electrolytes with different E/S ratios. The inset schematics illustrate the cell assembly. (b) The cycling behavior of the optimized HATN/CNT-S cathode at 0.1 C, 1 C = 1000 mAh g<sup>-1</sup>. (d) The cycling stability of the GM C-S cathode showing the same capacity decay tendency with the University of California, San Diego, nano C-S (Figure 127a). .... 211
- Figure 133. GM data: electrochemical performance of  $5.2 \text{ mg}_{\text{sulfur}}/\text{cm}^2$  sulfur cathode electrode (a) charge-discharge profiles and (b) discharge-charge capacities and Coulombic efficiency versus cycle number. .... 211
- Figure 134. Electrochemical cycling performance and Coulombic efficiency of POFM1-S electrode cycled between 1.8-2.8 V at C/20 and 1.7-2.8 V at C/10 current rates. .... 215
- Figure 135. Electrochemical cycling performance along with areal discharge capacity of MCA4 electrode cycled at 1 mA current for 1 hour for alloying and de-alloying, respectively, for 30 cycles. .... 215
- Figure 136. (a) Cycling performances of optimized SPC and SPAN cathodes in carbonate electrolyte at current density of  $100 \text{ mA g}^{-1}$ . The SPC cathodes show much improved specific capacity (initial specific capacity > 1000 mAh g<sup>-1</sup> based on SPC weight, or > 800 mAh g<sup>-1</sup> based on cathode weight) over that of the routine SPAN cathode. (b) Cyclic voltammetry curves of SPC and SPAN cathode-based batteries at scan rate of  $0.1 \text{ mV s}^{-1}$ ..... 219
- Figure 137. (a) Charge-discharge curves of optimized SPC cathode-based battery at a current density of  $100 \text{ mA g}^{-1}$  in carbonate electrolyte. (b) Cycling performance and Coulombic efficiency evolution of optimized SPC cathode-based battery at a current density of  $100 \text{ mA g}^{-1}$  in carbonate electrolyte..... 220
- Figure 138. (a) Deep discharge of Li-O<sub>2</sub> using carbon paper and using SEI-coated carbon paper at  $50 \mu\text{A cm}^{-2}$  until  $3 \text{ mAh cm}^{-2}$  or until voltage cutoff of 2 V versus Li<sup>+</sup>/Li is reached. Potentiostatic hold of Li-O<sub>2</sub> battery at 2.5 V versus Li<sup>+</sup>/Li. (b) The cumulative capacity by integrating the current response. (c) The current response of the carbon paper and the SEI-coated carbon paper. (d) Expanded view of the current response showing details of the current peak, indicating passivation..... 223

Figure 139. Microscopy of discharge product. Scanning electron microscopy (SEM) of SEI-carbon paper (a) before and (b) after discharge. SEM of carbon paper (c) before and (d) after discharge. (e) Cryogenic transmission electron microscopy of discharge product clearly indicating the $\text{Li}_2\text{O}_2$ spatially sits over the SEI layer rather than inside. (f) Select area electron diffraction of the discharge product indicating it is mostly $\text{Li}_2\text{O}_2$ .....	224
Figure 140. Density functional theory calculations for (a) initial and final structure of $\text{SnI}_2$ reacting on a Li-metal (100) surface and for (b) initial and final structure of $\text{SnI}_2$ reacting on a SnS surface.....	226
Figure 141. Cycling results of Li- $\text{CO}_2$ batteries with (a) Te-based and S-based cathode, and (b) $\text{MoS}_2$ -, Au-, Pt-, and Te-based cathodes under a current density and capacity of $1 \text{ mA/cm}^2$ and $0.2 \text{ mAh/cm}^2$ , respectively. ....	229
Figure 142. Cycling results of Li- $\text{CO}_2$ batteries with Te-based cathode under a current density of $1 \text{ mA/cm}^2$ at a capacity of $0.2 \text{ mAh/cm}^2$ . ....	229
Figure 143. Copper $\text{L}_3$ edge (left panel) and oxygen K-edge (right panel) for P3-NaCuMnO at pristine state, charged to 3.66 V, and charged to 4.10 V. The vertical dotted lines indicate the position of main peak, and the upward arrows indicate the rising of shoulder peaks and their positions. ....	233
Figure 144. X-ray diffraction pattern (a-b), voltage profile (c-d), and cycle performance (e-f) of NMF-111 (a/c/e) and NMF-112 (b/d/f); ( $i = 10 \text{ mA/g}$ for the 1 <sup>st</sup> three cycles and $30 \text{ mA/g}$ for the next cycles). ....	236
Figure 145. <i>Operando</i> synchrotron X-ray diffraction (XRD) analysis of NMF-111 and NMF-112. (a) <i>Operando</i> XRD of NMF-112 during the initial charge. (b) Comparison of the phase transition as a function of the sodium content. (c-d) Selected XRD patterns during the initial charge, and (e/f) after the 1 <sup>st</sup> cycles up to different cut-off voltages: NMF-111 (c/e) and NMF-112 (d/f).....	237
Figure 146. Gas evolution in the initial two cycles of sodium half cells made with $60^\circ\text{C}$ -heated sodium titanate anodes, or NTOs, (a) with and (b) without 10 minutes of air-exposure, and (c) $500^\circ\text{C}$ . The cells were cycled at a current rate of $32 \text{ mA g}^{-1}$ using $0.5 \text{ M NaBPh}_4$ in DEGDM as the electrolyte. The $\text{CO}_2$ signals observed during the open circuit voltage (OCV) period were from residual $\text{CO}_2$ in the instrument. The $\text{H}_2$ signals detected during the second OCV period are mostly from the residual $\text{H}_2$ generated during the previous charge. ....	240
Figure 147. Sodium stripping/plating efficiency in two different electrolytes (testing condition: plating $4 \text{ mAh cm}^{-2}$ and fully stripping to 1 V and cycling for 10 cycles at $0.5 \text{ mA cm}^{-2}$ ). ....	243
Figure 148. Cycling performance of half-cell $\text{Na}    \text{NVP}$ cathode in 10 cycles at 0.2C. ....	243
Figure 149. (a) Initial charge-discharge profile of $\text{Cu}    \text{NVP}$ cell in two electrolytes. (b) Cycling performance of the anode-free cells for 50 cycles (formation cycle: 1 <sup>st</sup> cycle: $0.1 \text{ C}$ , charge cyclic voltammetry (CV), cycling: 2 <sup>nd</sup> – 7 <sup>th</sup> cycle: $0.2 \text{ C}$ , charge CV, 8 <sup>th</sup> cycle: $0.3 \text{ C}$ , discharge $0.2 \text{ C}$ , charge CV; NVP loading mass: $3\text{-}4 \text{ mg/cm}^2$ ). ....	244

Figure 150. (a) X-ray photoelectron spectroscopy study of coin-cell components. (b) Heat evolved for NMC-811 with the M47 electrolyte using the aluminum protected Hohsen and MTI cells. (c-d) Studies of X4 (PNNL) and FDMB (Stanford) electrolytes. <i>Ex situ</i> differential scanning calorimetry profiles of electrolyte alone, electrolyte + Targray NMC-811 charged to 4.8 V, and electrolyte + Li-metal anode after charge. (e-f) Cycling and heat evolution of coin cells cycled between 4.4 V and 2.8 V at C/10 current rate. ....	246
Figure 151. (a) Schematic illustrations of the localized saturated electrolyte (LSE). (b-c) Effect of solvents (b) and diluents (c) on the cycling stability of LiNiO <sub>2</sub> . The cycling was conducted at room temperature with 2 mA h cm <sup>-2</sup> loading of the cathode material. The charge rate was C/2 and the discharge rate was 1C in the voltage range of 2.8 V – 4.4 V. (d-e) X-ray photoelectron spectra for the SEI formed on Li-metal anode (d) and the CEI formed on LiNiO <sub>2</sub> cathode (e). (f-g) Quantitative analysis of different elemental components of the SEI (f) and the CEI (g). ....	248
Figure 152. (a) The molecular structures and estimated bond lengths (in Å) of EC, EMC, FEC, and PF <sub>6</sub> <sup>-</sup> molecules. The size of a general contact ion pair (CIP) and aggregate (AGG) is also labeled. (b-c) Experimental pair distribution function (PDF) data in the range of 0.8-2.5 Å for different electrolytes. (d-e) Experimental small-angle X-ray scattering (SAXS) data of different electrolytes. (f) Proposed solvation structure evolution from a low concentration electrolyte (LCE) to a saturated electrolyte (SE) to a localized saturated electrolyte (LSE) based on the PDF and SAXS measurements. ....	249
Figure 153. (a) Aurbach Coulombic efficiency of Li  Cu cell in different electrolytes. (b) Charge curves of different electrolytes with various resting time. (c) Electrochemical performance of the NMC-811  Li coin cells tested in different electrolytes. (d) Wettability of the electrolytes on Celgard separators and lithium metals after 1 <sup>st</sup> charge. ....	251
Figure 154. Morphology of Li-metal anode after 10 cycles: (a-c) top-view scanning electron microscopy images and (d-f) cross-view images of lithium anodes in different electrolytes. ....	251
Figure 155. (a) Average Coulombic efficiency (CE) of Li  Cu cells with high-concentrated electrolytes with six solvating solvents. (b) Average CE of Li  Cu with SS4-based localized high-concentration electrolytes and E-baseline. (c) Lithium deposition morphologies on copper electrodes at a current density of 0.5 mA cm <sup>-2</sup> for a capacity of 1 mAh cm <sup>-2</sup> . ....	252
Figure 156. Charging/discharging profiles of Li  SPAN cells at a current density of C/20 with (a) E-baseline, (b) SS4-LHCE-1, and (c) SS4-LHCE-2. (d) Performances of Li  SPAN cells with studied electrolytes at a current density of C/5 in the voltage range of 1-3 V. ....	253
Figure 157. (a) Ionic conductivities at different temperatures. (b) Charge-rate capability of Li  SPAN cells with the studied electrolytes at a constant discharging current density of C/5 in the voltage range of 1-3 V. ....	253

- Figure 158. Chemical structures, compositions, and ionic conductivities of the three weakly solvating electrolytes under investigation. Notably, the ionic conductivities in Celgard 2325 separator (left blue axis) are lower by an order of magnitude than those without a separator (orange right axis)..... 254
- Figure 159. Full-cell performance at various charge rates and 1C discharge rate ( $1C = 4 \text{ mA cm}^{-2}$ ). Coin cells were assembled with NMC-811 (ca.  $4.5 \text{ mAh cm}^{-2}$ ),  $50\text{-}\mu\text{m}$  thick lithium foil ( $N/P \sim 2$ ), and relatively lean electrolyte amount ( $E/C \sim 8.9 \text{ mL Ah}^{-1}$ ). All cells were cycled between 2.8 V and 4.4 V versus  $\text{Li}^+/\text{Li}$ . Two formation cycles at C/10 charge and discharge rates were performed, followed by long-term cycling at various charge rates (labeled on the graph) and 1C discharge rate. A constant voltage step was applied at the end of charging until the current fell below C/10. (a-f) Discharge capacity and Coulombic efficiency (CE) over cycling for 1 M LiFSI in 1:3 (v/v) DEE:FDEB (a-b), 1.54 M LiFSI in 1:3.6 (v/v) DME:TTE (c-d), and 1 M LiFSI in FDMB (e-f). The replicated cells are shown in the same color and different symbols. (g) The dependence of cycle life on charge rates. Cycle numbers were calculated from the champion cell at each charge rate. The end of cycle life was defined as  $< 70\%$  discharge capacity of the 3<sup>rd</sup> cycle or  $< 90\%$  CE starting from the 4<sup>th</sup> cycle. (h-i) Voltage profiles showing soft shorting characteristics at 1C charge rate in 1.54 M LiFSI in 1:3.6 (v/v) DME:TTE (h) and 1 M LiFSI in FDMB (i)..... 255
- Figure 160. (a) Degradation of lithium salts into LiF under  $\text{Ar}^+$  sputtering of X-ray photoelectron spectroscopy (XPS) measurements. (b) XPS analyses of unwashed copper electrode after cycling in a Li/Cu cell at 0-1 V for 100 times in DME / 1 M LiFSI electrolyte, revealing crucial fingerprint species of SEI chemistry. (c) Schematic of three basic steps of breaking down FSI<sup>-</sup> anion at  $\text{Li}^0$ -metal potential based on XPS analyses. .... 256
- Figure 161. Initial data showing no significant impact to the specific capacity as a function of cathode thickness..... 258
- Figure 162. Characterizations of thin-film SPAN. (a) Photo of thin-film SPAN synthesized on top of titanium substrate. (b) Focused ion beam – scanning electron microscopy (FIB-SEM) image of the cross-section of thin-film SPAN on titanium substrate. Top-view SEM images for the (c) precursor (polyacrylonitrile) thin film and (d) SPAN thin film. (e) Scanning transmission electron microscopy – energy dispersive X-ray spectroscopy mapping of thin-film SPAN. (f) Fourier transform infrared spectra of the powder and thin-film SPAN. (g-h) Schematic and results of the electrical conductivity test for SPAN thin film before and after the 1<sup>st</sup> cycle. .... 259
- Figure 163. Potential energy profiles for Reaction 2 ( $\text{Li}_2\text{S}_2 \rightarrow \text{Li}_2\text{S} + \text{S}^*$ ) for the two types of functional electrocatalysts considered..... 260
- Figure 164. Coulombic efficiency versus areal density for four different current collector structures. .... 261
- Figure 165. Top-view (left) and cross-sectional view (right) of electrochemically deposited lithium metal on copper foam in LHCE..... 262
- Figure 166. Normal distribution curve of unit weight of  $12\text{-}\mu\text{m}$  and  $20\text{-}\mu\text{m}$  thick aluminum foils. .... 263

---

Figure 167. Single-layer pouch cell using baseline electrode. ....	264
Figure 168. (a) Cycling stability of the single-layer pouch cell. (b) Voltage profiles for the first 5 cycles.....	264
Figure 169. (a) Optimization of slurries for doctor-blade casting reproducible and high-quality SPAN electrodes. (b) Discharge curves of a typical SPAN electrode. (c) Discharge capacities versus cycling number for six batches of SPAN electrodes based on the Gen 2 recipe. ....	265
Figure 170. (a) (111) and (200) LiH/D X-ray diffraction (XRD) peaks from Li  NMC cell SEI using 100% H-DME, 50% H-DME + 50% D-DME, and 100% D-DME. (b) Lattice parameters obtained from the XRD fitting. (c) Lithium 1s and oxygen 1s X-ray photoelectron spectra of fresh lithium foil. (d) XRD results of SEI inside Li  NMC after formation cycle and after 50 cycles. ....	267
Figure 171. Nano secondary ion mass spectrometry elemental mapping of SEI formed on copper at 30 mV versus Li <sup>+</sup> /Li as a function of hold time. ....	268
Figure 172. Chromatograms of samples of different concentrations of (a) Me <sub>2</sub> S <sub>2</sub> , (b) Me <sub>2</sub> S <sub>3</sub> , and the calibration curves for (c) Me <sub>2</sub> S <sub>2</sub> and (d) Me <sub>2</sub> S <sub>3</sub> .....	270
Figure 173. X-ray micro fluorescence maps for nickel, cobalt, and manganese of a pristine NMC-811 electrode using 1 μm focusing optics.....	270
Figure 174. X-ray absorption near-edge spectra taken at 32 different points of a NMC cathode inside a pouch cell after 600 cycles. ....	271

## TABLE OF TABLES

Table 1. Stability of LLZO–NMC-111 under varying lithium chemical potential. ....	46
Table 2. Stability of LLZO–NMC-111 interface under varying O <sub>2</sub> chemical potential.....	46
Table 3. Domain spacing and glass transition temperature (T <sub>g</sub> ) of crosslinked PEO and PFPE membranes.....	75
Table 4. The final ten novel fast lithium-conducting frameworks discovered in this Task.....	139
Table 5. Coherent interfacial models built for the cluster-based solid electrolytes and coating Li <sub>3</sub> PO <sub>4</sub> . In each case, surfaces (according to the miller indices hkl) are chosen due to the minimum matching area (MA) between the solid electrolyte and Li <sub>3</sub> PO <sub>4</sub> . The strain at the interface is measured by the von Mises strain. The number of formula units (FU) and the thickness (in atomic layers) of the solid electrolyte and Li <sub>3</sub> PO <sub>4</sub> are given.....	148
Table 6. NiO <sub>2</sub> cell parameter and energies for different oxygen stacking sequences and density functionals.....	160
Table 7. Compositions of the prepared electrolyte solutions.....	200
Table 8. ΔH interface for c <sub>Li</sub> = 5 at% in the different multicomponent alloys (MCAs) considered.....	217
Table 9. Normalized H <sub>2</sub> generation (μmols/mg <sub>active material mass</sub> ) in the initial two cycles of sodium half cells made with sodium titanate anodes (NTOs).....	240
Table 10. The values indicating the performance of sodium anode-free cells in two electrolytes. ....	244
Table 11. Coulombic efficiency data for commercial foil and foam using four electrolytes. ....	262

## A MESSAGE FROM THE MANAGERS: ADVANCED BATTERY MATERIALS RESEARCH AND BATTERY500 CONSORTIUM

The Advanced Battery Materials Research (BMR) Program within the Office of Energy and Renewable Energy (EERE) comprises seven topic areas: Solid-State Electrolytes, Advanced Diagnostics, Modeling, Metallic Lithium, Lithium-Sulfur Batteries, Lithium-Air Batteries, and Sodium-Ion Batteries. The BMR Program's goal is to develop next-generation, high-performance batteries for electric vehicles. EERE also supports the Battery500 Consortium, a multi-institution program focused on developing lithium-metal anode cells capable of delivering 500 Wh/kg and 1,000 charge/discharge cycles. Scientific advancements made in these two programs can be followed in our quarterly reports, accessible on the BMR website (<https://bmr.lbl.gov/>).

A few notable achievements from BMR investigators during the July 1, 2022, through September 30, 2022, quarter are summarized below:

- P. Zhang's group at Solid Power cycled 2 Ah Li/NMC pouch cells containing a sulfide solid-state electrolyte between 2.8-4.2 V, with a charge and discharge rate of C/5 at 45°C. Cells demonstrated 750 cycles with 87% capacity retention before the Coulombic efficiency (CE) started to drop, indicating the formation of a soft short. Surface modification of the lithium anode may be needed to further improve cycling stability.
- G. Ceder's group at University of California, Berkeley, has identified new lithium conductors based on the rationale that corner-sharing frameworks enable high conductivity. Using high-throughput (HT) screening, the team discovered ten, fast lithium-conducting frameworks. To validate the HT screening method, the team produced one of the novel candidates,  $\text{LiGa}(\text{SeO}_3)_2$ , using solid-state synthesis and densifying the material into a pellet using spark plasma sintering. The data show remarkably high bulk ionic conductivity of 0.11 mS/cm at room temperature.
- Z. Bao and Y. Cui's Stanford University group showed that a salt-philic, solvent-phobic ( $\text{SP}^2$ ) polymer coating on lithium-metal anodes improved the cycle life of cells containing carbonate electrolyte. Li/NMC cells went from 100 cycles to 250 cycles (80% capacity retention) with the coating. These data highlighted the promise of the  $\text{SP}^2$  approach.
- W. Chueh's group at Stanford/SLAC National Accelerator Laboratory conducted *operando* scanning electron microscopy (SEM) microprobe experiments on a strained LLZO cantilever to observe the initiation of lithium penetration (termed intrusions) into the solid electrolyte at various compressive stresses. They demonstrated that a strain as small as 0.070% strongly influences the direction of intrusion propagation immediately following initiation.

A few notable achievements from the Battery500 Team this quarter include:

- The Pennsylvania State University team formulated an electrolyte achieving a 99.5% lithium CE in Li/Cu cells. The electrolyte shows good wettability of separators and electrode surfaces. Li/NMC-811 coin cells, utilizing a high areal capacity ( $4.0 \text{ mAh cm}^{-2}$ ) cathode, 50- $\mu\text{m}$  thin Li-metal anode, and lean electrolyte ( $5.5 \mu\text{L/mAh}$ ), displayed 80% capacity retention after 280 cycles.
- The Pacific Northwest National Laboratory team developed new localized high-concentration electrolytes (LHCEs) for Li/SPAN cells. The lithium deposition morphologies in the new electrolytes show larger particle size and denser packing compared to the ether-baseline electrolyte. Cells containing the new electrolyte exhibit capacity retentions of 92.5% after 150 cycles at the C/5 rate. Despite a lower ionic conductivity than that of the ether-baseline electrolyte, cells using the LHCEs deliver better charge-rate capability.

- The University of California, San Diego, team confirmed that the electronic conductivity of SPAN increases after the 1<sup>st</sup> cycle due to the increase in degree of conjugation resulting from the loss of non-aromatic S/N.
- The Brookhaven National Laboratory team has identified LiOH on the surface of pristine Li-metal anode as an important contributor to the formation of LiH. LiOH converts into LiH and Li<sub>2</sub>O during cycling of the Li||NMC-811 cell.
- The General Motors team completed the large-batch, sulfur-cathode development process. The 500 mL mixer procedure can provide a 5-meter long continuous single-side coating, or a 2-meter long double-sided coating electrode. Electrodes fabricated by this process will be distributed to the various lithium-sulfur teams to ensure uniformity of experiments.

Our next quarterly report is anticipated in April 2023.

Sincerely,

*Tien Q. Duong*

Tien Q. Duong  
Manager, Advanced Battery Materials Research Program & Battery500 Consortium  
Batteries & Electrification R&D  
Office of Energy Efficiency and Renewable Energy  
U.S. Department of Energy

*Simon Thompson*

Simon T. Thompson, Ph.D.  
Manager, Battery Technology Development  
Vehicle Technologies Office  
Office of Energy Efficiency and Renewable Energy  
U.S. Department of Energy

## TASK 1 – Solid-State Electrolytes

Team Lead: Andrew Westover, Oak Ridge National Laboratory

### Summary and Highlights

The U. S. Department of Energy (DOE) has made a clear goal of realizing next-generation batteries that have an energy density greater than 500 Wh/kg, that can cycle for more than 300 cycles, and that can demonstrate high-rate capabilities. To achieve this step-change in battery performance, a significant change in the battery chemistry and cell design is needed. This task focuses on developing solid-state electrolytes (SSEs) that enable Li-metal anodes and high-energy cathodes to achieve just such a step change. This task includes 12 projects centered in DOE national laboratories and 13 in companies and universities. These projects span the gamut of different materials for SSEs, interfacial design strategies to enable Li-metal anodes, and high-energy cathodes. Together, they can significantly impact the successful realization of the DOE battery performance targets.

In summary, the projects focus on research and development of a range of solid electrolytes (SEs), including:

- sulfur ceramics and glasses (1.1 – 1.9),
- oxide ceramics (1.10 – 1.13),
- halides and anti-perovskites (1.13 – 1.15),
- polymers (1.16 – 1.18),
- composites (1.19 – 1.22),
- multiple electrolytes / full cells (1.23 – 1.24), and
- Li-metal – SSE interface (1.25).

These projects encompass common research themes essential to achieving high-energy solid-state batteries (SSBs), including:

- engineering high ionic conductivity  $> 1$  mS/cm,
- developing electrolytes that are stable with various high-energy cathodes, including layered oxide cathodes, high-voltage spinels, and conversion cathodes such as sulfur and  $\text{FeF}_3$ ,
- developing electrolytes or interfaces that are stable with lithium metal,
- developing thin SEs 20-100  $\mu\text{m}$  thick, and
- understanding the mechanics of SSBs.

### Highlights

The highlights for this quarter are as follows:

- J. Connell’s group at Argonne National Laboratory (ANL) used density functional theory (DFT) modeling to determine the band gap of argyrodite electrolytes with differing amount of oxygen substitutions. The DFT calculations showed that adding oxygen can significantly improve the bandgap and thus the expected interfacial stability with lithium metal, with full oxygen substitutions resulting in a calculated band gap of 7.04 eV.
- G. Xu’s ANL team showed that a two-step calcination process enables the successful synthesis of  $\text{Li}_{5.5}\text{PS}_{4.4}\text{O}_{0.1}\text{Br}_{1.5}$  SE that has improved electrochemical and air stability while mitigating ionic conductivity reduction.

- Y. Cui's group at Stanford University synthesized a high-purity  $\text{Li}_{10}\text{B}_{10}\text{S}_{20}$  SE with an ionic conductivity of  $\sim 3.4 \times 10^{-4}$  S/cm that forms a stable passivating interface with a resistance of  $\sim 50 \Omega \text{ cm}^2$ .
- J. Nanda's SLAC National Accelerator Laboratory team compared full-cell batteries utilizing  $\text{LiNi}_{0.8}\text{Mn}_{0.1}\text{Co}_{0.1}$  combined with  $\text{Li}_6\text{PS}_5\text{Cl}$  SEs to those using  $\text{Li}_3\text{InCl}_6$ . They anticipated that the electrochemically stable  $\text{Li}_3\text{InCl}_6$  would help reduce capacity fade in the cathode due to electrochemical decomposition of the electrolyte. Instead, they found that the two cathodes showed a similar amount of capacity fade, highlighting that electrochemical decomposition is not the primary mechanism for capacity fade in their cathodes.
- D. Lu's group at Pacific Northwest National Laboratory synthesized  $\text{Li}_7\text{P}_2\text{S}_8\text{Br}_{0.5}\text{I}_{0.5}$  and measured the interfacial resistance as a function of time showing that the addition of the iodide reduces the interfacial resistance with lithium metal from  $2.65 \Omega \text{ cm}^2$  to  $1.08 \Omega \text{ cm}^2$ . They then demonstrated  $\text{Li}/\text{Li}_7\text{P}_2\text{S}_8\text{Br}_{0.5}\text{I}_{0.5}/\text{Li}$  symmetric cycling for 1000 hours at a current density of  $0.5 \text{ mA}/\text{cm}^2$  and a per-cycle capacity of  $0.25 \text{ mAh}/\text{cm}^2$  at  $20^\circ\text{C}$ .
- S. Martin's Iowa State University team successfully drew their mixed Li-Si-P-S-O glass electrolytes to a thickness of  $60 \mu\text{m}$  without any observable change in the composition and short-range structure, as measured by X-ray photoelectron spectroscopy (XPS).
- P. Zhang's group at Solid Power showed full NMC-Li cycling results tested at 2.8-4.2 V, with a charge and discharge rate of C/5 at  $45^\circ\text{C}$ . The pouch cell showed 750 cycles with 87% capacity retention before the Coulombic efficiency started to drop, indicating the formation of a soft short.
- D. Wang's Pennsylvania State University team developed three different alloy anodes using ball milling. While the first alloy led to internal shorting after 29 cycles, two subsequent alloy compositions enable more than 150 cycles with greater than 80% capacity retention at a charge rate of 0.1C at  $60^\circ\text{C}$ .
- T. Yersak's General Motors group used X-ray tomography to understand crack formation in a fully solid cell. Because the confined lithium metal could not relieve stress, resulting in electrolyte cracking, the design of a semi-solid system was determined to be necessary to dissipate the stresses at the SSE/Li interface.
- J. Ye's team at Lawrence Livermore National Laboratory attempted to co-sinter Li-La-Zr-Ta-O SEs with both  $\text{LiCoO}_2$  and  $\text{LiNi}_{0.6}\text{Mn}_{0.2}\text{Co}_{0.2}$  (NMC-622) cathodes at  $750^\circ\text{C}$  and  $900^\circ\text{C}$ . The NMC-622 cathodes had significant degradation in the NMC-622 capacity, emphasizing the difficulty with conventional sintering methods for solid-state NMC cathodes. They proposed a rapid laser sintering to mitigate these negative effects.
- J. Sakamoto's University of Michigan group reported development of the use of a catholyte tailored to sulfur-based cathodes that forms a kinetically stable interface with a resistance of  $30 \Omega \text{ cm}^2$ . This interface enabled the use of Li-La-Zr-O (LLZO) with sulfur cathodes. Initial performance shows a capacity of  $\sim 1300 \text{ mAh}/\text{g}_{\text{sulfur}}$  over three cycles.
- E. Wachsman's team at University of Maryland successfully coated NMC-622 with  $\text{Al}_2\text{O}_3$  and  $\text{Li}_2\text{SiO}_3$ . Based on X-ray diffraction data, the coatings have successfully reduced formation of unwanted perovskite phases on co-sintering.
- Z. Chen and T. Li's ANL group explored hot pressing of  $\text{Li}_2\text{HOCl}_{0.75}\text{Br}_{0.25}$  powders with ionic conductivities of  $\sim 10^{-5}$  S/cm at room temperature. The hot-pressing process at  $200^\circ\text{C}$  significantly improves the pellet densities, reducing the number and size of voids.
- R. Sacci's team at Oak Ridge National Laboratory (ORNL) performed initial full-cell testing with  $\text{LiNi}_{0.85}\text{Mn}_{0.1}\text{Co}_{0.05}\text{O}_2 - \text{Li}_3\text{InCl}_6$  cathodes, a  $\text{Li}_3\text{InCl}_6$  electrolyte, and  $\text{LiIn}$  anodes. The cell cycling showed rapid capacity fade. Using scanning electron microscopy, they identified that the failure was due to significant delamination of the  $\text{Li}_3\text{InCl}_6$  electrolyte from the NMC cathode.
- D. Qu's University of Wisconsin, Madison group explored the mechanical evolution of their prelithiated silicon anode ( $\mu\text{-Li}_x\text{Si}$ ). Using a  $\text{Li}_4\text{Ti}_5\text{O}_{12}$  counter electrode, they demonstrated that the silicon anode reaches a stable "breathing" state where the pressure change is uniform from cycle to cycle.

- N. Balsara's team at University of California, Berkeley (UCB) demonstrated that poly(pentyl malonate) electrolytes have a higher oxidative stability than standard poly(ethylene oxide) (that is, PEO) electrolytes with no substantial electrolyte degradation until ~ 5.2 V versus Li/Li<sup>+</sup>.
- Z. Bao and Y. Cui's Stanford University group showed Stanford's salt-philic solvent-phobic (SP<sup>2</sup>) electrolyte coating improved the cycle life of Li-metal anodes, with 10 mAh/cm<sup>2</sup> excess lithium from 100 cycles with 80% capacity retention to 250 cycles with 80% capacity retention. These data highlighted the promise of their SP<sup>2</sup> approach.
- L. Madsen's team at Virginia Polytechnic Institute and State University showed full-cell data for batteries using the molecular ionic composites (MIC) SEs. The data showed the MIC composites have minimal degradation up to 4.5 V and at 60°C.
- S. Tepavcevic's ANL group calculated the estimated ceramic electrolyte fiber fraction to reach an ionic percolation threshold for ceramic fibers with different aspect ratios. For the target fibers with an aspect ratio of ~ 10, the needed threshold is ~ 20 wt%. Experimental work shows that the interfacial resistance between the fibers and the polymer electrolytes (PEs) and between fibers is limiting the ionic percolation in practical films.
- X. C. Chen's team at ORNL clearly determined the morphology of 60% perfluoropolyether (PFPE) – 40% PEO to have a significant amount of phase segregation at the nanoscale. These nanodomains both decreased the PEO segmental dynamics and increased the tortuosity, resulting in poor ionic conductivity. The work clearly showed that the PFPE-PEO approach is not suitable for optimal SSBs.
- B. McCloskey's UCB group compared two methods to synthesize p-Glycerol carbonate methacrylate electrolyte additives using a dimethylsulfoxide (DMSO) and acetonitrile solvents. While the DMSO resulted in a higher yield, the acetonitrile-based synthesis is more straightforward and efficient.
- E. Hu's Brookhaven National Laboratory team used X-ray total scattering to determine changes in the short range ordering of polyvinylidene fluoride with both lithium bis(trifluoromethanesulfonyl)imide (LiTFSI) and lithium bis(sulfonyl fluoride)imide salts. In both cases, the addition of the salts significantly decreases the crystallinity of the polymer films.
- G. Cedar's team at UCB tested three carbon-metal nanoparticle buffer layers identifying a carbon-Mg buffer layer as a potential alternative to expensive silver in Task 1. Task 2 explored synthesis of Li<sub>3</sub>YCl<sub>6</sub>, successfully demonstrating electrolytes with conductivities as high as 0.3 mS/cm to be used as ionically conductive additives to their composite cathodes. In this way, they can successfully protect the SE from the carbon while maintaining the active area. Task 3 optimized the tape-casting procedure to form thin LLZO membranes by changing the binder burnout temperature and sintering temperature, minimizing the warping of the LLZO membranes. The LLZO fracture toughness was also measured to be 1.37 MPA m<sup>0.5</sup>. Task 4 compared the use of solution precipitation with different polymer content. The results clearly show that this method successfully creates a uniform dispersion of the ceramic and the PEO polymer in the composite electrolyte.
- A. Burrell's National Renewable Energy Laboratory materials characterization team synthesized the ionic LiBH<sub>4</sub>-doped argyrodite electrolytes with an ionic conductivity of ~ 8 × 10<sup>-3</sup> S/m. The materials characterization team also developed and demonstrated a virtual XPS measurement technique allowing them to observe solid electrolyte interphase formation *in situ* for argyrodite SEs and showed progress on Kelvin force probe microscopy measurements. Finally, the cell building team demonstrated initial pouch-cell cycling for a full cell using an argyrodite SE, a LiNi<sub>0.9</sub>Mn<sub>0.05</sub>Al<sub>0.05</sub>O<sub>2</sub> cathode, and a Si-based anode.
- A. Westover's ORNL team tested five lithium sources with PEO-LiTFSI and argyrodite SEs. For the PE, the interfacial resistance directly correlated to the thickness of the surface layers and varied from 100-500 Ω cm<sup>2</sup>. They also found that while the resistance correlates to the surface layers, the ultimate failure of the cells is determined by other factors, likely including the microstructure and the ability of lithium to diffuse within lithium metal.

## Task 1.1 – Multifunctional Gradient Coatings for Scalable, High-Energy-Density Sulfide-Based Solid-State Batteries (Justin Connell, Argonne National Laboratory)

**Project Objective.** This task seeks to develop scalable approaches to synthesize gradient-coated sulfide solid-state-electrolyte (SSE) particles to improve their air/moisture tolerance and provide chemical compatibility with Li-metal anodes and high-voltage oxide cathodes. The compositional gradient is targeted to provide the additional advantage of lower interfacial impedance due to mitigation of detrimental, spontaneously formed space-charge layers and/or elemental interdiffusion at the sulfide SSE-oxide cathode interface.

**Impact.** Development of coated SSE materials that provide stable, low-impedance interfaces with both anode and cathode will enable high-energy-density, all-solid-state full cells with improved cyclability at high rates relative to benchmarked, uncoated materials. Coating the SSE directly will also remove the need for separate anode and cathode coatings, significantly reducing the cost and complexity associated with materials processing while maintaining compatibility with roll-to-roll manufacturing.

**Approach.** The team will leverage a surface science-based, integrated experimental-theoretical approach to synthesize gradient-coated SSE powders, characterize the structure, composition, and intrinsic stability of coated SSEs in contact with reactive electrodes, and directly correlate this understanding with their electrochemical performance. Gradient coatings will be developed using atomic layer deposition (ALD) and/or physical mixing methodologies viable at the kg/ton scale, ensuring technical and commercial relevance of the final, optimized coating process. Well characterized, model surfaces will be used to understand the electronic structure and chemical stability of the gradient coatings as a function of gradient composition and thickness to understand the effect of space-charge layers and chemical reactions on interface resistance. They will accelerate development and optimization of the gradient coatings for improved performance in full cells by establishing a tight feedback loop between materials synthesis and experimental/computational characterization of interfacial (electro)chemistry.

**Out-Year Goals.** The out-year goals are to demonstrate high-energy-density, low-impedance full cells assembled from fully optimized, gradient-coated SSE powders, high-energy-density cathodes, and Li-metal anodes. The team will also significantly improve the ability to manipulate the formation of space-charge layers at sulfide SSE-oxide cathode interfaces based on mechanistic understanding of the extent to which they can be mitigated to reduce overall cell impedance.

**Collaborations.** This project funds work within multiple divisions and directorates at Argonne National Laboratory and includes in-kind contributions from Solid Power.

### Milestones

1. Baseline Li||Li symmetric cell testing and characterization of uncoated argyrodite SSEs. (Q2, FY 2022; Completed)
2. Chemical stability characterization of gradient coatings for argyrodite SSEs. (Q3, FY 2022; Completed)
3. Computational assessment of electronic structure of candidate gradient coating chemistries. (Q4, FY 2022; Completed)
4. Identification of multiple gradient coating chemistries that deliver > 50% reduction in weight gain during humidified air exposure. (Q1, FY 2023; In progress)

## Progress Report

Sulfide SSEs with argyrodite-type structure and  $\text{Li}_{7-y}\text{PS}_{6-y}\text{X}_y$  (LPS-X; X = Cl, Br, I) composition have high ionic conductivities (over 10 mS/cm), wide band gaps and favorable mechanical and processing properties, making them particularly promising candidate materials for all-solid-state batteries. The team's experimental work in previous quarters focused on studies of coatings for the LPSCl composition, which exemplifies all of these advantages and enables investigations of interfacial properties critical to the operation of these SSEs. Computational studies in this report address reactivity and electronic properties for the coatings at interfaces of argyrodite particles aimed at mitigating interfacial impedance. These studies are performed in conjunction with experimental characterization of the stability of LPSCl materials to coating via ALD and their performance. Specifically, ALD alumina coatings on LPSCl were shown last quarter to significantly improve stability against lithium metal with minimal reactivity of the underlying SSE material.

To analyze the electronic structure of coatings, the team started with density functional theory calculations for LPSCl with different degrees of oxygen substitution. Two levels of theory have been used: a generalized gradient approximation and a hybrid functional, with the latter providing more accurate band gap values. The electronic density of states (Figure 1) shows an increase of the bandgap from 3.32 eV to 3.55 eV when 5% of sulfur atoms are substituted by oxygen. Calculations for the isostructural analogue where all sulfur atoms are substituted by oxygen atoms produces an even larger increase in band gap to 7.04 eV; however, the lattice constant of argyrodite decreases considerably. Substituting oxygen into chlorine positions was found to be less energetically favorable than substitution into tetrahedral sulfur positions, and substitution of oxygen atoms into phosphorus positions is unfavorable. Their results point to the possibility that ALD coatings of oxide or oxysulfide materials will result in lower electronic conductivity because of an increased band gap deriving from exchange of some sulfur for oxygen at the interface.

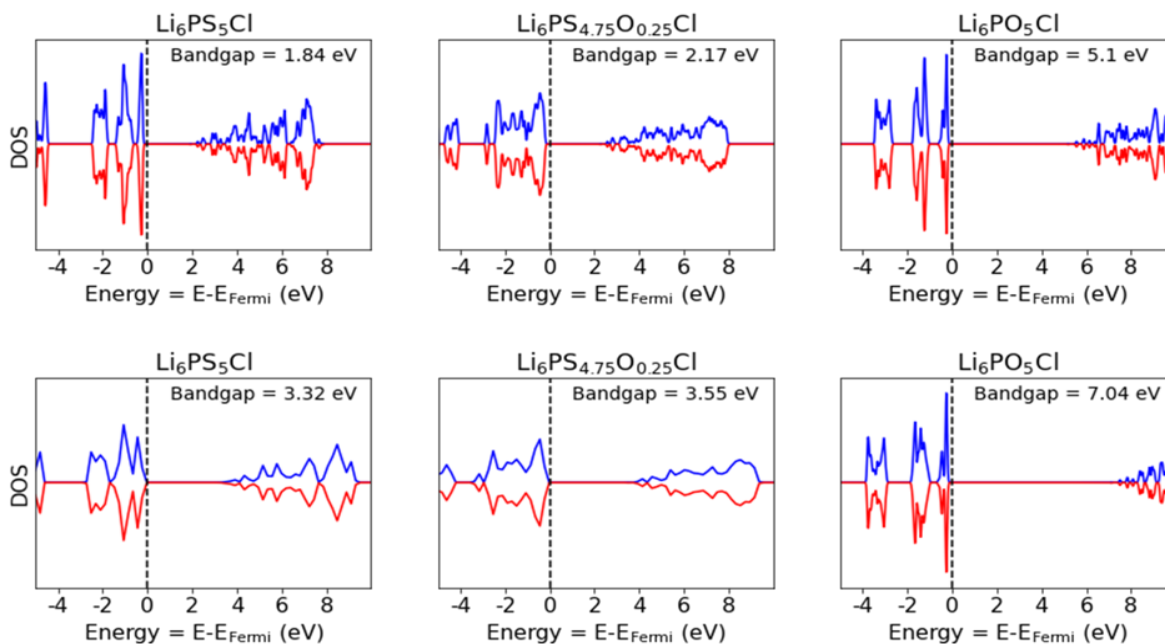


**Figure 1.** Calculated density of states (DOS) for LPSCl solid-state electrolyte with varying concentrations of oxygen at generalized gradient approximation (top row) and hybrid functional (bottom row) levels of theory.

To gain further insight into the stability and transport properties of oxide coatings, the team considers computational models of LPSCl with ALD alumina coatings. First, they have calculated the work functions for amorphous alumina and LPSCl to determine relative band alignment at the interface. The results (Figure 2)

show that work function for LPSCl (4.6 eV) is considerably smaller than the work function for amorphous alumina (average 6.5 eV). The team's calculations for amorphous LPSCl with the same composition as a crystalline argyrodite in Figure 2 produce a work function very close to the value for the crystal. This suggests that electronic transport through LPSCl interfaces is easier than through alumina-LPSCl interfaces.

As prior X-ray photoelectron spectroscopy (XPS) results indicate a thin, but detectable, reaction layer formed at the alumina-LPSCl interface, they also need to consider electronic and ionic transport properties for reaction products that could be present at interfaces, depending on synthesis and processing conditions. Considering possible chemical reactivity between argyrodite and the alumina coatings, they have determined two compositions in the range between  $\text{Li}_6\text{PS}_5\text{Cl}$  and  $\text{Al}_2\text{O}_3$  corresponding to the points on the convex hull according to the following reactions:



Notably, LPSCl decomposition is found to be favorable, resulting in formation of  $\text{Li}_2\text{S}$  and lithiated aluminum oxides/sulfides. This result is consistent with the XPS results that indicate formation of a thin layer of  $\text{Li}_2\text{S}$  and reduced aluminum species (either  $\text{LiAlO}_x$  or  $\text{LiAlS}_x$ ) after ALD coating. Calculations of barriers for  $\text{Li}^+$  hopping through some of these interfacial phases, some of which could impede ionic transport, produce the lowest values

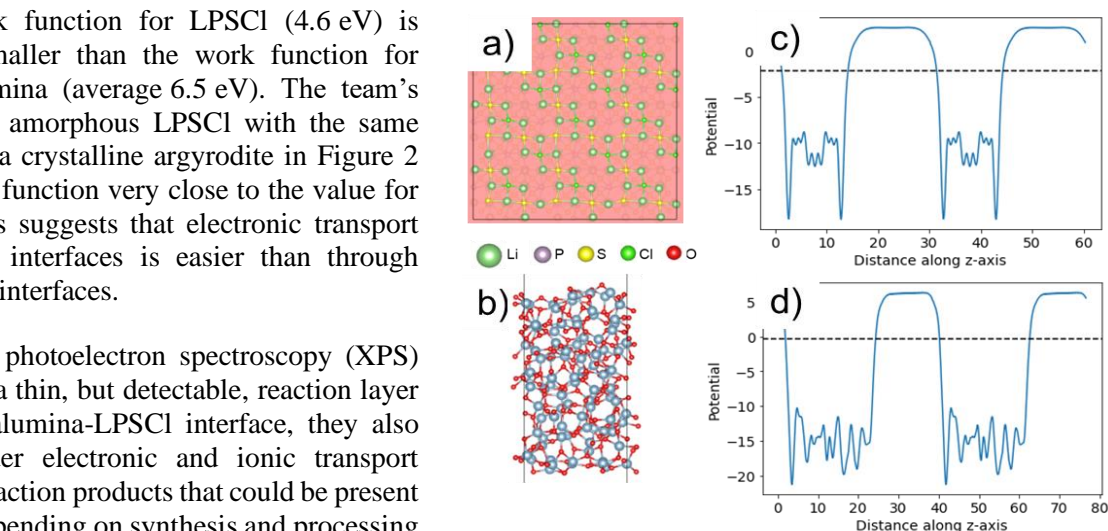


Figure 2. Computed structures of (a) argyrodite (001) surface (top view), and (b) amorphous alumina (side view) were used to determine work functions from (c-d) potential profiles normal to these surfaces, respectively. The Fermi levels are shown with dashed lines.

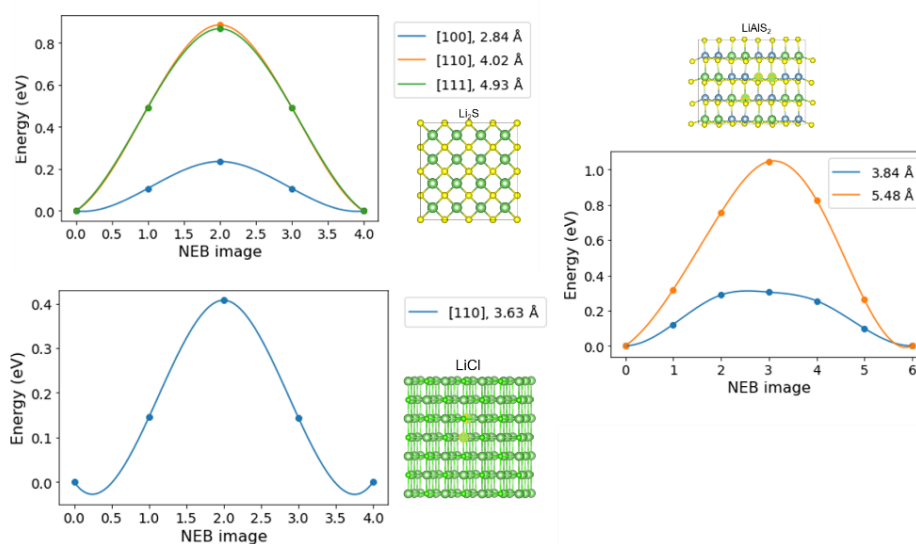


Figure 3. Calculated barriers for lithium hopping in several products of reaction of alumina with LPSCl indicate feasibility of lithium ionic transport through the interfacial layers.

for the barriers in  $\text{LiAlS}_2$ ,  $\text{LiCl}$ , and  $\text{LiS}_2$ , which range from about 0.2 eV to 0.4 eV (Figure 3). These relatively low transport barriers indicate the feasibility of lithium ionic transport through reaction products that may form at the interface between ALD alumina and LPSCI.

Taken together, these results provide a baseline for assessing potential coating chemistries for development via the team's ALD coating strategy. Electronic band structure, work functions, interface reaction enthalpies, and barriers for Li-ion transport will be assessed for candidate chemistries to further establish their contributions to possible space-charge layer formation at interfaces and resulting increases in interfacial impedance. Continued development of screening criteria for target chemistries and compositional distributions across the interfaces will target materials stability and electrochemical properties as well, providing a framework for design of new coatings that is guided by both computation and experiment.

### Patents/Publications/Presentations

The project has no patents, publications, or presentations to report this quarter.

## Task 1.2 – Electrolytes for High-Energy, All-Solid-State, Lithium-Metal Batteries (Guiliang Xu, Argonne National Laboratory)

**Project Objective.** The project objective is to develop ultrathin ( $< 30 \mu\text{m}$ ) sulfide solid-state electrolytes (SSEs) with high room-temperature ionic conductivity ( $> 0.01 \text{ S/cm}$ ) and high chemical/mechanical/electrochemical stability, and further integrate them with lithium metal and high-loading Se-doped sulfur cathodes through rational interface engineering to develop all-solid-state Li-S batteries (ASSLSBs) with high energy density and long cycle life.

**Impact.** The project is related to development and mass production of high-performance sulfide SSEs for high-energy all-solid-state Li-S pouch cells. The project's success in meeting or exceeding U. S. Department of Energy targets can promote practical implementation of Li-S battery in electric vehicles, electric aviation, and grid energy storage, and hence significantly reduce oil dependence and emissions of carbon dioxide. It can also mitigate the domestic supply challenge on the critical raw battery materials (for example, nickel and cobalt).

**Approach.** The thickness and chemical/interfacial stability of sulfide SSEs are the critical challenges for energy density, cycle life, and mass production of all-solid-state Li-S pouch cells. The team will combine innovative material design, electrode architecture fabrication, and advanced diagnostics tools to address these challenges. Specifically, the approaches include: (1) improving air stability and ionic conductivity of sulfides through synthetic control and cation/anion doping, and (2) fabrication of flexible thick SeS cathode supported thin sulfide electrolytes to ensure intimate contact and increase energy density, (3) stabilizing Li-metal/sulfide electrolytes interface via interlayer and additives design to increase critical current density of lithium stripping/plating, (4) advanced Li-S pouch-cell design, and (5) multiscale advanced diagnostic such as *in situ* X-ray diffraction (XRD), X-ray absorption spectroscopy, X-ray imaging, and focused ion beam – scanning electron microscopy to understand and overcome the degradation pathways.

**Out-Year Goals.** The out-year goals are to scale up the optimal sulfide SSEs to develop Ah-level all-solid-state Li-S pouch cells that can reach a cell energy density of  $> 500 \text{ Wh/kg}$  with 80% capacity retention for  $> 300$  cycles at a current density of  $> 1 \text{ mA/cm}^2$ .

**Collaborations.** The team is closely collaborating with top scientists at University of Chicago (X. Huang) and at Advanced Photon Source (C. Sun, W. Xu, D. Zhang, and J. Deng) and Center for Nanoscale Materials (Y. Liu and M. Chan) of Argonne National Laboratory for *in situ* diagnostics on the synthesis and aging mechanism of the proposed sulfide SSEs.

### Milestones

1. Set up a dedicated lab for synthesis, processing, and characterization of sulfide SSEs. (Q1, FY 2022; Completed)
2. Reveal the formation and degradation mechanism of sulfide SSE. (Q2, FY 2022; Completed)
3. Complete composition tuning of sulfide SSE. (Q3, FY 2022; Completed)
4. Develop doped sulfide SSE with high room-temperature ionic conductivity ( $> 1 \text{ mS/cm}$ ) and air stability. (Q4, FY 2022; Completed)

## Progress Report

In the last two quarters, the team has focused on efforts to synthesize  $\text{Li}_{1-x}\text{PS}_{5-x-y}\text{O}_y\text{Br}_{1+x}$ . The oxygen dopant is aimed to improve the air stability of argyrodite sulfide electrolytes, which, however, would cause reduction of ionic conductivity. Thus, they further increased the content of bromine to increase the percentage of site disorder and thus compensate the ionic conductivity. However, when simultaneously introducing oxygen and bromine, the synthesis process of pure phase  $\text{Li}_{1-x}\text{PS}_{5-x-y}\text{O}_y\text{Br}_{1+x}$  became more complex; in particular, a large amount of LiBr residue was found in the high-Br doping samples. To successfully dope oxygen and bromine in the  $\text{Li}_6\text{PS}_5\text{Br}$ , this quarter the team has developed a two-step calcination process to successfully synthesize pure phase  $\text{Li}_{5.5}\text{PS}_{4.5}\text{Br}_{1.5}$  and  $\text{Li}_{5.5}\text{PS}_{4.4}\text{O}_{0.1}\text{Br}_{1.5}$ .

In contrast to the team's previous one-step calcination process, in which the precursor mixture ( $\text{Li}_2\text{S}$ ,  $\text{LiBr}$ , and  $\text{P}_2\text{S}_5$ ) is directly heated from room temperature to 500-600°C, they pre-calcined the mixture at 300°C for 12 hours because their previous *in situ* XRD results showed that  $\text{Li}_6\text{PS}_5\text{Br}$  started to form at ~ 300°C. They then used *in situ* synchrotron XRD to monitor the phase transition process during heating of the pre-calcined mixture. As shown in Figure 4, before heating, the pre-calcined mixture shows clear XRD peaks that belong to  $\text{Li}_6\text{PS}_5\text{Br}$ . Meanwhile, signature XRD peaks of LiBr can be observed. During heating from 25°C to 550°C, all the peaks gradually shift to lower 2-theta degree, corresponding to thermal expansion. When the temperature is higher than 550°C, the (111), (200), (220), (311), (400), (331), (420), (422), (511), (531), and (442) peaks of LiBr suddenly disappear, accompanied by the emergence of (111), (200), (220), (311), (222), (422), (333), (440), (620), (533), (622), (642), and (553) peaks of  $\text{Li}_6\text{PS}_5\text{Br}$ . The results indicate that the pre-calcination step is important to successfully dope high bromine content into  $\text{Li}_6\text{PS}_5\text{Br}$  and synthesize pure-phase  $\text{Li}_{5.5}\text{PS}_{4.5}\text{Br}_{1.5}$ .

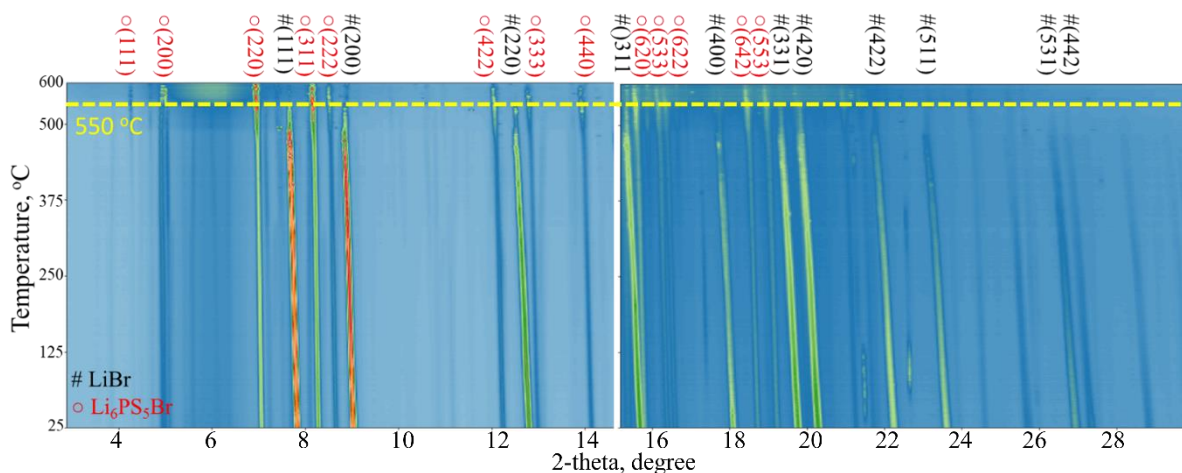


**Figure 4.** Contour plot of *in situ* X-ray diffraction (XRD) pattern during synthesis of  $\text{Li}_{5.5}\text{PS}_{4.5}\text{Br}_{1.5}$  from 25°C to 600°C. The heating rate is 5°C/min, and the time interval between two successive XRD patterns is 30 seconds. The colors represent intensity, with blue and red representing low and high, respectively.

The team further studied the case of  $\text{Li}_{5.5}\text{PS}_{4.4}\text{O}_{0.1}\text{Br}_{1.5}$ , in which both oxygen and bromine are introduced. Their previous experiment by single-step calcination showed a significant amount of LiBr residue. By sharp contrast, as shown in Figure 5, the synthesis of  $\text{Li}_{5.5}\text{PS}_{4.4}\text{O}_{0.1}\text{Br}_{1.5}$  via two-step calcination undergoes a similar process as that of  $\text{Li}_{5.5}\text{PS}_{4.5}\text{Br}_{1.5}$ . At a temperature of ~ 520°C, the formation of pure phase  $\text{Li}_{5.5}\text{PS}_{4.4}\text{O}_{0.1}\text{Br}_{1.5}$  is observed, indicating both oxygen and bromine have been successfully doped into  $\text{Li}_6\text{PS}_5\text{Br}$ .

They have conducted Rietveld refinement to compare the lattice parameters and percentage of site disorder in the  $\text{Li}_6\text{PS}_5\text{Br}$ ,  $\text{Li}_6\text{PS}_{4.8}\text{O}_{0.2}\text{Br}$ ,  $\text{Li}_{5.5}\text{PS}_{4.5}\text{Br}_{1.5}$ , and  $\text{Li}_{5.5}\text{PS}_{4.4}\text{O}_{0.1}\text{Br}_{1.5}$ . As shown in Figure 6, a higher amount of oxygen doping causes decrease of both lattice parameter and percentage of  $\text{Br}^+/\text{S}^{2-}$  site disorder, and hence would cause reduction of ionic conductivity. High bromine content could compensate for both lattice parameter and percentage of  $\text{Br}^+/\text{S}^{2-}$  site disorder and would thus improve ionic conductivity.

Furthermore, the team has investigated the effect of holding time on the crystal structures of final products during quenching or rapid cooling ( $\sim 30^\circ\text{C}/\text{min}$ ). Figure 7a shows the results of XRD patterns after holding at  $600^\circ\text{C}$  for 0.5 hours and rapid cooling to  $25^\circ\text{C}$ . A generation of new peaks belonging to LiBr is observed during rapid cooling, indicating holding at high-temperature for a short period of time is not enough to maintain the argyrodite crystal structure. By contrast, a process of 12-hour holding can lead to maintained pure phase  $\text{Li}_{5.5}\text{PS}_{4.4}\text{O}_{0.1}\text{Br}_{1.5}$  during rapid cooling (Figure 7b).

In brief, through the first year, the team has used *in situ* synchrotron XRD to reveal the formation mechanism of pure phase  $\text{Li}_{6-x}\text{PS}_{5-x-y}\text{O}_y\text{Br}_{1+x}$  as well as the relationship between synthetic conditions and bulk/local crystal structure. Next fiscal year, they will use these guidelines to accelerate development of  $\text{Li}_{6-x}\text{PS}_{5-x-y}\text{O}_y\text{Br}_{1+x}$  with both high ionic conductivity and air stability. They will also use the optimal electrolyte to achieve high sulfur utilization in ASSLSBs.

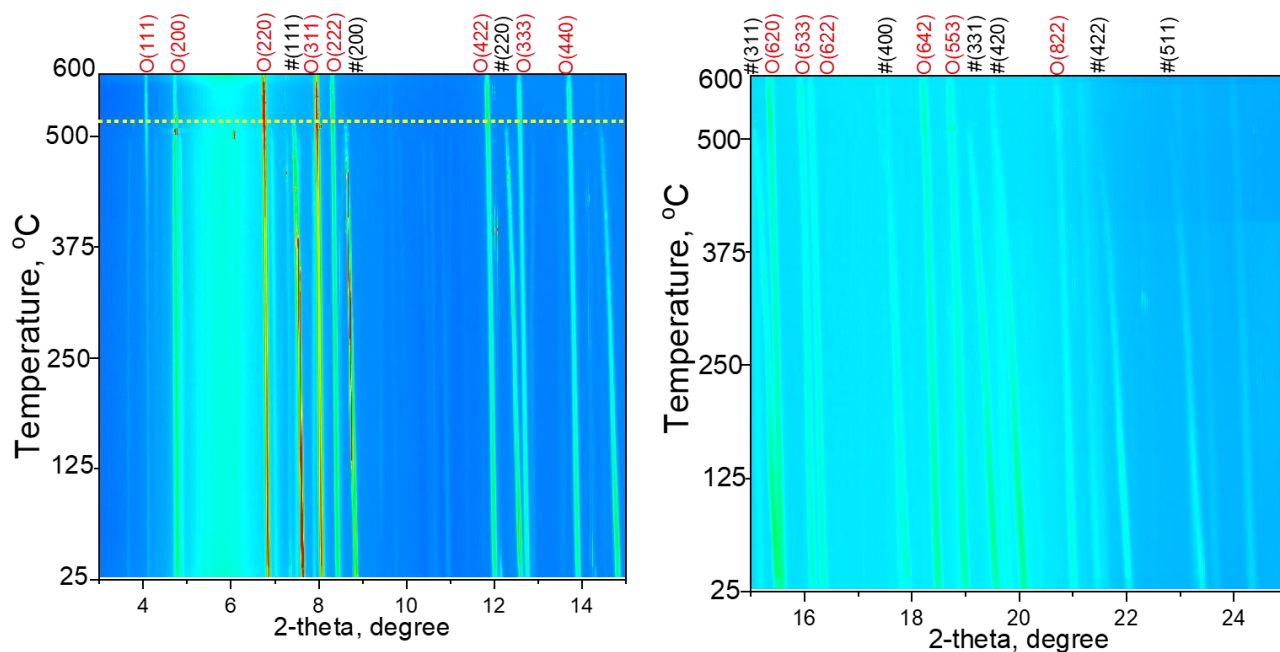


Figure 5. Contour plot of *in situ* X-ray diffraction (XRD) pattern during synthesis of  $\text{Li}_{5.5}\text{PS}_{4.4}\text{O}_{0.1}\text{Br}_{1.5}$  from  $25^\circ\text{C}$  to  $600^\circ\text{C}$ . The heating rate is  $5^\circ\text{C}/\text{min}$ , and the time interval between two successive XRD patterns is 30 seconds. The colors represent intensity, with blue and red representing low and high, respectively.

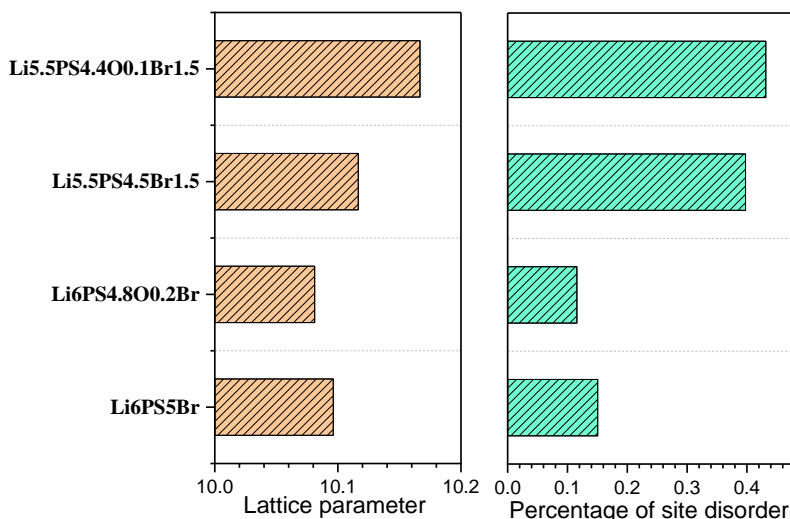


Figure 6. Comparison on the lattice parameter and percentage of site disorder of  $\text{Li}_6\text{PS}_5\text{Br}$ ,  $\text{Li}_6\text{PS}_{4.8}\text{O}_{0.2}\text{Br}$ ,  $\text{Li}_{5.5}\text{PS}_{4.5}\text{Br}_{1.5}$ , and  $\text{Li}_{5.5}\text{PS}_{4.4}\text{O}_{0.1}\text{Br}_{1.5}$ .

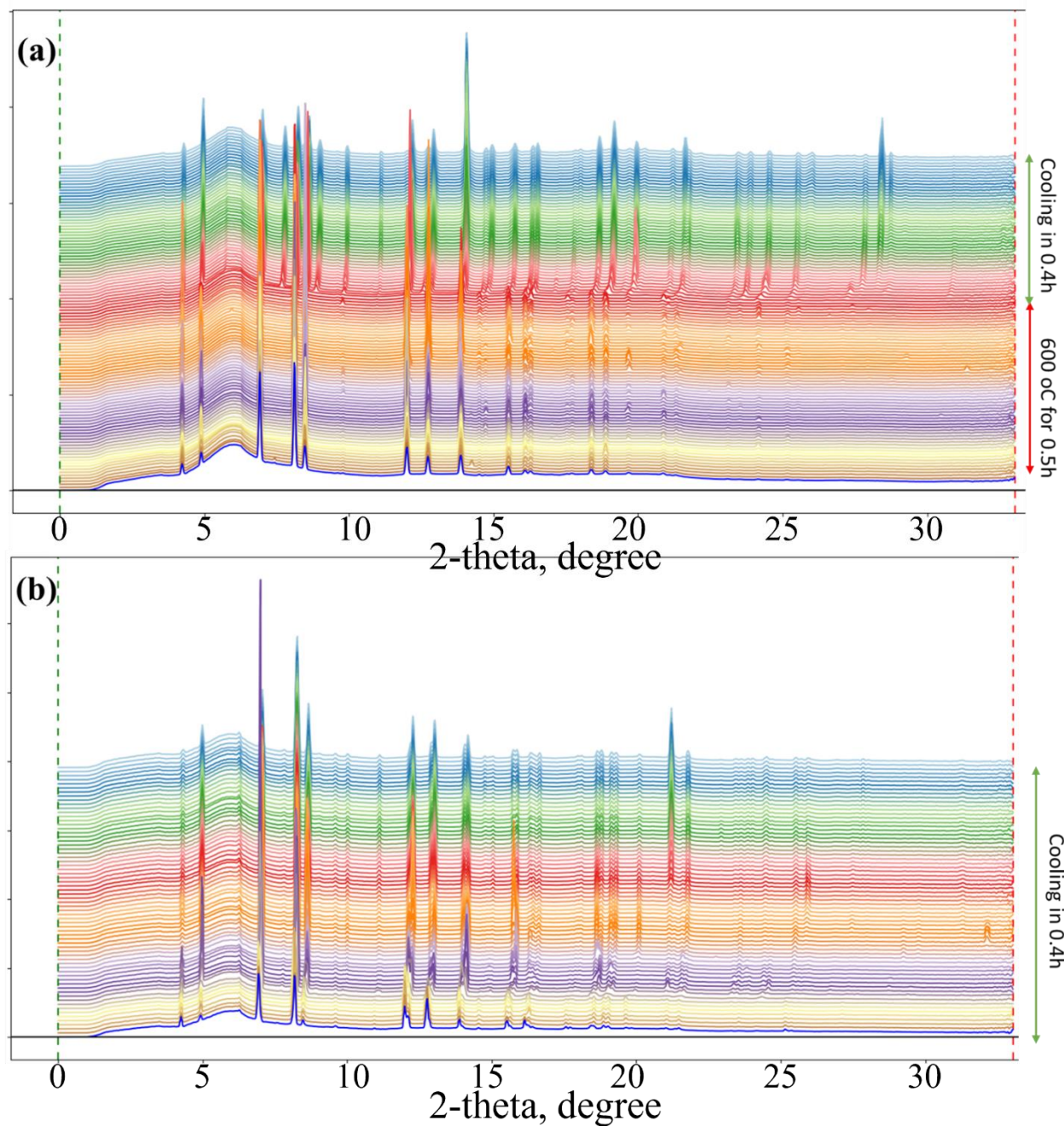


Figure 7. Effect of holding time on the crystal structures of final products during rapid cooling: (a) 0.5 hours, and (b) 12 hours.

## Patents/Publications/Presentations

### Presentation

- American Chemical Society Fall Meeting, Chicago, Illinois (August 21–25, 2022): “Probing the Degradation and Synthesis of Sulfides Solid Electrolytes by *In Situ* Synchrotron XRD”; G-L. Xu. Slide presentation.

## Task 1.3 – Thioborate Solid-State Electrolytes for Practical All-Solid-State Batteries (Yi Cui, Stanford University)

**Project Objective.** This project aims to develop novel lithium thioborates (Li-B-S, LBS) as a new class of solid-state electrolytes (SSEs) to realize high-performance all-solid-state batteries (ASSBs), with a particular focus on addressing the technical challenges in electrolyte synthesis, cell integration, failure diagnostics, and scale-up. The approach will be technologically transformative to the current solutions for ASSB development. For the final deliverables, ASSBs with the ability to reach an energy density of 500 Wh/kg and maintain 80% capacity for at least 300 cycles will be demonstrated.

**Impact.** The project approaches provide new directions toward developing high-conductivity and electrochemically stable sulfur-based electrolytes for ASSBs. Such high-performance electrolytes can enable the practical realization of ASSBs with a high energy density and improved safety.

**Approach.** The long-term project has a multistep approach toward integration of LBS with high-voltage cathodes, with steps 1-3 as the focus for this year:

1. Fabricate undoped LBS powders using an all-solid-state synthesis method to achieve high ionic conductivity, low electronic conductivity, and a wide operational voltage window.
2. Integrate LBS SSEs into symmetric Li/LBS/Li cells and into full batteries using high-voltage cathodes including lithium Ni-Mn-Co oxide.
3. Study atomic, particle, and cell-scale Li-metal-SSE interface development and dendrite growth mechanisms in SSEs using advanced characterization tools. Use knowledge to better develop SSEs and modify interfaces for stable cycling in full cells.
4. Fabricate doped LBS powders and develop particle/surface modifications to increase ionic conductivity as well as stability in full batteries and in air for glovebox-free synthesis.
5. Use density functional theory to guide development of new doped LBS materials and to explore interactions at solid-solid interfaces.

**Out-Year Goals.** In the following year, the team will develop solid-state reaction methods to synthesize undoped LBS powders and construct Li/LBS/Li symmetric cells to test the electrochemical performance of synthesized LBS. Meanwhile, the team will utilize advanced characterization tools [for example, cryogenic electron microscopy (cryo-EM), X-ray computed tomography (CT), etc.] to resolve the nanostructure of Li/LBS interphase and investigate the electrochemical stability between LBS and lithium metal.

**Collaborations.** The Y. Cui group is collaborating with W. Chueh's group (advanced characterization) and E. Reed's group (crystal structure computation) at Stanford University as well as with Y. Liu (advanced characterization) at SLAC National Accelerator Laboratory.

### Milestones

1. Develop solid-state reaction methods to synthesize undoped LBS powders with high ionic conductivity. (Q1, FY 2022; Completed)
2. Construct Li/LBS/Li symmetric cells for electrochemical characterizations. (Q2, FY 2022; Completed)
3. Study the evolution of Li/LBS interphase. (Q3, FY 2022; Completed)
4. Resolve the nanostructure of Li/LBS interphase using advanced characterizations (for example, cryo-EM, CT, etc.). Achieve ionic conductivity of LBS SSE of  $1.0 \times 10^{-3} \text{ S cm}^{-1}$ . (Q4, FY 2022; Completed)

## Progress Report

In a collaboration with the Reed group at Stanford, the team discovered that the theoretical ionic conductivity of LBS SSEs can reach  $74 \text{ mS cm}^{-1}$ . Motivated by these calculations and by the possibility of discovering a new class of SSEs made from earth-abundant elements, they are working to develop LBS SSEs with high ionic conductivity and high stability for application in full batteries. They have synthesized high-purity  $\text{Li}_{10}\text{B}_{10}\text{S}_{20}$  SSE with total resistance of  $220 \Omega$  and ionic conductivity of  $3.4 \times 10^{-4} \text{ S cm}^{-1}$  under 360 MPa pressure with stainless-steel electrodes. When in contact with lithium metal in a symmetric  $\text{Li-Li}_{10}\text{B}_{10}\text{S}_{20}\text{-Li}$  cell,  $\text{Li}_{10}\text{B}_{10}\text{S}_{20}$  is semi-stable, forming a slightly resistive interfacial layer (Figure 8a). The ionic conductivity remains stable over time in the  $\text{Li-Li}_{10}\text{B}_{10}\text{S}_{20}\text{-Li}$  cell, and the interfacial layer does not grow (Figure 8b).

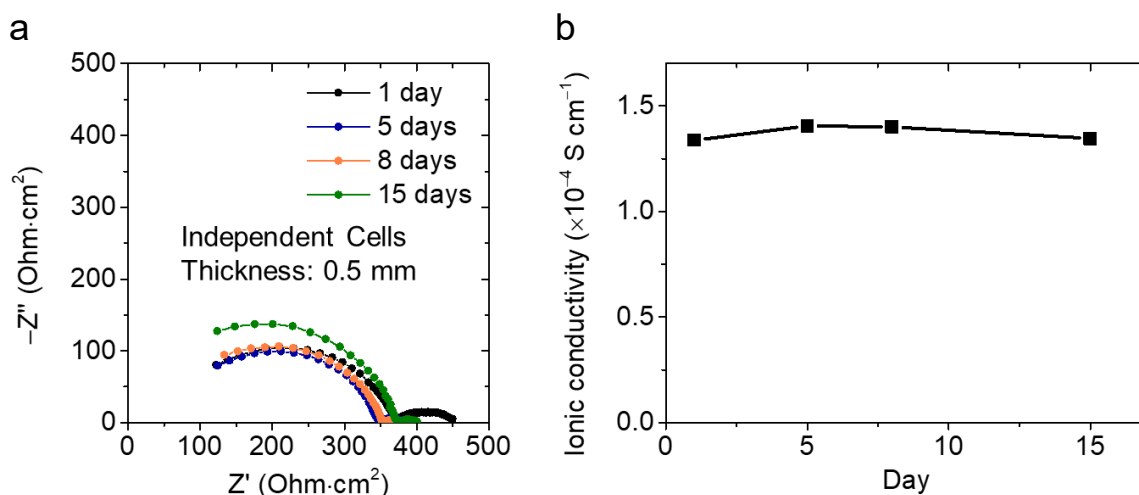


**Figure 8. (a) Nyquist plots of  $\text{Li-Li}_{10}\text{B}_{10}\text{S}_{20}\text{-Li}$  cells after rest from 1-15 days. (b) Ionic conductivity extrapolated from the Nyquist plots of the  $\text{Li-Li}_{10}\text{B}_{10}\text{S}_{20}\text{-Li}$  cells.**

To determine the suitability of  $\text{Li}_{10}\text{B}_{10}\text{S}_{20}$  as an SSE, the team has used X-ray photoelectron spectroscopy to analyze the species at the surface of  $\text{Li}_{10}\text{B}_{10}\text{S}_{20}$  before (Figure 9a-c) and after (Figure 9d-f) contact with lithium metal. They found that the new peaks appear after  $\text{Li}_{10}\text{B}_{10}\text{S}_{20}$  comes in contact with lithium (Figure 9d-f): in the boron 1s region, elemental boron appears, and in the lithium 1s and sulfur 2p regions,  $\text{Li}_2\text{S}$  peaks appear. Both boron and  $\text{Li}_2\text{S}$  peaks are small in comparison to  $\text{Li}_{10}\text{B}_{10}\text{S}_{20}$ , suggesting minimal reaction.

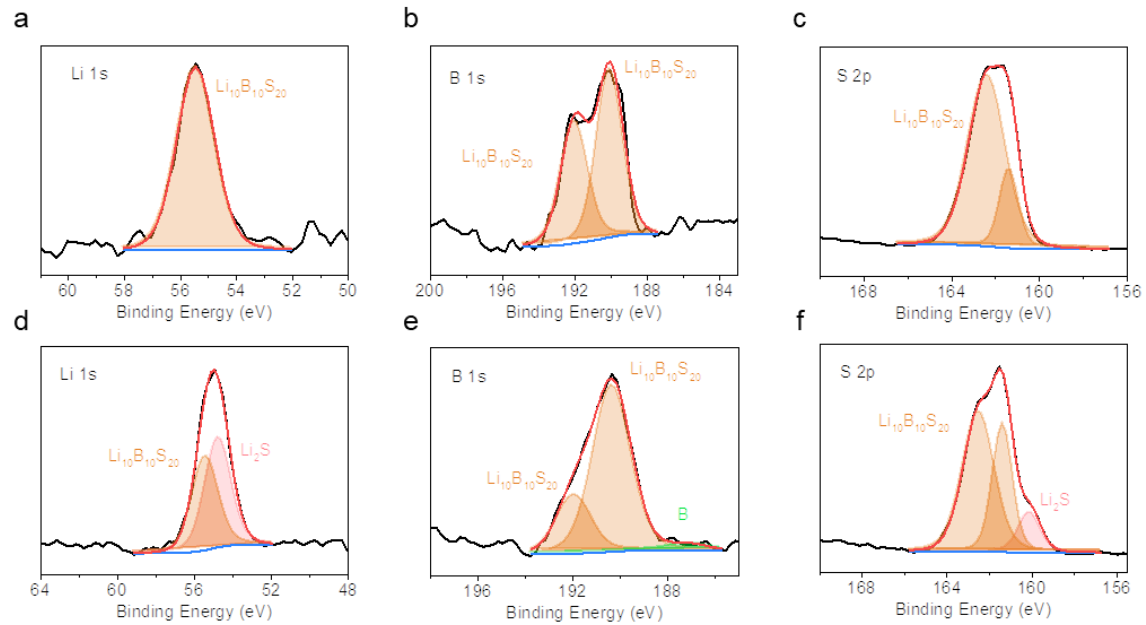


Figure 9. (a-c) X-ray photoelectron spectroscopy (XPS) of  $\text{Li}_{10}\text{B}_{10}\text{S}_{20}$  powder: (a) lithium 1s, (b) boron 1s, and (c) sulfur 2p. (d-f) XPS of  $\text{Li}_{10}\text{B}_{10}\text{S}_{20}$  powder after reaction with lithium metal: (d) lithium 1s, (e) boron 1s, and (f) sulfur 2p.

### Patents/Publications/Presentations

The project has no patents, publications, or presentations to report this quarter.

## Task 1.4 – Substituted Argyrodite Solid Electrolytes and High-Capacity Conversion Cathodes for All-Solid-State Batteries (Jagjit Nanda, SLAC Stanford Battery Research Center)

**Project Objective.** The project aims at synthesis and fabrication of Li-ion conducting argyrodite solid electrolytes (SEs) with nominal composition  $\text{Li}_6\text{PS}_5\text{X}$ , where X = chlorine and/or bromine. The team will combine alternating current impedance with complementary *in situ* spectroscopy and microscopy to identify buried interfacial side-reaction products and quantify the voltage losses associated with these side reactions. Specifically, they plan to investigate the interfacial reaction between various  $\text{Li}_6\text{PS}_5\text{X}$  SE and Li-ion cathodes belonging to different structural families [transition-metal-based sulfides and fluorides (for example,  $\text{FeS}_2$  and  $\text{FeF}_2$ ) and high-voltage layered oxides (for example,  $\text{LiNi}_{0.8}\text{Mn}_{0.1}\text{Co}_{0.1}\text{O}_2$ , NMC-811)]. New dopants such as niobium and partial substitution of sulfur with oxygen will be explored to improve stability of argyrodite SEs against lithium metal and high-voltage cathodes.

**Impact.** The proposed work addresses key technical barriers to achieve Li-metal solid-state batteries (SSBs) with energy densities of  $> 450 \text{ Wh/kg}$  and  $1,000 \text{ Wh/L}$ , which are critical for next-generation electric vehicles. Integrating new sulfide SEs prepared through scalable, low-cost solvent-mediated routes with high capacity, earth abundant conversion cathodes (for example, sulfur,  $\text{FeF}_3$ , and  $\text{FeS}_2$ ) will lower SSB cost to  $\$80/\text{kWh}$  and eliminate use of critical materials such as cobalt and nickel.

**Approach.** Scalable solution-based processing routes will be developed to produce freestanding sulfide/binder solid-state separators with thicknesses  $< 50 \mu\text{m}$  and area specific resistance  $< 50 \Omega \text{ cm}^2$ . These ultrathin separators will be integrated with Li-metal anodes and high areal capacity conversion cathodes (for example, sulfur,  $\text{FeS}_2$ , and  $\text{FeF}_3$ ) to demonstrate lab-scale prototype SSBs. As a cross-cut activity, various *in situ* and *ex situ* passivation methods will be combined with enabling characterization techniques to facilitate  $\text{Li}^+$  transport across electrode/SE interfaces.

**Out-Year Goals.** Optimize SSB performance by: (1) varying cathode composition, particle size, and porosity, (2) applying halide-rich and carbon layers at electrode/electrolyte interfaces, and (3) evaluating how stack pressure (0.1-10 MPa) and temperature (25-75°C) impact performance. Targets: room-temperature cycling with areal capacities  $> 5 \text{ mAh/cm}^2$ , current densities  $> 2 \text{ mA/cm}^2$ , stack pressures  $< 1 \text{ MPa}$ , and  $< 20\%$  capacity fade over 300 cycles.

**Collaborations.** D. Hallinan and his group are funded collaborators to develop the binder system for sulfide SEs and evaluate compatibility with cathode and Li-metal. P. Jena from Virginia Commonwealth University will be an unfunded collaborator on density functional theory modeling of bulk Li-ion transport and *ab initio* molecular dynamics at SE interfaces.

### Milestones

1. Produce  $\text{Li}_6\text{PS}_5\text{X}$  (X = Cl, Br, I) SEs using solvent-mediated routes with ionic conductivity  $\geq 1 \times 10^{-3} \text{ S/cm}^{-1}$  at room temperature. (Q1, FY 2022; Completed)
2. Optimize synthesis and annealing conditions to obtain phase-pure SE  $\text{Li}_6\text{PS}_5\text{X}$  powders. Evaluate structure using X-ray diffraction, Raman, and neutron scattering. (Q2, FY 2022; Completed)
3. Compare the structure and  $\text{Li}^+$  conductivity of  $\text{Li}_6\text{PS}_5\text{X}$  prepared through solvent-mediated versus mechano-chemical and solid-state routes. (Q3, FY 2022; Completed)
4. Integrate SSB using  $\text{Li}_6\text{PS}_5\text{X}$  SE with a working cathode and thin Li-metal anode for testing and capacity optimization. (Q4, FY 2022; Completed)

## Progress Report

Activities this quarter explored how different SEs impact the performance of SSBs containing composite NMC-811 cathodes. Unlike conventional sulfide SEs (for example,  $\beta$ - $\text{Li}_3\text{PS}_4$ , LPS), which are unstable at potentials  $>$  ca. 2.6 V versus  $\text{Li}/\text{Li}^+$ , halide-containing compositions, such as  $\text{Li}_6\text{PS}_5\text{Cl}$  (LPSCl) and  $\text{Li}_3\text{InCl}_6$  (obtained through a collaboration with R. Sacci's group at Oak Ridge National Laboratory), have outstanding oxidative stability, which is anticipated to facilitate formation of stable NMC/SE interfaces. As shown in Figure 10a-b, the team evaluated pellet-type cells containing: (i) a single-layer sulfide separator and catholyte (LPSCl), and (ii) a bilayer sulfide/halide LPSCl/ $\text{Li}_3\text{InCl}_6$  separator and  $\text{Li}_3\text{InCl}_6$  catholyte. The composite cathodes were prepared by blending NMC-811 (uncoated), SE powder (either LPSCl or  $\text{Li}_3\text{InCl}_6$ ), and carbon nanofibers on a Turbula T2F shaker. The cathodes were tested against In-metal anodes where the  $\text{Li}_x\text{In}$  alloy ( $0 < x < 1$ ) was electrochemically formed *in situ* during charging. Similar cells containing Li-metal anodes were also prepared and tested, but these results are not shown here due to internal shorts caused by lithium dendrites when the current density exceeded  $100 \mu\text{A}/\text{cm}^2$ .

Figure 10c-d shows the galvanostatic voltage profiles for SSBs containing single-layer (LPSCl) and bilayer (LPSCl+ $\text{Li}_3\text{InCl}_6$ ) separators, respectively. The voltage profiles suggest the charge compensation is almost entirely through NMC-811 active material, and neither LPSCl nor  $\text{Li}_3\text{InCl}_6$  exhibited significant oxidative decomposition during charge steps. The initial reversible capacity of the LPSCl cell was 13% higher than that of the LPSCl+ $\text{Li}_3\text{InCl}_6$  cell (161 mAh/g<sub>NMC</sub> and 142 mAh/g<sub>NMC</sub>, respectively), possibly due to the higher  $\text{Li}^+$  conductivity of LPSCl ( $\sim 2 \text{ mS}/\text{cm}$  at room temperature versus  $0.5 \text{ mS}/\text{cm}$  for  $\text{Li}_3\text{InCl}_6$ ). Both cells exhibited significant capacity fade and retained only  $\sim 25 \text{ mAh}/\text{g}_{\text{NMC}}$  after 40 cycles (see Figure 10e). Interestingly, the cells' operating voltage gradually increased during cycling due to the cumulative irreversible capacity losses that were potentially caused by: negative drifting of the  $\text{Li}_x\text{In}$  anode potential and/or positive drifting of the cathode's state of charge. After 40 cycles, the LPSCl and LPSCl+ $\text{Li}_3\text{InCl}_6$  cells had cumulative irreversible capacity losses of 2.04 mAh and 1.58 mAh, respectively. These losses correspond to anode stoichiometries of  $\text{Li}_{0.12}\text{In}$  and  $\text{Li}_{0.09}\text{In}$ , respectively, indicating the anodes remained within desired In/ $\text{Li}_x\text{In}$  two-phase region ( $0 < x < 1$ , 0.622 V versus  $\text{Li}/\text{Li}^+$ ) throughout the experiments. As such, the cells' potential drift during cycling was due to lithium inventory loss in the NMC active material. More specifically, the total irreversible capacity was 194 mAh/g<sub>NMC</sub> and 150 mAh/g<sub>NMC</sub> for the LPSCl and LPSCl+  $\text{Li}_3\text{InCl}_6$  cells, respectively. It is important to note the team used the same stack pressure for comparing the performance (Figure 10) for bilayer versus single-layer separators. It is possible that  $\text{Li}_3\text{InCl}_6$  separator and the catholyte require higher stack pressure for optimal performance.

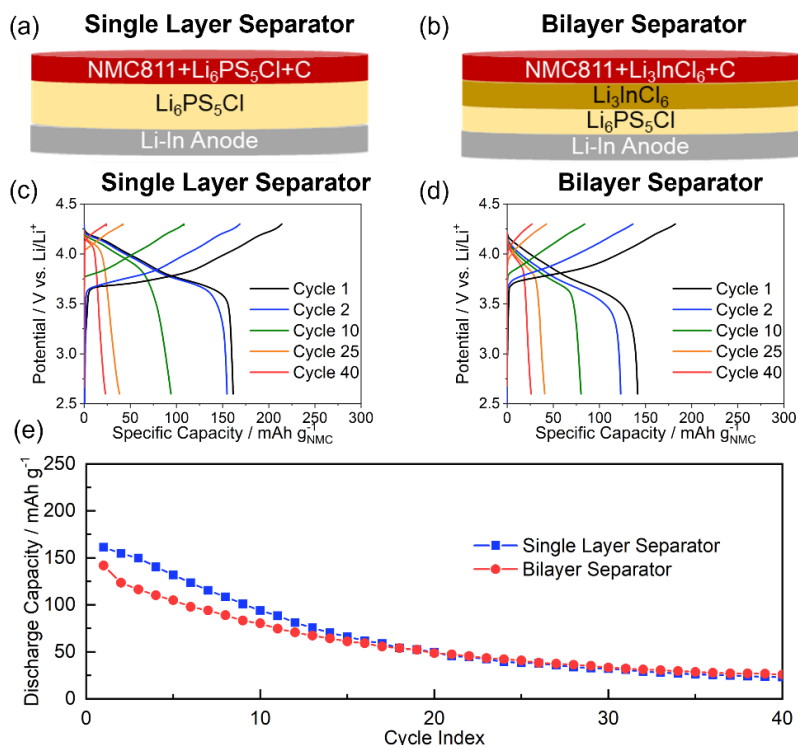


**Figure 10.** Electrochemical performance of solid-state batteries containing NMC-811 composite cathodes and  $\text{Li}_x\text{In}$  anodes. (a-b) Schematics of the cell designs. Voltage profiles for cells containing (c) single-layer  $\text{Li}_6\text{PS}_5\text{Cl}$  and (d) bilayer  $\text{Li}_6\text{PS}_5\text{Cl}/\text{Li}_3\text{InCl}_6$  separators. (e) Discharge capacity over 40 cycles. Cells were cycled by polarizing the cathode between 2.6 V – 4.3 V versus  $\text{Li}/\text{Li}^+$  at a constant current of  $\pm 66 \mu\text{A}/\text{cm}^2$  (cycle 1) and  $\pm 127 \mu\text{A}/\text{cm}^2$  (cycles 2-40). Due to the use of  $\text{Li}_x\text{In}$  anodes, potentials were referenced against  $\text{Li}/\text{Li}^+$  by adding 0.622 V to the measured cell potential.

Overall, these results demonstrate that incorporating oxidatively stable SEs in composite cathodes does not necessarily ensure formation of robust NMC/SE interfaces, and cumulative irreversible capacity losses in such cells can yield rapid performance decline. Rather than SE decomposition, the capacity fade in LPSCI-based and  $\text{Li}_3\text{InCl}_6$ -based SSBs is most likely due to active material isolation resulting from repeated volume changes during cycling. As such, an additional understanding of the mechanics of solid-solid interfaces will be critical to address key performance bottlenecks for Li-metal SSBs. Work in the next fiscal year will explore this topic by investigating how stack pressure and cathode composition (for example, carbon/SE content and particle morphology) impact cycling stability for cells prepared with argyrodite and/or halide SEs.

## Patents/Publications/Presentations

### Publication

- Self, E. C., W-Y. Tsai, A. S. Westover, K. L. Browning, G. Yang, and J. Nanda. “Benchmarking Solid-State Batteries Containing Sulfide Separators: Effects of Electrode Composition and Stack Pressure.” *Journal of Electrochemical Society* 169 (2022): 100510.
- Yang, G., E. C. Self, T. Brahmabhatt, A. Mills, W-Y. Tsai, D. T. Hallinan, X. Chen, F. M. Delnick, and J. Nanda. “Development of Argyrodite-Based Sulfide Electrolytes for Next-Generation Solid-State Li Batteries.” In *ECS242 Meeting Abstracts*, 202. Atlanta: Electrochemical Society, 2022.

## Task 1.5 – Stable Solid-State Electrolyte and Interface for High-Energy, All-Solid-State, Lithium-Sulfur Battery (Dongping Lu, Pacific Northwest National Laboratory)

**Project Objective.** The project objective is to address material and interfacial barriers of sulfide-based solid-state electrolyte (S-SSE) for deep cycling of Li-metal anode in all-solid-state lithium batteries (ASSLBs). All proposed work will be focused on development of highly conductive sulfide  $\text{Li}^+$  conductors with extremely low Li/SSE interfacial resistance and ultrathin multifunctional interlayer to enable deep and stable lithium cycling. The solid electrolytes (SEs) and interlayer assembly achieved in the project will be tested at practical conditions and validated in realistic Li-S pouch cells.

**Impact.** ASSLBs have the potential to achieve higher energy and power densities, extending the range of electric vehicles (EVs) and reducing charging time simultaneously. The success of the project would advance the research and deployment of superionic SEs and protective Li-compatible interlayers to support the U. S. Department of Energy Vehicle Technologies Office target of developing next-generation ASSLBs for EVs, accelerating market acceptance of long-range EVs required by the EV Everywhere Grand Challenge.

**Approach.** The project proposes the following approach: (1) to develop Li-compatible superionic S-SSEs and effective coating approaches, (2) to stabilize Li/SSE interface by employing a multifunctional interlayer, (3) to enable robust  $\text{Li}^+/\text{e}^-$  mixed conduction network for a high-loading sulfur cathode, (4) to develop dry processing for SSE film, cathode, and interlayer fabrication, and (5) to advance the mechanism study of the sulfur cathode, lithium anode, and interfaces by multiscale characterization and multiscale modeling.

**Out-Year Goals.** This project has the following out-year goals:

- Development of Li-metal-compatible S-SSEs with Li/SSE interfacial resistance  $< 5 \Omega \text{ cm}^2$  and room-temperature  $\text{Li}^+$  conductivity  $> 5 \text{ mS/cm}$ .
- Operation of lithium anode at critical current density (CCD)  $> 1 \text{ mA/cm}^2$ , and lithium cycling for at least 400 cycles.
- Ultrathin multifunctional interlayer to enable deep lithium cycling  $> 4 \text{ mAh/cm}^2$  to couple high areal-capacity cathode.
- Dry processing of an SSE/interlayer assembly with an overall ionic conductivity  $> 1 \text{ mS/cm}$ .
- Validation of the S-SSE, high-areal capacity cathode, and bilayer assembly in a realistic Li-S pouch cell.

**Collaborations.** This project engages in collaboration with the following: D. Y. Qu (University of Wisconsin, Madison), Z. K. Liu (Pennsylvania State University), C. M. Wang and J. Bao (Pacific Northwest National Laboratory), H. Du (Ampcera Inc.), and Z. Liu (Thermo Fisher Scientific).

### Milestones

1. Synthesis of lithium halides doped S-SSE to realize low Li/SSE areal interfacial resistance (AIR,  $< 5 \Omega \text{ cm}^2$ ) and high room-temperature  $\text{Li}^+$  conductivity ( $\sigma \sim 6 \text{ mS/cm}$ ). (Q1, FY 2022; Completed)
2. Development of surface treatment approach to improve moisture stability of S-SSE. (Q2, FY 2022; Completed)
3. Optimization, characterization, and simulation of Li/SSE interface and its dynamics. (Q3, FY 2022; Completed)
4. Optimization of external pressure to improve CCD ( $> 1 \text{ mA/cm}^2$ ) and Li/SSE/Li cycle life ( $> 400$  cycles). (Q4, FY 2022; Completed)

## Progress Report

This quarter, the team studied the interfacial stability of halide-doped S-SSEs ( $\text{Li}_7\text{P}_2\text{S}_8\text{Br}_{1-x}\text{I}_x$ ,  $0 \leq x \leq 1$ ) against lithium metal and its capability of supporting long-term cycling of Li/SSE/Li symmetrical cell.

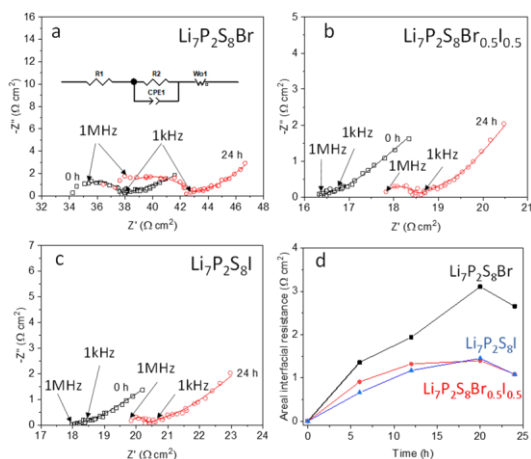


**Figure 11.** Nyquist plots of (a) Li/Li<sub>7</sub>P<sub>2</sub>S<sub>8</sub>Br/Li, (b) Li/Li<sub>7</sub>P<sub>2</sub>S<sub>8</sub>Br<sub>0.5</sub>I<sub>0.5</sub>/Li, and (c) Li/Li<sub>7</sub>P<sub>2</sub>S<sub>8</sub>I/Li cells with equivalent circuit fitting at 20°C. (d) Evolution of areal interfacial resistance of each cell with time at 20°C.

24 hours is only  $1.09 \Omega \text{ cm}^2$  and  $1.08 \Omega \text{ cm}^2$ , respectively. Moreover, both SSEs with LiI ( $\text{Li}_7\text{P}_2\text{S}_8\text{Br}_{0.5}\text{I}_{0.5}$  and  $\text{Li}_7\text{P}_2\text{S}_8\text{I}$ ) display an exceptionally stable and low AIR, indicating that the presence of LiI facilitates building a superior stable and highly  $\text{Li}^+$  conductive solid electrolyte interphase.

Thanks to the stable and low-resistance SSE/Li interface featuring a LiI-rich interface, the  $\text{Li}_7\text{P}_2\text{S}_8\text{Br}_{0.5}\text{I}_{0.5}$  enables long-term lithium cell cycling at different conditions. Figure 12a shows cycling performance of a Li/Li<sub>7</sub>P<sub>2</sub>S<sub>8</sub>Br<sub>0.5</sub>I<sub>0.5</sub>/Li cell at 20°C at  $0.5 \text{ mA cm}^{-2}$  with a charge/discharge capacity of  $0.25 \text{ mAh cm}^{-2}$ . No sign of shorting is observed throughout the cycling of 1000 hours. Stable cell cycling (1000 hours) is also achieved at 60°C at  $1 \text{ mA/cm}^2$  with a charge/discharge capacity of  $0.5 \text{ mAh cm}^{-2}$  and at 100°C at  $2 \text{ mA/cm}^2$  with charge/discharge capacity of  $1 \text{ mAh cm}^{-2}$ . Both the high ionic conductivity and the low interfacial resistance suggest that  $\text{Li}_7\text{P}_2\text{S}_8\text{Br}_{0.5}\text{I}_{0.5}$  is a promising SSE for all-solid-state Li-metal batteries.

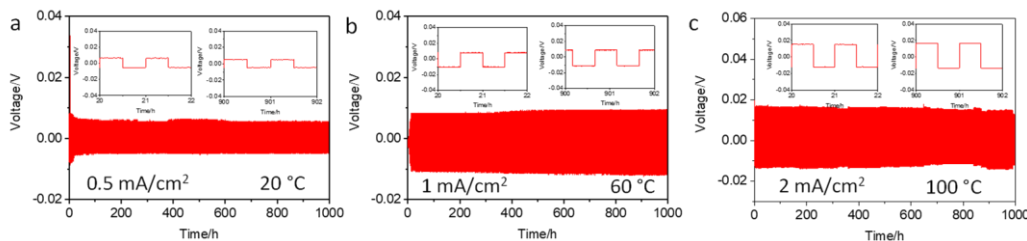


**Figure 12.** (a-c) Long-term cycling of a Li/Li<sub>7</sub>P<sub>2</sub>S<sub>8</sub>Br<sub>0.5</sub>I<sub>0.5</sub>/Li cell at (a)  $0.5 \text{ mA/cm}^2$  with a charge/discharge capacity of  $0.25 \text{ mAh cm}^{-2}$  at 20°C, (b)  $1 \text{ mA/cm}^2$  with a charge/discharge capacity of  $0.5 \text{ mAh cm}^{-2}$  at 60°C, and (c)  $2 \text{ mA/cm}^2$  with a charge/discharge capacity of  $1 \text{ mAh cm}^{-2}$  at 100°C.

## Patents/Publications/Presentations

### Patent

- Yu, Z., and D. Lu. Lithium-Metal Compatible Solid-State Electrolyte for All-Solid-State Battery. Patent Application, no. 17/945,447, no. PCT/US2022/043609.

### Publication

- Strange, L. E., M. H. Engelhard, Z. Yu, and D. Lu. “Li<sub>7</sub>P<sub>2</sub>S<sub>8</sub>Br<sub>0.5</sub>I<sub>0.5</sub> (LPSBI) Solid State Electrolyte by XPS.” *Surface Science Spectra* 29 (2022). doi: <https://doi.org/10.1116/6.0001963>.

### Presentation

- American Chemical Society Fall Meeting, Chicago, Illinois (August 22–25, 2022): “Highly Conductive and Li Stable Sulfide Solid-State Electrolytes for All-Solid-State Li Battery”; Z. Yu, D. Marty, and D. Lu.

## Task 1.6 – Development of Thin, Robust, Lithium-Impenetrable, High-Conductivity, Electrochemically Stable, Scalable, and Low-Cost Glassy Solid Electrolytes for Solid-State Lithium Batteries (Steve Martin, Iowa State University of Science and Technology)

**Project Objective.** The project objective is to develop new Li<sup>+</sup>-conducting mixed oxy-sulfide nitride (MOSN) glassy solid electrolytes (GSEs) that are impermeable to lithium dendrites, have high conductivities, are scalable through low-cost glass manufacturing, are chemically and electrochemically stable, and will enable low-cost, high-energy-density all-solid-state lithium batteries (ASSLBs). The ASSLBs constructed from these new GSEs will meet and exceed all program objectives: usable specific energy @ C/3  $\geq$  350 Wh/kg, calendar life of 15 years, cycle life (C/3 deep discharge with < 20% energy fade) of 1000, and cost  $\leq$  \$100/kWh.

**Project Impact.** This project will enable the team to demonstrate the following: (1) thin MOSN GSE films yield superior performance in a much safer, lower-cost, and Li-dendrite impenetrable form, and (2) high rate and long cycle life can be achieved in ASSLBs using thin-film MOSN GSEs. The new GSEs in ASSLBs are anticipated to increase energy density (anode basis) from  $\sim$  300 mAh/g to  $\sim$  4,000 mAh/g, enabling replacement of internal combustion engines in both light-duty and heavy-duty vehicles. Each 20% reduction in the  $\sim$  1.6 billion l of gasoline used per day in the United States would reduce CO<sub>2</sub> emissions by  $\sim$  4 billion kg or  $2 \times 10^{12}$  l of CO<sub>2</sub> per day. The team will also increase scientific and engineering knowledge of thin-film GSEs in ASSLBs.

**Approach.** The MOSN mixed glass former (MGF) glasses used for the GSEs in this project were developed in previous work to have the necessary thermal stability and high ionic conductivity for successful use as a drawn-film electrolyte. In this project, the glass chemistry will be tuned for even more desirable properties, by investigating structure-property relationships and testing variations in glass chemistry.

**Out-Year Goals.** Work will progress toward developing a glass capable of being drawn to 100- $\mu$ m thickness, while having high conductivity and electrochemical stability and good cycling ability.

**Collaborations.** The team is collaborating with S. Kalnaus and G. Veith (Oak Ridge National Laboratory) on the physical and mechanical properties of oxy-nitride glasses and with Y. Cui (Stanford University) and A. Sendek (Avionics) on new classes of polycrystalline lithium thioborate solid electrolyte. The team is also collaborating with T. Versak (General Motors) on testing of the GSEs in their solid-state cells.

### Milestones

1. Accomplish: Large MOSN MGF GSE preforms (10 cm  $\times$  0.5 cm  $\times$  30 cm) demonstrate < 1 vol% crystallization at 90°C above the glass transition temperature. (Q1, FY 2022; Completed)
2. Accomplish: Optimize draw conditions for MOSN GSE to achieve 5 m  $\times$  5 cm  $\times$  < 50  $\mu$ m thin films. (Q2, FY 2022; In progress)
3. Accomplish: Fabricate MOSN MGF Li|GSE|Li cells in intermediate area format,  $\sim$  2 cm<sup>2</sup>. (Q3, FY 2022; In progress)
4. *Go/No-Go Decision*: Fabricate MOSN MGF GSE cells in large format  $\sim$  5 cm<sup>2</sup>. Cells achieve targeted performance metrics. Analysis indicates technical approach capable of achieving performance targets. (Q4, FY 2022; In progress)

## Progress Report

### Optimized High Li<sup>+</sup> Conductivity MOSN MGF GSEs: Develop Preforms that do not Crystallize

Solid-state magic-angle spinning nuclear magnetic resonance (NMR) and X-ray photoelectron spectroscopy (XPS) were conducted on samples of the ISU-6 composition studied in previous reports. NMR and XPS were utilized to study and compare the structure and chemical composition of the bulk glass preform as synthesized and the thin drawn films. As seen in Figure 13, the composition analysis based on both NMR and XPS shows that the sulfur content is a bit lower and the oxygen content a bit higher than anticipated through the massed-out chemistry. This could be due to a minor reaction during the melting and remelting process or a slight contamination in the starting materials. However, the elemental analysis of other elements, (that is, lithium, silicon, phosphorus, and oxygen) appears to be within what is expected, with no systematic change observed when the thickness decreases, indicating that no significant compositional changes occur to the glass during the thin film drawing process.

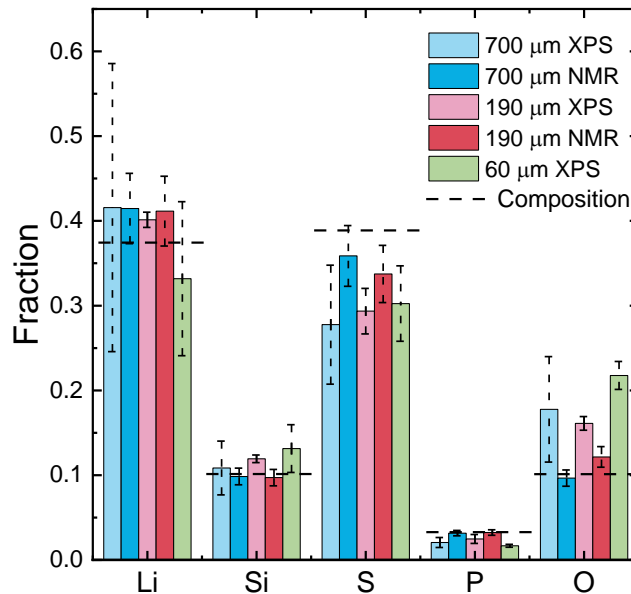


**Figure 13. Compositional analysis of bulk and drawn thin film ISU-6 via X-ray photoelectron spectroscopy (XPS) and nuclear magnetic resonance (NMR). NMR values were determined through fitting of the NMR spectra and charge compensation. XPS values were determined through survey scans after argon etching. Error bars for XPS are the standard deviation of two depth scans, while they are 10% of the value for the NMR.**

### Micro-Sheet Glass Ribbon Processing Facility for GSEs: Develop and Optimize

No work was done to further optimize the processing facility this quarter. Efforts focused on optimizing the process itself.

### Processing Conditions Micro-Sheet Ribbons of MOSN MGF GSEs: Optimize Draw Conditions for Optimized MOSN MGF GSEs < 50 μm

While concurrently synthesizing more glass for a new preform, a draw was attempted on an old preform made earlier. While this did not generate a large quantity of thin film, this draw did produce some MOSN GSE thin film on which the team has begun initial testing. An image of a piece of this 60-μm film is shown in Figure 14. Sections of this film were taken for characterization. X-ray diffraction confirmed that no Bragg reflections are shown other than a diffuse amorphous peak, indicating that the film is still vitreous.

After this draw, newly synthesized glass and the remainder of the previous preform were combined and melted into a new preform. This larger preform has presented a few issues, particularly with respect to thermal shock causing the preform to break prior to the draw starting. A possible solution has been tested by opening the furnace baffles to reduce the temperature gradient experienced by the preform, and this has shown promise. More work is being done to generate a large quantity of sub-50- $\mu\text{m}$  film and to overcome recently experienced issues.

### ASSLBs using GSEs in Large Area Planar Formats: Test Optimized MOSN MGF GSE in Intermediate Cell Format ASSLBs

Full-cell cycling of the batteries constructed with the ISU-6 chemistry as the GSE continued. A full 100 cycles of galvanostatic cycling with potential limits have recently been completed on a full cell at a rate of  $C/50$ . This cell architecture used a Li-foil anode, a bulk piece ( $\sim 1$  mm thick) of ISU-6 as the electrolyte, and a tape-cast  $\text{LiFePO}_4$  composite film as the cathode. At the electrolyte-cathode interface,  $0.5 \mu\text{L}$  of a triglyme+LiTFSI salt complex was added to ease ion transport across the solid-solid interface. Under these conditions, the cell had a specific capacity of over 100  $\text{mAh/g}$  at the beginning and maintained Coulombic efficiency (CE) over 99% for most of the cycling. Fluctuations in the specific capacity and CE due to accidental machine shutdowns and temperature fluctuations within the lab can be observed in Figure 15. Additionally, the cell shows a significant continuous decrease in its specific capacity during cycling, the causes of which have been investigated.



Figure 14. Image of 60- $\mu\text{m}$  thin film in a micrometer.

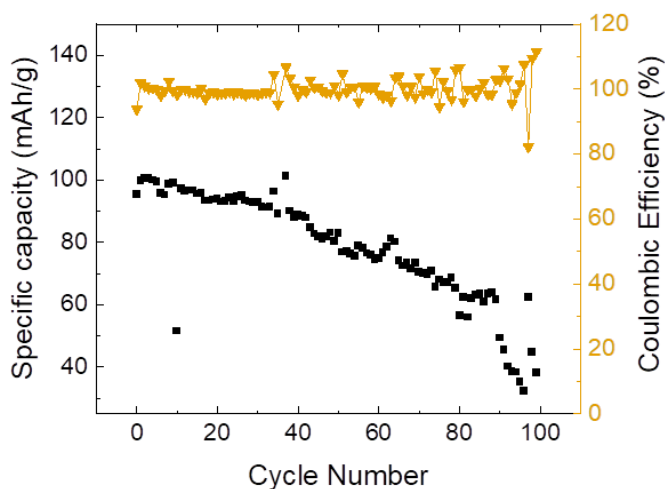


Figure 15. Galvanostatic cycling of a Li | ISU-6 | composite cathode film full cell at  $C/50$ .

In a continued effort to develop these full-cell architectures using the project's MOSN GSEs, progress has been made toward investigating cell degradation mechanisms due to cycling. Li | GSE | composite cathode film cells were prepared and cycled at  $C/20$  for 100 cycles. Pre- and post-mortem Raman spectroscopy was performed on both the GSE and the tape-cast composite cathode film. It was noted that no major chemical changes were seen in the GSE, shown in Figure 16a, from cycling. A growth in the D-band of the carbon doublet

~ 1500 wavenumbers was observed in the cathode film due to cycling, as seen in Figure 16b. The magnitude of this carbon band is often attributed to defects and disorder within the carbon structure; therefore, a growth in its magnitude implies that the carbon within the cathode is accumulating defects during cycling. From these data, it is proposed that one of the mechanisms for capacity fade within these constructed full cells is a continued breakdown of the structure of the cathode, leading to loss of conduction pathways and tri-junction points.

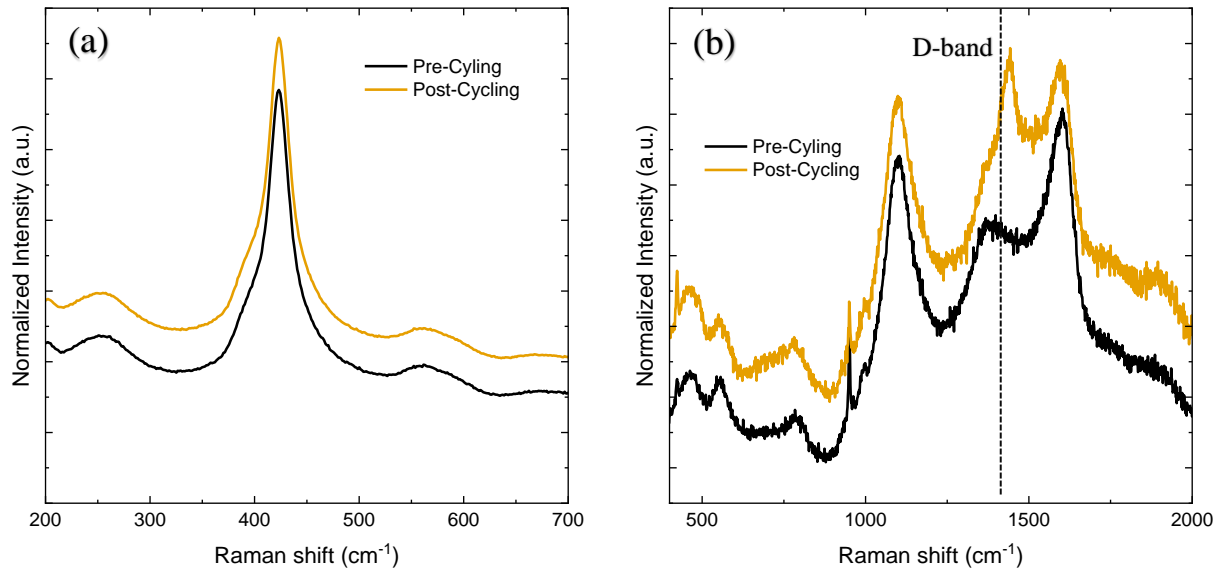


Figure 16. Pre- and post-mortem Raman spectroscopy of cycled cell components, the (a) ISU-6 glassy solid electrolyte and (b) composite cathode film.

## Patents/Publications/Presentations

### Publications

- Zhao, R., G. Hu, S. Kmiec, J. Wheaton, V. M. Torres, and S. W. Martin. “Grain-Boundary-Free Glass Solid Electrolytes Based on Sulfide Materials: Effects of Oxygen and Nitrogen Doping on Electrochemical Performance.” *Batteries and Supercaps* 5, no. 11 (2022): e2021000356-1-13. <https://doi.org/10.1002/batt.202100356>.
- Kmiec, S., M. Olson, M. Kenney, and S. W. Martin. “Interpretation of the Na<sup>+</sup> Ionic Conductivity in Na<sub>4</sub>P<sub>2</sub>S<sub>7-x</sub>O<sub>x</sub> Mixed Oxy-Sulfide (MOS) Glasses: Effects of Diverse Sodium Environments.” *Chemistry of Materials* 34, no. 21 (2022): 9479–9491. <https://pubs.acs.org/doi/10.1021/acs.chemmater.2c01934>.
- Olson, M., S. Kmiec, and S. W. Martin. “NaPON Doping of Na<sub>4</sub>P<sub>2</sub>S<sub>7</sub> Glass and its Effects on the Structure and Properties of Mixed Oxy-Sulfide-Nitride Phosphate Glass.” *Inorganic Chemistry* 61, no. 44 (2022): 17469–17484. <https://pubs.acs.org/doi/10.1021/acs.inorgchem.2c02300>.

### Presentations

- 242<sup>nd</sup> Meeting of the Electrochemical Society (ECS), Atlanta, Georgia (October 9–13, 2022): “Preparation of Li-Si-P-S-O-N Glasses: The Impact of Lipon Incorporation on Ionic Conductivity”; V. M. Torres, P. Philipp, and S. W. Martin.
- 242<sup>nd</sup> Meeting of ECS, Atlanta, Georgia (October 9–13, 2022): “Electrochemical Characterization of a Drawn Thin-Film Mixed Oxy-Sulfide Glassy Electrolyte Material for Solid-State Battery Applications”; J. Wheaton and S. W. Martin. Poster.
- 242<sup>nd</sup> Meeting of ECS, Atlanta, Georgia (October 9–13, 2022): “Development and Optimization of Composite Cathode Materials for Use with Thin-Film Glassy Solid Electrolytes in Solid-State Batteries”; W. Fettkether, J. Wheaton, and S. W. Martin. Poster.

## Task 1.7 – All-Solid-State Batteries Enabled by Multifunctional Electrolyte Materials (Pu Zhang, Solid Power Inc.)

**Project Objective.** The project objective is to develop Li-metal solid-state batteries enabled by multifunctional solid-state electrolytes (SSEs) for electric vehicle (EV) application. The ultimate goal is scalable production of large-format all-solid-state batteries (ASSBs) able to deliver  $\geq 350$  Wh/kg specific energy,  $\geq 1000$  cycle life, and  $\leq \$100/\text{kWh}$  cost.

**Project Impact.** The project is enabling scalable production of large-format ASSBs required by the vehicle market and is building domestic battery manufacturers as leaders in the global vehicle ASSB production. The proposed technology will address key limitations of state-of-the-art lithium batteries to meet U. S. Department of Energy EV battery targets and accelerate their adoption as large-format EV batteries for sustainable transportation technology.

**Approach.** The project will develop a high-performance Li-metal solid-state cell enabled by a multifunctional SSE. The new SSE will (1) have high conductivity (up to  $10 \text{ mS/cm}$ ), (2) be stable against lithium metal and high-voltage cathodes (0-4.5 V), (3) promote uniform lithium plating (enabling  $> 2\text{C}$  charge rate), and (4) be compatible with large-scale manufacturing processes. The specific cell chemistry to be demonstrated will be the SSE with Li-metal anode and high-nickel-content Li-metal oxide cathode. The solid-state cell will be assembled by scalable roll-to-roll processes developed by Solid Power.

**Out-Year Goals.** In Year 1, a multifunctional SSE will be developed with lithium ionic conductivity of  $\geq 3 \times 10^{-3} \text{ S/cm}$ . A critical current density of  $\geq 6 \text{ mA/cm}^2$  will be achieved in a symmetric lithium cell. The SSE design concept will be proven by demonstrating a cycle life of  $\geq 200$  in a full cell. In Year 2, SSE material will be optimized with lithium ionic conductivity of  $\geq 5 \times 10^{-3} \text{ S/cm}$ . Scalable cell assembly processes will be developed. A cycle life of  $\geq 500$  will be demonstrated in a full cell. In Year 3, large-format solid-state cells ( $> 2 \text{ Ah}$ ) will be assembled and tested to meet the final goal:  $\geq 350 \text{ Wh/kg}$ ,  $\geq 1000$  cycles, and  $\leq \$100/\text{kWh}$  cost.

**Collaborations.** The proposed team consists of Solid Power and a subcontractor, University of California, San Diego (UCSD). Solid Power (principal investigator, or PI: P. Zhang) will develop the multifunctional SSE and other cell components, assemble cells, and conduct cell tests. UCSD (PI: Y. S. Meng) will carry out material characterization by using advanced techniques such as X-ray photoelectron spectroscopy, cryogenic scanning transmission electron microscopy (cryo-STEM) imaging, cryo-STEM energy-dispersive X-ray spectroscopy, electron energy loss spectroscopy, and cryogenic focused ion beam milling. The UCSD team seeks to quantify the kinetics and evolution of each contributing factor and its impact on battery performance.

### Milestones

1. Charge rate  $\geq 2\text{C}$ . (Q1, FY 2022; Completed)
2. SSE film  $\geq 10 \text{ m}$  and  $\leq 40 \text{ }\mu\text{m}$ . (Q2, FY 2022; Completed)
3. Pouch cell  $\geq 2 \text{ Ah}$ . (Q3, FY 2022; Completed)
4. Cycle life  $\geq 1000$ . (Q4, FY 2022; 75% Completed)

## Progress Report

### Solid-State Cell Design

The SSE replaces all of the liquid electrolyte in a solid-state cell, but many cell designs are possible under the solid-state umbrella. The Solid Power SSEs enable an entire new cell platform that can incorporate a wide variety of existing and future anode and cathode materials.

On the anode side, lithium metal is an ultimate solution as it stores ultra-high energy per unit mass and it delivers low cost over the long term. Silicon is also attractive as it offers the quickest path to meeting all of the charge rate and low-temperature cycling requirements for future EVs in low-cost EV scale cells, while delivering similar volumetric energy density to lithium metal if enough silicon material can be packed into the anode layer.

On the cathode side, the sulfide electrolytes can be paired with the same Li-Ni-Mn-Co oxide (NMC) cathode materials being used today in Li-ion batteries, which is important for near-term market introduction. Conversion reaction type cathode chemistries such as iron sulfide, enabled by the sulfide SSE materials, would provide further gains in specific energy while being inexpensive and sustainable.

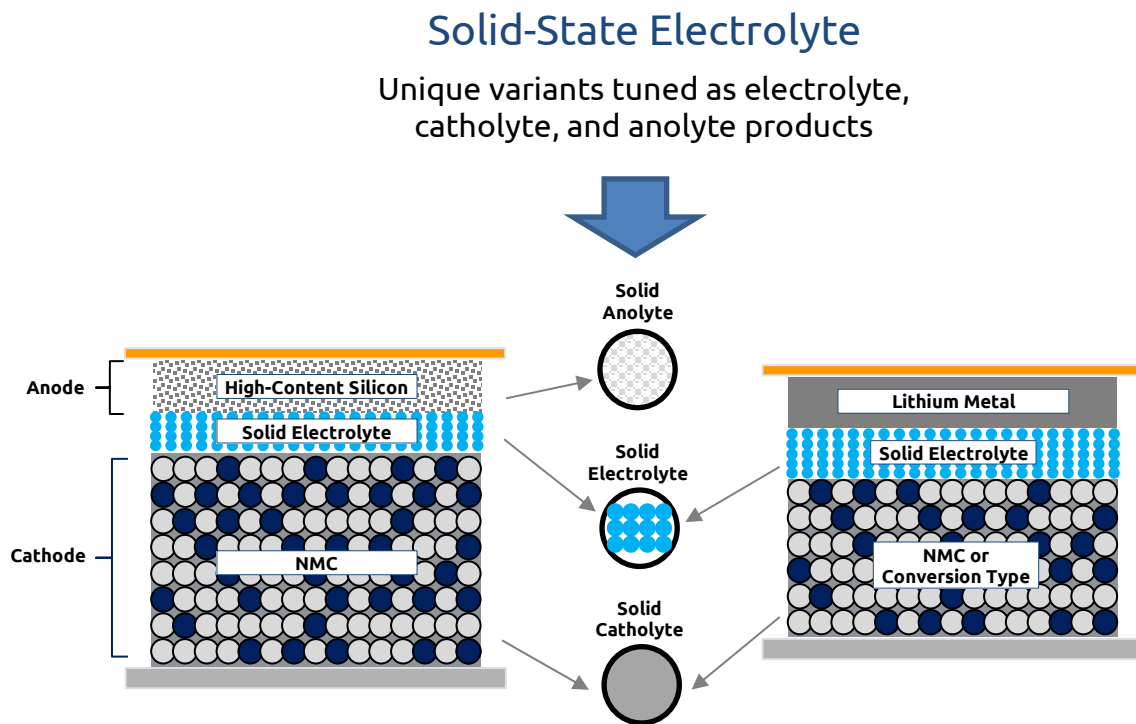


Figure 17. The sulfide solid-state electrolyte materials enabling a flexible platform that incorporates a variety of anode and cathode materials for a high-energy and low-cost all-solid-state-battery cell.

### Full-Cell Cycle Life Demonstration

Evaluation of the cycle life of the electrolyte continued in a lab-scale Li-NMC pouch cell to meet the final project goal of 1000 cycles. When tested at 2.8 V – 4.2 V, C/5 – C/5, and 45°C, the pouch cell showed 750 cycles with 87% capacity retention before the Coulombic efficiency (CE) started to drop. The CE drop indicates a soft-shortening issue due to lithium dendrite formation after 750 cycles. The cycle life data are shown in Figure 18. This will conclude the full-cell cycle life demonstration in the project. Surface modification of the lithium anode may be needed to further improve cycling stability.

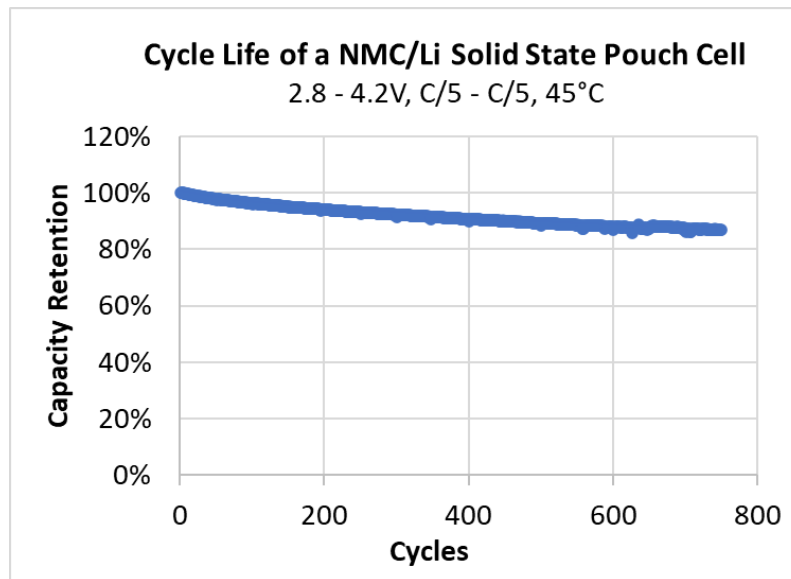


Figure 18. Cycle life of an NMC/Li-metal solid-state pouch cell with the multifunctional solid-state electrolyte at 45°C.

### Patents/Publications/Presentations

The project has no patents, publications, or presentations to report this quarter.

## Task 1.8 – Developing Materials for High-Energy-Density Solid-State Lithium-Sulfur Batteries (Donghai Wang, Pennsylvania State University)

**Project Objective.** The project objectives are to develop materials involving advanced S-C composite materials, solid additives, and sulfide-based solid-state electrolytes (S-SSEs) and also to acquire knowledge for all-solid-state Li-S batteries (ASSLSBs). These batteries—with large areal sulfur loading ( $\geq 5 \text{ mg cm}^{-2}$ ) and high sulfur content ( $\geq 50 \text{ wt\%}$  in cathode), and paired with lithium or Li-alloy anode—will deliver a high initial specific capacity  $> 1200 \text{ mAh g}^{-1}$  at high charge/discharge rate ( $> 0.3 \text{ C}$ ) for 500 cycles with over 80% capacity retention.

**Project Impact.** This project aims to develop new materials to enable ASSLSBs with high energy density, excellent cycling stability, and good rate performance, and thus to build knowledge for fabrication of prototype ASSLSBs. Specifically, the developed new materials will greatly increase the specific capacity of sulfur and sulfur utilization at high areal sulfur loading, alleviate the interfacial problem between S-C composite and SSE within sulfur cathode, boost Li-ion conductivity, and improve moisture stability of glass and glass-ceramic S-SSEs. Meeting the technical targets will potentially promote development of high-energy-density ASSLSBs and their practical application in electric vehicles (EVs) and plug-in hybrid EVs and will also reduce petroleum consumption in the transportation sector by helping battery-powered vehicles become more accepted by consumers as a reliable source of transportation.

**Approach.** The project goal will be accomplished through developing new materials, together with in-depth characterization of sulfur cathodes. Specifically, approaches to realize the project objectives include the following: (1) development of new carbon material with unique structure, high surface area, and large pore volume; (2) development of new S-C and S-C- $\text{M}_x\text{S}_y$  materials ( $\text{M} = \text{Li, Co, Ti, Mo, etc.}$ ) to facilitate electron/ion transport; (3) development of novel additives to tune interfacial behavior among components in the cathode; (4) development and optimization of new SSE through cation and anion doping with superior properties such as high ionic conductivity, good moisture, and stability; and (5) diagnostics, characterization, and cell tests on the developed new material or advanced sulfur cathode.

**Out-Year Goals.** The out-year goals are as follows: (1) develop and optimize sulfur cathode materials and synthesize new solid electrolytes (SEs; ionic conductivity  $> 5 \text{ mS cm}^{-1}$  at room temperature), and (2) conduct characterization and performance tests on both material and electrode levels. The final demonstration will be all-solid-state sulfur cathodes with  $> 1200 \text{ mAh g}^{-1}$  discharge capacity at  $0.3 \text{ C}$  discharge rate and  $50 \text{ wt\%}$  sulfur content for 500 cycles at room temperature.

**Collaborations.** There are no active collaborations.

### Milestones

1. Demonstrate sulfur cathode with high areal sulfur loading ( $\geq 5 \text{ mg cm}^{-2}$ ) and  $50 \text{ wt\%}$  sulfur content over  $1000 \text{ mAh g}^{-1}$  discharge capacity at  $0.1 \text{ C}$  rate at  $25^\circ\text{C}$  for 10 cycles. (Q1, FY 2022; Completed)
2. Demonstrate new SE with ionic conductivity  $> 3 \text{ mS cm}^{-1}$  at  $25^\circ\text{C}$ . (Q2, FY 2022; Completed)
3. Demonstrate sulfur cathode with high areal sulfur loading ( $\geq 5 \text{ mg cm}^{-2}$ ) and above  $50 \text{ wt\%}$  sulfur content over  $1000 \text{ mAh g}^{-1}$  discharge capacity at  $0.3 \text{ C}$  rate at  $25^\circ\text{C}$  for 50 cycles. (Q3, FY 2022; In progress)
4. Demonstrate sulfur cathode with high sulfur content ( $> 50 \text{ wt\%}$ ) and over  $1200 \text{ mAh g}^{-1}$  at  $0.3 \text{ C}$  rate for 500 cycles ( $< 20\%$  capacity decay) at room temperature, and new SEs with ionic conductivity  $> 5 \text{ mS cm}^{-1}$  at  $25^\circ\text{C}$ . (Q4, FY 2022; In progress)

## Progress Report

### New Sulfur Cathodes for ASSLSBs

Through post-analysis of ASSLSBs with high sulfur loading, the team has identified that the primary cause for the mediocre electrochemical performance is the poor ion transport through the sulfur cathode, which causes high internal resistance of the battery. Therefore, this quarter, they tried to enhance the ion transport efficiency in sulfur cathode by developing cathode materials and optimizing the composition (SE, additive, etc.) By doing so, they successfully prepared a sulfur cathode with superior electrochemical performance at high areal sulfur loading. As shown in Figure 19, the sulfur cathode with an areal sulfur loading of  $5.39 \text{ mg cm}^{-2}$  and sulfur content of 50 wt% delivered a high discharge specific capacity of over  $1200 \text{ mAh g}^{-1}$  based on the weight of sulfur at room temperature. After 10 cycles, the discharge specific capacity remained as high as  $\sim 1400 \text{ mAh g}^{-1}$  based on the weight of sulfur. Such performance fulfills the target for the milestone of the first quarter. They will continue optimizing the cathode compositions to enhance the ionic transport within sulfur cathodes toward achieving the remaining milestones and will evaluate the batteries at  $0.3 \text{ C}$  next quarter.

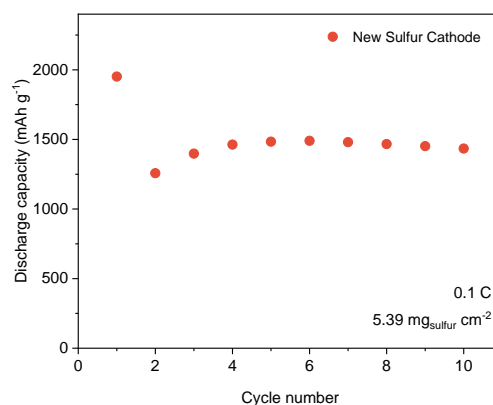


**Figure 19. Cycling performance of the all-solid-state Li-S batteries using the new sulfur cathode developed this quarter. The cell was tested at  $0.1 \text{ C}$  with high sulfur loading content under room temperature. Discharge capacities are based on the weight of sulfur in the cathodes.**

### Lithium Alloy Anodes for ASSLSBs

Further, the team synthesized various Li-alloy anodes by the high-energy ball-milling method for fabricating high-energy-density ASSLSBs. To avoid the interfacial issues between lithium metal and SEs, using alloy anodes could mitigate the interfacial resistance increase and the lithium dendrite growth. In addition, owing to the stable and reversible plating/stripping of alloy anodes, they can develop stable and durable ASSLSBs with high sulfur utilization (high discharge capacity). After optimizing the composition and synthesis procedures, they found a type of alloy anode (Lithium alloy-2) that can cycle stably and enable ASSLSBs with high discharge specific capacity, which remained  $1368.6 \text{ mAh g}^{-1}$  based on the weight of sulfur after 150 cycles, as shown in Figure 20 (blue). The full cells were cycled under  $0.1 \text{ C}$  at  $60^\circ\text{C}$ , and the sulfur cathode loading was  $\sim 2.19 \text{ mg cm}^{-2}$ . Besides that, the other two types of lithium alloy anode behaved differently. The ASSLSB using lithium alloy-1 exhibited a high initial discharge capacity of  $\sim 1400 \text{ mAh g}^{-1}$  based on the weight of sulfur, but suffered from short-circuit after 20 cycles (red). The ASSLSB with lithium alloy-3 (green) also had good reversibility and still showed a high discharge specific capacity of  $1162.4 \text{ mAh g}^{-1}$  based on the weight of sulfur after 150 cycles. It shows that the Li-alloy anodes could be utilized for ASSLSBs, delivering high discharge specific capacities and good capacity retention. The team is investigating the mechanism of the short-circuit behavior and trying to gain more knowledge of how different lithiation states of alloy anodes affect the stability and electrochemical performance of the full cells, which will provide guidance for them to fabricate ASSLSBs with prolonged and excellent electrochemical performance.

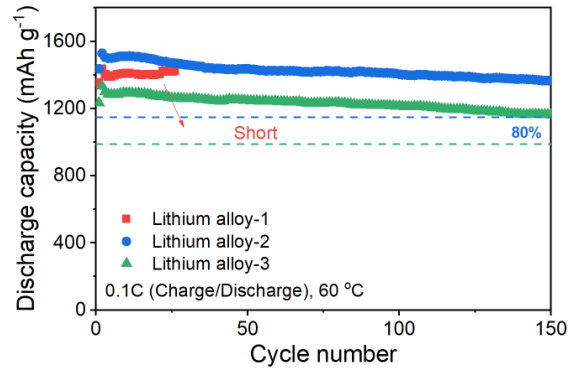


Figure 20. Cycling performance of the all-solid-state Li-S batteries using the as-synthesized alloy anodes. The cells were tested at 0.1 C under 60°C, and the specific capacity is based on the weight of sulfur

### Patents/Publications/Presentations

The project has no patents, publications, or presentations to report this quarter.

## Task 1.9 – Hot Pressing of Reinforced Lithium-NMC All-Solid-State Batteries with Sulfide Glass Electrolyte (Thomas Yersak, General Motors, LLC)

**Project Objective.** The project will research, develop, and test lithium – Ni-Mn-Co (Li-NMC) all-solid-state batteries (ASSBs) capable of achieving program performance metrics by implementing sulfide-glass solid-state electrolytes (SSEs) and hot-press processing in a dry-room environment. The performance of ASSBs with sulfide SSEs is limited because they are essentially green tapes with up to 20% porosity. In composite cathodes, the porosity limits energy density and power, while porosity in the separator acts as a conduit for Li-metal deposits if cycling conditions (C-rate, operating temperature, and pressure) are not strictly controlled. The project goal is to demonstrate that the hot-pressing method and appropriately formulated sulfide-glass SSEs can eliminate porosity to enable Li-NMC ASSBs with energy density of > 350 Wh/kg.

**Project Impact.** The hot-press processing method and appropriately formulated sulfide-glass SSEs may enable Li-NMC ASSBs with improved energy density > 350 Wh/kg. The General Motors (GM) processing technology depends on heating a sulfide-glass SSE above its transition temperature, at which point it can consolidate via viscoplastic flow. In the composite cathode, hot-pressing provides liquid-like contact between the NMC cathode and SSE to increase energy density and power by enabling thick composite cathodes with high active material loading. Furthermore, cathode-supported sulfide-glass separators can be made dense and thin by hot-pressing. A dense separator enables the use of Li-metal anodes because lithium deposits may be more effectively blocked, preventing cell shorting.

**Approach.** The sulfide SSE used in the composite cathode, otherwise known as the catholyte, will dictate the processing specifications for ASSB hot-pressing. Thermal stability can be achieved by NMC passivation and proper catholyte formulation. This project will systematically evaluate different NMC coatings, catholyte formulations, and hot-press processing specifications (that is, temperature, time, and pressure). The performance of hot-pressed ASSBs will be compared to green baseline ASSBs and hot-pressed control ASSBs consisting of the  $\beta$ -Li<sub>3</sub>PS<sub>4</sub> and Li<sub>6</sub>PS<sub>5</sub>Cl model SSEs. Electron microscopy will be employed to understand interfacial phenomena and track composite cathode microstructure before and after hot-pressing.

**Out-Year Goals.** In the second year of this project, a sulfide-glass SSE will be formulated specifically for use as the separator. The separator glass SSE formulation will be designed to achieve full densification under the hot-press processing specifications determined for the catholyte. Separator glass formulation design will also consider cathodic stability, moisture stability, and ionic conductivity. Once a system of separator glass SSE and catholyte has been determined, the third year of the project will demonstrate hot-pressed full cells at the coin-cell and single-layer pouch-cell levels, meeting program target performance metrics.

**Collaborations.** GM will lead this project with no subrecipients.

### Milestones

1. Report ionic conductivity of separators with multifunctional reinforcement. Decide whether to carry forward multifunctional reinforcement for the remainder of the project. (Q1, FY 2022; Completed)
2. Demonstrate that H<sub>2</sub>S generation of target separator glasses and catholytes can be cut by 50% in a -40°C dewpoint dry-room environment. Report functional characteristics of SSEs after exposure. (Q2, FY 2022; Completed)
3. Based on results collected during Budget Period 2, the best performing separator glasses will be carried forward for the remainder of the project. (Q3 FY 2022; Completed)
4. Retrofit glovebox: implement a simulated dry-room environment inside an inert glovebox by designing and installing custom equipment. (Q4, FY 2022; Completed)

## Progress Report

This report describes custom laboratory hardware and a semi-solid electrolyte system. First, the team presents custom laboratory hardware that will be used to simulate a dry-room environment. Demonstration of this hardware meets the Q4 milestone. Second, they outline a semi-solid electrolyte system based on SSE and solvate ionic liquid (SIL) that will be used to meet future project deliverables. Finally, micro – computed tomography (CT) images of all-solid-state separators *post-mortem* are presented to motivate the need for the aforementioned semi-solid electrolyte system.

A tabletop glovebox was modified with a custom moisture control system to conveniently simulate a dry-room environment at any moisture setpoint ranging from  $-80^{\circ}\text{C}$  to  $-40^{\circ}\text{C}$  dewpoint. For reference, an inert glovebox will have a moisture level of about  $-80^{\circ}\text{C}$  dewpoint, while a cell assembly dry room will have a moisture level of about  $-40^{\circ}\text{C}$  dewpoint. A picture of the setup is provided in Figure 21a. It consists of a moisture probe, a microcontroller, a solid-state relay, and a cartridge-based desiccant system. As shown in Figure 21b, the microcontroller is programmed to turn the cartridge-based desiccant system on and off to keep the moisture setpoint within a desired range.

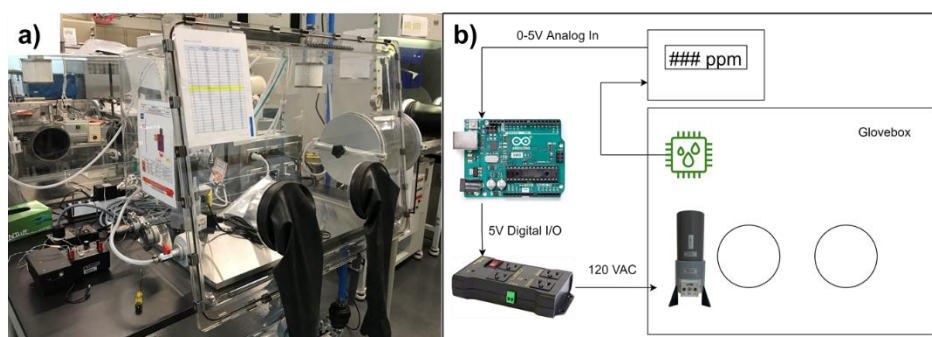


**Figure 21.** (a) Picture of the retrofitted glovebox. The glovebox is equipped with a custom system to maintain a dry-room environment within a predetermined moisture setpoint range. (b) Schematic of the glovebox moisture control system. It consists of a moisture probe, a microcontroller, a solid-state relay, and a cartridge-based desiccant system.

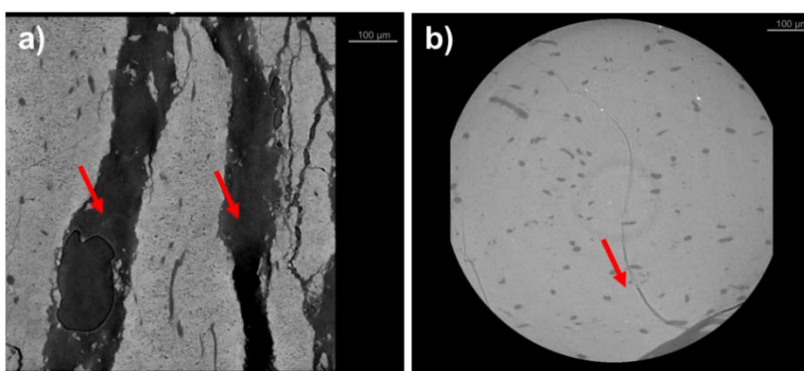


**Figure 22.** (a) Micro – computed tomography (CT) image of a cold-pressed separator after a critical current density (CCD) experiment. Red arrows point to Li-metal deposit. (b) Micro-CT image of a hot-pressed separator after a CCD experiment. A red arrow points to a lithium deposit that has expanded an incipient micro-crack. For both images, the vertical direction corresponds to the thru plane, transverse direction of the separator. Large speckles in both images are attributed to the Kevlar® reinforcing fibers.

X-ray micro-CT was used to image all-solid-state SSE separators after failure by internal shorting (Figure 22). The SSE was a glass powder with composition  $70\text{Li}_2\text{S}\cdot 25\text{P}_2\text{S}_5\cdot 5\text{A}$ , where A is a third glass component. The separators were fabricated by consolidating the glass powder into 13-mm-diameter Kevlar® fiber reinforced

pellets at room temperature (cold-pressed, CP) or 240°C (hot-pressed, HP) and 300 MPa. Symmetric Li/SSE/Li cells were constructed with these pellets and cycled at progressively higher current densities under a 3-Mpa stack pressure, as previously described.<sup>[1]</sup> The separators were collected after failure, sectioned into 2- $\mu\text{m}$   $\times$  2- $\mu\text{m}$   $\times$  0.5- $\mu\text{m}$  (that is, length  $\times$  width  $\times$  thickness) pieces, and embedded inside ultraviolet (UV) curable epoxy. The samples were scanned using a Zeiss Xradia Versa 520 three-dimensional (3D) X-ray microscope with diffraction contrast tomography module at a voxel size of 0.7  $\mu\text{m}$  and an X-ray voltage of 40 kV. The micro-CT image of the CP sample is provided in Figure 22a, and red arrows point to large deposits of lithium metal. Closer inspection reveals that the SSE is denser at the boundary with the lithium deposit. The micro-CT image of the HP sample is provided in Figure 22b, and a red arrow points to a lithium deposit expanding an incipient SSE microcrack. In both cases, high stresses are generated at the SSE/Li interface when lithium deposition is volumetrically confined under a high stack pressure. As a result, lithium deposits penetrate both CP and HP separators. The design of a semi-solid system is therefore required to dissipate the stresses at the SSE/Li interface.

Finally, the team evaluated the stability of a semi-solid electrolyte system. A secondary electrolyte phase reduces the need for a high stack pressure,<sup>[2]</sup> which may alleviate deleterious stresses generated at the SSE/Li interface during confined lithium deposition. An SIL was prepared by combining lithium bis(trifluoromethanesulfonyl)imide salt (LiTFSI) and triethylene glycol dimethyl ether (G3) in a molar ratio of 1:1. Dilute liquid electrolytes (LEs) were also prepared by combining LiTFSI and G3 in molar ratios of 1:2, 1:3, or 1:4. Glass electrolytes were prepared with varying content of a third glass component, according to the compositional formula  $70\text{Li}_2\text{S} \cdot (30-x)\text{P}_2\text{S}_5 \cdot x\text{A}$  ( $x = 0, 2, 5, 10$ ). Solubility tests were conducted by immersing SSE chunks in LE. After a week, the team measured the solids mass loss and conducted UV-Vis absorption spectroscopy with the liquid phase. The solids mass loss was measured by filtering the solutions and drying the remaining solids at 60°C; results are provided in Figure 23a. No mass loss was observed for SSEs soaked in Li(G3)TFSI, while significant mass loss was observed for SSE samples soaked in dilute LEs. The stability of SSEs in Li(G3)TFSI can be explained by the strong complexation of G3 with lithium salts.<sup>[3]</sup> In dilute LEs, oxygen in G3 attacks the electropositive elements (for example, phosphorus) of the sulfide SSEs by nucleophilic attack. The composition of the SSE also influences of the stability of the semi-solid electrolyte system. They find that solubility of glasses in dilute solutions decreases as A content increases. UV-Vis spectroscopy was conducted to corroborate the data outlined above; data are provided in Figure 23b-c. In conclusion, future work will employ use of a semi-solid electrolyte system containing Li(G3)TFSI SIL and SSE with A content.

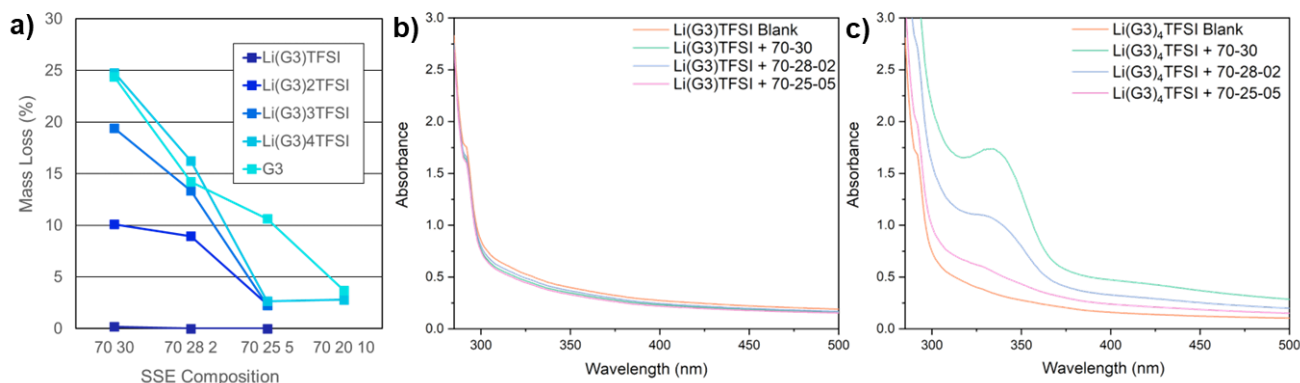


**Figure 23.** (a)  $70\text{Li}_2\text{S} \cdot (30-x)\text{P}_2\text{S}_5 \cdot x\text{A}$  solid-state electrolyte (SSE) solids mass loss after soaking in a variety of liquid electrolyte (LE) formulations. All SSEs soaked in Li(G3)TFSI solvate ionic liquid are stable. (b) UV-Vis molecular absorption spectroscopy results for  $70\text{Li}_2\text{S} \cdot (30-x)\text{P}_2\text{S}_5 \cdot x\text{A}$  SSE samples soaked in Li(G3)TFSI solvate ionic LE and (c) Li(G3)<sub>4</sub>TFSI LE.

## References

- [1] Yersak, T. A., et al. *ACS Applied Energy Materials* 2, no. 5 (2019): 3523–3531.
- [2] Yersak, T. A., et al. *Materials Advances* 3, no. 8 (2022): 3562–3570.
- [3] Oh, D. Y., et al. *Advanced Energy Materials* 5, no. 22 (2015): 1500865.

## Patents/Publications/Presentations

### Patents

- Yersak, T. A., I. Halalay, Y. Zhang, and A. Ketchum. Bicontinuous Separating Layers for Solid-State Batteries and Methods of Forming the Same. U. S. Patent Application; September 30, 2022.
- Malabet, H. J. G., Y. Zhang, and T. A. Yersak. Solid-State Electrolyte Materials for All-Solid-State Batteries. U. S. Patent Application, 17/824,584; May 25, 2022.

### Presentation

- American Chemical Society Fall Meeting, Chicago, Illinois (August 22, 2022): “Process Rheology of Oxysulfide Solid-State Electrolyte Separators for Solid-State Batteries”; T. A. Yersak. Invited.

## Task 1.10 – Three-Dimensional Printing of All-Solid-State Lithium Batteries (Jianchao Ye, Lawrence Livermore National Laboratory)

**Project Objectives.** The project has two primary objectives: (1) down select three-dimensional (3D) printing and post-processing approaches for solid-state electrolyte (SSE) / cathode integration, and (2) understand battery failure mechanisms via *ex situ* and *in situ* characterization.

**Impact.** The adoption of thin separator layer, thick cathode structure, and metallic lithium anode will lead to electric vehicle batteries with > 350 Wh/kg energy density for increased mileage per charge. The higher ionic conductivity with suppression of lithium dendrite growth will allow high critical current densities for fast charging applications. The improved electrode/electrolyte contact will increase battery cycle life for long-term service.

**Approach.** The technical approaches include advanced manufacturing based on 3D printing and related techniques, *ex situ* / *in situ* characterizations, and battery testing. Direct-ink writing 3D-printing techniques will be employed to fabricate thin-film SSEs (< 100 μm), gradient SSEs, and 3D interfaces for battery performance evaluation. Three approaches, including sintering-free, hybrid, and co-sintering, will be investigated. The knowledge obtained from these approaches is transferable and complementary to each technique.

**Out-Year Goals.** The long-term vision of the team is to 3D-print all components of the all-solid-state lithium battery (ASSLB) to facilitate the scale-up of ASSLB manufacturing. In this project, the team will tackle the issues emerging from integrating solid electrolyte with electrodes. The project goal is to demonstrate a successful 3D-printing approach to integrate SSE into electrodes and show reasonable capacity retention (that is, > 80%) after 300 cycles at current density  $\geq 1$  mA/cm<sup>2</sup>.

**Collaborations.** The team will work closely with a computational partner (Task 3.11 led by B. Wood) to better understand battery failure mechanisms and design new battery architectures and chemistries for performance improvement. The team is collaborating with Dr. S. Kim and Dr. G. Cheng from University of Illinois at Chicago on composite polymer electrolyte (CPE) development.

### Milestones

1. Determine the polymer /  $\text{Li}_{6.75}\text{La}_3\text{Zr}_{1.75}\text{Ta}_{0.25}\text{O}_{12}$  (LLZTO) interfacial chemistry effects on the total ionic conductivity and  $\text{Li}^+$  transference number. (Q2, FY 2022; Completed)
2. Improve conductivity and strength of CPEs. (Q3, FY 2022; Completed)
3. Obtain porous co-sintered LLZTO-SSE / Ni-Mn-Co (NMC) / C electrolyte/cathode bilayer structure. (Q4, FY 2022; Completed)

## Progress Report

The team previously showed co-sintering results for cathode composites made with 50 wt%  $\text{LiNi}_{0.6}\text{Mn}_{0.2}\text{Co}_{0.2}$  (NMC-622) / 50 wt%  $\text{Li}_{6.4}\text{La}_3\text{Zr}_{1.4}\text{Ta}_{0.6}\text{O}_{12}$  (LLZTO). To better approximate the conditions of an actual solid-state cell, the team recently studied co-sintering outcomes using cathode composites made with less electrolyte (75 wt% NMC-622 / 25 wt% LLZTO), as well as with  $\text{LiCoO}_2$  (LCO) as the cathode material (75 wt% LCO / 25 wt% LLZTO). To test the electrochemical performance of these co-sintered materials, the cathode and electrolyte were mixed with a small amount of binder and coated on top of pre-sintered LLZTO pellets (Figure 24a). The samples were then co-sintered at 750°C or 900°C for 2 hours in either air or argon to determine the effect of temperature and sintering environment on stability and performance (Figure 24b-c). For all the samples, a definite color change throughout the LLZTO pellet from white to green after co-sintering was observed, with the color intensity corresponding to the temperature and the environment. This is likely due to cobalt diffusion from the cathode into the LLZTO. Figure 24d shows an optical image of the back side of the LLZTO pellets after co-sintering, and a few trends can be observed. First, the green color change is more intense at higher temperatures and in argon versus air, indicating a greater degree of reaction under these conditions. Even after sintering at 750°C in air (the least reactive condition), the LLZTO pellet still changes to a yellow color for both LCO and NMC-622, suggesting some amount of cathode/electrolyte reaction. Second, the green color change is more significant for LCO compared to NMC-622, likely due to the greater cobalt content in LCO relative to NMC-622.

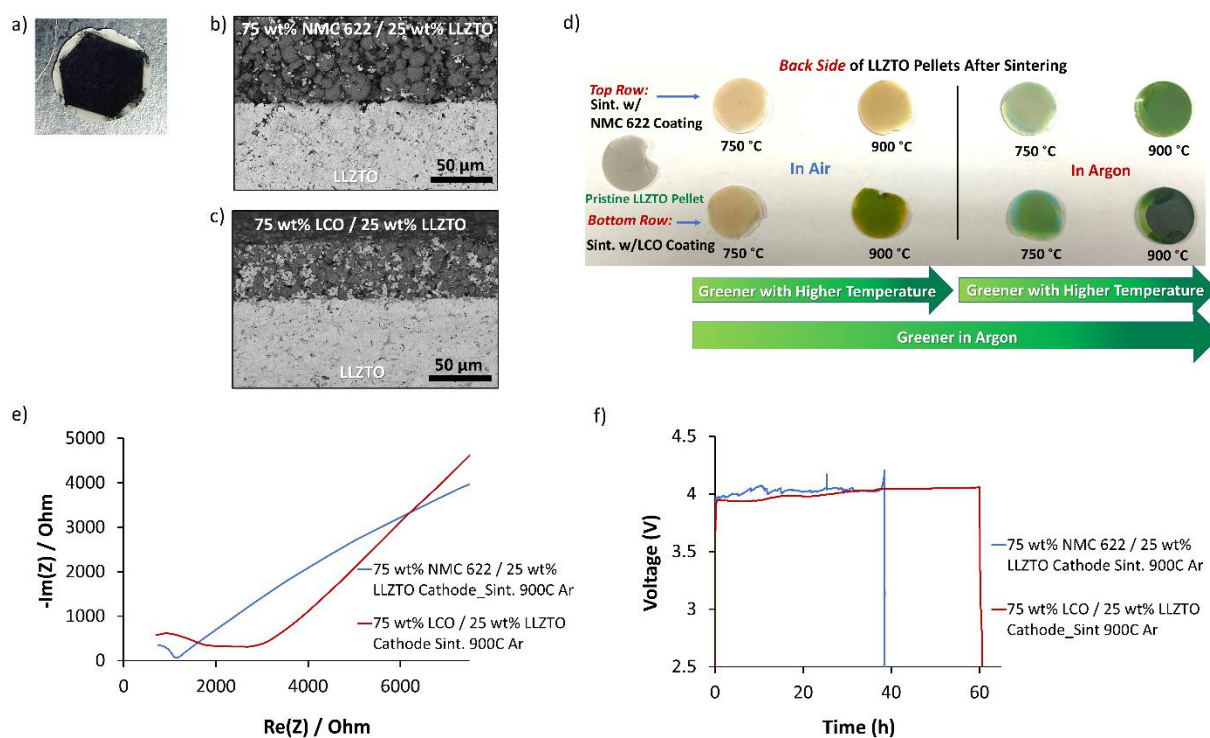


**Figure 24.** (b-c) Backscattered scanning electron microscopy cross-sections of composite cathodes coated on pre-sintered LLZTO pellets and co-sintered at 900°C for 2 hours in argon; (a) optical image before sintering. (d) Optical images of the back side of the LLZTO pellets after co-sintering at different temperatures and in different environments (air versus argon). Electrochemical measurements using lithium as the anode: (e) electrochemical impedance spectroscopy comparison before cycling. (f) Voltage profiles for the 1<sup>st</sup> charge/discharge cycle at C/20.

Electrochemical performance of these cells was evaluated by sputtering gold onto the cathode to form a conductive contact and assembling cells with lithium as the anode. All samples co-sintered at 750°C (in both air and argon) hit the upper cutoff voltage immediately. This is probably due to high resistance in the cell from the poor sintering between the cathode and electrolyte at these temperatures, which results in a discontinuous

ion transport pathway. For the LCO sample sintered at 900°C in argon, the cell continued to charge for a very long time and never hit the upper cutoff voltage (it hit the time limit set in the program instead), while the NMC-622 cell sintered at 900°C in argon also charged for a long time and had a bumpy voltage profile before finally hitting the upper cutoff voltage. Both cells hit the lower cutoff voltage very quickly on discharge (Figure 24f). This poor performance could be due to a combination of interfacial contact issues, cathode degradation, and secondary phase formation.

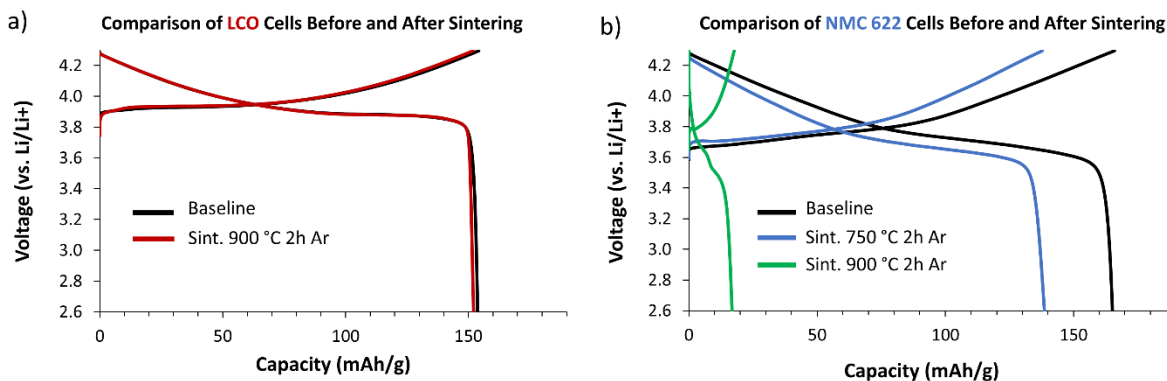


**Figure 25. Representative voltage versus capacity profiles for cathode materials sintered at 750°C and 900°C for 2 hours in argon before electrode preparation. Half cells were cycled at C/10 charge/discharge using liquid electrolyte (1.2 M LiPF<sub>6</sub> in 3:7 wt% EC/EMC) and lithium as the anode. (a) Comparison of LCO cells. (b) Comparison of NMC-622 cells.**

To determine if some of the observed degradation during co-sintering is due to degradation of the cathode material itself, the stability of each cathode at high temperatures was studied independently. To accomplish this, each cathode powder was pressed into a pellet (to mimic the co-sintering conditions) and then sintered at 900°C for 2 hours in argon. The pellets were then crushed into a powder, mixed with carbon black and binder to create a conventional cathode slurry, and tape cast. The cathodes were assembled into coin cells with liquid electrolyte (1.2 M LiPF<sub>6</sub> in 3:7 wt% ethylene carbonate / ethyl methyl carbonate) and cycled at C/10 to monitor capacity changes (Figure 25). For LCO, the capacity and voltage profiles are very similar before and after sintering at 900°C (154 mAh/g versus 152 mAh/g, respectively), indicating that the sintering does not cause initial capacity loss. However, for NMC-622, there is a substantial decrease in capacity from 165 mAh/g to 17 mAh/g after sintering at 900°C. Another set of NMC-622 samples was sintered at 750°C for 2 hours in argon as a comparison. While the capacity after sintering at this lower temperature is much better than after sintering at 900°C, there is still a significant decrease compared to the baseline (139 mAh/g versus 165 mAh/g). These results indicate that while co-sintering at these higher temperatures may be feasible for LCO, it must be done at much lower temperatures for NMC-622 to prevent degradation.

The team has recently been exploring laser sintering of LLZTO<sup>[1]</sup> and laser co-sintering as a way to minimize the detrimental effects of conventional high-temperature furnace sintering. Using rapid laser heating decreases the overall sintering time significantly (minutes compared to hours), which should help limit cathode/electrolyte reactions and help prevent formation of secondary phases. Figure 26 shows preliminary results for a 75 wt% LCO / 25 wt% LLZTO composite pellet sintered at 26 W for 90 seconds (~ 1215°C) using a 1000 nm laser diode array. The cross-sectional scanning electron microscopy images (Figure 26a) show a significant degree of sintering between the cathode and LLZTO particles, and the X-ray diffraction results (Figure 26b) indicate fewer secondary phases are formed during the short laser sintering period relative to the furnace sintered sample. The sintering parameters will be further tuned in the future, but these initial results demonstrate the potential for laser sintering to minimize interfacial reactions during co-sintering. Laser co-sintering will be further explored under this project.

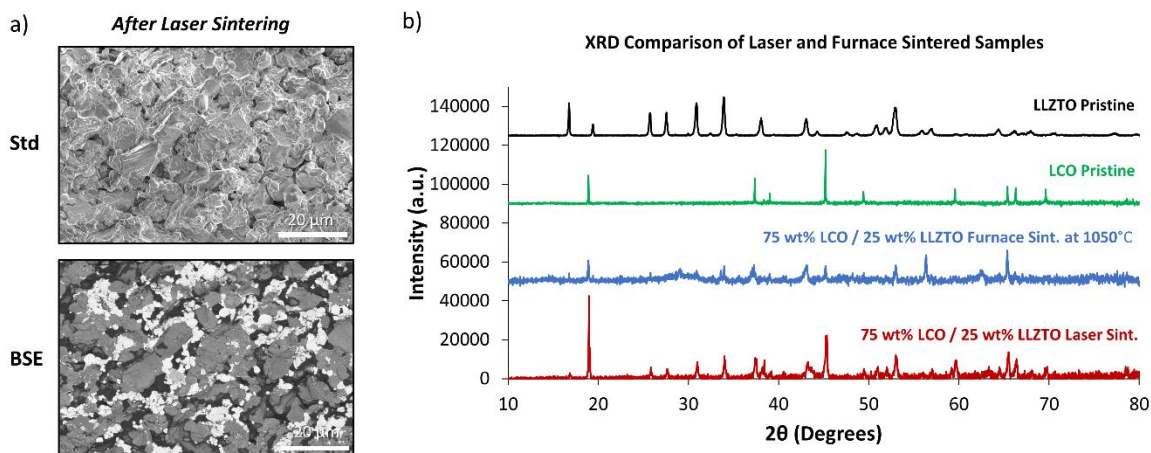


Figure 26. 75 wt% LCO / 25 wt% LLZTO pellets laser co-sintered at 26 W for 90 seconds using a laser diode array. (a) Standard and backscattered scanning electron microscopy images of cross-sections after co-sintering. (b) X-ray diffraction (XRD) comparison of laser and furnace co-sintered samples.

#### Reference

- [1] Ramos, E., et al. “CO<sub>2</sub> Laser Sintering of Garnet-Type Solid-State Electrolytes.” *ACS Energy Letters* 7 (2022): 3392–3400.

## Patents/Publications/Presentations

#### Presentation

- Solid-State Battery Summit, Chicago, Illinois (August 2022): “Additive Manufacturing of Solid State Batteries”; E. Ramos, A. Browar, M. Wood, J. Roehling, A. Santomauro, J. Forien, A. Martin, J. Yoo, J. Tong, and J. Ye.

## Task 1.11 – Physical and Mechano-Electrochemical Phenomena of Thin-Film Lithium-Ceramic Electrolyte Constructs (Jeff Sakamoto, University of Michigan)

**Project Objective.** While a small number of solid electrolytes (SEs) exhibit high ionic conductivity ( $\sim 1 \text{ Ms cm}$  at 298 K), few are stable against lithium metal. The garnet-type SE, based on the nominal formula  $\text{Li}_7\text{La}_3\text{Zr}_2\text{O}_{12}$  (LLZO), is unique in that it is a fast ion conductor and—as demonstrated in the team’s recent project (DE-EE-00006821)—is stable against lithium. Moreover, the team’s former project successfully demonstrated a decrease in Li-LLZO interface resistance from  $12,000 \Omega \text{ cm}^2$  to  $2 \Omega \text{ cm}^2$  and stable cycling at  $1 \text{ mA cm}^2$  for 100 cycles ( $\pm 15 \mu\text{m}$  of lithium per cycle). Although the past project demonstrated that LLZO is a viable SE for enabling batteries using metallic lithium, the studies used thick pellets (1 mm) and thick anodes ( $\sim 500 \mu\text{m}$ ). The goal of this project is to acquire a deep fundamental understanding of the physical and mechano-electrochemical phenomena that control the performance of cells consisting of thin LLZO ( $\sim 10 \mu\text{m}$ ), thin lithium anodes ( $\sim 20 \mu\text{m}$ ), and thin solid-state composite cathodes.

**Project Impact.** If successful, the project will gain knowledge to guide closely related commercialization efforts to scale up the production of LLZO-based solid-state batteries.

**Approach.** The team believes that to achieve a step increase in technology readiness level, the same performance characteristics previously shown should be demonstrated in technologically relevant cells, for example, thin LLZO and thin lithium.

**Out-Year Goals.** Out-year goals involve the following: custom thin-film composite (TFC) development, preliminary cycling studies, Vis cell development, lithium cycling, and polymer gel electrolyte (PGE) screening.

**Collaborations.** This project collaborates with N. Dasgupta and D. Siegel of University of Michigan (UM), Mechanical Engineering.

### Milestones

1. In thin lithium and thin LLZO TFC, determine the maximum plating critical current density ( $\text{CCD}^{\text{plating}}$ ) and stripping critical current density ( $\text{CCD}^{\text{stripping}}$ ) versus depth of discharge (DOD) at fixed lithium thickness ( $17 \mu\text{m}$ ). (Q1, FY 2022; Completed)
2. Long-term cycling tests to demonstrate  $\geq 80\%$  energy retention over 1000 cycles. (Q2, FY 2022; In progress)
3. In thin lithium and thin LLZO TFC, determine the max  $\text{CCD}^{\text{plating}}$  and  $\text{CCD}^{\text{stripping}}$  versus lithium thickness, DOD, stack press, and temperature. (Q3, FY 2022; Completed)
4. Optimize atomic layer deposition (ALD) coating technology to suppress reactions between the PGE and LLZO. (Q4, FY 2022; Completed)

## Progress Report

### Optimize ALD Coating Technology to Suppress Reactions Between the PGE and LLZO

Because initial success was achieved in stabilizing the sulfur catholyte and LLZO interface, the project resources were redirected from the study of ALD coatings to suppress potential reactions between LLZO and the organic electrolyte to treating the native LLZO interface. This work closely involves pre-PhD candidate M. Palmer at UM and L. Nazar and her PhD students, A. Shyamsunder and I. Kochetkov, from the University of Waterloo, Canada.

In this collaboration, it was determined that residual adventitious compounds on the LLZO surface react state-of-the-art Li-S organic electrolytes. A reaction pathway was hypothesized and validated, enabling the design and implementation of a treatment process to stabilize the native LLZO surface using 1,3-dioxolane / 1,2 dimethoxyethane (DOL/DME) 1.0 M lithium bis(trifluoromethanesulfonyl)imide (LiTFSI) as the catholyte. An interface resistance of  $30 \Omega/\text{cm}^2$  was achieved and exceeds the goal of  $40 \Omega/\text{cm}^2$ . To demonstrate the compatibility between LLZO and the liquid electrolyte, hybrid Li-S cells were made using LLZO to protect the lithium electrode and DOL/DME 1.0 M LiTFSI as the catholyte for S+carbon prototype cells (Figure 27). The goal of the initial cycling study was to demonstrate stable cycling and to demonstrate that LLZO can protect the lithium anode to protect fouling of the lithium anode with soluble polysulfides. The data in Figure 27 show that the Li-LLZO-S cell closely resembles a standard all-liquid Li-S, but it uses LLZO to protect the lithium anode. The fact that the profile closely resembles a liquid Li-S, shows potential as an effective cell configuration to ameliorate the side reactions that limit traditional Li-S cells, such as passivation of the lithium anode from deleterious side reactions with soluble polysulfides.

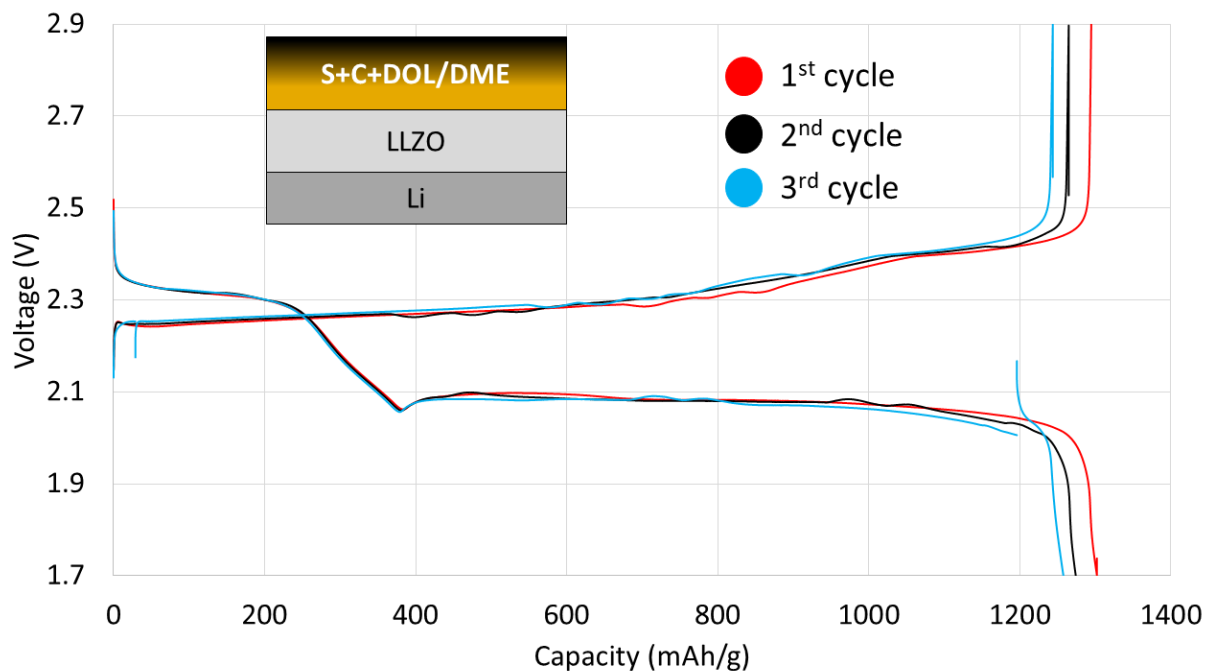


Figure 27. Cycling at  $108 \mu\text{A}/\text{cm}^2$  at room temperature with carbon paper. A Li-LLZO-DOL/DME/S hybrid battery can be discharged to 1,300 mAh/g and be cycled with minimal capacity loss.

## Patents/Publications/Presentations

### Patent

- A joint patent between UM and the University of Waterloo is planned before the end of the 2022 calendar year. The patent will involve treating the LLZO surface to enable compatibility with organic electrolytes used in Li-S cells.

### Publication

- Lee, K., E. Kazyak, M. J. Wang, N. P. Dasgupta, and J. Sakamoto. “Analyzing Void Formation and Rewetting of Thin *In Situ*-Formed Li Anodes on LLZO.” *Joule* 6, no. 11 (2022): P2457–2565. doi: <https://doi.org/10.1016/j.joule.2022.09.009>.

### Presentations

- National Academy of Sciences, Distinctive Voices Seminar, Beckman Center, Irvine, California (July 2022); J. Sakamoto. Invited.
- National Academy of Sciences, Distinctive Voices Seminar, Beckman Center, Irvine, California (July 2022); J. Sakamoto. Organized symposium on batteries and gave invited presentation.
- Solid-State Ionics Meeting, Boston, Massachusetts (July 2022); J. Sakamoto. Plenary presentation.

## Task 1.12 – Low Impedance Cathode/Electrolyte Interfaces for High-Energy-Density Solid-State Batteries

(Eric Wachsman and Yifei Mo, University of Maryland)

**Project Objective.** The project objective is to research, develop, and test Li-metal-based batteries that implement solid Li-ion conductors equipped with Ni-Mn-Co (NMC) cathodes integrated into the Li-metal / Li-La-Zr (LLZ) tri-layer architecture. Specifically, the team will achieve the following: (1) identify and demonstrate interfacial layers to achieve low-impedance and stable NMC/LLZ interfaces; (2) develop novel processing techniques to fabricate NMC/LLZ composite cathodes with low interfacial resistance; and (3) enable high-performance all-solid-state batteries (ASSBs) with an energy density of 450 Wh/kg and 1400 Wh/L and negligible degradation for 500 cycles.

**Project Impact.** Instability or high resistance at the interface of high-energy cathode materials with Li-garnet solid electrolytes (SEs) limits the high-energy-density all-solid-state lithium batteries. This project will lead to a fundamental understanding of solid-electrolyte/solid-cathode interfaces and a unique and transformative LLZ framework to enable high-energy-density, safe Li-metal batteries approaching ~ 400 Wh/kg.

**Approach.** In this new project, the team will build on their demonstrated expertise with garnet electrolytes and ASSB cells to accomplish the following: (1) engineer interfaces to overcome high NMC/LLZ interfacial impedance and interfacial degradation; (2) develop processing and fabrication techniques to achieve high-loading NMC/LLZ composite cathodes with low resistance and high cyclability; and (3) integrate the NMC/LLZ cathodes into all-solid-state Li-metal/LLZ cells to achieve high-energy-density batteries.

**Out-Year Goals.** The project will solve the current challenges of integrating garnet SE with a cathode to achieve a high-performance ASSB using a high-energy-density Li-metal anode. The resultant high energy density and stability using both high-energy-density Li-metal anodes and NMC cathodes will open new applications in portable electronics, electric vehicles, and beyond.

**Collaborations.** This project funds work at University of Maryland. The principal investigator (PI), E. Wachsman, will have management responsibility and will lead experimental efforts including garnet synthesis, interface processing, cell fabrication, and testing. The Co-PI, Y. Mo, will lead computational efforts on understanding stability between garnet and cathode and on identifying promising coating materials. In addition, Wachsman is actively collaborating with several universities and national laboratories through the U.S.–German cooperation on solid-state battery interfaces.

### Milestones

1. Thermochemical stability between LLZ and interface-coated NMC experimentally determined. (Q3, FY 2022; In progress, to be completed by November 2022)
2. Experimental results compared with computational results, and model refined for side reactions and process optimization. (Q4, FY 2022; In progress, to be completed by November 2022)
3. Ten-times reduction in interfacial impedance between coated LLZ/NMC and uncoated LLZ/NMC interfaces demonstrated by co-sintering. (Q4, FY 2022; In progress, to be completed by November 2022)
4. Fabricate tri-layer cell with composite NMC-LLZ cathode layer and evaluate. (Q1, FY 2023; In progress)
5. *Go/No-Go Decision*: Demonstrate final cell with achieved performance. (Q2, FY 2023; In progress)

**COVID-19 Impact.** Progress on experimental results was impacted by COVID-19, which closed labs for several months; this resulted in a six-month, no-cost extension reflected in the milestone dates above.

## Progress Report

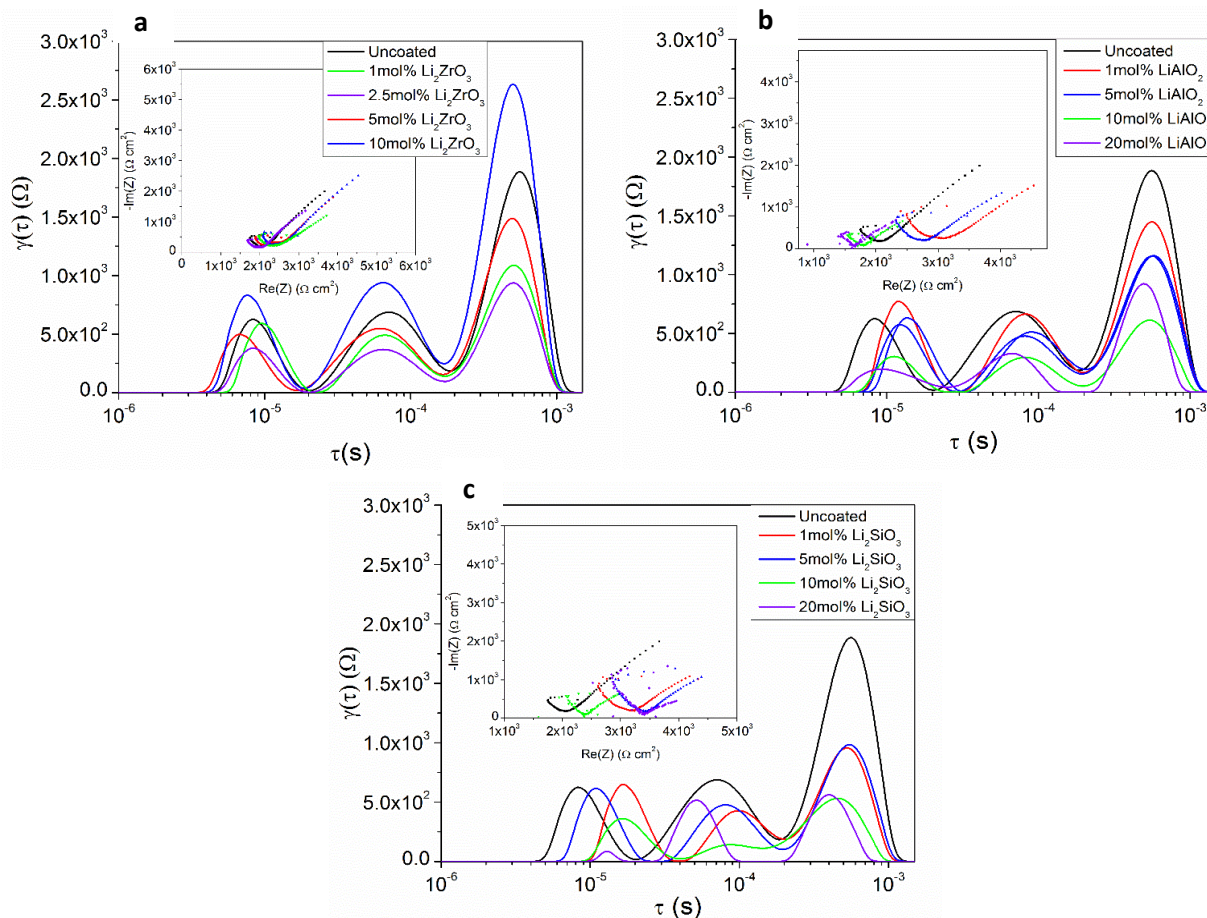


**Figure 28.** Nyquist plots and distribution of relaxation times analysis of electrochemical impedance spectroscopy of (a)  $\text{Li}_2\text{ZrO}_3$ -NMC-622, (b)  $\text{LiAlO}_2$ -NMC-622, and (c)  $\text{Li}_2\text{SiO}_3$ -NMC-622 co-sintered in a 1:1 wt ratio with  $\text{Li}_{6.75}\text{La}_3\text{Zr}_{1.75}\text{Ta}_{0.25}\text{O}_{12}$  onto LLZTO trilayers at  $1000^\circ\text{C}$  in  $\text{O}_2$ .

Various interlayer coatings as identified by previous computational work were synthesized on the surface of  $\text{LiNi}_{0.6}\text{Mn}_{0.1}\text{Co}_{0.1}$  (NMC-622) via a solution-based process. These include  $\text{LiAlO}_2$ ,  $\text{Li}_2\text{SiO}_3$ , and  $\text{Li}_2\text{ZrO}_3$ . These coated NMC powders were then co-sintered in a 1:1 weight ratio of NMC :  $\text{Li}_{6.75}\text{La}_3\text{Zr}_{1.75}\text{Ta}_{0.25}\text{O}_{12}$  (LLZTO) at  $1000^\circ\text{C}$  in  $\text{O}_2$  onto LLZTO trilayers to fabricate symmetric cells for electrochemical impedance spectroscopy (EIS) testing. These results for varying interfacial coating thicknesses are summarized in Figure 28. Shown in Figure 28a-b, 2.5 mol% was the optimal coating thickness for  $\text{Li}_2\text{ZrO}_3$ , leading to a  $2.5\times$  reduction in impedance versus uncoated NMC. For the  $\text{LiAlO}_2$  and  $\text{Li}_2\text{SiO}_3$  coatings, 10 mol% was optimal, with both leading to a  $4\times$  reduction in impedance.

Since the computational results indicate that the lithium concentration gradient between NMC and LLZTO is the main driving force for the reaction, more lithiated versions of the silicate and aluminate coatings ( $\text{Li}_5\text{AlO}_4$  and  $\text{Li}_4\text{SiO}_4$ ) were also synthesized and coated on NMC-622. These EIS results are shown in Figure 29. At the same molar concentration, the higher lithium content aluminate and silicate reduced the impedance  $2\times$  more than their less lithiated counterparts, confirming the computational results that reducing the difference in the lithium concentration at the interfaces attenuates the interfacial reaction of NMC and LLZTO.

Efforts to fabricate a full cell via sintering a tape-casted NMC/LLZTO composite cathode, dense LLZTO layer, and LLZTO porous anode for lithium metal are under way. However, the shrinkage mismatch between the

porous anode tape and the initial formulations of the composite NMC tapes are causing extreme curling. Further process optimization is in progress to obtain flat samples. This will include further analysis of the shrinkage rates using an optical dilatometer and adjusting the tape thickness and binder ratios.

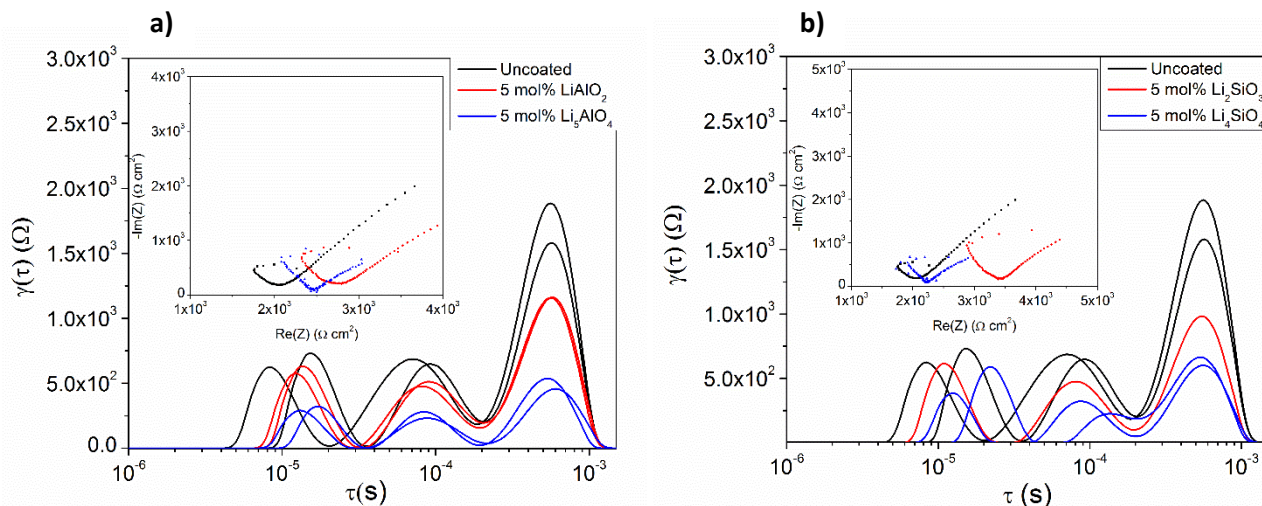


Figure 29. Nyquist plots (inset) and distribution of relaxation times analysis of the electrochemical impedance spectroscopy of (a)  $\text{LiAlO}_2\text{-NMC-622}$ , and (b)  $\text{Li}_2\text{SiO}_3\text{-NMC-622}$  co-sintered in 1:1 wt ratio with  $\text{Li}_{6.75}\text{La}_3\text{Zr}_{1.75}\text{Ta}_{0.25}\text{O}_{12}$  (LLZTO) onto LLZTO trilayers at  $1000^\circ\text{C}$  in  $\text{O}_2$ .

X-ray diffraction results additionally support the efficacy of the lithiated aluminate and silicate coating in preventing reaction between NMC and LLZTO. Figure 30 contains plots of the weight percentage of each phase present in a co-sintered NMC/LLZTO pellet as determined by Rietveld refinement. The uncoated NMC co-sintered with 40 mol% excess LLZTO produces 2 wt% of the decomposition phase (perovskite). The  $\text{Li}_2\text{SiO}_3$  coating shows similar amounts of perovskite compared to the uncoated NMC; however, the  $\text{LiAlO}_2$  coating shows no observable increase in the perovskite phase. These experiments continue and will be updated as new coating materials are tried.

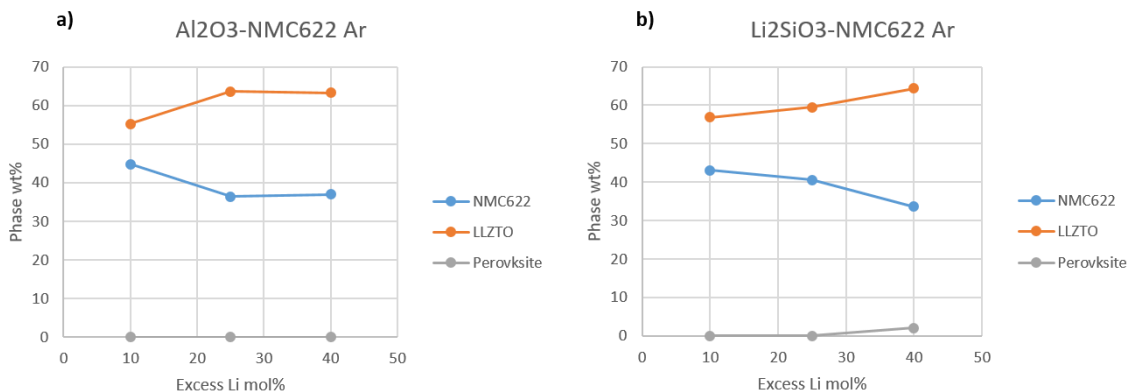


Figure 30. Rietveld refinement results of X-ray diffraction of (a)  $\text{LiAlO}_2\text{-NMC-622}$ , and (b)  $\text{Li}_2\text{SiO}_3\text{-NMC-622}$  co-sintered in a 1:1 wt ratio with  $\text{Li}_{6.75}\text{La}_3\text{Zr}_{1.75}\text{Ta}_{0.25}\text{O}_{12}$  (LLZTO) onto LLZTO trilayers at  $900^\circ\text{C}$  in argon.

The results for the computation model for the interface side reaction are also compared with experimental results. The experimental results reported the formation of delithiated phases as side products in agreement with the team's computation predictions. For the process optimization, experimental results show improvement in interface stability using oxygen gas environment. To improve their model to account for the process optimization, they include the sintering environment into their computation model using the grand potential phase diagram approach. In the improved model, the external environment is open to the interface for the

potential reaction evaluations. Their models consider the environment in two ways. One way is through the control of lithium chemical potential, which is a key element loss during sintering, and can strongly interact with the environment. Thus, the environment chemical potential can be translated into the lithium chemical potential. In their results, the team observes that having an appropriate range of lithium chemical potential can reduce lithium loss and promote formation of passivation layer, such as  $\text{Li}_2\text{O}$ , which can kinetically limit lithium loss and mitigate side reaction. In another model, they directly consider the oxygen gaseous environment. In this model, they observe significant stabilization of the cathode materials, in agreement with previously reported experimental results. In summary, the computation models for process optimization are achieving good agreement with experiments. In addition, as shown above, the experimental results for inter-layer materials are compared with previous computation results. The coating layer materials predicted by computation are now verified by experiments. These coating layers show good stabilities and good conductive properties, confirming and verifying the computation prediction of the stable coating between garnet and cathode.

**Table 1. Stability of LLZO–NMC-111 under varying lithium chemical potential.**

$\mu_{\text{Li}}$ (eV)	Ratio of NMC	Ratio of LLZO	Mutual Rxn. E. (meV/atom)	Phase Equilibria
0	0.43	0.57	-81	$\text{La}_2\text{O}_3, \text{Li}_2\text{O}, \text{ZrCo}_2, \text{ZrMn}_2, \text{ZrNi}_3$
-0.25	0.75	0.25	-29	$\text{La}_2\text{O}_3, \text{Li}_2\text{O}, \text{MnCo}, \text{Zr}_6\text{Co}_{23}, \text{ZrNi}_3$
-0.5	1.00	0.00	0.00	$\text{Co}, \text{Li}_2\text{O}, \text{MnCo}, \text{MnNi}_3$
-1	0.53	0.47	-27	$\text{Co}, \text{La}_2\text{MnCoO}_6, \text{Li}_2\text{O}, \text{Li}_6\text{Zr}_2\text{O}_7, \text{MnNi}_3$
-1.25	0.43	0.57	-87	$\text{Co}, \text{La}_2\text{MnCoO}_6, \text{Li}_2\text{O}, \text{Li}_6\text{Zr}_2\text{O}_7, \text{Ni}$
-1.75	0.43	0.57	-155	$\text{La}_2\text{MnCoO}_6, \text{Li}_2\text{O}, \text{Li}_6\text{CoO}_4, \text{Li}_6\text{Zr}_2\text{O}_7, \text{Ni}$
-2	0.43	0.57	-151	$\text{La}_2\text{MnCoO}_6, \text{Li}_2\text{O}, \text{Li}_6\text{Zr}_2\text{O}_7, \text{LiCoO}_2, \text{Ni}$
-2.25	0.43	0.57	-139	$\text{La}_2\text{MnCoO}_6, \text{Li}_2\text{O}, \text{Li}_6\text{Zr}_2\text{O}_7, \text{LiCoO}_2, \text{NiO}$
-2.75	0.43	0.57	-125	$\text{La}_2\text{MnCoO}_6, \text{Li}, \text{Li}_2\text{NiO}_3, \text{Li}_2\text{O}, \text{Li}_6\text{Zr}_2\text{O}_7, \text{LiCoO}_2$
-3	0.43	0.57	-138	$\text{La}_2\text{MnCoO}_6, \text{Li}, \text{Li}_2\text{NiO}_3, \text{Li}_2\text{O}_2, \text{Li}_6\text{Zr}_2\text{O}_7, \text{LiCoO}_2$
-3.25	0.43	0.57	-146	$\text{La}_2\text{MnCoO}_6, \text{Li}, \text{Li}_2\text{NiO}_3, \text{Li}_2\text{O}_2, \text{Li}_2\text{ZrO}_3, \text{LiCoO}_2$
-3.5	0.43	0.57	-140	$\text{La}_2\text{MnCoO}_6, \text{Li}, \text{Li}_2\text{NiO}_3, \text{LiCoO}_2, \text{O}_2, \text{ZrO}_2$
-3.75	0.43	0.57	-158	$\text{La}_2\text{MnCoO}_6, \text{Li}, \text{Li}(\text{CoO}_2)_2, \text{NiO}, \text{O}_2, \text{ZrO}_2$
-4	0.43	0.57	-168	$\text{CoO}_2, \text{La}_2\text{MnCoO}_6, \text{Li}, \text{NiO}, \text{O}_2, \text{ZrO}_2$

**Table 2. Stability of LLZO–NMC-111 interface under varying  $\text{O}_2$  chemical potential.**

$\mu_{\text{O}}$ (eV)	Ratio of NMC	Ratio of LLZO	Mutual Rxn. E. (meV/atom)	Phase Equilibria
0.00	0.43	0.57	-141	$\text{La}_2\text{MnCoO}_6, \text{Li}, \text{Li}_2\text{NiO}_3, \text{Li}_2\text{O}_2, \text{Li}_6\text{Zr}_2\text{O}_7, \text{LiCoO}_2$
-0.25	0.43	0.57	-145	$\text{La}_2\text{MnCoO}_6, \text{Li}, \text{Li}_2\text{NiO}_3, \text{Li}_2\text{O}_2, \text{Li}_2\text{ZrO}_3, \text{LiCoO}_2$
-0.50	0.43	0.57	-141	$\text{La}_2\text{MnCoO}_6, \text{Li}, \text{Li}_2\text{NiO}_3, \text{LiCoO}_2, \text{O}_2, \text{ZrO}_2$
-0.75	0.43	0.57	-160	$\text{La}_2\text{MnCoO}_6, \text{Li}, \text{Li}(\text{CoO}_2)_2, \text{NiO}, \text{O}_2, \text{ZrO}_2$
-1.00	0.43	0.57	-168	$\text{CoO}_2, \text{La}_2\text{MnCoO}_6, \text{Li}, \text{NiO}, \text{O}_2, \text{ZrO}_2$

## Patents/Publications/Presentations

### Publication

- Ren, Y., and E. D. Wachsman. “All-Solid-State Li/LLZO/LCO Battery Enabled by Alumina Interfacial Coating.” *Journal of The Electrochemical Society* 169 (2022): 040529.

### Presentation

- 23<sup>rd</sup> International Conference on Solid State Ionics, Boston, Massachusetts (July 17–22, 2022): “Enabling High Rate Metal Anodes by Tailored Structures and Interfaces.” Keynote.

## Task 1.13 – Development of All-Solid-State Battery Using Anti-Perovskite Electrolytes (Zonghai Chen and Tao Li, Argonne National Laboratory)

**Project Objective.** The objective of this project is to develop an optimized anti-perovskite electrolyte with a stabilized interface for scalable fabrication of liquid-free solid-state batteries.

**Impact.** The project will lead to impact on several areas: (1) establishing structure-property relationship of anti-perovskite electrolytes, (2) understanding and quantifying the interaction between the electrolytes and the environment, (3) understanding and mitigating the failure of all-solid-state batteries (ASSBs) at solid-solid interface, and (4) developing a scalable process for fabrication of ASSBs.

**Approach.** The project approach is multifold: (1) *chemistry design*: multiple doping at anion sites will be pursued to improve structural stability ionic conductivity and environmental compatibility; (2) *interfacial design*: surface coating will be deployed to improve the chemical and mechanical stability of solid/solid interface; and (3) *process development*: a scalable fabrication process based on melt-infiltration or dry lamination will be developed for fabrication of ASSBs.

**Out-Year Goals.** The project has the following out-year goals:

- Developing high-performance anti-perovskite electrolytes.
- Accessing the air stability and proton mobility of anti-perovskite electrolytes.
- Stabilizing the solid/solid interface through interfacial engineering.
- Prototyping liquid-free cells using anti-perovskite electrolytes.

**Collaborations.** This project collaborates with Y. Z. Liu and W. Q. Xu (Argonne National Laboratory), X. H. Xiao (Brookhaven National Laboratory), and H. Meng (University of Arkansas).

### Milestones

1. Setting up high-throughput synthesis capability. (Q1, FY 2022; Completed)
2. Optimizing synthesis condition for anti-perovskite electrolytes. (Q2, FY 2022; Completed)
3. Investigating structural stability of doped electrolytes. (Q3, FY 2022; Completed)
4. Investigating transport properties of doped electrolytes. (Q4, FY 2022; Completed)

## Progress Report

A series of phase pure anti-perovskite electrolyte,  $\text{Li}_2\text{HOCl}_{1-x}\text{Br}_x$  ( $0 < x < 1$ ), has been synthesized. Electrolyte pellets of these electrolytes were previously fabricated using a cold-press approach, and the measured Li-ion conductivity was in the range of  $10^{-5}$  S/cm. The best Li-ion conductivity was observed for the pellet made from  $\text{Li}_2\text{HOCl}_{0.75}\text{Br}_{0.25}$ . Figure 31 shows two typical scanning electron microscopy images of cold-pressed anti-perovskite electrolyte pellets. It can be clearly seen that the electrolytes were a mixture of big particles (micron-sized) and fine particles ( $\sim 100$ -nm in size). Particularly, big voids (up to micron in size) can be easily spotted in the cold-pressed pellet. The abundance of big voids in the pellet can greatly reduce the active Li-ion conducting pathways through the pellet, leading to a significantly lower nominal Li-ion conductivity measured for these pellets.

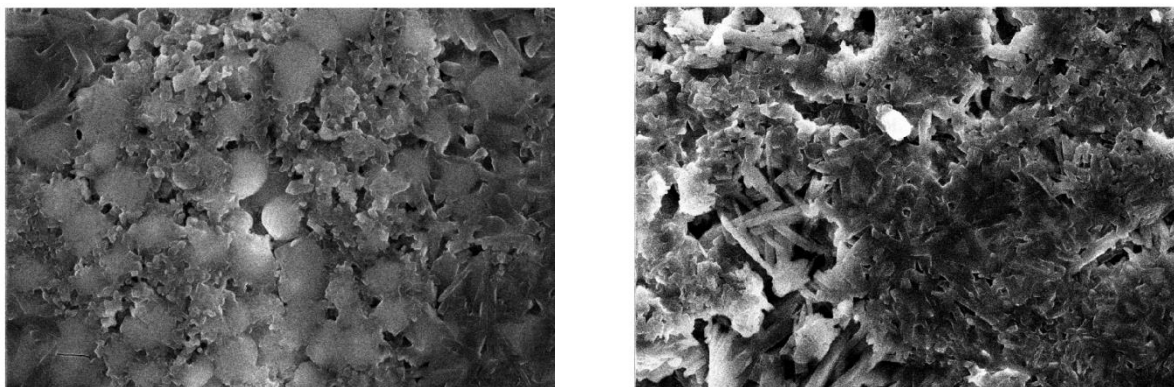


**Figure 31. Scanning electron microscopy images of cold-pressed electrolyte pellets from (a)  $\text{Li}_2\text{HOCl}$  and (b)  $\text{Li}_2\text{HO}_{0.75}\text{Br}_{0.25}$ , showing the presence of big voids, which can significantly reduce the nominal Li-ion conductivity of the electrolyte pellets.**

An effort was made to densify the electrolyte pellets using a hot-press approach. The electrolyte powder was heated to  $200^\circ\text{C}$ , and a pressure of 1000 MPa was applied to densify the pellet. Mechanically strong pellets were obtained through the hot-press approach. Figure 32 shows the measured Li-ion conductivity of anti-perovskite electrolyte pellets at various temperatures. A similar slope was observed for all electrolytes, implying a similar activation energy for Li-ion conduction. The linear fitting results show that the samples have an activation energy of  $\sim 0.6$  eV, which is very close to the numbers measured for cold-pressed pellets. This suggests that the hot-press process did not alter the chemical nature of the electrolytes. Compared to the conductivity measured for cold-pressed samples, the conductivity was generally improved two-to-three fold using the hot-press process. The current exercise was limited to  $200^\circ\text{C}$  with the intent to avoid the extra phase transformation that occurs at about  $250^\circ\text{C}$  (see Figure 33). A careful optimization of the hot-press process beyond  $250^\circ\text{C}$  will be conducted to further improve densification of anti-perovskite electrolyte pellets.

Figure 34 shows the team's latest progress on assembling an ASSB using an anti-perovskite electrolyte. The cell was assembled using  $\text{Li}_2\text{HOCl}_{0.75}\text{Br}_{0.25}$  electrolyte; the cathode is composed of  $\text{LiNi}_{0.6}\text{Mn}_{0.2}\text{Co}_{0.2}\text{O}_2$  (NMC-622), carbon black, and  $\text{Li}_2\text{HOCl}_{0.75}\text{Br}_{0.25}$  (catholyte), with lithium as the negative electrode. With their current optimization effort, the best Li-ion conductivity achieved is still at  $10^{-5}$  range at room temperature. Therefore, the cell was cycled at C/6 at  $60^\circ\text{C}$  between 2.5 V and 4.3 V. It is also observed that the cell delivered a capacity of 205 mAh/g at initial charge, which is comparable to the specific capacity obtained in cells using liquid electrolytes. However, the initial discharge capacity measured was  $\sim 165$  mAh/g, showing about 20% initial irreversible capacity loss, which is substantially higher than those for liquid cells ( $\sim 10\%$ ). The high initial irreversible capacity loss can potentially result from either (1) parasitic reactions between the cathode and the electrolyte to form the needed cathode/electrolyte interface, or (2) a loss of active material during discharge when the active cathode material particles contract.

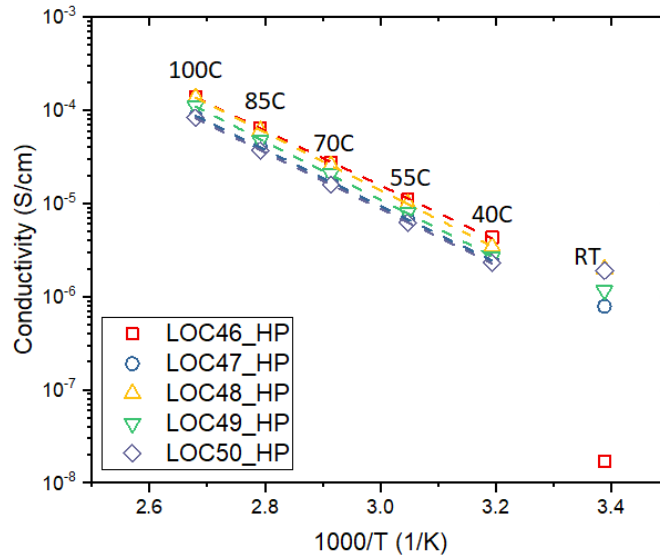


Figure 32. Measured Li-ion conductivity of hot-pressed anti-perovskite electrolyte pellets. The pellets were prepared at 200°C and 1000 MPa to reduce their porosity.

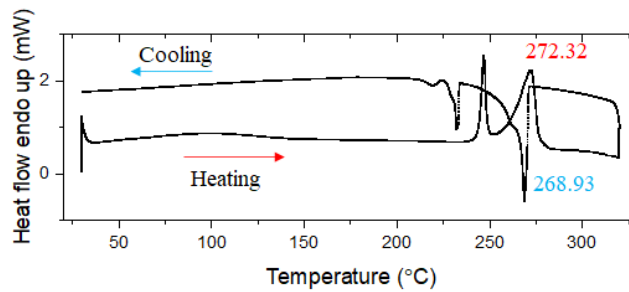


Figure 33. Differential scanning calorimetry of  $\text{Li}_2\text{HOC}_{10.75}\text{Br}_{0.25}$  showing the extra phase transformation before the melting of the electrolyte (at ~ 250°C).

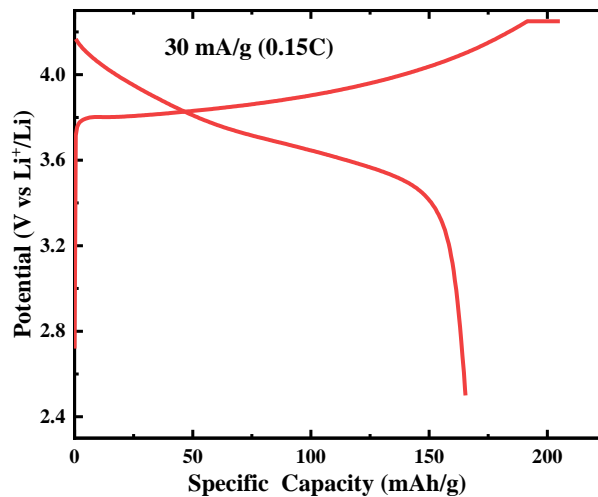


Figure 34. Initial voltage profile of all-solid-state cell using  $\text{LiNi}_{0.6}\text{Mn}_{0.2}\text{Co}_{0.2}\text{O}_2$  (NMC-622) as the cathode, and  $\text{Li}_2\text{HOC}_{10.75}\text{Br}_{0.25}$  as both the electrolyte and the catholyte.

## Patents/Publications/Presentations

The project has no patents, publications, or presentations to report this quarter.

## Task 1.14 – Lithium Halide-Based Superionic Solid Electrolytes and High-Voltage Cathode Interface (Robert Sacci, Oak Ridge National Laboratory)

**Project Objective.** The project aims to develop low-temperature solution-based synthesis strategy for high ionic conducting halide-based solid electrolyte (SE) and to enable approaches to develop a scalable process for integrating halide-based SE within porous high-voltage Li-ion cathode matrix. Years 1 and 2 aim at developing low-cost, solution-based synthesis routes to produce a halide class of superionic conductor belonging to  $\text{Li}_3\text{MX}_6$  (where  $\text{M} = \text{Sc}, \text{Y}, \text{La}, \text{Er}, \text{In}$ , and  $\text{X} = \text{Cl}, \text{Br}, \text{I}$ ) along with enabling electrochemical and structural characterization. Parallel efforts in years 2 and 3 target developing synthesis and processing methods where the high-voltage stable halide-based SEs can be readily infiltrated within the porous cathode structures such as  $\text{LiNi}_{0.6}\text{Mn}_{0.2}\text{Co}_{0.2}\text{O}_2$  (NMC-622), high-voltage Mn-Ni spinel ( $\text{LiMn}_{1.5}\text{Ni}_{0.5}\text{O}_4$ ), and recent fluorinated Mn-rich disorder rock salt cathodes. Years 3 and 4 focus on designing and fabricating thin halide SE separators with a thickness of 50  $\mu\text{m}$  or lower and optimizing the cathode microstructure. Finally, years 4 and 5 will target developing approaches for anode-free lithium plating and stripping on alloyed or engineered copper current collectors at relatively higher current densities aimed at improving the volumetric energy density of solid-state batteries (SSBs) with a high loading cathode and thin halide SE separator.

**Impact.** The proposed tasks and metrics aim at addressing the long-term Vehicle Technologies Office goal for developing SSBs at ambient temperature with energy density in the range of 500 Wh/Kg and 1000 Wh/L for electric drive vehicles. Advances in scalable processing of superionic SEs, stabilizing electrode-electrolyte interfaces, and promoting long cycle life are all needed to meet the energy density and cost targets for next-generation batteries for electric vehicles.

**Approach.** The project employs a multifaceted approach: (1) conduct solution-based synthesis of the metal halide superionic conductor as the platform to enable robust cathode-electrolyte interface processing for SSBs, (2) infiltrate pore structures using solution-based processing that deposits high-conductivity SEs within cathode pores, and (3) facilitate lithium transport and improve stability using cation doping (divalent to introduce lithium vacancies, and lanthanum to prevent indium redox).

**Out-Year Goals.** Demonstrate single-layer, pouch-cell SSB containing a thin halide SE separator coupled with high-voltage cathodes with 70% capacity retention over 300 cycles at 2  $\text{mA}/\text{cm}^2$  in an anode-free SSB configuration that can attain 1000 Wh/L in prototype cells.

**Collaborations.** Y. Yao and team at University of Houston (UH) are funded collaborators for halide-based SSB fabrication, testing, and interfacial studies. The project also involves unfunded collaboration with SLAC National Accelerator Laboratory for X-ray absorption spectroscopy and synchrotron X-ray diffraction of SEs.

### Milestones

1. Produce gram-scale quantities of  $\text{Li}_3\text{InCl}_6$  SE using solvent-phase synthesis. (Q1, FY 2022; Completed)
2. Obtain phase-pure  $\text{Li}_3\text{InCl}_6$  thin pellets with  $\sim 1 \text{ mS}/\text{cm}^{-1}$  conductivity. (Q2, FY 2022; Completed)
3. Utilize neutron diffraction, X-ray photoelectron spectroscopy, Raman, and electron microscopy to characterize  $\text{Li}_3\text{InCl}_6$  SE. (Q3, FY 2022; Completed)
4. Compare structure and  $\text{Li}^+$  conductivity of  $\text{Li}_3\text{InCl}_6$  prepared through solvent-mediated versus mechanochemical;  $> 5\text{g}$  batch with ionic conductivity in the range of  $1 \text{ mS}/\text{cm}^{-1}$ . (Q4, FY 2022; Completed)

## Progress Report

The team previously switched two quarterly objectives. Last quarter, they reported on synthesis and resulting properties of the  $\text{Li}_3\text{InCl}_6$  products. The summarized conclusions were: (1) 10% excess of rare-earth improves synthesis purity; (2) mechanical and  $\text{H}_2\text{O}$ -based synthesis have little grain boundary (GB) resistances while ethanol-based had significantly more, suggesting surface termination difference; and (3) excessive pressure induces structural or bulk alignment changes in bulk  $\text{Li}_3\text{InCl}_6$  that results in decreased overall conductivity (increased GB resistivity). Having thus completed the fourth quarter Go/No-Go decision point, they focused on preliminary testing of solution infiltration of membranes to form free-standing  $\text{Li}_3\text{InCl}_6$  films and on following the synthesis of  $\text{Li}_3\text{InCl}_6$  from ethanol. Y. Yao's group at UH is testing the project's  $\text{Li}_3\text{InCl}_6$  materials synthesized through ethanol and  $\text{H}_2\text{O}$ -mediated routes.

The team has made their first  $\text{Li}_3\text{InCl}_6$  infiltrated membrane, as pictured below. They tried infiltrating commercial polypropylene (Celgard); however, neither  $\text{H}_2\text{O}$  nor ethanol solutions wet the material and therefore do not penetrate. That said, it does appear visually that a thin, yet inhomogeneous  $\text{Li}_3\text{InCl}_6$  layer can be deposited atop this membrane. The successful infiltration occurred when they used a highly porous polyaramid membrane (that is, Dreamweaver Gold). The  $\text{Li}_3\text{InCl}_6$  coats the fibers from ethanol very well. They are in the process of pressing these membranes and taking conductivity measurements. They speculate that membranes with porosity of  $> 70\%$  and little-to-no micropores are required for successful infiltration and electrolyte synthesis in this form factor. Figure 35 shows that the  $\text{Li}_3\text{InCl}_6$ -coated separator becomes more textured and contains numerous small sparkling deposits. That said, the loading for this sample was poor, and the resulting conductivity nearly nonexistent. The team is progressing by using dip casting into hot ( $80^\circ\text{C}$  solutions), as they believe the poor loading is due to using overly dilute solutions.

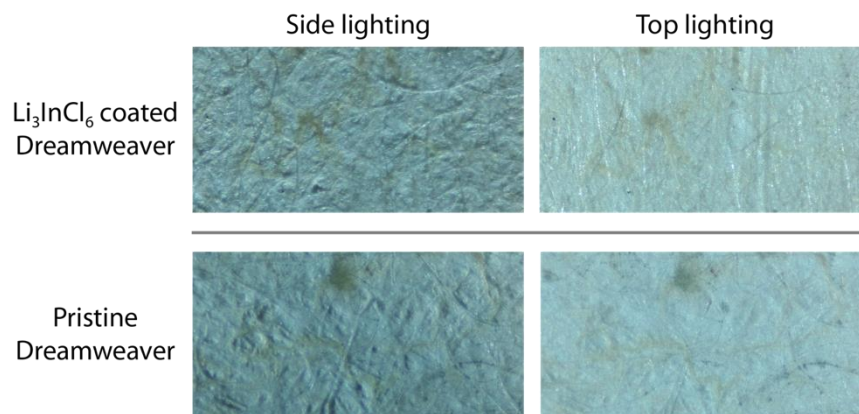


**Figure 35. Optical micrographs of Dreamweaver Gold porous membranes before and after  $\text{Li}_3\text{InCl}_3$  infiltration from ethanol solution precursor.**

The team has been successful in using neutron scattering to probe the difference between  $\text{H}_2\text{O}$ -mediated synthesis and ethanol-mediated synthesis of  $\text{Li}_3\text{InCl}_6$ . Figure 36 shows that ethanol-mediated synthesis occurs differently than  $\text{H}_2\text{O}$ -mediation. Here, they see that on a base drying at  $60^\circ\text{C}$ ,  $\text{LiCl}$  and  $\text{InCl}_3$  are seen along with a third unknown phase. Heating this solution to near  $100^\circ\text{C}$  shows that the  $\text{InCl}_3$  and the unknown phase drop out and are replaced by an intermediate phase. The presence of  $\text{LiCl}$  does not change, though the peaks corresponding to  $\text{LiCl}$  do decrease by 20%. Heating to  $120^\circ\text{C}$ , shows that the  $\text{Li}_3\text{InCl}_6$  product forms along with further decrease in  $\text{LiCl}$  signals. At  $150^\circ\text{C}$ , Pure product is achieved. For  $\text{H}_2\text{O}$  [reported in R. Sacci, et al. *Journal of Materials Chemistry A* 9 (2021): 990–996], there were two intermediate phases and no detection of  $\text{LiCl}$ . This suggests that for ethanol-synthesized samples,  $\text{LiCl}$  may exist in trace amounts or be more descriptive of the GBs. This key difference led the team to investigate how  $\text{Li}_3\text{InCl}_3$  synthesized from ethanol evolved during full-cell cycling.

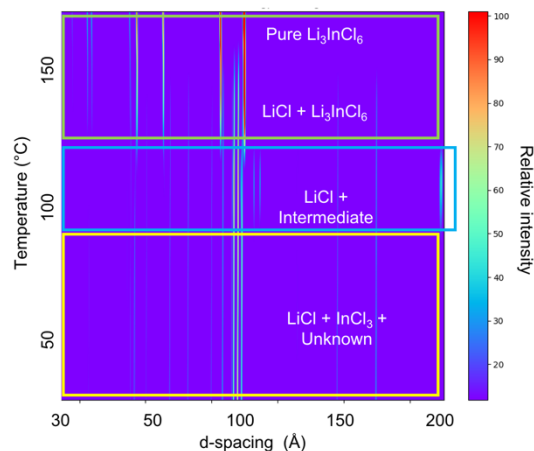


Figure 36. *In situ* neutron diffraction of  $\text{Li}_3\text{InCl}_6$  being synthesized from ethanol solution.

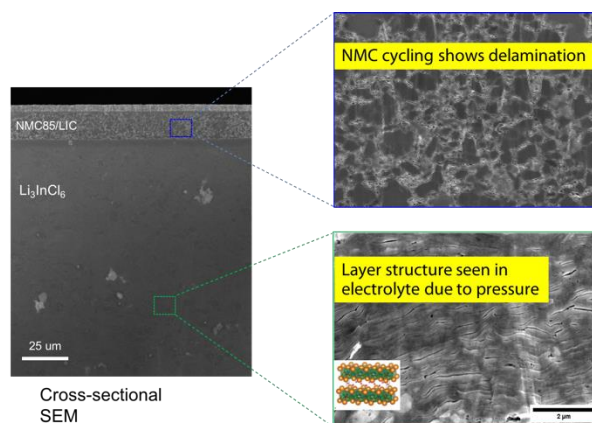


Figure 37. Scanning electron micrograph cross-sections of a Li-In alloy/ $\text{LiNi}_{0.85}\text{Mn}_{0.1}\text{Co}_{0.05}\text{O}_2$  full cell that uses ethanol-derived  $\text{Li}_3\text{InCl}_6$  as the bulk solid electrolyte and the electrolyte within the cathode. After 50 cycles, the team observes extensive delamination in both the cathode- $\text{Li}_3\text{InCl}_6$  composite and the bulk  $\text{Li}_3\text{InCl}_6$  itself.

The UH group has been testing the full-cell cycling stability of the  $\text{Li}_3\text{InCl}_6$  SEs. Thus far, the material has been used to access 170 mAh/g of the  $\text{LiNi}_{0.85}\text{Mn}_{0.1}\text{Co}_{0.05}\text{O}_2$ 's 220-mAh/g theoretical capacity during the 1<sup>st</sup> cycle; however, the capacity rapidly decays. These cells were pressurized at 5 MPa, which is significantly lower than literature reports of 200 MPa. Figure 37 reveals the likely cause of capacity fade is the SE delaminating from the NMC cathode. They can see that the grains become easy to distinguish in the scanning electron microscopy, and voids can be seen. Interestingly, in the bulk they see similar delamination and void formation. They saw evidence in the previous quarter that increased pressure results in mechanical relaxations that decrease bulk conductivity. Here, they see that pressure and/or cycling induces large-scale relaxations. Last quarter, they also saw that GB impedance is highest in ethanol-synthesized products. Putting all of this together, it seems that ethanol-synthesized samples may contain trace LiCl that may collect at grains. These nano-sized LiCl domains would then affect cycling performances, leading to increasing delamination that cannot be overcome by the mere addition of pressure.

They have concluded that alcohol-based synthesis is indeed faster and can occur at lower temperatures; however, LiCl forms during ethanol drying and then reacts with an intermediate phase. This means that trace LiCl may remain after heating to 150°C. They will test the overall performance of these materials after annealing at 200°C to see if they are more robust.

## Patents/Publications/Presentations

### Presentation

- American Chemical Society Fall Meeting, Chicago, Illinois (August 22–25, 2022): “Substituted Argyrodites and Halide-Based Solid Electrolytes for All-Solid-State Batteries”; R. Sacci and J. Nanda.

**Task 1.15 – Developing an *In Situ* Formed Dynamic Protection Layer to Mitigate Lithium Interface Shifting: Preventing Dendrite Formation on Metallic Lithium Surface to Facilitate Long Cycle Life of Lithium Solid-State Batteries**  
(Deyang Qu, University of Wisconsin, Milwaukee)

**Project Objective.** The objective of this project is to research, develop, and test Li-metal-based batteries that implement solid Li-ion conductors equipped with a formed dynamic protection layer. The proposed project aims to enable safe, long-cycle lithium anodes to achieve cell performance targets of 400 Wh/Kg, over 100 cycles, with a 15-year shelf life, and < \$100/KWh cost.

**Project Impact.** Project efforts are to contribute an in-depth understanding of the lithium interface and dendrite growth prevention to the field of Li-metal batteries, which will pave the way for eventual development of high-energy-density, low-cost, and long-lasting lithium batteries. This advancement could be a crucial selling point for the greater adoption of electric vehicles. This project will make possible the translation of fundamental research into practical implementation of high-energy lithium anodes, enabling eventual achievement of cell performance targets.

**Approach.** The novelty of this approach is that the team intends to mitigate the dendrite problem by creating a dynamic protection layer during the interface shift to prevent dendrite formation throughout battery operation.

**Out-Year Goals.** The project has three one-year goals: (1) *in situ* diagnostic tools are verified; (2) thin solid-state electrolyte (SSE) and cathode are made; and (3) all-solid-state cells are made.

**Collaborations.** The principal investigator (PI) is the Johnson Control Endowed Chair Professor, who has close and frequent collaboration with Johnson Controls’ scientists and engineers. The collaboration enables the team to validate the outcomes of fundamental research in pilot-scale cells. The PI also has been working closely with top scientists at Argonne National Laboratory, Brookhaven National Laboratory, Lawrence Berkeley National Laboratory, and Pacific Northwest National Laboratory, and with U. S. industrial collaborators, for example, General Motors, Millipore, and Clarios. In addition, the team works with international collaborators in China, Japan, and South Korea. These collaborations will be strengthened and expanded to give this project a vision with both today’s state-of-the-art technology and tomorrow’s technology in development, while incorporating feedback from material designers and synthesizers upstream, as well as from industrial end users downstream.

### Milestones

1. Coated lithium anode with dendrite suppression demonstrated. Demonstrate effectiveness of inorganic artificial protective layer. (Q1, FY 2022; Completed)
2. Lithium anode with suppressed dendrite growth demonstrated. Demonstrate effectiveness of artificial protective layer. (Q2, FY 2022; Completed)
3. Down select materials and cell fabrication method for final cell build. (Q3, FY 2022; Completed)
4. All-solid-state cell build and test. (Q4, FY 2022; Completed)
5. Dendrite suppression demonstrated; cell performance verified. (Q4, FY 2022; Completed)

## Progress Report

Last quarter, the team reported an all-solid-state lithium battery made with sulfur cathode and prelithiated silicon anode ( $\mu\text{-Li}_x\text{Si}$ ). 1200 mAh/g after 200 cycles @60°C was shown. 800 mAh/g after 500 cycles was demonstrated in the cell with 3.0 mg/cm<sup>2</sup> sulfur loading @25°C.

This quarter, they confirmed the reversibility of the prelithiated silicon anode in an all-solid-state cell. Figure 38a-d shows the stacking pressure change of the  $\mu\text{-Li}_x\text{Si}$  electrode during a constant volume cycling of a  $\mu\text{-Li}_x\text{Si} | \text{SSE} | \text{Li}_4\text{Ti}_5\text{O}_{12}$  (LTO) full cell. Since the phase transition of LTO cathode caused negligible volume change, the net stress change of the full cell was governed by the  $\mu\text{-Li}_x\text{Si}$  anode alone.

Theoretically, the stress change only depends on the quantity of the lithium inserted or extracted from the  $\mu\text{-Li}_x\text{Si}$  electrode. In reality, however, the stress change can be buffered due to the elastic deformation of SSE layer and the presence of pores and void spaces within the cell. For example, the thicker the SSE layer is, the smaller stress change would be detected. As shown in Figure 38a (bottom) and Figure 38d (bottom), a relatively large stress hysteresis (irreversibility of stress change) is revealed from the initial cycles, which gradually vanishes in the subsequent cycles. At the 5<sup>th</sup> cycle, the stress change became highly reversible on charge/discharging (Figure 38a, bottom); therefore, a stable or reversible “cell breathing” was achieved. Figure 38e-f shows the comparison of a prolonged cycling test at 4 mA cm<sup>-2</sup> and 4 mAh cm<sup>-2</sup> between a Li-In|SSE|Li-In cell and a  $\mu\text{-Li}_x\text{Si}$ |SSE| $\mu\text{-Li}_x\text{Si}$  cell. The Li-In|SSE|Li-In cell experienced a severe voltage hysteresis until reaching the cutoff voltage (-5 V) after 13 cycles (Figure 38f), while the  $\mu\text{-Li}_x\text{Si}$ |SSE| $\mu\text{-Li}_x\text{Si}$  cell remained stable cycling over 325 hours (Figure 38e).

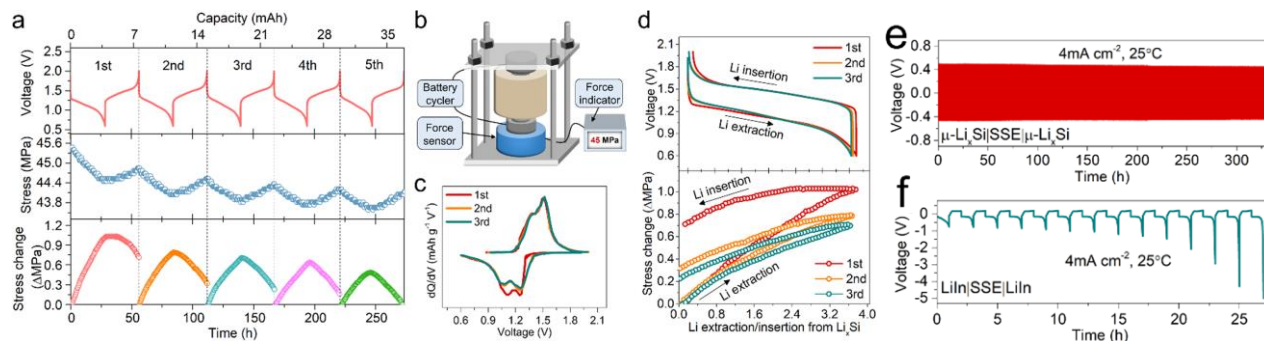


**Figure 38.** (a) The voltage profiles of  $\mu\text{-Li}_x\text{Si}|\text{SSE}|\text{LTO}$  cell (top) along with correlated evolution of stress (middle) and stress change (bottom). (b) Schematic of pressure-monitoring cell. (c) Corresponding  $dQ/dV$  curves. (d) Voltage and stress change plotted as a function of the molar amount of lithium extracted from or inserted into the  $\mu\text{-Li}_x\text{Si}$  phase. Prolonged cycling of (e) the  $\mu\text{-Li}_x\text{Si}|\text{SSE}|\mu\text{-Li}_x\text{Si}$  symmetric cell and (f) the Li-In|SSE|Li-In symmetric cell at 25°C.

In addition, this quarter the team made and began testing 2-inch × 3-inch all-solid-state pouch cells (full cell). Figure 39 shows the cell along with the cell under testing in a pressure fixture.



**Figure 39.** (left) All-solid-state pouch cell (full cell, 2 × 3 inch), and (right) cell under test in a pressure fixture.

## Patents/Publications/Presentations

### Publication

- Ji, W., X. Zhang, M. Liu, T. Ding, H. Qu, D. Qiu, D. Zheng, and D. Qu.\* “High-Performance All-Solid-State Li–S Batteries Enabled by An All-Electrochem-Active Prelithiated Si Anode.” *Energy Storage Material* 53 (2022): 613–620.

### Presentation

- American Chemical Society Fall Meeting, Chicago, Illinois (August 21, 2022): “An All-Solid-State Li-Oranosulfide Battery with an Ultrathin Flexible Solid-State Electrolyte.”

## Task 1.16 – Polyester-Based Block Copolymer Electrolytes for Lithium-Metal Batteries (Nitash Balsara, University of California, Berkeley)

**Project Objective.** The project objective is to design and synthesize polyester-based block copolymer electrolytes that can enable full-cell cycling at 1 mA/cm<sup>2</sup> or greater for 300 cycles. The cell comprises Li-metal anode, 4.5 V Ni-Mn-Co (NMC) cathode, and thin separators (20-50 μm) casted from the block copolymer.

**Impact.** Polymer electrolytes offer increased stability in lithium batteries in comparison to more widely used liquid electrolytes. Block copolymer-based electrolytes containing both soft, ion-conducting domains and rigid, nonconducting domains offer the opportunity to tune both mechanical and electrical properties separately. Most block copolymer electrolytes studied thus far comprise poly(ethylene oxide) (PEO) as the conducting domain. The team hopes to develop polyester-based electrolytes that exhibit much higher transport properties and limiting currents than PEO-based electrolytes. An all-solid full cell with this new block copolymer electrolyte, a Li-metal anode, and an NMC cathode will have much higher energy density than current Li-ion technology.

**Approach.** The team will begin by synthesizing several series of polyester homopolymers and fully characterizing their blends with lithium salts as polymer electrolytes in Li-Li symmetric cells. Next, they will make block copolymer electrolytes based on the most promising candidate and measure the electrochemical and mechanical properties thoroughly. Finally, they will assemble full cells with the optimum block copolymer electrolytes together with lithium metal and a 4.5 V NMC cathode.

**Out-Year Goals.** In the first year, the team will establish an efficient synthesis and characterization platform for polyester electrolytes. Several polyesters will be synthesized, and electrolytes will be made by blending each polymer with lithium salt. Transport properties (such as conductivity and current fraction) and limiting current of resulting electrolytes will be measured in Li-Li symmetric cells. The highest performing polymer electrolyte will be used as the conducting phase in the block copolymer design in the second year.

**Collaborations.** There are no active collaborations this quarter.

### Milestones

1. Establish synthesis platform: synthesize at least two polyester electrolytes. (Q1, FY 2022; Completed)
2. Conductivity: measure conductivity of at least two electrolytes. (Q2, FY 2022; Completed)
3. Symmetric cell characterization: measure salt diffusion coefficient and current fraction of at least two electrolytes. (Q3, FY 2022; Completed)
4. Complete characterization: measure thermodynamic factor and thereby complete characterization of at least one polyester electrolyte. (Q4, FY 2022; Completed)

## Progress Report

The conductivity, current fraction, and diffusion coefficient of poly(pentyl malonate) (PPM) of different salt concentration range of  $0.01 \leq r \leq 0.2$  (where  $r = [\text{Li}^+]/[\text{O}]$ ) was studied in detail last quarter. This quarter, the concentration cells were studied over the range of salt concentrations.

The concentration cell was prepared by creating a channel of (4-cm  $\times$  1.5-mm) dimensions in a 250- $\mu\text{m}$  thick silicone spacer. Half of the channel was filled by electrolyte of reference salt concentration ( $r = 0.08$ ), whereas the other half was filled by electrolytes of different salt concentrations,  $r$ . Nickel backed lithium electrodes were placed at the two sides of the channels, and the assembly was vacuum sealed. The cells were annealed at 90°C for 24 hours before the cell potential,  $U$ , was recorded. Experiments were repeated with 3-4 different cells at each salt concentration to ensure reproducibility. The team has made all measurements needed for complete characterization of PPM / lithium bis(trifluoromethanesulfonyl)imide electrolytes.

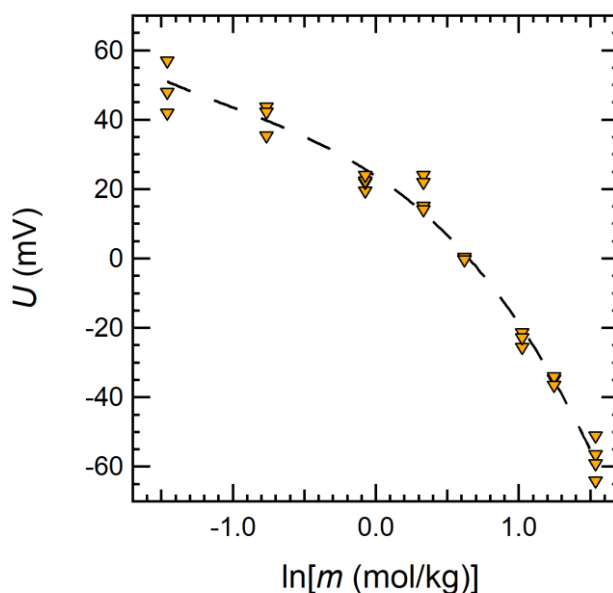


Figure 40. Concentration cell open-circuit potential ( $U$ ) as a function of natural log molality ( $\ln[m]$ ) at 90°C. The fit is shown in dashed line. Three data points at each salt concentration represent reproducibility of the data.

Finally, oxidative stability of the PPM electrolytes was compared against PEO electrolytes using linear sweep voltammetry technique in a lithium / polymer ( $r = 0.02$ ) / stainless-steel cell. Figure 41 shows that PEO-based electrolyte gave rise to oxidation currents above 0.01 mA/cm<sup>2</sup> in the 3.5-5 V window, whereas the PPM electrolyte exhibited current densities below 0.01 mA/cm<sup>2</sup> in the 3.5-5 V window. Thus, PPM exhibits higher oxidation current than PEO electrolyte.

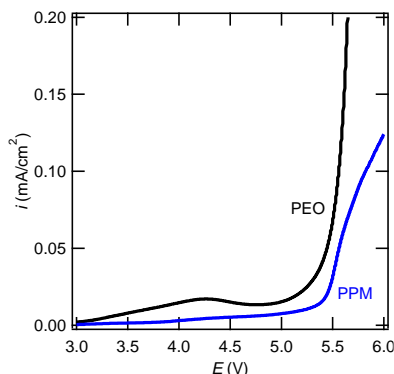


Figure 41. Linear sweep voltammetry (3-6 V versus Li<sup>+</sup>/Li) of PPM and PEO electrolytes at 90°C. The scanning rate is 1 mV/s.

The efficacy of PPM polymer to conduct Na-metal ion is tested by making electrolyte of PPM / sodium bis(trifluoromethylsulfonyl)imide at  $r = 0.06$  ( $r = [\text{Na}^+]/[\text{O}]$ ). Figure 42 represents the chronopotentiometry data of sodium / polymer ( $r = 0.06$ ) / sodium cells at a current density of  $0.125 \text{ mA/cm}^2$ . The inset represents the impedance spectra before and after the polarization. Based on the experiment, the conductivity ( $\kappa$ ) and current fraction ( $\rho_+$ ) of the electrolyte is  $\kappa = 6 \times 10^{-4} \text{ S/cm}$  and  $\rho_+ = 0.54$  at 80°C, and the electrolyte was found to be stable against Na-metal electrodes.

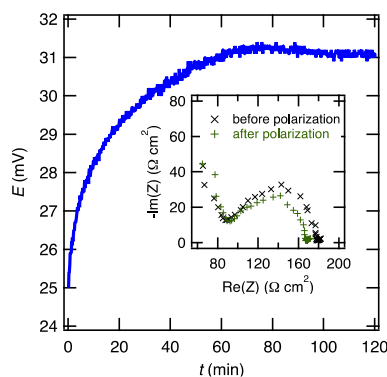


Figure 42. Chronopotentiometry curve of a sodium/polymer/sodium symmetric cell with a PPM/NaTFSI electrolyte at  $r = 0.06$ , under a current density of  $0.125 \text{ mA/cm}^2$  at 80°C. The inset is the normalized Nyquist plot before and after polarization.

## Patents/Publications/Presentations

### Publication

- Yu, X., Z. J. Hoffman, J. Lee, C. Fang, L. A. Gido, V. Patel, H. B. Eitouni, R. Wang, and N. P. Balsara. “A Practical Polymer Electrolyte for Lithium and Sodium Batteries: Poly(Pentyl Malonate).” *ACS Energy Letters* 7 (2022): 3791–3797.

## Task 1.17 – Advanced Polymer Materials for Batteries (Zhenan Bao and Yi Cui, Stanford University)

**Project Objective.** This project will develop new polymer materials for batteries. The team will develop polymer coatings with specific mechanical properties that can accommodate the volume expansion and contraction of the Li-metal anode associated with deposition and stripping (charging and discharging).

**Project Impact.** The cycling stability and Coulombic efficiency (CE) of Li-metal electrodes will be increased by implementation of a polymer-based protective layer that functions as an artificial solid electrolyte interphase (SEI) with desired properties. The improved performance will enable further development toward practical utilization of Li-metal anodes with higher cycling efficiency and less susceptibility to dendrite-based failure.

**Approach.** The project uses soft polymer coatings with dynamic crosslinking to give the resulting polymers liquid-like rheological properties and stretchable, self-healing properties. In previous work, the team has shown that such coatings resulted in uniform deposition/stripping of lithium metal and improved cycling stability of Li-metal electrodes. To understand the design rules for effective polymer coatings, they chose a few representative polymers to systematically understand structure property relationships. Here, they investigate the correlation between surface energy of the polymer and exchange current for lithium deposition.

**Out-Year Goals.** Work will progress toward the correlation between dielectric constant and exchange current. These findings will enable further understanding and development of various polymer coatings for protecting Li-metal anodes.

**Collaborations.** The team is collaborating with J. Qin at Stanford University.

### Milestones

1. New lithium anode coating design. Design the polymer chemistry through density functional theory and contact angle measurement to find salt affinitive and solvent phobic moieties. (Q1, FY 2022; Completed)
2. Characterize selective transport of salt over solvents for this polymer. (Q2, FY 2022; Completed)
3. Characterize impact of polymeric coating on lithium deposition morphology and short-term CE. (Q3, FY 2022; Completed)
4. Coat thin Li-metal electrodes with the polymeric coating and achieve stable lithium cycling for  $\geq 200$  cycles at  $2.5 \text{ mAh/cm}^2$  capacity and C/3 D/5 current density in lean electrolyte condition. (Q4, FY 2022; Completed)

## Progress Report

Since SP<sup>2</sup> (salt-philic solvent-phobic) coating showed improvement in carbonate electrolyte, SP<sup>2</sup> coated thin lithium anodes (50 μm) were also assembled into lithium | Ni-Mn-Co (NMC) cells. They were cycled at different C-rates, and the team found that reasonable capacity (> 200 mAh g<sup>-1</sup>) can be achieved at C/10 and C/3 for carbonate electrolyte (Figure 43a). They proceeded with C/5 charging and C/3 discharging in long-term cycling. Figure 43b shows the discharge capacity over cycles when pairing with 2.5 mAh cm<sup>-2</sup> NMC cathode for carbonate; a cycle life of ~ 250 was reached. The CE of each cycle is shown in Figure 43c.

Overall, the team developed SP<sup>2</sup> polymer coating on Li-metal anode. This coating allows selective transport of lithium salt instead of solvent molecules. When salt has a higher probability to be in physical contact with lithium metal, salt-derived SEI formation is promoted. SP<sup>2</sup> was found to be applicable to several typical electrolyte chemistries and showed improvement in cycling performance for ether, carbonate, and fluorinated ether electrolytes. The project's polymer coating polymer design is a marked improvement in full-cell cycle life versus capacity when compared with other state-of-the-art lithium anode modification strategies (Figure 43d).<sup>[1-12]</sup>

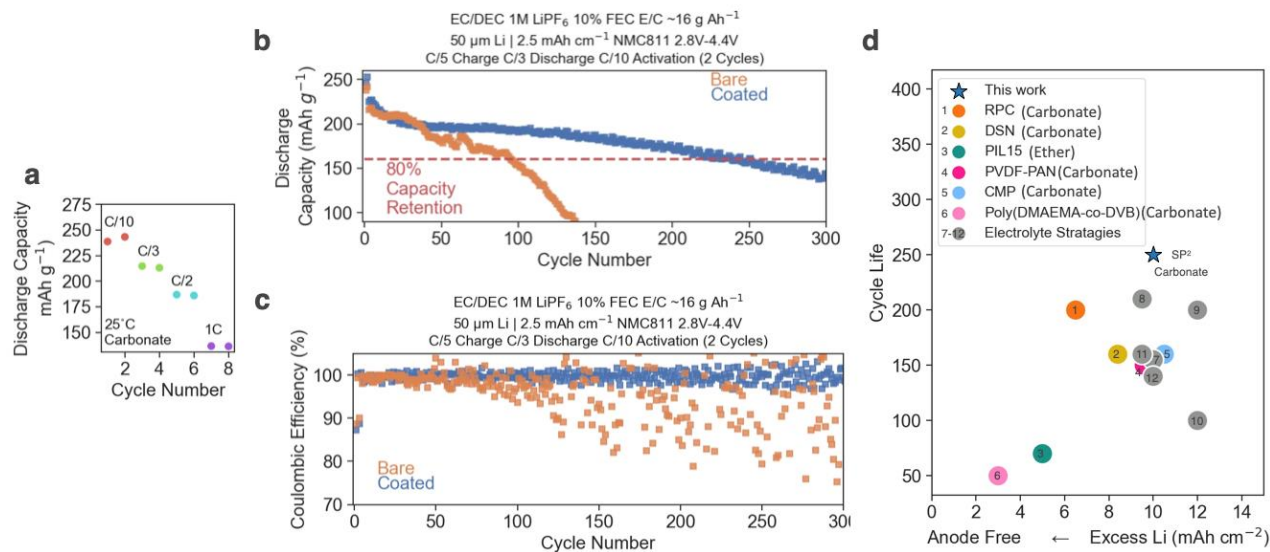


**Figure 43. Cycling of SP<sup>2</sup>-coated lithium anode in Li|NMC cells: (a) rate capabilities, (b) cycle life and capacity, and (c) Coulombic efficiency of each cycle. (d) Comparison of cycle life (80% capacity retention) plotted against excess lithium amount of the SP<sup>2</sup> coating with other coatings / electrolyte strategies. The x axis locations of 4, 5, 7, 11, and 12 are 10 mAh cm<sup>-2</sup>; they are adjusted slightly to dodge.**

### References

- [1] Gao, Y., Z. Yan, J. L. Gray, X. He, D. Wang, T. Chen, Q. Huang, Y. C. Li, H. Wang, S. H. Kim, T. E. Mallouk, and D. Wang. "Polymer–Inorganic Solid–Electrolyte Interphase for Stable Lithium Metal Batteries under Lean Electrolyte Conditions." *Nature Materials* 18, no. 4 (2019): 384–389. <https://doi.org/10.1038/s41563-019-0305-8>.
- [2] Yu, Z., D. G. Mackanic, W. Michaels, M. Lee, A. Pei, D. Feng, Q. Zhang, Y. Tsao, C. V. Amanchukwu, X. Yan, H. Wang, S. Chen, K. Liu, J. Kang, J. Qin, Y. Cui, and Z. Bao. "A Dynamic, Electrolyte-Blocking, and Single-Ion-Conductive Network for Stable Lithium-Metal Anodes." *Joule* 3, no. 11 (2019): 2761–2776. <https://doi.org/10.1016/j.joule.2019.07.025>.
- [3] Huang, Z., S. Choudhury, H. Gong, Y. Cui, and Z. Bao. "A Cation-Tethered Flowable Polymeric Interface for Enabling Stable Deposition of Metallic Lithium." *Journal of the American Chemical Society* 142, no. 51 (2020): 21393–21403. <https://doi.org/10.1021/jacs.0c09649>.

- [4] Wang, D., H. Liu, F. Liu, G. Ma, J. Yang, X. Gu, M. Zhou, and Z. Chen. “Phase-Separation-Induced Porous Lithiophilic Polymer Coating for High-Efficiency Lithium Metal Batteries.” *Nano Letters* 21, no. 11 (2021): 4757–4764. <https://doi.org/10.1021/acs.nanolett.1c01241>.
- [5] Zhang, K., W. Liu, Y. Gao, X. Wang, Z. Chen, R. Ning, W. Yu, R. Li, L. Li, X. Li, K. Yuan, L. Ma, N. Li, C. Shen, W. Huang, K. Xie, and K. P. Loh. “A High-Performance Lithium Metal Battery with Ion-Selective Nanofluidic Transport in a Conjugated Microporous Polymer Protective Layer.” *Advanced Materials* 33, no. 5 (2021): 2006323. <https://doi.org/10.1002/adma.202006323>.
- [6] Stalin, S., P. Chen, G. Li, Y. Deng, Z. Rouse, Y. Cheng, Z. Zhang, P. Biswal, S. Jin, S. P. Baker, R. Yang, and L. A. Archer. “Ultrathin Zwitterionic Polymeric Interphases for Stable Lithium Metal Anodes.” *Matter* 4, no. 11 (2021): 3753–3773. <https://doi.org/10.1016/j.matt.2021.09.025>.
- [7] Cao, X., X. Ren, L. Zou, M. H. Engelhard, W. Huang, H. Wang, B. E. Matthews, H. Lee, C. Niu, B. W. Arey, Y. Cui, C. Wang, J. Xiao, J. Liu, W. Xu, and J-G. Zhang. “Monolithic Solid–Electrolyte Interphases Formed in Fluorinated Orthoformate-Based Electrolytes Minimize Li Depletion and Pulverization.” *Nature Energy* 4, no. 9 (2019): 796–805. <https://doi.org/10.1038/s41560-019-0464-5>.
- [8] Cao, X., L. Zou, B. E. Matthews, L. Zhang, X. He, X. Ren, M. H. Engelhard, S. D. Burton, P. Z. El-Khoury, H-S. Lim, C. Niu, H. Lee, C. Wang, B. W. Arey, C. Wang, J. Xiao, J. Liu, W. Xu, and J-G. Zhang. “Optimization of Fluorinated Orthoformate Based Electrolytes for Practical High-Voltage Lithium Metal Batteries.” *Energy Storage Materials* 34 (2021): 76–84. <https://doi.org/10.1016/j.ensm.2020.08.035>.
- [9] Xue, W., Z. Shi, M. Huang, S. Feng, C. Wang, F. Wang, J. Lopez, B. Qiao, G. Xu, W. Zhang, Y. Dong, R. Gao, Y. Shao-Horn, J. A. Johnson, and J. Li. “FSI-Inspired Solvent and ‘Full Fluorosulfonyl’ Electrolyte for 4 V Class Lithium-Metal Batteries.” *Energy & Environmental Science* 13, no. 1 (2020): 212–220. <https://doi.org/10.1039/C9EE02538C>.
- [10] Xue, W., M. Huang, Y. Li, Y. G. Zhu, R. Gao, X. Xiao, W. Zhang, S. Li, G. Xu, Y. Yu, P. Li, J. Lopez, D. Yu, Y. Dong, W. Fan, Z. Shi, R. Xiong, C-J. Sun, I. Hwang, W-K. Lee, Y. Shao-Horn, J. A. Johnson, and J. Li. “Ultra-High-Voltage Ni-Rich Layered Cathodes in Practical Li Metal Batteries Enabled by a Sulfonamide-Based Electrolyte.” *Nature Energy* 6, no. 5 (2021): 495–505. <https://doi.org/10.1038/s41560-021-00792-y>.
- [11] Zhang, W., Z. Shen, S. Li, L. Fan, X. Wang, F. Chen, X. Zang, T. Wu, F. Ma, and Y. Lu. “Engineering Wavy-Nanostructured Anode Interphases with Fast Ion Transfer Kinetics: Toward Practical Li-Metal Full Batteries.” *Advanced Functional Materials* 30, no. 39 (2020): 2003800. <https://doi.org/10.1002/adfm.202003800>.
- [12] Li, S., W. Zhang, Q. Wu, L. Fan, X. Wang, X. Wang, Z. Shen, Y. He, and Y. Lu. “Synergistic Dual-Additive Electrolyte Enables Practical Lithium-Metal Batteries.” *Angewandte Chemie International Edition* 59, no. 35 (2020): 14935–14941. <https://doi.org/10.1002/anie.202004853>.

## Patents/Publications/Presentations

### Patents

- Cui, Y., Z. Bao, Y. Chen, and H. Gong. Fast-Charging of Hybrid Lithium-Ion/Lithium-Metal Anodes by Nanostructured Hard Carbon Flower Host. U. S. provisional patent filing; 63/405,319.
- Cui, Y., Z. Bao, Z. Huang, and J. Lai. A Salt-Philic Solvent-Phobic (SP<sup>2</sup>) Interfacial Coating Design for Lithium Metal Anodes. U. S. provisional patent filing; 63/402,427.

### Publications

- Oyakhire, S. T., H. Gong, Y. Cui, Z. Bao, and S. F. Bent. “An X-Ray Photoelectron Spectroscopy Primer for Solid Electrolyte Interphase Characterization in Lithium Metal Anodes.” *ACS Energy Letters* 7, no. 8 (2022): 2540–2546. <https://doi.org/10.1021/acseenergylett.2c01227>.
- Yu, W., Z. Yu, Y. Cui, and Z. Bao. “Degradation and Speciation of Li Salts during XPS Analysis for Battery Research.” *ACS Energy Letters* 7, no. 10 (2022): 3270–3275. <https://doi.org/10.1021/acseenergylett.2c01587>.
- Kim, S. C., J. Wang, R. Xu, P. Zhang, Y. Chen, Z. Huang, Y. Yang, Z. Yu, S. Oyakhire, W. Zhang, M. S. Kim, D. Boyle, P. Sayavong, J. Qin, Z. Bao, and Y. Cui. “High Entropy Electrolytes for Practical Lithium Metal Batteries.” *Chemistry* (2022). Preprint. <https://doi.org/10.26434/chemrxiv-2022-j40p4>.

### Presentations

- Gordon Research Conference on Electrochemistry, Ventura, California (September 11-16, 2022): “Electrochemical Dynamics: From Interface to Interphase”; W. Yu and Z. Bao. Poster.
- American Chemical Society (ACS) Fall Meeting, Chicago, Illinois (August 22-25, 2022): “Solving a Metal Issue with Organic (Macro)Molecules”; Z. Huang, Y. Cui, and Z. Bao.
- ACS Fall Meeting, Chicago, Illinois (August 22-25, 2022): “Advanced Polymer Coatings for Li-Metal Anodes”; Z. Huang, Y. Cui, and Z. Bao.
- ACS Fall Meeting, Chicago, Illinois (August 22-25, 2022): “Improving the Lithium Metal Battery Performance with a Polymer Layer”; Z. Huang, Y. Cui, and Z. Bao.
- ACS Fall Meeting, Chicago, Illinois (August 22-25, 2022): “Dynamic Enamine-One Bonds Enabled Sustainable Polymeric Materials”; Y. Lin and Z. Bao.

## Task 1.18 – Molecular Ionic Composites: A New Class of Polymer Electrolytes to Enable All-Solid-State and High-Voltage Lithium Batteries (Louis A. Madsen, Virginia Polytechnic Institute and State University)

**Project Objective.** Based on a newly discovered class of solid polymer electrolyte materials, that is, molecular ionic composites (MICs), the overall objective is to develop solid-state lithium conductors targeted for use in transportation applications. MICs form a mechanically stiff, electrochemically stable, and thermally stable matrix. Specific objectives include the following: (1) development of robust MIC electrolyte thin films ( $\sim 20 \mu\text{m}$ ) to serve as simultaneous nonflammable separators and dendrite-blocking  $\text{Li}^+$  conductors, (2) electrochemical quantification of key performance metrics including electrolyte stability, interfacial reactions, and suitability/compatibility with a range of electrode materials, and (3) comprehensive investigation of ion transport mechanisms and electrode-electrolyte interfacial reactivity under practical operating conditions using nuclear magnetic resonance (NMR) and synchrotron X-ray analyses.

**Project Impact.** Commercialization of solid-state Li-metal batteries is hampered by lack of a functional nonflammable solid electrolyte that can provide high ionic conductivity, wide electrochemical window, favorable mechanical properties to inhibit lithium dendritic growth, and low interfacial resistance. The tunable MIC materials platform has potential to fulfill these requirements with relatively simple fabrication techniques, and thus shows promise for enabling nonflammable solid-state batteries that can be optimized for low cost and high energy density.

**Approach.** MICs rely on a unique polymer that is similar to Kevlar<sup>®</sup> in its strength, stiffness, and thermal stability, but with densely spaced ionic groups that serve to form an electrostatic network that permeates mobile ions in the MIC. The team can tailor the ion concentrations and types to yield MIC electrolyte films that are electrochemically compatible with Li-metal anode as well as a range of high-voltage layered cathodes. They are searching the composition space of lithium salts, electrochemically compatible ionic liquids, and polymer [poly(2,2'-disulfonyl-4,4'-benzidine terephthalamide), or PBDT] molecular weight to determine best composition windows for MIC electrolytes. The team is also investigating best methods for casting thin films in terms of temperature, solvent/evaporation conditions, and control over the initial liquid crystalline gel formation point. Concurrently, they are testing MIC films in various electrochemical cells, quantifying transport and structural/morphology parameters with NMR and X-ray techniques, and measuring key mechanical (dynamic mechanical thermal analysis, stress-strain) and thermal (differential scanning calorimetry, thermal gravimetric analysis) properties.

**Out-Year Goals.** This year, the team will generate a predictive model to understand the relationship between the mobility of all ions and the MIC synthesis parameters. They will establish the testing protocol for NMR measurements under operating conditions. They will also study the surface chemistry of the MIC electrolyte before and after cycling. The team will identify methods to mitigate interfacial degradation. They will then test the final project electrolyte in full cell and develop specifications.

**Collaborations.** The team is collaborating with T. J. Dingemans' group at University of North Carolina, Chapel Hill, in which they are forming composites based on PBDT polymer and carbon materials such as graphene oxide and are beginning to develop charged rigid-rod polymers building on the PBDT structure. The team is exploring shear rheology and broadband dielectric spectroscopy collaboration with R. H. Colby at Pennsylvania State University. They are collaborating with D. Nordlund and Y. Liu at SLAC National Accelerator Laboratory and S-M. Bak at Brookhaven National Laboratory to conduct synchrotron X-ray studies on MIC films.

### Milestones

1. Multivariate analysis of experimental parameters and electrochemical properties. (Q1 FY 2022; Completed)

2. *In situ* experiments implementing NMR spectroscopy and diffusometry at different cell states of charge. (Q2, FY 2022; Completed)
3. Spectroscopic surface analysis of cathode, anode, and MIC electrolyte after various cycling history. (Q3, FY 2022; Completed)
4. Area specific resistance: MIC/Li  $\leq 10 \Omega \text{ cm}^2$  and cathode/MIC  $\leq 50 \Omega \text{ cm}^2 / \text{cells}$ . (Q4, FY 2022; In progress)

## Progress Report

This quarter, the team investigated ion dynamics within the MIC films at various states of charge and total cycling times in cells with  $\text{LiFePO}_4$  (LFP) cathodes as well as in cells with  $\text{LiNi}_{0.8}\text{Mn}_{0.1}\text{Co}_{0.1}$  (NMC-811) cathodes via NMR diffusometry. The composition of these films is 10 wt% PBDT, 10 wt% lithium bis(trifluoromethanesulfonyl)imide (LiTFSI) and 80 wt% pyrrolidinium (trifluoromethanesulfonyl)imide ( $\text{Pyr}_{14}\text{TFSI}$ ), consistent with the team's optimal/robust MIC formulation. To investigate ion dynamics in the film, they measured the diffusion coefficients of the mobile cations and anions,  $\text{Pyr}_{14}^+$  and TFSI $^-$ , respectively, from room temperature to  $80^\circ\text{C}$ , as shown in Figure 44. All samples measured had diffusion coefficients ranging from  $2 \times 10^{-12}$  to  $6 \times 10^{-11}$  (depending on temperature and history), with the uncycled films having somewhat higher diffusion coefficients than those MIC films collected from cycled cells. This may be due to some of the mobile ions being pushed out of the film and dispersed into the porous cathode when assembling the coin cell, or possibly due to degradation of some fraction of the ions. In comparison to the cation and anion diffusivities of uncycled MIC films reported in an earlier publication,<sup>[1]</sup> the diffusion coefficients of the uncycled films match within errors. The cell with the NMC cathode was charged to 4.4 V at  $60^\circ\text{C}$  with a charging rate of 0.1 C then disassembled at this charged state and sealed in an NMR tube

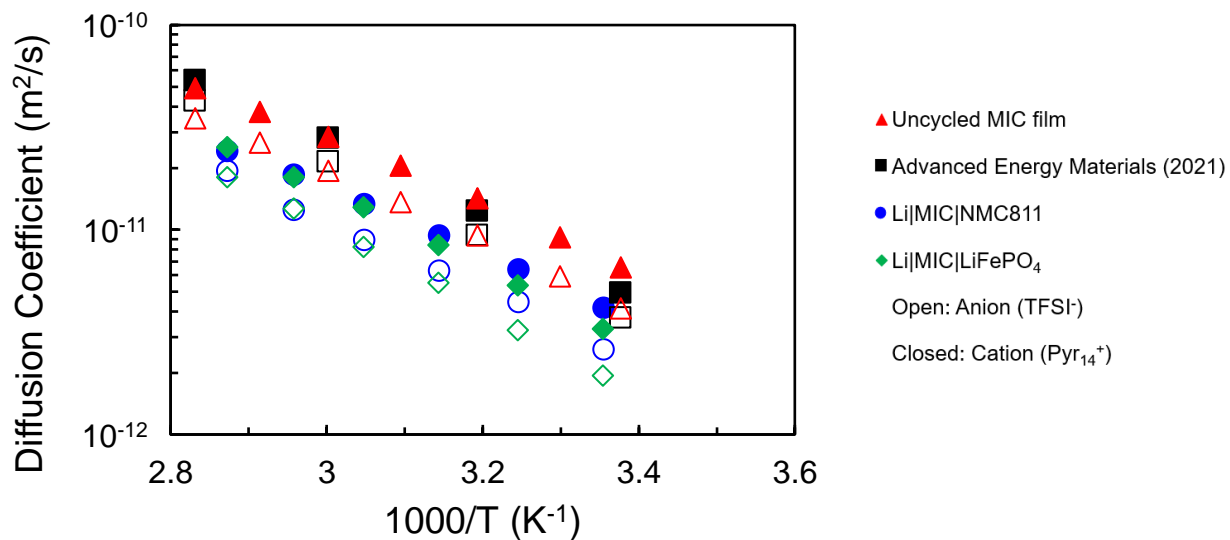


Figure 44. Temperature dependence of the cation ( $\text{Pyr}_{14}^+$ ) and anion (TFSI $^-$ ) diffusion coefficients in the cycled/charged molecular ionic composite (MIC) films. The solid data points represent the cation diffusion coefficients and the open data points represent the anion diffusion coefficients. The red triangles are the diffusion coefficients of the uncycled MIC film before assembly into a battery, and the diffusion coefficients agree with the uncycled MIC film reported in the *Advanced Energy Materials* paper (black squares). The blue circular data points are of the MIC film charged to 4.4 V in a Li/MIC/NMC-811 cell, and the green diamonds are of the MIC film after 20 cycles in a Li/MIC/LFP cell. Both MIC membranes collected after cell assembly, and then charging, and/or cycling have similar diffusion coefficients, which are half as high as the uncycled MIC material, possibly due to some mobile ions pushed into the porous cathode during cell assembly. These data provide critical information for further optimizing MIC composition, casting process, and cell assembly.

under vacuum before performing diffusometry experiments. The Li/MIC/LFP cells were cycled 20 times at room temperature before disassembly. The charge/discharge cycles were run 5 times at different constant current densities of 0.01 mA/cm<sup>2</sup>, 0.02 mA/cm<sup>2</sup>, 0.05 mA/cm<sup>2</sup>, and 0.1 mA/cm<sup>2</sup>. Both cells have comparable diffusion coefficients. These results indicate high overall film stability (that is, electrochemical, chemical, and structural) of MIC electrolytes up to 4.4 V and at 60°C. Figures 45 and 46 show the charging and cycling steps used for preparing these cells for NMR diffusometry measurements.

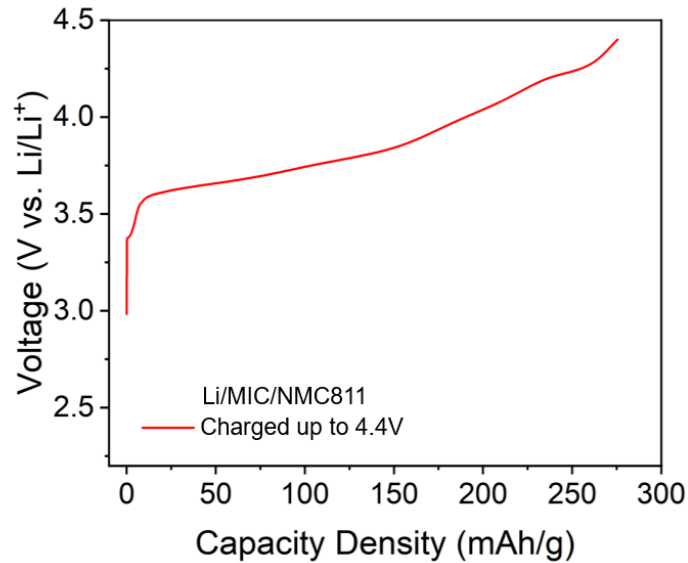


Figure 45. Constant current charging step of Li / molecular ionic composite / NMC-811 cell, run at 60°C with a 0.1C charging rate and an upper cut off voltage of 4.4 V.

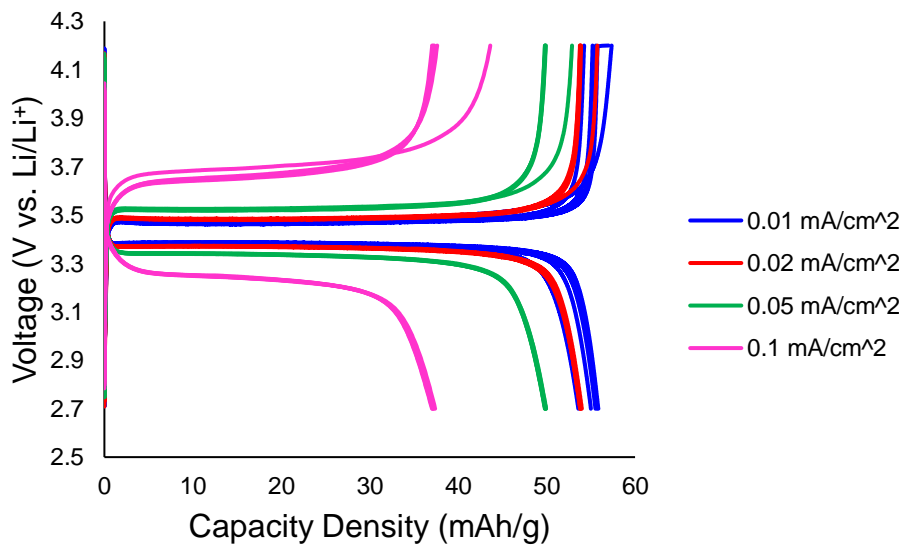
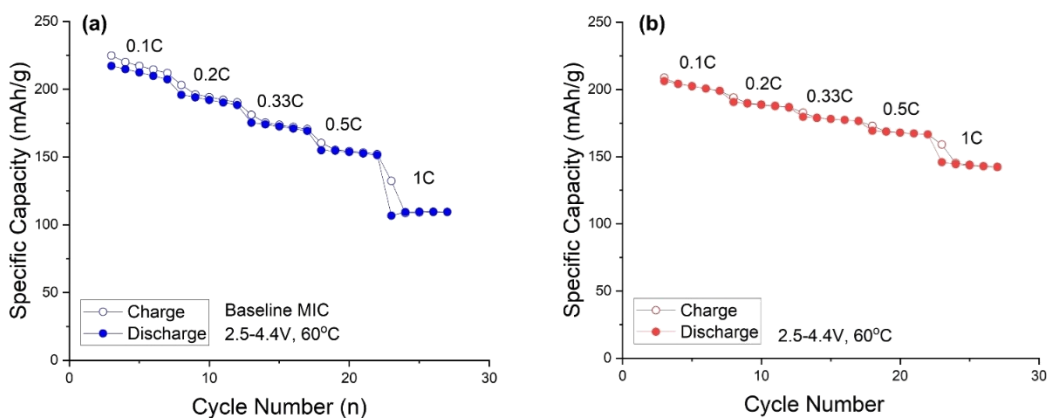


Figure 46. Charge/discharge profile of Li / molecular ionic composite / LiFePO<sub>4</sub> cell at room temperature. The cell was run at each constant current density for 5 cycles before increasing current density, for a total of 20 cycles.

The previous MIC electrolyte with 10 wt% PBDT, 10 wt% LiTFSI, and 80 wt % Pyr<sub>14</sub>TFSI shows good thermal stability, yet the rate capability is still very limited due to a low Li<sup>+</sup> transference number. This quarter, the team incorporated new mobile ions (Pyr<sub>13</sub><sup>+</sup> and FSI<sup>-</sup>) into the MIC electrolyte to improve its capability. Figure 47 shows a comparison of the specific capacity of Li/MIC/NMC-811 cells using the previous MIC and a new engineered MIC electrolyte. Incorporating a new ion composition increases rate capability.



**Figure 47. Specific capacity of Li / molecular ionic composite (MIC) / NMC-811 cells with (a) previous MIC composition and (b) modified MIC with mixed ion composition measured at 60°C when cycled between 2.5 V and 4.4 V.**

#### Reference

- [1] Yu, D., X. Pan, J. E. Bostwick, C. J. Zanelotti, L. Mu, R. H. Colby, F. Lin, and L. A. Madsen. “Room Temperature to 150°C Lithium Metal Batteries Enabled by a Rigid Molecular Ionic Composite Electrolyte.” *Advanced Energy Materials* 11 (2021): 2003559. doi: <https://doi.org/10.1002/aenm.202003559>.

## Patents/Publications/Presentations

#### Publication

- Yu, D., L. Mu, X. Feng, F. Lin, and L. A. Madsen. “Rigid-Rod Sulfonated Polyamide as an Aqueous-Processable Binder for Li-Ion Battery Electrodes.” *ACS Applied Energy Materials* 5, no. 10 (2022): 12531–12537. doi: <http://dx.doi.org/10.1021/acsaem.2c02173>.

#### Presentations

- Gordon Research Conference (GRC) on Polymer Physics, South Hadley, Massachusetts (July 24–29, 2022): “How are Ion Motions Separately Influenced by Molecular Environment and by Geometric Confinement?” L. A. Madsen,\* R. Zhang, A. G. Korovich, Y. Chen, and D. Troya.
- GRC on Polymer Physics, South Hadley, Massachusetts (July 24–29, 2022): “Formation, Multi-Scale Structure, and Dynamics of Molecular Ionic Composites for Energy Storage and Separations”; D. Yu,\* N. F. Pietra, C. J. Zanelotti, A. G. Korovich, J. E. Bostwick, R. H. Colby, F. Lin, and L. A. Madsen.
- GRC on Polymer Physics, South Hadley, Massachusetts (July 24–29, 2022): “Role of Intra-Domain Heterogeneity on Ion and Chain Dynamics in Block Polymer Electrolytes”; N. F. Pietra,\* A. G. Korovich, P. M. Ketkar, T. H. Epps, III, and L. A. Madsen.
- American Chemical Society Fall Meeting, Chicago, Illinois (August 21–25, 2022): “Polymer Electrolytes for High-Voltage Solid Lithium Batteries”; J. Min, Y. Zhang, M. Yuan, D. Yu, L. A. Madsen, and F. Lin.

## Task 1.19 – Synthesis of Composite Electrolytes with Integrated Interface Design (Sanja Tepavcevic, Argonne National Laboratory)

**Project Objective.** This project aims to develop well-controlled, scalable  $\text{Li}_7\text{La}_3\text{Zr}_2\text{O}_{12}$  (LLZO) nanofiber and composite polymer electrolyte (CPE) synthesis processes that will address the manufacturing challenges of current solid-state electrolytes (SSEs) and demonstrate the fabrication of large-area, thin CPE membranes with outstanding electro-chemomechanical properties.

**Impact.** The outcome of this proposal will be a transformative manufacturing solution that can create large-area, mechanically and (electro)chemically stable SSEs (0 V to 4.5 V versus  $\text{Li}/\text{Li}^+$ ) with  $\text{Li}^+$  conductivity of  $\geq 10^{-3}$  S/cm at room temperature enabling  $\geq 1$ C charging rates.

**Approach.** To commercialize all-solid-state Li-ion battery technology, further advances will require the application of knowledge, concepts, and tools from several fields including materials science, physics, engineering, theory, and interfacial electrochemistry. The team’s research philosophy is to establish a synthesis-material characterization-computation cycle that advances synthesis, chemistry, microstructure, interfaces, and transport in CPEs by a coordinated, interdisciplinary approach. The team’s diverse expertise will allow them to understand, create, and rapidly scale up composite electrolytes to meet ambitious conductivity, energy, and power density targets.

**Out-Year Goals.** The innovative design and synthesis of integrated SSE interfaces include the following goals: (1) achieve high room-temperature conductivity by optimizing composite microstructures, synthetically modifying the LLZO-polymer interface, and reducing CPE membrane thicknesses down to 20  $\mu\text{m}$ ; (2) create a stable and effective interface between the CPE and metallic lithium that yields low charge transfer resistance and enables high critical current density ( $> 3 \text{ mA}/\text{cm}^2$ ); and (3) modify the CPE-cathode interface to enable the use of different cathodes [that is, lithium iron phosphate,  $\text{LiCoO}_2$ , and Ni-Mn-Co] and achieve high energy and power density in batteries.

**Collaborations.** Computational researchers will further help the team to understand and design better all-solid-state batteries. They will work closely with L. A. Curtiss, P. Barai, K. Chavan, and V. Srinivasan (Argonne National Laboratory) to understand the molecular and mesoscopic characteristics and performance of the team’s CPEs.

### Milestones

1. Achieve uniform distribution of LLZO nanofibers within CPEs. (Q1, FY 2022; Completed)
2. Vary LLZO doping (aluminum, germanium, undoped) to improve conductivity and strength. (Q2, FY 2022; Completed)
3. Optimize LLZO nanofibers loading and processing to demonstrate good percolation and maximize conductivity. (Q3, FY 2022; Completed)
4. Use computational methods at the continuum level to gain understanding of the improved conduction pathways and lithium deposition mechanisms. (Q4, FY 2022; Completed)

## Progress Report

**Theoretical Estimation of Percolation Threshold for Randomly Oriented Fibers within Matrix.** Effective conductivity of a fiber-reinforced composite can be estimated using “effective medium theories.” In this approach, fibers are placed in the matrix material, the perturbation in the electric field due to presence of the foreign inclusion is calculated, and effective conductivity of the composite is estimated as a function of the corresponding conductivity and volume fraction of the fibers and the matrix material. During this effective property estimation process, the total current and electric fields are assumed to be volume average of the currents and electric fields in individual phases. The advantage of these effective medium theories is that they can successfully estimate the effective conductivity of the composite from very small ( $\sim 0.0$  vol %) to extremely large ( $\sim 100$  vol%) volume fractions of the fiber materials and are not limited by any dilute approximations. The magnitude of the percolation threshold is estimated from the expression of effective properties through the assumption of a completely insulating matrix phase. With an insulating matrix, the minimum volume fraction of fibers that leads to a non-zero magnitude of the effective conductivity of the composite is characterized as the percolation threshold. Interestingly, the magnitude of the percolation threshold does not depend on the conductivity of the individual phases and depends only on the geometry of the fibers. In the present context, percolation threshold for LLZO fibers in poly(ethylene oxide) (PEO) matrix is estimated using the “effective medium theory”-based technique described by Y. Wang and G. J. Weng.<sup>[1]</sup> Because of the isotropic conductivity demonstrated by LLZO fibers, the conductivity of both the fiber inclusions and PEO polymers is assumed to be isotropic. However, due to the geometric anisotropy associated with the shape of the fibers, the individual fibers are assumed to be randomly oriented, and an orientational averaging is conducted before estimating the effective conductivity and percolation threshold of the composite material.

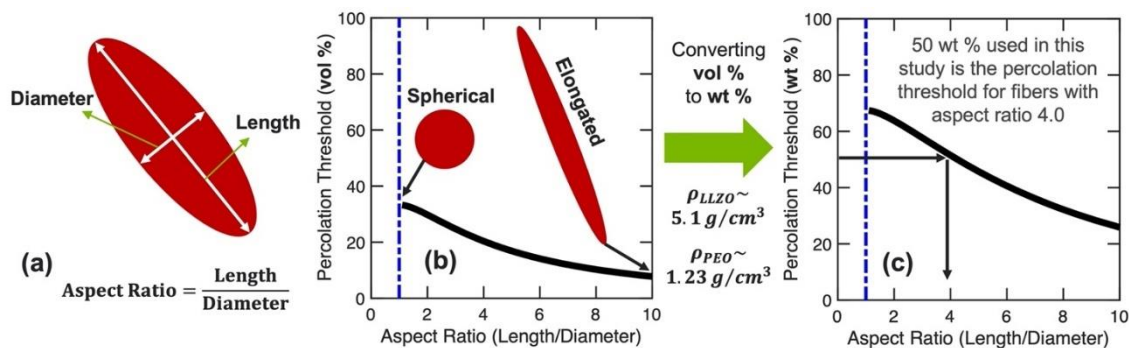


**Figure 48. Demonstration of computationally predicted percolation thresholds experienced by polymer/ceramic composites. (a) Geometrical approximation of an elongated fiber as an ellipsoid. Aspect ratio of the fiber is defined as the ratio between the length over the diameter of the fibrous inclusions. (b) Percolation threshold experienced by the fiber reinforced composites as a function of the aspect ratio of the fibers. Fiber content within the matrix is demonstrated as volume percentage. (c) Conversion of the percolation threshold from volume percentage to weight percentage. Given that the density of LLZO fibers is larger than that of the PEO matrix, the weight percentage of fibers needed for percolation is much larger than the volume percentage.**

In the effective medium theory, each fiber is approximated as an ellipsoid with a certain length and diameter as shown in Figure 48a. The percolation threshold in terms of the volume percentage of the LLZO fibers is demonstrated in Figure 48b. It is evident that as the aspect ratio of the fibers increase, percolation can be achieved with a smaller fraction of fibrous inclusions. The percolation thresholds in weight percentage of LLZO are provided in Figure 48c; they indicate that more than 20 wt% LLZO fibers are needed to obtain percolation with elongated fibers of aspect ratio 10. The theoretical analysis presented here has several approximations, such as the interface between the LLZO fiber, and the PEO matrix is assumed to be perfect and without any imperfections, which is very far from the realistic observations. In addition, the connection between individual fibers is expected to be perfect; therefore, as soon as two fibers touch each other, it is assumed that they start behaving as a single fiber. The interfacial resistance associated with ion transport from one fiber to the next is also neglected and is important to address in experiments.

### Determining LLZO Nanofiber Participation in Conductivity of Slot-Die Coated Composite Electrolytes.

CPEs were prepared via slot-die coating from a mixture of PEO, lithium bis(trifluoromethanesulfonyl)imide (LiTFSI), and LLZO nanofibers. Varying the weight percent of LLZO from 0 wt% to 50 wt% shows a small increase in bulk ionic conductivity with small amounts of LLZO, then a decrease in conductivity with higher LLZO (> 10 wt%), as shown in Figure 49a. Notably, at 50 wt% LLZO, the expected percolation threshold is exceeded, and high conductivity should be achieved if the nanofibers are in contact with each other in a percolation network. The results indicate that this is not the case. Scanning electron microscopy imaging in Figure 49b shows that the preparation method for coating from a concentrated ink results in the LLZO nanofibers being coated uniformly by the PEO-LiTFSI polymer matrix. This inhibits the percolation network since there is a high barrier for ion transport between LLZO and PEO. The team's future efforts will aim to ensure that LLZO fibers are in intimate contact during the coating process, and they will modify the LLZO surface to interact more with the polymer phase and increase Li<sup>+</sup> transport.

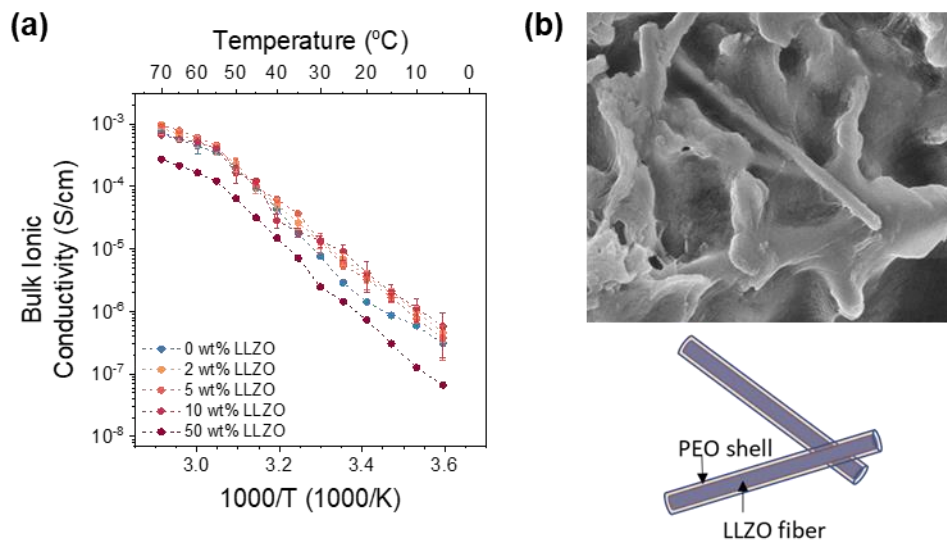


**Figure 49. (a) Ionic conductivity of composite polymer electrolytes with 0, 2, 5, 10, and 50 wt% LLZO nanofibers. 50 wt% corresponds to 20 vol% of the LLZO filler in the polymer matrix. (b) Scanning electron micrograph of the as-prepared composite electrolyte, showing that nanofibers are coated with thin layers of polymer and are likely not in direct contact with each other.**

#### Reference

- [1] Wang, Y., and G. J. Weng. "Electrical Conductivity of Carbon Nanotube- and Graphene-Based Nanocomposites." In *Micromechanics and Nanomechanics of Composite Solids*, edited by S. A. Meguid and G. J. Weng, 123–156. Springer Nature: Switzerland, 2018. [https://doi.org/10.1007/978-3-319-52794-9\\_4](https://doi.org/10.1007/978-3-319-52794-9_4).

## Patents/Publications/Presentations

### Presentations

- 23<sup>rd</sup> International Conference on Solid State Ionics, Boston, Massachusetts (July 17–22, 2022): “Advancing Cycling Capabilities of Composite Polymer Electrolytes with LLZO Nanofibers”; S. Tepavcevic.
- 2022 American Chemical Society Fall Meeting, Chicago, Illinois (August 21–25, 2022): “Interface Reactions and Transport in Polymer and Composite Polymer Electrolytes”; S. Tepavcevic. Invited.

## Task 1.20 – Polymer Electrolytes for Stable, Low-Impedance, Solid-State Battery Interfaces (X. Chelsea Chen, Oak Ridge National Laboratory)

**Project Objective.** The overall project objective is to develop stable polymer/cathode and polymer/anode interfaces with low interfacial impedance for integration of a thin solid composite electrolyte into a battery, to achieve chemical stability at the electrodes, high energy density (500 Wh/kg), high rate (1 mA/cm<sup>2</sup>), and long cycle life (80% capacity retention for 300 cycles), demonstrated in pouch cells.

**Impact.** Achieving stable, low-impedance interfaces at both the cathode and anode sides is critical to achieve high energy density with excellent safety, lifetime, and cycling efficiency. This project will identify key design strategies needed to prepare polymer electrolyte (PE) to achieve stable, low-impedance polymer/cathode and polymer/lithium interfaces and to develop processing procedure to integrate a thin composite electrolyte into a solid-state battery (SSB). Success will enable U. S. Department of Energy (DOE) technical targets: energy density of 500 Wh/kg with 80% capacity retention for at least 300 cycles.

**Approach.** The team's main design principle is to use an oxide ceramic as the main ion transporting phase in the electrolyte and a fluorinated polyether-based PE to form optimized interfaces as well as to provide flexibility to the electrolyte membrane. Compared with inorganic electrolytes, PEs are soft and flexible and capable of maintaining good contact at interfaces. However, several technical barriers remain. On the Li-metal side, the interface between PEs and thin-Li and Li-free anodes is still at an early stage of investigation. Interface optimization using thin-Li and Li-free designs is crucial to reaching the DOE 500 Wh/kg target. On the cathode side, studies on the polymer/cathode interface are scarce. The interface resistance between polymer (catholyte) and cathode active material is not well understood. In addition, with a target voltage stability of 0-4.5 V versus Li/Li<sup>+</sup>, a polymer with oxidative stability up to 4.5 V is needed. Fluorinated polyethers have the potential to form stable and low impedance interfaces at both the cathode side and the anode side. By systematically examining the effects of fluorine content, polymer chain length and structure, and plasticization on the interfacial resistance with the cathode and the anode, a balance between the desolvation kinetics of Li<sup>+</sup> and diffusion rate will be achieved to optimize the interface ion transport. A fundamental understanding of the origin of interfacial impedance with the cathode as well as Li-metal anode will be developed alongside the optimization process to generate design rules for polymers with optimized interfaces. The team will also develop a processing procedure to integrate a thin composite electrolyte that was previously developed into a full cell. The composite electrolyte features an interconnected ceramic structure with a thickness of 20 μm. It will be backfilled with the newly developed fluorinated PEs. The mechanical properties of the composite electrolytes will be optimized to accommodate roll-to-roll processing.

**Out-Year Goals.** In the second and third year of this project, the team will focus on optimizing the cathode/polymer as well as the Li-anode/polymer interface with maximized stability and minimized interfacial impedance. A fundamental understanding of parameters that determine the interfacial impedance and strategies to minimize the interfacial impedance will be developed. The fourth and fifth year of the project will be focused on integration of a thin composite electrolyte into a full cell to achieve high energy density, high rate, and long cycle life, as stated in the overall project objectives. Processing techniques and procedures for electrolyte integration will be investigated to achieve this goal.

**Collaborations.** Work is being conducted by B. Armstrong, S. Kalnaus, R. Sahore, X. Tang, A. Ullman, and X. C. Chen.

### Milestones

1. Synthesize fluoropolyether polymers with four fluorine concentrations. (Q1, FY 2022; Completed)
2. Quantify ionic conductivity, Li<sup>+</sup> transference number, oxidative stability, thermal stability, glass transition temperature (T<sub>g</sub>), and mechanical modulus as a function of fluorine concentration. (Q2, FY 2022; Completed)

- Optimize conductivity of composite electrolyte with a three-dimensional (3D) interconnected structure (at least  $5 \times 10^{-5}$  S/cm at room temperature). Measure flexural strength of the composite electrolyte with three compositions. (Q3, FY 2022; Completed)
- Quantify interfacial resistance and stability between the fluoropolyether polymers and lithium anode from two different sources. (Q4, FY 2022; Completed)
- Build a prototype SSB in a pouch cell using the interconnected composite electrolyte as the electrolyte layer. (FY 2022 Annual Stretch Milestone; paused due to equipment delay)

## Progress Report

### Synthesis of Fluorinated Polyether-Containing PEs

In the last two quarters, the team reported on the ionic conductivity and oxidative stability of fluorinated polyether-containing PEs. The conductivities of the dry crosslinked poly(ethylene oxide) (xPEO) / fluorinated polyether (PFPE) copolymer electrolytes were at least one order of magnitude lower than the dry xPEO electrolyte membrane ( $2\text{--}5 \times 10^{-6}$  versus  $5\text{--}6 \times 10^{-5}$  S/cm at  $70^\circ\text{C}$ ). This quarter, they conducted in-depth characterizations of xPEO/PFPE copolymer electrolyte membranes to understand the origin of the low ionic conductivity. The  $\text{Li}^+$  transference number and interface resistance with lithium metal are also evaluated.

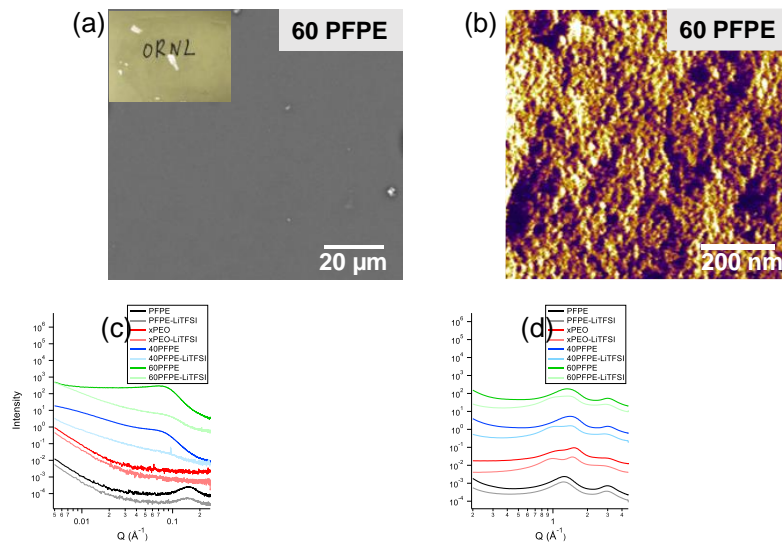


**Figure 50.** Morphology of dry xPEO/PFPE electrolytes. (a) Scanning electron microscopy image showing the surface morphology of 60PFPE electrolyte membranes at the micrometer scale. Inset: photo of the membrane. (b) Scanning probe microscopy phase image showing the surface morphology of 60PFPE electrolyte membranes at the nanometer scale. (c) Small-angle X-ray scattering (SAXS) profiles of PFPE, xPEO, 40PFPE, and 60PFPE in the pristine form and with LiTFSI salt. (d) Wide-angle X-ray scattering (WAXS) profiles of PFPE, xPEO, 40PFPE, and 60PFPE in the pristine form and with LiTFSI salt. SAXS and WAXS measurements were taken at room temperature.

Figure 50 shows the morphology of dry PFPE electrolyte membranes. The digital photo and scanning electron microscopy (SEM) image of 60PFPE (60:40 w/w PFPE:PEO copolymer) membrane in Figure 50a indicate that membranes prepared using the acetonitrile/hexafluorobenzene mixed solvents produced an optically transparent membrane that is homogeneous at the micron-scale level. The team used scanning probe microscopy (SPM) to further investigate the morphology of 60PFPE at a much smaller scale. In the SPM phase image shown in Figure 50b, the dark phase is the fluorocarbon (PFPE-rich) phase, whereas the bright phase is the hydrocarbon (PEO-rich) phase. The SPM image revealed a finely phase separated morphology of 60PFPE membrane, where PFPE-rich domains on the order of 10 nm in size dispersed homogeneously in the PEO-rich matrix.

To complement the SEM and SPM techniques, the team also examined the structure of the membranes using small-angle X-ray scattering (SAXS) and wide-angle X-ray scattering (WAXS) (Figure 50c-d). In SAXS (Figure 50c), xPEO did not show any features, indicating a homogeneous one phase morphology, both in the pristine form and after infusing with lithium bis(trifluoromethanesulfonyl)imide (LiTFSI) salt. Pristine PFPE membrane showed a peak at  $Q = 1.5 \text{ \AA}^{-1}$ , where  $Q$  is scattering wave vector. This peak arises due to the microphase separation between the hydrocarbon part of the PFPE molecules and the fluorocarbon part of the PFPE molecules. In 40PFPE (60:40 w/w PFPE:PEO copolymer) and 60PFPE membranes, a broad peak can be observed, indicating a microphase separated morphology in these membranes. The average domain spacing can be calculated using  $D = 2\pi/Q_{max}$ , where  $Q_{max}$  is the  $Q$  position of the peak maxima. The  $D$ -spacing results are summarized in Table 3. In pristine PFPE,  $D = 4.2$  nm. The addition of LiTFSI salt did not change this spacing. Since pristine PFPE is a fluorine-rich oligomer, the team interprets the morphology as small hydrocarbon domains dispersed in a fluorine-rich matrix, with the average nearest domain spacing being 4.2 nm. When PEO and PFPE were mixed and crosslinked together (40PFPE and 60PFPE), the copolymer became hydrocarbon rich. SAXS results of 40PFPE and 60PFPE copolymers suggest a microphase separated morphology where fluorocarbon-rich domains dispersed in a PEO-rich matrix, with the average  $D$ -spacing being 8.4 and 7.8 nm, respectively. Compared with pristine PFPE, the peaks in 40PFPE and 60PFPE are broader, indicating the distributions of the  $D$ -spacings in these two samples are larger. With the addition of salt, the intensity of the peak decreased. This indicates that LiTFSI was infused into both the PFPE-rich phase and the PEO-rich phase, which decreased the contrast between the two phases. On the other hand, the domain spacing did not change significantly with the addition of LiTFSI.

**Table 3. Domain spacing and glass transition temperature ( $T_g$ ) of crosslinked PEO and PFPE membranes.**

Sample	$D$ -spacing (nm)	$T_g$ -hydrocarbon (°C)	$T_g$ -fluorocarbon (°C)
xPEO	N/A	-64.6	N/A
xPEO-LiTFSI	N/A	-54.3	N/A
PFPE	4.2	10 - 20	-109.4
PFPE-LiTFSI	4.2	10 - 20	-109.8
60PFPE	7.8	-53.2	-113.5
60PFPE-LiTFSI	7.4	-47.0	-115.6
40PFPE	8.4	-48.7	-118.3
40PFPE-LiTFSI	7.4	-40.7	-118.0

Pristine PFPE showed two peaks in WAXS, and pristine xPEO showed three peaks in WAXS (Figure 50d). These peaks are associated with interchain spacings. The peaks of 40PFPE and 60PFPE are combinations of the peaks of pristine PFPE and xPEO, which makes sense given the microphase separated morphology from SAXS profiles.

Figure 51 shows the differential scanning calorimetry (DSC) of dry xPEO/PFPE electrolytes. Pristine xPEO showed one glass transition temperature ( $T_g$ ) at -64.6°C (Figure 51a, Table 3). After infusing with LiTFSI, the  $T_g$  increased to -54.3°C, due to the EO-Li<sup>+</sup> coordination. Pristine crosslinked PFPE showed a  $T_g$  at -109.4°C. With LiTFSI, the  $T_g$  remained very similar, at -109.8°C. This indicates that fluoroether does not form tight coordination with Li<sup>+</sup>, that is, the presence of Li<sup>+</sup> does not significantly influence the segmental

dynamics of the fluoroether. Looking very closely, the DSC thermogram of PFPE has another weak glass transition, in the 10°C to 20°C range. This glass transition has been reported in several other crosslinked PFPE systems.<sup>[1-2]</sup> It is the glass transition of the hydrocarbon portion of the crosslinked PFPE membranes. Although in the team's system, this transition is too weak to be determined accurately; they found that it actually plays a key role in the ion transport properties of the xPEO/PFPE copolymer.

In 40 PFPE and 60 PFPE copolymer membranes, two  $T_g$  levels are observed in the DSC thermograms, one near -110°C, which is associated with the PFPE-rich phase, and one near -50°C, which is associated with the PEO-rich phase. The temperatures as a function of PFPE weight percentage are plotted in Figure 51c. Evidently, the  $T_g$  of the PEO phase (the hydrocarbon phase) exhibited greater than 10°C increase compared with pristine xPEO. Since the hydrocarbon in PFPE is highly miscible with PEO and has high  $T_g$ , it significantly increased the  $T_g$  of the PEO phase. The  $T_g$  of the PFPE phase also increased with the weight percentage of the PFPE. This is likely due to the chain connectivity between the PFPE phase and PEO phase, since the domain sizes are small, and the domains are crosslinked together.

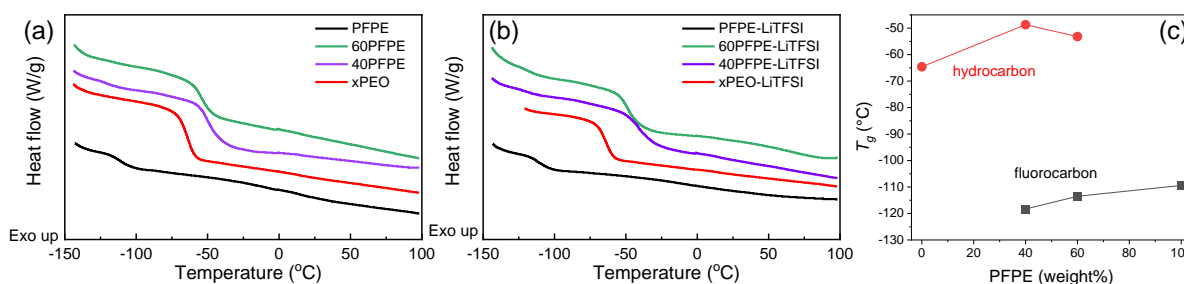


**Figure 51.** Differential scanning calorimetry (DSC) of dry xPEO/PFPE electrolytes. (a) DSC thermogram (2<sup>nd</sup> heating) of pristine xPEO, PFPE, 60PFPE, and 40PFPE. (b) DSC thermogram (2<sup>nd</sup> heating) of xPEO, PFPE, 60PFPE, and 40PFPE infused with LiTFSI salt. (c) Glass transition temperature ( $T_g$ ) of the hydrocarbon and fluorocarbon phases of the membranes as a function of PFPE wt%. The values used in this plot are from samples without LiTFSI salt.

To this end, the origin of the low ionic conductivity of dry xPEO/PFPE electrolyte membranes is clear. The team believes the low ionic conductivity is the result of two main contributing factors. The first is the increased  $T_g$  of the PEO-rich phase in the copolymer membrane. Since the  $\text{Li}^+$  transport is strongly coupled to the segmental motion of the PEO chains, an increase in  $T_g$  (decrease in the segmental mobility) leads to decreased  $\text{Li}^+$  mobility. Second, due to the finely phase separated morphology of the xPEO/PFPE membrane, the PEO phase tortuosity significantly increased. Lithium ions must move through a much more tortuous path to cross the membrane to reach the electrode. This also contributed to decreased  $\text{Li}^+$  transport rate.

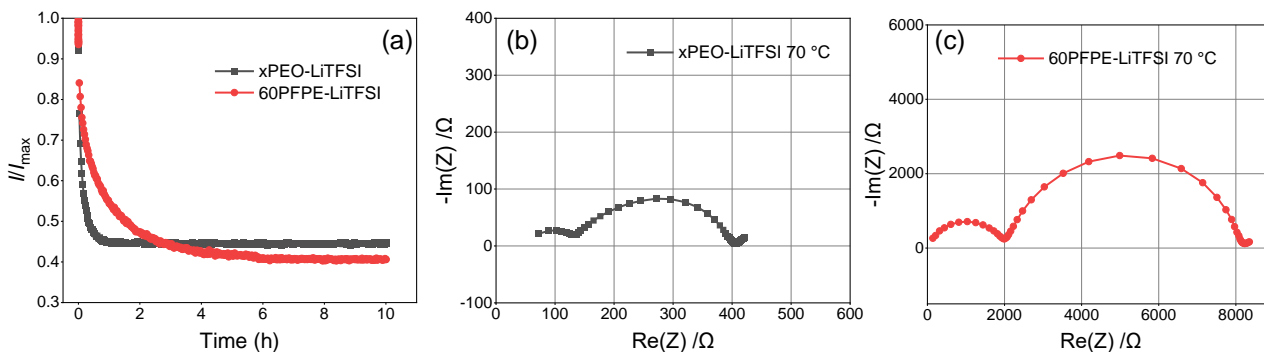


**Figure 52.** (a) Chronoamperometry measurement of xPEO-LiTFSI and 60PFPE-LiTFSI electrolytes at 70°C. (b) Interfacial impedance between lithium and xPEO-LiTFSI at 70°C. (c) Interfacial impedance between lithium and 60PFPE-LiTFSI at 70°C.

Lastly, the interface properties of xPEO/PFPE membranes with Li-metal anode were evaluated. To do this, the team performed chronoamperometry and impedance measurements on lithium symmetric cells at 70°C. The results are shown in Figure 52. The chronoamperometry of xPEO-LiTFSI and 60PFPE-LiTFSI samples showed very similar equilibrium current, indicating a similar concentration gradient was established in the lithium

symmetric cells. Indeed, the  $\text{Li}^+$  transference number calculated using the Bruce-Vincent method was 0.20 and 0.14, respectively. This suggests that the presence of PFPE did not improve the  $\text{Li}^+$  transference number of the electrolyte. This is likely because the main ion transport path is through the PEO-rich phase, not PFPE-rich phase. Furthermore, a very high interfacial impedance with lithium ( $\sim 8000 \Omega \cdot \text{cm}^2$ ) was found for 60PFPE-LiTFSI, versus  $350 \Omega \cdot \text{cm}^2$  for xPEO-LiTFSI. The decreased ion transport properties and large interfacial impedance with lithium have rendered dry PFPE-based electrolytes unsuitable for Li-metal solid-state batteries. In the next fiscal year, the team will evaluate the capabilities of plasticized PFPE membranes.

#### References

- [1] Hu, Z., L. Chen, D. E. Betts, A. Pandya, M. A. Hillmyer, and J. M. DeSimone. “Optically Transparent, Amphiphilic Networks Based on Blends of Perfluoropolyethers and Poly(Ethylene Glycol).” *Journal of the American Chemical Society* 130, no. 43 (2008): 14244–14252.
- [2] Lopez, G., B. Ameduri, and J-P. Habas. “A Versatile Strategy to Synthesize Perfluoropolyether-Based Thermoplastic Fluoropolymers by Alkyne-Azide Step-Growth Polymerization.” *Macromolecular Rapid Communications* 37, no. 8 (2016): 711–717.

### Patents/Publications/Presentations

#### Publication

- Tsai, W-Y.,\* X. C. Chen,\* S. Kalnaus, R. Sahore, Z. Du, and A. S. Westover. “Li Morphology Evolution during Initial Cycles in a Gel Composite Polymer Electrolyte.” *ACS Applied Energy Materials* 5, no. 9 (2022): 11362–11369. <https://doi.org/10.1021/acsaem.2c01856>.

## Task 1.21 – Ion Conductive High Li<sup>+</sup> Transference Number Polymer Composites for Solid-State Batteries

(Bryan McCloskey, University of California, Berkeley)

**Project Objective.** This project seeks to develop polymer-inorganic composites that have an optimal combination of conductivity, processability, and low interfacial resistance at both a Li-metal anode and a porous Li[Ni, Mn, Co]O<sub>2</sub> (NMC) cathode. In an effort to enable Li-metal anodes, mechanically rigid solid-state Li<sup>+</sup> conductors, such as Li<sub>7</sub>La<sub>3</sub>Zr<sub>2</sub>O<sub>12</sub> (LLZO), Li<sub>1+x</sub>Al<sub>x</sub>Ti<sub>2-x</sub>(PO<sub>4</sub>)<sub>3</sub> (LATP), and Li<sub>2</sub>S-P<sub>2</sub>S<sub>5</sub> (LPS) glasses, have been employed due to their high Li<sup>+</sup> ion conductivity and, when engineered to eliminate interfacial defects, appropriate stiffness to suppress Li-metal dendrite formation. However, for these materials to result in batteries that compete against current commercial cells in terms of energy density and cost per kWh, they would need to be manufactured at no more than 50- $\mu$ m thickness and cost no more than \$5 per square meter. These metrics are daunting for pure thin-film inorganic ion conductors, particularly when a porous, thick cathode also needs to be used to achieve competitive cell energy densities. To overcome these challenges, this project aims to develop polymer-inorganic composites, where high Li<sup>+</sup> transference number polymer electrolytes (PEs) serve as a binder for inorganic ion conducting particles.

**Impact.** By optimizing the composition of this composite electrolyte, the team aims to marry the processability and interfacial mechanical compliance of polymers with the impressive transport properties of inorganic composites, thereby enabling roll-to-roll manufacturing to allow thin (< 50  $\mu$ m) layers of high-conductivity solid-state conductors to be cost-effectively incorporated into batteries.

**Approach.** The project approach relies on the following key steps in FY 2022: (1) using monomers with (trifluoromethanesulfon)imide (TFSI) anions appended to them, synthesize and characterize polyanionic PEs with high Li<sup>+</sup> transference number and conductivity; (2) through systematic material structure-property characterization, understand how to reduce interfacial ion transport impedance between inorganic ion conductors (specifically, thin-film inorganic conductors such as Li-La-Zr-Ta-O (LLZTO), LATP, and LPS) and high Li<sup>+</sup> transference number PEs; and (3) characterize electrode-polymer and electrode-inorganic conductor interfacial resistances at a Li-metal anode.

**Out-Year Goals.** The overall project goal is to develop an optimized polymer-inorganic Li-ion conductor with superior conductivity (> 1 mS/cm), thin-film processability, and low electrode interfacial impedance. Of particular interest in the out years is development of a process to fabricate thick, porous, and electrochemically stable NMC cathodes using the polymer-inorganic composite as both the binder and electrolyte. The team aims to integrate the optimized high-loading cathode with a 25- $\mu$ m thin-film polymer-inorganic electrolyte to create an “anode-less” battery with 500 Wh/kg and 80% capacity retention after 300 cycles.

**Collaborations.** While this project has a single principal investigator (PI), B. McCloskey will leverage the collaborative battery research environment at Lawrence Berkeley National Laboratory (LBNL) and coordinate with other LBNL PIs in the BMR Program for materials and experimental development.

### Milestones

1. Establish polymer synthesis by making two neat TFSI-containing polymers. (Q1, FY 2022; Completed)
2. Measure conductivity of two polymers using Li-Li symmetric cells. (Q2, FY 2022; Completed)
3. Measure interfacial impedance evolution of polymer in a Li-Li cell. (Q3, FY 2022; Completed)
4. Synthesize a series of four copolymers with various ratios of TFSI monomer and a film-forming monomer. (Q4, FY 2022; Completed)

## Progress Report

Last quarter, the team began adding plasticizers to poly((trifluoromethane)sulfonimide lithium methacrylate) (PLiMTFSI) films because the freestanding PLiMTFSI was very brittle. However, the plasticizers they examined last quarter were small-molecule methacrylates, and large quantities (that is, 60 wt%) were required to observe appreciable mechanical changes in the film. Based on these observations, this quarter the team developed a new reversible addition-fragmentation chain transfer (RAFT) polymer synthesis of the methacrylates: glycerol carbonate methacrylate (GCMA) and acetonide-protected trimethylolpropane methacrylate (TMPMA). By using polymer blends of PLiMTFSI with polymerized GCMA and TMPMA, they hope to create systems that need less plasticizer to produce the same mechanical properties observed with the small-molecule additives.

This quarter, the team focused investigation on GCMA. Additionally, identification of a suitable solvent for the TMPMA polymer synthesis proved challenging, as the polymer was found to be insoluble in many common solvents. They used several procedures to synthesize a GCMA polymer with a molecular weight comparable to the PLiMTFSI. Figure 53 below details the nuclear magnetic resonance data for a RAFT synthesis using azobisisobutyronitrile (AIBN) in dimethylsulfoxide (DMSO) (top panel) and 4,4'-azobis(4-cyanopentanoic acid) (ACPA) in acetonitrile (bottom panel). The reaction in AIBN produced a conversion of near unity; however, removing the DMSO from the product has proven time consuming and detrimental to the reaction yield. On the other hand, the reaction in ACPA has a lower conversion (around 85%), so the need to purify the product impacted the yield.

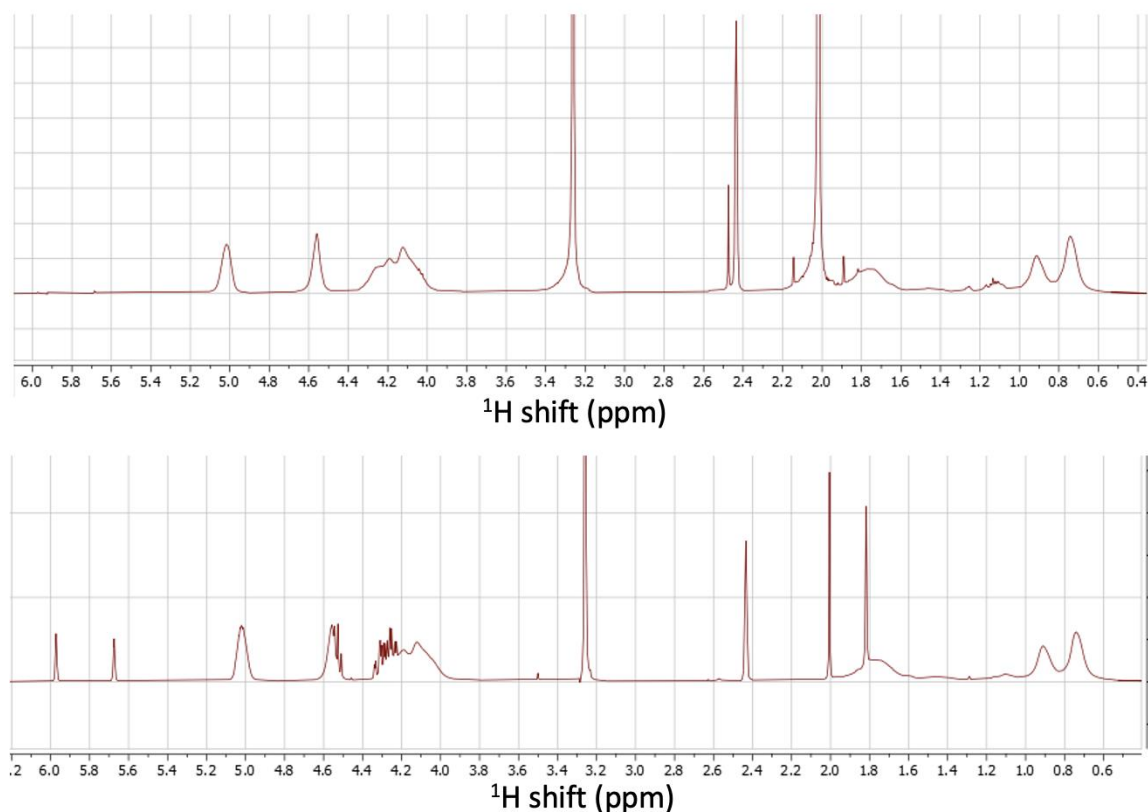


**Figure 53.** Nuclear magnetic resonance data for GCMA polymerization with AIBN in DMSO (top) and ACPA in acetonitrile (bottom). The peaks at 5.7 and 6.0 correspond to the monomer, while the double-humped peak from 0.6-1.0 represents the polymer.

The team has not done a complete characterization of GCMA/PMLiTFSI blends, which is a priority for next quarter; they would like to gain a fundamental understanding of how these polymers impact the mechanical properties of the films. Next quarter, their focus will be on the blends, as well as blends of PMLiTFSI and polyethylene glycol (PEG) of various molecular weights. The well-documented ability of PEG to form free-standing films ensures that this will be a viable solution to pursue while continuing to investigate the GCMA polymers the team has already synthesized. Once they find the optimal blend of PEG and PMLiTFSI, they will begin incorporating LLZO and will electrochemically characterize the electrolytes via symmetric cells.

### Patents/Publications/Presentations

The project has no patents, publications, or presentations to report this quarter.

## Task 1.22 – Inorganic-Polymer-Composite Electrolyte with Architecture Design for Lithium-Metal Solid-State Batteries (Enyuan Hu, Brookhaven National Laboratory)

**Project Objective.** This project targets the following goal: the composite electrolytes will be thin ( $< 100 \mu\text{m}$ ) and have high Li-ion conductivity ( $\geq 10^{-3} \text{ S/cm}$  at room temperature), low interfacial impedance, and desirable mechanical properties. When used in the solid electrolyte (SE) Li-metal battery, a current density  $> 1 \text{ mA/cm}^2$  and an areal capacity of  $2\text{-}3 \text{ mAh/cm}^2$  can be achieved with more than 300 cycles. The constructed  $\text{LiNi}_x\text{Mn}_y\text{Co}_{1-x-y}\text{O}_2$  (NMC) /  $\text{LiCoO}_2$  || composite electrolyte || Li-metal cell can be operated at up to  $4.5 \text{ V}$  versus  $\text{Li}^+/\text{Li}$ . The SE will also be compatible with high loading cathodes in achieving high energy density at the coin or pouch-cell level.

**Impact.** The results of this project will lead to advancement of solid-state batteries (SSBs), a beyond Li-ion battery option with better safety characteristics and higher energy density. The project will also provide valuable knowledge to U. S. industries in scaling up SSB production for vehicle applications, thus providing solutions to the clean energy strategy.

**Approach.** The project approaches are as follows: (1) design and synthesize polymer with anion-tether strategy for high transference number, (2) through theories and experiments, design hierarchical inorganic electrolyte for suppressing lithium dendrite penetration, (3) optimize the composite electrolyte composition and structure, (4) use additives for Li-metal anode and NMC cathode protection, and (5) use synchrotron and cryogenic electron microscopy characterization to understand the bulk electrolyte and interphases.

**Out-Year Goals.** The out-year goals are to synthesize single ion conducting solid polymer electrolyte (SPE) with high transference number and conductivity; to design hierarchical inorganic electrolyte with high ionic conductivity and good mechanical/electrochemical stability; and to use synchrotron total scattering to study the structure of ceramic/polymer electrolyte.

**Collaborations.** The principal investigator (PI) will work closely with co-PIs H. Xin of University of California, Irvine, and X. Li of Harvard University.

### Milestones

1. Synthesize single ion conducting SPE with high transference number and conductivity. Achieve formulation optimization to achieve transference number  $> 0.5$ . (Q1, FY 2022; Completed)
2. Design hierarchical inorganic electrolyte with high ionic conductivity and good mechanical/electrochemical stability. Develop inorganic electrolytes (sulfides, halides) with ionic conductivity  $> 1 \text{ mS/cm}$  and a hierarchy of voltage stability up to  $4.5 \text{ V}$  and down to near  $0 \text{ V}$  in cyclic voltammetry tests. (Q2, FY 2022; Completed).
3. Optimize composition for plastic hybrid electrolyte. Tune the SPE and inorganic electrolyte composition to enable compatibility. (Q3, FY 2022; delayed due to slow hiring process)
4. Use synchrotron total scattering to study the structure of ceramic/polymer electrolyte. Complete synchrotron pair distribution function (PDF) analysis of the ceramic/polymer electrolyte. (Q4, FY 2022)

## Progress Report

This quarter, synchrotron soft x-ray absorption spectroscopy (sXAS) and total scattering technique PDF characterization of polymer electrolytes (PEs) have been completed. The polymer used is polyvinylidene fluoride (PVDF) and the salts used include both lithium bis(trifluoromethanesulfonyl)imide (LiTFSI) and lithium bis(sulfonyl fluoride) imide (LiFSI). The PE was prepared by solvent casting method. PVDF and salts were first dissolved into N-methyl-2-pyrrolidone (NMP) and stirred for 24 hours, followed by vacuum drying at 60°C for one day to form the PE.

Carbon, oxygen, and fluorine K-edge sXAS of blank polymer (mixed with NMP and vacuum dried without adding the salts) are shown in Figure 54a, 54b, and 54c, respectively. All data are measured in partial fluorescence yield mode. In Figure 54a, the peaks at 288.4 eV, 292.8 eV, and 295 eV correspond to the excitation of core electrons to the C-H, C-F, and C-C antibonding orbitals, respectively. Surprisingly, Figure 54b shows there is clear oxygen signal from the blank polymer. Since PVDF itself does not contain any oxygen, the only possible oxygen source is the amide group in NMP, which is also known as lactam (cyclic amide). The 532.2 eV peak in Figure 54b indeed corresponds to the carbonyl antibonding associated with the amide group. Figure 54c shows the fluorine sXAS, which has the peak at ~ 689.8 eV corresponding to the  $\sigma$  C-F antibonding in PVDF. Figure 54d shows the PDF results of PVDF (pure powder without going through mixing with NMP), salts, and the PEs. In general, the PDF data can be divided into the short-range region associated with the local structure and the long-range region that indicates the crystallinity of the materials. In the short-range region, the first peak (shaded) at ~ 1.5 Å relates to the shortest bond in these materials, which can be C-F/C as in PVDF and S-O/N/F as in LiTFSI and LiFSI salts. The second shaded region at ~ 2.3 Å corresponds to indirect correlations between atoms that are not directly bonded to each other, but are connected through an atom bonding to both simultaneously. For example, it could be the correlation between two oxygen atoms in the sulfonyl group. In the long-range region, it is obvious that pristine PVDF, LiTFSI, and LiFSI all have good crystallinity as indicated by the strong oscillating peaks. After making them into PE, the magnitude of oscillation considerably decreases, suggesting loss of crystallinity during electrolyte making.

This study shows how the wet method affects the composition and crystallinity of the PE. Future studies will be devoted to understanding its influence on cell electrochemistry.

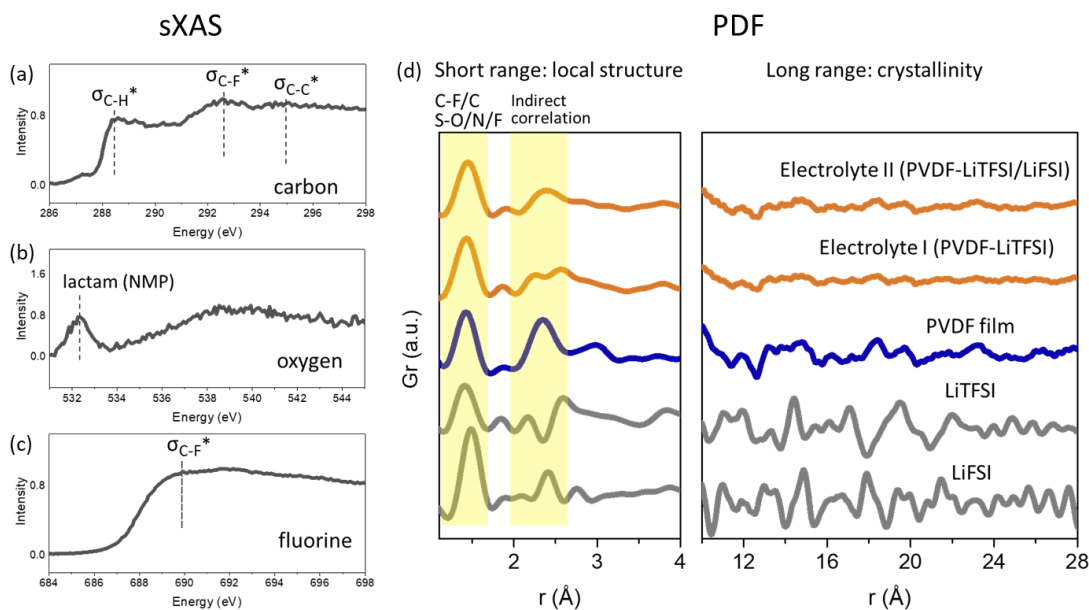


**Figure 54.** Soft X-ray absorption spectroscopy (sXAS) and pair distribution function (PDF) characterization of the polymer electrolytes (PEs). (a) Carbon, (b) oxygen, (c) fluorine K-edge sXAS of PVDF mixed with NMP and vacuum dried. (d) PDF results of polymer, salts, and PEs.

## Patents/Publications/Presentations

### Publication

- Shao, B., S. Tan, Y. Huang, L. Zhang, J. Shi, X-Q. Yang, E. Hu,\* and F. Han.\* “Enabling Conversion-Type Iron Fluoride Cathode by Halide-Based Solid Electrolyte.” *Advanced Functional Materials*. <https://doi.org/10.1002/adfm.202206845>.

## Task 1.23 – Solid-State Batteries with Long Cycle Life and High Energy Density through Materials Design and Integration (Gerbrand Ceder, University of California, Berkeley)

**Project Objective.** This project aims to create solid-state Li-metal batteries (SSLMBs) with high specific energy, high energy density, and long cycle life using scalable processing techniques. The team will achieve this by addressing fundamental challenges associated with (1) interfacial reactivity, (2) Li-metal plating, and (3) cathode loading. Addressing these challenges supports the broader Vehicle Technologies Office goal of solid-state batteries (SSBs) with increased cycle life and energy density.

**Impact.** Ultimately, this project will develop an understanding of how to prevent interfacial reactions, make uniform Li-metal plating, and increase cathode loading significantly. The knowledge obtained from this project will be used to design SSLMBs with high specific energy of 500 Wh/kg, 80% capacity retention for at least 300 cycles, and critical current density  $> 1 \text{ mA/cm}^2$ .

**Approach.** This project addresses several fundamental challenges and makes the SSLMB competitive, surpassing the specific energy, energy density, and cycle life of Li-ion batteries:

- Create homogeneous lithium deposition on the anode without penetration of lithium metal through the separator to achieve high cycle life and high safety. The team will achieve this with the use of an active buffer layer (ABL) that combines active and inactive components to homogenize lithium plating and to keep the lithium plating potential away from the solid electrolyte (SE) separator.
- Limit chemical reactivity and mechanical decohesion between the SE, carbon, and cathode material in the composite cathode so that high cycle life can be achieved. The team will limit chemical reactivity by protecting the carbon from the SE, by using novel cathode coatings designed to be stable to high voltage and that do not react with the SE, by using novel solid halide catholyte conductors, and by using inorganic/organic solid composite electrolytes in the cathode.
- Achieve high volumetric loading of the active cathode material in the composite cathode to achieve high energy density and high specific energy. The team will achieve high volumetric cathode loading by creating thin highly porous conductor scaffolds that are infiltrated with cathode, by tailored particle size distributions of deformable lightweight conductors, and by the use of organic/inorganic hybrids.
- Create inexpensive materials and processes to fabricate SSBs so that they can be cost-competitive with Li-ion batteries. The team will create solution-processable organic/inorganic hybrids to be used as separator and to blend in the composite cathode; they will use inexpensive, scalable ceramics processing techniques to create high loading composite cathodes.

**Out-Year Goals.** The ultimate project goal is to develop SSLMBs that achieve high specific energy of 500 Wh/kg, 80% of capacity retention after 300 cycles, and  $> 1 \text{ mA/cm}^2$  of critical density.

**Collaborations.** The principal investigator's (PI's) team collaborates with the following co-PIs: H. Kim, V. Battaglia, G. Chen, M. M. Doeff, G. Liu, M. Scott, M. Tucker, and J. Urban, all at Lawrence Berkeley National Laboratory (LBNL).

### Milestones

1. Demonstration of use of ABL in Li-metal cell with active component other than silver. (Project start in Q2, FY 2022; Completed)
2. Integration of  $\text{LiNi}_x\text{Mn}_y\text{Co}_{1-x-y}\text{O}_2$  (NMC) into three-dimensional (3D) carbon framework with cathode active material (CAM) loading  $> 80 \text{ wt}\%$ . (Q3, FY 2022; Completed)
3. Model studies to assess compatibility of cathode components. (Q4, FY 2022; Completed)

## Progress Report

### Buffer Layers to Stabilize Li/SE Interface and Create Uniform Lithium Plating (H. Kim, G. Ceder, V. Battaglia, M. Scott)

This task aims to (1) understand how the ABL of Ag-C composite works to ensure uniform lithium plating between a current collector and an ABL, and (2) design lower cost ABL replacing silver with inexpensive components. To understand the lithiation and lithium plating mechanisms when Ag-C ABL is used, it is vital to reproduce some parts of the full cell reported. The team has tested several SSB cell configurations, but those cells did not operate well. The cells deliver specific capacity below 10 mAh/g with a very large polarization over 1 V. The main reason of the failure is that the current SSB cell design can provide a low internal stacking pressure (maximum internal stacking pressure: 5 MPa). The team is rebuilding the SSB cells that can provide higher internal stacking pressure of 10-20 MPa or even higher.

Understanding the role of silver particles in Ag-C buffer layer is crucial to design new ABLs with an inexpensive active metal component. As an effort to understand the thermodynamics in the lithiation of silver in the Ag-C buffer layer, the team performed *ab initio* calculations to compute the formation energy and voltage profile of Ag-Li alloys. In these calculations, the team considered three types of lattice geometries: body-centered cubic (BCC), face-centered cubic (FCC), and  $\gamma$ -brass, as suggested by experiments. For each lattice type, the electronic energy of 150 different configurations was computed. A cluster-expansion model was fitted for each lattice type, from which ground-state structures were predicted. Figure 55 shows the density functional theory (DFT) formation energies and configurations of predicted ground states. Besides experimentally reported structures (for example, CsCl-type BCC structure, I41 FCC structure, and  $\gamma$ -Ag<sub>5</sub>Li<sub>8</sub>), other ordered ground-state structures have also been found (for example, FCC AgLi<sub>3</sub> structure, and  $\gamma$ -Ag<sub>2</sub>Li<sub>11</sub>). The team aims to further include phonon corrections with DFT electronic energies in the current cluster-expansion model to match the experimental phase stability and thus to calculate an accurate lithiation voltage profile for bulk Ag-Li system.

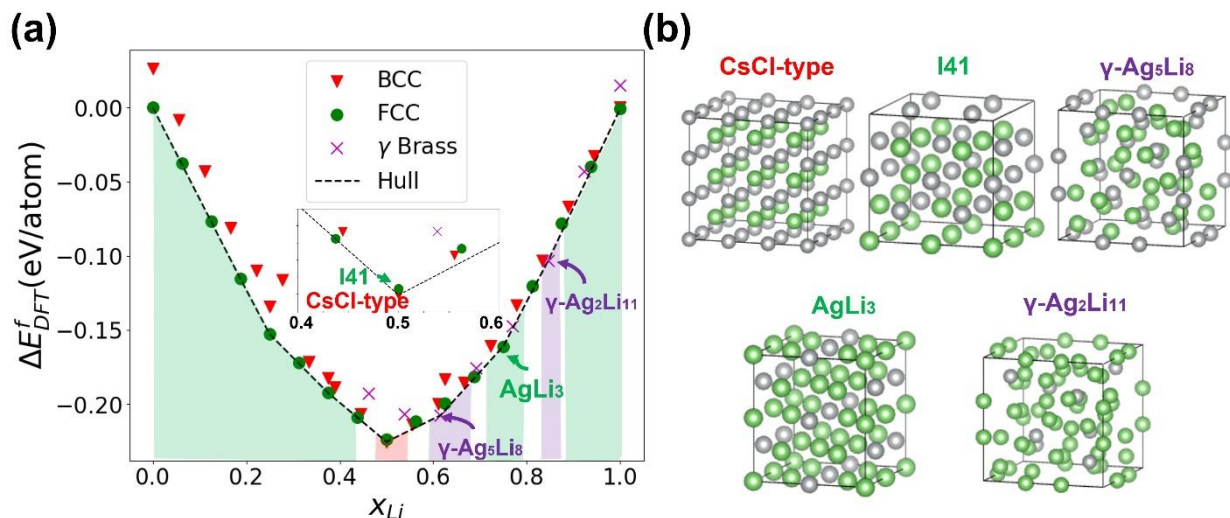


Figure 55. (a) Computed density functional theory formation energy for ground-state structures predicted by cluster expansion in BCC (red triangle), FCC (green dot), and  $\gamma$ -brass (magenta cross) lattice types. The convex hull of formation energy is marked with dashed line, under which single-phase regions are shaded with light red (BCC), light green (FCC), and light magenta ( $\gamma$ ). The composition range  $0.4 < x_{Li} < 0.6$  is enlarged in the middle. Phonon energy and entropy contributions are not included. (b) Predicted ground-state structures as marked with arrows in (a).

The team is also testing several metallic components (silver, tin, and magnesium nanoparticles) to investigate what materials can replace expensive silver as a buffer layer, but also to understand what properties of metallic components govern the lithium plating behaviors. All the metallic components were mixed with carbon (75 wt% of carbon and 25 wt% of metallic component). Then, electrode films of ABL mixtures were prepared using polytetrafluoroethylene (PTFE) binder (20 wt%). The thickness of the ABL used in this study is  $\sim 100 \mu\text{m}$ . Because their full-cell design was unsuccessful, the team used half-cell configuration (Li/Li<sub>6</sub>PS<sub>5</sub>Cl/ABL). Figure 56 shows the charge and discharge profiles of the SSBs. Sn-C buffer layer exhibits a very high overpotential  $> 1 \text{ V}$ , whereas Ag-C and Mg-C buffer layers show relatively low overpotentials  $< 0.1 \text{ V}$  without noticeable short-circuit behaviors. While further investigations are required, the team expects that Mg-C buffer layer can be a good alternative to Ag-C. The team is investigating how the lithiation mechanisms differ depending on the active components.

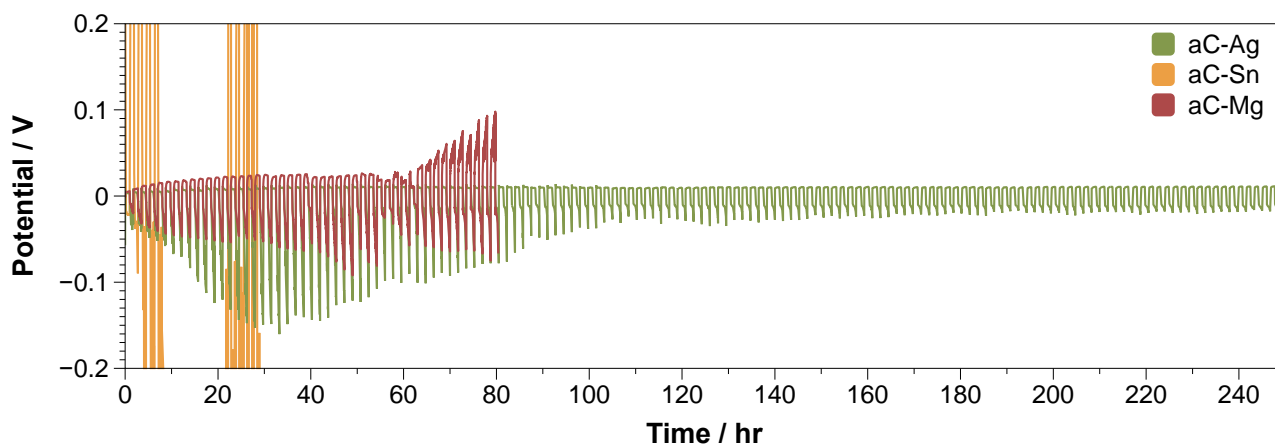


Figure 56. Charge-discharge voltage profiles of Li/Li<sub>6</sub>PS<sub>5</sub>Cl/ABL cells. Active buffer layers are Ag-C, Sn-C, and Mg-C composites at  $0.17 \text{ mA cm}^{-2}$ . All the tests were conducted at  $25^\circ\text{C}$ .

### Composite Cathode: High-Voltage Stability, Chemical, and Mechanical Degradation Issue (G. Chen, H. Kim, J. Urban, G. Ceder, M. Scott)

Li<sub>3</sub>REX<sub>6</sub>-family (RE = rare earth) of halides often crystallize in three types of phases: monoclinic (C2/m structure), trigonal (P-3m1 structure) and orthorhombic (Pnma structure). It is well recognized that polymorphic transformations are common among the halides, especially under thermal treatment conditions. However, the impact of crystal structure on halide properties is not well understood. This quarter, the team investigated the synthesis-composition-structure-property relationships in the Li-Y-Cl system. Three synthesis routes, solid-state (SS), co-melting (CM) and mechanochemical (MC) methods, were used to prepare Li<sub>3</sub>YCl<sub>6</sub>-type SEs. The precursors were heated at  $450^\circ\text{C}$  in SS synthesis and  $550^\circ\text{C}$  in CM synthesis, with the latter corresponding to synthesis under the melting condition of the precursors. High-energy ball milling was used in the MC synthesis.

Figure 57 shows X-ray diffraction (XRD) patterns obtained on various synthesized samples as well as the Nyquist plots from the electrochemical impedance spectroscopy (EIS) measurements. When the stoichiometric ratio (1:3) of YCl<sub>3</sub> and LiCl was used, Li<sub>3</sub>YCl<sub>6</sub> with the trigonal phase was obtained from both SS and CM synthesis (Figure 57a-b). Increasing the amount of YCl<sub>3</sub> precursor, on the other hand, leads to formation of nonstoichiometric Li<sub>3-x</sub>Y<sub>1+x</sub>Cl<sub>6</sub> compounds with the orthorhombic phase. This is clearly shown by the splitting of the diffraction peak at  $\sim 15.8^\circ$ , the absence of the peak at  $\sim 17.3^\circ$ , and the appearance of an additional peak at  $\sim 18.0^\circ$  on the XRD pattern in Figure 57a-b. They found that the synthesis method plays an important role as the trigonal-to-orthorhombic transition occurs at a different level of YCl<sub>3</sub> excess in SS and CM synthesis, with the former requiring a much higher amount than that in the latter. In comparison, the samples prepared by the MC method show significantly broader diffraction peaks. This is likely due to the lower crystallinity from high-energy ball milling synthesis as well as increased cation disordering in the lattice.

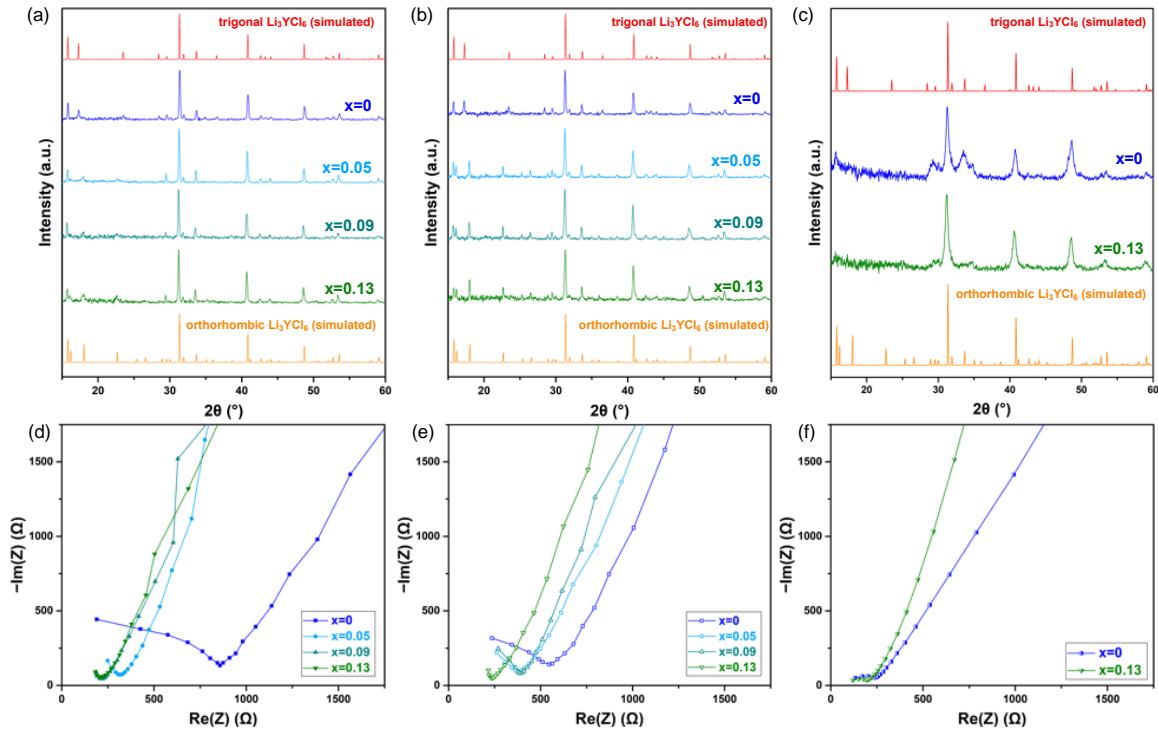


Figure 57. (a-c) X-ray diffraction patterns and (c-e) Nyquist plots of  $\text{Li}_{3-x}\text{Y}_{1+x}\text{Cl}_6$  ( $0 \leq x \leq 0.13$ ) samples prepared from solid state (a/d), co-melting (b/e), and mechanochemical synthesis (c/f).

Synthesis methods also affect the lattice dimension of  $\text{Li}_{3-x}\text{Y}_{1+x}\text{Cl}_6$ . Figure 58a shows the normalized unit cell volume ( $V/Z$ , where  $Z$  denotes the number of the chemical formula in the unit cell) obtained from the refinement of the XRD patterns. Among trigonal  $\text{Li}_3\text{YCl}_6$  samples prepared by the different methods, the  $V/Z$  value follows this order: MC > SS > CM. Room-temperature ionic conductivities ( $\sigma_{25}$ ) obtained from EIS measurements are also shown in Figure 58b. Consistent with previous reports, the values are  $0.049 \text{ mS cm}^{-1}$  and  $0.081 \text{ mS cm}^{-1}$  for SS- $\text{Li}_3\text{YCl}_6$  and CM- $\text{Li}_3\text{YCl}_6$ , respectively. The conductivity increases with the increase of yttrium content in the composition, reaching  $0.197 \text{ mS cm}^{-1}$  and  $0.187 \text{ mS cm}^{-1}$  for  $\text{Li}_{3-x}\text{Y}_{1+x}\text{Cl}_6$  ( $x = 0.13$ ) prepared by SS and CM, respectively. Overall, higher conductivities are obtained on ball-milled samples, achieving  $0.179 \text{ mS cm}^{-1}$  and  $0.233 \text{ mS cm}^{-1}$  for  $x = 0$  and  $x = 0.13$ , respectively (Figure 58b). The  $\sigma_{25}$  of nonstoichiometric  $\text{Li}_{3-x}\text{Y}_{1+x}\text{Cl}_6$  appears to be less dependent on the synthesis methods. These differences may be associated with the structural characteristics of trigonal and orthorhombic phases, such as the cation disorder and defect concentration, which will be further investigated in future research.

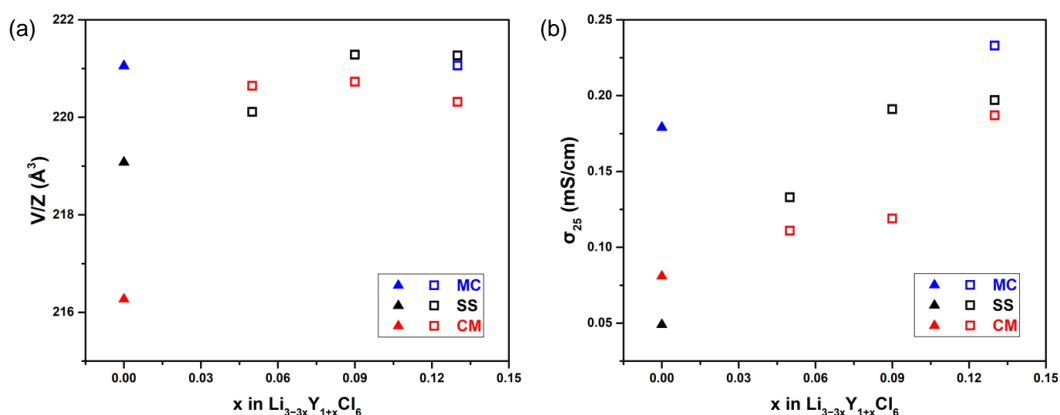


Figure 58. Comparison of normalized unit cell volumes (a) and room-temperature ionic conductivities (b) of  $\text{Li}_{3-x}\text{Y}_{1+x}\text{Cl}_6$  ( $0 \leq x \leq 0.13$ ) samples prepared by different synthesis methods.  $\blacktriangle$  indicates trigonal phase and  $\square$  indicates orthorhombic phase.

## High-Loading Composite Cathodes (M. Tucker, M. Doeff, G. Chen, G. Ceder)

The team aims to fabricate thin LLZO (that is, lithium lanthanum zirconium oxide) film via tape casting. To fabricate thin LLZO film (target thickness 20  $\mu\text{m}$ ), a tape casting and post-processing method has been developed. Continuing from previous quarters, they have optimized the process, including debinding and sintering conditions. First, a higher debinding temperature was tested to fully burn out additives and binders in a short time. The additives and binders must be fully removed, or they will inhibit densification of the LLZO film. Previously, debinding was conducted at 675°C. At this temperature, the weight decreased and reached a plateau after 12 hours. This result implies that more than 12 hours of dwelling is required for full burn-out. To shorten this long dwelling time, they tested a higher debinding temperature of 690°C. A faster green body weight loss was observed, and the weight stabilized after 4 hours. Second, the team has optimized the procedure to fabricate a flat LLZO film. The LLZO film was sintered under a dead weight to prevent curving (Figure 59). The loading should be heavy enough to prevent the curve, but it should not be so heavy that it breaks the sample. A graphite plate was used as a weight because it is chemically inert with LLZO at high temperatures. Different loadings from 1  $\text{g}/\text{cm}^2$  to 3  $\text{g}/\text{cm}^2$  were tested. As shown in Figure 59, the sintered LLZO film was severely curved with the 1  $\text{g}/\text{cm}^2$  loading. The 2  $\text{g}/\text{cm}^2$  loading resulted in less curving than the 1  $\text{g}/\text{cm}^2$ , but curving was still evident. The 3  $\text{g}/\text{cm}^2$  loading was enough to prevent curving without breaking the sample.

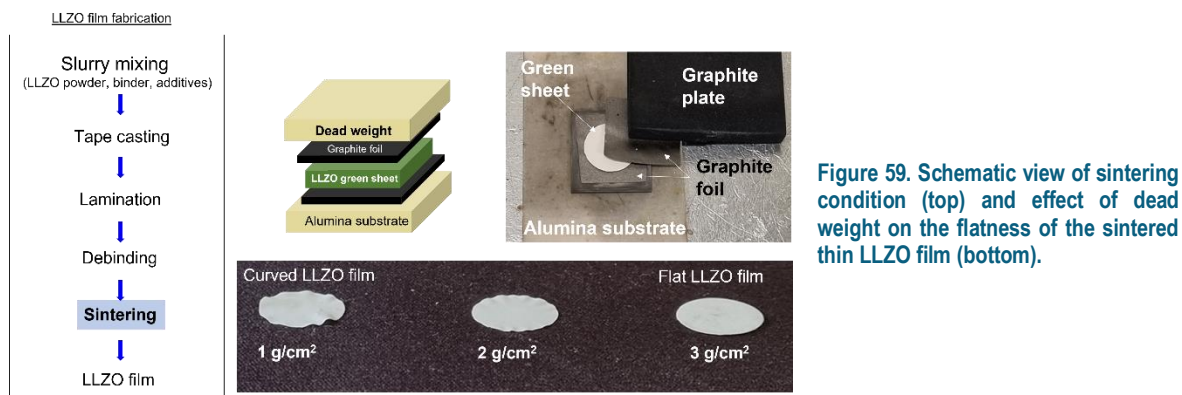


Figure 59. Schematic view of sintering condition (top) and effect of dead weight on the flatness of the sintered thin LLZO film (bottom).

Third, the sintering temperature was explored in the range of 1050°C to 1180°C. The sintering behavior of thin LLZO may be different from thick LLZO pellets because it can undergo relatively more lithium loss and more severe shrinkage during sintering. All the samples were sintered with 3  $\text{g}/\text{cm}^2$  loading under an argon atmosphere. Up to the sintering temperature of 1150°C, the LLZO films were flat and semi-translucent, as shown in Figure 60. However, a sample treated at 1180°C had a surface color change and relatively poor flatness. These results show that the optimum sintering temperature needs to be below 1180°C.

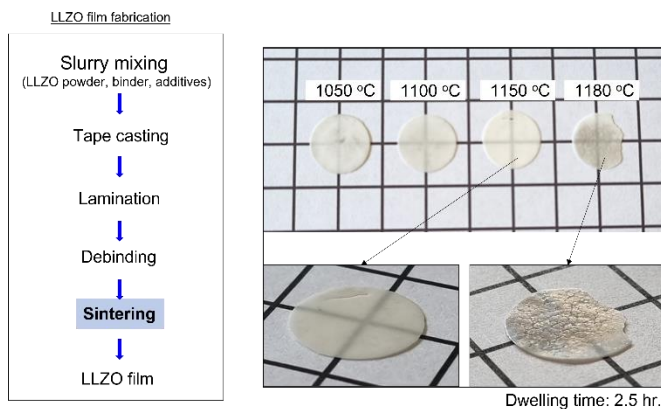


Figure 60. Picture of LLZO films after sintering at different temperatures.

The mechanical properties of thin LLZO films need to be characterized and enhanced because the thin LLZO is currently highly fragile. Preliminary mechanical property testing has been conducted with thick LLZO pellets (~ 700  $\mu\text{m}$ ) because the LLZO film synthesis needs more optimization. In this report, the team fabricated LLZO pellets at LBNL using the same recipe as for the LLZO thin films and evaluated mechanical properties such as hardness (H) and fracture toughness ( $K_{IC}$ ). Hardness was evaluated using micro-indentation. Indentation with five loads (that is, 50 gf, 100 gf, 300 gf, 500 gf, and 1000 gf) was conducted, and the diagonal lengths of the indented points were plotted. By fitting the diagonal length versus applied force, they obtained a hardness of 10.02 GPa, in the range of hardness reported in the literature for LLZO pellets. Fracture toughness was also evaluated using the direct crack length observation method. The length of the cracks at the corners of the indented points was measured. Using the above-obtained hardness and observed crack length, the fracture toughness could be obtained using the Niihara equation. The fracture toughness was  $1.367 \text{ MPa}\cdot\text{m}^{0.5}$ , again in good agreement with previously reported values of fracture toughness of LLZO pellets.

This quarter, the team has tested cathode composites containing secondary SEs. The cathode composite consists of CAM and secondary SE. In this study, they used NMC-111 ( $\text{Li}_{1.05}\text{Ni}_{0.33}\text{Mn}_{0.33}\text{Co}_{0.33}\text{O}_2$ ) as a CAM. As a secondary SE, succinonitrile (SN) with lithium salts was investigated because of its good oxidative stability and high  $\text{Li}^+$  ion conductivity. Lithium bis(trifluoromethanesulfonyl)imide (LiTFSI) was used as the lithium salt because it is known to be stable with LLZO. SN+LiTFSI was prepared by mixing molten SN and LiTFSI at  $80^\circ\text{C}$ . The ionic conductivity, electronic conductivity, and voltage stability window of the secondary SE were evaluated. Symmetric cells (SUS/SN+LiTFSI/SUS, SUS=stainless steel) were fabricated to evaluate ionic conductivity and electronic conductivity; then, EIS and direct current (DC) polarization were conducted. The Nyquist plots from the EIS are shown in Figure 61a. The diameter of the semicircle significantly decreased with higher LiTFSI concentrations, indicating that it has a higher ionic conductivity. The ionic conductivity increased more than 10 times from  $2.39 \times 10^{-4} \text{ S/cm}$  (1.6 mol%) to  $3.47 \times 10^{-3} \text{ S/cm}$  (5.0 mol%). DC polarization curves are shown in Figure 61b, and all the SN+LiTFSI samples showed similar electronic conductivity  $\sim 1 \times 10^{-9} \text{ S/cm}$ . These EIS and DC polarization results show that the SN+LiTFSI is highly ionic conductive, but electronically insulating. To observe the stable voltage window of the SN+LiTFSI, Li/SN+LiTFSI/SUS cells were fabricated, and linear sweep voltammetry was conducted (Figure 61c). Up to 4.7 V versus  $\text{Li/Li}^+$ , negligible current was detected for all the SN+LiTFSI samples. This indicates that SN+LiTFSI has a wide enough voltage window to be used with high-voltage CAMs. The team will further explore other secondary SEs, including other salts such as lithium bis(oxalate) borate and mixtures with LiTFSI, and will assess compatibility of secondary SEs with cathode materials. The team will also attempt to build liquid-free cells using a mixture of solid-state electrolyte, CAM, and conductive additives for the cathode, with LLZO separators.

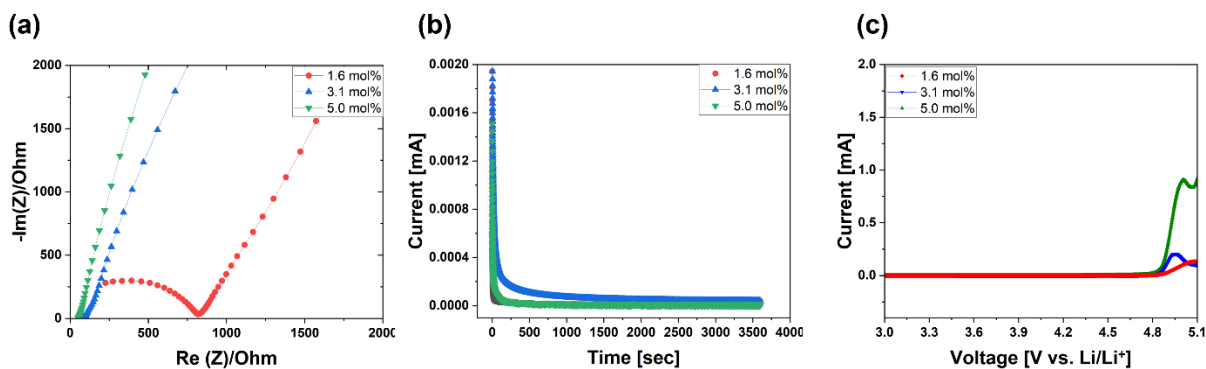


Figure 61. Property testing of different mol% of LiTFSI in succinonitrile. (a) Nyquist plot. (b) Direct current polarization. (c) Linear sweep voltammetry.

### Glass Composite SE by Low-Temperature Solution-Phase Synthesis (G. Liu)

The team aims to develop a sulfide glass separator that is both thin and resists lithium dendrite penetration from the Li-metal anode side. Solution processable separators would be more easily integrated with SSBs through low-cost processing. In addition, solution processable SEs could be directly integrated with cathode materials to form a composite cathode through conventional slurry coating. Their objective is therefore to develop the processes to synthesize hybrid SEs from inorganic conductors and polymer through solution-based processes, and which combine high ionic conductivities ( $> 10^{-3} \text{ S cm}^{-1}$ ) and high fracture toughness ( $> 10 \text{ MPa m}^{1/2}$ ). As discussed, there are three methods that can mix functional polymers with solid-state ceramic materials: direct mechanical mixing, slurry dispersion, and solution precipitation. Solution precipitation is the preferred method for this study. To evaluate the proposed solution-precipitation method, the team comparatively investigated the morphological and mechanical properties of the Li-P-S-CL (LPSCl)-polymer composites with the other preparation methods. First, they discuss the morphology of LPSCl – poly(ethylene glycol), or PEO, composites using scanning electron microscope (SEM) images in Figure 62. Regardless of the polymer content, all composites displayed similar morphology with crystal grain sizes between  $1 \mu\text{m}$  and  $10 \mu\text{m}$ . Unlike the size of LPSCl decreasing after precipitation without polymer, the feature size of the polymer composite appears to be preserved when precipitation was performed in the polymer solution. This result suggests that the polymer promotes LPSCl precipitation and possibly limits ethanol accessibility to LPSCl. Because they could not identify the polymer phase in SEM images, they performed transmission electron microscope (TEM) – energy dispersive X-ray spectroscopy (EDS) analyses to track how the polymer distributes on the composites. For the TEM analyses, they used an air-tight sample transfer TEM holder to avoid potential degradation of the composite due to air exposure. Figure 63 shows the comparative results between LPSCl-PEO composites by dispersion method (Figure 63a) and the composites via the solution-precipitation method (Figure 63b). Considering all sample preparation procedures were conducted without air exposure, oxygen elemental distribution in the EDS maps is expected to represent the presence of PEO along with the LPSCl phase. To compare the elemental distribution clearly, they put bi-elemental maps of P-O and P-Cl next to each scanning transmission electron microscopy (STEM) – high-angle annular dark field (HAADF) image. For the 2 wt% polymer composites prepared by the dispersion mix method, a non-uniform distribution of PEO is clearly observed, as shown in Figure 63a. In contrast, the solution-precipitation method creates a uniform distribution of PEO in LPSCl composites (Figure 63b). These results confirm a solution-precipitation method is better than the dispersion mix method to produce a uniform distribution of the polymer and ceramic phase.

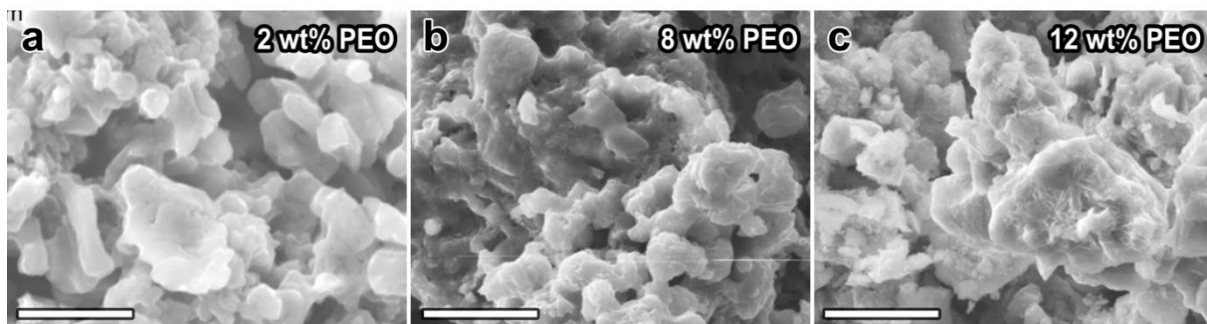


Figure 62. Scanning electron microscopy images of LPSCl-PEO composites with the polymer content of 2 wt%, 8 wt%, and 12 wt% (from left to right).

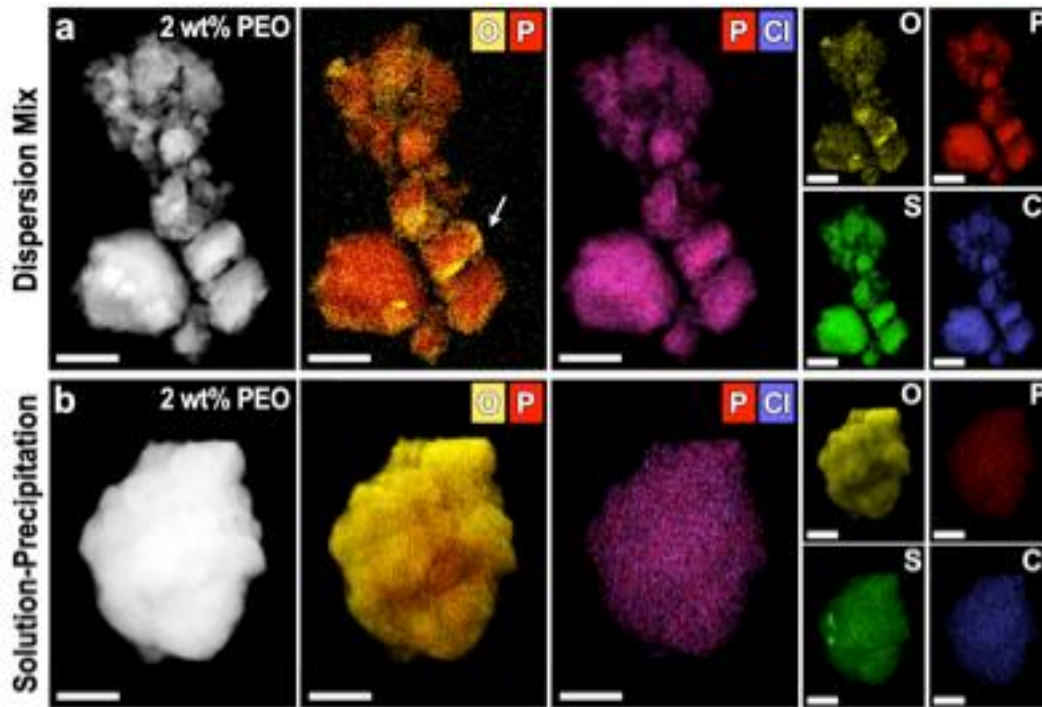


Figure 63. Chemical and mechanical evaluations of LPSCI-PEO composite. (a-b) Elemental mappings of oxygen, phosphorus, sulfur, and chlorine in LPSCI-PEO composites with 2 wt% polymer content. Note that the composites are prepared by two methods: (a) dispersion mix and (b) solution-precipitation methods.

## Patents/Publications/Presentations

### Publication

- Shen, H., K. Chen, J. Kou, Z. Jia, N. Tamura, W. Hua, W. Tang, H. Ehrenbert, and M. Doeff. “Spatiotemporal Mapping of Microscopic Strains and Defects to Reveal Li-Dendrite-Induced Failure in All-Solid-State Batteries.” *Materials Today* 57 (2022): 180–191. <https://doi.org/10.1016/j.mattod.2022.06.005>.

### Presentations

- 23<sup>rd</sup> International Conference on Solid-State Ionics, Boston, Massachusetts (July 17–22, 2022): “A Perspective on Solid-State Batteries with LLZO”; M. Doeff. Keynote address.
- American Society of Mechanical Engineers, Summer Heat Transfer Meeting, Philadelphia, Pennsylvania (July 11, 2022): “Thermal Wave Sensing of Electrochemical Information”; D. Chalise, Y. Zheng, B. Zhang, Y. Fu, F. Shen, Q. Zheng, R. Miao, S. Kaur, S. D. Lubner, M. C. Tucker, V. Battaglia, C. Dames, and R. S. Prasher.

## Task 1.24 – Low-Pressure All-Solid-State Cells (Anthony Burrell, National Renewable Energy Laboratory)

**Project Objective.** The goal of this project is to develop all-solid-state batteries (ASSBs) using four classes of solid-state electrolytes (SSEs), and/or electrode modifiers, that can be used to achieve the final 500 Wh/kg cell target. These materials will be down selected using full-cell testing and advanced characterization to achieve cell targets at cell pressures less than 100 psi.

**Impact.** Many factors limit ASSB performance, and this project seeks to address the interface stability of both the lithium interface and the high-voltage cathode. The combination of multiple ionic conductors coupled is specifically targeted to allow solution processing, and low-pressure cell outcome will enable lower cost deployment of solid-state cells in automotive applications.

**Approach.** To achieve the goal of low-pressure ASSBs, the team is utilizing three classes of solid ion conductors, sulfide materials, melt-processable lithium carboranes, and multinary metal halides. These materials can be chemically modified to optimize ionic conductivity and voltage stability in single conductor modes or in combinations to effect interface modification for full-cell development. Specifically, the use of flexible ionic conductors at the cathode interface will enable the mechanical effects of cathode expansion and contraction to be mitigated. In combination with the materials discovery work, the project has an extensive characterization team to help determine the impacts of interface, chemical, electrochemical, and mechanical factors on system performance. Full-cell assembly and development, targeting approaches that are readily scalable and compatible with roll-to-roll process, will drive the materials innovation and development.

**Out-Year Goals.** The out-year goal is demonstration of 2 Ah cells that achieve 500 Wh/kg and lifetimes exceeding 300 cycles at functional pressures below 100 psi.

**Collaborations.** There is a joint effort for this project between National Renewable Energy Laboratory, M. Toney at the University of Colorado, and A. Maughan at the Colorado School of Mines.

### Milestones

1. Prepare electrochemical cells using lithium carboranes. (Q1, FY 2022; Completed)
2. Prepare electrochemical cells using  $\text{Li}_y\text{MCl}_z$ . (Q2, FY 2022; Completed).
3. Prepare electrochemical cells using sulfur-polymer-coated cathodes. (Q3, FY 2022; Completed)
4. Demonstrate full-cell design that enables accurate, repeatable internal pressure control for ASSBs. (Q4, FY 2022; Completed)

## Progress Report

Over the past few months, the synthesis of borohydride substituted variants of the chloride argyrodite ( $\text{Li}_6\text{PS}_5\text{Cl}$ , or LPSCl) have focused on eliminating an obvious impurity phase. Multiple synthetic adjustments were made to suppress the formation of the impurity phase, including the use of unpyrolyzed ampules, adjusting annealing temperature and time, and adjusting precursor mix to be  $\text{LiBH}_4$  rich. These strategies had limited success; however, the root cause of the impurity phase has been tentatively identified as an impurity present in the  $\text{LiBH}_4$  precursor.

Although work has centered around troubleshooting problematic syntheses, a phase pure borohydride substituted argyrodite has been prepared and preliminary electrochemical impedance spectroscopy data have been collected. The data are promising, as the material exhibited an ionic conductivity well in excess of what has been previously reported ( $8 \times 10^{-3} \text{ S/cm}$  versus  $4 \times 10^{-4} \text{ S/cm}$  and  $< 1.2 \times 10^{-4} \text{ S/cm}$ ), even without cold isostatic pressing of the pellet.<sup>[1-2]</sup> Next steps will consist of preparing borohydride substituted argyrodites using fresh  $\text{LiBH}_4$  and thorough characterization of their electrochemical properties as well as an investigation of borohydride dynamics in the argyrodite. On confirming the phase purity and ionic conductivities of as-prepared argyrodites, virtual electrode X-ray photoelectron spectroscopy (XPS) measurements will be performed to monitor the surface chemistry of the electrolyte as it is cycled.

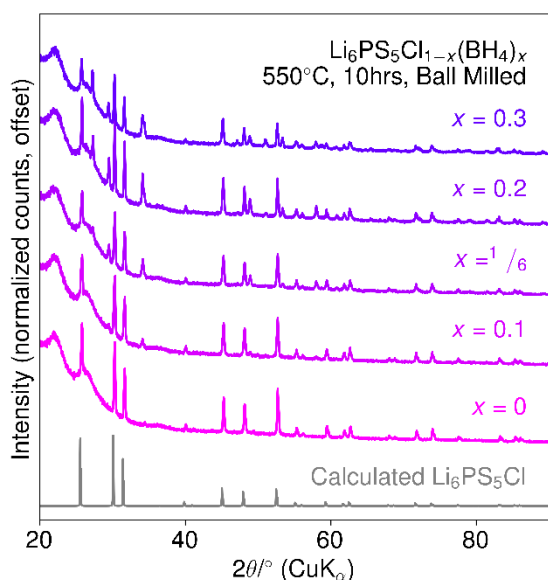


**Figure 64.** Powder X-ray diffraction patterns of borohydride-substituted argyrodites.

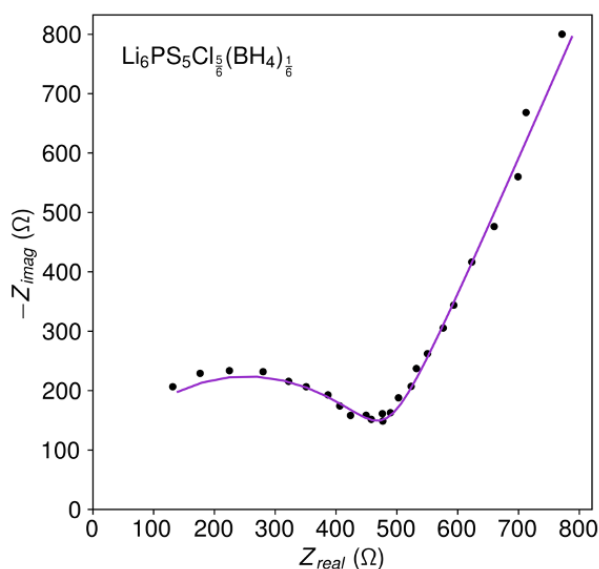


**Figure 65.** Nyquist plot of phase pure substituted argyrodite, ionic conductivity =  $8 \times 10^{-3} \text{ S/cm}$ .

Argyrodites such as  $\text{Li}_6\text{PS}_5\text{Br}$  are known for their excellent Li-ion conductivity. However, the stability of these materials with the other battery components is less than desirable. Recently, reports have indicated that certain aspects of stability such as air-stability have been improved through replacing  $\text{P}^{5+}$  with  $\text{Sb}^{5+}$ .<sup>[3-4]</sup> Efforts have been focused on the synthesis of  $\text{Li}_{6.5}\text{Sb}_{0.5}\text{Ge}_{0.5}\text{S}_5\text{I}$ . To better characterize  $\text{Li}_{6.5}\text{Sb}_{0.5}\text{Ge}_{0.5}\text{S}_5\text{I}$ , the team has successfully synthesized the material using a salt flux approach that will be optimized to grow single crystals. Future work will include detailed characterization and measuring the ionic conductivity of this material.

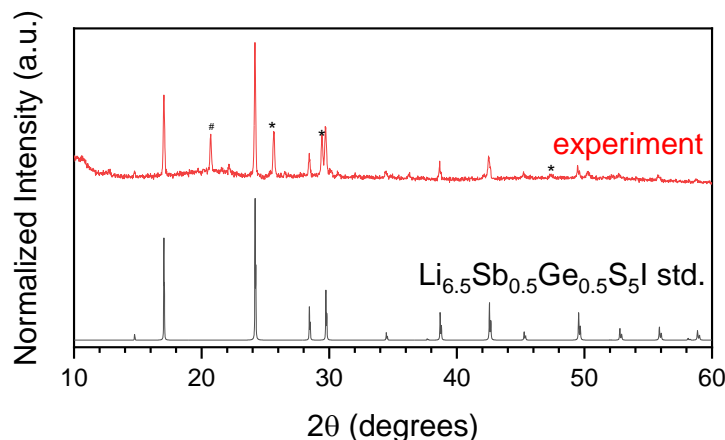


Figure 66. Powder X-ray diffraction of  $\text{Li}_{6.5}\text{Sb}_{0.5}\text{Ge}_{0.5}\text{S}_5\text{I}$  synthesized with a salt flux method. Peaks with (\*) come from the salt flux while (#) is an unidentified phase.

Synthesis of other materials with structural relations to the argyrodites is also in progress.  $\text{Li}_4\text{SiS}_4$  has similar structural units (isolated tetrahedrons) and has been demonstrated to be a poor ion conductor,<sup>[5]</sup> yet with aliovalent substitution of silicon with phosphorus, the ionic conductivity was improved by 4 orders of magnitude.<sup>[6]</sup>  $\text{Li}_4\text{SiS}_4$  will be used as a precursor to form new materials with isolated tetrahedrons. Currently, near phase-pure synthesis of  $\text{Li}_4\text{SiS}_4$  has been achieved. Exploratory syntheses are in progress.

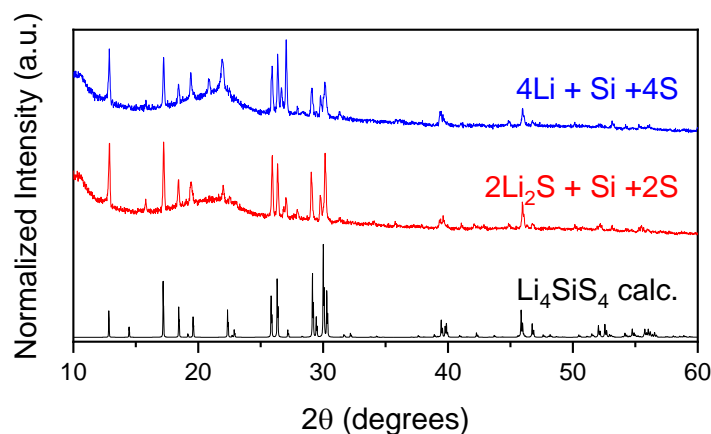
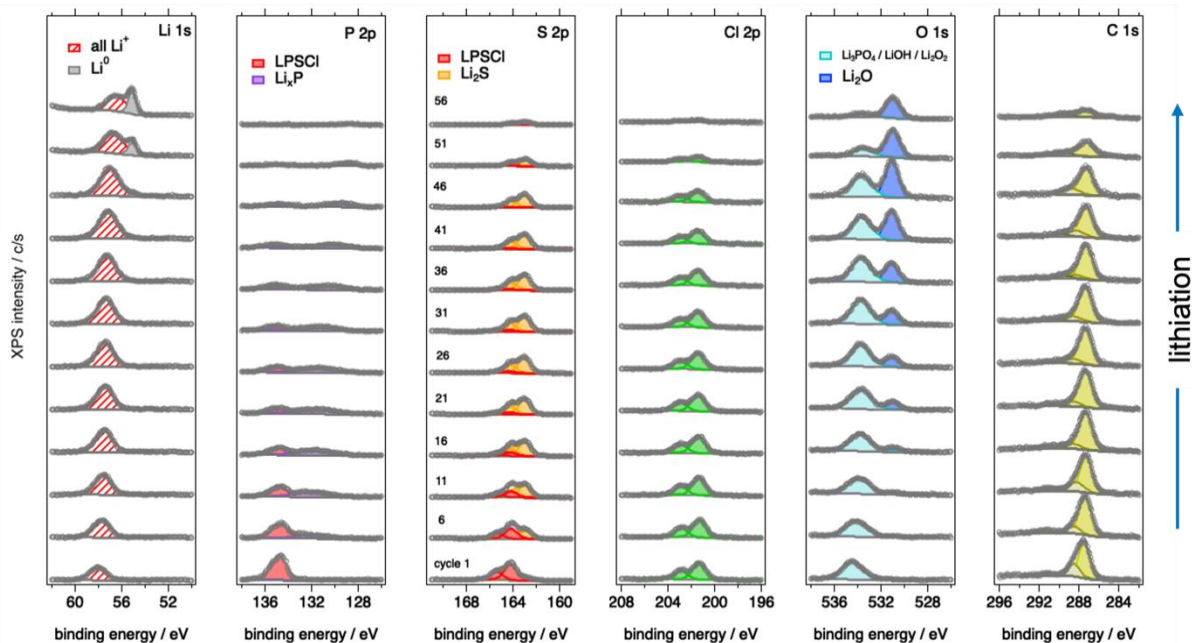


Figure 67. Powder X-ray diffraction of different synthetic preparations of  $\text{Li}_4\text{SiS}_4$  (blue, red) compared with the calculated pattern (black).

### Virtual-Electrode XPS (VE-XPS)

This quarter, the team also continued analysis of the VE-XPS experiments performed on LPSCl argyrodite SSE materials. In these experiments, XPS measurements are performed while the exposed sample surface is biased *in situ* via a low-energy electron source, which in turn drives bulk  $\text{Li}^+$  migration toward the surface. On SSE materials, this approach enables direct observation of solid electrolyte interphase (SEI) formation and evolution at the SSE/Li-metal interface.

Figure 68 shows elemental core levels acquired during a VE-XPS experiment on a composite LPSCI/S-polymer sample. This experiment probes SEI formation, where excess  $\text{Li}^+$  arrives at the surface and is neutralized via  $\text{Li}^+ + \text{e}^- \rightarrow \text{Li}^0$ . Initially, the neutral  $\text{Li}^0$  exists only transiently, as it very quickly reacts with LPSCI to form Li-rich secondary phases. In the as-received sample, peaks associated with the argyrodite LPSCI are observed, and in addition peaks are observed in the oxygen 1s and carbon 1s core levels that are associated with  $\text{Li}_3\text{PO}_4$  and carbonaceous contamination, respectively. The Li-rich phases that form due to the reaction of  $\text{Li}^0$  with LPSCI include primarily  $\text{Li}_2\text{S}$ ,  $\text{Li}_x\text{P}$ . The formation of  $\text{Li}_2\text{O}$  is also observed, likely due in part to the decomposition of  $\text{Li}_3\text{PO}_4$  into  $\text{Li}_2\text{O}$  and  $\text{Li}_x\text{P}$ , but also to some extent through reactions with residual gases in the vacuum chamber. Eventually the SEI passivates and stops growing, at which point metallic  $\text{Li}^0$  is observed plating on the surface.



**Figure 68.** Subset of curve-fitted spectra acquired during virtual-electrode X-ray photoelectron spectroscopy (VE-XPS) experiment on baseline argyrodite LPSCI+S-based polymer composite / lithium foil sample. These XPS core-level spectra reveal formation and passivation of the SEI (primarily comprised of  $\text{Li}_2\text{S}$ ,  $\text{Li}_x\text{P}$ ,  $\text{Li}_3\text{PO}_4$ , and  $\text{Li}_2\text{O}$ ) followed by plating of metallic lithium on the free surface that occurs beginning at approximately cycle 46.

Peak areas (corrected for elemental sensitivity factors) associated with the LPSCI composite material and SEI phases over the course of the VE-XPS experiment are plotted in Figure 69a. As the SEI forms, the  $\text{Li}^+$  peak area grows, consistent with the interpretation that the SEI is composed of Li-rich secondary phases. The onset of  $\text{Li}^0$  plating occurs abruptly at cycle 46, signaling that the SEI has passivated. Figure 69b shows the evolution of XPS binding energies for sulfur 2p (in LPSCI) and sulfur 2p (in  $\text{Li}_2\text{S}$ ). Peak positions are not plotted beyond cycle 45 due to attenuation of signals caused by  $\text{Li}^0$  plating.

As indicated in Figure 69b, small but measurable binding energy shifts are observed both for the LPSCI composite and  $\text{Li}_2\text{S}$ . Binding energy shifts in VE-XPS experiments are caused by a combination of doping effects and changes to interfacial dipoles, both of which contribute to interfacial energy-band alignments. In some cases, transient charging phenomena associated with either the photoelectron current or electron beam current bias can also cause shifts in core-level binding energies, but those effects can be ruled out in the present case based on measurement conditions. Doping effects are related to changes in native point defect concentrations in response to variations in lithium chemical potential,  $\mu_{\text{Li}}$ . The magnitudes of interfacial dipoles depend sensitively on the distribution of charge at the interface, including defects, which can also be influenced by  $\mu_{\text{Li}}$ . In Figure 69b, the change in interfacial valence-band offset (DVBO) is calculated by subtracting the shift in the sulfur 2p core level associated with  $\text{Li}_2\text{S}$  from that associated with the LPSCI. It is interesting to note that although initially a substantial DVBO value  $> -0.2$  eV is observed, this value steadily decreases toward zero as the SEI grows and essentially passivates by  $\sim$  cycle 45.

In future work on this project, additional VE-XPS experiments will be performed on LPSC1-based samples, as well as other SSE materials being synthesized within the project. In addition to electron current bias,  $\text{Li}^+$  current bias VE-XPS experiments will be performed to further explore interfacial energy-band alignments, as well as the contributions of various SEI phases to impedance at SSE/Li interfaces.

### Characterizations by Atomic Force Microscopy (AFM)-Based Nano-Probes

The quality of the interface between the SSE and the lithium metal is critical for Li-ion transport and preventing lithium dendrite growth. However, challenges have been encountered at the interfaces when integrating the SSE into full cells. The SEI grows due to chemical reactions of lithium metal with the SSE and impedes ion transport. In addition, a space-charge region around the electrode/SSE interface should exist with even a simple material interface that has no extensive chemical reactivity. The space-charge regions can have a major impact on the ion transport at the interface. Chemical and structural characterizations at the interface have been reported by large numbers of research groups, including this team. However, electrical characterizations, such as the electrical potential across the interface, have received much less attention. C. S. Jiang's team has measured the electrical potential in nm-scale resolutions by using Kelvin probe force microscopy (KPFM) on cross-sections of Li/SSE. The SSE is a composite with 90% argyrodite and 10% sulfur polymer. KPFM is an AFM-based technique with spatial resolution of  $\sim 30$  nm and energy resolution of  $\sim 10$  meV. The cross section was made by cleaving the electrolyte/lithium puck, followed by ion milling using 6 kV argon ion for 10 hours to generate a flat surface for analysis.

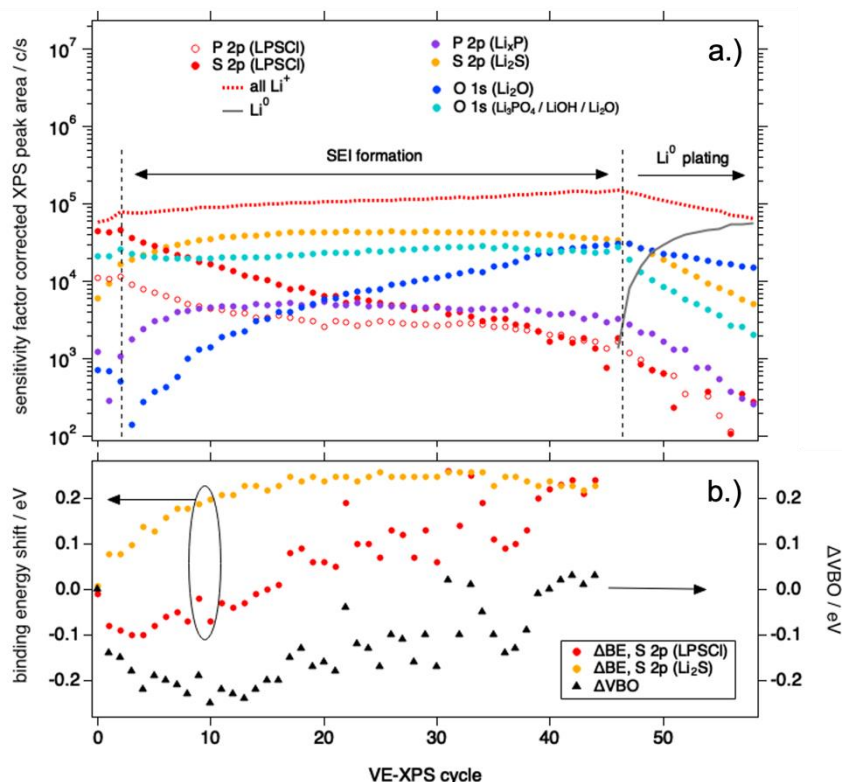
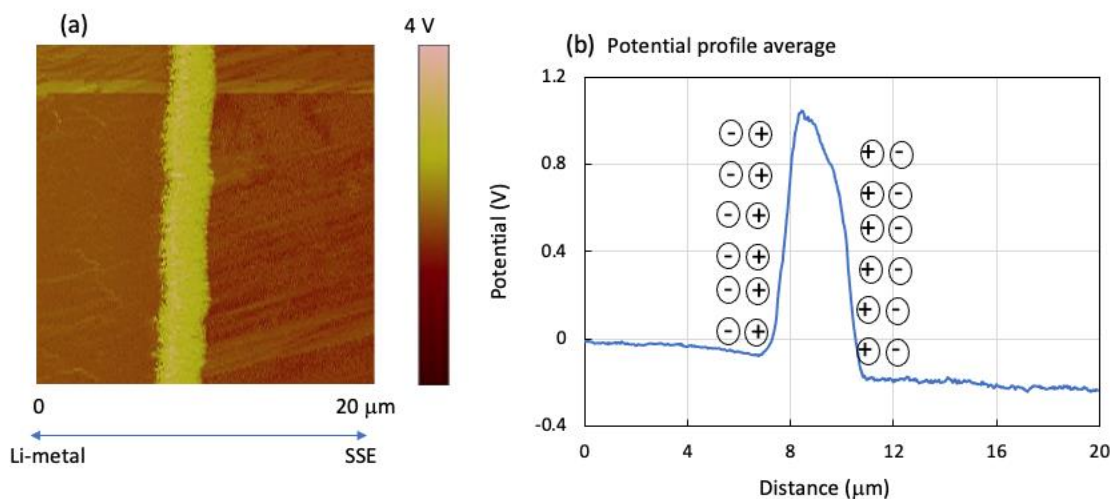


Figure 69. (a) Plot of peak areas and (b) binding energy shifts for the LPSC1 and  $\text{Li}_2\text{S}$  during the virtual-electrode X-ray photoelectron spectroscopy experiment on an LPSC1/S-polymer composite. In these experiments, binding energy shifts can be interpreted in terms of changes in doping levels in materials, as well as changes to interface defect populations that affect the interfacial dipole, and thus reveal changes in interfacial energy band alignments.

The KPFM image (Figure 70a) shows a very large unexpected potential barrier at the Li/SSE interface, with an amplitude of  $\sim 1$  V and a width of  $\sim 2$   $\mu\text{m}$ . Differing from the potential barrier previously observed at an SSE/cathode interface,<sup>[7]</sup> this potential barrier exhibits a large peak and a much smaller difference ( $\sim 200$  mV) between the lithium and SSE sides (Figure 70b). This potential peak illustrates a structure with two electrical double layers (inside; Figure 70b) that is different from a single electrical double layer raised by a charge transfer between the lithium metal and SSE due to Fermi-level alignment. This interface potential profile suggests the presence of a thick and complicated SEI layer at the interface that increases the interface impedance  $\sim 150\times$  by a simple estimate that  $R$  is proportional to  $\exp(1\text{ V}/200\text{ mV})$ , where 1 V and 200 mV are the potential barriers with and without the potential peak. Indeed, AFM-based ion transport imaging has detected no ion current by applying a bias voltage in 1 V order between the lithium metal and AFM probe, with the setup of probe/SSE/Li/sample-holder stack. The current amplifier detection range is  $10^{-3}$ - $10^{-14}$  A, and their previous measurement in the same setup with a healthy interface showed more than  $10^{-12}$  A current detected.<sup>[8-9]</sup> Considering the impedance of the SSE, the interface impedance dominates the overall impedance for ion transport in this sample. These measurements indicate that the interface engineering is critical for integration of the SSE and lithium metal into solid-state batteries (SSBs).



**Figure 70. (a) Potential map on the interface of the solid-state electrolyte and lithium metal. (b) Potential profile averaged along the vertical in (a); (b) inside, showing two electrical double layers that raise the two sides of the potential peak.**

## Cell Builds

The cell build team has primarily focused on the incorporation of high-energy-density active materials into a solid-state system. The cathode of interest is the no-cobalt, nickel-rich cathode  $\text{LiNi}_{0.9}\text{Mn}_{0.05}\text{Al}_{0.05}\text{O}_2$  (NMA) capable of generating 230 mAh/g.<sup>[10]</sup> This NMA has been atomic layer deposition coated with  $\text{Al}_2\text{O}_3$  to mitigate known side reactions between transition metal oxides and the chlorinated argyrodite ( $\text{Li}_6\text{PS}_5\text{Cl}$ ) used in the team's solid-state system. A mixture of NMA (65 wt%), argyrodite (30 wt%), vapor-grown carbon fibers (VGCF, 2.5 wt%), and Oppanol<sup>®</sup> (2.5 wt%) combined with xylene was mixed in a mortar and pestle. The slurry was blade coated onto aluminum foil and dried in a glovebox with a loading of 0.7 mAh/cm<sup>2</sup>. The anode consists of silicon nanoparticles (Paraclete Energy, Batch G18) mixed with a 0.5 wt% solution of polyvinylidene (di)fluoride (PVDF) in NMP such that the silicon nanoparticles and the dissolved PVDF were 99 wt% and 1 wt% of the mixture, respectively. While the cathode must contain both SSE and carbon to increase the electrode's ionic and electronic conductivity, the silicon electrode does not need to contain carbon due to its higher conductivity ( $3 \times 10^{-5}$  S cm<sup>-1</sup> for silicon and  $\sim 10^{-6}$  to  $10^{-4}$  S cm<sup>-1</sup> for NMA) and can avoid the degradation that occurs at the SSE//carbon interface.<sup>[11]</sup> The slurry was mixed with a planetary mixer and was blade coated onto a copper foil with a roughened surface using a wet gap of 75  $\mu\text{m}$ . The resulting electrode was dried under vacuum at 80°C for 12 hours before being calendered.

An SSE electrolyte layer was printed onto both the silicon and NMA electrodes with a slurry consisting of 95 wt% argyrodite and 5 wt% Oppanol<sup>®</sup> with a thickness of 40  $\mu\text{m}$  and 70  $\mu\text{m}$ , respectively. A separate SSE film was coated on a polished stainless-steel surface and dried in a glovebox. This film was removed with a carbon-steel blade and was used as a free-standing electrolyte layer (30  $\mu\text{m}$  thickness) between the electrolyte coated cathode/anode (Figure 71); this gives a total electrolyte thickness of 140  $\mu\text{m}$ . Punches were then removed from the electrodes and placed into a coin cell, which was placed pressed in a high-pressure setup at approximately 125 MPa.

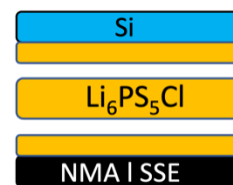


Figure 71. Illustration showing electrode and electrolyte stack.

Results from the NMA versus silicon cell are shown in Figure 72. As expected, there is a large disparity between the 1<sup>st</sup> charge and discharge that can be caused by several aspects including: (1) chemical diffusion between the electrolyte and active material, (2) consumption of the active materials, (3) formation of a space-charge layer, and (4) change in chemical composition in the interface between the solid electrolyte and the contraction of NMA particles during delithiation.<sup>[12]</sup> The low specific capacity of 100 mAh/g of subsequent cycles can partially be attributed to the conservative charge voltage (4.2 V). To the team’s knowledge, this is the first report of an NMA versus silicon SSB. Future work will aim to increase the specific capacity of these Si/NMA SSE systems and to develop methods for low-pressure cycling.

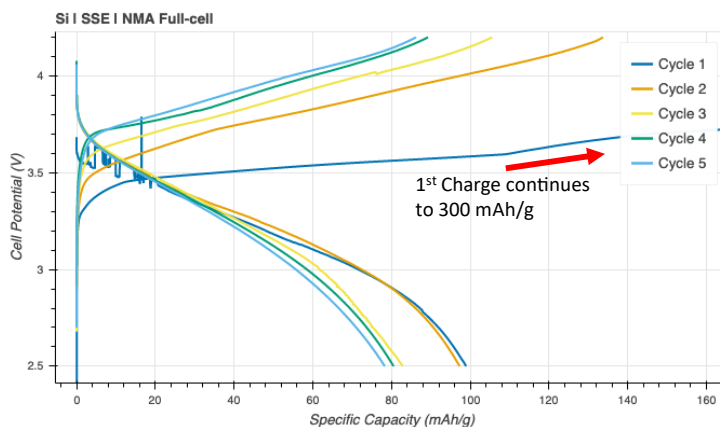


Figure 72. Cycling data for the NMA versus silicon cell cycled at room temperature and C/20. Erratic voltage profiles for the 1<sup>st</sup> charge/discharge can be caused by a loss of physical contact between active particles and the electrolyte.

## References

- [1] Dao, A. H., P. López-Aranguren, R. Černý, O. Guiader, J. Zhang, F. Cuevas, M. Latroche, and C. Jordy. “Improvement of the Ionic Conductivity on New Substituted Borohydride Argyrodites.” *Solid State Ionics* 339 (2019): 114987. <https://doi.org/10.1016/j.ssi.2019.05.022>.
- [2] Wang, H., L. Gao, Z. Lu, Y. Tang, D. Ye, G. Zhao, H. Zhao, and J. Zhang. “Borohydride Substitution Effects of  $\text{Li}_6\text{PS}_5\text{Cl}$  Solid Electrolyte.” *ACS Applied Energy Materials* 4, no. 11 (2021): 12079–12083. <https://doi.org/10.1021/acsaem.1c02892>.
- [3] Lee, Y., J. Jeong, H. J. Lee, M. Kim, D. Han, H. Kim, J. M. Yuk, K-W. Nam, K. Y. Chung, H-G. Jung, and S. Yu. “Lithium Argyrodite Sulfide Electrolytes with High Ionic Conductivity and Air Stability for All-Solid-State Li-Ion Batteries.” *ACS Energy Letters* 7, no. 1 (2022): 171–179. <https://doi.org/10.1021/acseenergylett.1c02428>.
- [4] Zhou, L., A. Assoud, Q. Zhang, X. Wu, and L. F. Nazar. “New Family of Argyrodite Thioantimonate Lithium Superionic Conductors.” *Journal of the American Chemical Society* 141, no. 48 (2019): 19002–19013. <https://doi.org/10.1021/jacs.9b08357>.
- [5] Ahn, B. T., and R. A. Huggins. “Synthesis and Lithium Conductivities of  $\text{Li}_2\text{SiS}_3$  and  $\text{Li}_4\text{SiS}_4$ .” *Materials Research Bulletin* 24, no. 7 (1989): 889–897. [https://doi.org/10.1016/0025-5408\(89\)90053-6](https://doi.org/10.1016/0025-5408(89)90053-6).

- [6] Murayama, M., R. Kanno, M. Irie, S. Ito, T. Hata, N. Sonoyama, and Y. Kawamoto. “Synthesis of New Lithium Ionic Conductor Thio-LISICON—Lithium Silicon Sulfides System.” *Journal of Solid State Chemistry* 168, no. 1 (2002): 140–148. <https://doi.org/10.1006/jssc.2002.9701>.
- [7] Jiang, C-S., K. Park, A. K. Burrell, and M. M. Al-Jassim. “Direct Imaging of Space Charges Around the Interface between Solid Electrolyte and Electrode of Solid-State Batteries.” The Electrochemical Society Meeting Abstract, V. MA2020-02, Section A05 (2020): 934.
- [8] Jiang, C-S., N. Dunlap, Y. Li, H. Guthrey, P. Liu, S-H. Lee, and M. M. Al-Jassim. “Nonuniform Ionic and Electronic Transport of Ceramic and Polymer/Ceramic Hybrid Electrolyte by Nanometer-Scale *Operando* Imaging for Solid-State Battery.” *Advanced Energy Materials* 10 (2020): 2000219.
- [9] Jiang, C-S., Y. Yin, H. Guthrey, K. Park, S-H. Lee, and M. M. Al-Jassim. “Local Electrical Degradations of Solid-State Electrolyte by nm-Scale *Operando* Imaging of Ionic and Electronic Transports.” *Journal of Power Sources* 481 (2021): 229138.
- [1] Li, W., et al. “High-Nickel NMA: A Cobalt-Free Alternative to NMC and NCA Cathodes for Lithium-Ion Batteries.” *Advanced Materials* 32, no. 33 (2020): 2002718. <https://doi.org/10.1002/adma.202002718>.
- [2] Tan, D. H., et al. “Carbon-Free High-Loading Silicon Anodes Enabled by Sulfide Solid Electrolytes.” *Science* 373, no. 6562 (2021): 1494–1499. <https://doi.org/10.1126/science.abg7217>.
- [3] Chen, T., L. Zhang, Z. Zhang, P. Li, H. Wang, C. Yu, X. Yan, L. Wang, and B. Xu. “Argyrodite Solid Electrolyte with a Stable Interface and Superior Dendrite Suppression Capability Realized by ZnO Co-Doping.” *ACS Applied Materials & Interfaces* 11, no. 43 (2019): 40808–40816. <https://doi.org/10.1021/acsami.9b13313>.

### Patents/Publications/Presentations

The project has no patents, publications, or presentations to report this quarter.

## Task 1.25 – Precision Control of the Lithium Surface for Solid-State Batteries (Andrew Westover, Oak Ridge National Laboratory)

**Project Objective.** The overall goal of this project is to understand and engineer the surface and purity of thin Li-metal anodes to enable batteries with an energy density of 500 Wh/kg and a cycle life > 300 cycles.

**Impact.** The knowledge of lithium surface engineering and the implications for cell design of Li-metal batteries will improve commercialization efforts for solid-state Li-metal batteries. There is very little standard knowledge about variations in the impurity level in different lithium sources, the surface chemistry of different lithium surfaces, and their impact on performance. Furthermore, the strategies developed to engineer the surface of the lithium metal for integration into Li-metal batteries will provide significant performance increases, ideally enabling successful commercialization.

**Approach.** This project is broken into two parts. First, the team is focused on thoroughly understanding the purity, mechanics, and surface chemistry of multiple lithium sources and how these parameters impact performance. Second, they will focus on intentional engineering of the lithium purity and surface chemistry to control the mechanical properties, electrochemical stability, and electrochemical performance. They will explore three approaches to engineer the surfaces: gas-phase passivation, deposition of thin metal coatings, and deposition of thin inorganic coatings. To test electrochemical performance, they will use standard ceramic and polymer electrolytes to demonstrate the impact of purity and surface chemistry. The program will also employ a range of standard and specialized characterization techniques, including a significant focus on understanding the mechanics of lithium metal using nanoindentation and adhesion measurements using surface probe microscopy.

**Out-Year Goals.** In FY 2023, the program plans to finish gaining a deep understanding of different lithium sources, purity, and surface conditions, and of how they affect performance in Li-metal cells with both ceramic and polymer electrolytes. In FY 2024 through FY 2027, the primary goal is to develop strategies to carefully control and engineer the surface of lithium metal to optimize performance, enabling batteries that can achieve 500 Wh/kg and cycle for more than 300 cycles at mid-to-high current densities.

**Collaborations.** The primary collaborator for this project is E. Herbert at Michigan Technological University, who is focused on mechanical measurements of Li-metal anodes and electrolytes in inert environments. The project also includes R. Sahore, S. Kalnaus, W-Y. Tsai, and R. Sacci of Oak Ridge National Laboratory (ORNL). The team anticipates the BMR program will also foster significant collaborations with other teams who have a complementary focus on lithium metal. H. Meyer from ORNL helped with the X-ray photoelectron spectroscopy (XPS) measurements and data analysis this quarter.

### Milestones

1. Obtain lithium sources. (Q1, FY 2022; Completed)
2. Conduct chemical characterization of lithium surfaces. (Q2, FY 2022; Completed).
3. Conduct nanoindentation of various lithium sources. (Q3, FY 2022; Completed)
4. Establish baseline electrochemical performance of multiple lithium sources. (Q4, FY 2022; Completed)

## Progress Report

In prior quarters, the ORNL team obtained and characterized the surface of five lithium sources, including four from different commercial suppliers and one made by lithium evaporation at ORNL. The surface characterization found that each lithium source has a different surface layer that varies from source to source. The focus this quarter was to develop baseline electrochemical performance comparing multiple lithium sources.

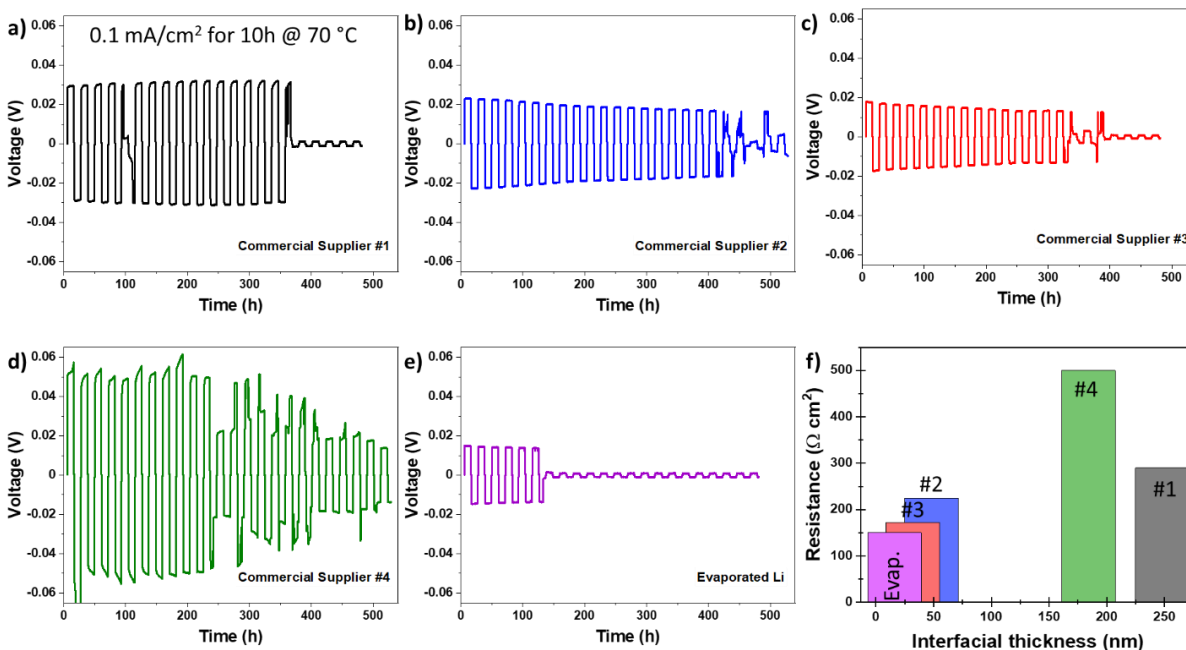


**Figure 73.** Li/PEO-LiTFSI/Li symmetric cycling. All cells were cycled under the same conditions at 0.1 mA/cm<sup>2</sup> for 10 hours at 70°C. (a) Commercial Supplier #1. (b) Commercial Supplier #2. (c) Commercial Supplier #3. (d) Commercial Supplier #4. (e) Evaporated lithium. (f) Plot of the thickness of the estimated interface including the surface layer and distinct Li<sub>2</sub>O layers (excluding the mixed Li<sub>2</sub>O / lithium metal layer) versus the resistance determined from the plating overpotential.

Figure 73 shows symmetric Li/electrolyte/Li cell cycling of the five lithium sources using a standard poly(ethylene oxide) (PEO) – lithium bis(trifluoromethanesulfonyl)imide (LiTFSI) electrolyte tested at 0.1 mA/cm<sup>2</sup> for 10 hours (1 mAh/cm<sup>2</sup>) at 70°C. The polymer electrolyte (PE) membrane was prepared by the solution casting method, where a 5 wt% solution of linear PEO (M.W. 400,000) and LiTFSI salt (3:1 by weight) in acetonitrile was cast into a Teflon dish and ambient dried. The membrane is further heat dried (50-60°C) under vacuum before transferring to a glovebox for coin-cell assembly. The electrolyte used for all tests was made in the same batch. It is difficult to precisely control pressure in a coin-cell format; however, the number of spacers per coin cell was adjusted to keep the total stack thickness roughly constant to account for the variation in thickness of lithium foils from different sources. Each source had different performance in the symmetric cell tests. The first key difference was the overpotential. For the most part, the overpotential directly correlates with the thickness of the interphase as measured by XPS, which can be seen in Figure 73f. The films with the highest resistance were Suppliers #1 & #4, which both had thick distinct Li<sub>2</sub>CO<sub>3</sub> and Li<sub>2</sub>O layers. These were followed by Suppliers #2 & #3, which had silicone-based and organic-based surface layers followed by thin Li<sub>2</sub>O layers. The lowest resistance was for the evaporated lithium metal, which also had the thinnest interphase. The second key difference was in the capacity plated and stripped before failure. The best performance was from Suppliers #2 & #3, which had the organic surface and thin interphase. The quickest sample to fail, though, was the ORNL evaporated lithium, which had the thinnest interphase. This discrepancy cannot be explained simply based on surface chemistry alone. It is possible that the microstructure of the lithium metal itself also plays a key role in dictating the capacity plated before failure. Regardless, in all cases, the cells

failed before reaching 25 cycles or 25 mAh/cm<sup>2</sup> of cumulative capacity plated in each direction. The dramatic difference in overpotential and subsequent failures also emphasizes the effect that lithium source-to-source variation can have on performance, even with nominally the same solid electrolyte (SE).

In addition to developing a baseline with the standard PEO-LiTFSI electrolyte, the team is also developing baselines for argyrodite (Li<sub>6</sub>PS<sub>5</sub>Cl) sulfide SEs (NEI corporation, 3-5 μm particle size) and Li-La-Zr-Ta-O (Toshima LLC). Figure 74 shows initial results from the argyrodite SEs, in collaboration with J. Nanda's team, tested in symmetric Li/argyrodite/Li cells. In this case, the cells used an argyrodite electrolyte powder that was directly compacted in a polyether ether ketone cell along with Li-metal electrodes. For these cells, the argyrodite powder separators were consolidated using pressure alone. The team compared here two different lithium sources, that is, Supplier #3 and the evaporated lithium. The cells were tested at room temperature, at a current density of 0.1 mA/cm<sup>2</sup> for 10 hours (the same as for the PEs) under 5-6 MPa of pressure. Here, one can see that the initial overpotential is virtually the same, which could be due to the high pressures being used. While the 1<sup>st</sup> cycles for both lithium sources are almost the same, from the 2<sup>nd</sup> cycle onward there is a rapid rise in resistance for the evaporated lithium cell that gets worse each cycle. This voltage rise has been identified with voiding during stripping resulting in contact loss. This can be further confirmed as the overpotential during the rest period after cycling returns to 0 V, suggesting that there is still lithium remaining at the surface. Notably, the mechanical nanoindentation data reported last quarter show that the lithium from Supplier #2 had on average a lower hardness at the small length scales compared to the evaporated lithium metal. This is directly related to the ability of lithium to self-diffuse relieving stress. This difference correlates with this rapid rise in voltage for the evaporated Li-metal cells.

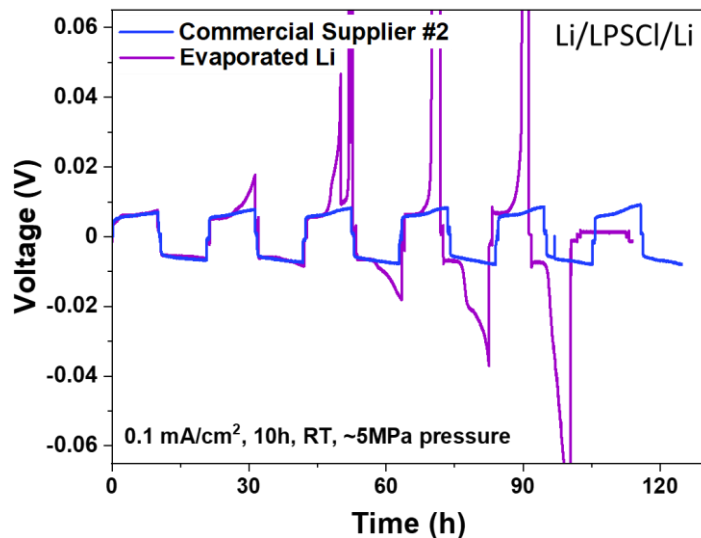


Figure 74. Li/LiPSCI argyrodite (NEI) / lithium test under 5 MPa of pressure at room temperature at a current density of 0.1 mA/cm<sup>2</sup> for 10 hours. Blue: Commercial Supplier #2. Purple: Evaporated lithium.

Based on both the polymer and sulfide argyrodite electrolytes, the team can see that lithium source clearly plays a key role in determining the performance and ultimate failure. The data also suggest that while the overpotential is strongly influenced by the surface layers, the failure may also be significantly impacted by the microstructure or differences in the bulk lithium metal.

## Patents/Publications/Presentations

### Publication

- Tsai, W-Y., X. C. Chen, S. Kalnaus, R. Sahore, Z. Du, and A. S. Westover. “Li Morphology Evolution during Initial Cycles in a Gel Composite Polymer Electrolyte.” *ACS Applied Energy Materials* 5, no. 9 (2022): 11362–11369.

## TASK 2 – ADVANCED DIAGNOSTICS

Team Lead: Guoying Chen, Lawrence Berkeley National Laboratory

### Summary and Highlights

To meet the goals of the Vehicle Technologies Office programs on next-generation electric vehicles, low-cost and abuse-tolerant batteries with higher energy density, higher power density, better safety, and longer lifetimes are needed. In pursuit of these goals, high cell operating voltages and demanding cycling conditions are used, which leads to unprecedented chemical and mechanical instabilities in cell components. Successful implementation of promising electrode materials (such as silicon anode and high-voltage cathodes) and new cell chemistry (such as high-energy Li-metal cells combined with solid-state electrolytes, or SSEs) requires better understanding of fundamental processes, especially those at the interface/interphase of both anode and cathode. Identifying and understanding structure-property-electrochemical performance relationships in materials and various failure modes in cell chemistry are therefore more pressing than ever, not only in guiding battery development activities but also the scale-up efforts needed for commercialization.

Task 2 takes on these challenges by combining model systems, *ex situ*, *in situ*, and *operando* approaches, with an array of state-of-the-art analytical and computational tools. Numerous subtasks are tackling the chemical processes and reactions at the electrode/electrolyte interfaces in Li-metal batteries. Researchers at Lawrence Berkeley National Laboratory (LBNL) use surface- and bulk-sensitive techniques, including Fourier transform infrared (FTIR), attenuated total reflectance – FTIR, near-field infrared and Raman spectroscopy/microscopy, and scanning probe microscopy to characterize changes in materials and the physio-chemical phenomena occurring at the interface of Li-metal electrode. General Motors is developing *in situ* diagnostic techniques, including atomic force microscopy, nano-indentor, dilatometer, and stress-sensor, to be combined with atomic/continuum modeling schemes to investigate the coupled mechanical/chemical degradation of the solid electrolyte interphase (SEI) layer as well as the microstructural evolution at the interface/interphase of Li-metal anode. Argonne National Laboratory aims to develop high-conductivity ceramic electrolytes through cation doping and to identify mechanistic barriers that limit chemical, mechanical, and electrochemical durability of solid/solid interfaces. University of Houston is developing multidimensional diagnostic tools, including focused ion beam – scanning electron microscopy, time-of-flight secondary ion mass spectrometry, and *in situ* scanning electron microscopy nanoindentation, to probe structural, chemical, and mechanical evolution at the interfaces of solid-state lithium batteries. At LBNL, model systems of electrode, SSE, and their interfaces with well-defined physical attributes are being developed and used for advanced diagnostic and mechanistic studies at both bulk and single-particle levels. These controlled studies remove the ambiguity in correlating a material's physical properties and reaction mechanisms to its performance and stability, which is critical for further optimization. Subtasks at Brookhaven National Laboratory (BNL) and Pacific Northwest National Laboratory (PNNL) focus on the understanding of fading mechanisms in electrode materials, with the help of synchrotron-based X-ray techniques (diffraction and hard/soft X-ray absorption) at BNL and high-resolution transmission electron microscopy / scanning transmission electron microscopy and related spectroscopy techniques at PNNL. The final subtask at Stanford / SLAC National Accelerator Laboratory develops and utilizes an integrated X-ray characterization toolkit to investigate and generate insights on solid-state batteries (SSBs), by tracking the evolution of nanoscale chemistry as well as structure, microstructure, and transport properties. The diagnostics team not only produces a wealth of knowledge key to developing next-generation batteries, but they also advance analytical techniques and instrumentation with a far-reaching effect on material and device development in various fields.

## Highlights

The highlights for this quarter are as follows:

- The BNL (X. Yang / E. Hu) team used soft X-ray absorption spectroscopy to reveal the chemical compositions and their spatial distribution in the cathode electrolyte interphase between a sulfurized polyacrylonitrile cathode and the electrolyte. The influence of the electrolyte choice was also demonstrated.
- G. Chen's LBNL group used electrochemical impedance spectroscopy to demonstrate the advantage of using single-crystalline (SC) cathode active particles in SSBs. The superior mechanical properties of the SC particles enables improved  $\text{Li}^+$  ion diffusion pathways on continuous cell cycling.
- The PNNL (C. Wang) group used cryogenic transmission electron microscopy to demonstrate the impact of dissolved transition metals on the chemistry and microstructure of the SEI formed at the Li-metal anode.

## Task 2.1 – Characterization and Modeling of Lithium-Metal Batteries: Model-System Synthesis and Advanced Characterization (Guoying Chen, Lawrence Berkeley National Laboratory)

**Project Objective.** This project will use a rational, non-empirical approach to design and develop solid-state electrolyte (SSE) materials and interfaces for next-generation Li-metal batteries. Combining a suite of advanced diagnostic techniques with carefully prepared model-system samples, the project will perform systematic studies to achieve the following goals: (1) obtain understanding on the role of SSE grain and grain boundaries (GBs) on ion conduction and dendrite formation, (2) obtain fundamental knowledge on rate-limiting and stability-limiting properties and processes in SSEs when used in Li-metal batteries, (3) investigate the reactivities between SSE and electrodes, and gain insights on the dynamic evolution of the interfaces, and (4) design and synthesize improved SSE materials and interfaces for safer and more stable high-energy Li-metal batteries.

**Impact.** The project will focus on fundamental understanding of SSE and relevant interfaces to enable its use in Li-metal batteries. Knowledge gathered from model-system-based studies will guide the design and engineering of advanced materials and interfaces. The use of the non-empirical, rational-design approach will develop high-energy battery systems with improved commercial viability.

**Approach.** The project will combine model-system synthesis and advanced diagnostic studies to investigate ion conduction and interfacial chemistry of SSE in Li-metal batteries. Single crystalline (SC), polycrystalline (PC), and amorphous model SSE samples with various grain and GB properties will be synthesized. Model interfaces between the SSE and electrodes with controlled properties will also be developed. Both bulk-level and single-grain-level characterization will be performed. Global properties and performance of the samples will be established from the bulk analyses, while the single-grain-based studies will utilize time-resolved and spatially-resolved analytical techniques to probe the intrinsic redox transformation processes and failure mechanisms under battery operating conditions.

**Out-Year Goals.** In the out years, the project will deliver fundamental knowledge on the role of SSE microstructure in  $\text{Li}^+$  conduction and lithium dendrite formation/propagation. Insights on performance-limiting physical properties and phase transition mechanisms as well as dynamic evolution of SSE/electrode interfaces will be obtained. Mitigating approaches, such as use of surface coating or a “buffer layer” in stabilizing SSE/electrode interfaces, will be evaluated. Further, advanced SSE materials and interfaces for improved high-energy Li-metal batteries will be designed and synthesized.

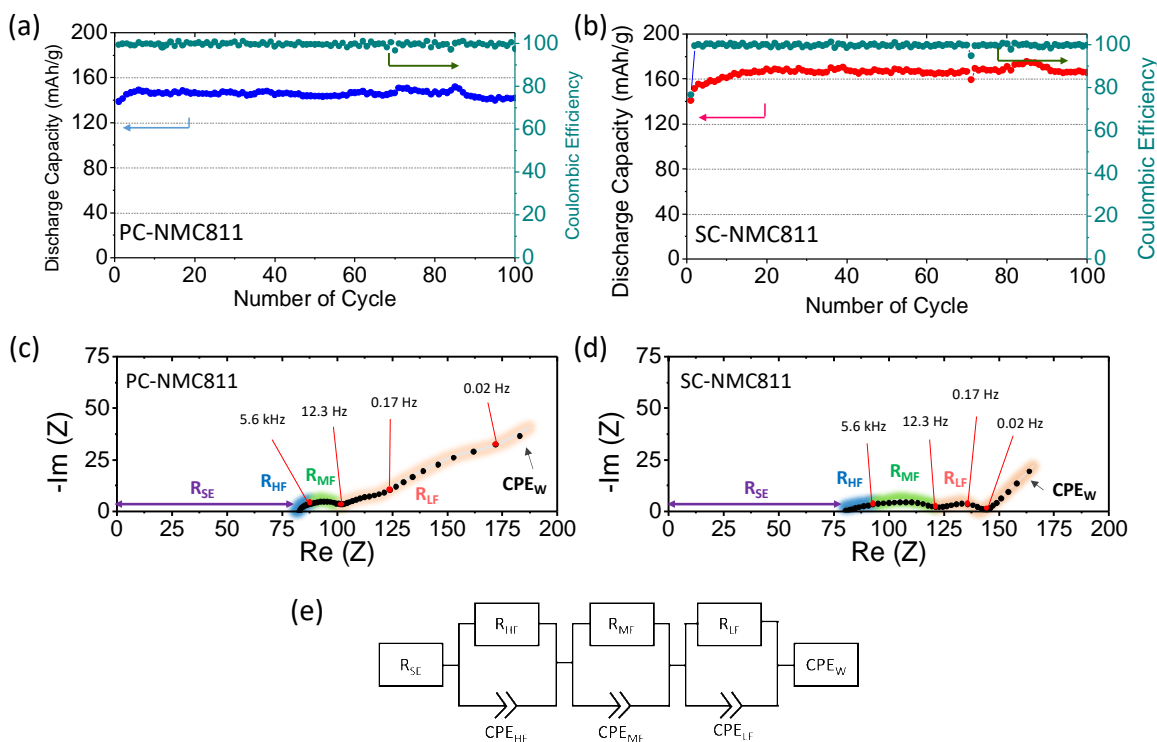
**Collaborations.** This project collaborates with the following principal investigators: G. Ceder, K. Persson, M. M. Doeff, B. McCloskey, R. Kostecki, and R. Prasher (Lawrence Berkeley National Laboratory); W. Yang (Advanced Light Source); D. Nordlund and Y. Liu (Stanford Synchrotron Radiation Lightsource); C. Wang (Pacific Northwest National Laboratory); and J. Nanda (SLAC National Accelerator Laboratory).

### Milestones

1. Develop SSE/cathode model systems for studying the cathode interfaces. (Q1, FY 2022; Completed)
2. Synthesize SSE model samples and model SSE/cathode interfaces. (Q2, FY 2022; Completed)
3. Advanced diagnostic studies of SSE/cathode interfaces. (Q3, FY 2022; Completed)
4. Obtain mechanistic understanding and deliver design strategies to improve SSE/cathode interfaces. (Q4, FY 2022; Completed)

## Progress Report

To obtain mechanistic understanding of the interface between the cathode active material (CAM) and the solid electrolyte (SE), the team employed electrochemical impedance spectroscopy (EIS) to compare the dynamic interfacial evolution during the cycling of PC and SC CAM composite cathodes. The electrodes were prepared by mixing PC- or SC- $\text{LiNi}_{0.8}\text{Mn}_{0.1}\text{Co}_{0.1}\text{O}_2$  (NMC-811) with  $\text{Li}_3\text{YCl}_6$  (LYC) SE and carbon in a weight ratio of 57:40.5:2.5. Figure 75a-b shows the capacity retention and Coulombic efficiency obtained from the PC and SC all-solid-state battery (ASSB) cells cycled at C/2 rate between 3 V and 4.3 V (V versus  $\text{Li}^+/\text{Li}$ ), respectively. While the PC cell delivered an initial discharge capacity of  $\sim 140$  mAh/g and experienced gradual capacity decay in the following cycles (Figure 75a), the SC cell delivered a higher discharge capacity of  $\sim 165$  mAh/g and showed improved capacity retention (Figure 75b).



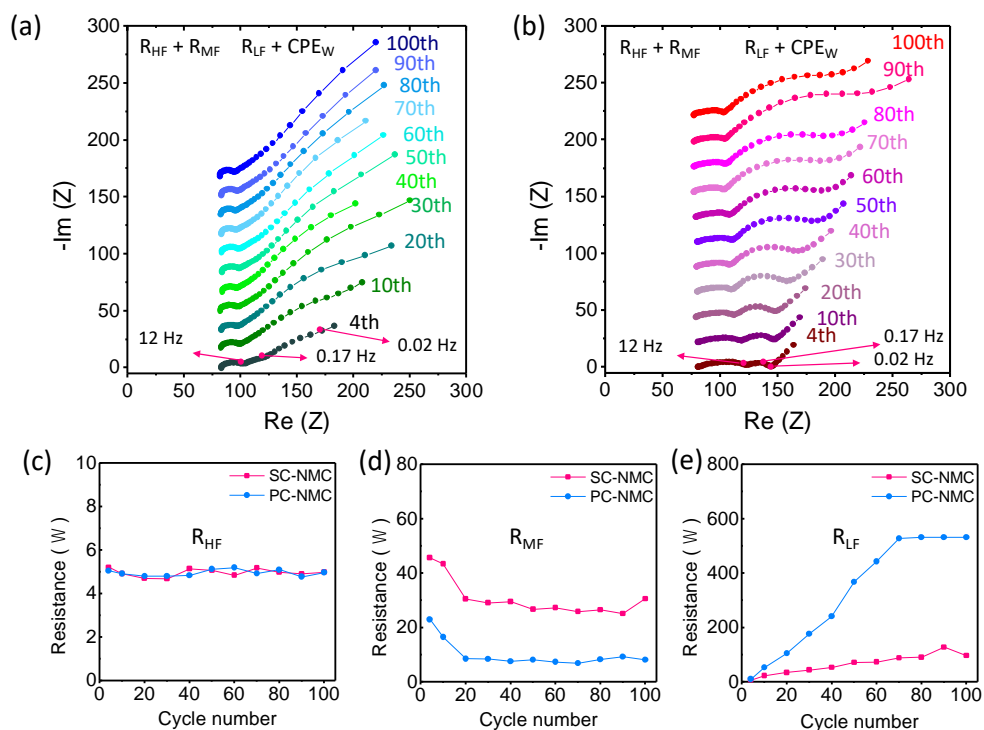
**Figure 75.** Electrochemical performance (a-b) and Nyquist plots (c-d) collected at 3.67 V during the 4<sup>th</sup> discharge of the all-solid-state batteries with polycrystalline – NMC-811 (a/c) and single crystalline – NMC-811 (b/d) cathode active material. (e) Equivalent circuit model for fitting the electrochemical impedance spectroscopy data. The colored lines in (c) and (d) are shown to guide the placement of the various semi-circle components on the Nyquist plots.

Figure 75c-d compares the Nyquist plots obtained at open circuit voltage, after a 2-hour relaxation following the 4<sup>th</sup> discharge of the PC and SC cells to 3.67 V, respectively. The voltage of 3.67 V was chosen due to the known high diffusion coefficient at the corresponding state of charge of NMC-811, allowing better differentiation of impedance components in the ASSB cell. In both cases, the typical semi-circle shape, along with the Warburg element, appears in the examined frequency region (1 MHz - 1 mHz). According to previous reports, the bulk SE resistance from the separator layer ( $R_{SE}$ ) appears at a very high-frequency region of  $> 1$  MHz, while the charge transfer resistance within the GBs of SE evolves in the frequency region of 1 MHz - 1 kHz ( $R_{HF}$ ). The semi-circle that appears in the mid-frequency region of 1 kHz - 10 Hz ( $R_{MF}$ ) can be attributed to the charge transfer resistance at the interface between NMC-811 CAM and LYC SE. In addition, the semi-circle at the low-frequency region of  $< 10$  Hz ( $R_{LF}$ ) can be assigned to the interfacial resistance between the LYC SE layer and the In-Li alloy anode as well as  $\text{Li}^+$  ion diffusion impedance within the CAM. The latter component is also reflected in the subsequent Warburg region ( $CPE_W$ ). The corresponding equivalent circuit is shown in Figure 75e.

Figure 76a-b compares the Nyquist plots of the 4<sup>th</sup> as well as every 10<sup>th</sup> discharge of the PC and SC cells to 3.67 V, respectively. In both cases, the  $R_{SE}$  resistance of the LYC SE separator layer was determined to be  $\sim 80 \Omega$ , corresponding to an electrolyte layer thickness of  $\sim 350 \mu\text{m}$  and an ionic conductivity of  $0.3 \text{ mS}\cdot\text{cm}^{-1}$  in LYC. The  $R_{SE}$  values stay more or less constant throughout cycling. The GB resistance ( $R_{HF}$ ) of the LYC electrolyte evolves similarly in the frequency range of 0.15 MHz to 5.6 kHz. The  $R_{MF}$  component

between 5.6 kHz and 12.3 Hz appears smaller in the PC cell, and the differences are likely a result of initial contact made between the CAM and the SE. While the PC particles are largely spherical and better for making surface contact, the SC particles are irregularly shaped. Furthermore, the measured Brunauer–Emmett–Teller surface areas of the PC – NMC-811 and SC – NMC-811 samples are  $0.64 \text{ m}^2/\text{g}$  and  $0.27 \text{ m}^2/\text{g}$ , respectively, suggesting that more surface contact area is available for the SE connection in the former. Regardless of

the initial  $R_{MF}$  size, both cells showed a gradual reduction over the first 20 cycles, indicating a “break-in” process that establishes effective  $\text{Li}^+$  ion migration pathways between NMC-811 particles and LYC SE. This facilitates  $\text{Li}^+$  ion migration on initial cycling, which is reflected by the small capacity increase in both cells (Figure 75a-b). The  $R_{MF}$  component remained more or less constant in the subsequent cycles. The main differences between the two cells are observed in the  $R_{LF}$  and  $CPE_W$  region below 12 Hz, which includes impedance contribution from the SE and Li-In anode interface (12.3–0.17 Hz) as well as  $\text{Li}^+$  diffusion within the CAM particles ( $< 0.17 \text{ Hz}$ ). As shown in Figure 76a-b, this component in both cells increases with cycling; however, the extent is significantly more severe in the PC cell. Further analysis was carried out by fitting the EIS data using the equivalent circuit shown in Figure 75e; the results are plotted in Figure 76c-e. The initial  $R_{LF}$  values of  $\sim 7\text{--}10 \Omega$  are similar, consistent with the properties of the pristine materials before cell cycling. Cycling leads to a continuous increase in  $R_{LF}$  in both cells. After 100 cycles, a large increase of over  $60\times$  was observed in the PC cell, whereas in the SC cell, a much smaller increase of  $\sim 10\times$  was observed. Although the impedance evolution at the interface between LYC SE and Li-In anode also contributes to the increase in the  $R_{LF}$  component, it is expected that both cells experience similar changes at the anode interface, as the same configuration was used for the study and the depth of discharge was carefully controlled during the experiment.  $\text{Li}^+$  diffusion resistance within NMC-811 CAM particles, therefore, is considered as the main contributor to the observed differences in the  $R_{LF}$  and  $CPE_W$  components. The study demonstrates the unique advantage of using SC particles, which provide improved  $\text{Li}^+$  ion diffusion pathways on continuous cell cycling due to their better mechanical properties.



**Figure 76.** Nyquist plots obtained at 3.67 V during the discharge of polycrystalline – NMC-811 (a) and single crystalline – NMC-811 (b) all-solid-state battery cells at the indicated cycle numbers. (c-e) Resistance values obtained from fitting the corresponding Nyquist plots in (a) and (b).

## Patents/Publications/Presentations

The project has no patents, publications, or presentations to report this quarter.

## Task 2.2 – Interfacial Processes – Diagnostics (Robert Kostecki, Lawrence Berkeley National Laboratory)

**Project Objective.** The project objective is to establish specific design rules toward the next generation of low-impedance Li-metal rechargeable batteries that are capable of performing 1000 deep discharge cycles at Coulombic efficiency > 99.9% and suppressing lithium dendrite formation at high current densities (> 2 mA/cm<sup>2</sup>). This project aims at the following: (1) establishing general rules between Li<sup>+</sup> transport properties in novel liquid/solid electrolytes, and (2) determining the mechanism of the solid electrolyte interphase (SEI) layer (re)formation. The other goal is development and application of far- and near-field optical probes and synchrotron-based advanced X-ray techniques to obtain insight into the mechanism of Li<sup>+</sup> transport and interfacial reactions in lithium/liquid model systems. Through an integrated synthesis, characterization, and electrochemistry effort, this project aims to develop a better understanding of lithium / liquid electrolyte (LE) interface so that rational decisions can be made as to their further development into commercially viable Li-metal cells.

**Project Impact.** Chemical instability and high impedance at the interface of Li-metal electrodes limit electrochemical performance of high-energy-density batteries. A better understanding of the underlying principles that govern these phenomena is inextricably linked with successful implementation of high-energy-density materials in Li-metal-based cells for plug-in hybrid electric vehicles (PHEVs) and electric vehicles (EVs). New state-of-the-art techniques to identify, characterize, and monitor changes in materials structure and composition that take place during battery operation and/or storage will be developed and made available to BMR participants. The work constitutes an integral part of the concerted effort within the BMR Program, and it supports development of new electrode materials for high-energy, Li-metal-based rechargeable cells.

**Approach.** Pristine and cycled composite electrode and model thin-film electrodes will be probed using various surface- and bulk-sensitive techniques, including Fourier transform infrared (FTIR), attenuated total reflectance (ATR) – FTIR, near-field infrared and Raman spectroscopy/microscopy, and scanning probe microscopy to identify and characterize changes in materials structure and composition. Novel *in situ* / *ex situ* far- and near-field optical multifunctional probes in combination with standard electrochemical and analytical techniques are developed to unveil the structure and reactivity at interfaces and interphases that determine electrochemical performance and failure modes of materials.

**Out-Year Goals.** In the out-years, the project aims to achieve the following: (1) understand factors that control performance and degradation processes, (2) unveil structure and reactivity at hidden or buried interfaces and interphases that determine electrochemical performance and failure modes, and (3) propose effective remedies to address inadequate Li-metal-based battery calendar/cycle lifetimes for PHEV and EV applications.

**Collaborations.** Diagnostic studies will be carried out in sync with other diagnosticians (that is, G. Chen, B. McCloskey, R. Prasher, and L-W. Wang) and theory/computational scientists (that is, G. Ceder and K. Persson).

### Milestones

1. Fundamental physicochemical and electrochemical characterization of the considered primary and secondary Li-metal cell chemistries. (Q1, FY 2022; Completed)
2. *In situ* Fourier transform infrared nano-spectroscopy (nano-FTIR) experimental setup for probing Li/LE interface designed, built, and tested. Preliminary tests and results delivered. (Q2, FY 2022; Completed)

- Near- and far-field optical and X-ray photoelectron spectroscopy characterization of the baseline Li-metal cell chemistries and relevant interfacial phenomena and processes completed. (Q3, FY 2022; Completed)
- Correlation of electrolyte chemistry and Li/SEI compositional structure in Li-metal baseline LE and solid electrolyte systems determined. (Q4, FY 2022; Completed)

## Progress Report

This quarter, the team focused research efforts on understanding the evolution of the SEI layer on lithium surfaces during the 1<sup>st</sup> electrochemical oxidation-reduction cycle (formation cycle). They prepared Li-metal electrodes in a solvent-free glovebox and exposed their surfaces to pure liquid GEN 2 electrolyte (ethylene carbonate / ethyl methyl carbonate 1.2 M LiPF<sub>6</sub>). In this way, they created an artificial SEI without introducing any unwanted components (for example, those that may form on a thermodynamically spontaneous reaction between solvent vapor and a clean lithium surface). This approach ensures minimal contamination of the

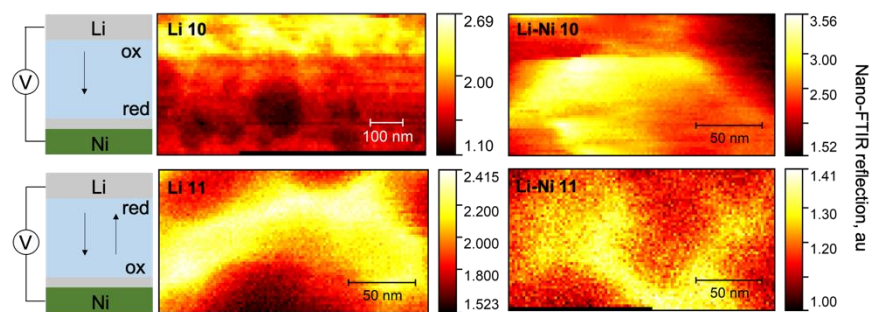


**Figure 77.** Nanoscale “white light” imaging of SEI layer on Li-metal surface under various electrochemical conditions: (top left) Li-metal electrode after oxidation under galvanostatic conditions. (top right) Nickel electrode after plating lithium under galvanostatic conditions. (bottom left) Li-metal electrode after an oxidation-reduction cycle under galvanostatic conditions. (bottom right) Nickel electrode after a cycle of plating and stripping of lithium.

were dried under vacuum for ~ 1 hour to allow residual electrolyte to vaporize. In another cell, after the lithium plating step, the polarity of the cell was reversed, and lithium was stripped via similar but inverted protocols, leaving a reduced Li-metal counter electrode (referred to as “Li 11” in the Figures) and nickel working electrode with electrically disconnected (or “dead”) lithium on the surface. These *ex situ* electrodes were analyzed by infrared near-field imaging and nano-FTIR.

Figure 77 shows “white light” (WL) imaging of the electrodes’ surfaces, showing a heterogenous distribution of infrared (IR) reflection at the nanoscale. Since IR reflectivity can be correlated with the electronic conductivity of a material, Figure 77 likely shows the local distribution of SEI components with various electronic densities. Notably, Li 11 and Li-Ni 11 electrodes exhibit a similar pattern, with ~ 50 nm domains.

Figure 78 shows nano-FTIR spectra collected from the electrodes compared to the ATR-FTIR spectrum of dried electrolyte to reveal spectroscopic features of

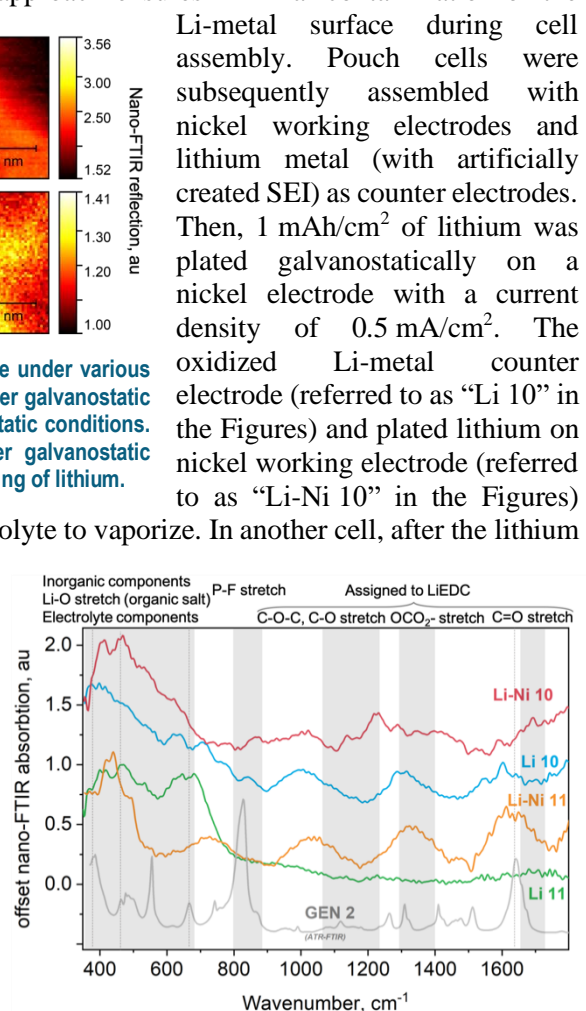


**Figure 78.** Nano - Fourier transform infrared (FTIR) spectroscopy of SEI layer under various electrochemical conditions. Plated lithium on nickel (red trace), oxidized lithium surface (blue trace), plated and stripped lithium “dead lithium” (orange trace), and reduced lithium surface after oxidation cycle (green trace). Attenuated total reflectance FTIR spectrum of dried GEN 2 electrolyte (gray trace).

SEI components in each electrode. The data were collected at the Lawrence Berkeley National Laboratory Advanced Light Source, Beamline 2.4 (capable of Synchrotron-based nano-FTIR and near-field imaging), which allows using a bright and broadband IR light source and a detector that allows probing vibrations at lower cutoff frequency  $\sim 350\text{ cm}^{-1}$ ; this in turn opens an opportunity to probe inorganic SEI components. Figure 78 shows that the majority of the spectral features are located in the region below  $800\text{ cm}^{-1}$ . Oxidized electrodes, namely Li 10 and Li-Ni 11 show broad features above  $1000\text{ cm}^{-1}$ , which can be attributed to the organic electrolyte components as well as organic lithium salts that are known to be present in the SEI layer. A feature at  $400\text{--}450\text{ cm}^{-1}$  is present only on the working electrode, while a broad peak at  $600\text{--}650\text{ cm}^{-1}$  is found in both Li-metal electrodes and could be attributed to LiF. Notably, the reduced Li-metal electrode surface contains no significant peaks above  $1000\text{ cm}^{-1}$ , indicating the minimal presence of organic components on the SEI.

The team has also progressed toward the characterization of relevant interfaces and interphases, and the unveiling of key structures, chemistries, and mechanisms that originate therein, by proposing an *in situ* electrochemical cell. They find motivation from their recently published work<sup>[1]</sup> to develop a new *in situ* cell (Figure 79a) that is compatible with non-polymer solid-state electrolytes (SSEs). While this device form should accommodate numerous SSE chemistries, the team's first intended target will be lithium aluminum germanium phosphate (LAGP). With that in mind, before cell fabrication, they collected atomic force microscopy data (Figure 79b), infrared WL images, and spatially dependent nano-FTIR (Figure 79c) data on an LAGP sample. Their initial exploratory data indicate that chemical heterogeneities exist on a spatial scale that can only be spectroscopically resolved with novel near-field techniques capable of sub-diffraction-limit characterization ( $\approx 3$  micron spacing); this is similar to their recent work.<sup>[1]</sup> These results complete progress toward this quarter's milestone and support continuation of this research trajectory, as mitigating such intrinsic heterogeneities and corresponding deleterious effects will be crucial for advanced energy storage schemes; likewise, understanding such heterogeneities, and related phenomena, is a necessary first step toward this end.

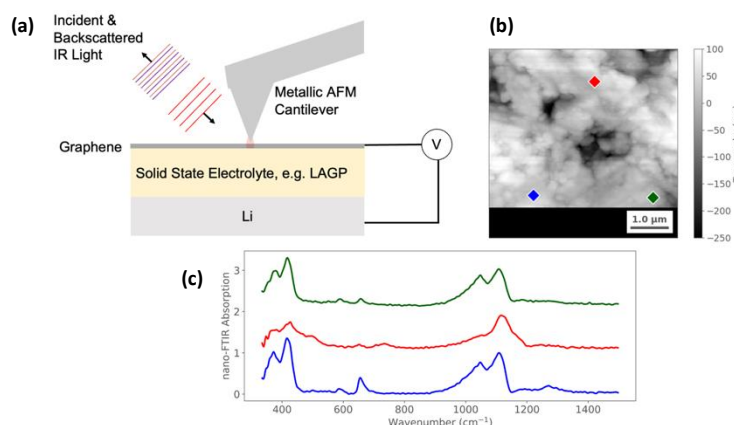


**Figure 79.** (a) Schematic of conceptualized *in situ* solid-state electrochemical cell to be prepared. (b) Atomic force microscopy topography data of a pristine LAGP surface. Colored diamonds indicate locations where nano – Fourier transform infrared (nano-FTIR) data were collected. (c) Spatially dependent nano-FTIR absorption data that show sub-diffraction-limit chemical heterogeneity across the LAGP surface; traces are color matched to the corresponding spatial locations shown in (b).

## Reference

- [1] He, X., J. M. Larson, H. A. Bechtel, and R. Kostecki. “*In Situ* Infrared Nanospectroscopy of the Local Processes at the Li/Polymer Electrolyte Interface.” *Nature Communications* 13, no. 1 (2022): 1–10.

## Patents/Publications/Presentations

The project has no patents, publications, or presentations to report this quarter.

## Task 2.3 – Advanced *In Situ* Diagnostic Techniques for Battery Materials (Xiao-Qing Yang and Enyuan Hu, Brookhaven National Laboratory)

**Project Objective.** The primary objective of this project is to develop new advanced *in situ* material characterization techniques and to apply these techniques to support development of new cathode and anode materials with high energy and power density, low cost, good abuse tolerance, and long calendar and cycle life for beyond Li-ion battery systems to power plug-in hybrid electric vehicles (PHEVs) and battery electric vehicles. The diagnostic studies will focus on issues relating to capacity retention, thermal stability, cycle life, and rate capability of beyond Li-ion battery systems.

**Project Impact.** The Vehicle Technologies Office Multi-Year Program Plan describes the goals for battery: “Specifically, lower-cost, abuse-tolerant batteries with higher energy density, higher power, better low-temperature operation, and longer lifetimes are needed for development of the next-generation of HEVs [hybrid electric vehicles], PHEVs, and EVs [electric vehicles].” The results of this project will be used for development of technologies that will significantly increase energy density and cycle life and will reduce cost. This will greatly accelerate deployment of EVs and reduce carbon emission associated with fossil fuel consumption.

**Approach.** This project will use a combination of synchrotron X-ray diffraction and pair distribution function and of neutron diffraction and pair distribution function; X-ray spectroscopies including hard/soft X-ray absorption spectroscopy (XAS), X-ray photon emission spectroscopy; and imaging techniques including X-ray fluorescence microscopy, transmission X-ray microscopy (TXM), and transmission electron microscopy.

**Out-Year Goals.** The out-year goals are to develop spectro-tomography, X-ray diffraction (XRD), XAS, and pair distribution function (PDF) techniques, and to apply these techniques on Li-ion battery cathode, Na-ion battery cathode, and solid-state electrolyte (SSE).

**Collaborations.** The Brookhaven National Laboratory team will work closely with material synthesis groups at Argonne National Laboratory (Y. Shin and K. Amine) for the high-energy composite, at Pacific Northwest National Laboratory for the S-based cathode and Li-metal anode materials, and with Oak Ridge National Laboratory on neutron scatterings. This project will also collaborate with industrial partners, as well as with international collaborators.

### Milestones

1. Complete XRD and X-ray PDF studies on SSE  $\text{Li}_7\text{P}_2\text{S}_8\text{I}_{0.5}\text{Br}_{0.5}$  to understand its degradation mechanism at high voltage. (Q1, FY 2022; Completed)
2. Complete cryogenic electron microscopy study to understand the positive role of  $\text{LiNO}_3$  additive in solid electrolyte interphase formation on Li-metal anode. (Q2, FY 2022; Completed)
3. Complete many-particle TXM studies on  $\text{LiNi}_{0.8}\text{Mn}_{0.1}\text{Co}_{0.1}\text{O}_2$  cathode to understand its chemical and morphological heterogeneities at the electrode level. (Q3, FY 2022; Completed)
4. Complete *ex situ* XAS and TXM studies on polymeric sulfur cathode to understand its redox mechanism and morphological evolutions during cycling. (Q4, FY 2022; Completed)

## Progress Report

This quarter, *ex situ* soft X-ray absorption spectroscopy (sXAS) studies have been completed for polymeric sulfur (sulfurized polyacrylonitrile, or SPAN) cathode to understand how electrolytes influence the cathode electrolyte interphase (CEI). The work is done in collaboration with University of California, San Diego. Three types of electrolytes were used: (1) localized high concentration electrolyte (LHCE): 1.8 M LiFSI in DEE/BTFE [DEE: diethyl ether; BTFE: bis(2,2,2-trifluoroethyl)ether; weight ratio 1:4], (2) carbonate electrolyte: 1 M LiPF<sub>6</sub> in EC/EMC (EC: ethylene carbonate; EMC: ethyl methyl carbonate; volume ratio 3:7), and (3) ether electrolyte: 1 M LiTFSI in DOL/DME (DOL: 1,3-dioxolane; DME: dimethoxyethane; volume ratio 1:1). The data were collected in both total electron yield (TEY) mode and partial fluorescence yield (PFY) mode, which have a probing depth of 2~5 nm and > 10 nm, respectively.

The carbon K-edge sXAS results are shown in Figure 80. In the pristine sample, the peaks at ~ 285.5 eV and ~ 288.5 eV arise from different antibonding orbitals associated with the C=C bond in the SPAN pyridine rings. Other peaks corresponding to various functional groups in SPAN are indicated in Figure 80. On cycling, new peaks arise and evolve, and their ways of evolution are highly dependent on the electrolyte used. Comparing the TEY data among different electrolytes, it is obvious that carbonate electrolyte leads to Li<sub>2</sub>CO<sub>3</sub> formation in the CEI, as indicated by the peak located at ~ 290.5 eV. Ether electrolyte generates semi-carbonates in the CEI, as the corresponding peak is slightly lower in energy. This is probably due to the ring-opening and polymerization of DOL solvents. In contrast, LHCE does not generate any carbonate in the CEI. Instead, it may generate some esters, as indicated by the growth of the peak at 288.6 eV. In all the electrolytes used, there are vinyl-group-containing species formed in the CEI, as indicated by the peak at ~ 285.2 eV and close to the pyridinic  $1\pi_{C=C}^*$  peak. Comparing among different cycles, LHCE forms a stable CEI even in the formation cycle, as the spectra show little change from 1<sup>st</sup> cycle to the 50<sup>th</sup> cycle. However, both carbonate and ether electrolytes cannot form a stable CEI, and the spectra keep evolving during cycling.

The PFY results are different from that of the TEY results, suggesting that CEI chemical compositions have depth-dependence. For example, the carbonate (either Li<sub>2</sub>CO<sub>3</sub> or semi-carbonate) and ester peaks are much weaker in PFY than in TEY, indicating that these species are more likely on the top layer of CEI and on the side close to the electrolytes. Interestingly, PFY have peaks at ~ 284.1 eV that are absent in the TEY data. These low energy peaks typically arise from multi-ring molecules such as fused benzene/pyridine rings or their various derivatives with nitrogen substitution. Considering their close relationship to the SPAN structure, which is built on the network of pyridines, it is likely that these multi-ring molecules are the decomposition product of SPAN and lie in the bottom of CEI and on the side close to SPAN electrode.

This study reveals the chemical composition and spatial distribution of SPAN CEI and how these are influenced by the electrolyte used.

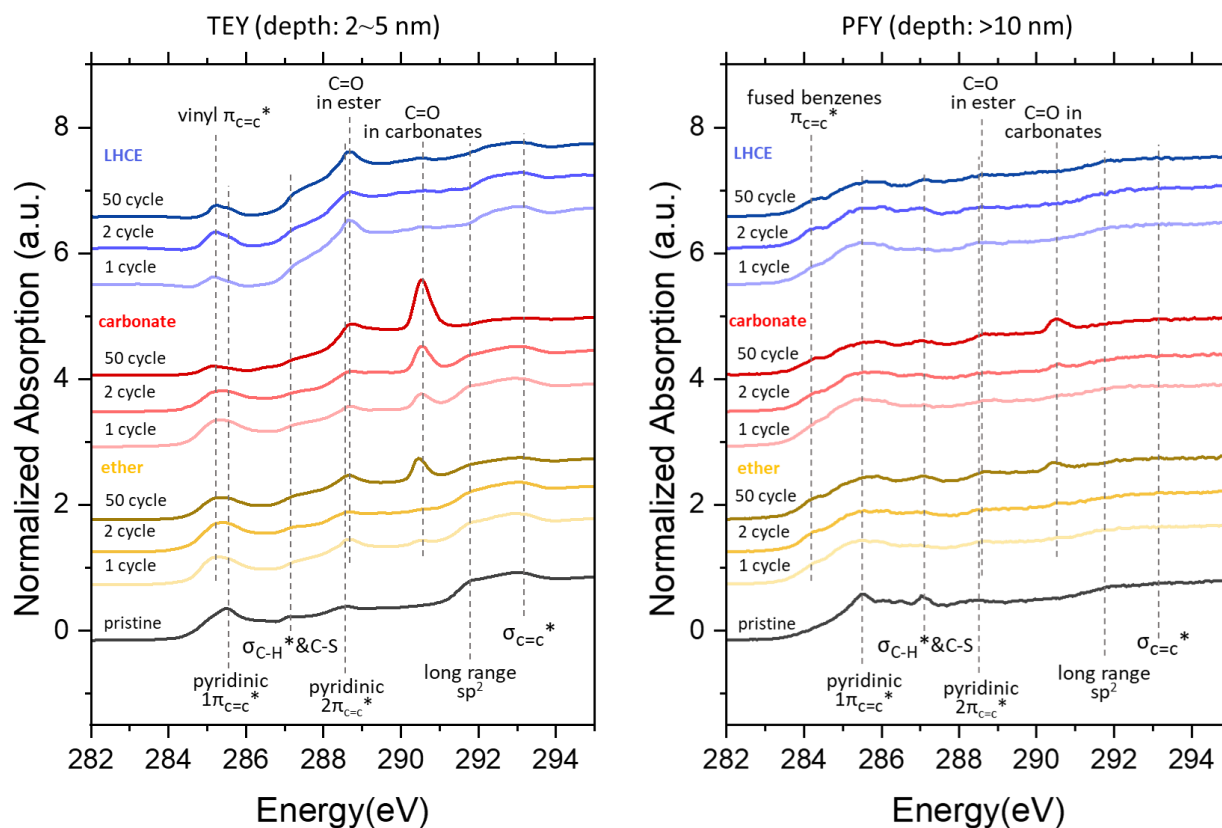


Figure 80. Carbon K-edge X-ray absorption spectroscopy both in total electron yield (TEY, left panel) and partial fluorescence yield (PFY, right panel) of *ex situ* SPAN electrodes cycled in various electrolytes.

### Patents/Publications/Presentations

The project has no patents, publications, or presentations to report this quarter.

## Task 2.4 – Probing Interfacial Processes Controlled Electrode Stability in Rechargeable Batteries (Chongmin Wang, Pacific Northwest National Laboratory)

**Project Objective.** The main objective is to explore interfacial phenomena in rechargeable Li-ion batteries of both solid-state electrolyte (SSE) and liquid electrolyte (LE) configuration to identify the critical parameters that control the stability of interface and electrodes as well as solid electrolyte (SE). The outcome will be establishing correlations between structural-chemical evolution of active components of batteries and their properties. These correlations will provide insight and guidance to battery materials development groups for developing high-performance battery materials.

**Project Impact.** The proposed characterization work focuses on atomic-level structural and chemical analysis and direct correlation with battery fading properties. The work can be directly used to guide design of electrode materials with tailored microstructure and chemistry for enhanced properties of increasing the energy density of Li-ion batteries and to accelerate market acceptance of electric vehicles (EVs), especially for plug-in hybrid electric vehicles as required by the EV Everywhere Grand Challenge.

**Approach.** The project will use integrated advanced microscopic and spectroscopic techniques, including *in situ* and *ex situ* scanning transmission electron microscopy (STEM), environmental STEM, cryogenic electron microscopy, and *in situ* liquid secondary ion mass spectrometry, in collaboration with theoretical modeling, to directly probe the structural and chemical information of active materials in rechargeable batteries. Cryogenic STEM (cryo-STEM) with analytical tools, such as energy dispersive X-ray spectroscopy (EDS) and electron energy loss spectroscopy (EELS), will be used to gain chemical and electronic structural information at the interface between lithium metal and electrolyte of both solid-state and liquid configuration, which will allow direct correlation between the morphology and chemistry. STEM – high-angle annular dark-field atomic-level imaging and EDS/EELS will be used to probe the interface and bulk lattice stability of cathode and SE in solid-state batteries. The work will be in close collaboration with the battery development group within the BMR and U. S. – Germany Collaboration on Energy Storage.

**Out-Year-Goals.** This project has the following out-year goals:

- Atomic-level multiscale *ex situ* / *in situ* and *operando* STEM and cryo-STEM investigation on the fading mechanisms of energy-storage materials and devices in the system of both LE and SE; gain a fundamental understanding of electronic and ionic transport characteristics and kinetics in energy-storage system.
- Develop new *in situ* and *ex situ* STEM capability for probing challenging questions related to energy storage technology for both SSE and LE energy storage systems.

**Collaborations.** This project collaborates with G. Chen (Lawrence Berkeley National Laboratory, LBNL); J. Nanda (SLAC National Accelerator Laboratory); Y. Yao (University of Houston); K. Amine (Argonne National Laboratory); D. Wang (Pennsylvania State University); A. Manthiram (University of Texas, Austin); W. Tong (LBNL); Y. Cui (Stanford University); J. Zhang, J. Liu, P. M. L. Le, W. Xu, X. Jie, and D. Lu (Pacific Northwest National Laboratory); X. Xiao (General Motors); and M. S. Whittingham (State University of New York, Binghamton).

### Milestones

1. Measure electronic properties of solid electrolyte interphase (SEI) layer and electrical double layers, identifying their effects on electrochemical properties. (Q1, FY 2022; Completed)
2. Identify correlation between electrical properties of SEI layer and lithium structural features, such as how mossy lithium and crystalline lithium form. (Q2, FY 2022; Completed)

3. Reveal the nature of reaction product between cathode and S-based SE. (Q3, FY 2022; Completed)
4. Identify the effect of transition metal (TM) dissolution on SEI growth in Li-metal battery. (Q4, FY 2022; Completed)

## Progress Report

The formation and continuous growth of SEI consume active lithium ions, becoming the main cause of the irreversible capacity loss in the initial and following cycles. TM (for example, nickel) ions dissolved from layered-structured Ni-rich cathodes can migrate to the anode side and accelerate the failure of Li-ion batteries. Incorporation of the TM ions into the SEI on graphite anode has been considered as a primary failure mechanism of Li-ion batteries for using carbonaceous anodes. Despite significant progress on the understanding of the effects of dissolved TM ions on the performance of graphite anode, the impact of TM ions on the SEI layer formed on Li-metal anode is rarely investigated. It has been noticed that a Ni-rich cathode paired with a Li-metal anode fades faster than the same cathode paired with a graphite anode, indicating a dramatic difference in SEI behavior on graphite and Li-metal anode. This work will investigate the effect of TM ions on the SEI layer formed on Li-metal anode, intending to gain crucial insight on the failure mechanism of Li-metal batteries.

The team uses cryogenic transmission electron microscopy (cryo-TEM) to study how nickel impurities in electrolytes from cathode dissolution change the SEI on Li-metal anodes. They designed two cell systems: Li||Cu with localized high concentration electrolyte (LHCE) with and without 400 ppm nickel, and Cu||LiNi<sub>0.8</sub>Mn<sub>0.1</sub>Co<sub>0.1</sub>O<sub>2</sub> (NMC-811 secondary particle) with LHCE with and without 400 ppm nickel. The LHCE is composed of lithium bis(fluorosulfonyl)imide (LiFSI), 1,2-dimethoxyethane (DME), and 1,1,2,2-tetrafluoroethyl-2,2,3,3-tetrafluoropropyl ether (TTE) as the diluent at a molar ratio of 1:1.2:3, to yield LiFSI-1.2DME-3TTE (in molar ratio).

Figure 81 shows the TEM, STEM, and selected area electron diffraction (SAED) images of deposited lithium with different electrolytes using a coin cell. The deposited lithium is featured with particle morphology, while with few whiskers (Figure 81, first column). The SEI layer formed in Cu||NMC coin cell is thicker than that in Li||Cu coin cell. It is apparent that the SEI layer formed in electrolyte with nickel is thicker than that in electrolyte without nickel. This result clearly indicates that the dissolution of TMs in NMC cathode strongly affects the SEI formation and growth on Li-metal anode. The SAED patterns (Figure 81, third column) of the deposited lithium indicate that the deposited lithium are all crystalline lithium metal. The atomic resolution TEM images (Figure 81, fourth column) and corresponding fast Fourier transform patterns (Figure 81, inset of fourth column) reveal the microstructure of SEI layers formed on the deposited lithium, indicating that the SEI layer is an amorphous matrix with Li<sub>2</sub>O nano crystals embedded. The addition of nickel to electrolyte appears to lead to an increase of the concentration of Li<sub>2</sub>O nano crystals in SEI layers.

The team further investigated the chemical composition of SEI layers by EELS, revealing the elemental distribution at high spatial resolution. Figure 82 illustrates the EELS elemental maps, showing the spatial distribution of elements in SEI layers on the lithium particles formed in four electrolytes. Based on elemental maps, all SEI layers are mainly composed of lithium, oxygen, and sulfur, with dilute concentration of carbon, nitrogen, and fluorine. In addition, as shown in lithium elemental maps, the outer layer is enriched with lithium, while the inner layer is lean in lithium.

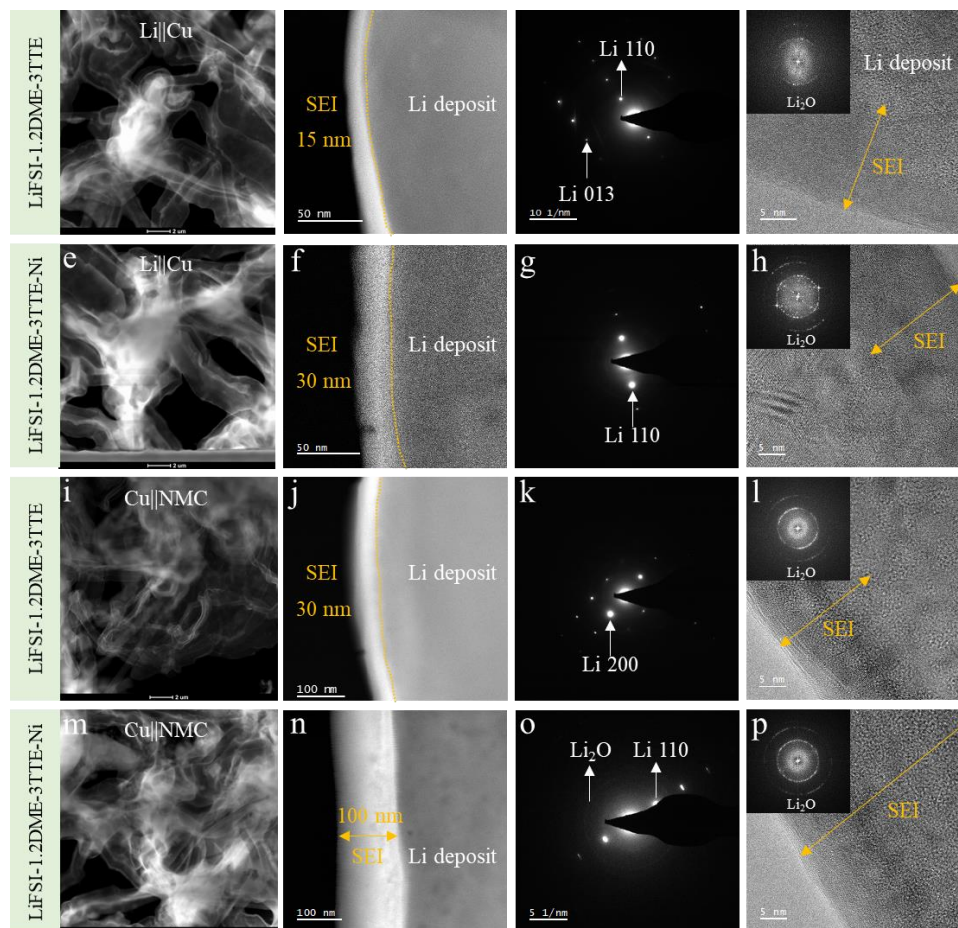


**Figure 81. Transmission electron microscopy and scanning transmission electron microscopy images of deposited lithium from Li||Cu and Cu||NMC coin cells in the localized high-concentration electrolyte (LHCE) without and with nickel impurities. (a-d) Morphology and microstructure of deposited lithium and SEI from Li||Cu in the LHCE without nickel. (e-h) Morphology and microstructure of deposited lithium and SEI from Li||Cu in the LHCE with nickel. (i-l) Morphology and microstructure of deposited lithium and SEI from Cu||NMC in the LHCE without nickel. (m-p) Morphology and microstructure of deposited lithium and SEI from Cu||NMC in the LHCE with nickel.**

The spatial distribution of oxygen, sulfur, and carbon across the SEI layer appears to be affected by the nickel in the SEI layer. In the Li||Cu coin cell with LHCE without nickel, oxygen is uniformly distributed across the SEI, while sulfur is concentrated in the outer layer. With the addition of nickel in the LHCE, the sulfur and carbon appear to be concentrated in the outer SEI layer. For the Cu||NMC coin cells, SEI formed in LHCE without nickel shows high content of carbon and sulfur in the outer SEI layer. However, SEI formed in LHCE with nickel has less carbon and sulfur. Most importantly, the team cannot detect nickel clusters across the SEI layers, which is contrasted with the case of the SEI layer formed on graphite anode, where the TMs could incorporate into the SEI during the initial cycles. Dissolution of TMs aggravates significantly on cycling. It is generally speculated that the capacity fade associated with TM dissolution from NMC cathode is likely caused by the disruption of electronic property of the SEI.

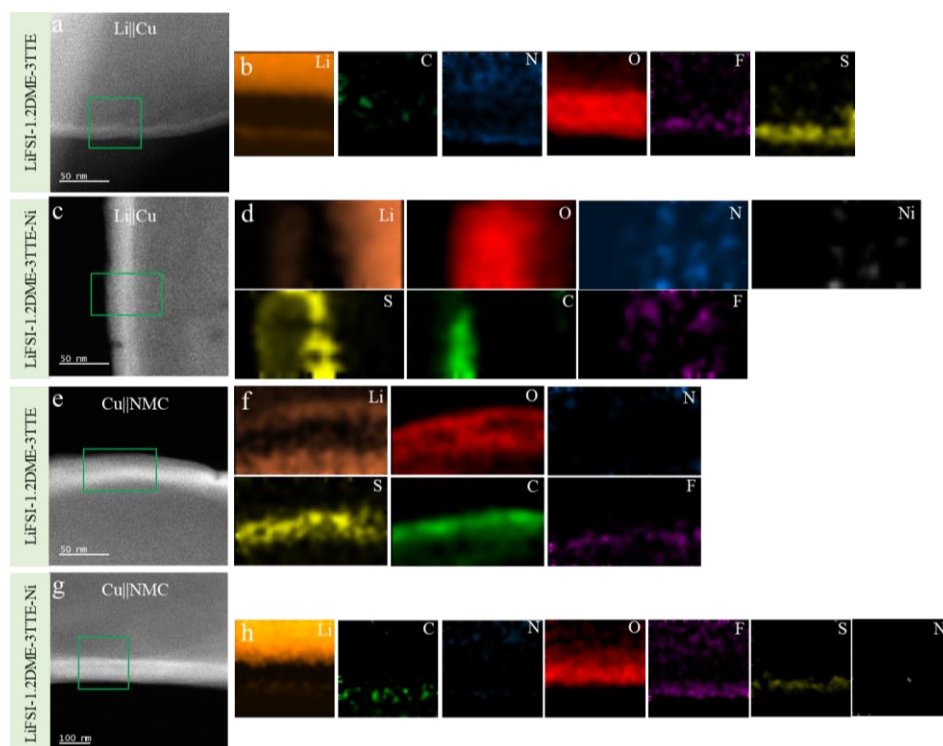


**Figure 82.** Elemental composition of lithium deposits and their SEIs formed in different electrolyte in a coin cell. (a) Cryogenic scanning transmission electron microscopy – high-angle annular dark-field (cryo-STEM-HAADF) image reveals the SEI layer on the lithium particle formed in Li||Cu coin cell using localized high-concentration electrolyte (LHCE) without nickel. (b) Corresponding electron energy loss spectroscopy (EELS) elemental maps show the elemental distribution of SEI. (c) Cryo-STEM-HAADF image reveals the SEI layer on the lithium particle formed in Li||Cu coin cell using LHCE with nickel. (d) Corresponding EELS elemental maps show the elemental distribution of SEI. (e) Cryo-STEM-HAADF image reveals the SEI layer on the lithium particle formed in Cu||NMC coin cell using LHCE without nickel. (f) Corresponding EELS elemental maps show the elemental distribution of SEI. (g) Cryo-STEM-HAADF image reveals the SEI layer on the lithium particle formed in Cu||NMC coin cell using LHCE with nickel. (h) Corresponding EELS elemental maps show the elemental distribution of SEI.

In summary, the team reveals the effect of dissolved nickel on the SEI formation process on Li-metal anode by cryo-TEM. They found that the impacts of dissolved TMs on the SEI on graphite and Li-metal anode differ. A trace concentration of nickel impurities in the electrolyte could not only affect SEI microstructure, but also modify the SEI chemistry, accelerating electrolyte reduction in the Li||Cu coin cell, which is further manifested in the Cu||NMC coin cell. The absence of nickel clusters in the SEI layer indicates the dissolved TMs will not reduce into metallic state and subsequently incorporate into the SEI layer. The team postulates that the mechanism of TMs on SEI layer formation appears to be associated with a catalytic effect. The result provides new insights on the effect of dissolved TMs on the SEI layer on Li-metal anode.

## Patents/Publications/Presentations

### Publications

- Li, Q. Y., R. Yi, Y. B. Xu, X. Cao, C. M. Wang, W. Xu, and J-G. Zhang. “Failure Analysis and Design Principles of Silicon-Based Lithium-Ion Batteries Using Micron-Sized Porous Silicon/Carbon Composite.” *Journal of Power Sources* 548 (2022): 232063.
- Kim, J-M., M. H. Engelhard, B. Y. Lu, Y. B. Xu, S. Tan, B. E. Matthews, S. Tripathi, X. Cao, C. J. Niu, E. Y. Hu, S-M. Bak, C. M. Wang, Y. S. Meng, J-G. Zhang, and W. Xu. “High Current-Density-Charging Lithium Metal Batteries Enabled by Double-Layer Protected Lithium Metal Anode.” *Advanced Functional Materials* (2022): 2207172. <https://doi.org/10.1002/adfm.202207172>.

### Presentation

- 2022 Molecular Foundry User Meeting, LBNL, Berkeley, California: “Dynamic Observation of Lithium Transport in Solid-State Electrolyte Using In-Situ TEM”; Y. B. Xu.

## Task 2.5 – Integrated Atomic-, Meso-, and Micro-Scale Diagnostics of Solid-State Batteries (Yi Cui, William Chueh, and Michael Toney; Stanford University / SLAC National Accelerator Laboratory)

**Project Objective.** By developing a characterization toolkit that tackles length scales (Å to mm), cell pressure (1-100 bars), and dynamics (during synthesis, fabrication, and cycling), the project aims to generate insights to engineer solid-state batteries (SSBs) for deployment in electric vehicles. This interdisciplinary team aims to achieve this objective by merging a broad range of characterization approaches as well as modeling to track the evolution of nanoscale chemistry and structure, microstructure, and transport.

**Project Impact.** The project will have an impact in several areas: (1) accelerate rational design of coatings and artificial solid electrolyte interphases (SEIs) in SSBs; (2) inhibit the root causes leading to cell shorting, and enable high current cycling; (3) accelerate design of cathode coating and composite electrode architectures; and (4) reduce degradation and variability during SSB manufacturing via composition and surface engineering.

**Approach.** The project has a multifold approach that will encompass the following: (1) resolve nanoscale structure and chemistry of SEIs via cryogenic transmission electron spectroscopy (cryo-TEM); (2) track solid electrolyte (SE) and lithium microstructure evolution in three dimensions via X-ray micro and diffraction tomography; (3) visualize nanoscale ionic and electronic transport at grain boundaries via conducting atomic force microscopy; (4) map current distribution in cathodes via scanning transmission X-ray microscopy; and (5) monitor nanoscale SE evolution with gas impurity via *in situ* environmental TEM.

**Out-Year Goals.** The project will develop an integrated characterization toolkit to characterize SSBs within a single cycle and over hundreds of cycles, spanning a wide range of relevant length scales.

**Collaborations.** Project collaborations include work with Stanford Synchrotron Radiation Lightsource, Advanced Light Source, and Advanced Photon Source synchrotron light sources.

### Milestones

1. Quantify effect of microindentation pressure on fracture formation of  $\text{Li}_7\text{La}_3\text{Zr}_2\text{O}_{12}$  (LLZO) SE using *in situ* electrochemical scanning emission microscopy (SEM). (Q1, FY 2022; Completed)
2. Quantify degree of H/Li exchange for acid-treatment LLZO before and after heat treatment. (Q2, FY 2022; Completed)
3. Characterize chemical nature of the Ag-LLZO interface via cryo-TEM. (Q3, FY 2022; Completed)
4. Characterize lithium plating on LLZO coated with five metallic electrodes using *in situ* electrochemical SEM. (Q4, FY 2022; Completed)

## Progress Report

Throughout this year, the team has developed *operando* characterization for lithium plating in LLZO SE. Until this quarter, they focused on indentation experiments and effects the local critical current density. This quarter, they expanded the technique beyond local stresses to global stresses.

They conducted *operando* SEM microprobe experiments on a strained LLZO cantilever. As schematically shown in Figure 83, a 15-mm-long LLZO cantilever (attached to a thin layer of lithium and copper) was clamped at one end and pushed upward at the free end. This setup results in a linear variation in strain along the length of the cantilever, in which there is zero strain at the free end and maximum strain at the clamped end. This geometry enables local examination of the LLZO surface under different mechanical strains along the same cantilever.

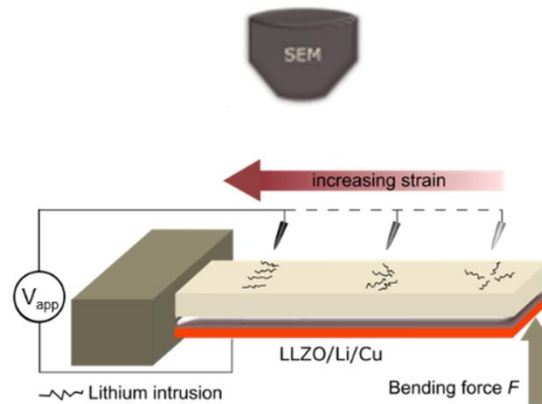


**Figure 83.** *Operando* microprobe scanning electron microscopy (SEM) setup on LLZO cantilever.

As in the earlier experiments, here the team observes lithium intrusion at various compressive stresses while flowing ionic current between the top and the bottom surface of the cantilever. Figure 84a reveals that lithium intrusions are randomly oriented at 0% strain (free end of cantilever), indicating the random nature of the pre-existing defect distribution. At 0.033% compressive strain (the middle of the cantilever), the lithium intrusions start to show more geometric alignment, as shown in Figure 84b. Strikingly, at the base of the cantilever where the compressive strain is only  $\sim 0.070\%$ , the intrusions exhibit a strong alignment along the cantilever longitudinal direction, that is, along the compressively strained direction (see Figure 84c). Tests were consistently performed in the low contact force regime ( $0.1 \pm 0.03$  mN). To rule out the possibility that the rotational angle between the microprobe and sample influences the intrusion direction, they conducted experiments on a cantilever that was rotated 20 and 45 degrees relative to the probe (Figure 84d-e) and found lithium intrusions remained predominantly aligned along the cantilever longitudinal direction rather than perpendicular to the microprobe.

The team proposes that the directional propagation of intrusions occurs because the uniaxial compression facilitates crack closure and increases the effective fracture toughness in the transverse direction, as schematically shown in Figure 84f. These results show that mechanical strain controls the propagation of intrusions after their initiation and provides further evidence of the mechanical origin of Li-metal intrusions.

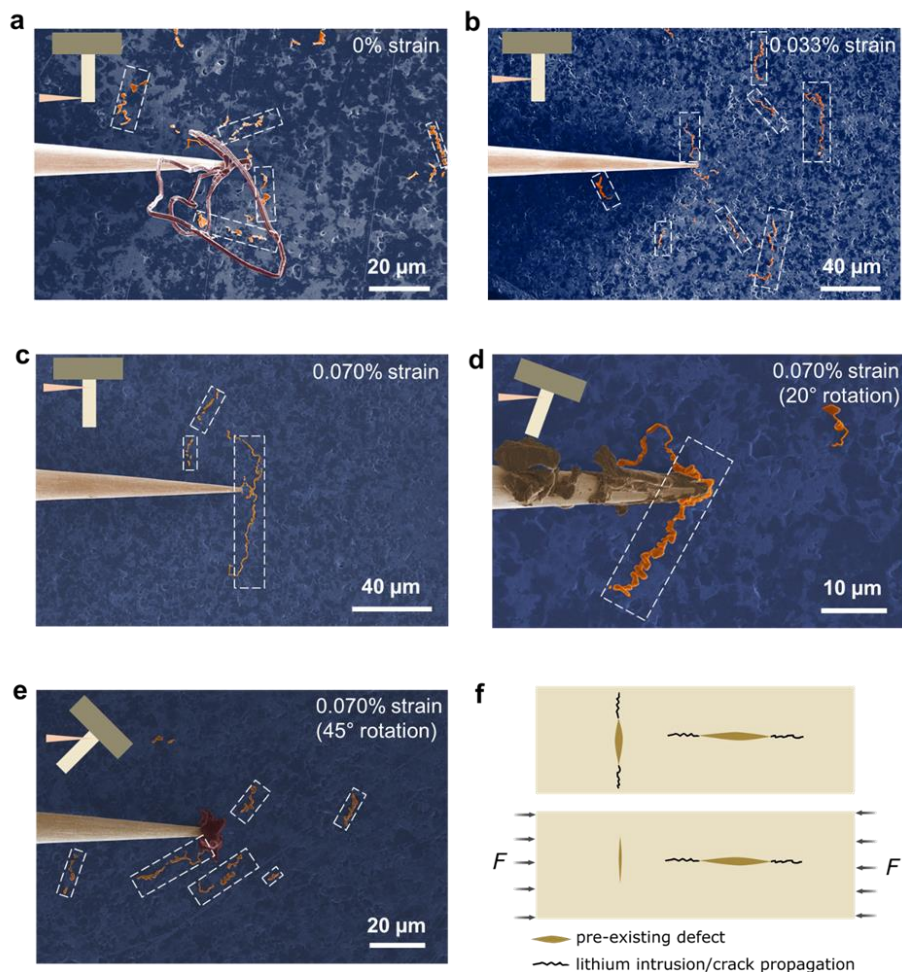


Figure 84. *Operando* LLZO cantilever bending experiments revealing a strong mechanical strain effect on regulating the intrusion propagation behavior. Colorized scanning electron microscopy images showing intrusions at (a) 0% strain (free end of the cantilever), (b) 0.033% strain (center of the cantilever), and (c-e) 0.070% strain (base of the cantilever). The intrusion propagates in random directions at 0% strain and becomes gradually more aligned along the longitudinal direction of the cantilever with increasing compressive strain. (d-e) Intrusion propagation at 0.070% with the cantilever rotated by 20° and 45° relative to the microprobe. The intrusion propagation direction remains along the cantilever. (f) Schematic showing the crack closure effect of external compressive strain to the pre-existing cracks normal to the strain direction.

## Patents/Publications/Presentations

### Publication

- McConohy, G., X. Xu, T. Cui, E. Barks, S. Wang, E. Kaeli, C. Melamed, X. W. Gu, and W. C. Chueh. “Mechanical Origins of Lithium-Metal Intrusions into Garnet Solid Electrolytes Revealed by Failure Statistics.” *Nature Energy* (2022). Working Paper. Doi: <https://doi.org/10.26434/chemrxiv-2022-33210>.

### Presentations

- International Society of Electrochemistry Annual Meeting, Virtual (September 16, 2022); W. C. Chueh.
- Gordon Research Conference on Electrochemistry, Ventura, California (September 11, 2022); W. C. Chueh.
- International Conference on Solid State Ionics, Boston, Massachusetts (July 19, 2022); W. C. Chueh.

## Task 2.6 – Fundamental Understanding of Interfacial Phenomena in Solid-State Batteries (Xingcheng Xiao, General Motors)

**Project Objective.** The project objective is to develop a comprehensive set of *in situ* diagnostic techniques combined with atomic/continuum modeling schemes to investigate and understand the coupled mechanical/chemical degradation associated with dynamic interfacial phenomena in solid-state batteries (SSBs). Specifically, *in situ* observations and characterizations of lithium plating-stripping processes, lithium dendrite formation, interphase formation, and the induced interfacial stresses, as well as the mechanical and electrochemical properties of interfaces and interphases, are paramount. The study will provide useful guidelines for optimizing cell structure design and engineering interfaces and interphases to enable SSBs.

**Project Impact.** The project will provide fundamental understanding of the dynamic interfacial phenomena and the coupled mechanical and chemical degradation. In addition, it will establish a critical guideline to design safe and durable SSBs with energy density > 500 wh/kg for electric vehicle (EV) applications.

**Approach.** The multiscale *in situ* diagnostic tools, including atomic force microscopy, nanoindentation, dilatometer, stress sensors, and pressure cells, will be used to investigate mechanical behavior and microstructure evolution at interface/interphase during lithium plating and stripping. The information (along with Li-ion transport properties and microstructure evolution obtained using the advanced spectroscopic ellipsometry, and *in situ* transmission electron microscopy) will be correlated with electrochemical performance toward high cycle efficiency and dendrite-free SSBs. The goal of this understanding is to develop strategies for surface and interface engineering, apply them to commercially available solid electrolytes (SEs) including powder, pellets, and foils, and assemble SSBs for further validation and optimization, eventually extending cycle life for EV application.

**Out-Year Goals.** The project seeks to develop SSB model systems to capture critical mechanical properties and probe the coupled mechanical-chemical degradation by further developing comprehensive *in situ* diagnostic tools. All results obtained from these *in situ* studies, combined with advanced postmortem analysis and modeling, will be correlated with the cycling stability of SSBs. The *in situ* tools developed will be applied to the following two periods to deeply understand the coupled mechanical and chemical degradation of interface/interphase.

**Collaborations.** The principal investigators involved in experiments and simulation will be as follows: B. W. Sheldon and Y. Qi (Brown University), and Y-T. Cheng and A. Seo (University of Kentucky, or UK).

### Milestones

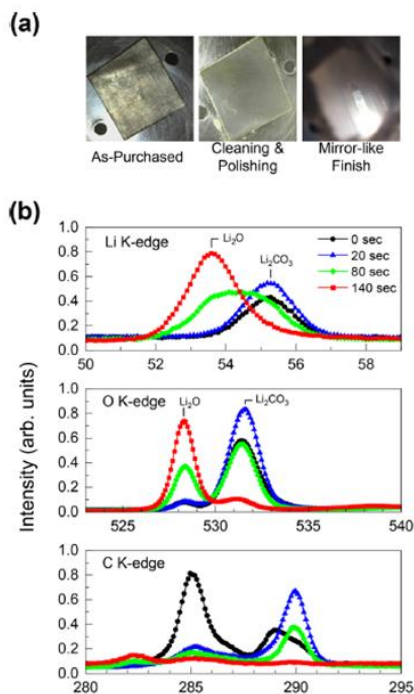
1. Artificial interlayer can regulate mechanical/chemical properties of interfaces. (Q1, FY 2022; Completed)
2. Artificial interphase has good ionic conductivity and chemical stability. (Q2, FY 2022; Completed)
3. Model to predict the governing mechanical and material properties of interfaces responsible for failures. (Q3, FY 2022; Completed)
4. Pouch cells of SSBs with optimized interlayers with energy density > 350 Wh/kg and cycle life > 500 cycles. (Q4, FY 2022; In progress – will be completed in no-cost extension period)

## Progress Report

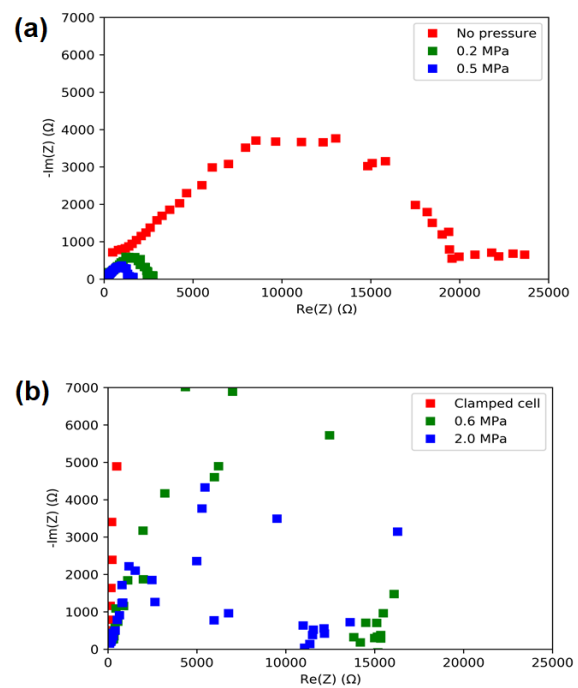
Many of the project’s models of the interface between lithium metal and SEs assume an ideal contact, where only pure lithium metal is in contact with the SE. Here, the team reports an *in situ* spectroscopic study conducted at UK demonstrating that even when lithium metal is rigorously polished and cleaned, there still exists a surface layer that is tens of nanometers thick.

Figure 85 shows X-ray photoemission spectroscopy (XPS) of the surface of cleaned and polished lithium foil as the surface is etched with an argon ion beam. The XPS data reveal that  $\text{Li}_2\text{CO}_3$  and  $\text{Li}_2\text{O}$  both still exist near the top surface after cleaning and polishing. XPS does not provide any information on the thickness of these layers since the etching rate of these layers is unknown. An *in situ* optical spectroscopic ellipsometry study was conducted to measure the thickness of the surface layer as it is exposed to air. It was found that the thickness of the top surface layer is a function of exposure time to air. Up until 5 minutes, the film is initially about 50-nm thick and increases linearly in time at a rate of 24 nm/min. This indicates that the initial growth of the film is an interface-controlled process rather than a diffusion-controlled process. A future study will look at how this process depends on temperature.

To help mitigate this surface layer formation and to decrease interfacial resistance between the lithium foil and SE in all-solid-state batteries, researchers are looking into coating an artificial solid electrolyte interphase onto lithium foil. Here, the team presents measurements on interfacial resistance of coated lithium foil and its dependence on applied external pressure. Lithium foil was coated in a solution of dimethyl ether – trimethylolpropane – lithium nitrate (DTL). DTL coated and uncoated Li-foil samples were prepared at General Motors Global Research and Development Center. Samples were then assembled and vacuum sealed in a pouch cell for pressure cell studies. Figure 86 shows electrochemical impedance spectroscopy data that suggest that the interfacial resistance significantly decreases when lithium foil is coated with DTL, and that under externally applied pressure, both coated and uncoated samples show significant decrease in interfacial resistance.



**Figure 85.** (a) Photos of lithium foil as it is cleaned and polished. (b) X-ray photoelectron spectroscopy at the K-edge of lithium, oxygen, and carbon, respectively, as its surface layer is slowly removed by the Ar-ion milling process.



**Figure 86.** (a) Electrochemical impedance spectroscopy (EIS) spectra taken on DTL-coated lithium symmetric pouch cell. (b) Bare lithium symmetric pouch cell EIS data.

## Patents/Publications/Presentations

### Patent

- Xiao, X. A Process to Reduce the Interfacial Impedance in All Solid-State Batteries; GM patent number, P103667.

### Publication

- Feng, M., C-T. Yang, and Y. Qi. “The Critical Stack Pressure to Alter Void Generation at Li/Solid-Electrolyte Interfaces during Stripping.” *Journal of The Electrochemical Society* 169 (2022): 090526.

## Task 2.7 – Multidimensional Diagnostics of the Interface Evolutions in Solid-State Lithium Batteries (Yan Yao, University of Houston)

**Project Objective.** The project objective is to develop a platform combining focused ion beam – scanning electron microscopy (FIB-SEM) tomography, time-of-flight secondary ion mass spectrometry (TOF-SIMS), and *in situ* scanning electron microscopy (in-SEM) nanoindentation-based stiffness mapping for structural, chemical, and mechanical characterizations in solid-state lithium batteries (SSLBs). Assessment of the influence of cell design and testing conditions (that is, external pressure, current density, and temperature) on the evolutions of interfaces will be performed.

**Project Impact.** The consolidated *in situ* structural–chemical–mechanical diagnostic platform established in this project will provide unprecedented insights into the failure mechanisms of SSLBs.

**Approach.** Space- and time-resolved structural, chemical, and mechanical characterizations of the cathode-electrolyte and anode-electrolyte interfaces will be performed on lithium all-solid-state batteries using FIB-SEM, TOF-SIMS, and in-SEM nanoindentation. Tasks include the following: (1) development of solid-state cell thin stacks and test-cell configurations that are suitable for *in situ* characterizations; (2) quantitative characterization and *in situ* tracking of interfacial voids formation within composite cathode and electrolyte layer; (3) identification and *in situ* tracking of the chemical composition, spatial distribution, and mechanical properties of electrolyte decomposition products at the lithium- and cathode-electrolyte interfaces; and (4) visualization, chemo-mechanical properties detection, and *in situ* tracking of lithium dendrites grown within the solid electrolyte (SE) layer.

**Out-Year Goals.** In the out years, the project will develop thin-stack solid-state cells, micro-cells, in-SEM nanoindentation, and testing protocols. The correlation between structural evolution, electrolyte decomposition, and interfacial resistance increase will be investigated.

**Collaborations.** The University of Houston team (that is, Y. Yao, Z. Fan, and Y. Liang) works closely with the Rice University team (that is, J. Lou and H. Guo).

### Milestones

1. Multiscale structural investigations. (Q1, FY 2022; Completed)
2. Composition and spatial distribution study. (Q2, FY 2022; Completed)
3. Selected region mechanical property probing. (Q3, FY 2022; Completed)
4. Real-time monitoring of structural evolutions. (Q4, FY 2022; Completed)
5. Real-time monitoring of chemical products evolutions. (Q1, FY 2023; Completed)
6. Real-time monitoring of chemical products evolutions. (Q2, FY 2023; In progress)

## Progress Report

The team has demonstrated the capability to monitor the microstructural and chemical evolution of a solid-state Li-metal cell using TOF-SIMS. A custom-built *in situ* biasing stage was used to operate the cell in a TOF-SIMS chamber, which allows electrochemical biasing and TOF-SIMS imaging simultaneously. A typical solid-state Li-metal cell with the structure of composite cathode/sulfide electrolyte/silver-carbon interlayer/lithium anode (Figure 87, left) was assembled and polished with an Ar-ion polisher to expose the cross-section. A  $100 \times 100 \mu\text{m}^2$  area at the interface between the electrolyte and interlayer was chosen for the *operando* characterization.

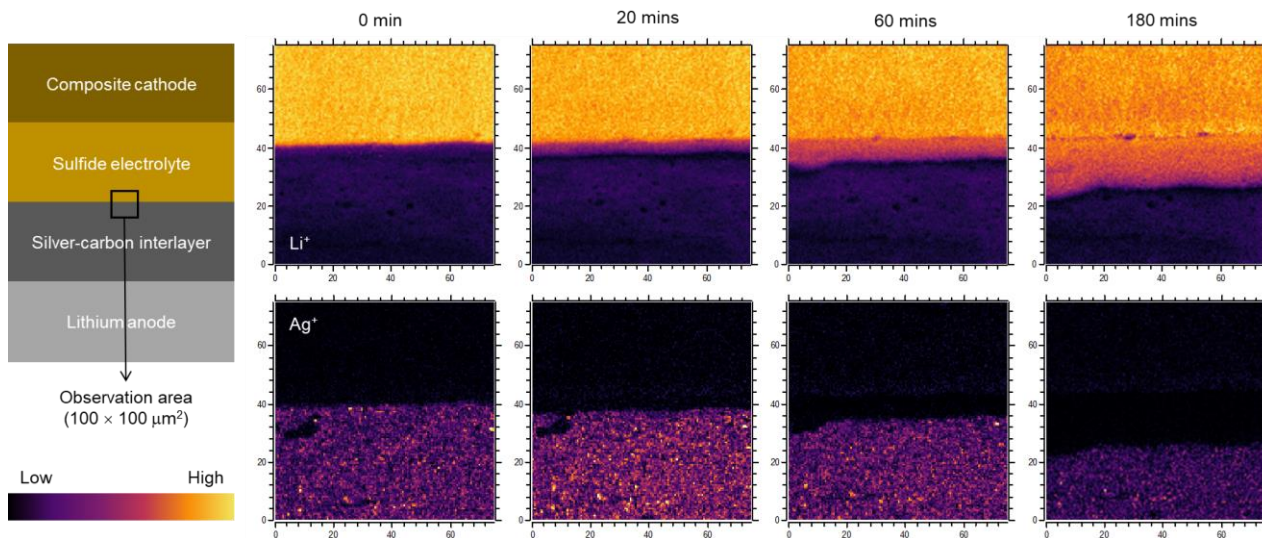


**Figure 87.** *Operando* time-of-flight secondary ion mass spectrometry mapping of  $\text{Li}^+$  and  $\text{Ag}^+$  at the electrolyte – silver-carbon interface. The x-axis and y-axis represent the spatial coordinates in  $\mu\text{m}$ . The brightness in color represents the ion count. (Left column) Structure of the solid-state Li-metal cell used in the observation; the observation area is marked with a black square. (Top row) Mapping of  $\text{Li}^+$ ; the strong  $\text{Li}^+$  signal in the top region ( $40 < y < 75$ ) originates from the solid electrolyte. (Bottom row) Mapping of  $\text{Ag}^+$ ;  $\text{Ag}^+$  signal is only present within the silver-carbon layer ( $y < 40$ ).

The TOF-SIMS mapping of the cell during a 3-hour charging is shown in Figure 87. Before charging (0 minutes), there is a clear distinction between the SE layer and the interlayer, characterized by  $\text{Li}^+$  and  $\text{Ag}^+$  signals, respectively. As charging proceeds,  $\text{Li}^+$  signal gradually extends into the interlayer, indicating lithiation and/or lithium growth. The moving front of  $\text{Ag}^+$  signal retreats as  $\text{Li}^+$  progresses, which may be interpreted either as a decrease of silver element in the lithiated region or  $\text{Ag}^+$  signal being overwhelmed by the more intensive  $\text{Li}^+$  signal.

The signal intensity of both  $\text{Ag}^+$  and  $\text{Li}^+$  is plotted against distance and compared in Figure 88. Both signals show gradient distribution in the lithiation front, indicating a gradual, possibly multi-step lithiation process. These intensity–distance profiles can be fed into modeling of diffusion and reveal the lithiation and lithium growth mechanism in the interlayer. Further efforts on distinguishing different silver and lithium species, from which details on the chemical status of the lithiated species can be extracted, are ongoing. With an improved understanding of the working mechanism of the interlayer, further engineering can be done for improvement.

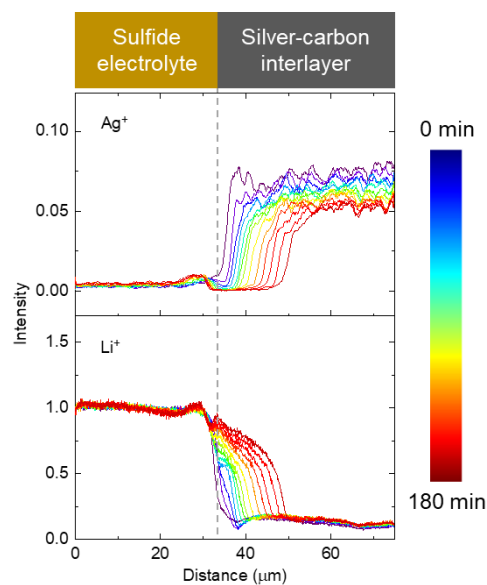


**Figure 88.** Evolution of spatial distribution of  $\text{Ag}^+$  and  $\text{Li}^+$  during charging. Curves processed from time-of-flight secondary ion mass spectrometry spectra such as those displayed in Figure 87.

The *operando* chemical monitoring with spatial resolution can be readily applied to other interfaces and bulk phases in the same cell. Application of the method to material evolution in the cathode, anode, and related interfaces will shed light on a series of questions of interest, including passivation, material failure, and dendrite growth. The method is complementary to the team’s previously reported *operando* methods concerning microstructural and mechanical evolution. Their air-free transfer vessels allow spatially aligned cross-reference between these methods.

## Patents/Publications/Presentations

### Presentations

- American Chemical Society (ACS) Fall 2022 Meeting, Chicago, Illinois (August 23, 2022): “Redox-Active Polymers for Energy Storage.” Invited.
- ACS Fall 2022 Meeting, Chicago, Illinois (August 22, 2022): “Understanding Solid Electrolyte-Lithium Interfaces via *Operando* Characterizations.” Invited.
- ACS Fall 2022 Meeting, Chicago, Illinois (August 21, 2022): “Rational Design of High-Power Mg Batteries: from Intercalation to Conversion Chemistry.” Invited.
- 2022 Molecular Foundry User Meeting, Berkeley, California (August 19, 2022): “Multidimensional Characterizations for All-Solid-State Batteries.” Invited.
- Hong Kong Polytechnic University, Department of Industrial and Systems Engineering Seminar, Virtual, (September 15, 2022): “Next-Generation Batteries for Electric Vehicles and Stationary Storage.” Invited.

## TASK 3 – MODELING

Team Lead: Venkat Srinivasan, Argonne National Laboratory

### Summary and Highlights

Achieving the performance, life, and cost targets outlined by the Vehicle Technologies Office will require moving to next-generation chemistries, such as higher capacity Li-ion intercalation cathodes, silicon and other alloy-based anodes, Li-metal anode, and sulfur cathodes. However, numerous problems plague development of these systems, from material-level challenges in ensuring reversibility to electrode-level issues in accommodating volume changes, to cell-level challenges in preventing cross talk between the electrodes. In this task, a mathematical perspective is applied to these challenges to provide an understanding of the underlying phenomenon and to suggest solutions that can be implemented by the material synthesis and electrode architecture groups.

The effort spans multiple length scales, from *ab initio* methods to continuum-scale techniques. Models are combined with experiments, and extensive collaborations are established with experimental groups to ensure that the predictions match reality. Efforts also focus on obtaining parameters needed for the models, either from lower-length scale methods or from experiments. Projects also emphasize pushing the boundaries of the modeling techniques used to ensure that the task stays at the cutting edge.

A major focus of the effort is around Li-metal-based solid-state batteries. While these chemistries hold promise, numerous challenges such as reactivity, conductivity, and mechanical stability prevent their commercialization. Mathematical models are ideal to provide the guidance and insights needed to solve these issues.

In the area of Li-metal anodes, the focus is on understanding how materials can be designed to prevent dendrite growth using continuum modeling approaches, combined with calculations on mobility in solid conductors. The results are used to guide materials development by providing the properties needed to prevent dendrites, while also achieving the energy and power goals. Models examine the role of the solid electrolyte interphase on the morphology of the dendrite and describe the mechanical-electrochemical coupled effects that are critical for dendrite formation. Finally, efforts are focused on discovery of new solid ion conductors with properties that far exceed existing materials. The focus is on using these models as a guide before embarking on extensive experimentation.

Lithium metal with solid electrolytes will be paired with cathode materials, often intercalative in nature. Models are being developed to examine the solid-cathode interface in Li-metal-based systems, where side reactions and interface debonding issues are known to limit cycling. These models are being used to understand how to prevent chemo-mechanical failure at the interface. Coatings, an effective strategy for high-voltage operation, are being explored with the aim of providing a rational design approach for new coating materials. In addition, focus is paid to porous electrodes with cathode particles to predict the impact of heterogeneities on electrode behavior.

**Highlight.** The G. Ceder group has identified new lithium conductors based on the rationale that corner-sharing frameworks enable high conductivity. Based on a high-throughput (HT) screening, the team discovered ten novel fast Li-conducting frameworks. To demonstrate the prediction of the team's HT screening, they synthesized one of the candidates,  $\text{LiGa}(\text{SeO}_3)_2$ , using solid-state synthesis and densifying into a dense pellet using spark plasma sintering. The data show remarkably high bulk ionic conductivity of 0.11 mS/cm at room temperature.

## Task 3.1 – Characterization and Modeling of Lithium-Metal Batteries: First-Principles Modeling and Machine Learning (Kristin Persson, Lawrence Berkeley National Laboratory)

**Project Objective.** This project supports Vehicle Technologies Office programmatic goals by developing next-generation, high-energy cathode materials and enabling stable cathode operation at high voltages through target particle morphology design, functional coatings, and rational design of electrolytes. The end-of-project goals include the following: (1) understanding of the factors that govern charge transport in nonaqueous, superconcentrated liquid electrolytes (LEs), (2) critical surface and coating design and optimization strategies that will improve cycling of Li-ion battery cathodes by reducing cathode degradation from oxygen loss, and (3) simulation and machine learning (ML) of the early formation of the solid electrolyte interphase (SEI) on Li-metal electrodes.

**Project Impact.** This project is aimed at providing fundamental insights into the atomistic mechanisms underlying surface reactivity and performance of Li-ion cathode materials and electrolytes, with the goal being to suggest improvement strategies, such as coatings, surface protection, novel electrolyte formulations, and particle morphology design. Transport modes as a function of solvent and salt concentrations will be clarified, and a data-driven reaction network framework will be designed and implemented to predict early SEI formation on lithium metal.

**Approach.** First-principles calculations, both static and dynamic approaches, are used to model solid-state electrolyte material thermodynamics and kinetics. LEs are modeled through coupled classical molecular dynamics and first-principles methods to accurately capture solvation structure as well as reactivity of the liquid system. The reaction network is built on large-scale first-principles data, using graph theory and ML models.

**Out-Year Goals.** Electrolyte work will be aimed toward understanding the atomistic interactions underlying performance of lithium electrolytes, specifically elucidating conductivity (as a function of salt concentration) and impact on the charge transport mechanisms at play. Amorphous coatings will be evaluated based on ionic transport metrics and thermodynamic stability. The reaction network will be tested against known interfacial species forming on lithium metal in  $\text{LiPF}_6$ /ethylene carbonate (EC) electrolytes.

**Collaborations.** This project is highly collaborative among several BMR principal investigators: G. Chen (Lawrence Berkeley National Laboratory), G. Ceder (University of California, Berkeley), and R. Kostecki (Argonne National Laboratory). Improved coating formulations will be examined by Chen and Ceder, and interfacial reactivity insights will be corroborated by Kostecki.

### Milestones

1. Correlate electrolyte chemistry, and Li/SEI compositional structure determined for Li-EC-based electrolyte. (Q1, FY 2022; Completed)
2. Determine sensitivity of molecular dynamics (MD) parameters to diluent effect on transport in at least one superconcentrated electrolyte. (Q2, FY 2022; Completed)
3. Develop high-throughput infrastructure for MD simulations. (Q3, FY 2022, Completed)
4. Determine chemistry and structural motifs that control cathode amorphous coating performance, screening over 50,000 compositions. (Q4, FY 2022; Completed)

## Progress Report

This report presents the team’s recent progress in determining chemistry and structural motifs that control cathode amorphous coating performance. A coating material that participates in the redox reaction during extensive cycling may cause degradation of the surface film, thus a loss of the surface protection. Therefore, the team retains only electrochemically stable compounds that can sustain the desirable voltage window. In this study, they select the compounds that exhibit a reduction limit smaller than 3 V and an oxidation limit above 4 V. Figure 89a illustrates the reduction and oxidation limits of the compounds that are thermodynamically stable. The electrochemical stability of each category is denoted by two violin plots: the left and right represent oxidation and reduction limits, respectively. They find that in general, fluorides, such as  $\text{AlF}_3$  and  $\text{LiAlF}_4$ , have the largest electrochemical stability window with high oxidation limits and low reduction limits. On the other hand, metal oxides, such as  $\text{BaO}$  and  $\text{Bi}_2\text{O}_3$ , exhibit low oxidation limit, and nonmetal oxides, such as  $\text{P}_2\text{O}_5$  and  $\text{SeO}_2$ , have high reduction limit. The bar graph in Figure 89a summarizes the numbers of compounds for each category of materials that passes the electrochemical stability screening. After this screening tier, polyanionic oxides have the largest number of candidates, followed by fluorides and chlorides. There are only 12 metal oxides and 1 nonmetal oxide,  $\text{B}_2\text{O}_3$ , left for further screening.

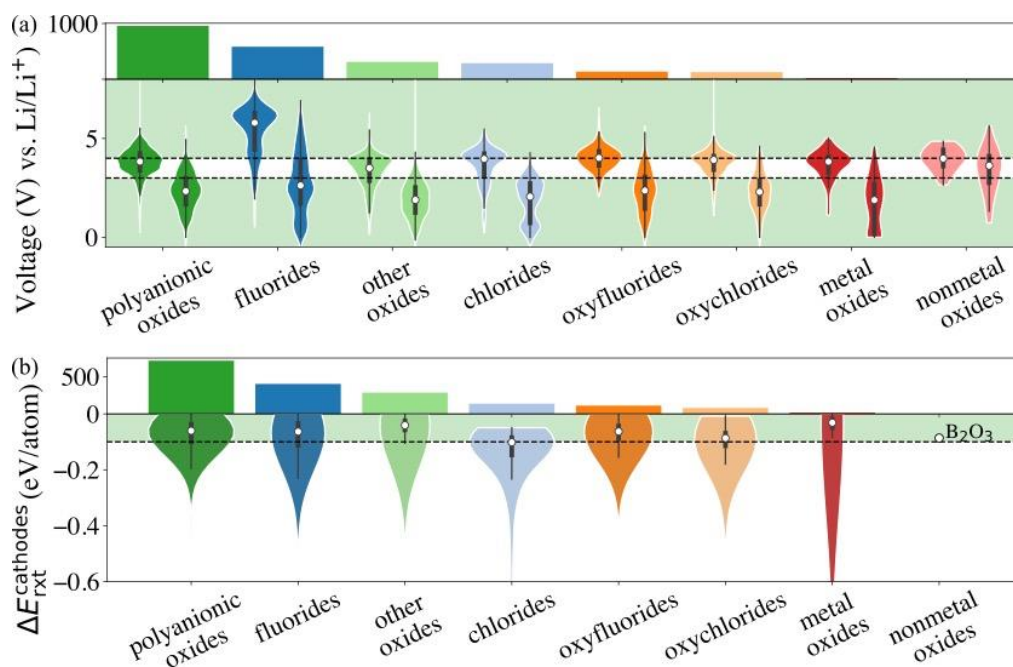


**Figure 89.** (a) Distribution of the reduction and oxidation limits for each category that passes thermodynamic stability descriptor. (b) Distribution of the reaction energy with  $\text{LiNiO}_2$ ,  $\text{LiCoO}_2$ ,  $\text{LiMn}_2\text{O}_4$ , and  $\text{LiFeOP}_4$  cathodes for each category that passes electrochemical stability descriptor. The horizontal dash lines represent the limits of the descriptors. The histograms in (a) and (b) illustrate the numbers of compounds for each category that passes the descriptors.

Next, the team selects cathode coatings that are inert to chemical reactions with both cathodes and electrolytes. The reaction energy  $\Delta E_{\text{rxt}}$  is calculated using density functional theory computed energies of the reactants and products, and a more negative  $\Delta E_{\text{rxt}}$  indicates a more reactive chemical reaction. They set the criterion for chemically stable cathode coatings as:  $\Delta E_{\text{rxt}} \geq -0.1$  eV per atom. They calculate  $\Delta E_{\text{rxt}}$  between cathodes and coating materials using the commonly used cathodes, layered  $\text{LiNiO}_2$  and  $\text{LiCoO}_2$ , spinel  $\text{LiMn}_2\text{O}_4$ , and olivine  $\text{LiFeOP}_4$ . Figure 89b shows that oxide coatings are less prone to react with cathodes than fluorides and chlorides. Specifically, all the electrochemically stable metal oxides exhibit low reactivity with common cathodes and pass the chemical stability descriptor. This round of screening returns 1790 compounds for further consideration, with polyanionic oxides having the largest number of candidates (714).

Similarly, the team calculates  $\Delta E_{\text{rxt}}$  between coating materials and representative electrolyte components. In this study, they consider the commonly used  $\text{Li}_3\text{PS}_4$  solid electrolyte and  $\text{LiPF}_6$ -based non-aqueous LEs, respectively, and categorize the coating materials based on their reactivity. In the case of  $\text{LiPF}_6$ -based electrolytes, they calculate  $\Delta E_{\text{rxt}}$  between coating materials and HF, which is known to react strongly with both cathodes and coating materials. Figure 90 illustrates the distribution of  $\Delta E_{\text{rxt}}$  with  $\text{Li}_3\text{PS}_4$  and HF for the compounds that are chemically stable with the cathodes. They find that most fluorides and chlorides have lower chemical reactivity with both  $\text{Li}_3\text{PS}_4$  and HF than oxides compounds, and thus are chemically compatible with both the cathodes and electrolytes. On the other hand, most oxides compounds are not chemically inert in  $\text{LiPF}_6$ -based LEs due to a high reactivity with HF. This round of screening returns 902 and 508 coating candidates that are chemically compatible with  $\text{Li}_3\text{PS}_4$  and  $\text{LiPF}_6$  based electrolytes, respectively.

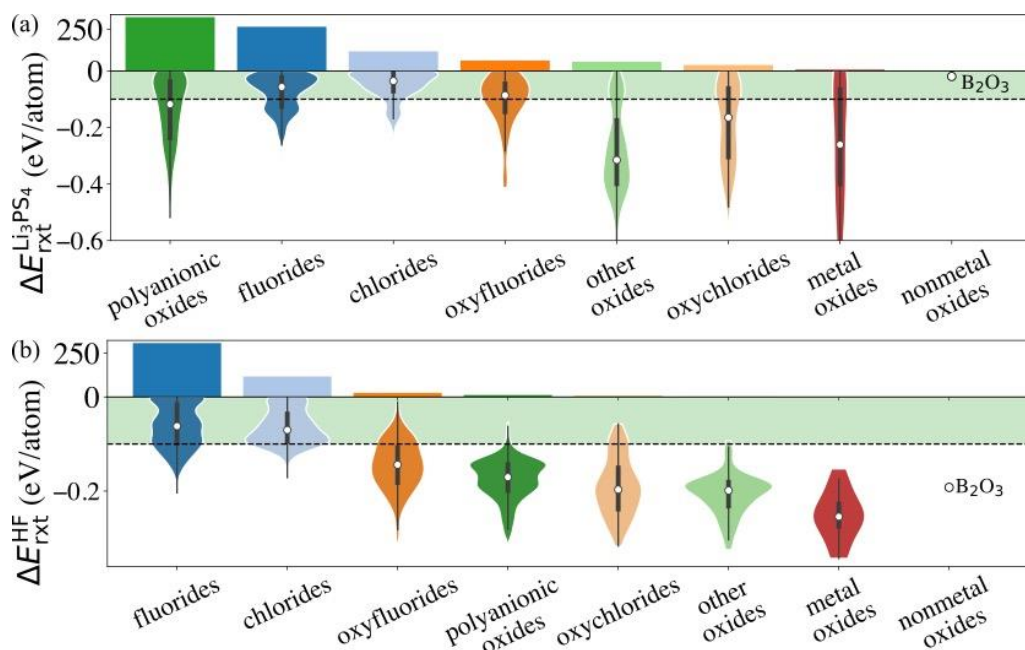


**Figure 90.** Distribution of the reaction energy  $\Delta E_{\text{rxt}}$  with  $\text{Li}_3\text{PS}_4$  (a) and HF (b) for each category that passes chemical stability with the cathodes descriptor. The horizontal dash lines represent the limits of the descriptors. The histograms in (a) and (b) illustrate the numbers of compounds for each category that passes the descriptors.

In addition, the team finds a correlation between  $\text{Li}^+$  and  $\text{O}^{2-}$  diffusion, which can be explained by ionic conduction mechanism in amorphous structures. Their previous study showed that  $\text{Li}^+$  and  $\text{O}^{2-}$  diffusion consists of discrete vibrational and translational motions. During vibrational motions,  $\text{Li}^+$  is bonded to more  $\text{O}^{2-}$  ions than during translational motions, and its translation to another vibration site is activated by the Li-O bond breaking/formation process, which effectively explains the correlated transport between  $\text{Li}^+$  and  $\text{O}^{2-}$ .

## Patents/Publications/Presentations

### Publication

- Cheng, J., K. D. Fong, and K. A. Persson. “Materials Design Principles of Amorphous Cathode Coatings for Lithium-Ion Battery Applications.” *Journal of Materials Chemistry A* 10 (2022): 22245-22256. doi: <https://doi.org/10.1039/D2TA06051E>.

### Presentation

- Telluride Science Research Center, Telluride, Colorado (July 14, 2022): “Computational Design of Surface Coating and Targeted Doping for Li-ion Batteries.”

## Task 3.2 – Electrode Materials Design and Failure Prediction (Venkat Srinivasan, Argonne National Laboratory)

**Project Objective.** The main project objective is to develop computational models for understanding the various degradation mechanisms for next-generation Li-ion batteries. This year's goal is to use the continuum-based mathematical model to estimate the conduction pathway through the solid electrolytes (SEs) and investigate interfacial stability between Li-metal electrodes and SEs during deposition and dissolution of lithium under externally applied currents. Electrolytes comprised of soft polymers, hard ceramics, and a combination of the two in the form of polymer-ceramic composites, will be investigated. SEs are expected to enable high-energy-density and liquid-free, safe, next-generation Li-ion batteries, while combined with thin Li-metal anodes. During charge, lithium dendrites are observed through the SEs, which are supposed to occur because of the non-uniform current distribution at the Li/electrolyte interface. Due to their lack of conformability, hard-ceramic-based SEs [such as  $\text{Li}_7\text{La}_3\text{Zr}_2\text{O}_{12}$  (LLZO) and Li-Al-Ti-P] are expected to experience loss of electrochemically active surface area during lithium plating and stripping, which can eventually lead to current focusing and subsequent dendrite growth. Sulfide-based soft ceramics Li-P-S and Li-P-S-Cl, and/or polymer-ceramic composite electrolytes are expected to maintain better contact with the Li-metal electrode because of their higher deformability. The possibility of stabilizing the lithium deposition with composite electrolytes consisting of poly(ethylene oxide)-based soft-polymer matrix and LLZO-type hard ceramic fillers will be studied. Proper conduction pathways through the polymer and ceramic domains, and their influence on the effective conductivity of the SE, will be elucidated. Other soft SEs, such as polystyrene-*b*-poly(ethylene oxide) polymer and sulfide-based soft ceramics, will be investigated for their capability to stabilize the lithium deposition on metallic anodes.

**Project Impact.** Findings from this research will give a better understanding of the ion transport mechanism within the polymer and ceramic domains of the composite SEs and will help elucidate the factors influencing the deposition of lithium at the electrode/electrolyte interface.

**Project Approach.** In the present project, mesoscale models are developed based on mass conservation, charge balance, and force balance relations at the continuum level to describe the physical processes occurring in the electrochemical systems during charge and discharge, which is then compared with the experimental observations for appropriate validation. The models are then used to provide insights and guidance for strategizing new design concepts and materials for the stabilization of Li-metal anodes.

**Out-Year Goals.** In this project, a computational framework will be presented that can capture the ionic transport through composite electrolytes and predict lithium deposition at the electrode/electrolyte interface.

**Collaborations.** This project collaborates with L. A. Curtiss, A. T. Ngo, S. Tepavcevic, and Y. Zhang at Argonne National Laboratory.

### Milestones

1. Investigating the current, focusing on the interface between Li-metal electrode and polymer/ceramic composite electrolyte. (Q1, FY 2022; Completed)
2. Elucidating ion transport mechanism through the polymer and ceramic phases in a composite electrolyte. (Q2, FY 2022; Completed)
3. Deciphering the influence of stress state on the exchange current density experienced by Li-metal electrodes in contact with solid polymer electrolytes during lithium deposition and stripping processes. (Q3, FY 2022; Completed)

4. Understanding the impact of grain boundaries (GB) in soft inorganic SEs on the lithium deposition process and subsequent dendrite growth. (Q4, FY 2022; Completed)

## Progress Report

**Understanding the Impact of GBs in Soft Inorganic SEs on the Lithium Deposition Process and Subsequent Dendrite Growth.** Due to the extremely high stiffness of garnet-type SEs (such as, LLZO), they do not conform to the depositing lithium, which can eventually lead to loss of contact between the Li-metal electrode and the SE. This decrease in electrochemically active surface area can eventually lead to current focusing and dendrite growth within LLZO-type stiff SEs. Sulfide-based soft inorganics have been investigated due to their enhanced conformability and possibility of having enhanced electrochemically active surface area with Li-metal electrode. However, similarly to garnets, sulfide-based soft inorganics also demonstrate grain/GB microstructure. It was reported earlier that softer GBs of LLZO act as points for current focusing, which can eventually lead to cracking of the SE; dendrites can grow through those crack openings. Since current focusing at the GBs is assumed to be the main culprit that causes the formation and propagation of dendrites, the extent of current focusing at the GBs for sulfide-based soft inorganic SEs is worth investigating. Accordingly, reaction current distribution at the triple junction of lithium electrode, grain interior, and GB of the SE is investigated using the computational mesh shown in Figure 91a. The Butler-Volmer prescribed reaction current distribution at the lithium/electrolyte interface is plotted in Figure 91b, which contains contribution from electrochemical potential as well as mechanical stress. Enhanced reaction current at the GB is evident, which increases with time, as is clearly demonstrated in Figure 91c. The blue dashed line indicates the applied current.

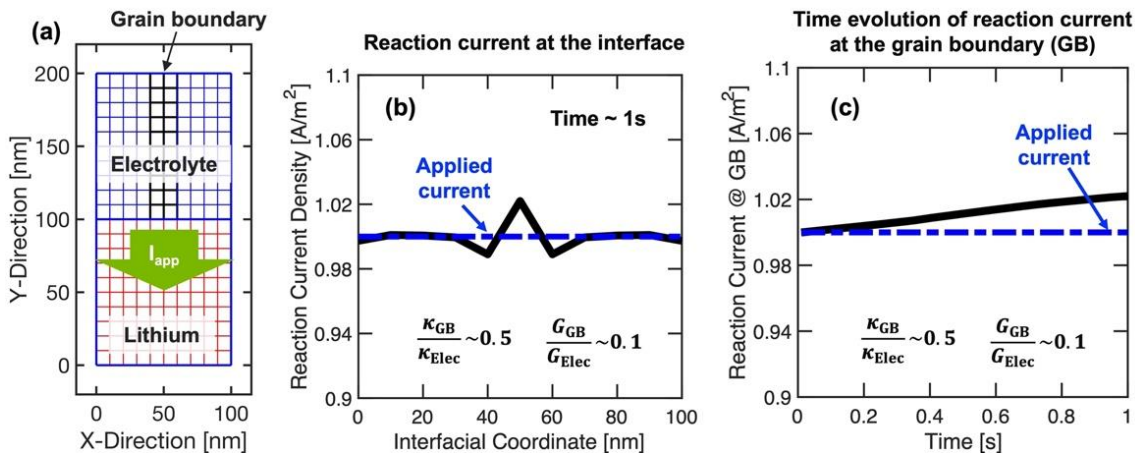


**Figure 91.** (a) Lithium/solid-electrolyte mesh used in the present analysis. The grain interior and grain boundaries (GBs) are denoted by the blue and black regions, respectively. Butler-Volmer reaction current is implemented at the lithium/solid-electrolyte interface. (b) Distribution of reaction current at the electrode/electrolyte interface (black line) after 1 second for GB conductivity and shear modulus being 50% and 10% of the grain interior, respectively. (c) Increase in reaction current density at the GB region with time, which demonstrates an increasing trend. In (b) and (c), the blue dashed line indicates the applied current density.

The extent of current focusing at the GBs depends on the conductivity and shear modulus of the GB region, which is demonstrated in Figure 92a-b. It is evident that the current focusing at the GBs can be eliminated by the adoption of mechanically stiff GB domains (Figure 92b, right side). Investigation of the current focusing at the GBs of sulfide-based soft inorganic SEs completes this quarter's milestone.

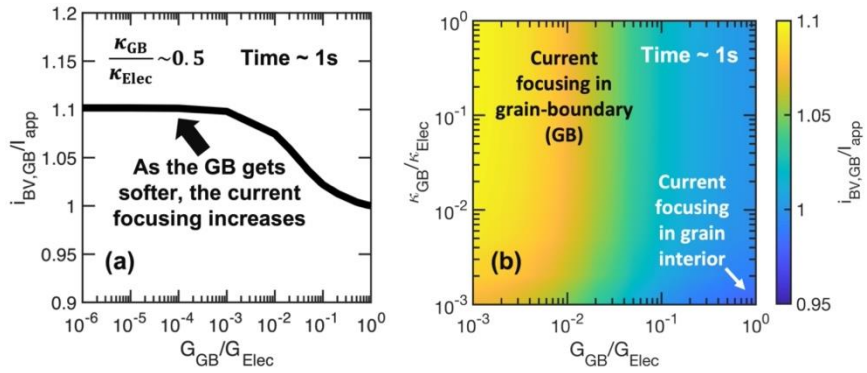


Figure 92. (a) Current focusing at the grain boundary (GB) region after 1 second as a function of the shear modulus of the GBs. Decreasing the GB modulus enhances the current focusing. (b) Phase map between conductivity and shear modulus of the GBs indicating regions where current focusing should occur at the GBs (yellow domain). Homogeneous distribution of reaction current can be achieved by adopting stiff GBs.

## Patents/Publications/Presentations

The project has no patents, publications, or presentations to report this quarter.

### Task 3.3 – Modeling of Amorphous Solid-State Conductors (Gerbrand Ceder, University of California, Berkeley)

**Project Objective.** Solid-state batteries are promising to achieve high energy density. The project objective is to determine the design principles needed to create solid-state electrolytes with high Li-ion conductivity, while also achieving stability against common Li-ion cathodes and Li-metal anodes.

**Project Impact.** The project will lead to understanding the factors that control Li-ion motion in crystalline and amorphous solids and will develop strategies to create stable interfaces against lithium metal and high-voltage cathode materials. The understanding of such processes is necessary to determine design principles to develop reliable all-solid-state batteries (ASSBs).

**Approach.** High-throughput (HT) computation is used to screen suitable solid electrolytes (SEs) with high electrochemical stability and high ionic conductivity, by incorporating nudged elastic band and an *ab initio* molecular dynamics (AIMD) method. Meanwhile, density functional theory is used to calculate bulk elastic constants of materials, surface energies, and interface decohesion energies of grain boundaries. Thermodynamic interface stability is assessed from *ab initio* computed grand potential phase diagrams in which the lithium voltage can be controlled. Kinetic limits for SE decomposition are assessed by topotactic lithium insertion and removal from the SE.

**Out-Year Goals.** Future goals include the following: (1) gain insight into what creates high Li-ion conduction in sulfide and oxide solids, and (2) develop stable, processable solid-state conductors that can be applied in ASSBs.

**Collaborations.** There are no collaborative activities this quarter.

#### Milestones

1. Investigate lithium diffusion mechanism in activated network structures. (Q1, FY 2022; Completed)
2. Conduct diffusion network analysis in low-density structures. (Q2, FY 2022; Completed)
3. Perform detailed lithium transport modeling in one novel conductor. (Q3, FY 2022; Completed)
4. Conduct stability analysis of novel Li-ion conductor. (Q4, FY 2022; Completed)

## Progress Report

### HT Screening of Novel Lithium Oxide Superionic Conductors with Corner-Sharing Frameworks (CSFs)

Based on the team’s rationalization of the high ionic conductivities enabled in CSFs, they performed HT screening to discover new lithium oxide superionic conductors that share the same feature of CSFs. They started with all of quaternary lithium containing oxides from the Materials Project database. Among them, they identified 2,822 compounds in 637 distinct CSFs. Then, the team removed compounds with a band gap smaller than 2 eV or compounds containing elements unsuitable for SEs. Finally, they prioritized only the experimentally reported compounds, yielding 122 compounds in 56 distinct groups. For one representative compound per group, the team performed multi-step AIMD simulations to find the final candidates that have sufficiently high ionic conductivity (0.1 mS/cm) at 300 K.

Table 4 lists the final ten novel fast lithium-conducting frameworks discovered in this work. Including previously reported or predicted superionic conductors, the HT screening using the feature of CSF gave a success rate of 39%. It is noted that the team’s screening used the strictest criteria. By imposing less strict criteria, they anticipate that even more lithium superionic conductors may be discovered.

**Table 4. The final ten novel fast lithium-conducting frameworks discovered in this Task.**

Materials Project ID	ICSD ID	Pristine Composition	Target Composition	$\sigma_{300\text{K}}$ (mS/cm)	$E_a$ (eV)	Pristine $E_{\text{ball}}$ (eV/atom)	Target $E_{\text{ball}}$ (eV/atom)	$E_d$ (eV/defect)
mp-1198930	250868	LiGa(SeO <sub>3</sub> ) <sub>2</sub>	LiGa(SeO <sub>3</sub> ) <sub>2</sub>	0.212 (0.013, 3.57)	0.320 ± 0.070	0.0	0.0	N/A
mp-973966	422056	LiIn(IO <sub>3</sub> ) <sub>4</sub>	LiIn(IO <sub>3</sub> ) <sub>4</sub>	18.0 (3.57, 90.9)	0.155 ± 0.040	0.0	0.0	N/A
mp-559441	39761	LiTiPO <sub>5</sub>	Li <sub>1+1/16</sub> Ti <sub>1-1/16</sub> Ga <sub>1/16</sub> PO <sub>5</sub>	1.70 (0.098, 29.7)	0.212 ± 0.071	0.013	0.019	0.79
mp-14646	65025	Li <sub>2</sub> Mg <sub>2</sub> (SO <sub>4</sub> ) <sub>3</sub>	Li <sub>2+1/4</sub> Mg <sub>2</sub> (S <sub>11/12</sub> P <sub>1/12</sub> O <sub>4</sub> ) <sub>3</sub>	2.74 (0.145, 52.0)	0.232 ± 0.073	0.0	0.011	0.81
mp-552663	161499	LiScAs <sub>2</sub> O <sub>7</sub>	Li <sub>1+3/8</sub> Sc <sub>1-3/8</sub> Mg <sub>3/8</sub> As <sub>2</sub> O <sub>7</sub>	23.3 (4.26, 128)	0.177 ± 0.042	0.0	0.021	0.64
mp-1020018	428002	Li <sub>5</sub> B(SO <sub>4</sub> ) <sub>4</sub>	Li <sub>5+1/4</sub> B(S <sub>15/16</sub> P <sub>1/16</sub> O <sub>4</sub> ) <sub>4</sub>	0.330 (0.0368, 4.90)	0.330 ± 0.061	0.008	0.023	1.56
mp-1020022	248343	Li <sub>3</sub> B(PO <sub>4</sub> ) <sub>2</sub>	Li <sub>3+1/8</sub> B(P <sub>15/16</sub> Si <sub>1/16</sub> O <sub>4</sub> ) <sub>2</sub>	0.166 (0.00721, 3.83)	0.326 ± 0.078	0.014	0.028	1.63
mp-1020015	192496	Li <sub>2</sub> B <sub>3</sub> PO <sub>8</sub>	Li <sub>2+1/8</sub> B <sub>3</sub> P <sub>7/8</sub> Si <sub>1/8</sub> O <sub>8</sub>	0.251 (0.00744, 8.44)	0.269 ± 0.087	0.0	0.015	1.67
mp-1222376	260590	LiZnBO <sub>3</sub>	Li <sub>1+2/16</sub> Zn <sub>1-1/16</sub> BO <sub>3</sub>	0.605 (0.0104, 35.3)	0.220 ± 0.101	0.008	0.009	0.12
mp-556799	94355	Li <sub>3</sub> In(BO <sub>3</sub> ) <sub>2</sub>	Li <sub>3+1/8</sub> In <sub>7/8</sub> Zn <sub>1/8</sub> (BO <sub>3</sub> ) <sub>2</sub>	0.121 (0.0027, 5.33)	0.300 ± 0.094	0.004	0.009	0.50

To demonstrate the prediction of their HT screening, the team selected LiGa(SeO<sub>3</sub>)<sub>2</sub> for experimental investigation. This material has previously been synthesized, but it has never been considered as a Li-ion conductor. By synthesizing this material using a solid-state method and densifying into a dense pellet using spark plasma sintering, they were able to measure a remarkably high bulk ionic conductivity of 0.11 mS/cm at room temperature. These experimental results are in excellent agreement with the team’s computational predictions, suggesting a vast new structural space for consideration as materials for SEs in ASSBs.

## Patents/Publications/Presentations

### Presentation

- 23<sup>rd</sup> International Conference on Solid State Ionics, Boston, Massachusetts (July 17, 2022): “The Complex Mechanisms that Create High Li-Ion Mobility in Oxides and Sulfides”; K. Jun and G. Ceder. Keynote Talk.

## Task 3.4 – *In Situ* and *Operando* Thermal Diagnostics of Buried Interfaces in Beyond Lithium-Ion Cells (Ravi Prasher, Lawrence Berkeley National Laboratory)

**Project Objective.** Transport at various interfaces in beyond Li-ion cells will play a major role in electrochemical performance and reliability. It has not yet been possible to thermally profile a Li-metal cell during operation to provide a spatially resolved map of thermal transport properties throughout the cell. The objective of this research is to create a metrology capable of spatially resolved *in operando* thermal property profiling, and then to relate thermal property to the quality of electrodes and interfaces, and to use the developed thermal metrology to understand electrochemical processes in Li-metal batteries, such as dendrite growth, interface kinetics, and ionic transport.

**Project Impact.** Characterizing electrochemical processes in Li-metal cells such as lithium deposition and dendrite growth at interfaces is of great significance for understanding and enhancing their electrochemical performance and reliability. *In situ* and *operando* micro electrothermal sensors can provide significant information regarding the impact of buried interfaces as a function of time, material, voltage, current, temperature, etc. Therefore, it is important to develop *operando* micro electrothermal sensors and develop models relating those signals to electrochemical performance for beyond Li-ion cells. The physics-based model relating thermal and electrochemical properties based on these measurements can facilitate future design of Li-metal batteries.

**Approach.** To accomplish project goals, the team will utilize an in-house adapted 3-omega ( $3\omega$ ) technique to probe thermal properties of a Li-metal cell while it is in operation, without affecting the operation of the cell. The  $3\omega$  sensors will be deposited and fabricated on Li-metal cells based on previous learning on  $3\omega$  sensor fabrication. The characteristic depth of the thermally probed region is defined by the wave's "thermal penetration depth,"  $\delta_p = \sqrt{D/2\omega}$ , where  $D$  is the sample's thermal diffusivity, and  $2\omega$  is the heating frequency of the thermal wave. By depositing the project's  $3\omega$  sensors on the battery's outer surface and adjusting  $\omega$ , the team controls  $\delta_p$  to span the full range from the top to the bottom layer, thereby noninvasively probing the thermal transport in subsurface layers and interfaces within the bulk of the battery. Thermal transport can be related to quality of the interfaces. By doing concurrent thermal transport and electrochemical performance measurements, the team plans to relate thermal transport to electrochemical performance. As frequency-based thermal measurement techniques provide excellent spatial resolution within the cell, the team also plans to study heat generation at the electrolyte/Li-metal interface and to relate the thermal signals to the interface kinetics and ionic transport. The frequency dependence of heat generated due to transport resistance is different from that due to kinetic resistance. The team plans to utilize this difference to separate the contributions of kinetic and transport resistance at the interface, which will enable understanding of interface kinetics and transport at the Li-metal / solid-state electrolyte (SSE) interface.

**Out-Year Goals.** The project will design, build, and implement the adapted  $3\omega$  metrology to examine thermal properties and a general frequency-dependent thermal metrology to examine heat generation. This will involve developing and testing the metrology itself along with accompanying theory, designing compatible battery samples, and applying the technique to live cells. The team will measure thermal transport properties of battery materials provided by collaborators. Combined with the electrochemical performance measurement, this will provide significant information relating the thermal signal to the electrochemical process.

**Collaborations.** This project collaborates with two Lawrence Berkeley National Laboratory groups: V. Battaglia's for cell assembly for  $3\omega$  studies, and R. Kostecki's for pristine battery active material growths for studies of thermal signals related to electrochemical process.

## Milestones

1. Identification of theoretical model relating the interface morphology to thermal contact resistance (TCR). (Q1, FY 2022; Completed)
2. Measured change to TCR/morphology with cell cycling correlated with electrochemical impedance spectroscopy. (Q2, FY 2022; Completed)
3. *Ex situ* characterization of interface morphology to validate the theory relating the morphology to TCR. (Q3, FY 2022; Completed)
4. Effect of temperature on TCR and self-heating study of thermally insulated  $\text{Li}_7\text{La}_3\text{Zr}_2\text{O}_{12}$  (LLZO) cycling. (Q4, FY 2022; Completed)

## Progress Report

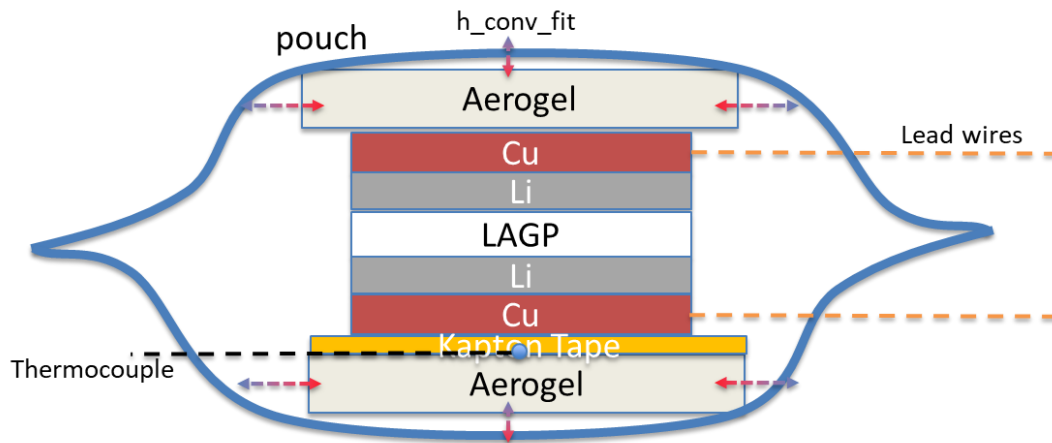
This quarter, the team carried out a self-heating study of thermally insulated solid-state cells. Because Li-Al-Ge-P (LAGP) is not air sensitive and is easy to make with the laboratory's cold pressing and sintering process, they choose LAGP instead of LLZO as the electrolyte in the self-heating study. Currently, the cycling of solid-state cells is investigated under the citation under high-frequency alternate current (AC) from function generator. The symmetric cells with lithium metal at each side were assembled first.

For the thermal insulation, the cell stacks are sandwiched by the aerogel material, and the power is supplied by copper wires instead of aluminum tabs. A small thermocouple is inserted between the aerogel and the Kapton film to monitor the temperature rise. The LAGP-Li cell is set on the Kapton film with additional Kapton tape for fastening. The solid-state cell is cycled under ~ 300 kPa pressure to enable good contact and electrochemical performance. The electrochemical impedance frequency response of the cell is measured before the insulated heating experiments. The generated heat under high frequency AC is calculated from Reference [1]:

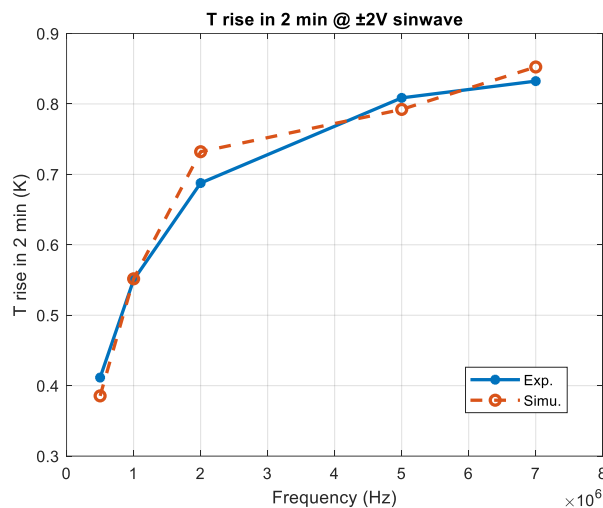
$$Q = U^2 * \frac{R_e}{|Z|^2}$$

The recorded temperature rise under different frequencies of AC voltage is modeled using COMSOL. The required heat capacities of SSE are measured from differential scanning calorimetry. Other parameters are used from literature. From the results shown in Figure 93, the simulation and experiments results agree well, with the heat transfer coefficients fitted well.

(a)



(b)



(c)

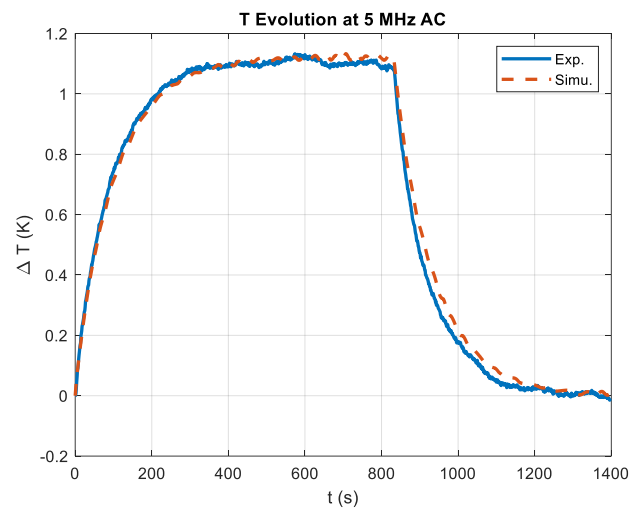


Figure 93. (a) The structure schematic of the assembled lithium aluminum germanium phosphate (LAGP) symmetric cell and insulation setup. (b) The temperature rises in 2 minutes under different frequency  $\pm 2V$  sin wave. (c) The example of fitting result between COMSOL simulation and experiments.

#### Reference

- [1] Qin, Y., et al. "A Rapid Lithium-Ion Battery Heating Method Based on Bidirectional Pulsed Current: Heating Effect and Impact on Battery Life." *Applied Energy* 280 (2020): 115957. doi: <https://doi.org/10.1016/j.apenergy.2020.115957>.

### Patents/Publications/Presentations

The project has no patents, publications, or presentations to report this quarter.

## Task 3.5 – Multiscale Modeling of Solid-State Electrolytes for Next-Generation Lithium Batteries (Anh Ngo, Larry A. Curtiss, and Venkat Srinivasan, Argonne National Laboratory)

**Project Objective.** This project is part of a multiscale modeling effort to obtain an in-depth understanding of the interaction of the electrode and the solid electrolyte (SE) aimed at developing highly efficient solid-state electrolyte (SSE) batteries for vehicle applications. Input parameters needed for mesoscale (continuum) level calculations are being obtained from atomistic calculations including density functional theory (DFT) and classical molecular dynamics simulations. This atomistic input will enable a multiscale computational procedure for SSEs that is capable of successfully capturing the physicochemical aspects during charge and discharge process, including lithium transport mechanisms, interfacial phenomena during the insertion and extraction of lithium ions, and mechanical deformation of SSE.

**Project Impact.** A major safety concern experienced with commercially available Li-ion batteries under some scenarios is leakage of the liquid electrolyte (LE), which can potentially catch fire. Replacement of the LE is necessary to decrease the fire hazard and improve safety associated with present-day Li-ion batteries. In addition, use of SEs provides a path to prevent dendrites in Li-metal anodes, thereby leading to batteries with significantly higher energy density. The impact of this project will be to help in development of good SSEs as a replacement for the commercially used organic LEs to improve safety and energy density in Li-ion batteries.

**Approach.** Parameters needed for mesoscale modeling of grain interior, grain boundary (GB), and electrode-electrolyte interface will be calculated by DFT-based calculations along with Monte Carlo and molecular dynamics simulations. The calculations will be used to determine properties of the electrode with the SE as well as in GB regions of the SE. This will include calculations of structure, stability, ionic conductivity, Young's modulus, fracture toughness, exchange current density, and other properties.

**Out-Year Goals.** The out-year goals of this work are to calculate other properties such as fracture toughness and include other SSEs and coatings in the multiscale modeling.

**Collaborations.** This project collaborates with Y. Cui at Stanford University.

### Milestones

1. Determine the stable phase of  $\text{Li}_7\text{P}_3\text{S}_{11}$  (LPS) amorphous/disordered glass-ceramic SSE and S-C cathode /  $\text{Li}_7\text{P}_3\text{S}_{11}$  interface. (Q1, FY 2022; Completed)
2. Conduct *ab initio* molecular dynamics (AIMD) study of an electrochemical interface between S-C cathode / amorphous LPS interface. (Q2, FY 2022; Completed)
3. Investigate Li-ion transport of the S-C cathode / amorphous LPS interface. (Q3, FY 2022; Completed)
4. Compute the exchange current density associated with charge transfer from amorphous LPS glass-ceramic SSE to the S-C cathode. (Q4, FY 2022; Completed)

## Progress Report

This quarter, the team computed the exchange current density associated with charge transfer from an amorphous LPS used in glass-ceramic SSEs to a S-C cathode. The activation energy barrier associated with the transfer of lithium ions from the amorphous LPS SEs to the C-S cathodes was calculated last quarter through the AIMD technique. Depending on the type of carbon framework, whether it is graphene type or carbon-nanotube (CNT) type, the energy barriers for lithium transport can be different. For example, AIMD calculations revealed that during operation at elevated temperatures ( $T > 1000$  K), the activation energy for charge transfer at LPS/graphene-S interface is 0.42 eV, whereas the energy barrier for LPS/CNT-S interface is  $\sim 0.48$  eV. This quarter, they used the climbing image nudged elastic band (cNEB) method, and the energy barrier for lithium transport at room temperature from amorphous LPS to the C-S cathode is  $\sim 0.58$  eV and 0.905 eV, if CNT and graphene type carbon are used, respectively. The corresponding jumping frequencies for lithium transport from LPS to the C-S cathode are also estimated using the transition state theory. The red circles shown in the right axis of Figure 94 denote the calculated jumping frequencies, which increase with increasing energy barrier; however, the overall magnitude is not much different.

The exchange current densities ( $i_0$ ) are estimated from the energy barriers ( $E_a$ ) and jumping frequencies ( $\nu$ ), as shown in the expression below:

$$i_0 = F\nu \exp(-E_a/k_B T) \cdot \text{sqrt}(c_{\text{Li}_7\text{P}_3\text{S}_{11}} \cdot c_{\text{Li}_2\text{S}}) \quad (1)$$

where,  $F$  denotes the Faraday constant,  $k_B$  is the Boltzmann's constant,  $T$  is temperature (assumed to be  $\sim 300$  K),  $c_{\text{Li}_7\text{P}_3\text{S}_{11}}$  ( $\sim 36300$  mol/m<sup>3</sup>) is the concentration of lithium in the SE domain, and  $c_{\text{Li}_2\text{S}}$  ( $\sim 3800$  mol/m<sup>3</sup>) indicates the concentration of lithium in the lithium sulfide discharge product. The final dimension of the exchange current density is current per unit area. The black squares along the left axis of Figure 94 indicate the estimated exchange current densities, which decrease exponentially with increasing energy barrier (note the left y-axis in Figure 94 is in log scale).

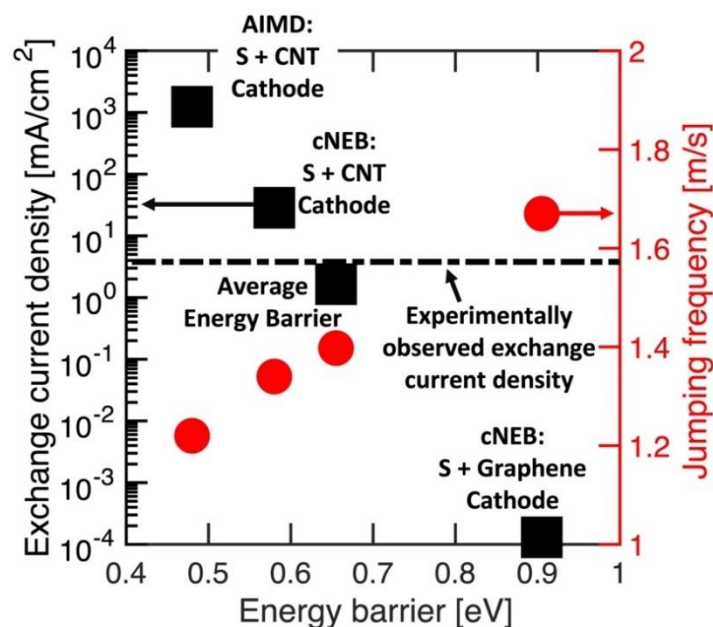


Figure 94. Exchange current density (black squares along left axis) and jumping frequencies (red circles along right axis) for different energy barriers, which is demonstrated along the x-axis. *Ab initio* molecular dynamics calculations reveal smaller energy barriers ( $\sim 0.48$  eV), which lead to larger exchange current densities ( $\sim 10^3$  mA/cm<sup>2</sup>). Climbing image nudged elastic band (cNEB) calculations provide relatively higher energy barrier,  $\sim 0.58$  eV for CNT+S cathode and 0.905 eV for graphene+S cathodes. The exchange current densities follow a similar trend with higher energy barrier providing a smaller magnitude of the exchange current density. The experimentally observed exchange current density between Li<sub>7</sub>P<sub>3</sub>S<sub>11</sub> and C-S cathode is  $\sim 3.8$  mA/cm<sup>2</sup>, which is shown by the black dashed line. The average energy barrier ( $\sim 0.655$  eV) leads to the best correlation with experimental results. Jumping frequencies increase with increasing energy barrier, but their magnitude is similar.

The experimentally observed exchange current density at the interface between LPS SE and C-S cathode is extracted from existing literature,<sup>[1]</sup> which provides a value of 3.8 mA/cm<sup>2</sup> and is depicted by the black dashed horizontal line in Figure 94. It is evident that the energy barrier estimated by neither the AIMD nor the cNEB techniques provides exchange current densities that correlate well with the experimental observations. Rather, the averaged energy barrier demonstrates the best correlation with experiments, which indicates a possible mixture of CNT and graphene type phases within the carbon cathode backbones. This estimation of exchange current density from the energy barrier predicted by atomistic calculations completes this quarter's milestone.

#### Reference

- [1] Han, Q., et al. "Outstanding Cycle Stability and Rate Capabilities of the All-Solid-State Li-S Battery with a Li<sub>7</sub>P<sub>3</sub>S<sub>11</sub> Glass-Ceramic Electrolyte and a Core-Shell S@BP2000 Nanocomposite." *Journal of Materials Chemistry A* 7 (2019): 3895–3902. doi: <https://doi.org/10.1039/C8TA12443D>.

### Patents/Publications/Presentations

The project has no patents, publications, or presentations to report this quarter.

## Task 3.6 – First-Principles Modeling of Cluster-Based Solid Electrolytes (Puru Jena, Virginia Commonwealth University)

**Project Objective.** The objective of the project is to use cluster-ions, which are stable atomic clusters that mimic the chemistry of individual atoms, as the building blocks of new solid electrolytes (SEs) for Li-ion batteries and the corresponding battery system. The advantages of using cluster-ions to replace elemental ions is that the size, shape, and composition of the former can be tailored to achieve higher superionic conductivity, electrochemical stability, and charge transfer across the solid-state ions than the conventional materials. More specifically, the goal is to develop superior SEs based on cluster-ions and to model these SEs and their interfaces with electrodes, especially with the Li-metal anode, for successful integration into high-performance solid-state batteries (SSBs) for electric vehicles (EVs). The team will model and screen cluster-based solid electrolytes (CSEs) that, compared to conventional SEs, have low activation energies, practical room-temperature ionic conductivities, wide electrochemical stability windows, and desired mechanical properties that, for example, can inhibit the Li-metal anode dendrite growth. They will provide a fundamental understanding of the ionic conduction mechanism in the newly developed CSEs and will identify means to further improve property metrics via chemical and defect engineering. The team will model the interfacial properties, such as the structural, chemical, electrochemical, and ion/charge transfer properties, between the CSEs and electrodes at the atomic level, as well as find the interfacial coating materials with desired properties. Based on accumulated data from modeling, they will establish links between the basic parameters of the cluster-ions and the bulk/interface properties, which can directly guide experiments. Meanwhile, the team will work closely with experimentalists in the BMR Program to complement the project's theoretical efforts and to guide them in focused development of the predicted CSEs and the interfaces.

**Project Impact.** The proposed project will open a new avenue for guiding experiments in the synthesis of SSBs equipped with CSEs and capable of operating over a wide temperature range. Modeling and understanding of the ionic conduction of CSEs and their interfacial properties with electrodes, especially with Li-metal anode, will enrich current battery science and also train the future workforce in SSB development for next-generation EVs by supporting postdoctoral fellows.

**Approach.** This project will employ multiscale theoretical methods and computational techniques.

**Out-Year Goals.** The out-year goals involve modeling development of new CSE materials and database.

**Collaborations.** The team is working with J. Nanda of SLAC Stanford Battery Research Center (formerly of Oak Ridge National Laboratory), Y. Wu of Ohio State University, and D. Mitlin of University of Texas, Austin, on SEs.

### Milestones

1. Complete phase analysis for interfaces between the CSE and electrodes. (Q1, FY 2022; Completed)
2. Model structural properties of CSE interfaces. (Q2, FY 2022; Completed)
3. Model chemical/electrochemical and transport properties of CSE interfaces. (Q3, FY 2022; Completed)
4. Identify potential coating materials, and model electrolyte-coating-electrode interfaces. (Q4, FY 2022; Completed)

## Progress Report

This quarter, the team has selected the coating materials to stabilize the interfaces between CSEs and the electrodes, in particular, the Li-metal anode. This is first done using phase diagram and reactivity analyses, and then, using explicit interface modeling at room temperature. The results show that the selected coating materials, including  $\text{Li}_2\text{S}$  and  $\text{Li}_3\text{PO}_4$ , can stabilize the CSE interfaces.

It is found that, unlike the CSEs containing mono-anion clusters  $\text{BH}_4^-$ ,  $\text{CN}^-$ , and  $\text{BF}_4^-$ , the SEs containing the  $\text{SCN}^-$  cluster are not stable against Li-metal anode due to the breaking-up of the cluster to sulfur and C-N, as shown in Figure 95. Figure 95a shows the modeled structure after 20 ps simulation at room temperature (300 K). The original Li-metal phase is clearly destroyed in contact with the SE. The highlighted area (in yellow) shows that some  $\text{SCN}^-$  clusters are broken into CN clusters and individual sulfur, which are in turn migrating into the lithium metal. The cluster completeness analysis in Figure 95b shows that, besides the known reduction of phosphorus and the P-S bond breaking of the argyrodite,  $\text{SCN}^-$  clusters will indeed break into sulfur and CN.

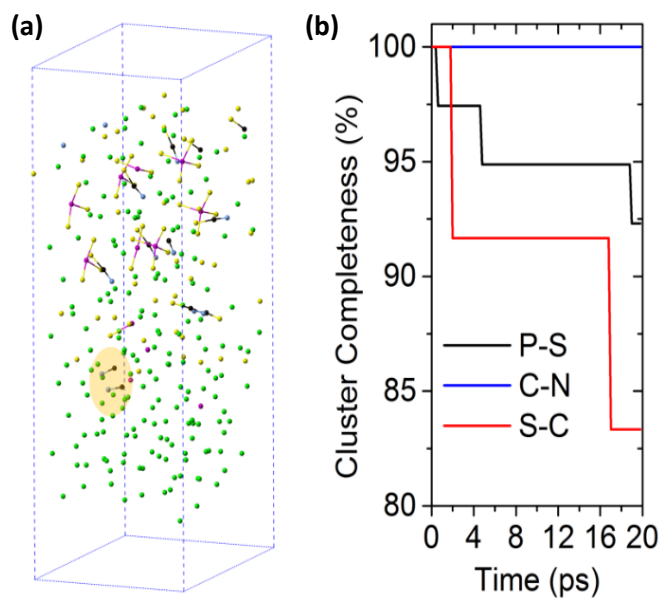


**Figure 95.** (a) Model structure of the  $\text{Li}_6\text{PS}_5(\text{SCN})$ -Li interface from the simulation at 300 K. (b) Bond completeness for the clusters against the simulation time.

The team found that  $\text{Li}_2\text{S}$  can serve as a coating layer to stabilize the  $\text{Li}_6\text{PS}_5(\text{SCN})$ -Li interface. Phase and reactivity analysis under the thermodynamically equilibrium condition predicts that  $\text{Li}_2\text{S}$  is stable against lithium metal, as shown in Figure 96a. To see if the SE  $\text{Li}_6\text{PS}_5(\text{SCN})$  is stable against  $\text{Li}_2\text{S}$ , the team conducted explicit modeling of the  $\text{Li}_6\text{PS}_5(\text{SCN})$ - $\text{Li}_2\text{S}$  interface using coherent interfacial models, with different terminal atomic groups in contact with  $\text{Li}_2\text{S}$ . Simulations based on these interfacial models show that  $\text{Li}_6\text{PS}_5(\text{SCN})$  is stable against  $\text{Li}_2\text{S}$  without any reactions. Figure 96b-c shows that both phases will remain intact at the interface, and the  $\text{SCN}^-$  anion clusters will not break. The  $\text{PS}_4^{3-}$  clusters from the argyrodite component will be also stable, regardless of the different terminal groups in contact with  $\text{Li}_2\text{S}$ . Further radial distribution function analyses on P-S, C-S, and C-N pairs show that crystalline phases and the long-range structures of the active materials at the interface are stable.

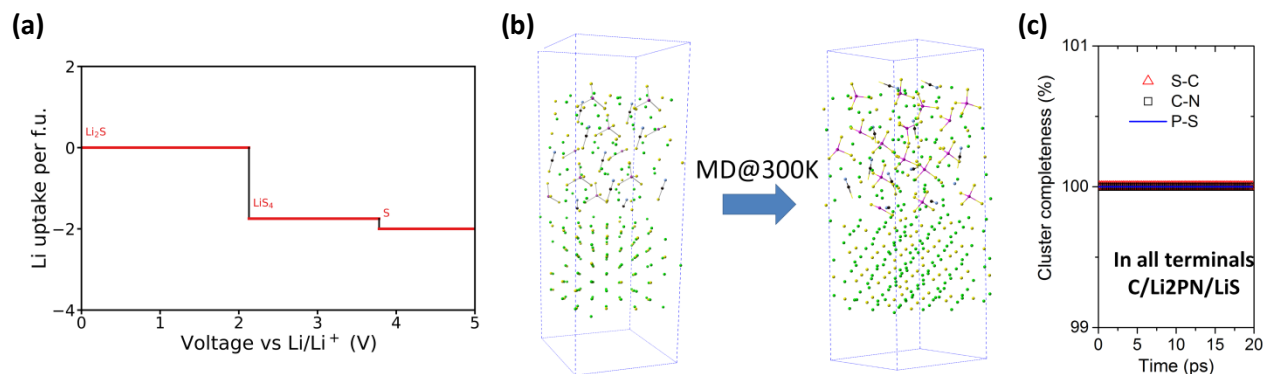


Figure 96. (a) Li-uptake plot of Li<sub>2</sub>S against the voltage. (b) Modeled structures at the Li<sub>6</sub>PS<sub>5</sub>(SCN)-Li<sub>2</sub>S interface before and after the simulation run. (c) Analysis on cluster completeness of the interfacial models with different terminal groups.

The team also found that Li<sub>3</sub>PO<sub>4</sub> can serve as the coating material to stabilize the SE-electrode interfaces for all the CSEs, according to the phase diagram analysis, reactivity predictions, and explicit interface simulations based on the interfacial model built in Table 5.

Table 5. Coherent interfacial models built for the cluster-based solid electrolytes and coating Li<sub>3</sub>PO<sub>4</sub>. In each case, surfaces (according to the miller indices hkl) are chosen due to the minimum matching area (MA) between the solid electrolyte and Li<sub>3</sub>PO<sub>4</sub>. The strain at the interface is measured by the von Mises strain. The number of formula units (FU) and the thickness (in atomic layers) of the solid electrolyte and Li<sub>3</sub>PO<sub>4</sub> are given.

Materials	hkl	MA (Å <sup>2</sup> )	von Mises Strain	Thickness (layer)	FU	Terminal	Li <sub>3</sub> PO <sub>4</sub>	
							hkl	Thickness (layer)
Li <sub>6</sub> PS <sub>5</sub> (BH <sub>4</sub> )	(110)	90.57	0.020	5	10	H <sub>2</sub>	(110)	5
Li <sub>6</sub> POS <sub>4</sub> (SH)	(110)	232.71	0.017	5	20	LiHO	(100)	3
Li <sub>6</sub> PS <sub>5</sub> (CN)	(110)	314.25	0.017	5	20	LiCS <sub>2</sub>	(100)	3
Li <sub>6</sub> PS <sub>5</sub> (SCN)	(100)	89.30	0.024	5	10	S	(110)	5
Li <sub>6</sub> PS <sub>5</sub> (BF <sub>4</sub> )	(110)	162.30	0.012	4	12	LiF	(101)	5

They also studied the link between the intrinsic properties of the individual clusters and the bulk properties of the corresponding CSEs, by using unsupervised clustering of machine learning. Initial results suggest that there is certain correlation between the ionic radius, electron affinity and microstructure of the cluster, and the activation energy of the bulk CSE. The team is exploring the possibility of including new descriptors/features for the cluster to possibly improve clustering.

## Patents/Publications/Presentations

The project has no patents, publications, or presentations to report this quarter.

## Task 3.7 – Predictive Engineering of Interfaces and Cathodes for High-Performance All-Solid-State Lithium-Sulfur Batteries (Badri Narayanan, University of Louisville)

**Project Objective.** The primary project goal is to leverage data-driven methods and machine-learning (ML) strategies to develop accurate multiphysics models for all-solid-state Li-S battery (ASSLSB) materials that can capture electrochemical and transport phenomena over atomic-to-mesoscopic length/timescales; these models will be rigorously validated by synthesis and advanced characterization experiments. The team will leverage the predictive power of these models, alongside synthesis/characterization experiments and battery fabrication, to address longstanding issues at the electrode/electrolyte interfaces in ASSLSBs. The project’s proposed technology involves the following: (1) halide-doped solid sulfide electrolytes that can concurrently provide high  $\text{Li}^+$  ion conductivity and suppress dendrite growth; (2) novel mesoporous cathode composed of interconnected carbon nano-cages co-infiltrated with sulfur and sulfide electrolyte, which hold potential to allow high sulfur loading and optimal ion/electron pathways; and (3) functionalization of sulfide electrolyte with ionic liquids (ILs) to improve physical contact and minimize impedance at the cathode electrolyte interphase (CEI).

**Project Impact.** ASSLSBs remain far from commercialization due to poor understanding of fundamental electrochemical/chemical and transport processes that occur at the interfaces, especially at atomic-to-mesoscopic scales. Successful development of proposed predictive models (at multiple scales) will bridge this knowledge gap and will advance fundamental understanding of reaction chemistry, kinetics, charge transfer, and dendrite growth at electrified solid-state ions. This will enable predictive design of effective strategies to mitigate interfacial problems in ASSLSBs, including poor interfacial contact, interfacial impedance to  $\text{Li}^+$  ion transport, and poor electron/ion conduction within cathodes. Ultimately, the fundamental knowledge gained will lead to development of high-performance ASSLSBs that meet U. S. Department of Energy targets of specific energy (that is, 350 Wh/kg @C/3), sulfur loading (that is, > 6 mg/cm<sup>2</sup>), and high cycle life (that is, 1000).

**Approach.** The project brings together innovative solutions in multiscale materials modeling, electrolyte synthesis, fabrication of cathode architecture, and electrolyte functionalization to overcome the issues at electrode/electrolyte interfaces in ASSLSBs. The central idea is to employ a data-driven and ML-based approach to develop accurate multiphysics battery models at atomic-to-mesoscopic scales. This approach overcomes critical problems with existing model development methods by foregoing the need for pre-defined functional forms, introducing deep-learning technique to describe reactivity, and employing optimization methods that do not require human intuition. Multiscale simulations based on the newly developed models will provide insights into electrochemical phenomena at electrode/electrolyte interfaces.

**Out-Year Goals.** In Year 3, the goal is to optimize the composite cathode, functionalize CEI, and understand interfacial reactions to design ASSLSBs with high-sulfur loading (that is, > 4 mg/cm<sup>2</sup>) and good capacity retention (that is, ~ 1000 mAh/g, 100 cycles @C/10).

**Collaborations.** The team collaborates with the groups under A. Ngo and L. A. Curtiss at Argonne National Laboratory for quantum simulations of battery systems; they plan to collaborate with J. Nanda at Oak Ridge National Laboratory for advanced spectroscopic *in situ* characterization of interfaces.

### Milestones

1. Optimize cathode architecture to achieve good sulfur utilization at high sulfur loading. (Q1, FY 2022; Completed)
2. Develop composite cathodes and optimize CEI to achieve good electrochemical performance at high sulfur loading using insights from simulations and experiment. (Q2, FY 2022; Completed)

- Utilize reactive molecular dynamics and advanced sampling to gain insights into defect chemistry, microstructural evolution, and interfacial processes. (Q3, FY 2022; Completed)
- Fabricate batteries that meet performance metrics. (Q4, FY 2022; Completed)

## Progress Report

This quarter, the team employed a combination of density functional theory (DFT) calculations, liquid-based synthesis, and characterization experiments to (1) develop solid-state argyrodite sulfide electrolytes doped with I/F that show high  $\text{Li}^+$  ion conductivity alongside excellent electrochemical stability against Li-metal, and (2) improve the cathode formulation to enhance the extent of sulfur utilization in composite sulfur cathodes at high sulfur loading.

### Development of Highly Conductive Iodine and Fluorine Dual-Doped Argyrodite Sulfide Electrolyte for Li-Metal Batteries

The argyrodite-class  $\text{Li}_7\text{PS}_6$  sulfide electrolyte and its halogen-doped derivatives  $\text{Li}_6\text{PS}_5\text{X}$  ( $\text{X} = \text{Cl}, \text{Br}, \text{I}$ ) have received attention owing to their high Li-ion conductivity (among solid-state materials), and tunable interfacial stability against lithium metal. In particular, the halide dopants are known to introduce anion site-disorder by partially replacing the  $\text{S}^{2-}$  ions in  $4a/4d$  crystallographic sites; such disorder can introduce facile pathways for  $\text{Li}^+$  hops and, in turn, enhance  $\text{Li}^+$  ion conduction by 3-4 times that for pristine  $\text{Li}_7\text{PS}_6$ . More importantly, the halogen dopants (particularly fluorine) can produce a stable solid electrolyte interphase (SEI) against lithium metal, which enhances electrochemical stability against lithium metal, as shown by their work in Year 1 on F- and Cl- doped sulfide electrolytes. However, previous solid-state synthesis works have shown that I-doped argyrodite possesses  $\text{Li}^+$  conductivity (1-2 orders of magnitude lower than its Cl/Br counterparts) due to lack of disorder in its crystal structure; specifically, unlike Cl/Br, I anions do not coinhabit both the  $4a$  and  $4d$  sites, preferring to reside only in the former. In this work, the team introduced disorder in I-doped argyrodites using their liquid-phase synthesis method (developed in Year 1) in two ways: (a) heat-treatment schedule that causes segregation of I-, and (b) dual-doping with I<sup>-</sup> and F<sup>-</sup> anions to achieve favorable anion site-disorder.

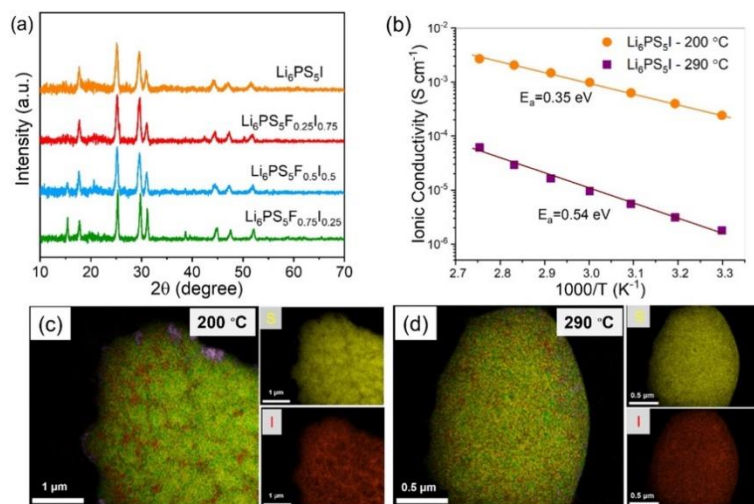


**Figure 97. Solvent-based synthesis of I- and F- doped argyrodite electrolytes. (a) X-ray diffraction patterns for as-synthesized  $\text{Li}_6\text{PS}_5\text{I}$ ,  $\text{Li}_6\text{PS}_5\text{F}_{0.25}\text{I}_{0.75}$ ,  $\text{Li}_6\text{PS}_5\text{F}_{0.5}\text{I}_{0.5}$ , and  $\text{Li}_6\text{PS}_5\text{F}_{0.75}\text{I}_{0.25}$  indicating high phase purity of the argyrodites. (b) Arrhenius plots of solvent synthesized  $\text{Li}_6\text{PS}_5\text{I}$  after two different heating treatment temperatures (200°C and 290°C). Transmission electron microscopy elemental mapping of synthesized  $\text{Li}_6\text{PS}_5\text{I}$  argyrodite after heating treatment at (c) 200°C and (d) 290°C. Note: sulfur in yellow; iodine in red; and oxygen in pink.**

### Heat Treatment Schedule to Introduce Structural Disorder

The team synthesized  $\text{Li}_6\text{PS}_5\text{I}$ ,  $\text{Li}_6\text{PS}_5\text{F}_{0.25}\text{I}_{0.75}$ , and hybrid-doped  $\text{Li}_6\text{PS}_5\text{F}_{0.25}\text{I}_{1-x}\cdot(x-0.25)\text{LiF}$  ( $x = 0.5, 0.75$ ) argyrodites using their solvent-based approach (Figure 97). The X-ray diffraction (XRD) patterns of the as-synthesized sulfide electrolytes show characteristic diffraction peaks at  $2\theta = 17.7^\circ, 25.2^\circ, 29.6^\circ,$  and  $31.0^\circ$ ,

corresponding to the planes of (200), (220), (311), and (222) in argyrodite structure, indicating high phase purity (especially in I-only case) (Figure 97a). Notably, while synthesized  $\text{Li}_6\text{PS}_5\text{I}$  is a pure phase argyrodite, the addition of 0.25 mols of F to synthesize  $\text{Li}_6\text{PS}_5\text{F}_{0.25}\text{I}_{0.75}$  appears to make it difficult for iodine to fully incorporate, as small secondary peaks corresponding to  $\text{LiI}$  can be observed at  $2\theta = 42.4^\circ$  and  $50.2^\circ$  (Figure 97a). With higher F-doping content, the  $\text{LiI}$  peaks disappear. Instead, a minor impurity peak at  $2\theta = 39.1^\circ$  starts to appear, which is attributed to a small amount of secondary  $\text{LiF}$  phase (Figure 97a). Nevertheless, at any composition, the structure of the as-synthesized sample is primarily argyrodite. This is further evidenced by Raman spectroscopy; for all compositions, they observed strong bands around  $420\text{ cm}^{-1}$ , with smaller bands appearing at  $575\text{ cm}^{-1}$  and  $200\text{ cm}^{-1}$ , both associated with  $\text{PS}_4^{3-}$  tetrahedra. To understand the effect of heat-treatment schedule on the structure (and consequent  $\text{Li}^+$  conductivity), the team synthesized  $\text{Li}_6\text{PS}_5\text{I}$  using two heat treatment temperatures ( $200^\circ\text{C}$  and  $290^\circ\text{C}$ ). At room temperature, the  $290^\circ\text{C}$ -treated  $\text{Li}_6\text{PS}_5\text{I}$  sample shows an ionic conductivity of  $1.8 \times 10^{-6}\text{ S cm}^{-1}$ , which is consistent with previous reports from solid-state synthesis methods (Figure 97b). In contrast, lower heat treatment temperature at  $200^\circ\text{C}$  results in  $\text{Li}_6\text{PS}_5\text{I}$  displaying a high ionic conductivity of  $2.5 \times 10^{-4}\text{ S cm}^{-1}$  at room temperature, which is among the highest values for  $\text{Li}_6\text{PS}_5\text{I}$  argyrodite reported thus far (Figure 97b). This conductivity is even higher than that reported for solid-synthesized  $\text{Li}_6\text{PS}_5\text{I}$  after additional high-energy ball-milling treatment ( $2 \times 10^{-4}\text{ S cm}^{-1}$ ), which introduces extra structural disorder. In addition, the  $200^\circ\text{C}$ - $\text{Li}_6\text{PS}_5\text{I}$  not only exhibits higher ionic conductivity than the  $290^\circ\text{C}$ -sample in the temperature range of  $30\text{--}90^\circ\text{C}$ , but also shows much lower activation energy ( $0.34\text{ eV}$  versus  $0.55\text{ eV}$ , respectively). Transmission electron microscopy was performed to analyze the morphology and elemental distribution of  $\text{Li}_6\text{PS}_5\text{I}$  samples after  $200^\circ\text{C}$  and  $290^\circ\text{C}$  heat treatments, respectively (Figure 97c-d). Compared to the homogenous distribution of sulfur and iodine elements for the  $290^\circ\text{C}$ -sample (Figure 97d), the  $200^\circ\text{C}$ -treated sample displays a mismatched distribution with iodine aggregating at the edges, while the sulfur remains in the inner region. Such elemental distribution is considered to contribute to the observed fast ion transport in  $200^\circ\text{C}$ -treated  $\text{Li}_6\text{PS}_5\text{I}$ , similar to the reduced impedance at grain boundaries seen in previous reports.

### Dual-Doping with Fluorine and Iodine to Introduce Anion-Site Disorder

The team performed DFT calculations to elucidate the energetics of anion-disorder during dual doping of argyrodite with F and I (Figure 98). They found that  $\text{Li}_6\text{PS}_5\text{I}$  exhibits a perfect argyrodite structure with face-centered cubic symmetry (space group:  $Fm\bar{3}m$ ) consisting of  $\text{PS}_4^{3-}$  building blocks (Figure 98a), and iodine atoms at the corners/face centers (that is,  $4a$  Wyckoff sites). The sulfur atoms belonging to the  $\text{PS}_4^{3-}$  occupy the Wyckoff  $16e$  sites, while other sulfur occupies the  $4d$  sites. The lithium atoms partially occupy the  $48h/24g$  positions, which form a cage-like structure around the S-atoms placed at the  $4d$  sites (Figure 98a) consistent with previous DFT work. Notably, their DFT-predicted lattice parameter ( $10.3\text{ \AA}$ ) is close (within 2%) to those obtained from their XRD measurements in Figure 97a ( $10.12\text{ \AA}$ ). Li-ion transport through such an atomic structure has been reported to consist of three types of jumps: (1) localized jumps between adjacent  $48h$  sites (doublet), (2) jumps within a cage centered at a given S/X atom at  $4d$  site, and (3) inter-cage jumps, the latter

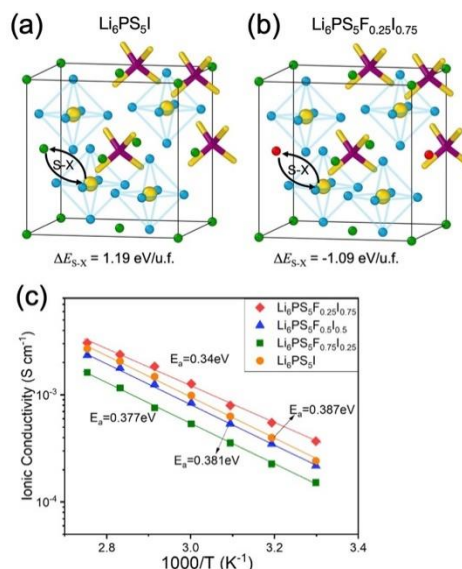


**Figure 98.** Anion-disorder in dual-doped argyrodite solid electrolytes and the impact on Li-ion conduction. Atomic-scale structures of (a)  $\text{Li}_6\text{PS}_5\text{I}$  and (b)  $\text{Li}_6\text{PS}_5\text{F}_{0.25}\text{I}_{0.75}$  optimized by density functional theory. In each panel, the energy change associated with swapping a sulfur atom at  $4d$  site (cage-center) with a halogen [iodine in panel (a), and fluorine in panel b)] are indicated. The lithium, phosphorus, sulfur, fluorine, and iodine atoms are depicted as blue, purple, yellow, red, and green spheres, respectively. (c) Arrhenius plots ( $30\text{--}90^\circ\text{C}$ ) of  $\text{Li}_6\text{PS}_5\text{I}$  and hybrid-doped argyrodites obtained from electrochemical impedance spectroscopy measurements.

of which is the primary bottleneck for Li-ion mobility. As opposed to the fast ion transport in  $\text{Li}_6\text{PS}_5\text{Cl}$  and  $\text{Li}_6\text{PS}_5\text{Br}$  argyrodites,  $\text{Li}_6\text{PS}_5\text{I}$  has been reported to exhibit poor ionic conductivity due to the absence of anion site disorder. Consistent with these reports, the team's DFT calculations show that inducing an anti-site disorder by swapping a pair of sulfur and iodine between  $4d$  and  $4a$  is significantly endothermic  $\sim 1.19$  eV/u.f. (Figure 98a). Such energetic penalty against anion-disorder in  $\text{Li}_6\text{PS}_5\text{I}$  can be attributed to the substantially larger size of I ( $2.06$  Å) as compared to  $\text{S}^{2-}$  ( $1.85$  Å). On the other hand, in F/I co-doped  $\text{Li}_6\text{PS}_5\text{F}_{0.25}\text{I}_{0.75}$ , an anti-site defect involving sulfur and fluorine atoms (with smaller ionic radius:  $1.33$  Å) is thermodynamically favorable, with the anion-disordered structure being  $\sim 1.09$  eV/u.f. lower in energy than the pristine case (Figure 98b). This energetic preference for halogen disorder in F/I co-doped  $\text{Li}_6\text{PS}_5\text{F}_{0.25}\text{I}_{0.75}$  would enhance the frequency of inter-cage hops, owing to the difference in electronegativity between sulfur and fluorine ions, as suggested by previous DFT studies. Indeed, their DFT predictions are consistent with their electrochemical impedance spectroscopy measurements (Figure 98c), which show that the addition of small amounts of F- into the  $\text{Li}_6\text{PS}_5\text{I}$  argyrodite to obtain  $\text{Li}_6\text{PS}_5\text{F}_{0.25}\text{I}_{0.75}$  increases the ionic conductivity at room temperature ( $3.5 \times 10^{-4}$  S  $\text{cm}^{-1}$ ), as compared to  $\text{Li}_6\text{PS}_5\text{I}$  ( $2.5 \times 10^{-4}$  S  $\text{cm}^{-1}$ ). However, additional F-doping content results in slightly slower ion transportation, with  $\text{Li}_6\text{PS}_5\text{F}_{0.25}\text{I}_{0.5} \cdot 0.25\text{LiF}$  and  $\text{Li}_6\text{PS}_5\text{F}_{0.25}\text{I}_{0.25} \cdot 0.5\text{LiF}$  samples showing ionic conductivities of  $2.4 \times 10^{-4}$  S  $\text{cm}^{-1}$  and  $1.5 \times 10^{-4}$  S  $\text{cm}^{-1}$ , respectively. The decreased ionic conductivity is attributed to the increased secondary phase (LiF) content in argyrodite structure (see XRD in Figure 97a).

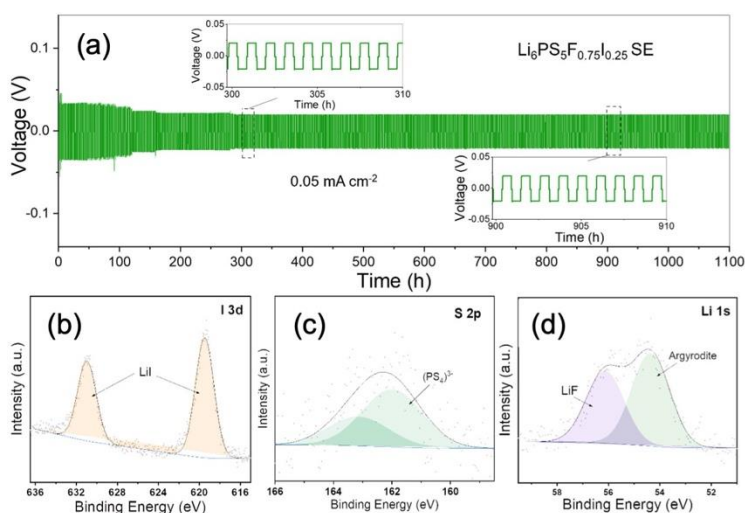


**Figure 99. Electrochemical stability of  $\text{Li}_6\text{PS}_5\text{F}_{0.25}\text{I}_{0.25}$  sulfide electrolyte against Li-metal obtained from cycling performance of Li-symmetric cell. (a) Voltage profiles of  $\text{Li}_6\text{PS}_5\text{F}_{0.25}\text{I}_{0.25} \cdot 0.5$  LiF-based symmetric cell cycling up to 1100 hours ( $0.05$  mA  $\text{cm}^{-2}$ ). X-ray photoelectron spectra of cycled symmetric cell with  $\text{Li}_6\text{PS}_5\text{F}_{0.25}\text{I}_{0.25} \cdot 0.5$  LiF sulfide electrolyte: (b) iodine 3d, (c) sulfur 2p, and (d) lithium 1s.**

The electrochemical stability of  $\text{Li}_6\text{PS}_5\text{I}$  and hybrid-doped argyrodites toward metallic lithium anode was examined by cycling in lithium symmetric cells (Figure 99). The team observed that the polarization voltage of the  $\text{Li}_6\text{PS}_5\text{I}$ -based cell increases from its initial value of  $0.18$  V to  $0.37$  V after 100 cycles, while those containing fluorine showed very stable voltage profiles. Among them, the  $\text{Li}_6\text{PS}_5\text{F}_{0.25}\text{I}_{0.25} \cdot 0.5\text{LiF}$ -based cell shows the lowest polarization voltage at  $0.03$  V, suggesting that the most stable interface is formed between  $\text{Li}_6\text{PS}_5\text{F}_{0.25}\text{I}_{0.25} \cdot 0.5\text{LiF}$  and lithium metal. Such a stable interface is further confirmed by the comparison between the impedance spectra of  $\text{Li}_6\text{PS}_5\text{F}_{0.25}\text{I}_{0.25} \cdot 0.5\text{LiF}$ -based lithium symmetric cell before and after 100 cycles under  $0.05$  mA  $\text{cm}^{-2}$  in which a minor variation of total resistance ( $2,950$  Ω versus  $2,780$  Ω) is observed. Figure 99a presents the long-term cycling stability of the lithium symmetric cell using  $\text{Li}_6\text{PS}_5\text{F}_{0.25}\text{I}_{0.25} \cdot 0.5\text{LiF}$  as sulfide electrolyte, which runs continuously for 1,100 hours without short circuit. The initial polarization of  $\sim 0.03$  V is slightly dropped to  $0.025$  V over the first 150 hours due to interfacial reactions. After this, the formation of stable SEI layer contributes to a stable voltage ( $\sim 0.022$  V) and cycling for the remaining 950 hours. X-ray photoelectron spectroscopy (XPS) was performed on the  $\text{Li}_6\text{PS}_5\text{F}_{0.25}\text{I}_{0.25} \cdot 0.5\text{LiF}$ -based cell after lithium plating/stripping to investigate the chemical compositions and to understand the reactions occurring at the interface. In the XPS spectra of  $\text{Li}_6\text{PS}_5\text{F}_{0.25}\text{I}_{0.25} \cdot 0.5\text{LiF}$  sulfide electrolyte, the doublet peaks for iodine 3d (Figure 99b) at  $619.4$  eV and  $630.5$  eV originated from Li-I bonding, while the peak at  $56.2$  eV for lithium 1s (Figure 99d) is attributed to Li-F bonding. This observation indicates that interfacial reactions between  $\text{Li}_6\text{PS}_5\text{F}_{0.25}\text{I}_{0.25} \cdot 0.5\text{LiF}$  and lithium metal form an SEI layer that contains both LiF and LiI during the long-term

cycling of lithium symmetric cells. Moreover, high F-doping content in  $\text{Li}_6\text{PS}_5\text{F}_{0.25}\text{I}_{0.25}\cdot 0.5\text{LiF}$  results in an increase of interfacial LiF, which has been shown to play a prominent role in both interface stabilization and prevention of lithium dendrites. At the interface between halide-doped argyrodites ( $\text{Li}_6\text{PS}_5\text{X}$ ; X = Br, Cl) and lithium metal, the participation of halide ions  $\text{X}^-$  has been reported to form  $\text{LiX}$  (X = Br, Cl), which contributes to the enhancement of interfacial stability. In this study, the observed behaviors of dual-doped argyrodites suggest that the dopant composition has significant impact on both interfacial reactions and electrochemical stability at the interface. A manuscript based on this work is under review at *Journal of Power Sources*.

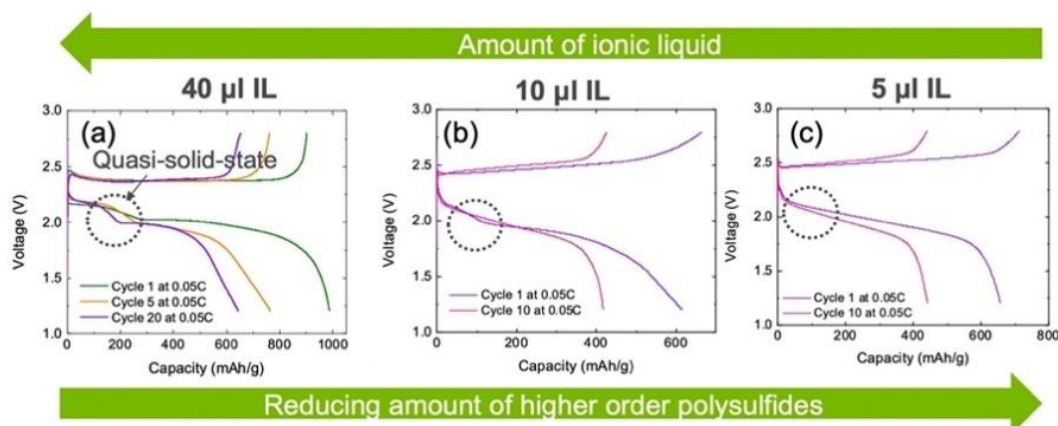


**Figure 100.** Effect of amount of functionalizing ionic liquid (IL) on the discharge profiles for batteries consisting of lithium anode, SP-S cathode with  $4.0 \text{ mg/cm}^2$  loading and 30% sulfide electrolyte, and  $\text{Li}_6\text{PS}_5\text{F}_{0.5}\text{Cl}_2$  electrolyte. Discharge profiles at selected cycles are shown for different amounts of functionalizing IL (LiTFSI in Pyr:DOL(1:3) at 3M) at the cathode-SSE interface at  $30^\circ\text{C}$ , namely, (a)  $40 \mu\text{L}$ , (b)  $10 \mu\text{L}$ , and (c)  $5 \mu\text{L}$ . As the amount of IL decreases, the discharge profile changes from a two-plateau (at  $40 \mu\text{L}$ ) indicative of a quasi-solid-state behavior, to a single slope (at  $5 \mu\text{L}$ ) akin to an all-solid-state Li-S battery.

### Improvement of Cathode Formulation at High Sulfur Loading to Enhance Sulfur Utilization

In previous quarters, the team successfully incorporated sulfide electrolyte ( $\text{Li}_6\text{PS}_5\text{F}_{0.5}\text{Cl}_2$ ) into the cathode (Super-P C-S) at high sulfur loading ( $4 \text{ mg/cm}^2$ ) by pressing it together. This was possible after they learned how to handle the entire battery assembly, including the cathode formulation inside the glovebox. In all cases, cathode containing solid-state electrolyte (SSE) powder (balled milled together) was pressed together with the SSE powder in a stainless-steel pellet die inside the glovebox, and a prescribed amount of IL [lithium bis(trifluoromethanesulfonyl)imide in pyrrolidinium : 1,3-dioxolane (Pyr:DOL, 1:3 at 3 M)] to ensure sufficient wetting. First, they systematically investigated the effect of the amount of functionalizing IL on electrochemical performance of the batteries during cycling for cathodes containing 30%  $\text{Li}_6\text{PS}_5\text{F}_{0.5}\text{Cl}_2$  (Figure 100). At high amount of IL ( $40 \mu\text{L}$ ), the discharge profile indicates two plateaus at  $\sim 2.2 \text{ V}$  and  $\sim 2.0 \text{ V}$ , showing formation of higher-order polysulfides, and is indicative of a quasi-solid-state battery (Figure 100a). As the amount of IL decreases, the two-plateau profile changes to a single-slope behavior, which resembles an all-solid-state battery (Figure 100b-c). They find that  $5 \mu\text{L}$  of IL provides sufficient wetting, while still maintaining a near-all-solid-state-like discharge profile (Figure 100c). The quasi-solid-state behavior in the batteries

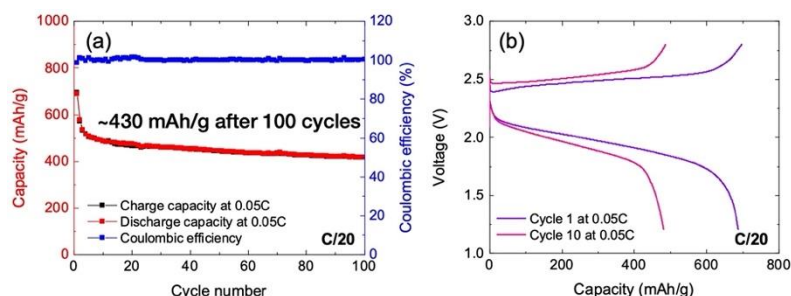


**Figure 101.** Electrochemical cycling performance of batteries consisting of lithium anode, SP-S cathode with  $4.0 \text{ mg/cm}^2$  loading pressed with 25% sulfide electrolyte,  $\text{Li}_6\text{PS}_5\text{F}_{0.5}\text{Cl}_2$  sulfide electrolyte with  $5 \mu\text{L}$  of ionic liquid [LiTFSI in Pyr:DOL(1:3) at 3M] at the cathode – solid-state-electrolyte interface. (a) Capacity variation, and Coulombic efficiency as a function of cycles at  $60^\circ\text{C}$  at C/20. (b) Discharge profiles at selected cycles.

containing a high amount of functionalizing IL affords a higher initial discharge capacity of  $\sim 1000$  mAh/g; however, the capacity fades quickly and yields  $\sim 200$  mAh/g after 100 cycles, possibly due to burn out of the IL. At lower amounts of IL, although the initial discharge capacity reduces to  $\sim 650$  mAh/g, it fades slowly (Figure 100c).

The team optimized the amount of sulfide electrolyte in the cathode, while keeping the amount of IL fixed at  $5 \mu\text{L}$  to further enhance the  $\text{Li}^+$  ion conductivity of the cathode, and consequently, its capacity. They find that the battery with 25% SSE in the cathode showed the best performance, with an initial discharge capacity of  $\sim 700$  mAh/g, and retention of  $\sim 430$  mAh/g after 100 cycles (@C/20) at  $60^\circ\text{C}$  (Figure 101). Indeed, the discharge profiles show a solid-state-like behavior, which shows that the  $5 \mu\text{L}$  of IL is still low enough to suppress formation of higher-order polysulfides (Figure 101b). Interestingly, the capacity fade is appreciable only over the initial 5 cycles (where it drops from  $\sim 700$  mAh/g to  $\sim 480$  mAh/g); thereafter, the capacity remains nearly stable, with a slow drop down to  $\sim 430$  mAh/g at 100 cycles. This indicates that the interphase at the CEI does not form fully in the first few cycles; they are running a few battery tests with slow-rate for the initial discharge, before beginning cycling tests.

Furthermore, the team studied the effect of pressure on initial discharge capacity using a specially designed pressure-controlled split cell (Figure 102, left). Cells with cathode [SP-S : carbon nanotube : SSE (30:45:25), sulfur loading:  $4 \text{ mg/cm}^2$ , 25% sulfide electrolyte],  $5 \mu\text{L}$  of functionalizing IL at CEI, and lithium anode were assembled and tested inside the Ar-filled glovebox using the Autolab (Nova 2.1) system. The battery tests under applied pressures showed that initial discharge capacities increased marginally with applied pressure (up to 20 bar) (Figure 102, right); beyond this pressure, batteries failed due to short-circuit issues. Although initial discharge capacity shows little pressure dependence, at an optimal 10 bar pressure, the plateau of  $\sim 2.1$  V has become more prominent, implying improved reaction forming  $\text{Li}_2\text{S}$ . This shows that the applied pressure facilitates the kinetics of interphase formation at CEI.

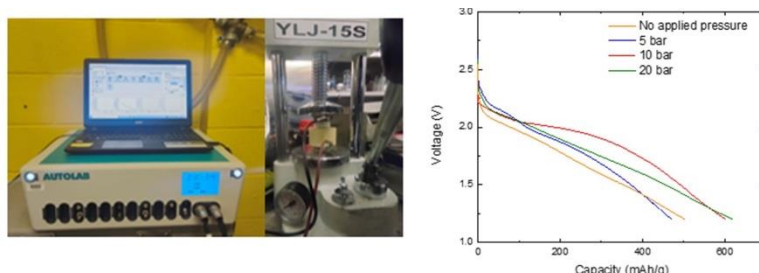


**Figure 102.** Electrochemical cycling performance of batteries consisting of lithium anode, SP-S cathode with  $4.0 \text{ mg/cm}^2$  loading pressed with 25% sulfide electrolyte,  $\text{Li}_6\text{PS}_5\text{F}_{0.5}\text{Cl}_2$  sulfide electrolyte with  $5 \mu\text{L}$  of ionic liquid [LiTFSI in Pyr:DOL(1:3) at 3M] at the cathode – solid-state electrolyte interface under applied pressure. (left) Picture of the specialized cell being tested inside the glovebox under applied pressure. (right) Initial discharge curve at 0.05 C for batteries tested under 0, 5, 10, and 20 bar.

## Patents/Publications/Presentations

### Presentation

- American Chemical Society Fall Meeting, Energy Storage Beyond Li-Ion Batteries, Chicago, Illinois (August 21–25, 2022): “Atomic-Scale Understanding of Ion-Transport and Interfacial Stability in Lithium Argyrodite Electrolytes for Solid-State Lithium-Metal Batteries”; B. Narayanan. Invited.

## Task 3.8 – Predicting the Nucleation and Evolution of Interphases in All-Solid-State Lithium Batteries (Sabrina (Liwen) Wan, Lawrence Livermore National Laboratory)

**Project Objective.** The goal of this project is to develop and apply a suite of new computational tools to predict early-stage formation of metastable interphases in solid-state batteries (SSBs). To achieve this goal, this project focuses on meeting three primary objectives corresponding to different regimes within the early-stage interphase formation: (1) identify chemical motifs for pre-nucleation; (2) predict possible interphase structures; and (3) model the kinetics of interphase formation.

**Project Impact.** Degradation of solid-state electrolyte and formation of undesired secondary interphases at the solid electrolyte/electrode interfaces are some of the key issues that limit SSB technology from practical applications. The computational tools developed in this project will allow modeling of nucleation and formation of interphases with quantum-level accuracy as well as significantly improved efficiency compared to currently available methods. Completion of this project will also provide valuable insights into the correlation between local chemistry and interphase formation, which can be used to inform design of interfacial structures to lower interfacial resistance, and to extend cycling life of SSBs.

**Approach.** The project approach centers on close integration of *ab initio* molecular dynamics (AIMD) simulations, machine learning (ML), and stochastic methods to probe chemistry and nucleation across broad ranges of time and length scales. First, the team will identify chemical motif, which acts as chemical precursor for pre-nucleation based on ML and large-scale AIMD simulations. Second, they will predict possible interphase structures based on stochastic minimizations of population-weighted chemical motifs identified from the molecular dynamics (MD) simulations. Third, they will model the kinetics of interphase formation and evolution using metadynamics and solid-state nudged elastic band (SS-NEB) methods. To test the general applicability of the proposed computational methods, the team considers various commercially viable solid electrolyte (SE) and cathode materials, including cubic  $\text{Li}_7\text{La}_3\text{Zr}_2\text{O}_{12}$  (LLZO) and LiPON SEs, and Li-Co-O (LCO) and Li-Fe-P (LFP) cathodes. These materials also represent a range of degrees of stability arising from their intrinsic properties—in particular, LiPON|LCO, LLZO|LCO, and LLZO|LFP are expected to form stable, less stable, and reactive interfaces, respectively.

**Out-Year Goals.** The future goal is to predict practical strategies either (1) to facilitate formation of the desired interphase that allows for fast  $\text{Li}^+$  diffusion and is stable on cycling, or (2) to suppress formation of undesired interphase to reduce interfacial impedance of all-solid-state batteries.

**Collaborations.** There are no collaborative activities this quarter.

### Milestones

1. Establish a library of meta-stable interphase structures. (Q1 FY 2022; Completed)
2. Identify initial phase transformation pathways. (Q2, FY 2022; Completed)
3. Obtain lowest energy phase transformation pathways. (Q3, FY 2022; Completed)
4. Extract phase transformation kinetics as a function of composition. (Q4, FY 2022; In progress)

## Progress Report

**MD Simulations of LLZO|LCO Interfacial Evolution Using ML Interatomic Potentials.** This quarter, the team further validated the machine-learning force field (MLFF) for LLZO|LCO interface by predicting properties of small LLZO|LCO mixed structures that have not been provided during ML training. They found that the force errors were lower than  $0.3 \text{ eV/\AA}$ . In addition, the radial distribution functions, vibrational spectra, and the diffusivity predicted by their MLFF are similar to those calculated by AIMD simulations. These results imply good generalizability of their MLFF to accurately model the atomic interactions at the highly disordered, heterogeneous LLZO|LCO interfaces. Here, they applied this MLFF to directly probe the initial evolution of LLZO|LCO interface on contact. Figure 103 showcases the atomic structure of LLZO(001)|LCO(104) interface ( $\sim 17,000$  atoms) after 10 ns of large-scale MD simulation at 1500 K. The atomic model has two distinct interfaces with different initial chemical environments, that is, Li/O sufficient and deficient. The Li/O-deficient interface underwent severe structural disordering of LCO near the interface and evidenced cation interdiffusion across the interface. In contrast, the Li/O-sufficient interface shows a separation of Zr/Li (closer to LCO side) and lanthanum (to LLZO side) with relatively less structural disordering. These results highlight the ability of their MLFF to directly probe the atomic evolution of complex interface toward establishing the correlation between chemical configuration and its propensity for degradation.

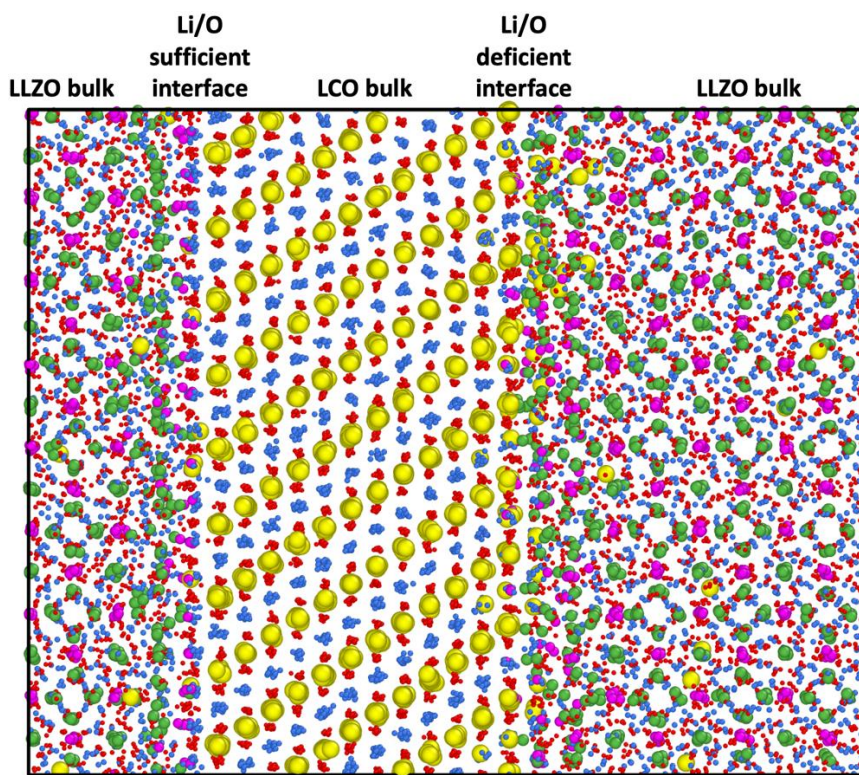


Figure 103. Snapshot of LLZO(001)|LCO(104) interface after 10 ns of large-scale molecular dynamic simulation at 1500 K using the team's recently developed machine-learning force field. The atomic model shows two distinct interfacial regions with different initial chemical compositions. The blue, green, magenta, red, and yellow spheres represent lithium, lanthanum, zirconium, oxygen, and cobalt atoms, respectively.

**First-Principles Predictions of Phase Transformation Kinetics.** Previously, the team has predicted the phase evolution kinetics of  $\text{LaCoO}_3$  using the 10-atom cells from SS-NEB simulations. This quarter, they extended their simulations to the 40-atom cells, which allows them to sample additional atomic configurations with reduced symmetry and compare their relative stabilities under different long-range chemical environments. The

larger system size also provides a more accurate description of the initial nucleation site for secondary phase formation. Using the Basin Hopping approach, the team has identified a number of intermediate states along the phase evolution pathway of  $\text{LaCoO}_3$  following its initial chemical environment observed at the LLZO|LCO interface to the most stable bulk configuration (global minimum). In addition to the  $\text{LaCoO}_3$  composition, they have extended the work to predict the phase evolution kinetics of  $\text{Li}_{0.5}\text{La}_2\text{Co}_{0.5}\text{O}_4$ , which is a new compound that has recently been observed at the LLZO|LCO interface prepared under rapid heating and quenching. The results of comparing both the thermodynamics and kinetics of forming various Li-La-Co-O compounds will provide valuable insight into which phase would be dynamically formed under different experimental conditions and what impact it will exert on Li-ion transport kinetics.

### Patents/Publications/Presentations

The project has no patents, publications, or presentations to report this quarter.

## Task 3.9 – Design of Strain Free Cathode – Solid-State Electrolyte Interfaces Using Chemistry-Informed Deep Learning (Hakim Iddir, Argonne National Laboratory)

**Project Objective.** The main objective of this project is to use state-of-the-art machine learning (ML) techniques and high-performance computing (HPC) to model complex oxide materials that will allow the team to develop cathode / solid electrolyte interfaces that exhibit minimal or no strain as well as provide chemical stability at the interface between the cathode material and the solid-state electrolyte (SSE). A deep understanding and control of the cathode/SSE interface (including its chemical and mechanical stability) is needed to develop an effective solid-state battery (SSB). The active cathode material changes volume during cycling, particularly at high state of charge (SOC). This volume change leads to strained interfaces triggering loss of contact and delamination, and hence reduction/elimination of electron and ion transport pathways. The increased strain could also generate cracks within the SSE, creating new paths for lithium dendrite growth channels. These structural changes degrade the electrochemical performance of the battery. Several strategies have had limited success in alleviating these drawbacks, including mixed SSE, buffer layers between the cathode and the SSE, and dopants to improve chemical stability of the interface. These approaches, although promising, could not resolve issues with both the chemical and mechanical stability of the interface. In this project, the team proposes a new approach that takes advantage of well-established ML techniques and HPC to screen for candidate dopants of high-Ni-content Ni-Mn-Co (NMC) cathodes that would both reduce the volume expansion and the chemical reactivity (mixing) at the interface, with minimum impact on electrochemical performance and energy density of the cathode.

**Project Impact.** Structure-property relationships are at the heart of most fundamental scientific approaches. However, the link between structure and property remains a challenge in the materials science of complex systems, such as the oxides that form battery components. In particular, the chemical and mechanical stability of the cathode-SSE interface presents a challenge to development of SSBs. High-performance density functional theory (DFT) calculations provide the necessary framework to understand such systems. Unfortunately, given the limited number of atoms and time scales accessible by the method, along with the myriad calculations required to achieve satisfactory results, the computational cost of simulating all the possible configurations of a multicomponent oxide is prohibitive. In this work, the team augments the DFT data with ML (especially deep learning) techniques that allow them to access the large system sizes and longer time scales necessary to build thermodynamic models. They focus on understanding the nature of benchmark  $\text{Li}_{1-\alpha}\text{Ni}_{1-x-y-z}\text{Mn}_x\text{Co}_y\text{M}_z\text{O}_2$  structures (M dopant,  $\alpha, x, y, z < 1$ ), their volume change with lithium content, the nature and concentration of the dopants, and chemical stability of the SSE-cathode interface. The DFT and ML approach will provide new cathode compositions that will reduce the strain of the SSE-cathode interface and hence improve its mechanical and chemical stabilities.

In this project, the team aims at developing a methodology that will allow them to explore and expand the configurational space using HPC approaches in a systematic and efficient way. The methodology will encompass DFT, *ab initio* molecular dynamics (AIMD), molecular dynamics (MD), and ML. The methodology will also take advantage of various software already developed at Argonne National Laboratory (ANL) and at other U. S. Department of Energy laboratories (for example, Balsam) to automate, manage, and control the large number of calculations needed to achieve the project goal.

**Approach.** All calculations will be performed by spin-polarized DFT as implemented in the Vienna *ab initio* simulation package (VASP). After geometry optimization within the DFT+U framework, electronic relaxation will be performed using a single-point calculation with the hybrid functional HSE06. For production calculations, they will use the message-passing interface (MPI) parallelized version of VASP.

Exploration of the potential energy surface is needed to predict the structure of solid materials and interfaces. Such calculations are infeasible using MD or DFT calculations alone. Thankfully, the potential energy surface of a system can be represented by the sum of the energies of the local neighborhoods surrounding each atom.

This enables the use of ML surrogate models trained with DFT calculations to capture the energies in local neighborhoods. The input to the ML surrogate must be a unique representation of the system under study. Consequently, the local environment of each ion is described using a local environment descriptor that renders the atomic configuration invariant to rotations, translations, and permutations of the atoms. In recent years, several different descriptors have come to prominence with advantages and disadvantages. Once the ML surrogate is trained, the total energy and forces over all the ions of any structural configuration can be determined. Such information can be used for atomistic simulations, namely, MD and Monte Carlo.

In this project, the team proposes to use the open-source DeepMDkit python/C++ package to construct the ML potential energy surface and force fields. The promise of DeepMDkit in this work is to provide near-DFT accuracy at orders-of-magnitude lower computational expense, comparable to traditional MD simulations. Efficiency in training is facilitated through integration with TensorFlow and MPI / graphics processing unit support.

One of the challenges of developing ML potential energy surface is achieving accurate predicted forces and energies across the entire configurational space, while minimizing the total number of calculations required for training. In recent years, active learning has been highlighted for its ability to target training examples most likely to improve the model quality or to achieve some other objective (that is, maximizing a predicted material property). DP-GEN, an open-source python package based on DeepMDkit, implements a similar active learning scheme with HPC support, and has been employed to construct ML potential energy surface with accuracy approaching DFT and sometimes exceeding embedded atom potential for experimentally measured properties of interest. In this work, the team proposes to leverage DeepMDkit and DP-GEN to efficiently generate ML potential energy surfaces for cathode-electrolyte systems including a variety of dopants.

**Out-Year Goals.** One out-year goal involves developing a DFT-trained ML model on NMC /  $\text{Li}_7\text{La}_3\text{Zr}_2\text{O}_{12}$  (LLZO) interface, ready to use for large screening of new cathodes, SSE compositions, and cathodes/SSE interfaces. A second is to provide fundamental understanding on critical parameters limiting performance and stability of the cathode/SSE interface and hence of the SSB.

**Collaborations.** Project collaborators include J. Croy, C. Johnson, and E. Lee from ANL Chemical Sciences and Engineering Division for the synthesis phase of the project.

### Milestones

1. Determine cationic distribution in  $\text{LiNi}_{0.8}\text{Mn}_{0.1}\text{Co}_{0.1-y}\text{X}_y\text{O}_2$  (NMCX) for X (X = Ti, Zr, Al, Fe, Ca, Mg, Y, W, Nb, B, La). (Q1, FY 2022; Completed)
2. Determine elemental segregation, volume changes, and phase transformation during charging of doped (including fluorine anionic substitution)  $\text{LiNi}_{0.8}\text{Mn}_{0.1}\text{Co}_{0.1}$  (NMC-811) using the developed DFT-trained ML model. (Q2, FY 2022; Completed)
3. Determine doped NMC-811-LLZO interface reactivity and structural stability. (Q3, FY 2022; In progress)
4. Screen for compositions with low interfacial strain, and elemental mixing (NMCX-LLZO). (Q4, FY 2022; In progress)

## Progress Report

### Influence of Proton Defects on Phase Transition at High SOC in Ni-Rich Cathodes

This quarter, the team has studied the effect of dopants on the doped NMC-LLZO interface energies of several configurations, as well as AIMD to explore new possible low energy configurations that could favor elemental mixing at the interface. The results will be reported next quarter. To provide a possible explanation for the experimental observation of the O1 phase at high SOC, they studied the effect of proton defects in the phase transformations at high SOC of Ni-rich materials. This effort has resulted in a paper being submitted for review. The team and others have examined the relative energy of O1 and O3 stacking in NiO<sub>2</sub> with several flavors of DFT. Gradient corrected DFT with van der Waals terms favor O1 stacking, while DFT+U, meta-functionals, and hybrid exchange with van der Waals terms favor O3 stacking. Table 6 contains the lattice constants, volumes, energies, and relative energies for O1 and O3 stacking of NiO<sub>2</sub> calculated with five density functionals and experiments.

**Table 6. NiO<sub>2</sub> cell parameter and energies for different oxygen stacking sequences and density functionals.**

	O1 NiO <sub>2</sub>				O3 NiO <sub>2</sub>				E(O1-O3) (eV/cell)
	a (Å)	c (Å)	Volume (Å <sup>3</sup> )	Energy (eV/cell)	a (Å)	c (Å)	Volume (Å <sup>3</sup> )	Energy (eV/cell)	
Experiment (Ref. [4])	2.822	13.04	89.93						
optB86b-vdW (Ref. [1])	2.808	12.834	87.63	-31.8204	2.806	13.061	89.08	-31.8080	-0.0124
optB86b-vdW+U	2.779	13.082	87.51	-19.6138	2.779	13.200	88.26	-19.6139	0.0001
R2SCAN+D4 (Ref. [2])	2.785	13.119	88.10	-80.5317	2.784	13.218	88.75	-80.5350	0.0033
HSE06+DFTd4 (Ref. [3-4])	2.765	13.253	87.74	-69.0278	2.766	13.238	87.72	-69.0341	0.0063

Although the optB86b-vdW predicts a geometry in reasonable agreement with experiment for structural parameters for layered materials, strong correlation is needed to predict accurate energies with changes in oxidation state associated with charging Li<sub>x</sub>NiO<sub>2</sub>.<sup>[1]</sup> Note that optB86b-vdW+U gives the best agreement with experiment for the c lattice parameter.

R2SCAN+D4 yields a unit cell volume that agrees the best with experiment. All the methods, which include strong correlation, have c lattice parameters that are slightly longer than experiment. All density functionals in Table 6 predict lattice constants within 2% of the experimental lattice constant. DFT correctly ranks the relative energies of phases that differ by less than 10 meV/atom about 80% of the time. The team's results are consistent with perfect crystals of O1 and O3 NiO<sub>2</sub> having essentially the same energy. However, DFT is reliable for larger energy differences, which is the focus of this study.

The team has decided to use the R2SCAN+D4 functional for calculations involving supercells needed for defect calculations and MD. R2SCAN+D4 includes dispersion and predicts the lattice energies of molecular crystals to within 1 kcal/mol. Although R2SCAN+D4 is not as accurate as a nonlocal functional, it is significantly less expensive and approaches the accuracy of hybrid functionals.

The team finds that a proton defect favors O1 stacking over O3 in a Ni<sub>36</sub>O<sub>72</sub> supercell by 90 meV. Figure 104 compares the geometries of proton defects for O1 and O3 stacking of NiO<sub>2</sub>. For O3 stacking, the proton points between two oxygen atoms above the hydroxyl. For O1 stacking, the O-H bond points directly at an oxygen atom in the layer above the hydroxyl. This leads to shorter (1.725 Å) and stronger H-bonds favoring O1 stacking over O3 stacking. Higher proton concentrations are expected to further enhance stability of O1 over O3 phase.

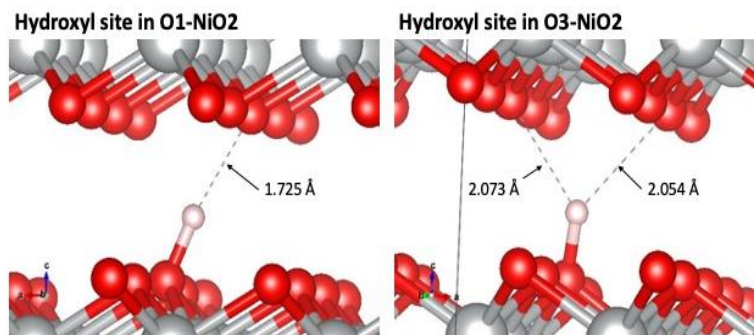


Figure 104. Comparison of a proton defect in O1-NiO<sub>2</sub> (left) and O3-NiO<sub>2</sub> (right).

The team has also carried out AIMD simulations for proton motion between layers of NiO<sub>2</sub>. Figure 105 shows an AIMD trajectory of a proton. The proton is bonded to oxygens in different layers at the start and end of the trajectory. Movement this fast is consistent with small barriers to proton transfer observed in the nudged elastic band calculation.

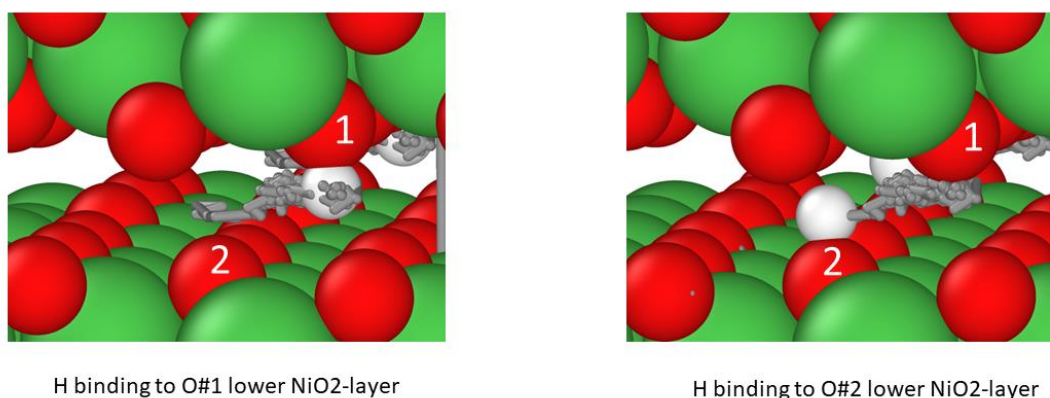


Figure 105. A trajectory for proton motion in NiO<sub>2</sub>.

Reactions with the electrolyte and air generate protons that diffuse into the bulk of NiO<sub>2</sub>. The team predicts that proton defects favor the O1 phase over the O3 phase. They show that protons can diffuse in the space between layers of NiO<sub>2</sub>. Protons combined with oxygen defects drive the transformation from O3 stacking to O1 stacking in NiO<sub>2</sub>. Although O1 stacking may be thermodynamically stable relative to O3 stacking, proton defects and oxygen defects favor O1 stacking and drive the transition from O3 to O1 stacking. Modifications to NiO<sub>2</sub>, which suppress the proton insertion or oxygen loss, will minimize the thermodynamics driving the change from O3 to O1 stacking and prevent structural damage to Li<sub>x</sub>NiO<sub>2</sub> at a high SOC.

### Experimental Validation

In previous reports, the team has shown that dopants with the greatest impact in decreasing volume change on delithiation are preferentially located in the lithium layer. On delithiation, these dopants stay in their octahedral position in the lithium layer, acting as pillars. They found that for calcium, the lithium slab space decreases from 2.66 Å to 2.45 Å, a 7.8% total decrease (compared to 9.8% for the undoped system). For lanthanum, the lithium slab space changes from 2.68 Å to 2.49 Å, a 7.0% total decrease. Last quarter, they were using an ensemble of previously trained machine learning force fields to predict the total energies for a large number of configurations and employ a batch Bayesian optimization strategy to identify a lowest energy structure via DFT.

Based on the results of the dopant screening, they have started experimental validation of the results. They have started the solubility study of lanthanum in NMC-811. The doped material was prepared mixing  $\text{La}(\text{NO}_3)_3$  with  $\text{Ni}_{0.8}\text{Mn}_{0.1}\text{Co}_{0.1}(\text{OH})_2$ ; it was dried overnight in a  $\text{N}_2$  atmosphere, and then calcined at  $720^\circ\text{C}$  for 12 hours in an oxygen atmosphere. They tested 1%, 3%, and 5% target lanthanum compositions. According to preliminary data, the solubility of lanthanum in NMC-811 is less than 1%. A side phase is formed during synthesis. As seen in the X-ray diffraction in Figure 106, the phase  $\text{La}_2\text{Li}_{0.5}\text{M}_{0.5}\text{O}_4$  ( $\text{M} = \text{Ni}, \text{Co}$ ) is present. However, the lattice parameter of the doped material changed with respect to pure NMC-811. This may be evidence of some lanthanum insertion. Refinement of experimental conditions and lattice parameters on delithiation is in progress.

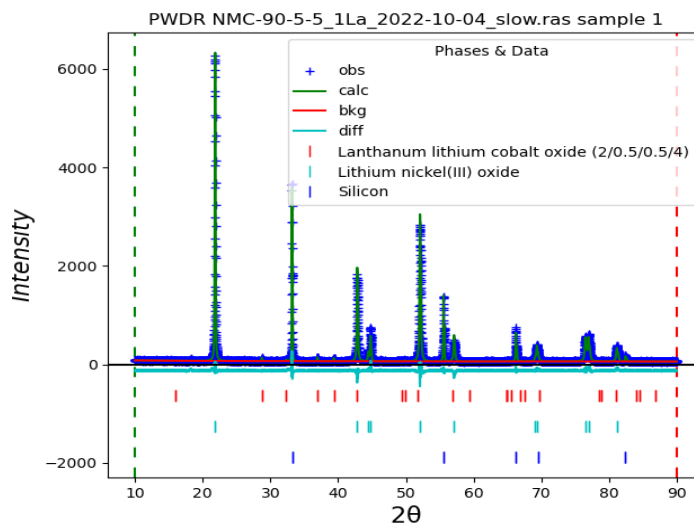


Figure 106. X-ray diffraction of La-doped NMC-811 material.

#### References

- [1] Klimeš, J., D. R. Bowler, and A. Michaelides. “Chemical Accuracy for the van der Waals Density Functional.” *Journal of Physics: Condensed Matter* 22 (2010): 022201.
- [2] Ehlert, S., U. Huniar, J. Ning, J. W. Furness, J. Sun, A. D. Kaplan, J. P. Perdew, and J. G. Brandenburg. “r2SCAN-D4: Dispersion Corrected Meta-Generalized Gradient Approximation for General Chemical Applications.” *The Journal of Chemical Physics* 154 (2021): 061101.
- [3] Krukau, A. V., O. A. Vydrov, A. F. Izmaylov, and G. E. Scuseria. “Influence of the Exchange Screening Parameter on the Performance of Screened Hybrid Functionals.” *The Journal of Chemical Physics* 125 (2006): 224106.
- [4] Seo, D-H., A. Urban, and G. Ceder. “Calibrating Transition-Metal Energy Levels and Oxygen Bands in First-Principles Calculations: Accurate Prediction of Redox Potentials and Charge Transfer in Lithium Transition-Metal Oxides.” *Physical Review B* 92 (2015): 115118.

## Patents/Publications/Presentations

### Publication

- Garcia, J. C., J. Gabriel, N. H. Paulson, J. Low, M. Stan, and H. Iddir. “Insights from Computational Studies on the Anisotropic Volume Change of  $\text{Li}_x\text{NiO}_2$  at High States of Charge ( $x < 0.25$ ).” *Journal of Physical Chemistry C* 125, no. 49 (2021): 27130–27139. doi: <https://doi.org/10.1021/acs.jpcc.1c08022>.

## Task 3.10 – Tackling Solid-State Electrochemical Interfaces from Structure to Function Utilizing High-Performance Computing and Machine-Learning Tools (Shinjae Yoo, Feng Wang, and Deyu Lu, Brookhaven National Laboratory; Nongnuch Artrith and Alexander Urban, Columbia University)

**Project Objective.** This project aims at elucidating the structural evolution and other dynamic properties of the interphases at the solid-state ions (SSIs) in solid-state batteries (SSBs) under processing and electrochemical cycling conditions that strongly impact cell performance. By leveraging synergies of first-principles theory, high-performance computing, machine learning (ML), and computational/experimental spectroscopy, this project involves a comprehensive investigation of solid electrolyte systems and SSIs that may enable the practical use of lithium anodes and high-Ni Ni-Mn-Co cathodes in SSBs. Specific project objectives are as follows: (1) develop realistic atomic-scale structure models of the heterostructural SSIs, (2) determine the impact of structural evolution on stability and transport properties of SSIs, and (3) identify the coating/doping chemistry that may stabilize SSIs during formation and electrochemical cycling.

**Project Impact.** Interfacial properties and the dynamical evolution of interphase structures are crucial for the stability and performance of SSBs. This project will lead to fundamental understanding of current materials limits and will identify key materials parameters for optimizing the performance of SSBs. By corroborating atomic-scale theory with experiment, the project will identify structure–property relationships of the heterostructural SSIs in SSB systems that are relevant for electric vehicles (EVs). The outcomes of this project will therefore accelerate development of high-energy-density, safe SSBs for EVs.

**Approach.** Accurate ML potentials will be trained on an extensive database from density functional theory calculations to simulate the structure evolution and electrochemical properties of the SSIs. Using a second ML model, key physical descriptors will be extracted from electron energy loss spectroscopy and X-ray absorption spectroscopy (XAS) measurements. This spectral fingerprinting will enable the automated interpretation of spectroscopy measurements, thereby bridging between atomistic modeling and experiment. An experimental platform will be developed to integrate experimental/computational spectroscopy and modeling of SSIs. In combination, the two ML models and the spectroscopic data will facilitate the construction of a physics-based model to unravel the structure-property relationships of the SSIs.

**Out-Year Goals.** The project will progress toward establishing dynamic composition-structure-property relationships for interface stability and transport within and across the electrochemical SSIs in SSBs. The ML approach will be further developed to a general model for thermodynamic and transport properties of dynamic heterostructural electrochemical interfaces and will eventually be applied to the practical SSB systems.

**Collaborations.** The project is collaborating with Y. Du at Brookhaven National Laboratory.

### Milestones

1. Determine electrochemical stability of Li-P-S (LPS)/lithium interfaces during cycling through spectroscopy characterization aided by ML, data-analysis, and modeling. (Q1, FY 2022; Completed)
2. Analyze impact of halide-substitution on chemical and electrochemical stabilities of LPS-X (X = Cl, Br, I) systems in contact with lithium metal. (Q2, FY 2022; Completed)
3. Identify key limitations to interfacial stability of LPS and LPS-X systems in contact with lithium metal through combined computational/experimental investigations. (Q3, FY 2022; Completed)
4. Establish doping/coating-based approaches for enabling long cycling stability of the LPS-X based half and full cells at high current density. (Q4, FY 2022; Completed)

## Progress Report

This quarter, the team applied ML methods to analyze the sulfur K-edge X-ray absorption near-edge structure (XANES) in LPS and studied the reaction process of the argyrodite electrolyte  $\text{Li}_6\text{PS}_5\text{Cl}$  (LPSCl) at the atomic scale to gain insights into its stability. They first used unsupervised ML to analyze the spectral features in the simulated LPS sulfur K-edge XANES dataset and associated them with structural descriptors. The established structure-spectrum relationship provides insights into the structural evolution of LPS during delithiation, characterized by atomic-scale local structure changes of sulfur atoms. The distinct phosphorus (see last quarter's report) and sulfur K-edge XANES spectral features identified from the simulated LPS dataset were used as fingerprints to analyze the local environment in LPSCl. Experimentally, they performed XAS measurement of LPSCl during redox reactions at different delithiation stages and analyzed the spectra using simulated phosphorus and sulfur K-edge XAS spectral features obtained from LPS. They conclude that S-S bridging bonds and LiCl are formed during the first delithiation, and that the reactions are partially reversible during the lithiation process. Unlike LPS, the distortion of the  $\text{PS}_4$  tetrahedra in LPSCl is greatly alleviated, which is likely due to the presence of Cl-doping atoms and the formation of LiCl. Their study suggests that the origin of better stability of argyrodite electrolytes may come from the more stable  $\text{PS}_4$  structure.

### Unsupervised Learning Analysis of Sulfur K-edge XANES

Last quarter, the team developed a structural database to study the delithiation process of LPS and reported data-driven phosphorus K-edge XANES analysis. This quarter, they performed a similar analysis of sulfur K-edge XANES data using the developed structural database. Specifically, they performed sulfur K-edge XANES calculations using the Vienna *ab initio* simulation package (VASP) for a total of ~ 8000 sulfur sites in the structural database. The spectral calculations were benchmarked on compounds with known experimental spectra standards (see the second quarter's report). The simulated sulfur XANES spectra were first aligned to the first major peak position and then clustered into six groups via the K-Means algorithm, as shown in Figure 107a-f. In principle, they can choose to use any number of groups in the K-Means algorithm. Six was chosen because the structural descriptors in each cluster can be better interpreted in the material science point of view, and the properties of different clusters can be better differentiated. Figure 107g-i shows the average values of structural descriptors within each cluster. The six clusters are arranged in descending order by lithium stoichiometry.

In Cluster 1, the sulfur sites have an average of three lithium neighboring atoms and no sulfur neighbors. These configurations also have relatively high lithium stoichiometry, suggesting that these sulfur sites are from pristine and slightly delithiated  $\beta$ -LPS. It is important to note that the stoichiometry of a configuration is determined for the whole supercell as an average quantity, and it does not necessarily reflect the number of lithium neighbors at a particular sulfur site in that configuration. In a configuration with low lithium stoichiometry, there could still be sulfur sites with three or two lithium neighbors.

Clusters 2 and 3 contain sulfur sites with an average of two and one lithium neighbor(s), respectively. Similar to Cluster 1, these sulfur sites have no sulfur neighbors. As compared to the spectra of Cluster 1, the main difference is the intensity change at the valley between the first and the second peaks, at ~ 2473 eV. The team has observed a similar feature in their experiments. Figure 107j shows the spectrum of a slightly delithiated LPS sample. The sample was delithiated to 3.4 V, while the fully delithiated sample should be cycled to 5 V. Comparing to the spectrum of pristine LPS, the spectrum of the 3.4 V sample shows an increase in intensity at 2473 eV, as indicated by the arrow.

The spectra of Cluster 4 and 5 exhibit different features from the first three clusters. The spectra show an increase in the intensity of the first major peak. This peak is the origin of the 2473 eV peak observed in the experimental spectra after the first and the second delithiation. The structural descriptors show that S-S bonds start to form (Figure 107h). The distance between sulfur atom and its neighboring phosphorus atom is larger in

Cluster 5 than in Cluster 4, as shown in Figure 107i. Further analysis shows that some sulfur atoms lose their phosphorus neighbors, which corresponds to the formation of  $\text{PS}_3$  structure in the analysis of phosphorus spectra in last quarter's report.

They note two important technical details. First, all the VASP spectra were aligned to the first major peak (the first local maximum), which is physically consistent for the pristine and slightly delithiated sulfur sites. However, this does not work well for sulfur sites with S-S bond, because the first peak of these sites is at a higher energy, so the computational spectra do not align well with experimental spectra. More sophisticated energy alignment procedures are being investigated; however, they become much more challenging as more lithium atoms are removed. In summary, the scope of this analysis can be understood as limited to the spectral variations instead of absolute features. Second, peak intensities in Cluster 4 and Cluster 5 are much higher than experimental spectra. This is because there are both sulfur sites with and without a sulfur neighbor in one configuration. Cluster 4 and Cluster 5 only select sulfur sites with sulfur neighbors, while the experimental spectra are combinations of all sulfur sites in the sample.

Cluster 6 seems to be an outlier at first glance, as it has the lowest lithium stoichiometry but does not show any S-S bonds. This is also due to a configuration having different sulfur sites. Sulfur sites with a S-S bond tend to be found in configurations with low lithium stoichiometry; however, this does not mean that every sulfur site in these configurations has an S-S bond. Cluster 6 includes the sulfur atoms without sulfur neighbors, but with lithium neighbors.

To summarize their findings in data-driven sulfur spectra analysis, the team shows that the delithiation of LPS starts with the decrease of lithium neighbors of sulfur atoms, which then leads to the formation of S-S bonds and gives rise to the observed new peak at 2473 eV in sulfur K-edge XANES. This information will be used in the interpretation of argyrodite electrolyte delithiation process in the next section. In combination with the results presented last quarter, they know that S-S bond formation is accompanied by the distortion of the  $\text{PS}_4$  structure. In the second delithiation cycle, some phosphorus atoms lose their sulfur neighbors and form  $\text{PS}_3$  structure. Further study is needed to reveal why the first two cycles have different atomic-scale processes. To their knowledge, this study is the first to explain the changes in the XANES spectra of LPS material during delithiation with atomic-scale insights and can largely benefit the development of sulfide electrolytes.

### Resolving LPSCI Redox Reactions with XAS

The team performed XAS measurements on the Cl-doped argyrodite electrolyte LPSCI to study its stability under oxidation (delithiation). The sample preparation was the same as described in the first quarter's report.

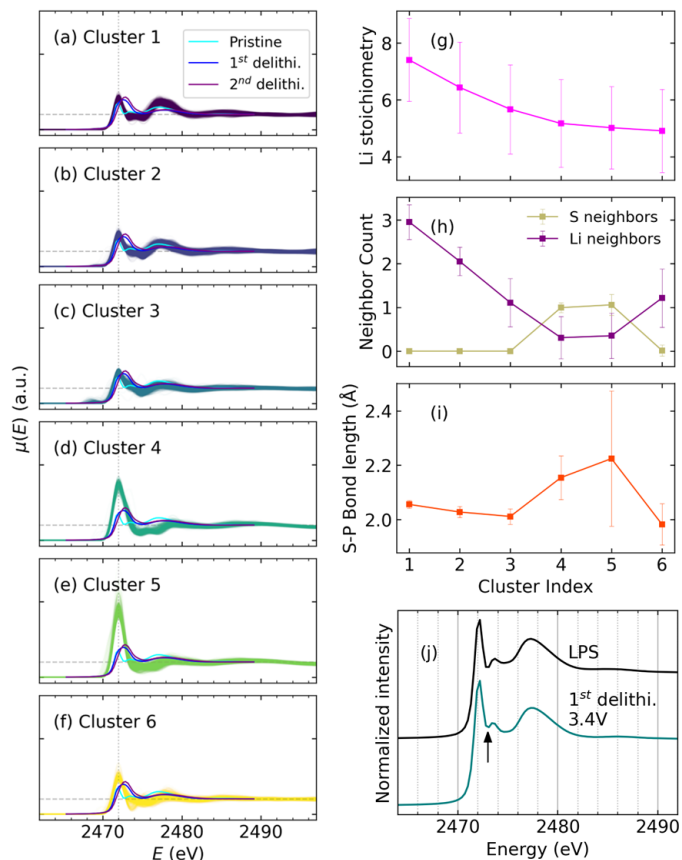


**Figure 107.** Clustering of simulated sulfur XANES spectra in the LPS dataset. The left column (a-f) plots the spectra in all six clusters, as well as experimental spectra measured on pristine LPS and LPS after the first and second delithiation. The right column (g-i) plots the extracted structure descriptors. The markers show the mean values of the descriptors within each cluster, with error bars representing the standard deviation. (j) Experimentally measured pristine and slightly delithiated LPS spectra.

They measured the phosphorus, sulfur, and chlorine K-edges of LPSCl-carbon electrodes cycled to different stages at the TES beamline of NSLS-II. The data are shown in Figure 108 along with the cyclic voltammetry curve.

During the first delithiation (pristine  $\rightarrow$  cyc1-5V), the intensity of the phosphorus K-edge white line peak decreases, and the peak slightly broadens due to the slight distortion of the  $\text{PS}_4$  tetrahedra (see last quarter's report). The team notes that although some of the sulfur sites are replaced by halide ions, the tetrahedra around phosphorus atoms, that is, 16e sites in argyrodite structure, are still fully occupied by  $\text{S}^{2-}$  anions.<sup>[1]</sup> Therefore, the information on the  $\text{PS}_4$  motif evolution in LPS can be transferred to the analysis of the structural changes in LPSCl. In the sulfur K-edge spectra, a peak at 2473 eV appears after delithiation, indicating the formation of S-S bond, as explained in the previous section. The change in chlorine K-edge spectra is due to the formation of LiCl, as described in the second quarter's report.

During lithiation (cyc1-5V  $\rightarrow$  cyc1-0V  $\rightarrow$  cyc2-2.3V), the spectral changes are partially reversible for all three elements. In addition, they observed a shoulder peak at  $\sim 2145$  eV in the phosphorus K-edge spectra. This peak may be due to the formation of P-P bond or Li-P bond during lithiation, and the analysis of the lithiation process is in progress.

The spectrum at the second delithiation (cyc2-5V) is similar to the one at the first delithiation (cyc1-5V). This is different from the behavior of the baseline LPS electrolyte (see last quarter's report). In LPS, after the second delithiation, a broad new peak at  $\sim 2150$  eV appears in phosphorus spectrum, which is due to the large distortion in  $\text{PS}_4$  structure and formation of  $\text{PS}_3$  local motif (see last quarter's report). The absence of new peaks in LPSCl indicates that the  $\text{PS}_4$  structure maintains stably without large distortions in the second (cyc2-5V) and following cycles (multi-cyc), which may be the origin of the good stability of argyrodite electrolytes. The second lithiation (cyc2-5V  $\rightarrow$  cyc2-0V) shows a similar behavior to the first delithiation.

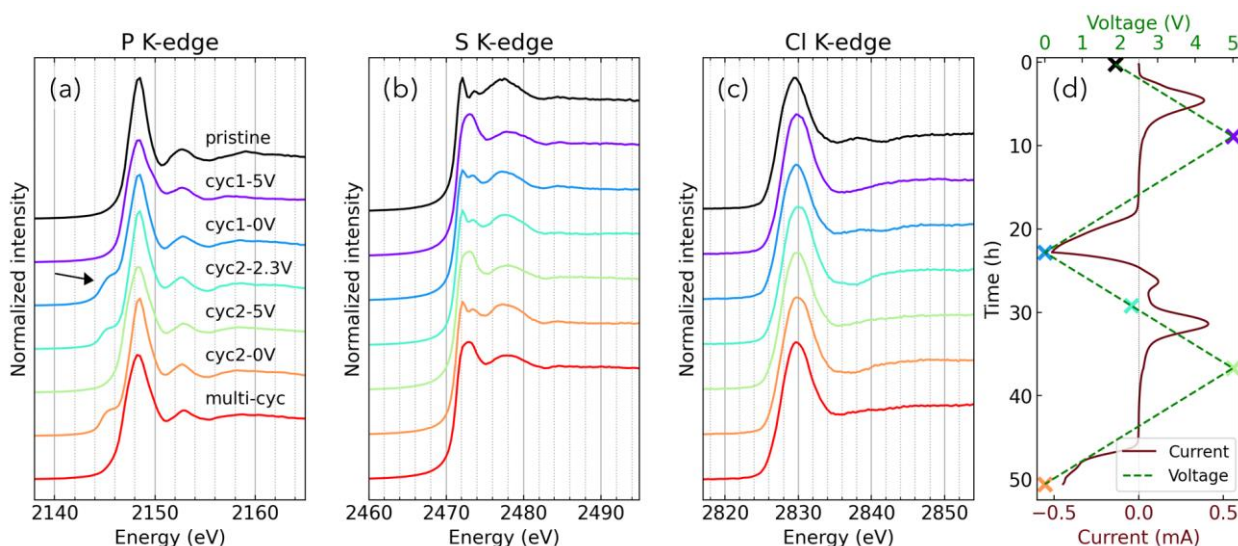


**Figure 108.** Experimentally measured X-ray absorption near-edge spectroscopy (XANES) spectra of (a) phosphorus, (b) sulfur, and (c) chlorine K-edges on LPSCl sample cycled to different stages with cyclic voltammetry (CV). XANES data were measured in fluorescence mode at the TES beamline of NSLS-II. (d) Electrochemistry profile of CV measurement, with current and voltage represented by solid and dashed lines, respectively. CV measurements were conducted at 0.1 mV/s over 0–5 V versus  $\text{Li}^+/\text{Li}$  voltage range. The markers in (d) indicate the states in which the batteries were disassembled and the electrodes were collected for X-ray absorption measurements.

In summary, the team has measured the XAS spectra during the redox reactions of LPSCl and interpreted the data using the phosphorus and sulfur XANES spectral features obtained from LPS. They draw the following conclusions. First, S-S bonds form during both the first and the second delithiations of LPSCl, accompanied by slight distortions of the  $\text{PS}_4$  tetrahedra. LiCl formation is also observed during delithiation. Second, these reactions are partially reversible during lithiation. Third, comparing the delithiation reactions of LPS and

LPSCl, LPS shows large distortions of the PS<sub>4</sub> tetrahedra and the formation of PS<sub>3</sub> motif in the second and following cycles, while the PS<sub>4</sub> structure in LPSCl remains stable after multiple cycles. This study provides a more complete picture of the redox process in LPSCl electrolytes and reveals the origin of the better stability of argyrodite electrolytes over the baseline LPS electrolyte. In future studies, they plan to measure the spectroscopy data of argyrodite electrolytes with other halide species, such as LPSBr and LPSCl<sub>0.5</sub>Br<sub>0.5</sub>, to determine the effect of halide species on interface reactions. Structural and spectral databases of LPS-X (X = Cl, Br) will be developed to provide more information on the local structure change of phosphorus, sulfur, and halide ions during the redox reactions.

#### Reference

- [1] Yu, C., et al. “Recent Development of Lithium Argyrodite Solid-State Electrolytes for Solid-State Batteries: Synthesis, Structure, Stability and Dynamics.” *Nano Energy* 83 (2021): 105858. doi: <https://doi.org/10.1016/j.nanoen.2021.105858>.

### Patents/Publications/Presentations

The project has no patents, publications, or presentations to report this quarter.

## Task 3.11 – Integrated Multiscale Model for Design of Robust, Three-Dimensional, Solid-State Lithium Batteries (Brandon Wood, Lawrence Livermore National Laboratory)

**Project Objective.** This project is developing and applying multiscale, multiphysics models that connect composition, microstructure, and architecture to mechanical integrity in three-dimensional (3D) solid-state batteries (SSBs). The models integrate multiple computational methods, informed and validated through collaborations with complementary experimental efforts. The project scope addresses three objectives: (1) develop multiphysics, multiscale chemomechanics models; (2) assess interface- and microstructure-induced mechanical failure thresholds; and (3) simulate chemomechanical evolution under battery operating conditions.

**Impact.** This project will deliver multiscale, multiphysics models that connect composition, microstructure, and architecture to mechanical integrity in 3D SSBs. The tools will be used to examine common interfaces in commercially viable electrolyte and cathode materials and to provide design principles for maintaining mechanically robust operation. The modeling framework will address the shortcomings of existing modeling strategies that either lack coupling of the multiphysics nature of various processes active in 3D batteries or fail to incorporate processes at different length scales to understand function. Connections will be made to understand the limits of operability and to co-optimize ionic conductivity and mechanical robustness in solid electrolyte-cathode matrix composites.

**Approach.** The project approach integrates atomistic, mesoscale, and continuum simulation methods to predict chemomechanical properties of interfaces in ceramic (Li-La-Zr-O, or LLZO) and halide-based solid electrolytes (SEs). Both internal grain boundaries (GBs) and interfaces with LiCoO<sub>2</sub> (LCO) and Ni-Mn-Co cathode materials are considered. The project is aligned along three tasks, each of which uses simulations to probe a different fundamental length scale relevant to the performance of 3D-SSB architectures. First, atomic-scale interfacial properties are computed using density functional theory and machine learning approaches. These include local bond strength and mechanical response, as well as stress distributions associated with formation of cracks. Second, using digital reproductions of 3D electrodes and electrolytes, the local stress distributions and stress hotspots in SEs and cathode-electrolyte composites are computed within a mesoscale model. Third, materials performance is coupled to cycling conditions within an operating device by incorporating phase-field models that can simulate rate-dependent fracture likelihood under cycling and extract microstructure-fracture-transport relationships.

**Out-Year Goals.** The team will focus on the following out-year goals: use *ab initio* methods to generate models for GBs and cathode electrolyte interphases (CEIs); compute local bond strength and mechanical response of model interfaces; reconstruct microstructures of electrodes and electrolytes using phase-field models; and develop a phase-field model for cathode-induced volume evolution on cycling.

**Collaborations.** This project collaborates with N. Adelstein from San Francisco State University on atomistic diffusion modeling, and J. Ye from Lawrence Livermore National Laboratory (LLNL) on 3D printing of SSB materials. They also partner with T. Danner and A. Latz from Deutsches Zentrum für Luft- und Raumfahrt on impedance modeling and electro-chemo-mechanical interface models, with P. Zapol from Argonne National Laboratory on modeling of interfaces in LLZO, and with D. Fattakhova-Rohlfing from Forschungszentrum Jülich and E. Wachsman from University of Maryland on properties of LLZO with varying densities and microstructures as part of the U. S.–Germany partnership on SSB research.

### Milestones

1. Complete atomistic CEI models. (Q1, FY 2022; Completed)
2. Determine composition profiles of CEIs. (Q2, FY 2022; Completed)

3. Set up model for local stress mapping. (Q3, FY 2022; Completed)
4. Train machine learning force fields (MLFFs) for disordered interfaces. (Q4, FY 2022; Completed)

## Progress Report

**Machine-Learning Interatomic Potentials for Accelerated Atomistic Simulations.** As part of the U. S.–Germany collaboration, this quarter the team has modeled 20 LLZO GBs using their developed MLFF. They varied the tilting axis and GB planes to create a series of initial GB configurations and further introduced local structural perturbations to generate realistic GB structures. It is found that the structural and chemical stability of GBs is highly sensitive to the local symmetry and atomic arrangement. For example, the  $\Sigma 5(130)/[001]$  GB shows well-ordered zirconium sublattice and relatively less disordered lanthanum sublattice, whereas the  $\Sigma 13(230)/[001]$  GB shows larger disordering of zirconium and lanthanum sublattices after perturbation via the same process (Figure 109). They will further investigate the structure-property relationship using these GB models and report the results next quarter.

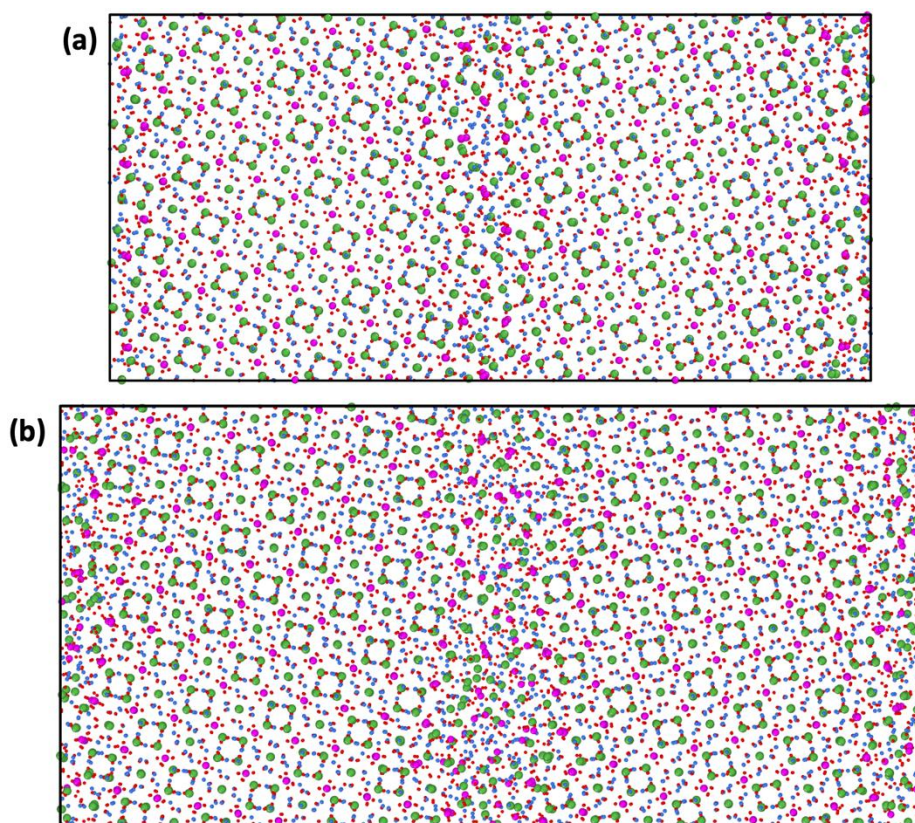
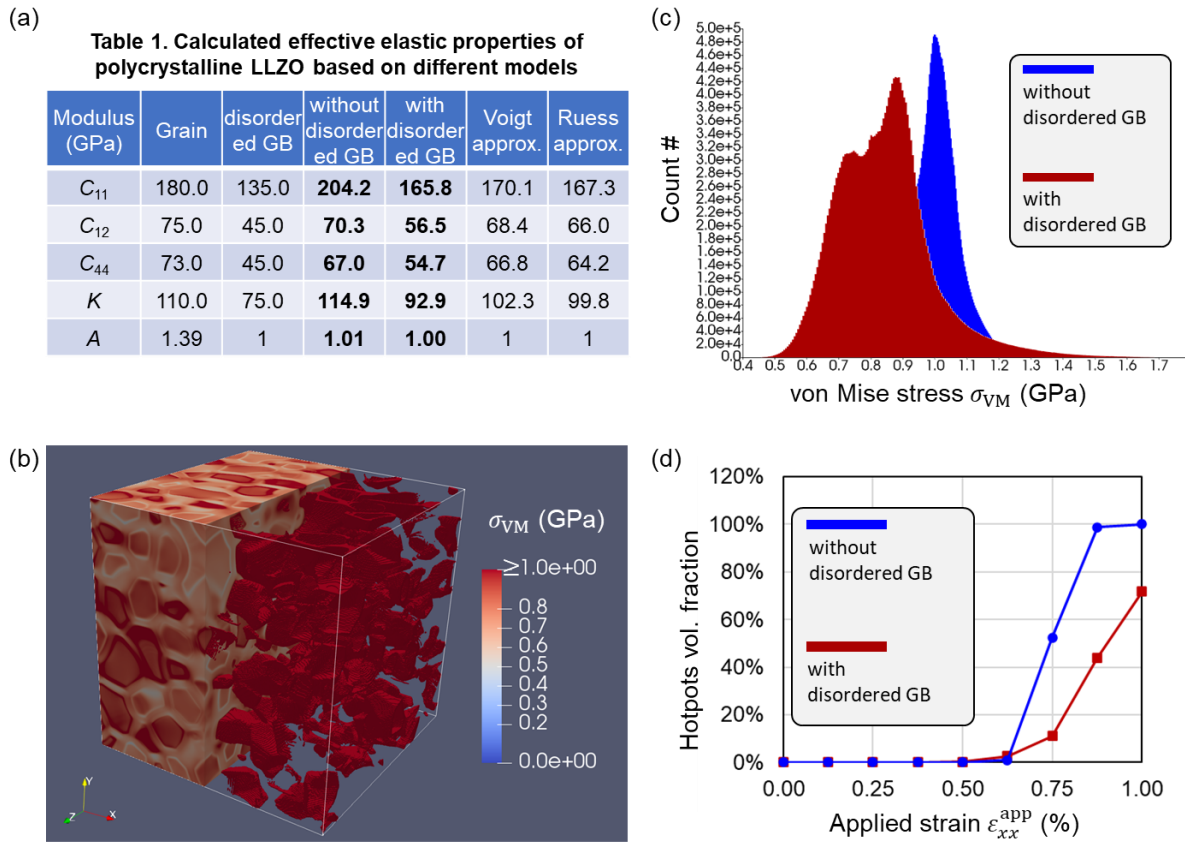


Figure 109. (a)  $\Sigma 5(130)/[001]$  and (b)  $\Sigma 13(230)/[001]$  symmetric tilt grain boundaries of LLZO. Lithium, lanthanum, zirconium, and oxygen atoms are shown in blue, green, magenta, and red, respectively.

**Microstructure-Aware Mesoscale Modeling and Atomistic Simulation-Informed Effective Property Calculation of Dense Polycrystalline (PC) LLZO SE.** This quarter, the team’s mesoscale modeling effort was made on assessing the mechanical responses of polycrystalline LLZO SE with input materials parameters from their MLFF-based atomistic calculations. Preliminary results are summarized in Figure 110. They first reconstructed the 3D representation of a compact PC microstructure of LLZO using the LLNL in-house phase-field grain growth simulator. The grains are modeled as a crystalline phase with cubic

symmetry, while the GBs are modeled as an isotropic disordered phase. Their atomistic calculations show that the cubic crystalline phase exhibits anisotropic characteristics in the elastic stiffness, as measured by the asymmetry factor,  $A = \frac{2C_{44}}{C_{11} - C_{12}} \approx 1.4$ , while the disordered GB phase is nearly isotropic, with a bulk modulus  $K = 75$  GPa. They also assumed randomly oriented grains, leading to spatially inhomogeneous local elastic properties. They then used the LLNL *MesoMicro* code framework to compute the effective elastic properties and simulate the micromechanical responses of the prepared elastically inhomogeneous LLZO microstructure.



**Figure 110.** Microstructure-aware mesoscale modeling and calculation of the mechanical properties of LLZO. (a) Calculated effective elastic properties of polycrystalline (PC) LLZO based on different models.  $C_{11}$ ,  $C_{12}$ ,  $C_{44}$ : elastic stiffness tensor components,  $K$ : Bulk modulus,  $A$ : asymmetric factor. (b) Calculated von Mises stress  $\sigma_{VM}$  distribution within a 3D polycrystalline microstructure of LLZO generated by phase-field grain growth simulations. The color corresponds to the value of  $\sigma_{VM}$ , and a threshold of  $\sigma_{VM}^{thres} = 1.0$  Gpa is applied to the half of the 3D structure to illustrate the mechanical hotspots. (c) Histograms of  $\sigma_{VM}$  in the PC models with and without considering the grain boundary phase to be disordered. (d) Volume fraction of hotspots as a function of applied longitudinal strain  $\epsilon_{xx}^{app}$  along  $x$ .

To quantify the effect of the disordered GB phase, they performed comparative simulations with and without consideration of the disordered GBs. They also compared their numerical computations with the results based on commonly used analytical models with the isotropic assumptions ignoring detailed microstructural features (for example, Voigt and Ruess models); see Table 1 in Figure 110. They verified that the computed effective mechanical properties such as the bulk modulus  $K$  can vary by  $\sim 20$  GPa depending on the GB models. These results indicate the importance of the elastic property of the GB phase in determining the microstructure-aware effective elastic moduli. In addition, they found that their microstructure-aware effective elastic moduli deviate from those obtained by simple analytical models, indicating the significance of local microstructural features in elastically inhomogeneous SEs.

The team also performed mechanical hotspot analysis based on the computed local von Mises stress,  $\sigma_{VM}$  (Figure 110b-d). Figure 110b shows the statistical distribution of  $\sigma_{VM}(\mathbf{x})$  in PC LLZO. For better representation, the identified mechanical hotspots ( $\sigma_{VM} > \sigma_{VM}^{thres} = 1.0$  GPa) are illustrated in the half of the employed LLZO microstructure, which are mostly concentrated on the disordered GBs. To show the influence of the GB elastic property on the mechanical hotspots, they compared the statistics of  $\sigma_{VM}$  computed with and without consideration of the disordered GBs (Figure 110c). They observed explicit impacts of disordered GBs on the stress distribution. Specifically, the disordered GBs relax the overall  $\sigma_{VM}$  level and lead to the wider statistical distribution of  $\sigma_{VM}$ . Motivated by this observation, the team performed a further parametric study on the evolution of the mechanical hotspots fraction with the increasing loading (see an example with the case of applied longitudinal strain  $\varepsilon_{xx}^{app}$  in Figure 110d). As expected, they verified the reduction of mechanical hot spots when the disordered GBs are incorporated due to their less-stiff elastic properties. In addition, the hot spot fraction increase is less sensitive to the applied loading with the disordered GBs. These simulation results may have implications for determining mechanical failure mechanisms (for example, delamination and fracture) in PC SEs.

In the coming quarters, they plan to utilize the workflow described above to perform more systematic study and sensitivity analysis on the effective mechanical responses in dense/porous LLZO and LLZO/LCO composite microstructures. Moreover, this micromechanical model will be integrated with the lithium transport model in a self-consistent way to quantitatively investigate chemo-mechanical coupling effects that determine how the lithium transport and mechanical response affect each other in PC LLZO.

### Patents/Publications/Presentations

The project has no patents, publications, or presentations to report this quarter.

## TASK 4 – METALLIC LITHIUM

Team Lead: Jagjit Nanda, SLAC Stanford Battery Research Center

### Summary and Highlights

The use of a metallic lithium anode is required for advanced battery chemistries like Li-ion, Li-air, and Li-S to realize dramatic improvements in energy density, vehicle range, cost requirements, and safety. However, use of metallic lithium with liquid and solid polymer or ceramic electrolytes has so far been limited due to parasitic solid electrolyte interphase reactions and dendrite formation that eventually short circuit the battery. Adding excess lithium to compensate for such losses negates the high-energy-density advantage of a Li-metal anode and leads to further concern for battery safety. For a long lifetime and safe anode, it is essential that no lithium capacity is lost either (1) to physical isolation by roughening, dendrites, or delamination processes, or (2) to chemical isolation from side reactions. The key risk, and current limitation, for this technology is the gradual loss of lithium over the cycle life of the battery. To address these issues, there is need for a much deeper analysis of the degradation processes and new strategies to maintain a dense, fully connected lithium and a dendrite-free electrolyte so that materials can be engineered to fulfill the target performance metrics for electric vehicle application, namely 1000 cycles and a 15-year lifetime, with adequate pulse power. Projecting the performance required in terms of just the lithium anode, this requires a high rate of lithium deposition and stripping reactions, specifically about 30  $\mu\text{m}$  of lithium per cycle, with pulse rates up to 10 nm/s and 20 nm/s (15 mA/cm<sup>2</sup>) charge and discharge, respectively, with little or no excess lithium inventory.

The efficient and safe use of metallic lithium for rechargeable batteries is then a great challenge, and one that has eluded research and development efforts for years. This project takes a broad look at this challenge for both solid-state batteries and batteries continuing to use liquid electrolytes (LEs). Electrolytes reported here include conventional LEs such as localized high concentrated electrolytes, gel type polymer-in-a-salt, composites of ceramic polymer phases, common and novel polymer electrolytes, and both oxide and sulfide ceramic electrolytes. Researchers are typically working toward cycling of full cells with relevant and balanced capacities using both thin lithium metal and anode-free configuration, prelithiation methods, and post-cycling observation of the disassembled cell components to assess stability of the Li-metal/electrolyte interface.

### Highlights

The highlights for this quarter are as follows:

- Y. Cui's group at SLAC National Accelerator Laboratory / Stanford University has demonstrated a solvent-free prelithiation method. Prelithiation reagents are added to the battery during the battery assembly step, and prelithiation occurs *in situ* during the cell resting period based on shorting mechanism. This quarter, they have developed an *in situ* optical cell to visualize lithium diffusion within silicon anode. At electrode/electrolyte interface, the color changes happen faster compared to locations further away from the interface, revealing a gradual lithium diffusion from electrode surface to the bulk.
- J. Zhang's group at Pacific Northwest National Laboratory reports that lithium deposition in anode-free lithium batteries is relatively porous in the center and denser on the edge of cells after the cell is charged to 4.5 V. This non-uniformity is directly related to the non-uniform thickness of commercial stainless-steel spacers and springs used in coin cells, which can exert a non-uniform pressure on copper substrate. The non-uniform pressure distribution leads to poor cycling performance.

## Task 4.1 – Lithium Dendrite Prevention for Lithium Batteries (Wu Xu, Pacific Northwest National Laboratory)

**Project Objective.** The objective of this project is to enable lithium metal to be used as an effective anode in Li-metal batteries with good thermal stability and safety. The investigation in FY 2022 will focus on the following aspects: (1) continuing evaluation of separators with high thermal stability in Li-metal batteries, (2) developing three-dimensional (3D)-structured, lightweight, flexible current collectors for Li-metal anode and Li-metal batteries, and (3) obtaining mechanistic insight on Li-metal deposition/stripping behavior.

**Project Impact.** Lithium metal is an ideal anode material for next-generation, high-energy-density, rechargeable batteries. However, the application of Li-metal anode has been hindered by concern for safety and short cycle life. The safety concern regarding Li-metal batteries mainly arises from lithium dendrite growth and electrolyte flammability; the short cycle life is largely associated with the high reactivity of lithium metal with electrolyte and the lithium loss due to formation of solid electrolyte interphase (SEI) and electrochemically inactive or “dead” lithium during cycling. Although much progress has been achieved in suppressing lithium dendrites and increasing lithium Coulombic efficiency in liquid electrolytes (LEs) in recent years, the intrinsic problems of Li-metal anode still exist. This fiscal year, the Pacific Northwest National Laboratory (PNNL) team will continue to evaluate the effectiveness of separators with high thermal stability in improving the thermal stability of Li-metal batteries. Meanwhile, the team will develop 3D porous current collectors for Li-metal anode to suppress lithium dendrite growth, increasing the utilization of lithium metal and consequently extending the cycle life of Li-metal batteries. The success of this project will increase safety and cycle life of lithium batteries and accelerate market acceptance of electric vehicles (EVs), as required by the EV Everywhere Grand Challenge.

**Approach.** The approach will encompass the following areas: (1) continue comparative evaluation of separators with high thermal stability in lithium || LiNi<sub>0.6</sub>Mn<sub>0.2</sub>Co<sub>0.2</sub> (NMC-622) cells during cycling and heating process, (2) develop current collectors with 3D structure for Li-metal anode to suppress lithium dendrite growth, increase lithium utilization, and extend cycle life of Li-metal batteries, and (3) conduct mechanistic studies on lithium deposition behavior to lay groundwork for future improvement of Li-metal batteries.

**Out-Year Goals.** The long-term goal of the proposed work is to enable Li-metal and Li-ion batteries with a specific energy of > 350 Wh/kg (in cell level), 1000 deep-discharge cycles, 15-year calendar life, and less than 20% capacity fade over a 10-year span to meet the goal of the EV Everywhere Grand Challenge.

**Collaborations.** This project collaborates with C. Wang of PNNL on characterization by transmission electron microscopy / scanning emission microscopy (SEM); K. Xu and M. Ding of U. S. Army Research Laboratory on differential scanning calorimetry (DSC) measurements; A. Bates, Y. Preger, and L. Torres-Castro of Sandia National Laboratory on DSC microcell tests; Y. Zhang and A. Simmons of Argonne National Laboratory on electrospinning polyimide, polysulfone, and polycarbonate porous membranes; and X. Shan and G. Xia of University of Houston on studying SEI formation using reflection interference microscope.

### Milestones

1. Evaluate thermal properties of polyimide and polyethylene separators in Li||NMC cells during heating. (Q1, FY 2022; Completed)
2. Evaluate cell performance and thermal properties of other separators in Li||NMC cells. (Q2, FY 2022; Completed)
3. Fabricate 3D-structured current collectors and characterize their physical properties; elucidate influencing factors on lithium deposition/stripping behavior by *in situ* characterization. (Q3, FY 2022; Completed)

4. Evaluate effect of new separator and 3D-structured current collector on cycling performance of Li||NMC cells. (Q4, FY 2022; Completed)

## Progress Report

This quarter, the process of synthesizing 3D current collector of Cu-coated polyimide fibers (Cu@PI) was optimized. The SEM and energy-dispersive X-ray spectroscopy (EDS) images, shown in Figure 111, demonstrate that the copper is fully and uniformly coated on the polyimide fibers, not only on the surface (Figure 111a), but also the inside (Figure 111b) of the polyimide membrane after the synthesis optimization. The EDS mapping images also indicate that the optimized synthesis process can provide a conductive 3D current collector. Lithium in the amount of  $4 \text{ mAh cm}^{-2}$  was deposited on both two-dimensional copper foil (bare copper) and the Cu@PI at a current density of  $0.4 \text{ mA cm}^{-2}$ ; the morphologies are shown in Figure 112. On the top surface, the lithium deposits on bare copper (Figure 112a) and Cu@PI (Figure 112b) show very similar morphologies with the same lithium particle size. However, the cross-sectional images exhibit distinct morphologies (Figure 112c-d). The lithium deposited on bare copper is more porous and less dense than that deposited on Cu@PI. The thicknesses of lithium deposited on copper and Cu@PI are  $\sim 20 \mu\text{m}$  and  $\sim 15 \mu\text{m}$ , respectively. This suggests that the lithium deposited on Cu@PI may have less surface area, less contact, and fewer side reactions with LE, thus leading to longer cycling stability.

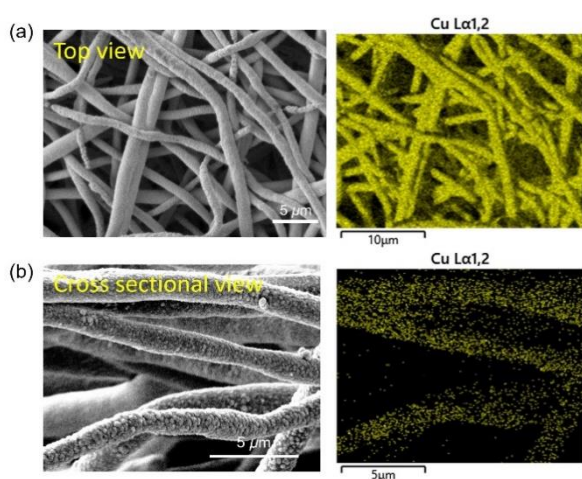


Figure 111. Scanning electron microscopy images and X-ray energy dispersive spectroscopy mapping images for copper distribution on Cu@PI mat of (a) top-view and (b) cross-sectional view.

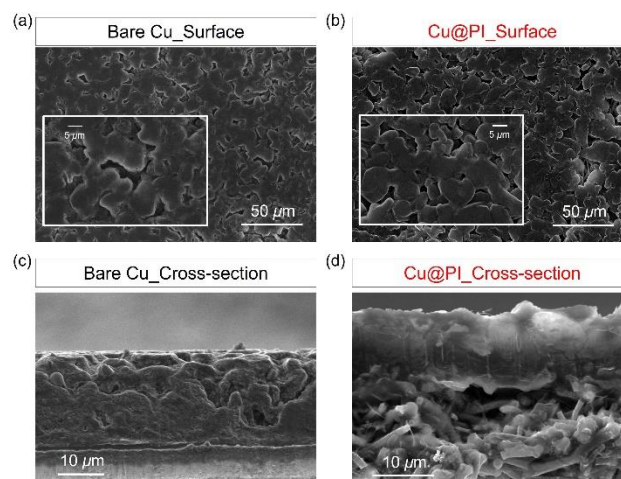


Figure 112. Scanning electron microscopy images of deposited lithium morphologies on (a/c) bare copper foil and (b/d) Cu@PI mat.

To investigate the effect of Cu@PI 3D current collector on Li-metal battery performance, Li||NMC-622 coin cells were assembled and tested. Each cell contains  $50\text{-}\mu\text{m}$  lithium metal,  $4 \text{ mAh cm}^{-2}$  NMC-622,  $20 \mu\text{m}$  of polyethylene separator, and  $75 \mu\text{L}$  electrolyte of lithium bis(fluorosulfonyl)imide in 1,2-dimethoxyethane and 1,1,2,2-tetrafluoroethyl-2,2,3,3-tetrafluoropropyl ether at 1:1.2:3 by mol. The cycling performance of the Li||NMC-622 cells is conducted at a current density of  $C/10$  for charging and  $C/3$  for discharging under a voltage range from 2.8 V to 4.4 V (versus  $\text{Li/Li}^+$ ) after two formation cycles at  $C/10$ , where  $1C = 4.0 \text{ mA cm}^{-2}$ . The Li||NMC-622 cell with Cu@PI current collector has very similar performance to the Li||NMC-622 cell with the bare copper foil up to 30 cycles (Figure 113). Longer cycling stability and other cell performance are measured and will be updated in the next quarterly report.

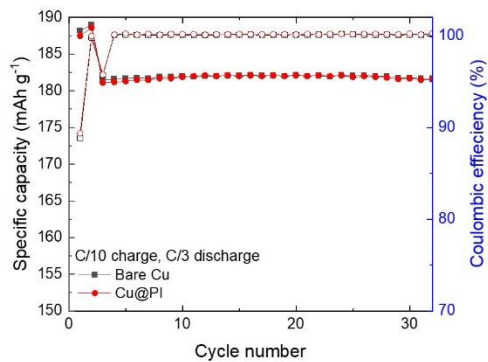


Figure 113. Room-temperature cycling performance of Li||NMC-622 coin cells using Cu@PI and bare copper current collectors.

## Patents/Publications/Presentations

The project has no patents, publications, or presentations to report this quarter.

## Task 4.2 – Prelithiation for High-Energy Lithium-Ion Batteries (Yi Cui, Stanford University)

**Project Objective.** Prelithiation of high-capacity electrode materials is an important means to enable those materials in high-energy batteries. This study pursues three main directions: (1) development of facile and practical methods to increase 1<sup>st</sup>-cycle Coulombic efficiency (CE) of anodes, (2) synthesis of fully lithiated anode to pair with high-capacity, Li-free cathode materials, and (3) prelithiation from the cathode side.

**Project Impact.** Prelithiation of high-capacity electrode materials will enable those materials in the next generation of high-energy-density Li-ion batteries. This project's success will make high-energy-density Li-ion batteries for electric vehicles.

**Approach.** Silicon electrode film will be prepared by coating the slurry of silicon nanoparticles, carbon black, and binder mixture on copper foil through a doctor-blading method. The silicon electrode film will be prelithiated by pressing a Li-metal foil on top of it and heating it in an argon glovebox for a certain time. Then, Li<sub>x</sub>Si electrode film can be obtained by removing the redundant lithium foil through a peeling-off approach. The redundant lithium foil is reusable for the next prelithiation. The structure, morphology, and other properties can be analyzed by scanning electron microscopy, transmission electron microscopy, X-ray photoelectron spectroscopy, Raman spectroscopy, X-ray diffraction, etc. In the first year, the team aims to fabricate Li<sub>x</sub>Si freestanding electrode film and improve its air stability. In the second year, the team aims to improve the electrochemical stability in full cells.

**Out-Year Goals.** Materials containing a large quantity of lithium will be synthesized for pre-storing lithium ions inside batteries. Materials and processes will be developed to be compatible with battery electrode and cell fabrication. First-cycle CE of anodes will be improved and optimized by prelithiation materials. Materials for prelithiation from the cathode side will be developed.

**Collaborations.** This project engages in collaboration with the following: BMR principal investigators; SLAC National Accelerator Laboratory: M. Toney (*in situ* X-ray); and Stanford University: W. Nix (mechanics).

### Milestones

1. Demonstrate a new solvent-free dry prelithiation strategy through *in situ* prelithiation. (Q1, FY 2022; Completed)
2. Demonstrate that the *in situ* prelithiation strategy can delicately control the prelithiation amount. (Q2, FY 2022; Completed)
3. Demonstrate that the *in situ* prelithiation strategy can achieve uniform prelithiation. (Q3, FY 2022; Completed)
4. Investigate the prelithiation kinetics in the *in situ* prelithiation strategy. (Q4, FY 2022; Completed)

## Progress Report

Substantial improvements on energy density of Li-ion batteries require development of high-capacity electrodes. Silicon anodes, which have high theoretical capacities (3579 mAh/g)—ten times higher than the conventional graphite anodes (372 mAh/g), hold great potential for application in high-energy Li-ion batteries. However, silicon anodes exhibit a low initial CE of 50-80%, which means 20-50% of battery capacity will be lost after 1<sup>st</sup> cycle due to side reactions. Therefore, a strategy to compensate the initial active lithium loss and improve initial CE is urgently needed to prevent battery capacity degradation.

In their previous reports, the team has presented a new solvent-free *in situ* prelithiation method. Prelithiation reagents are added to the battery in the battery assembly step, and prelithiation *in situ* takes place in the cell resting period based on shorting mechanism. This *in situ* prelithiation process addresses the challenges of cell reassembly and solvent compatibility in traditional prelithiation methods. They have demonstrated controllable prelithiation and investigated the uniformity of *in situ* prelithiation method. Here, they further investigate lithium diffusion within electrodes in the prelithiation process to provide more fundamental understandings of the prelithiation methods.

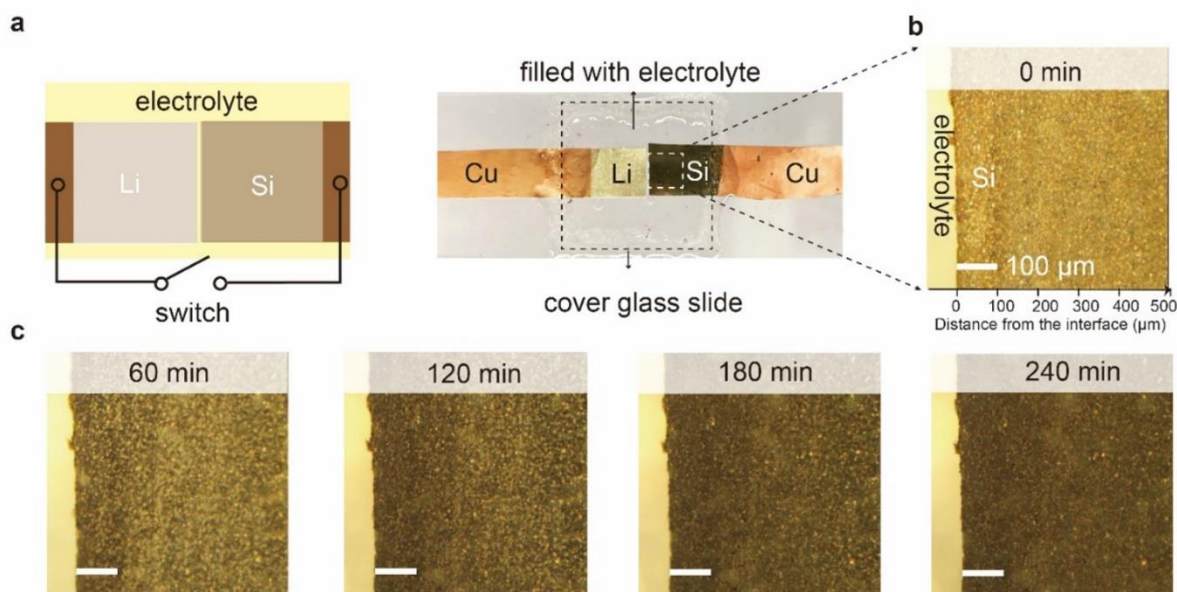


**Figure 114.** Kinetics studies of the lithium diffusion in the prelithiation process. (a) The *in situ* optical cell used to visualize the lithium diffusion process within silicon electrodes; left: schematic, and right: photo of the device. (b) The optical microscopy image of the area of interest before shorting (time = 0 min) with labeled components and scales. (c) *In situ* dark-field optical microscopy image displaying the prelithiation process within electrodes, scale bar = 100  $\mu\text{m}$ .

Lithium diffusion kinetics within the electrodes is an important, yet unanswered, question in the prelithiation process. Here, the team has designed an *in situ* optical cell to reveal the lithium diffusion process based on the gray-scale of the electrodes (Figure 114a). They chose a thin silicon anode with a thickness of  $\sim 3 \mu\text{m}$  to laterally visualize the bulk  $\text{Li}^+$  diffusion. All the components were placed between a glass substrate and a transparent cover glass slide and sealed with epoxy to enable *in situ* optical observation. An outer circuit with a switch controls shorting precisely. Figure 114b shows the interfacial silicon electrode before shorting with labeled components and scales. The snapshots are taken at different shorting time to reveal a gradual color change from yellow to black with prelithiation process (Figure 114c). These color changes of the electrodes toward darker colors after prelithiation have been widely observed and reported, indicating the transformation from silicon to  $\text{Li}_x\text{Si}$ . At electrode/electrolyte interface, the color changes happen faster compared to locations further away from the interface, revealing a gradual lithium diffusion from electrode surface to the bulk. In practical terms, this distance from the interface indicates the thickness of the electrodes. This optical cell study provides an insight of the lithium diffusion process along the thickness of silicon electrodes.

## Patents/Publications/Presentations

The project has no patents, publications, or presentations to report this quarter.

## Task 4.3 – Anode-Free Lithium Batteries (Ji-Guang Zhang and Xia Cao, Pacific Northwest National Laboratory)

**Project Objective.** The main objective of this project is to explore the feasibility of anode-free lithium batteries (AFLBs) for high-energy-density energy storage systems. An AFLB is an extreme case of Li-metal battery and Li-ion battery, where all active lithium is stored in cathode in the as-assembled batteries. Because of the many similarities among AFLBs, Li-metal batteries, and Li-ion batteries, extensive experiences and approaches developed for Li-metal and Li-ion batteries can be applied to AFLBs. Likewise, new approaches and knowledge to extend the cycle life and calendar life of AFLBs can also be used for development of Li-metal and Li-ion batteries, thus accelerating the market penetration of Li-based rechargeable batteries.

**Project Impact.** The ever-increasing need for electric vehicles (EVs) continually pushes the boundary of high-density energy storage systems. To date, the state-of-the-art Li-ion batteries consisting of graphite anode and high-voltage lithium intercalation cathodes cannot satisfy the energy demand from these applications. By replacing graphite anode with Li-metal anode, the specific energy density of Li-metal batteries can increase by more than 50% because Li-metal anode has a much higher specific capacity ( $3820 \text{ mAh g}^{-1}$ ) than that of graphite ( $372 \text{ mAh g}^{-1}$ ). To further increase the energy density of lithium batteries, the concept of AFLBs has been explored. An as-assembled or fully discharged AFLB consists of a cathode and an anode current collector (such as copper). All lithium source is stored in cathode. This cell design not only increases energy density of the battery, but also improves battery safety because no lithium metal is present in the battery in its as-assembled or discharged state. However, the cycle life of AFLBs is still very limited due to loss of active lithium during the cycling process. Therefore, there is an urgent need to understand the correlation between lithium Coulombic efficiency (CE), cathode CE, and electrolyte (including its electrochemical properties and consumption), as well as lithium dendrite growth and the formation of “dead” lithium, so that AFLBs and Li-metal batteries can be designed to achieve desired energy density and cycle life. In the end, the combination of these two efforts will accelerate the understanding and application of high-energy-density rechargeable batteries for EV applications.

**Approach.** This task will investigate the main factors affecting the performance of AFLBs and identify the solutions to enable long-term cycling and safety of these batteries. The lithium loss due to solid electrolyte interphase (SEI) formation and “dead” lithium generation by dendrite growth in the lithium deposition and stripping processes will be analyzed. The lithium dendrite suppressing principles and strategies for both liquid and solid-state AFLBs, ranging from materials design (that is, electrolytes, cathodes, and current collectors), cell fabrication, and operation controls (that is, pressure, temperature, and cycling protocol) will also be investigated.

**Out-Year Goals.** The long-term goal of the proposed work is to enable lithium batteries with a specific energy of  $> 350 \text{ Wh/kg}$  (in cell level), 1000 deep-discharge cycles, 15-year calendar life, and less than 20% capacity fade over a 10-year span to meet the goal of the EV Everywhere Grand Challenge.

**Collaborations.** This project collaborates with the following: C. S. Wang of University of Maryland on approaches to improve the CE of lithium cycling; C. M. Wang of Pacific Northwest National Laboratory on characterization by transmission electron microscopy / scanning electron microscopy; and Battery500 principal investigators on understanding and approaches to improve the calendar life of lithium batteries.

### Milestones

1. Optimize cycling parameters of AFLBs to improve cycle life using localized high-concentration electrolyte (LHCE) with high CE and safety. (Q1, FY 2022; Completed)
2. Develop approaches to treat copper substrate to minimize lithium loss during cycling. (Q2, FY 2022; Completed)

3. Improve CE efficiency of electrolyte by forming a lithiophobic SEI layer. (Q3, FY 2022; Completed)
4. Extend the cycle life of AFLBs to be more than 100 cycles. (Q4, FY 2022; Completed)

## Progress Report

Electrolyte is one of the most important factors determining the cycle life of AFLBs. Last quarter, several advanced LHCEs with different additives were investigated. When tested in Cu||Li cells, these electrolytes led to very high lithium CEs of 99.45%-99.7%, as shown in Figure 115a. AFLBs (Cu||LiNi<sub>0.8</sub>Mn<sub>0.1</sub>Co<sub>0.1</sub>, or Cu||NMC-811) with E1, E3, and E4 electrolyte show stable cycling behavior. As shown in Figure 115b-d, the cell with E4 electrolyte demonstrates the best cycling stability with a capacity retention of 74.5% after 100 cycles. This electrolyte has been used in the team's subsequent work for the effect of pressure uniformity on the performance of AFLBs.

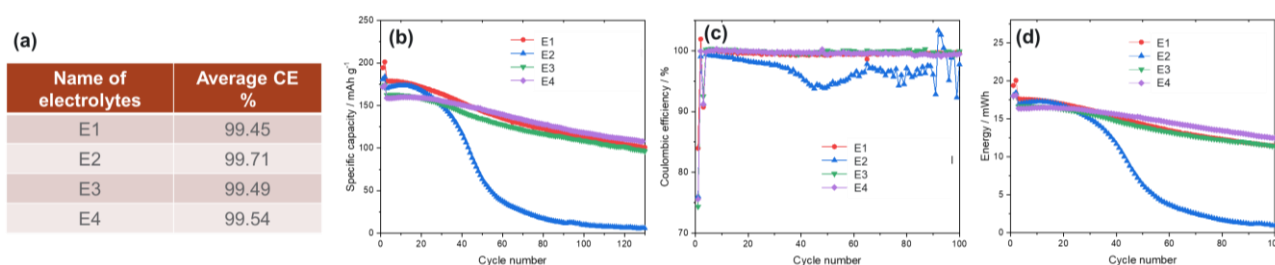


**Figure 115. (a) Average lithium Coulombic efficiency (CE) of Cu||Li cells using the standard CE protocol. (b-d) Cycling performance of Cu||NMC-811 cell cycled between 3.5 V – 4.4 V with the commercial 2032 coin-cell set.**

This quarter, the team investigated the pressure effect on the coin cells by introducing different combinations of spacers. For the anode-free batteries, the uniform/dense lithium deposition is critical for long-term cell operation. However, when a coin-type cell is used to investigate battery performance, non-uniform pressure introduced by the spacer and spring used in coin cells may lead to non-uniform deposition of lithium, premature local failure, and shortened cycle life of batteries. This is especially important for AFLBs that have no cushion layer (such as Li-metal anode in the case of Li-metal batteries, or graphite anode in the case of Li-ion batteries) to mitigate the pressure non-uniformity in a typical coin cell. During this quarter, they found that lithium deposition in AFLBs is more porous in the center, but denser on the edge of cells (Figure 116b-c) after the cell was charged to 4.5 V (Figure 116a). This non-uniformity is directly related to the non-uniform thickness of commercial stainless-steel spacers and springs used in coin cells, which can exert a non-uniform pressure on copper substrate, as shown in Figure 116d). The non-uniform pressure distribution leads to poor cycling performance (Figure 116e). Although coin cell is a convenient battery structure for testing of conventional batteries, non-uniform pressure distribution in coin cells is a clear barrier for investigation of AFLBs, which are highly sensitive to pressure uniformity. Next quarter, a small pouch cell with more uniform distribution of pressure will be used to investigate the performance of AFLBs.

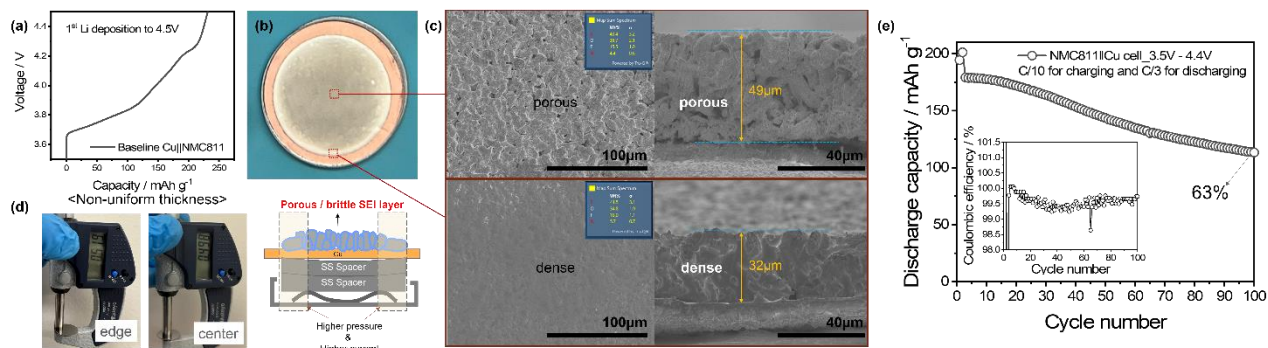


**Figure 116. (a) Voltage profile of Li||NMC-811 baseline cell charged to 4.5 V. (b) Digital photograph of copper electrode after the first lithium deposition to 4.5 V. (c) Scanning electron microscopy images with X-ray energy dispersive spectroscopy data (insets) for the top (left) and cross-sectional (right) views of the center (upper) and edge (lower) regions of the copper electrode after the first lithium deposition to 4.5 V. (d) Digital photographs displaying the non-uniform thickness of the stainless-steel spacer with a schematic illustration of the non-uniform lithium deposition leading to a porous/brittle SEI layer by non-uniform pressure/current distribution on copper electrode. (e) Cycling performance of Cu||NMC-811 cell cycled between 3.5 V – 4.4 V with the commercial 2032 coin-cell set.**

## Patents/Publications/Presentations

The project has no patents, publications, or presentations to report this quarter.

## TASK 5 – LITHIUM-SULFUR BATTERIES

Team Lead: Prashant N. Kumta, University of Pittsburgh

### Summary

The collected work of the projects in this Task encompasses the following areas:

- Conducting focused fundamental research on the mechanism of “shuttle effect” inhibition for rechargeable Li-S batteries.
- Developing electrode and electrolyte systems that can mitigate the “shuttle effect” so the low self-discharge and long cycle life can be achieved.
- Synthesizing sulfur composite materials with an emphasis on polymer sulfur composite materials.
- Developing creative electrode-making processes to improve processability and areal capacity; for example, polymeric sulfur composites may not be suitable for the traditional slurry casting process.
- Developing a novel  $S_xSe_y$  cathode material for rechargeable lithium batteries with high energy density and long life, as well as low cost and high safety.
- Delivering an electrochemically responsive self-formed hybrid Li-ion conductor as a protective layer for Li-metal anodes, enabling them to cycle with high efficiency.
- Developing high-energy, low-cost Li-S batteries with long lifespan.

### Highlights

The highlights for this quarter are as follows:

- K. Amine’s group at the Argonne National Laboratory (ANL) continued their studies in Li-S systems to improve cycling performance and suppress the self-discharge of Li-S batteries during charge/discharge at a wide temperature range (0-50°C). They prepared the ordered mesoporous sulfur host (OMSH) with a pore diameter of ~ 180 nm infiltrated with ~ 80 wt% Se-doped sulfur (Se:S = 1:9 in mass ratio) via molten-diffusion method at a temperature of 155°C for 12 hours, resulting in a new phase of Se/S contributing to improved electronic conductivity and reversibility. They determined the Se/S content in the OMSH-Se/S to be 79.11 wt% by thermogravimetric analysis. They also used hydrofluoroether (HFE)-based electrolyte to suppress the Li-polysulfide solubility, reducing the shuttle effect, and showed that OMSH-Se/S at an areal loading of 5.8 mg cm<sup>-2</sup> can deliver an areal capacity of 5.47 mAh cm<sup>-2</sup> at 200 mA g<sup>-1</sup> corresponding to a specific capacity of 943.10 mAh g<sup>-1</sup>, which validates the ability of OMSH-Se/S to enhance electrochemical redox kinetics. The system also exhibits a high Coulombic efficiency (CE) of > 99.2% with a retention rate of 71.77% for 100 cycles at the same loading. Finally, they showed that the HFE-based electrolyte resulted in a 20-mV drop in voltage after a 1-week rest, compared to the 205-mV drop registered by the 1,2-dimethoxyethane-based electrolyte for OMSH-Se/S system with a loading of 6.3 mg cm<sup>-2</sup> and maintaining an areal capacity of 5.44 mAh cm<sup>-2</sup> after 50 cycles at 167.6 mA g<sup>-1</sup>. These results demonstrate the promise of their OMSH-Se/S system for attaining high energy density of 500 Wh kg<sup>-1</sup>.
- D. Lu and J. Liu’s group at the Pacific Northwest National Laboratory attempted to improve the sulfur content in their S/C large particle cathode by optimizing the structures of the sulfur host materials, and they identified that the pore connectivity is an important factor for designing the large-sized secondary host materials. Accordingly, they studied N-doped integrated Ketjen Black (NKB) particles with different conductivity by integrating the KB carbon particles with poly(melamine-co-formaldehyde) methylation (PMF) at different PMF/KB ratios, followed by sulfur infiltration at 155°C (80 wt% sulfur). They showed that NKB11 with a PMF/KB = 1:1 had better distribution of sulfur within the composite by nano-computed

tomography. Similarly, the NKB11/S electrode after 40 cycles exhibited a reversible capacity of  $800 \text{ mAh g}^{-1}$ , confirming that PMF:KB = 1:1 is an optimal ratio. They also demonstrated the ability to scale up to  $\sim 40 \text{ g}$  per batch. With a 50% porosity cathode, with overall sulfur content of 72%, and  $5 \text{ mg cm}^{-2}$  loading, the system exhibits an initial discharge capacity of  $\sim 1000 \text{ mAh g}^{-1}$  under lean electrolyte conditions of an electrolyte-to-sulfur (E/S) ratio of  $4 \text{ }\mu\text{L/mg}_s$ . The system also maintains a capacity of  $817 \text{ mAh g}^{-1}$  after 40 cycles. With addition of polymer additives, the dense sulfur cathodes (35% porosity) at E/S of  $4 \text{ }\mu\text{L/mg}_s$ , the system shows a capacity of  $\sim 900 \text{ mAh g}^{-1}$  for 50 cycles, showing the promise of these systems for high-energy-density Li-S batteries.

- Y. Cui's group at Stanford University continued work using 1,5-bis(2-(2-(2-methoxyethoxy)ethoxy)ethoxy)anthra-9,10-quinon (AQT) as a redox mediator (RM) in developing all-solid-state Li-S batteries (ASSLSBs). They have further fabricated a high mass-loading of lithium sulfide ( $\text{Li}_2\text{S}$ ) cathodes with AQT and tested their cycling performance in 2032 Li-S coin-cell batteries using solid polymer electrolytes. They report that the  $\text{Li}_2\text{S}@AQT$  cell realized an areal capacity of  $2.3 \text{ mAh cm}^{-2}$  with a high mass-loading of  $\text{Li}_2\text{S}$  ( $3.7 \text{ mg cm}^{-2}$ ) at  $60^\circ\text{C}$  corresponding to a high cell-level energy density of  $416 \text{ Wh kg}^{-1}$  using the total mass of the cathode excluding the current collector, the solid electrolyte with RMs, and the anode. The cells also showed good rate capability achieving a discharge capacity of  $1214 \text{ mAh g}^{-1}$ ,  $827 \text{ mAh g}^{-1}$ ,  $577 \text{ mAh g}^{-1}$ , and  $406 \text{ mAh g}^{-1}$  based on commercial  $\text{Li}_2\text{S}$  at 0.06C, 0.12C, 0.24C, and 0.48C, respectively. These results demonstrate the promise of AQT in enabling high performance in ASSLSBs.
- E. Hu's group at Brookhaven National Laboratory in partnership with D. Qu at University of Wisconsin, Milwaukee, continued work in testing a novel bio-inspired N-doped carbon with a unique pore structure. They have expanded the electrochemical test in pouch cells ( $1 \text{ inch} \times 1.25 \text{ inch}$  pouch). They showed that under lean electrolyte conditions of E/S =  $10 \text{ }\mu\text{L}$ , following activation at C/20 for two cells, cells showed a capacity of  $\sim 900\text{-}950 \text{ mAh g}^{-1}$  at C/5. Cells with higher electrolyte exhibited rapid decay in capacity in the initial 70 cycles, and the capacity stabilized at  $\sim 600 \text{ mAh g}^{-1}$ . They also studied the polysulfide ion distribution in the electrolyte. Their result showed few polysulfide ions in the electrolyte during charge and discharge, and the only species detected was elemental sulfur, suggesting the role of nitrogen atoms in disproportionation of sulfur ions mitigating their shuttling to the lithium anode. They also postulate that high surface area and pore volume of N-doped carbon are effective in trapping more sulfur, suggesting the beneficial role of nitrogen doping and porous host structure demonstrating promise for high-energy-density Li-S batteries.
- G. Liu's group at the University of California, Berkeley, continued their work exploring new micellar electrolytes for Li-S batteries. They showed that the capacity retention of the Li-S battery with TF(1:5)DLiTFSI, TF(1:10)DLiTFSI, and TF(1:20)DLiTFSI electrolyte solutions was excellent, even though only 0.5 M LiTFSI salt concentration was used (lower than the standard salt concentration for Li-S batteries), which may correspond to the formation of a good solid electrolyte interphase layer by  $\text{F}_4\text{EO}_2$  additive on the surface of the lithium anode, while preventing degradation of the TFSI anion. TF refers to the presence of 1,1,2,2-tetrafluoroethyl-2,2,3,3-tetrafluoropropyl ether and  $\text{F}_4\text{EO}_2$  moieties. These systems also showed CE of 100%, 99.93%, and 99.92%, respectively, after 20 cycles. Further, they showed that the Li-S battery cells containing TF(1:5)DLiTFSI electrolyte solution exhibited superior performances in both the initial specific discharge capacity, or  $C_{\text{sp}}$ , and CE compared to the Li-S battery cells with TF(1:5)DLLiTFSILiFSI, and TF(1:5)DLLiFSI electrolyte solutions, likely due to different surface chemistry phenomena occurring on the Li-metal anode combined with better chemical stability of the TFSI anion compared to the FSI anion. These results show the promise of these new electrolytes for high-energy-density Li-S batteries.
- Y. S. Meng's group at the University of California, San Diego, (UCSD) continued demonstrating the efficacy of the new hexaazatrinaphthylene (HATN) polymer-sulfur composite electrode architectures in Li-S batteries. Major activities included successful demonstration of reproducibly synthesizing the HATN monomer from the laboratory-scale trials of 2-g batches with on-site collaboration between UCSD and Ampcera. This will lay the path for the team realizing the goal of generating a 50-g batch. The

second accomplishment included quantifying the  $\text{LiNO}_3$  consumption in bulk C-S cathode and nano C-S cathode following electrochemical cycling using high-performance liquid chromatography – ultraviolet spectroscopy techniques showing that the nano C-S cathode consumed much larger amounts of  $\text{LiNO}_3$  compared to bulk C-S cathode due to the high surface area. The third aspect included improving the specific capacity of the sulfur cathode to achieve  $\sim 1250 \text{ mAh g}_{\text{sulfur}}^{-1}$  of the HATN / carbon nanotube (CNT) polymer-sulfur composite electrodes with the baseline electrolyte via electrochemical sulfur infusion achieved by mixing bulk sulfur with the HATN/CNT composite. The fourth aspect included investigating the sulfur cathode volume change after discharging into the  $\text{Li}_2\text{S}$  cathode under lean electrolyte conditions of  $6 \mu\text{L mg}_{\text{sulfur}}^{-1}$ , and they show that the HATN/CNT-S cathode can accommodate a large volume change during charge and discharge. A fifth accomplishment involved the team updating the cyclability of the HATN/CNT-S cathode with a high areal capacity of  $\sim 5.5 \text{ mAh cm}^{-2}$  for Li-S batteries in coin cell under lean electrolyte ( $< 5 \text{ g Ah}^{-1}$ ) and low N/P ratios [ $< 2.6$ ; that is, the capacity ratio between anode (negative electrode) and cathode (positive electrode)]. Finally, the team evaluated the electrochemical performance of the General Motors C-S cathode for further study under lean electrolyte conditions. The studies show the promise of the HATN/CNT-S system for high-energy-density Li-S batteries.

- P. N. Kumta's group at the University of Pittsburgh, Pennsylvania, reported on new sulfur confinement cathode, new dendrite-free current collectors for Li-metal anodes, and theoretical understanding of interfacial energy for dendrite resistant alloying of current collectors. Accordingly, the team demonstrated the generation of porous organic framework materials (POFM1) with pre-designed and customized properties comprised of lightweight elements with repeat units of monomers modifying the electrode interface. Following melt infiltration of sulfur into the POFM1 structures, the cathodes were cycled with a sulfur loading of  $3.2 \text{ mg cm}^{-2}$  electrode area. The electrodes show an initial discharge capacity of  $\sim 950 \text{ mAh g}^{-1}$  stabilizing to  $\sim 625 \text{ mAh g}^{-1}$  after the 10<sup>th</sup> cycle. Following prolonged cycling at 0.1C, the electrode shows a very stable capacity of  $\sim 480\text{-}490 \text{ mAh g}^{-1}$  for over 230 cycles with an E/S ratio of  $8 \mu\text{L mg}^{-1}$ . In the area of anodes, the team studied the system of multicomponent alloys (MCAs) as a dendrite-free anode material synthesized using high-energy mechanical milling. Structurally isomorphous alloys are generated showing similar lattice registry to lithium, preventing lithium dendrite growth by forming solid solution with lithium ions electrochemically presented from metallic lithium as the counter anode. As a result, the system shows excellent alloying and dealloying behavior affording a stable areal capacity of  $\sim 1 \text{ mAh cm}^{-2}$  for continuous 30 cycles. Finally, the team used a macroscopic atomic model to estimate the interfacial enthalpy between the lithium layer and the various MCA compositions and then identified the best alloys showing interfacial enthalpy of  $+0.07 \text{ kJ/mol}$  and  $-0.3 \text{ kJ/mol}$  for lithium concentration of 5 at% in the different alloys. Interfacial enthalpies of these systems will also be optimal at higher lithium concentrations, rendering them promising as dendrite-free anodes and current collectors. The studies thus show the promise of these cathode and anode systems for high-energy-density Li-S batteries.
- D. Wang's group at Pennsylvania State University utilized the optimizing strategy for the sulfurized polyacrylonitrile baseline reported before to further improve the electrochemical performances of the teams' sulfur polymerized composite (SPC) derived active material. The team has demonstrated polysulfide-free SPC cathodes with a high initial discharge capacity of  $600 \text{ mAh g}^{-1}$  at an E/S ratio  $< 10 \mu\text{L mg}^{-1}$ . Additionally, the team also worked on parameter optimization of the synthesis conditions. Thus, they reduced the heating time and temperature and then tested in carbonate electrolytes. They showed that after optimization and activation, the SPC cathode would reach  $> 700 \text{ mAh g}^{-1}$ . The system also showed cycling stability with capacity retention  $> 90\%$  after 100 cycles. The systems are also durable over an enlarged cutoff window of 0.5 to 3.0 V showing an initial specific capacity of  $750 \text{ mAh g}^{-1}$  based on the total weight of cathode, which is also maintained on cycling in carbonate electrolyte. The results obtained thus far by the team show the potential and promise of these SPC systems as promising electrode systems for next-generation, high-energy-density Li-S batteries.

## Task 5.1 – Novel Chemistry: Lithium Selenium and Selenium Sulfur Couple (Khalil Amine, Argonne National Laboratory)

**Project Objective.** The project objective is to develop novel  $S_xSe_y$  cathode materials and advanced liquid electrolytes for rechargeable lithium batteries with high energy density and long life, as well as low cost and high safety.

**Project Impact.** Development of a new battery chemistry is promising to support the goal of plug-in hybrid electric vehicle and electric vehicle applications.

**Approach.** The dissolution of lithium polysulfides (LiPS) in nonaqueous electrolytes has been the major contribution to the low energy efficiency and short life of Li-S batteries. In addition, insulating characteristics of both end members during charge/discharge (sulfur and  $Li_2S$ ) limit their rate capacity. To overcome this problem, sulfur or  $Li_2S$  is generally impregnated in a carbon-conducting matrix for better electronic conductivity. However, this makes it difficult to increase the loading density of practical electrodes. It is proposed to solve these barriers using the following approaches: (1) partially replace sulfur with selenium, (2) nano-confine the  $S_xSe_y$  in a nanoporous conductive matrix, and (3) explore advanced electrolytes with suppressed shuttle effect.

**Out-Year Goals.** This new cathode will be optimized with the following goals:

- A cell with nominal voltage of 2 V and energy density of 600 Wh/kg.
- A battery capable of operating for 500 cycles with low capacity fade.

**Collaborations.** This project engages in collaboration with the following: C. Sun and X. Zuo of Advanced Photon Source at Argonne National Laboratory (ANL), Y. Liu of the Center for Nanoscale Materials at ANL, and L. Cheng of the Materials Science Division at ANL.

### Milestones

1. Fabrication of single-layer Li-S pouch cell with stable cycle life and *in situ* diagnostics. (Q1, FY 2022; Completed)
2. Development of 1 Ah Li-S pouch cell with a cell energy density of  $> 300$  Wh/kg and stable cycle life. (Q3, FY 2022; Completed)
3. Time-of-flight secondary ion mass spectrometry studies on the cycled lithium metal and sulfur cathode and optimization of Li-S pouch cells: cell-level diagnostic, electrolytes, and interlayer optimization. (Q3, FY 2022; Completed)
4. Development of novel SeS cathode with high areal capacity of  $> 4$  mAh/cm<sup>2</sup> for 100 cycles. (Q4, FY 2022; Completed)

## Progress Report

This quarter, the team has targeted improving the cycling performance and suppressing the self-discharge of Li-S batteries during charge/discharge at a wide temperature range (0-50°C). This would require both control on the cathode structures and electrolyte structures to simultaneously suppress the shuttle effect and stabilize the lithium stripping/plating process.

The team prepared the ordered macroporous sulfur host (OMSH). As shown in the scanning electron microscopy image of OMSH (Figure 117a), the ordered macroporous structure with a pore diameter of ~180 nm was successfully constructed. They then infiltrated ~80 wt% Se-doped sulfur (Se:S = 1:9 in mass ratio) into the hollow chamber of OMSH through the molten-diffusion method at a temperature of 155°C for 12 hours. The obtained cathode material was denoted as OMSH-Se/S. The transmission electron microscopy image of OMSH-Se/S (Figure 117b) shows that the macropores of OMSH are filled with Se-doped sulfur particles. The energy-dispersive X-ray spectroscopy images of OMSH-Se/S (Figure 117c) indicate that sulfur and selenium elements are uniformly distributed inside the cathode material, confirming the successful encapsulation of Se/S into the ordered macroporous structure. Meanwhile, the uniform distribution of zinc and cobalt elements suggests the existence of double-end binding sites inside the OMSH-Se/S, which can enhance the electrochemical kinetics of redox. X-ray photoelectron spectroscopy characterization of OMSH-Se/S (Figure 117d) reveals the existence of selenium bonding, as the selenium 3p1/2 (168.31 eV) and Se 3p3/2 (161.82 eV) can be identified. Meanwhile, the Se-S (56.0 eV and 57.0 eV) and Se-Se (55.49 eV and 56.35 eV) bonds in OMSH-Se/S cathode material (Figure 117e) confirmed the formation of a new phase of Se/S compound after selenium doping, rather than a simple physical mixture of selenium and sulfur. The formation of the Se/S phase can enhance the electronic conductivity and reversibility of cathode composite in comparison with pure sulfur phase. The content of Se/S in the OMSH-Se/S was measured to be 79.11 wt% by thermogravimetric analysis (Figure 117f).

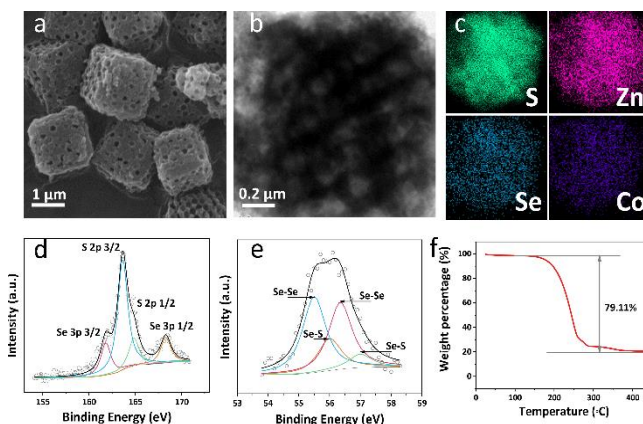


**Figure 117. Structure and composition analysis of cathode material.** (a) Scanning electron microscopy image of OMSH host material. (b-c) Transmission electron microscopy and corresponding X-ray energy dispersive spectroscopy chemical mapping of OMSH-Se/S (interesting elements are sulfur, zinc, selenium, and cobalt). (d-e) High-resolution X-ray photoelectron spectra of (d) sulfur 2p and (e) selenium 3d of OMSH-Se/S cathode material. (f) Thermal gravimetric analysis curve of OMSH-Se/S cathode material under argon atmosphere from room temperature to 450°C.

In the hydrofluoroether (HFE)-based electrolyte, the LiPS solubility can be effectively suppressed, leading to suppressed shuttle effect. Meanwhile, selenium doping and the ordered macroporous host structure can greatly enhance the electrical conductivity and the ion transport of the cathode composite even under high sulfur content conditions. Thus, as shown in Figure 118a, the OMSH-Se/S cathode material can deliver a reversible specific capacity of 1065.25 mAh g<sup>-1</sup> and a high Coulombic efficiency (CE, > 99.5%) at a current density of 160 mA g<sup>-1</sup>. Moreover, a high-capacity retention rate of 81.77% for 300 cycles can be achieved with an areal Se/S loading of 2 mg cm<sup>-2</sup>. The team also characterized the electrochemical performance of OMSH-Se/S cathode under higher areal Se/S loading and controlled electrolyte-to-sulfur ratio (10 μL mg<sup>-1</sup>). As shown in Figure 118b, when increasing the areal Se/S loading to 3.0 mg cm<sup>-2</sup>, the cell can deliver a high areal capacity of 3.82 mAh cm<sup>-2</sup> at 200 mA g<sup>-1</sup> and maintain 2.70 mAh cm<sup>-2</sup> after 100 cycles. Moreover, when they further increased the areal Se/S loading to 5.8 mg cm<sup>-2</sup>, the cathode can still deliver 5.47 mAh cm<sup>-2</sup> at 200 mA g<sup>-1</sup> (Figure 118b-c), corresponding to a specific capacity of 943.10 mAh g<sup>-1</sup>. The high active material utilization of OMSH-Se/S under high areal Se/S loading indicates that the ordered macroporous host combined with selenium doping can

effectively enhance the electrochemical redox kinetics. As a result, the OMSH-Se/S can achieve a high CE of > 99.2% and a high-capacity retention rate (71.77% for 100 cycles) even under high areal Se/S loading ( $5.8 \text{ mg cm}^{-2}$ ) conditions.

Due to the LiPS high solubility in the conventional 1,2-dimethoxyethane (DME)-based electrolyte, the severe self-discharge will lead to sharp capacity decay and corrosion of Li-metal anode, especially under high areal sulfur loading conditions. To validate the effectiveness of retarding self-discharge by using HFE-based electrolyte, the team recorded the open-circuit voltage of the resting cells in both DME- and HFE-based electrolyte after two initial cycles for one week. As shown in Figure 118d, in the conventional DME-based electrolyte, the voltage dropped 205 mV after resting for one week. In sharp contrast, the cell with HFE-based electrolyte dropped only 20 mV after resting for one week (Figure 118e). The much smaller voltage drops in the HFE-based electrolyte further confirmed that the HFE-based electrolyte can effectively reduce the LiPS self-discharge rate. More importantly, even after resting for one week, when they resumed the cycling test, the areal capacity of the cell could immediately recover to  $5.53 \text{ mAh cm}^{-2}$  and maintained as  $5.44 \text{ mAh cm}^{-2}$  after 50 cycles at  $167.6 \text{ mA g}^{-1}$  (Figure 118f).

Hence, the team has successfully improved the cycling stability and self-discharge of Li-S batteries under high areal sulfur loading through selenium doping and use of HFE electrolytes.

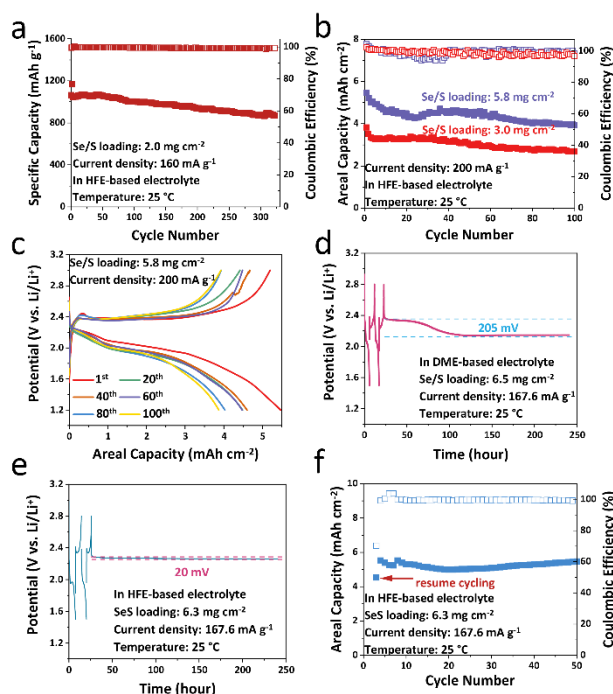


**Figure 118. Electrochemical characterizations of OMSH-Se/S cathode material.** (a) Cycling performance of OMSH-Se/S cathode in HFE-based electrolyte at  $160 \text{ mA g}^{-1}$  with an areal Se/S loading of  $2 \text{ mg cm}^{-2}$ . (b) Cycling performance of OMSH-Se/S cathode with higher areal Se/S loading conditions ( $3.0 \text{ mg cm}^{-2}$  and  $5.8 \text{ mg cm}^{-2}$ ) in HFE-based electrolyte at  $200 \text{ mA g}^{-1}$ . (c) Voltage profiles of various cycles of OMSH-Se/S cathode under high areal Se/S loading ( $5.8 \text{ mg cm}^{-2}$ ) condition in HFE-based electrolyte. (d-e) Voltage profiles of OMSH-Se/S cathode ( $\sim 6.5 \text{ mg cm}^{-2}$ ) that rested for one week after two initial cycles in (d) DME-based and (e) HFE-based electrolytes. (f) Cycling performance of OMSH-Se/S cathode after resting for one week in HFE-based electrolyte. Hollow and solid symbols in (a), (b), and (f) represent Coulombic efficiency and discharge capacity, respectively.

## Patents/Publications/Presentations

### Patent

- Zhao, C., G-L. Xu, and K. Amine. High Energy Metal Sulfur or Selenium-Sulfur Battery. U. S. Patent application, filed on September 28, 2022; no. 17/954,939.

### Publication

- Lee, B. J., C. Zhao, J-H. Yu, T-H. Kang, H-Y. Park, J. Kang, Y. Jung, X. Liu, T. Li, W. Xu, X. Zuo, G-L. Xu\*, K. Amine,\* and J. Yu.\* “Development of High-Energy Non-Aqueous Lithium-Sulfur Batteries via Redox-Active Interlayer Strategy.” *Nature Communications* 13 (2022): 4629.

## Task 5.2 – Development of High-Energy Lithium-Sulfur Batteries (Dongping Lu and Jun Liu, Pacific Northwest National Laboratory)

**Project Objective.** The project objective is to develop high-energy, low-cost Li-S batteries with long lifespan. All proposed work will employ thick sulfur cathode ( $\geq 4 \text{ mg/cm}^2$  of sulfur) at a relevant scale for practical applications. The diffusion process of soluble polysulfide out of thick cathode will be revisited to investigate cell failure mechanism at different cycling. The fundamental reaction mechanism of polysulfide under the electrical field will be explored by applying advanced characterization techniques to accelerate development of Li-S battery technology.

**Project Impact.** The theoretical specific energy of Li-S batteries is  $\sim 2300 \text{ Wh/kg}$ , which is almost three times higher than that of state-of-the-art Li-ion batteries. The proposed work will design novel approaches to enable Li-S battery technology and accelerate market acceptance of long-range electric vehicles (EVs) required by the EV Everywhere Grand Challenge.

**Approach.** The project proposes the following approach: (1) to identify and address key issues of applying high-energy sulfur cathodes including materials, binders, electrode architectures, and functional electrode additives, (2) to advance the mechanism study of sulfur cathode and electrolyte by using *in situ* / *ex situ* techniques and custom-designed hybrid cell setup, and (3) to verify effectiveness of the new approaches with coin/pouch cells by using high-loading electrodes ( $> 4 \text{ mg/cm}^2$ ), limited lithium ( $< 200\%$  lithium excess), and lean electrolyte (electrolyte-to-sulfur, or E/S, ratio  $< 4 \mu\text{L/mg}$ ).

**Out-Year Goals.** This project has the following out-year goals:

- Fabricate Li-S pouch cells with thick electrodes to understand sulfur chemistry/electrochemistry in environments similar to those witnessed in real application.
- Leverage the Li-metal protection project funded by the U. S. Department of Energy and Pacific Northwest National Laboratory (PNNL) advanced characterization facilities to accelerate development of Li-S battery technology.
- Develop Li-S batteries with a specific energy of  $400 \text{ Wh/kg}$  at cell level, 1000 deep-discharge cycles, improved abuse tolerance, and less than 20% capacity fade over a 10-year period to accelerate commercialization of EVs.

**Collaborations.** This project engages in collaboration with the following: X-Q. Yang (Brookhaven National Laboratory, BNL), M. Cai (General Motors), J. Bao (PNNL), P. Khalifah (BNL), and Z. Liu (Thermo Fisher Scientific).

### Milestones

1. Build three-dimensional (3D) electrode models to understand electrolyte transport and sulfur reactions in high-loading and low-porosity sulfur electrodes. (Q1, FY 2022; Completed)
2. Optimize S/C material and electrode architecture to realize sulfur utilization  $> 1100 \text{ mAh/g}$  in high loading electrode ( $> 4 \text{ mg S/cm}^2$ ) with sulfur content  $> 70\%$  and porosity  $< 35\%$ . (Q2, FY 2022; Completed)
3. Study impacts of electrode architecture and topography on sulfur utilization rate and cell cycling. (Q3, FY 2022; Completed)
4. Process high-loading ( $> 4 \text{ mg/cm}^2$ ) and dense ( $< 35\%$  porosity) sulfur electrodes at a relevant scale for pouch-cell fabrication. (Q4, FY 2022; Completed)

## Progress Report

Last quarter, the team studied sulfur reactions in high-loading and low-porosity sulfur electrodes (45% porosity) and their dependence on cathode particle size and structures. Compared with small particle cathode, the S/C large particle cathode (LPC) can deliver higher discharge capacity at a smaller cell polarization, which is ascribed to the promoted electrode wetting of the low-tortuosity LPC. To further improve cathode energy density, in this quarter, they attempted to improve the sulfur content by optimizing the structures of the sulfur host materials and identified that pore connectivity is an important factor that should be considered carefully when designing the large-sized secondary sulfur host materials. The optimized materials were scaled up and validated through the cell test at practical conditions (35% porosity, E/S ratio 4  $\mu\text{L}/\text{mg}_\text{S}$ ).

The N-doped integrated Ketjen Black (NKB) particles with different pore conductivity (NKB11, NKB12, and NKB15) were synthesized by integrating KB particles by poly(melamine-co-formaldehyde) methylated (PMF) at different PMF/KB ratio, where PMF acts as both an integration reagent and nitrogen resource. After sulfur was infiltrated at 155°C (80 wt% sulfur), the sulfur distribution in different NKBs was studied by X-ray nano-computed tomography (nano-CT). Figure 119a-c demonstrates the reconstructed 3D images of NKB/S materials, the red color represents a high contrast of sulfur, and the evolution from red to blue color indicates a decrease of relative sulfur concentration. In the NKB11/S (Figure 119a), the red and yellow areas are close to the center part of the secondary particle, while the blue and green areas are around the surface region. This indicates that during heat treatment sulfur tends to concentrate at the center of NKB11, exhibiting a descent in the sulfur concentration gradient from inside to outside. This is due to the high pore connectivity of the NKB11 at a lower integration degree (PMF/KB = 1/1). Driven by the capillarity, such high surface area, as well as sufficient pore connectivity, facilitates sulfur diffusion and distribution. On the contrary, with an increase of PMF/KB ratio from 2:1 to 5:1, bigger size sulfur aggregation was observed across the particle. This is because with increase of amorphous carbon content, both NKB particle surface and inside pores get blocked, reducing both the pore volume and connectivity as proved by the Brunauer–Emmett–Teller analysis (not shown here)

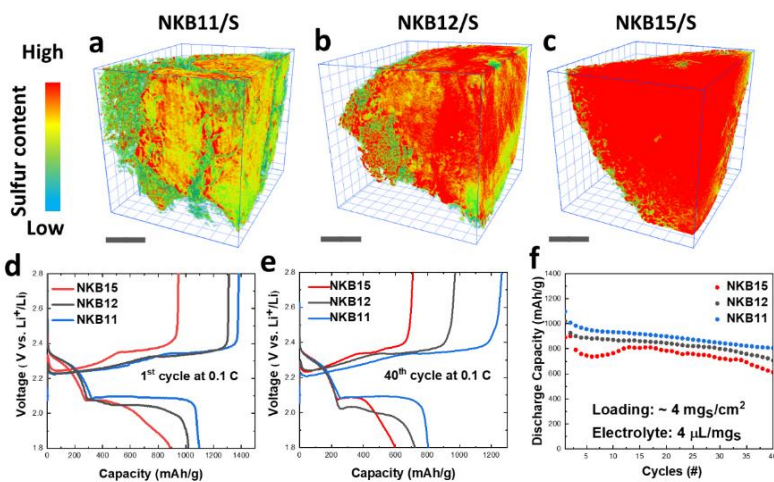


**Figure 119.** X-ray nano-computed tomography images of sulfur concentration distribution in (a) NKB11, (b) NKB12, and (c) NKB15, respectively. The scale bar is 6  $\mu\text{m}$ . (d) Discharge/charge curves of different NKB/S electrodes in the 1<sup>st</sup> cycle. (e) Discharge/charge curves of different NKB/S electrodes after 40 cycles. (f) Cycling performance of different NKB/S electrodes in 40 cycles at low E/S ratio.

utilization rate from 1100 mAh/g, to 1020 mAh/g, to 890 mAh/g. A close comparison of the discharging profiles indicates that all three NKB/S materials show similar capacities of  $\sim 250$  mAh/g for the first discharge plateau at 2.3 V, suggesting a similar conversion extent from elemental sulfur to LiPS. An obvious performance deviation was observed for the second discharge plateau: bigger polarization and lower discharge capacity at

and nano-CT analysis. As a result, the fused sulfur has a limited accessibility to the mesopores of the NKB. Instead, the sulfur stays in the voids between the individual KB particles and forms such a connected sulfur framework, which has a high contrast in CT.

Effects of KB integration degree and sulfur distribution on cell performance were studied in coin cells. The electrochemical performance of different NKB/S materials was evaluated at practical conditions of high sulfur loading ( $\geq 4$   $\text{mg}/\text{cm}^2$ ) and lean electrolyte (E/S ratio 4  $\mu\text{L}/\text{mg}_\text{S}$ ). Figure 119d-e compares the discharge/charge curves of different NKB/S materials at the 1<sup>st</sup> and 40<sup>th</sup> cycles. With an increase of PMF/KB ratio, the cell shows a decreasing trend of sulfur

higher PMF/KB ratio. Such a trend was maintained during cycling. After 40 cycles, NKB11/S has a reversible capacity of 800 mAh/g with a similar discharge voltage, while the NKB12/S and NKB15/S suffer from an increased polarization and a quicker capacity fading. This performance deviation was ascribed to the differences of NKB structures and sulfur distribution. As proved by nano-CT and X-ray energy dispersive spectroscopy (not shown here), NKB11 has a more open structure and better pore connectivity, forming a decreasing sulfur distribution from inside to outside. The sulfur-lack carbon shell provides more active sites for polysulfides deposition before diffusing outside of the particles. While NKB12 and NKB15 have lower surface area and less pore accessibility, sulfur has slower reaction kinetics and more serious irreversible loss. As a result, the generated polysulfides will either directly deposit on the particle surface or diffuse outside secondary particles, causing capacity loss of the second discharge plateau. Without sacrificing the rigidity and processability of the secondary particles, PMF:KB = 1:1 is an optimal ratio for the synthesis of high performance NKB/S cathode.

The NKB11/S was scaled up to ~ 40 g per batch at the laboratory for large-area electrode processing. Feasibility of the materials was further validated by increasing both sulfur content in the NKB/S composite and sulfur loading of the electrode. For the 50% porosity cathode with overall sulfur content of 72%, the 5 mg/cm<sup>2</sup> electrode still delivers a high discharge capacity of ~1000 mAh g<sup>-1</sup> under lean electrolyte conditions (E/S ratio of 4) (Figure 120a-b). Compared to the 64% sulfur electrodes, although the discharge specific capacity was decreased slightly from ~ 1100 mAh g<sup>-1</sup> to ~ 1000 mAh g<sup>-1</sup> in a 72% sulfur electrode, the overall specific capacity (based on whole weight of the electrode) was instead improved from 704 mAh/g to 720 mAh/g because of the reduction of parasitic weight. After 40 cycles, the cell can maintain a capacity of 817 mAh/g, 80% of its initial capacity. By integrating the team's recently developed polymer additives, the very dense sulfur cathode (35% porosity) can still deliver a large discharge capacity and maintain stable cycling of 50 cycles at a low E/S ratio of 4 (Figure 120c-d). This further validates the feasibility of the NKB11/S for next-step large-area electrode coating and Li-S pouch fabrication.

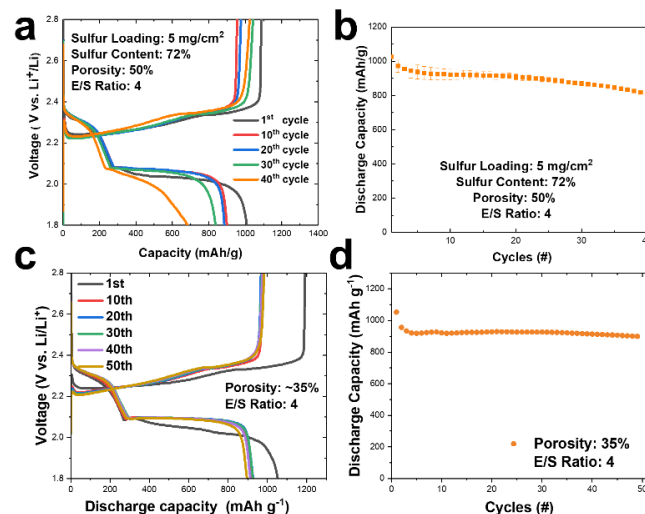


**Figure 120.** (a) Discharge/charge curves of 5 mg/cm<sup>2</sup> NKB11/S electrode at different cycles. (b) Cycling performance of the 5 mg/cm<sup>2</sup> NKB11/S electrode. (c) Discharge/charge curves of NKB11/S-Polymer electrodes at different cycles. (d) Cycling performance of NKB11/S-Polymer cathodes.

## Patents/Publications/Presentations

### Publications

- Feng, S., J. Liu, X. Zhang, L. Shi, C. Anderson, Y. Lin, M-K. Song, J. Liu, J. Xiao, and D. Lu.\* “Rationalizing Nitrogen-Doped Secondary Carbon Particles for Practical Lithium-Sulfur Batteries.” *Nano Energy* 103 (2022): 107794.
- Feng, S., R. K. Singh, Y. Fu, Z. Li, Y. Wang, J. Bao, Z. Xu, G. Li, C. Anderson, L. Shi, Y. Lin, P. G. Khalifah, W. Wang, J. Liu, J. Xiao, and D. Lu.\* “Low-Tortuous and Dense Single-Particle-Layer Electrode for High-Energy Lithium-Sulfur Batteries.” *Energy & Environmental Science* 15 (2022): 3842–3853.

### Presentation

- 242<sup>nd</sup> Electrochemical Society Meeting, Atlanta, Georgia (October 9–13, 2022): “Effects of Sulfur Cathode Topography on Cycling of Practical Li–S Batteries”; L. Shi, C. S. Anderson, J. Liu, J. Xiao, and D. Lu.

## Task 5.3 – Nanostructured Design of Sulfur Cathodes for High-Energy Lithium-Sulfur Batteries (Yi Cui, Stanford University)

**Project Objective.** The charge capacity limitations of conventional transition metal oxide cathodes are overcome by designing optimized nano-architected sulfur cathodes. This study aims to enable sulfur cathodes with high capacity and long cycle life by developing sulfur cathodes from the perspective of nanostructured materials design, which will be used to combine with Li-metal anodes to generate high-energy Li-S batteries. Novel sulfur nanostructures as well as multifunctional coatings will be designed and fabricated to overcome issues related to volume expansion, polysulfide dissolution, and the insulating nature of sulfur.

**Project Impact.** The capacity and cycling stability of sulfur cathodes will be dramatically increased. This project's success will allow Li-S batteries to power electric vehicles and decrease the high cost of batteries.

**Approach.** The approach involves three main efforts:

- Advanced nanostructured sulfur cathodes design and synthesis, including (1) engineer empty space into sulfur cathode to solve the problem of electrode volume expansion, (2) develop novel sulfur nanostructures with multifunctional coatings for confinement of S/Li polysulfides to address issues of active materials loss and low conductivity, (3) develop/discover optimal nanostructured materials that can capture the polysulfide dissolved in the electrolyte, (4) develop space-efficiently-packed nanostructured sulfur cathode to increase volumetric energy density and rate capability, and (5) identify interaction mechanism between sulfur species and different types of oxides/sulfides, and find optimal materials to improve capacity and cycling of sulfur cathode.
- Structure and property characterization, including *ex situ* scanning electron microscopy, X-ray photoelectron spectroscopy analysis, and *in operando* X-ray diffraction and optical microscopy.
- Electrochemical testing including coin cells and pouch cells as well as a set of electrochemical techniques.

**Out-Year Goals.** The cycle life, capacity retention, and capacity loading of sulfur cathodes will be greatly improved (200 cycles with 80% capacity retention, > 0.3 mAh/cm<sup>2</sup> capacity loading) by optimizing material design, synthesis, and electrode assembly.

**Collaborations.** This project collaborates with the following: BMR principal investigators; SLAC National Accelerator Laboratory: M. Toney (*in situ* X-ray); and Stanford University: W. Nix (mechanics) and Z. Bao (materials).

### Milestones

1. Designing redox mediators (RMs) to facilitate Li<sub>2</sub>S activation for all-solid-state Li-S Batteries (ASSLSBs). (Q1, FY 2022; Completed)
2. Understanding redox chemistry in ASSLSBs using *operando* X-ray absorption measurements. (Q2, FY 2022; Completed)
3. Demonstrating cycling performance of ASSLSBs with designed RMs. (Q3, FY 2022; Completed)
4. Enabling ASSLSBs with high area capacity and high energy density. (Q4, FY 2022; Completed)

## Progress Report

Last quarter, the team proved the efficacy of 1,5-bis(2-(2-(2-methoxyethoxy)ethoxy)ethoxy)anthra-9,10-quinone (AQT) beyond the first activation cycle in ASSLSBs. After incorporating AQT, lithium polysulfides prefer to stay on the cathode side, and are rapidly oxidized/reduced during charging/discharging. This quarter, the team further fabricated the high mass-loading lithium sulfide ( $\text{Li}_2\text{S}$ ) cathodes with AQT ( $\text{Li}_2\text{S}@AQT$ ) and tested their cycling performance in the Li-S batteries (type 2032) with solid polymer electrolytes. The  $\text{Li}_2\text{S}@AQT$  cell obtained an areal capacity of  $2.3 \text{ mAh cm}^{-2}$  with a high mass-loading of  $\text{Li}_2\text{S}$  ( $3.7 \text{ mg cm}^{-2}$ ) at  $60^\circ\text{C}$  (Figure 121a), which corresponds to a high cell-level energy density of  $416 \text{ Wh kg}^{-1}$ . The energy density is calculated from the average discharge voltage (2.1 V), cell capacity ( $2.3 \text{ mAh cm}^{-2}$ ), and total mass of the cathode ( $6.1 \text{ mg cm}^{-2}$ , excluding current collector), the solid electrolyte with RMs ( $2.9 \text{ mg cm}^{-2}$ ), and the anode ( $2.6 \text{ mg cm}^{-2}$ ). Figure 121b displays the cycling performance of the high-loading Li-S battery at a current density of  $0.25 \text{ mA cm}^{-2}$ . The cycling shows a slight capacity decay for the initial equilibrium cycles and remains stable with a discharge capacity of  $640 \text{ mA h g}^{-1}$  after 15 cycles.

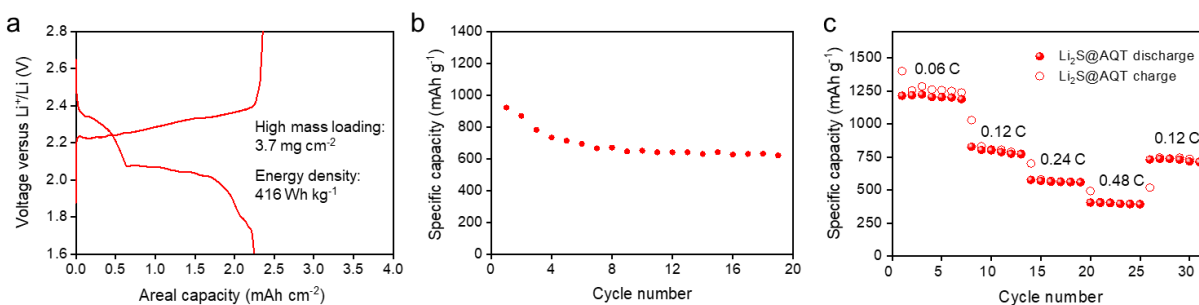


**Figure 121. Electrochemical performance of  $\text{Li}_2\text{S}$  cathodes with AQT redox mediator in all-solid-state Li-S batteries. (a) Voltage profile at the 2<sup>nd</sup> cycle of the  $\text{Li}_2\text{S}@AQT$  cell with a high mass-loading ( $3.7 \text{ mg cm}^{-2}$ ) at a current density of  $0.25 \text{ mA cm}^{-2}$ . (b) Cycling performance of the high loading cell. (c) Specific capacity of  $\text{Li}_2\text{S}@AQT$  cathodes cycled from 0.06 C to 0.48 C. All cells are operated at  $60^\circ\text{C}$ .**

Finally, the rate performance of as-prepared cathodes is investigated by cycling cells at different C-rates (Figure 121c). The  $\text{Li}_2\text{S}@AQT$  cell, benefiting from the effective AQT-enhanced Li-S reaction kinetics, shows a good rate capability, achieving a discharge capacity of  $1214 \text{ mAh g}^{-1}$ ,  $827 \text{ mAh g}^{-1}$ ,  $577 \text{ mAh g}^{-1}$ , and  $406 \text{ mAh g}^{-1}$  based on commercial  $\text{Li}_2\text{S}$  at 0.06 C, 0.12 C, 0.24 C, and 0.48 C, respectively. These results show that AQT promoted both reaction kinetics and stability to achieve high-performance ASSLSBs.

## Patents/Publications/Presentations

The project has no patents, publications, or presentations to report this quarter.

## Task 5.4 – Investigation of Sulfur Reaction Mechanisms (Enyuan Hu, Brookhaven National Laboratory; Deyang Qu, University of Wisconsin, Milwaukee)

**Project Objective.** The primary objectives are as follows:

- To optimize and down select polymeric sulfur electrode. The team will focus on the overall dissolution of polysulfide in an electrolyte and effectiveness of polymeric sulfur electrodes.
- To develop small organosulfur materials for all-solid-electrolyte Li-S batteries.
- To continue developing alternative anode materials having low reactivity with dissolved polysulfide ions.
- To continue investigating the interaction of polysulfides in the cathode solid phase.

**Project Impact.** The results of this project will be used for development of technologies that will significantly increase energy density and cycle life and will reduce the cost of beyond Li-ion battery systems. This will greatly accelerate deployment of electric vehicles and reduce carbon emission associated with fossil fuel consumption and help in the direction of building the U. S.-based energy storage manufacture chains.

**Approach.** The team will first down select the cross-linked polymerized sulfur compounds, in which sulfur is attached to the conductive backbone with covalent bonds; therefore, the polysulfides can be immobilized within the matrix. They will also explore the small organosulfur molecules in all-solid-state Li-S batteries (ASSLSBs). They will continue exploring alternative anode materials that can cycle well and do not react with dissolved polysulfide and sulfur in the electrolyte to mitigate the “shuttle effect.” In addition, they will continue to engage in fundamental *in situ* electrochemical investigations of the sulfur redox mechanisms to guide material and engineering designs. They will also continue optimizing alternative electrode fabrication processes.

**One-Year Goals.** The interim goal is to develop a Li-S battery with S-containing cathode of 600-800 mAh/g capacity with mitigation of the “shuttle effect.”

**Collaborations.** The principal investigator (PI) works closely with beamline scientists at synchrotron facilities to develop novel Li-S characterization tools. The PI and co-PI collaborate closely with top scientists at Argonne National Laboratory, Lawrence Berkeley National Laboratory, and Pacific Northwest National Laboratory, as well as U. S. industrial collaborators at General Motors, Duracell, Clarios, etc. The PI and co-PI also collaborate with scientists in China, Japan, and South Korea. These collaborations will be strengthened and expanded to give this project a vision on both today’s state-of-the-art technology and tomorrow’s technology in development, with feedback from the material designer and synthesizers upstream and from industrial end users downstream.

### Milestones

1. Selection of small organosulfur compounds and complete design of all-solid-state testing. (Q1, FY 2022; Completed)
2. Complete initial testing of prelithiated tin anode. Complete initial testing of small organo-sulfur molecules in an ASSLSB. (Q2, FY 2022; Completed)
3. Complete testing of full Li-S cell with alternative prelithiated anode. Complete synthesis of potential polymeric sulfur materials. (Q3, FY 2022; Completed)
4. Complete testing full cell with selected polymeric sulfur, small organosulfur cathodes, and alternative anode. (Q4, FY 2022; Completed)

- Complete investigations on the sulfur redox reaction mechanism in the solid phase in cathode and the interplay between dissolved polysulfide ions in electrolyte and sulfide compounds in the solid. Complete and continue testing of polymeric sulfur cathode, small organosulfur cathode, and alternative anode in full cell format. (Annual milestone; In progress)

## Progress Report

Last quarter, the team reported the synthesis and testing of a novel bio-inspired N-doped carbon with a unique pore structure. The carbon was used as the carbon host of a sulfur cathode. Good performance was reported in a coin-cell test. They hypothesized that the carbon could trap high-order polysulfides and enhance interaction with long-chain polysulfide ions.

This quarter, they expanded the electrochemical test in pouch cells (1-inch  $\times$  1.25-inch pouch), shown in Figure 122. They also started investigation of the mechanism of the sulfur redox reaction on the carbon. Figure 123 shows the charge and discharge curves and cycle results of the pouch cells made with different electrolyte per mg of sulfur. As shown in Figure 123c, under a starved electrolyte condition, it is hard for a large cell to become activated, for example, for all the surface to be wetted. For instance, it took 50 cycles for the cell with electrolyte-to-sulfur (E/S) ratio of 10  $\mu\text{L}$  to reach its highest capacity. After activated at 0.05C for two cycles, both cells with 10  $\mu\text{L mg}^{-1}$  and 20  $\mu\text{L mg}^{-1}$  of electrolyte delivered a specific capacity of  $\sim 900\text{-}950 \text{ mAh g}^{-1}$  at 0.2C. The cell with more electrolyte experienced a faster capacity decay in the initial 70 cycles, and its capacity became stabilized at  $\sim 600 \text{ mAh g}^{-1}$ . The fast capacity decay can be ascribed to the loss of active sulfur that crystalized on the surface of NC800 in an excess electrolyte. The specific capacity of the pouch cell with 10  $\mu\text{L mg}^{-1}$  of electrolyte gradually increased in the initial 50 cycles, which is ascribed to a slow penetration of electrolyte during the discharge and charge process.

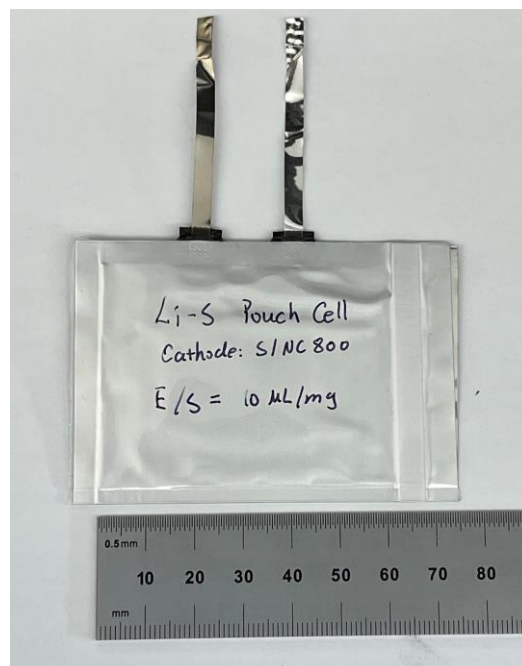


Figure 122. Li-S pouch cell.

To understand the good performance of the carbon materials in a Li-S battery, analysis was done to investigate the polysulfide distribution in the electrolyte. The preliminary results showed little polysulfide ions in the electrolyte during the charge and discharge of the Li-S cell. The only detectable specie dissolved in the electrolyte was elemental sulfur. Therefore, it can be speculated that the nitrogen atoms of NCs play a critical role for the disproportionation of  $\text{S}_n^{2-}$  and mitigate their shuttling toward a lithium anode during the cycling process. In addition, due to the relatively high specific surface area and pore volume, NC800 can effectively trap more sulfur. Therefore, both optimal porous structure and nitrogen content contributed to the good performance of NC800.

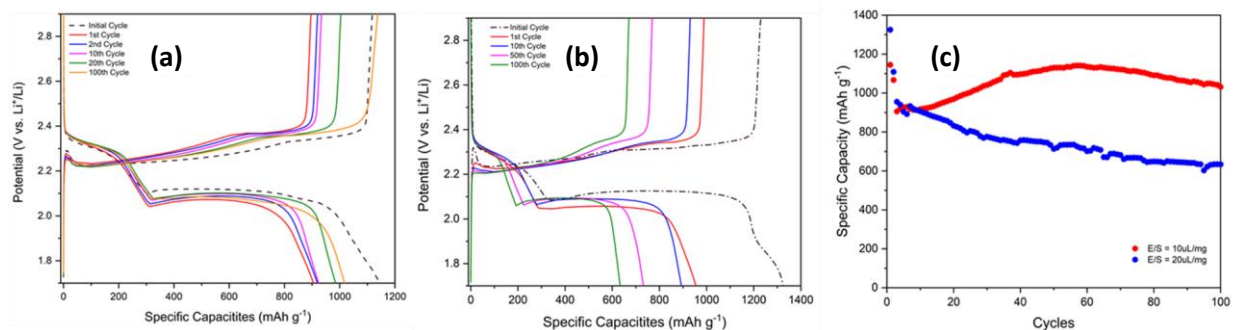


Figure 123. (a) Charge and discharge curves for an S/NC800 pouch cell with E/S ratio of 10  $\mu\text{L}$ . (b) Charge and discharge curves for the S/NC800 pouch cell with E/S ratio of 20  $\mu\text{L}$ . (c) Comparison of the 1<sup>st</sup> 100 cycles for the pouch cells made with S/NC800 with E/S ratio of 10  $\mu\text{L}$  and 20  $\mu\text{L}$ . The cells were tested under 0.2 C rate.

## Patents/Publications/Presentations

### Publication

- Ji, W., X. Zhang, M. Liu, T. Ding, H. Qu, D. Qiu, D. Zheng, and D. Qu. \* “High-Performance All-Solid-State Li-S Batteries Enabled by an All-Electrochem-Active Pre lithiated Si Anode.” *Energy Storage Material* 53 (2022): 613–620.

### Presentation

- American Chemical Society Fall Meeting, Sulfide-Based Solid-State Electrolytes & Batteries, Chicago, Illinois (August 21, 2022): “An All-Solid-State Li-Oranosulfide Battery with an Ultrathin Flexible Solid-State Electrolyte.”

## Task 5.5 – New Electrolytes for Lithium-Sulfur Battery (Gao Liu, Lawrence Berkeley National Laboratory)

**Project Objective.** The project objective is to develop new electrolytes, additives, and electrode compositions for Li-S battery with high ion-conductivity, stable toward polysulfide, and promoting the polysulfide affiliation with the electrode substrate to prevent polysulfide dissolution.

**Project Impact.** This work will address the high cost and low energy density of Li-ion rechargeable batteries. The emerging Li-S batteries could feature both high energy density and low cost. This project enables applications of the low-cost, abundant sulfur element as a major chemical component for electrical energy storage. This project will develop new approaches for electrolytes and electrode compositions of Li-S rechargeable batteries.

**Approach.** This project aims to develop new electrolytes and additives for Li-S battery. The properties of the ideal electrolyte for sulfur electrode would be high ion conductivity, stable toward polysulfide, and promoting the polysulfide affiliation with the electrode substrate to prevent polysulfide dissolution. The project is designed to first understand the electrode substrate interaction with the polysulfides in different electrolytes. This will lead to better understandings of the polysulfide nucleation and precipitation mechanisms in common electrolytes. The second stage of the project will focus on chemically modifying the structures of the solvent and salt electrolyte molecules to increase electrolyte stability and ionic conductivity, to prevent polysulfide dissolution, and to promote polysulfide precipitation.

**Out-Year Goals.** The team will also investigate the contribution of Li-metal electrodes to overall Li-S battery performance and will develop methods to stabilize Li-metal surface.

**Collaborations.** This project collaborates with J. Guo and C. Zhu (Advanced Light Source / Lawrence Berkeley National Laboratory, LBNL), A. Minor (National Center for Electron Microscopy at LBNL / University of California, Berkely), G. Nagy and W. Heller (Neutron National Science User Facility / Oak Ridge National Laboratory), and P. B. Balbuena (Texas A&M University).

### Milestones

1. Synthesize and formulate amphiphilic electrolytes using combination solvents, salts, and ionic liquids. (Q1, FY 2022; Completed)
2. Optimize sulfur positive electrode to balance ionic and electronic conductivity, as well as dissolution and precipitation properties. (Q2, FY 2022; Completed)
3. Implement at least one strategy to stabilize Li-metal anode electrode. (Q3, FY 2022; Completed)
4. Combine the electrolyte, sulfur electrode, and Li-metal stabilization strategies to achieve stable cell cycling. (Q4, FY 2022; Completed)

## Progress Report

The performance of the Li-S batteries with the prepared electrolyte solutions is consistent with their electrochemical stability and with the ionic conductivity results. More importantly, the capacity retention of the Li-S batteries with TF(1:5)DLiTFSI, TF(1:10)DLiTFSI, and TF(1:20)DLiTFSI electrolyte solutions is excellent, even though only 0.5 M lithium bis(trifluoromethanesulfonyl)imide (LiTFSI) salt concentration was used (lower than the standard salt concentration for Li-S batteries), which may correspond to formation of a good solid electrolyte interphase layer by  $F_4EO_2$  additive on the surface of the lithium anode and protect the degradation of (trifluoromethanesulfonyl)imide (TFSI) anion. (Note: For acronym meanings, refer to Table 7; for results, refer to Figure 124). The Coulombic efficiency (CE) of the Li-S batteries with TF(1:5)DLiTFSI, TF(1:10)DLiTFSI, and TF(1:20)DLiTFSI electrolyte solutions were ca. 100%, 99.93%, and 99.92%, respectively, after 20 cycles (Figure 124b). Correspondingly, the CE significantly decreased after 20 cycles of the Li-S batteries with TDLiTFSI, TF(1:5)DLiTFSILiFSI, and TF(1:5)DLiFSI electrolyte solutions, with values of ca. 99.32%, 88.18%, and 88.79%, respectively. However, the Li-S battery cell with TF(1:5)DLiTFSI electrolyte solution exhibited superior performance in both the initial capacity and CE compared to the Li-S battery cells with TF(1:5)DLiTFSILiFSI, and TF(1:5)DLiFSI electrolyte solutions; this may be due to the presence of different anion in the electrolyte solutions and, hence, resulting in different surface chemistry phenomena occurring on the Li-metal anode after cycling. The TFSI anion is more chemically stable toward lithium metal compared to that of the bis(fluorosulfonyl)imide (FSI) anion, which may be helpful for improving electrochemical stability of lithium salt toward different kinds of reactive intermediates, generated during the cycling of Li-S batteries.

**Table 7. Compositions of the prepared electrolyte solutions.**

Electrolyte Solution	Ratio of TTE and $F_4EO_2$ in Solution A		Amount of DOL (vol%) with respect to Solution A	Molar concentration of LiTFSI	Molar concentration of LiFSI
	TTE	$F_4EO_2$			
TDLiTFSI	5	-	10%	0.5 M	-
TF(1:5)DLiTFSI	5	1	10%	0.5 M	-
TF(1:10)DLiTFSI	10	1	10%	0.5 M	-
TF(1:20)DLiTFSI	20	1	10%	0.5 M	-
TF(1:5)DLiTFSILiFSI	5	1	10%	0.25 M	0.25 M
TF(1:5)DLiFSI	5	1	10%	-	0.5 M

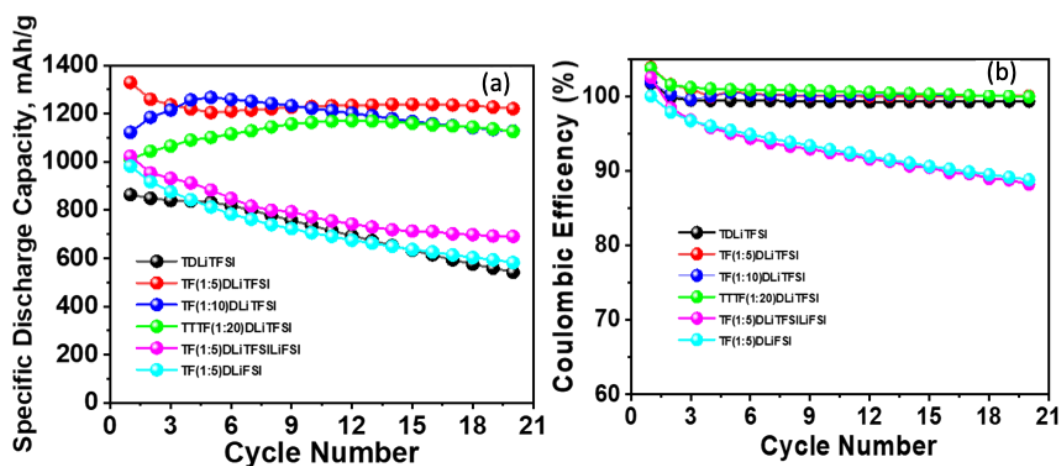


**Figure 124. Cell cycling plots of the as-prepared electrolytes-based S/C//electrolyte//Li half-cell at 0.1 C rate. (a) Specific discharge capacity plots of the cells as a function of cycles at 0.1 C. (b) Coulombic efficiency of the Li-S batteries with as-prepared electrolytes as a function of cycles. Note: For acronym meanings, see Table 7.**

## Patents/Publications/Presentations

### Presentation

- Advanced Lithium Batteries for Automobile Applications (ABAA-13) Conference, Marrakech, Morocco (October 16–19, 2022): “Comparative Study of Imide-Based Electrolyte Salts for Li-S Battery: A Micelle-Based Electrolyte Additive Potentiating the Cycling Performance”; F. Ahmed, C. Feng, D. Li, Q. Miao, and G. Liu.

## Task 5.6 – Strategies to Enable Lean Electrolytes for High Loading and Stable Lithium-Sulfur Batteries (Y. Shirley Meng, University of California, San Diego)

**Project Objective.** The project aims to develop high energy density ( $> 500$  Wh/kg) and low cost ( $< 65$  \$/kWh) Li-S pouch cells.

**Impact.** The project focuses on addressing the fundamental bottleneck in enabling high-energy-density Li-S batteries. This has been identified as the need to reduce liquid electrolyte excess and enable high areal loading electrodes. The challenges are overcome via the use of a dense polymer – sulfur electrode composite, which significantly reduces electrode porosity in conventional C-S systems while improving capacity retention. These capabilities, combined with project collaborator Ampcera’s material scaling and collaborator General Motor’s (GM’s) pouch prototyping capability using thin lithium metal, will result in breakthroughs in next-generation Li-S battery chemistries that meet the energy density ( $> 500$  Wh/kg) and cost goals ( $< \$65$ /kWh) of this project.

**Approach.** Novel electrode architectures using hexaazatriphthylene polymer – sulfur (HATN-S) composite electrode will be explored to reduce the porosity and increase the active loading of the composite electrode. Additionally, advanced electrolyte systems and optimization of Li-metal anode will be applied to further increase energy density of the Li-S pouch cell. If successful, the proposed HATN-S electrode should have less than 20% porosity with high areal capacities of  $> 10$  mAh cm<sup>-2</sup>, which will enable lean electrolyte conditions  $< 2$  g/Ah in the full Li-S pouch cell.

**Out-Year Goals.** The out-year goals involve demonstration of baseline cell chemistries with reduced cathode porosity and increased cathode areal loading pairing with limited electrolyte and lithium inventory. The conventional electrode drying process (solvent evaporation) limits sulfur loading in the electrode, as higher loading leads to cracking. Thus, the HATN-S electrode will be prepared by optimizing the electrode architecture to increase sulfur loading and reduce electrode porosity. The electrolyte system will be optimized to reduce lithium usage [low N/P ratio; that is, capacity ratio between anode (negative electrode) and cathode (positive electrode)] and improve cell stability.

**Collaborations.** Project collaborators include GM and Ampcera. This quarter, the work was accomplished by University of California, San Diego (UCSD). Ampcera reproduced synthesis of hexaazatriphthylene (HATN) monomer and polymer with assistance from UCSD by on-site visiting. GM has provided thin lithium metal (100  $\mu$ m) and has been working on the conventional C/S cathode with various sulfur loadings for this project.

### Milestones

1. Achieve a benchmark performance metric of 80% capacity retention of HATN-S electrodes after 200 cycles using baseline electrolyte system. (Q1, FY 2022; Completed)
2. Process synthesis to demonstrate HATN-S electrode with reduced porosity and increased areal loading. (Q2, FY 2022; Completed)
3. Demonstrate cyclability of optimized HATN-S electrode with limited electrolyte and lithium inventory. (Q3, FY 2022; Completed)
4. Demonstrate stable cycling of optimized HATN-S electrode, which should be able to cycle with limited electrolyte ( $< 2$  g/Ah) and low N/P ratios ( $< 1.2$ ). (Q4, FY 2022; In progress)
5. Demonstrate stable cycling of optimized HATN / carbon nanotube (CNT) – sulfur (that is, HATN/CNT-S) composite electrode ( $\sim 5.5$  mAh cm<sup>-2</sup>) under lean electrolyte ( $< 5$  g Ah<sup>-1</sup>) and low N/P ratios ( $< 2.6$ ). (Q4, FY 2022; Completed)

## Progress Report

The project objective is to develop high energy density ( $> 500$  Wh/kg) and low cost ( $< 65$  \$/kWh) Li-S pouch cells. To achieve that, novel electrode architectures using the HATN-S electrode will be explored to achieve low cathode porosity and high sulfur active loading of the composite electrode. Additionally, advanced electrolyte systems and optimization of the Li-metal anode will be applied to further increase energy density of the Li-S pouch cell. If successful, the proposed HATN-S electrode will achieve less than 20% porosity, significantly decreasing electrolyte usage with high areal capacities of  $> 10$  mAh cm<sup>-2</sup>, enabling lean electrolyte conditions  $< 2$  g Ah<sup>-1</sup> in the full Li-S pouch cell. This quarter, major activities include the following: (1) reproducing the synthesis of HATN monomer (laboratory trial of 2-g batch) by on-site collaboration between UCSD and Ampcera, (2) quantifying LiNO<sub>3</sub> consumption in bulk C-S cathode and nano C-S cathode, (3) improving the S-specific capacity ( $\sim 1250$  mAh g<sub>sulfur</sub><sup>-1</sup>) of the HATN/CNT-S composite electrodes with the baseline electrolyte via electrochemical sulfur infusion, (4) investigating the sulfur cathode volume change after discharging into the Li<sub>2</sub>S cathode under lean electrolyte conditions, (5) updating the cyclability of the HATN/CNT-S cathode with a high cycling areal capacity of  $\sim 5.5$  mAh cm<sup>-2</sup> for Li-S batteries (coin-cell) under lean electrolyte ( $< 5$  g Ah<sup>-1</sup>) and low N/P ratios ( $< 2.6$ ), and (6) evaluating electrochemical performance of the GM C-S cathode for study under lean electrolyte conditions.

Specifically, the synthetic setup was installed at Ampcera by on-site visit from UCSD, and a laboratory trial of a 2-g batch of HATN monomer has been synthesized at Ampcera. The setup for synthesis scale-up was designed, and the target materials and precursors are to be stored in a designated glovebox. This quarter, LiNO<sub>3</sub> consumption in the cathodes of bulk and nano C-S has been quantified with high-performance liquid chromatography (HPLC) methodology, showing the high importance of decreasing the cathode porosity to conserve the electrolyte reservoir. The HATN/CNT-S cathode was prepared by mixing HATN/CNT with bulk sulfur instead of the conventional sulfur melt infusion. After the formation cycle with a high S-specific capacity of  $\sim 1250$  mAh g<sub>sulfur</sub><sup>-1</sup>, the cathode porosity of the HATN/CNT-S cathode was suppressed to be 29%, the same as that of bare HATN-S cathode (29%; first quarter). It also features a super low average two-dimensional (2D) tortuosity of 1.22 within 1.57 of a semicircle, which facilitates electrolyte wettability. This demonstrates that the electrochemical infusion of sulfur species into the host material of HATN/CNT is a highly efficient strategy under the lean electrolyte condition.

Also this quarter, the S-specific capacities of UCSD nano C-S, HATN/CNT-S (electrochemical infusion and melt infusion), and GM C-S cathodes were evaluated by using an electrolyte-to-sulfur (E/S) ratio of  $\sim 6$   $\mu$ l mg<sub>sulfur</sub><sup>-1</sup> for HATN/CNT-S and an E/S ratio of  $\sim 10$   $\mu$ l mg<sub>sulfur</sub><sup>-1</sup> for C-S based on the porosity difference. It is shown that HATN/CNT-S (electrochemical infusion) presents the highest S-specific capacity (high sulfur utilization) and the highest discharge plateau (fast polysulfide kinetics) under the lean electrolyte condition. Further, the cathode volume change was investigated by comparison between the GM C-S and HATN/CNT-S cathodes after discharging. It is illustrated that the HATN/CNT-S cathode accommodates the volume change from sulfur to Li<sub>2</sub>S, while the C-S cathode suffers from a large volume change. By using a lean baseline electrolyte (E/S ratio of  $\sim 6$   $\mu$ l mg<sub>sulfur</sub><sup>-1</sup> or electrolyte-to-capacity ratio of  $\sim 5$  g Ah<sup>-1</sup>) and pairing with 100- $\mu$ m Li-metal foils (N/P ratio of 2.6) received from the team's collaborators at GM, the HATN/CNT-S cathode delivers a high cycling areal capacity of  $\sim 5.5$  mAh cm<sup>-2</sup> at 0.1 C in Li-S batteries (coin cell). In addition, the GM C-S cathode was evaluated under the E/S ratio of  $\sim 10$   $\mu$ l mg<sub>sulfur</sub><sup>-1</sup>, presenting a similar limited cycling behavior to the UCSD nano C-S cathode with drastic capacity decay (first through third quarters). The milestone of an initial areal capacity of 5 mAh cm<sup>-2</sup> has been achieved, and future work will be focused on the assembly of a small pouch cell to make the most use of the electrolyte for high energy density.

### Reproducible Synthesis of HATN Monomer and the Design for Future Scaled-Up Synthesis (UCSD & Ampcera)

Firstly, the UCSD team has synthesized a 5-g batch of HATN monomer and designed a vacuum sealing setup to prepare a 10-g batch of HATN/CNT composite in the laboratory. In efforts to meet the scale-up targets by Ampcera, the synthesis of HATN monomer with high purity must be reproduced before the

HATN/CNT synthesis is transferred to Ampcera's production site. Following on-site visit, the synthesis setup of the Schlenk line was installed at Ampcera with the connection to an argon tank and a vacuum pump (Figure 125a). A laboratory trial of a 2-g batch of HATN monomer has been synthesized at Ampcera (Figure 125b). It has a color difference from the UCSD batch (beige yellow), which was sent for further nuclear magnetic resonance (NMR) validation. To preclude the factor of precursors, both the hex-ketone and diamino-benzonitrile precursors were validated by NMR. Figure 125c-d shows the hydrogen NMR spectra of diamino-benzonitrile of Ampcera and UCSD batches. According to the peak attributions and integrations, they are identical to each other; however, the Ampcera batch needs a recrystallization process like the inset of Figure 125d to improve the purity. Further, since the TCI company has discontinued precursors with large quantities, UCSD and Ampcera have reached out to vendors from various countries. These chemicals will be validated by NMR before being used.

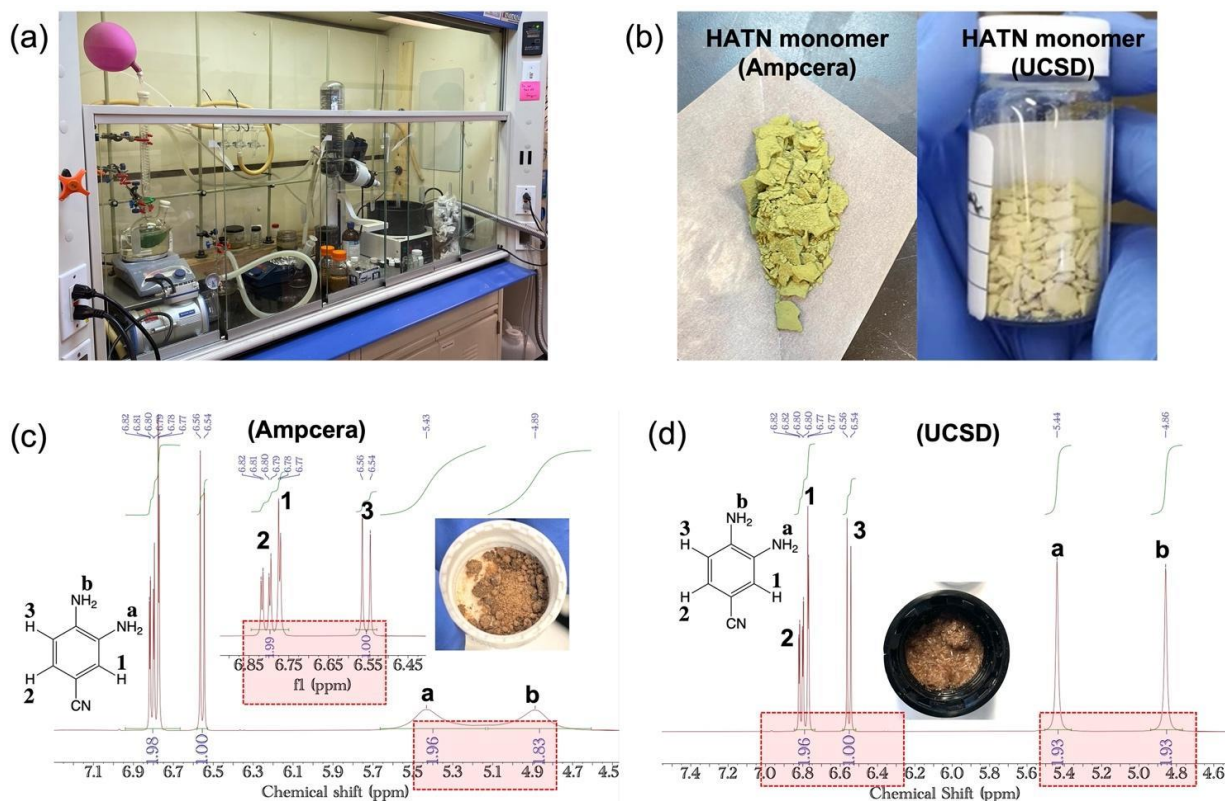


**Figure 125.** (a) The organic synthetic setup installed at Ampcera with on-site visiting by University of California, San Diego (UCSD). (b) Photos of the HATN monomer synthesized by Ampcera and UCSD. (c-d) The hydrogen – nuclear magnetic resonance spectrum of the synthesis precursor of diamino-benzonitrile with its physical appearance (insets) used at Ampcera (c) and UCSD (d).

Using a proprietary polymerization process, Ampcera has been able to prepare the HATN polymer, which will be validated by UCSD using Fourier transform infrared and Brunauer–Emmett–Teller analysis. Further, Ampcera has already established the setup of scaling-up of the synthesis of the HATN monomer (Figure 126a-b). The precursors and target materials will be stored in a designated glovebox to avoid chemical deterioration and contamination. Moreover, Ampcera has large vacuum sealing setups to realize the goal of 50 g per batch. Once the baseline is established, the monomer synthesis will be scaled up to deliver 50-g batches by the end of Year 1. Although the synthesis technology was reproduced at Ampcera, the production of the high-purity HATN monomer has been delayed owing to the discontinuation of the precursors with high purity.

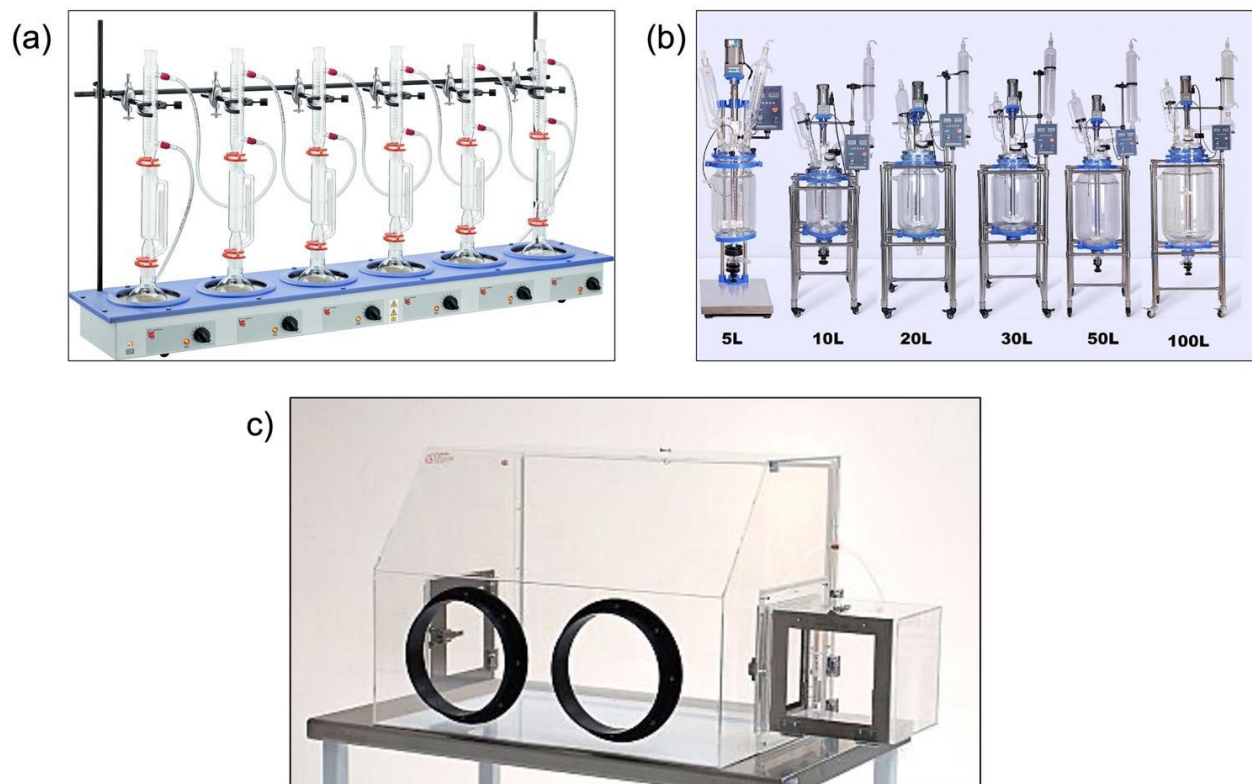


Figure 126. (a-b) The potential scaling-up setup design for the synthesis of HATN monomer. (c) The designated glovebox for materials storage at Ampcera.

### Quantification of $\text{LiNO}_3$ Depletion in Bulk C-S and Nano C-S Cathodes (UCSD)

It is of utmost importance to understand what the limiting factors are for Li-S batteries under lean electrolyte conditions. Apart from the lithium anode and the sulfur cathode, the HPLC – ultraviolet (HPLC-UV) methodology was introduced to quantify the consumption of electrolyte, that is,  $\text{LiNO}_3$ . The cycled cell was disassembled and dissolved by 1,3-dioxolane / 1,2-dimethoxyethane (DOL/DME) solvent, which generated a homogeneous liquid sample (electrolyte). The samples were injected into the HPLC column chromatography for separation and then characterized by the UV detector. It is known that cathode porosity and tortuosity impact electrolyte usage and wettability. This quarter, to investigate the influence on electrolyte consumption, both the nano C-S cathode and the bulk C-S cathode were evaluated for comparison (Figure 127a). Note that the bulk C-S cathode was prepared by a simple mix of bulk sulfur and super phosphorus (low surface area). These two cathodes are using the same E/S ratio of  $10 \mu\text{l mg}_{\text{sulfur}}^{-1}$ , and the lithium anodes are still excessive. The sulfur utilization (practical S-specific capacity / sulfur theoretical capacity) can vary due to the difference in electrolyte utilization. Figure 127a shows that the bulk C-S cathode delivers a similar S-specific capacity to that of the nano C-S cathode, indicating a similar sulfur utilization.

However, the bulk C-S cathode sustains superior cycling in sharp contrast to the nano C-S cathode, which has a poor cycle life. It has been verified that the consumption of  $\text{LiNO}_3$  in the nano C-S cathode is severe, while there is minor  $\text{LiNO}_3$  depletion in the bulk C-S cathode (Figure 127b-c). It is evidenced that the  $\text{LiNO}_3$  peak intensity of the cell after nano C-S cycling in baseline electrolyte is fragile, suggesting the depletion of  $\text{LiNO}_3$ . This huge difference in the  $\text{LiNO}_3$  depletion is correlated to the high surface area of the carbon host and sulfur. Since the sulfur redox chemistry is an interfacial reaction on the conductive carbon host materials, the nano C-S consumes far more  $\text{LiNO}_3$  during the charge and discharge. Hence, to achieve lean electrolyte utilization for high energy density, the sulfur cathode should be less porosity and tortuosity instead of the conventional cathode design principle of the nanostructured C-S cathode.

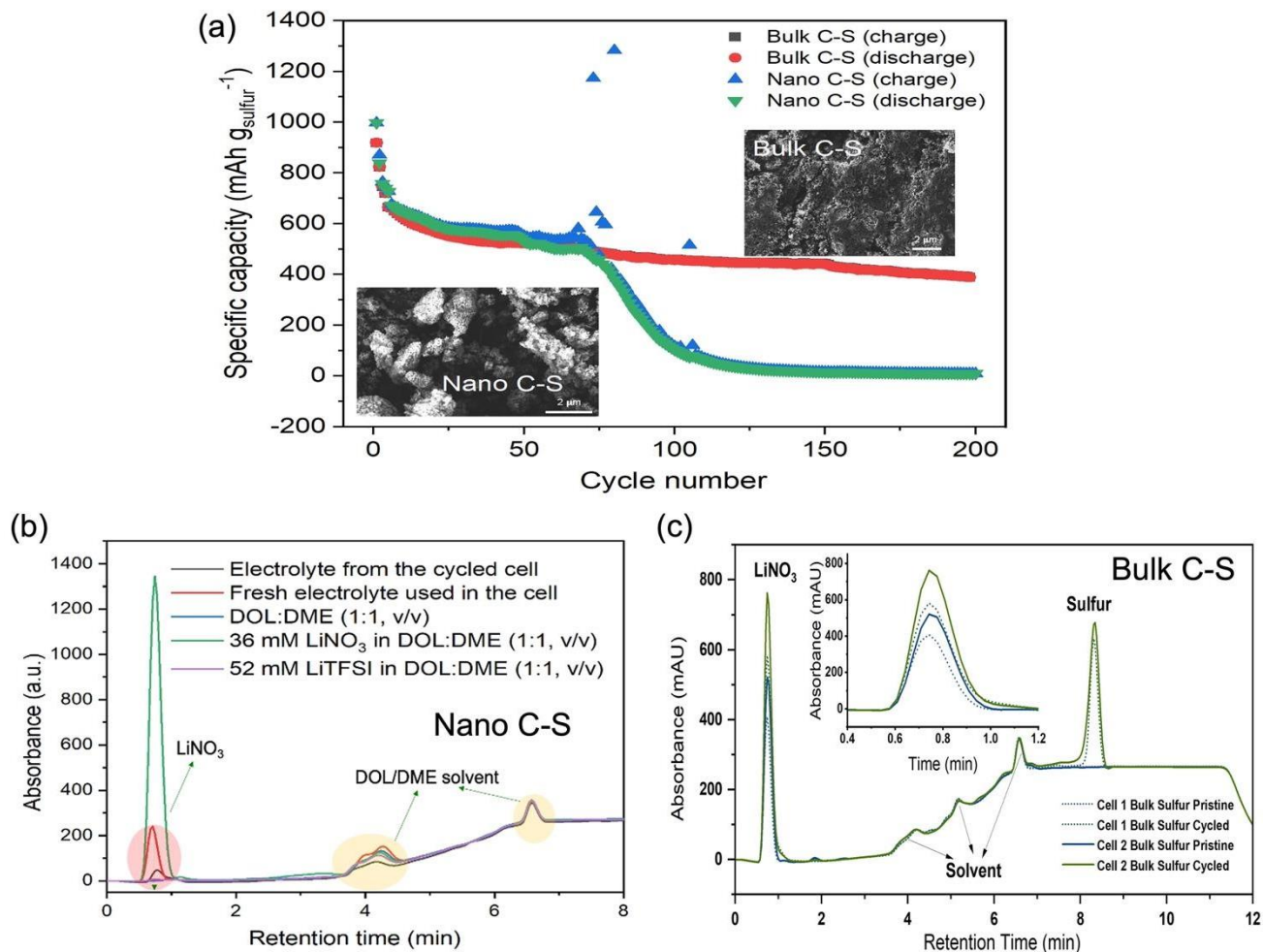


Figure 127. (a) Cycling behavior of the nanostructured C-S and the bulk C-S cathode in baseline electrolyte with E/S ratio of 10 ml mg<sub>sulfur</sub><sup>-1</sup> and 100 mm lithium. The sulfur loading of is 3.8 mg<sub>sulfur</sub> cm<sup>-2</sup> of the nano C-S and 2.52 mg-sulfur cm<sup>-2</sup> of the bulk C-S. (b) high performance liquid chromatography – ultraviolet (HPLC-UV) spectra of the fresh electrolyte, DOL/DME solvent, LiNO<sub>3</sub> and LiTFSI in DOL/DME solvent, and the cycled electrolyte of the nano C-S cathode. (c) HPLC-UV spectra of the pristine electrolyte and cycled electrolyte for bulk C-S cathode.

### Introducing Electrochemical Infusion of Sulfur Species in HATN/CNT-S Cathode (UCSD)

The HATN/CNT composite was prepared to construct a good ion and electron conduction network (third quarter). The HATN/CNT-S cathode was obtained by sulfur melt infusion subsequently (third quarter). Then, a slurry recipe containing HATN/CNT-S composite, a small amount of binder, and carbon additive (super phosphorus) was applied to prepare the cathode electrode sheet using C-coated aluminum foil as the current collector for better adhesion, which contains a sulfur content of 64% (in the entire cathode). A low cathode porosity of ~ 35% was achieved versus ~ 29% for the bare HATN-S cathode. HATN/CNT-S delivers a higher S-specific capacity of ~ 1050 mAh g<sub>sulfur</sub><sup>-1</sup> than ~ 900 mAh g<sub>sulfur</sub><sup>-1</sup> for HATN-S (second and third quarters). Inspired by the simple mix of bulk sulfur and super phosphorus in the preparation of the bulk C-S cathode, the electrochemical sulfur infusion is introduced by simply mixing bulk sulfur with the as-prepared HATN/CNT. This strategy was initially designed for achieving a better wettability of electrolyte, and active sulfur liquid (evidenced from the sulfur HPLC peak) since the intrinsic pores of HATN polymer and CNT are readily filled

up. As illustrated in Figure 128, the HATN/CNT composite was prepared by putting CNTs into the melting polymerization process of the HATN polymer, in which the intrinsic porosity of HATN polymer and CNTs can be maintained to trap the sulfur species. In addition, lithium polysulfide generated during the charge and discharge processes of Li-S batteries can bind to the C = N of the HATN molecular cores (reported mechanism).

On these attributes, the active sulfur species undergoes fast reaction kinetics within the HATN/CNT matrix, and the cathode is expected to boast high S-specific capacity (high sulfur utilization) under the lean electrolyte condition.

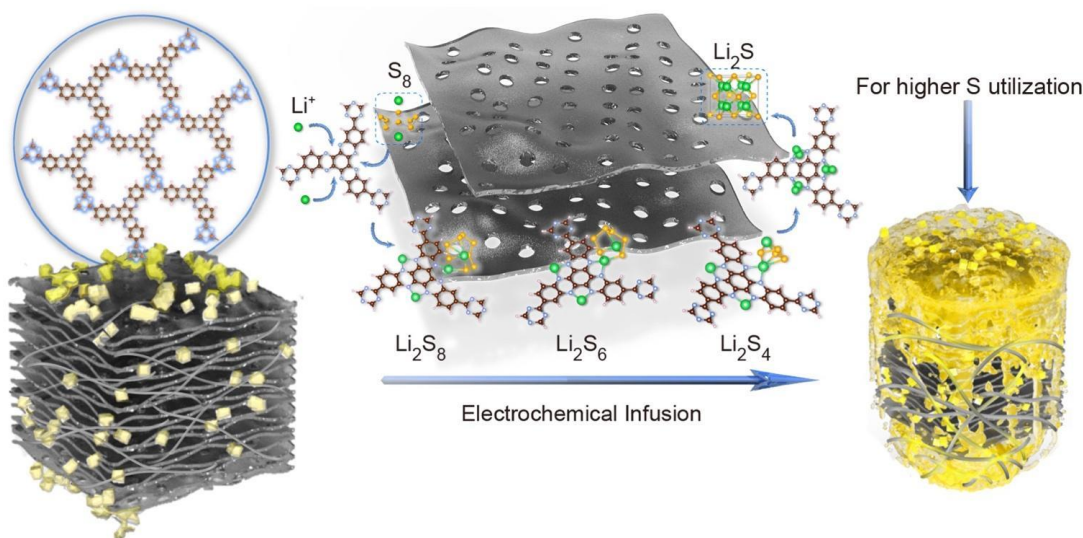


Figure 128. Schematic of the electrochemical infusion of sulfur species in the HATN/CNT-S cathode.

Figure 129a shows that despite lean electrolyte usage, the second discharge plateau of the optimized HATN/CNT cathode typically lies at a higher voltage of  $\sim 2.1$  V at the formation cycle ( $0.05$  C,  $1C = 1000 \text{ mAh g}^{-1}$ ) than that using conventional sulfur infusion. This indicates faster polysulfide redox reaction kinetics for better sulfur redistribution in the cathode under lean electrolyte conditions. The coin cells were assembled by pairing against the  $100\text{-}\mu\text{m}$  Li-metal foil obtained from the team's collaborator, GM, and a lean electrolyte (E/S ratio of  $\sim 6 \mu\text{l mg}_{\text{sulfur}}^{-1}$ ) using baseline electrolyte [1 M LiTFSI in a DOL/DME mixture (1:1, v/v) with 2 wt%  $\text{LiNO}_3$ ]. HATN/CNT-S delivers a higher S-specific capacity of  $\sim 1250 \text{ mAh g}_{\text{sulfur}}^{-1}$  than either  $\sim 900 \text{ mAh g}_{\text{sulfur}}^{-1}$  for the HATN-S cathode (second quarter) or  $\sim 1050 \text{ mAh g}_{\text{sulfur}}^{-1}$  for the HATN/CNT-S cathode via sulfur melt infusion (third quarter). Furthermore, an areal capacity of  $\sim 3.0 \text{ mAh cm}^{-2}$  at  $0.05$  C was achieved. Figure 129b shows the cryogenic focused ion beam scanning electron microscopy (cryo-FIB SEM) image of the cross-section of the UCSD nano C-S cathode as a reference, which is highly porous. However, the HATN/CNT-S cathode via electrochemical infusion features a bulk particle size of  $>10 \mu\text{m}$  (Figure 129c) with a low porosity of  $\sim 29\%$ , the same as that of bare HATN-S cathode ( $29\%$ , first quarter). Further, the quantification of the 2D tortuosity of this optimized HATN/CNT-S cathode is based on a simplified mathematical equation ( $\tau = C/L$ ), wherein  $C$  is the electrolyte diffusion curve length and  $L$  is the distance between the curve ends. Thus,  $\tau = 1$ ,  $\tau = 1.57$ , and  $\tau = \infty$  are defined as paths of a straight line, a semicircle, and a circle, respectively. Herein, three diffusion paths in the above cross-section were measured, exhibiting a low average 2D tortuosity ( $\tau$ ) of 1.22 based on  $\tau_1 = 1.14$ ,  $\tau_2 = 1.15$ , and  $\tau_3 = 1.37$  within 1.57 of a semicircle path. The X-ray energy dispersive spectrum of Figure 129d corresponds to the uniform S-element distribution of the HATN/CNT-S cathode. Its low cathode porosity decreases the electrolyte usage, and the low cathode tortuosity facilitates electrolyte wettability, which ultimately yields a high sulfur utilization and a high working voltage. These results show the effectiveness of the electrochemical sulfur infusion into a bulk ion/electron conductive network.

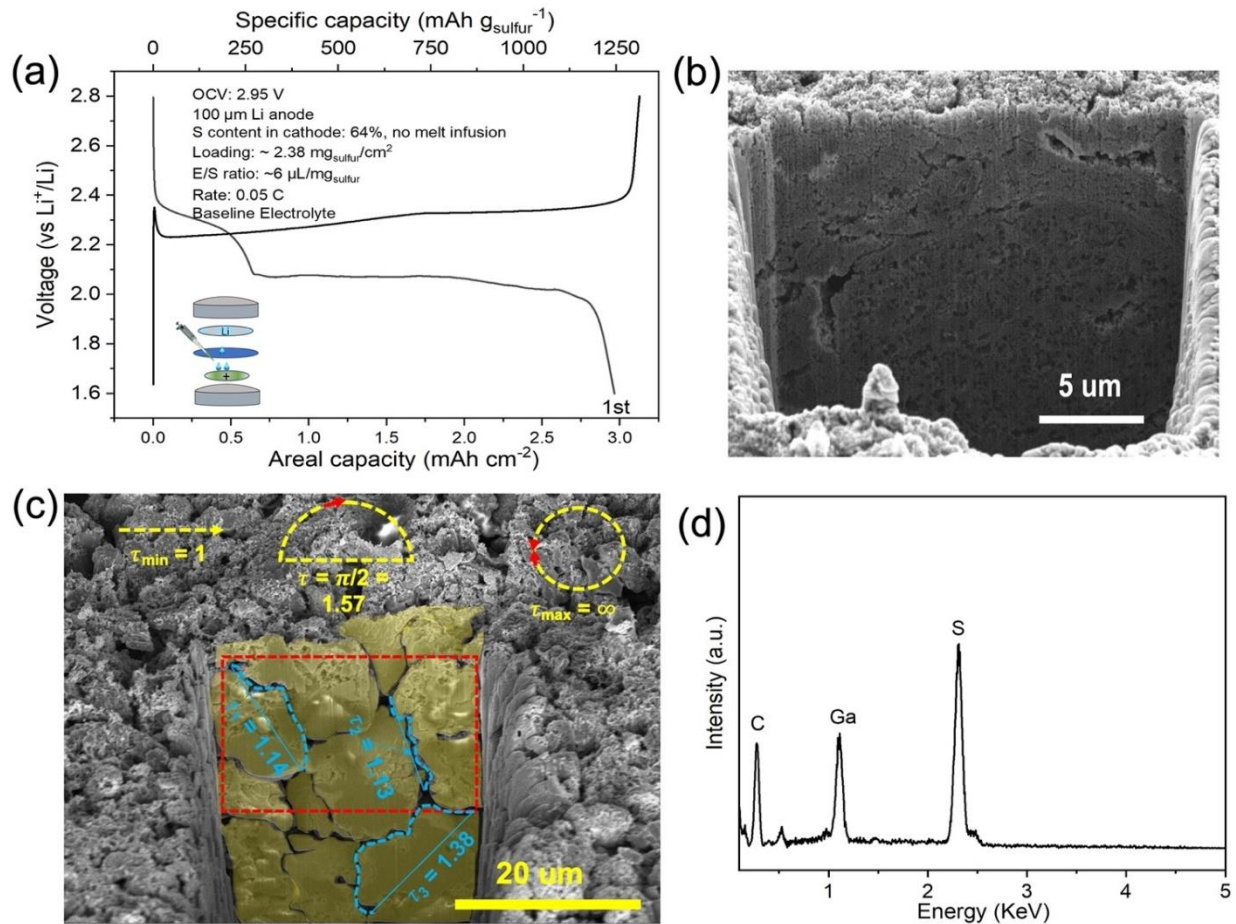
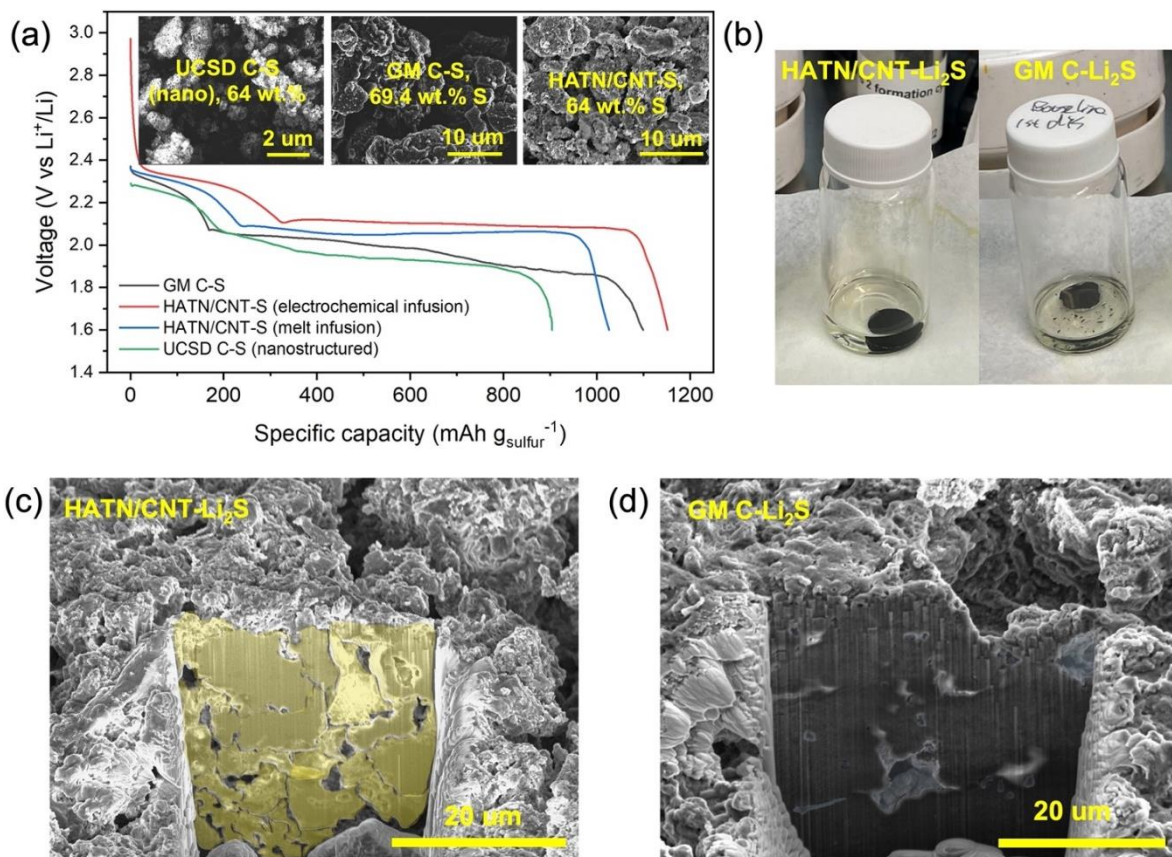


Figure 129. (a) The voltage profile of HATN/CNT-S cathode without sulfur melt infusion in baseline electrolyte of 1 M LiTFSI in a DOL/DME mixture (1:1, v/v) with 2 wt% LiNO<sub>3</sub>, using 100 μm lithium and E/S ratio of 6 μL mg<sub>sulfur</sub><sup>-1</sup>. (b) The cryogenic focused ion beam scanning emission microscopy (cryo-FIB SEM) image of the cross-section of the University of California, San Diego, nano C-S cathode with highly porous structure. (c) The cryo-FIB SEM image of the cross-section of the HATN/CNT-S cathode via electrochemical infusion, which is highlighted with a low average 2D tortuosity ( $\tau$ ) of 1.22 and a bulk particle size of > 10 μm. (d) X-ray energy dispersive spectrum of the selected area (red rectangle in Figure 129c), showing the successful electrochemical sulfur infusion.

### Investigating Volume Change of the HATN/CNT-S Cathode after Discharging (UCSD)

The destruction of electrode structural integrity during cycling is one of the bottleneck problems of Li-S batteries because the conversion of sulfur (2.07 g·cm<sup>-3</sup>) into Li<sub>2</sub>S (1.66 g·cm<sup>-3</sup>) intrinsically results in a large volume expansion of 180% ( $V_{\text{Li}_2\text{S}}/V_{\text{S}}$ , normalized to 1 mol) or a volume change of 80% ( $V_{\text{Li}_2\text{S}} - V_{\text{S}}/V_{\text{S}}$ , normalized to 1 mol). Thus, the selection and design of sulfur cathodes are of great importance. Figure 130a summarizes the 1<sup>st</sup> discharge curves and SEM images (inset) of the cathodes of GM C-S, UCSD C-S, and HATN/CNT-S with/without sulfur melt infusion with a similar sulfur loading of ~ 5 mg cm<sup>-2</sup>. The cells were assembled by using 100-μm lithium anodes and baseline electrolytes with the E/S ratio of 10 μL mg<sub>sulfur</sub><sup>-1</sup> for C-S and 6 μL mg<sub>sulfur</sub><sup>-1</sup> for HATN/CNT-S. It is shown that the GM C-S cathode delivers a high discharge capacity of ~ 1100 mAh g<sub>sulfur</sub><sup>-1</sup> (1<sup>st</sup> cycle) at such a high sulfur content in the cathode of 69.4%. However, both UCSD C-S and GM C-S (Figure 130a) cathodes present a lower working voltage of < 2.0 V, resulting from slower polysulfide diffusion even with a higher E/S ratio of 10 μL mg<sub>sulfur</sub><sup>-1</sup> owing to a higher cathode porosity and tortuosity of C-S. Notably, the HATN/CNT-S cathode (no melt infusion) delivers a higher S-specific capacity of ~ 1150 mAh g<sub>sulfur</sub><sup>-1</sup> than ~ 1050 mAh g<sub>sulfur</sub><sup>-1</sup> for HATN/CNT-S cathode (melt infusion) at a formation current density of 0.05 C (1C = 1000 mAh g<sup>-1</sup>). The initial discharge plateau of ~ 2.1 V is consistent with that under excessive electrolyte. This reconfirms the effectiveness of electrochemical infusion by simply

mixing HATN/CNT with sulfur. Figure 130b presents the washed cathodes of HATN/CNT-S and GM C-S after discharging. By contrast, the GM C-S cathode has a peeling-off issue, suggesting that the volume change can destroy the electrode (GM C-Li<sub>2</sub>S). The cryo-FIB characterization technology has been utilized to track the evolution of sulfur cathodes after discharging the cells (Figure 130c-d). From the cross-section view of the HATN/CNT-Li<sub>2</sub>S cathode (discharged, Figure 130c), the volume change is observed to be minor, while the GM C-Li<sub>2</sub>S cathode boasts a super small pore volume due to the wrap-up of Li<sub>2</sub>S (Figure 130d).



**Figure 130.** (a) The summary of the 1<sup>st</sup> discharge curves and scanning emission microscopy (SEM) images (inset) of the cathodes of GM C-S, University of California, San Diego (UCSD) C-S, and HATN/CNT-S with/without sulfur melt infusion with a similar sulfur loading of  $\sim 5 \text{ mg cm}^{-2}$ . The cells were assembled by pairing against 100- $\mu\text{m}$  lithium anodes in baseline electrolyte with E/S ratios of  $10 \mu\text{l mg}_{\text{sulfur}}^{-1}$  for C-S and  $6 \mu\text{l mg}_{\text{sulfur}}^{-1}$  for HATN/CNT-S. (b) The photos of the discharged cathodes of GM C-S and the optimized HATN/CNT-S, washed by DOL/DME solvent. (c-d) The cryogenic focused ion beam SEM images of the cross-sections of the HATN/CNT-Li<sub>2</sub>S cathode and the GM C-S cathode (discharged, 1<sup>st</sup> cycle). The particles are highlighted in (c), while the pores are identified in (d).

Figure 130c-d demonstrates that the team's HATN/CNT-S cathode can accommodate the large volume change during the charge and discharge processes. Figure 131 exhibits the top view of the cryo-FIB SEM images of HATN/CNT-S and GM C-S cathodes from the pristine (Figure 131a/c) to the discharged (Figure 131b/d) under a small magnification, which is for analysis of cathode volume change from a broad perspective. Figure 131c/d shows that a bare HATN/CNT host can contain the active liquid sulfur species (Li<sub>2</sub>S) much better than a sulfur solid infused HATN/CNT host (melt infusion). This distinguishes it from the GM C-S cathode, which suffers from a huge volume expansion because of Li<sub>2</sub>S encapsulation (Figure 131a-b). It is worth mentioning that the sulfur content of the GM C-S cathode is high, up to 69.4%.

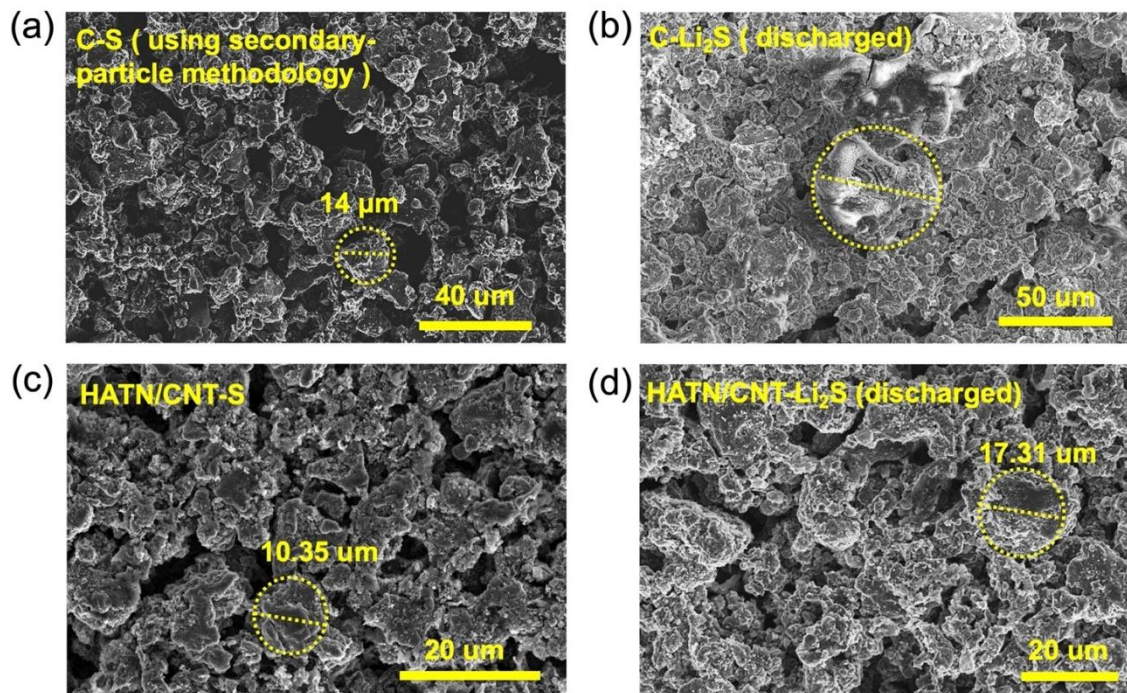


Figure 131. The top-view of scanning electron microscopy images of the pristine GM C-S cathode using the secondary-particle technology and the pristine HATN/CNT-S cathode (a/c) and after 1<sup>st</sup> discharge in Figure 130a (b/d) with a similar sulfur loading of  $\sim 5 \text{ mg cm}^{-2}$  under a small magnification.

### Updating Cyclability of HATN/CNT-S Cathode with High Cycling Areal Capacity of $\sim 5.5 \text{ mAh cm}^{-2}$ for Li-S Batteries

To achieve high-energy-density Li-S batteries, the cathode porosity of HATN/CNT-S needs to be decreased, and the sulfur loading needs to be increased. Previously, the HATN/CNT-S cathode with a small areal capacity of  $2.5 \text{ mAh cm}^{-2}$  was achieved with a stable cycling behavior (680 cycles, third quarter). This quarter, the focus is mainly on preparing high-areal-capacity HATN/CNT-S cathodes by increasing the S-specific capacity via electrochemical infusion (Figure 132a). The milestone of a starting areal capacity of  $5 \text{ mAh cm}^{-2}$ , recommended by the U. S. Department of Energy, has been completed by increasing the sulfur loading to  $6.30 \text{ mg}_{\text{sulfur}} \text{ cm}^{-2}$ . The areal discharge capacity can reach up to  $\sim 7.4 \text{ mAh/cm}^2$  initially under the first  $0.05 \text{ C}$  ( $0.315 \text{ mA cm}^{-2}$ ) formation cycle with a low N/P ratio of 2.6 and a low E/S ratio of  $6 \text{ } \mu\text{l mg}_{\text{sulfur}}^{-1}$  or  $5 \text{ g Ah}^{-1}$ , which quickly stabilized at  $5.5 \text{ mAh/cm}^2$  after switching to the  $0.1 \text{ C}$  discharge current rate for the following cycles (Figure 132b). Notably, the initial discharge plateaus are consistent with the subsequent, which reflects the good wettability and polysulfide diffusion in the HATN/CNT cathode. The cell is ongoing stably with high-capacity retention after 18 cycles. The cells of the HATN/CNT-S cathodes were prepared using  $100\text{-}\mu\text{m}$  lithium anodes (inset of Figure 132a), while the cells of the GM C-S cathodes were assembled by pairing against the thick lithium chips ( $1 \text{ mm}$ , inset of Figure 132c).

Figure 132c shows that the GM C-S delivers a high S-specific capacity of  $\sim 1150 \text{ mAh g}_{\text{sulfur}}^{-1}$ , and an areal capacity of  $\sim 6.2 \text{ mAh cm}^{-2}$  at a formation current density of  $0.05 \text{ C}$  ( $0.268 \text{ mA cm}^{-2}$ ) was achieved, which is consistent with the performance in Figure 133a. The GM C-S cathode also shows major capacity decay by using the lean electrolyte. The cell only lasts for 58 cycles until a drastic capacity decay takes place, even though the lithium is highly excessive (Figure 132d). There are some capacity variations between UCSD and GM data (Figure 132c and Figure 133a), while the cycling decay tendency is similar. After GM had a personnel change this quarter, the GM C-S cathodes with smaller sulfur loadings were prepared with an aim of good consistency. The electrochemical performance, especially the cycling performance, of the C-S cathodes will be evaluated (Figure 133b) before sending them to UCSD. Late this quarter, UCSD will quantify the  $\text{LiNO}_3$  and the Li-metal anode of the cycled GM C-S cathode (Figure 132d) to verify the cycling limitation factor of  $\text{LiNO}_3$  depletion

under lean lithium and electrolyte conditions. Further, UCSD and GM will work closely to prepare single-layer or few-layer pouch cells using even leaner electrolyte with a target of  $< 3 \text{ g Ah}^{-1}$  electrolyte amount, demonstrating cyclability of pouch cells.

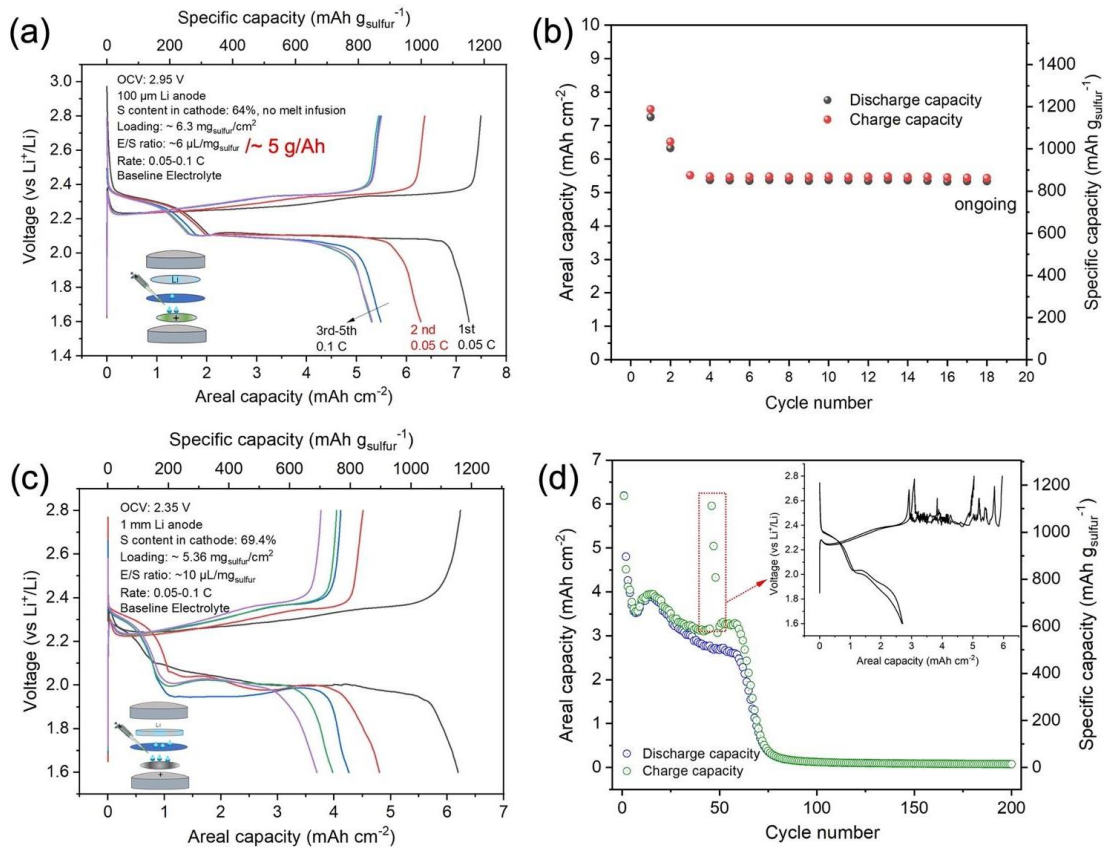


Figure 132. Voltage profiles of (a) the HATN/CNT-S cathode with  $6.30 \text{ mg}_{\text{sulfur}}/\text{cm}^2$  and (c) the GM C-S cathode with  $5.36 \text{ mg}_{\text{sulfur}}/\text{cm}^2$  in baseline electrolytes with different E/S ratios. The inset schematics illustrate the cell assembly. (b) The cycling behavior of the optimized HATN/CNT-S cathode at 0.1 C,  $1 \text{ C} = 1000 \text{ mAh g}^{-1}$ . (d) The cycling stability of the GM C-S cathode showing the same capacity decay tendency with the University of California, San Diego, nano C-S (Figure 127a).

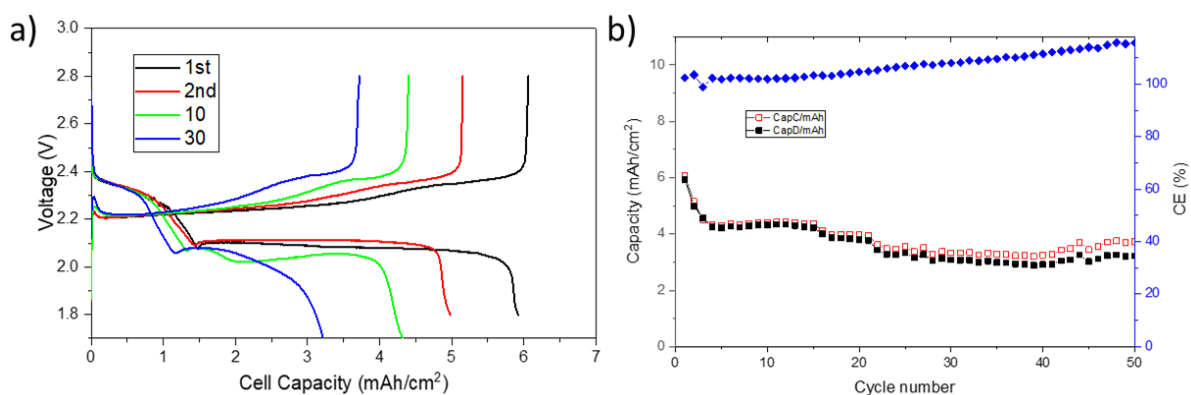


Figure 133. GM data: electrochemical performance of  $5.2 \text{ mg}_{\text{sulfur}}/\text{cm}^2$  sulfur cathode electrode (a) charge-discharge profiles and (b) discharge-charge capacities and Coulombic efficiency versus cycle number.

## Patents/Publications/Presentations

The project has no patents, publications, or presentations to report this quarter.

## Task 5.7 – New Engineering Concepts to High-Energy-Density Lithium-Sulfur Batteries (Prashant N. Kumta, University of Pittsburgh)

**Project Objective.** The major objectives of this project are to develop a Li-S pouch cell with a cell capacity > 300 mAh with energy density  $\geq 500$  Wh/kg,  $\geq 750$  Wh/L with cycling over 1000 cycles @C/3 rate, cycle life of 1000 at C/3 and  $\leq 20\%$  fade in energy @ C/10-C/3, and  $\leq \$80/\text{kWh}$ . To achieve the proposed objectives, the following major goals will be successfully attained over the first year of the project: (1) identification of effective electrocatalysts and Li-ion conductors (LICs) lowering the activation barrier; (2) *in situ* synthesis of electrocatalysts and LIC dispersed complex carbon-based framework material (CFM) and sulfur nanocomposite with sulfur content  $\geq 90$  wt%; (3)  $\sim 15$  mAh/cm<sup>2</sup> areal capacity of sulfur electrode with sulfur loading  $\geq 10$  mg/cm<sup>2</sup>; (4) Li-containing structurally isomorphous alloy (Li-SIA) of  $\geq 1000$  cycles with 15 mAh/cm<sup>2</sup> areal capacity @C/3 rate; and (5) identification of optimal electrolyte compositions giving Li<sup>+</sup> conductivities  $\sim 10^{-2}$  S/cm and polysulfide dissolution < 1 ppm.

**Impact.** The work from this project will have a strong impact on development of high-energy-density Li-S batteries. The results of this work will lead to new knowledge on identification and generation of high-capacity sulfur cathodes and dendrite-free Li-metal anodes using scalable synthesis and fabrication approaches. Both fundamental and applied knowledge will be gathered from the study. Systematic characterization will provide new scientific insights into the mechanisms contributing to the corresponding response in coin-cell and pouch-cell formats. Results of this work also will likely have an impact on other fields such as electrocatalysts for water splitting and fuel cells and other fields engaged in electrochemistry. Plans are also in place to engage under-represented minority undergraduate students to gain research experience in various aspects of the project. With new materials identified as the project is executed, opportunities will emerge for filing invention disclosures, and provisional/non-provisional patent applications. The training and opportunities presented by this project to undergraduate and graduate students as well as postdoctoral research associates will foster next-generation work force training, equipping workers with the necessary skillsets to transform the quality of life all over the globe by generating high-energy-density systems that can be deployed in electric vehicles as well as in laptops and cell phones including innumerable portable and wireless devices, opening the doors to a new green and sustainable energy environment improving overall quality of life.

**Approach.** Work involves executing a theory-driven study directed at identification of electrocatalysts for efficient conversion of polysulfides to Li<sub>2</sub>S during the forward discharge process and backward charge process to elemental sulfur and lithium. Also, first-principles computational approaches will be applied to identify solid-state LICs with conductivity  $> 10^{-4}$  S/cm. Employing expertise in the principal investigator's laboratory, suitable low-temperature (< 240°C) scalable synthesis techniques will be used to generate theoretically identified electrocatalysts and LICs. Low polysulfide solubility and stable solid electrolyte interphase forming electrolytes will then be prepared from commercially available solvents, additives, and salts. The effectiveness of the electrocatalysts and LICs to improve the polysulfide to Li<sub>2</sub>S transformation kinetics and the ability to achieve the targeted specific capacity by trapping polysulfides, including desired structural transformation during charging/discharging, will be assessed; accordingly, suitable modification of electrocatalysts and LICs will be performed to generate the ideal microstructures. Suitable modification if required of lithium alloy as anode will also be performed by alloying with other metals to improve the Li-ion diffusivity kinetics and the Gibbs-Thomson parameter. The scalable approaches developed will be further refined to optimize sulfur utilization in the cathode, engineer the surface and bulk structure of the novel Li-SIA and lithium multicomponent alloy (Li-MCA) anodes to yield the desired areal capacity with optimal Coulombic efficiency, and finally optimize the electrolyte structure to minimize and eliminate polysulfide dissolution with desired Li<sup>+</sup> conductivities. Finally, the developed systems will be scaled up, fabricated, and tested in pouch-cell configurations.

**Out-Year Goals.** The following goals will be achieved in subsequent years: (1) determine optimal cell component design parameters such as electrode thickness and porosity exhibiting minimal polarization while maintaining cathode capacity  $\geq 1500$  mAh/gS, (2) demonstrate excellent cycle life of  $> 1000$  cycles with  $> 80\%$  capacity retention, (3) electrochemically test cells with dendrite-free Li-alloy anodes comprising Li-SIA and Li-MCA of areal capacity of  $\sim 15$  mAh/cm<sup>2</sup>, (4) electrochemically test cells with modified electrolytes at charge-discharge rates of C/3 as well as other C-rates of C/10-C/3, (5) fabricate  $> 300$ -mAh pouch cell giving energy density greater or equal to 500 Wh/kg at C/3 rate and demonstration of acceptable performance at other C-rates of C/10-C/3, and (6) demonstrate cyclability of a minimum of 1000 charge/discharge cycles with  $< 20\%$  fade rate for operation in  $-40^{\circ}\text{C}$  to  $+40^{\circ}\text{C}$  temperature ranges with temperature measured external to the pouch cell.

**Collaborations.** The project involves collaboration with G. E. Blomgran of Blomgren Consulting Services, Ltd.

### Milestones

1. Computational identification of electrocatalysts and LICs will be completed: 80% lower activation barrier of polysulfide to Li<sub>2</sub>S transformation and a 10× improvement of reaction kinetics will be achieved. (Q4, FY 2022; In progress, October 2022)
2. Synthesis and characterization of  $\sim 20$ -nm-sized electrocatalysts and LICs homogeneously dispersed in the CFM/S will be completed. (Q1, FY 2023; In progress, January 2023)
3. Dendrite-free growth study will be completed, and  $\geq 1000$  cycles cyclability tests @C/3 rate will be completed for dendrite-free anode technology innovation. (Q2, FY 2023; In progress, April 2023)
4. Modified electrolyte with high Li-ion conductivity ( $\sim 10^{-2}$  S/cm) and minimum polysulfide solubility ( $< 1$  ppm) will be achieved. (Q3, FY 2023; In progress, July 2023)

## Progress Report

This quarter, the team initiated preliminary work on fabrication of new sulfur confinement cathodes. With the goal of generating advanced cathode architectures, they attempted to modify the porous organic framework materials (POFM1) with pre-designed and customized properties that have been employed as sulfur storage cathode materials for Li-S batteries. These POFM1 materials are composed of lightweight elements, including carbon and oxygen, and are connected by covalent bonds with the functional group additives. The lightweight elements containing functional cathode materials comprise repeating units of monomer that not only finetune the dissolution of polysulfides, but also serve to modify the electrode interface due to the multifunctional cathode chemistry. Therefore, the team conducted studies on the synthesis of the POFM1 useful for sulfur cathodes. The POFM-1 electrode can play a vital role in improving cycle life of Li-S batteries. Accordingly, this report describes the use of functional monomer with repeating cyclic metal-carbon-oxygen ring or new monomer molecule serving as a promising stabilizer for use in Li-S batteries to improve cycle life. The team observed that during electrochemical cycling, the POFM1 – short-chain polysulfides complexes likely formed during charge-discharge processes not only modify the kinetics of formation of short-chain polysulfides, but also reduce polysulfide dissolution. Results to date highlight the importance of use of appropriate functional monomer units of the POFM1 system with the porous organic framework matrix serving as the sulfur host material facilitating efficient functioning of the functional groups with repeating cyclic monomer units in Li-S batteries.

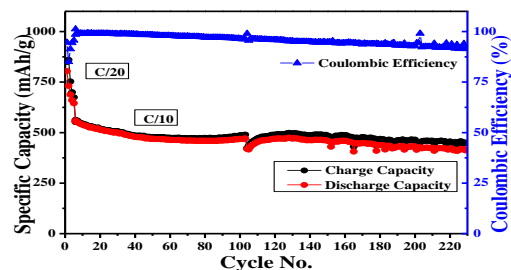


Figure 134. Electrochemical cycling performance and Coulombic efficiency of POFM1-S electrode cycled between 1.8-2.8 V at C/20 and 1.7-2.8 V at C/10 current rates.

The electrochemical cycling performance of the sulfur-infiltrated POFM1, termed as POFM1-S, cathodes containing the organic solvent-based polymer binder, tested in Li-S battery, is shown in Figure 134. The POFM1-S electrodes were cycled at 0.05C for the initial cycling with an average electrode loading of  $3.2 \text{ mg cm}^{-2}$  electrode area for the entire test. The POFM1-S electrode shows an initial discharge capacity of  $\sim 950 \text{ mAh g}^{-1}$ , which stabilizes at  $\sim 625 \text{ mAh g}^{-1}$  after the 10<sup>th</sup> cycle. On prolonged cycling at 0.1C, the POFM1-S electrode shows a very stable capacity of  $\sim 480\text{-}490 \text{ mAh g}^{-1}$  for over 230 cycles. The electrolyte-to-sulfur ratio used here was  $8 \mu\text{l mg}^{-1}$ . At present, there is still a challenge to accurately design an optimal matrix material that can provide suitable pore-size environment to trap the soluble intermediate lithium polysulfides. Efforts to increase the sulfur loadings with use of *in situ* synthesized LICs and functional electrocatalysts identified by theoretical studies to enhance the specific capacity are ongoing and will be detailed in subsequent reports.

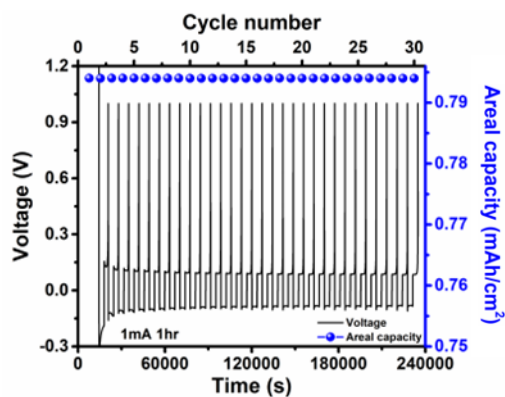


Figure 135. Electrochemical cycling performance along with areal discharge capacity of MCA4 electrode cycled at 1 mA current for 1 hour for alloying and de-alloying, respectively, for 30 cycles.

The team also studied the system of multicomponent alloy (MCA) as a dendrite-free anode material that was synthesized by high-energy mechanical milling process. The structurally isomorphous system, MCA4 having similar lattice registry to metallic lithium, prevents lithium dendrite growth by forming a solid solution with the reacting Li-ions electrochemically presented to it from the metallic lithium serving as the counter electrode. The ensuing electrochemical alloying reaction allows a significant amount of lithium to solubilize into the parent MCA4 alloy, causing minimal change in volume due to the solid solution formation. The crystallographic arrangements of atoms in the MCA4 alloy being similar to that of lithium thus serves

to preserve the overall crystallographic symmetry and allows the formation of a solid solution with optimal interfacial energy. The MCA4 alloy also improves the lithium diffusion, preventing surface segregation while continuing to maintain dendrite-free cycling, hence serving as effective anodes as well as current collectors in Li-S batteries. The MCA4 alloy was generated by high-energy alloying, and the anode electrode for electrochemical testing was prepared by standard slurry casting method followed by electrochemical testing in a coin-cell configuration, as shown in Figure 135. The MCA4 cells were cycled for 1 mAh/cm<sup>2</sup> at 1 C-rate with an average electrode loading of 3.2 mg cm<sup>-2</sup>. The MCA4 cells show excellent plating/stripping behavior, affording a stable areal capacity of ~ 1 mAh cm<sup>-2</sup> for continuous 30 cycles. The propensity of the MCA4 alloy electrode to demonstrate reversible lithium cycling (plating/stripping) is seen in Figure 135, as the overpotential of the cell decreases with cycle number. Further electrochemical testing of the cells with the various other MCA electrodes continues. Additionally, efforts are being directed at fabricating freestanding dense pellets of the MCAs to serve as dendrite-resistant anode current collectors for reversibly cycling lithium ions. Results of the ongoing current studies conducted on the MCA electrodes and the electrochemical testing results of the dense pellet of MCAs serving as current collectors will be detailed in subsequent reports.

Another related research effort undertaken this quarter involved computational studies executed with the goal to identify MCA anodes that can not only function as functional dendrite-free anodes, but also serve as dendrite-resistant anode current collectors validating the experimental results described above. These MCA anodes were identified using density functional theory methods during the last two quarters of the project. These alloys demonstrated the unique ability to form uniformly disordered, metastable, *bcc* solid solution isostructural with metallic lithium. One criteria for generating a morphologically stable interface preventing dendrite formation is the design of an alloy exhibiting the *bcc* alloy structure with matched interfacial enthalpy, resulting in optimal values (close to zero) and thereby preventing dendrite formation. Using the macroscopic atom model, the team estimated the interfacial enthalpy between lithium layer and various MCA compositions and thereby identified the best alloys satisfying this criterion. The following equations have been used for the calculations:

$$\Delta H_{Li\ in\ ABC\ (bcc)}^{inter} = c^{Li\ in\ ABC} (x \Delta H_{Li\ in\ A}^{inter} + y \Delta H_{Li\ in\ B}^{inter} + (1 - x - y) \Delta H_{Li\ in\ C}^{inter}) \quad (1)$$

$$\Delta H_{inter}^{Li-A} = \frac{V_{Li}^{2/3}}{(\eta_{ws}^{1/3})_{av}} \left[ -P(\Delta\phi^*)^2 + Q \left( \eta_{ws}^{1/3} \right)^2 \right] \quad (2)$$

$(\eta_{ws}^{1/3})_{av}$  – the average value of the electron density at the boundary of Wigner Seitz cell

$\Delta\phi^*$  – the difference between  $\phi_{Li}^*$  and  $\phi_A^*$  defined as the work function of the pure metals lithium

$V_{Li}$  – atomic volume of lithium

$P = 14.2 \text{ kJ}/(\text{mol cm}^2 \text{ V}^2 (\text{density unit})^{1/3})$

$Q = 133.5 \text{ kJ}/(\text{mol cm}^2 (\text{density unit}))$

All the parameters are tabulated and available in the literature and can also be calculated from first principles for elements not documented in the literature. Table 8 shows the calculated interfacial energy of the different MCAs considered in the present study with lithium metal at zero-degree temperature. Table 8 shows that MCA4 and MCA5 alloys demonstrate interfacial energies very close to zero value for 5 at% of lithium. Furthermore, it can be construed that the values will not be too large even at higher Li-concentration, in contrast to the other three MCAs collected in the Table. Thus, MCA4 and MCA5 could be considered as promising Li-anode materials exhibiting favorable conditions for suppressing dendrite formation during electrochemical cycling.

The experimental validations of these theoretical findings are already demonstrated for the MCA4 alloy generated by high-energy alloying. The electrochemical cycling results of this alloy are also shown in Figure 135. Experimental synthesis of the other alloys and the corresponding electrochemical cycling studies for these other alloys are in progress as planned and will be reported next quarter.

**Table 8.  $\Delta H$  interface for  $c_{Li} = 5$  at% in the different multicomponent alloys (MCAs) considered.**

MCAs	$\Delta H_{int}$ in kJ/mol
MCA1	+1.5
MCA2	+1.8
MCA3	+1.4
MCA4	+0.07
MCA5	-0.3

## Patents/Publications/Presentations

### Presentation

- 242<sup>nd</sup> Electrochemical Society Symposium, Research and Development of Primary and Secondary Batteries, Atlanta, Georgia (October 9–12, 2022): “From Lithiated Transition Metal Oxides to Silicon and Lithium-Sulfur Systems: An Evolution of Electrochemically Active Materials”; P. N. Kumta, O. Velikokhatnyi, and R. Kuruba. Invited.

## Task 5.8 – Development of Lithium-Sulfur Battery Cells with High Energy Density and Long Cycling Life (Donghai Wang, Pennsylvania State University)

**Project Objective.** The objective of this project is to develop a new soluble-polysulfide-free sulfur cathode with a high sulfur content ( $> 50$  wt%) and high discharge specific capacity ( $> 700$  mAh g<sup>-1</sup>, based on the weight of the whole cathode), and to demonstrate performance of the sulfur electrode at high electrode capacity ( $> 7$  mAh cm<sup>-2</sup>), low N/P ratio [ $< 2$ ; that is, capacity ratio between anode (negative electrode) and cathode (positive electrode)], and low electrolyte-to-sulfur (E/S) ratio ( $< 2.5$  μL mg<sup>-1</sup>). Prototype Li-S pouch cells with predicted energy density of 400 Wh kg<sup>-1</sup> and 80% capacity retention for over 300 cycles using conventional electrolyte and Li-metal anodes with a protective layer developed by the team will be demonstrated.

**Impact.** This project aims to develop new sulfur composite active materials and functional polymer binders that enable polysulfide-free, high-performance, low-cost sulfur cathode. The use of these high-performance and low-cost sulfur cathodes, in turn, enables Li-S batteries with high energy density and long cycle life. Such Li-S batteries, made using the developed cathodes paired with a Li-metal anode, can lead to 50% greater energy density than conventional Li-ion batteries. Meeting the technical targets will potentially develop high-energy-density lithium batteries, promote increased adoption of electric vehicles and plug-in hybrid electric vehicles, and reduce petroleum consumption in the transportation sector by helping battery-powered vehicles become accepted by consumers as a reliable source of transportation.

**Approach.** The overall approach will focus on synthesizing and optimizing a novel polysulfide-free sulfur composite active material and functional binders. Specifically, approaches to realize the project objectives include the following: (1) development of novel polysulfide-free sulfur composite active materials, (2) development of new functional polymer binders to facilitate Li<sup>+</sup> transport and trap residual lithium polysulfide; and (3) diagnostics, characterization, theoretical simulation, and cell tests on the developed materials in Li-S batteries.

**Out-Year Goals.** The out-year goals are as follows: (1) develop new sulfur composite active materials, and (2) conduct characterization, simulation, and performance tests on material and electrode levels. The *Go/No-Go Decision* will be demonstration of Li-S batteries using the developed sulfur composite active materials with an initial discharge specific capacity  $> 600$  mAh g<sup>-1</sup> (based on cathode weight) at an areal capacity of 4 mAh cm<sup>-2</sup> and E/S ratio  $< 8$  μL mg<sup>-1</sup>.

**Collaborations.** Pennsylvania State University will collaborate with the University of Illinois at Chicago on theoretical simulation.

### Milestones

1. Demonstrate sulfur cathode using sulfur composite active material (generation 1) with an initial discharge capacity  $> 500$  mAh g<sup>-1</sup> (based on cathode weight), at E/S ratio  $< 10$  μL mg<sup>-1</sup>. (Q1, FY 2022; Completed)
2. Demonstrate sulfur cathode using sulfur composite active material (generation 2) with an initial discharge capacity  $> 500$  mAh g<sup>-1</sup> (based on cathode weight), at E/S ratio  $< 10$  μL mg<sup>-1</sup>. (Q2, FY 2022; Completed).
3. Demonstrate sulfur cathode using sulfur composite active material (generation 1) with an initial discharge capacity  $> 600$  mAh g<sup>-1</sup> (based on cathode weight), at E/S ratio  $< 10$  μL mg<sup>-1</sup>. (Q3, FY 2022; Completed)
4. Demonstrate sulfur cathode using sulfur composite active material (generation 2) with an initial discharge capacity  $> 600$  mAh g<sup>-1</sup> (based on cathode weight), at E/S ratio  $< 10$  μL mg<sup>-1</sup>. (Q4, FY 2022; In progress)

## Progress Report

This quarter, the team utilized the optimizing strategy for the sulfurized polyacrylonitrile (SPAN) baseline reported previously to further improve the electrochemical performance of their sulfur polymerized composite (SPC) derived active material. Based on their experimental results, after optimization, they demonstrated polysulfide-free SPC cathodes with a high initial discharge capacity of over 600 mAh g<sup>-1</sup> (based on cathode weight) at an E/S ratio < 10 μL mg<sup>-1</sup>. Besides cycling stability, they also worked on the other electrochemical properties of optimized SPC cathodes and SPAN baseline to understand the improvements. The team first worked on synthetic parameter optimization and evaluating the electrochemical performance of the SPC cathode material in carbonate electrolytes.

The heating procedure is important to the SPC preparation because it determines the sulfur content in the resultant SPC material and, thus, the specific capacity. The composition and micro-structures in the resultant cathode composite may also be affected by the heating procedure on synthesis. Previously, the team showed that a SPAN baseline with much improved specific capacity could be obtained by reducing the heating time and decreasing the heating temperature. Therefore, in this quarter, they applied an optimized synthetic strategy and parameters to the preparation of their SPC cathode materials. Specifically, they reduced the heating time and the heating temperature of SPC cathode materials and then tested them in carbonate electrolytes (Figure 136). For electrochemical performance evaluation, sulfur cathodes using the above SPC powders were fabricated with 80 wt% of active material and an areal loading of ~ 2 mg SPC cm<sup>-2</sup>. The corresponding electrochemical performances were tested in carbonate electrolytes (Figure 136a). After optimization, the initial discharge-specific capacity of the SPC cathode after activation could reach > 700 mAh g<sup>-1</sup> (based on the weight of the whole cathode). Such initial discharge-specific capacity fulfills the target for this reporting period. The optimized SPC also showed cycling stability with capacity retention > 90% after 100 cycles. Two voltage plateaus at 2.35 V and 2.16 V were well defined on discharging, which was in line with their cyclic voltammetry (CV) profiles (Figure 136b). Reduced polarization of SPC was also found according to the CV analysis compared with that of the SPAN baseline, demonstrating the enhanced kinetics of the team's synthesized SPC cathodes.

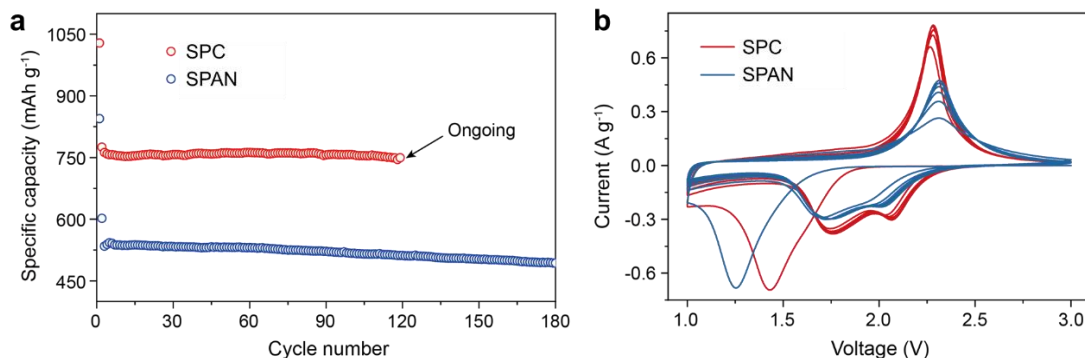


**Figure 136.** (a) Cycling performances of optimized SPC and SPAN cathodes in carbonate electrolyte at current density of 100 mA g<sup>-1</sup>. The SPC cathodes show much improved specific capacity (initial specific capacity > 1000 mAh g<sup>-1</sup> based on SPC weight, or > 800 mAh g<sup>-1</sup> based on cathode weight) over that of the routine SPAN cathode. (b) Cyclic voltammetry curves of SPC and SPAN cathode-based batteries at scan rate of 0.1 mV s<sup>-1</sup>.

The optimized SPC cathode material is durable on enlarged cutoff window from 0.5 V to 3.0 V, demonstrating its electrochemical stability (Figure 137). Batteries based on optimized SPC cathode demonstrated initial specific capacity over 750 mAh g<sup>-1</sup> (based on the total weight of cathode) at cutoff window of 0.5 V to 3.0 V (Figure 137a). Such initial discharge capacity meets the target for this reporting period. This high specific capacity could also be well maintained on cycling in carbonate electrolyte, as shown in Figure 137b.

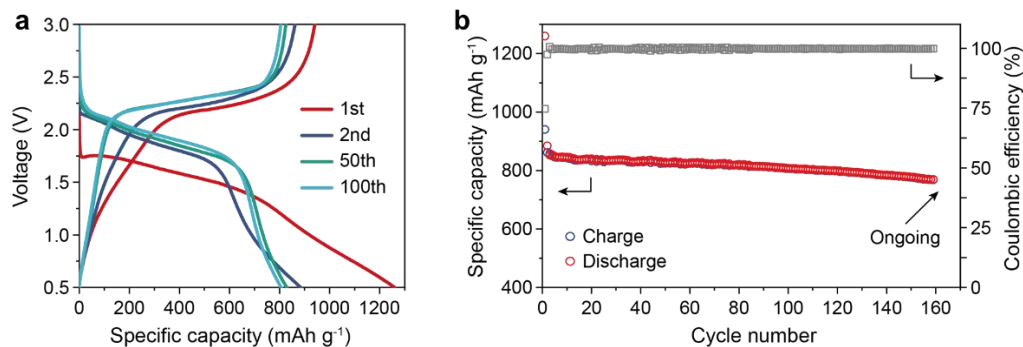


**Figure 137. (a) Charge-discharge curves of optimized SPC cathode-based battery at a current density of  $100 \text{ mA g}^{-1}$  in carbonate electrolyte. (b) Cycling performance and Coulombic efficiency evolution of optimized SPC cathode-based battery at a current density of  $100 \text{ mA g}^{-1}$  in carbonate electrolyte.**

Next quarter, the team will screen and optimize the electrolyte for the optimized SPC materials and further improve the specific capacities of SPC materials in both carbonate and ether electrolytes. This quarter's milestone is expected to be completed next quarter by demonstrating a sulfur cathode using sulfur composite active material (generation 2) with an initial discharge capacity  $> 600 \text{ mAh g}^{-1}$  (based on cathode weight) at an E/S ratio  $< 10 \text{ } \mu\text{L mg}^{-1}$ . In addition, they will continue optimizing the synthetic parameters of SPAN baseline, SPC-1, and SPC-2 cathode materials.

### Patents/Publications/Presentations

The project has no patents, publications, or presentations to report this quarter.

## TASK 6 – LITHIUM-AIR BATTERIES

Team Lead: Ji-Guang Zhang, Pacific Northwest National Laboratory

### Summary and Highlights

The Task objective is to develop rechargeable Li-O<sub>2</sub> batteries with long-term cycling stability through in-depth research on more stable electrolytes and highly efficient catalysts for air electrodes, protection of Li-metal anodes, and deeper understanding on the oxygen reduction reaction and oxygen evolution reaction mechanisms behind the electrochemical performance of Li-O<sub>2</sub> cells.

### Highlights

The highlights for this quarter are as follows:

- The Argonne National Laboratory (ANL) team further investigated the effect of the solid electrolyte interphase (SEI) from carboxyl groups formed after exposure to pure O<sub>2</sub>, possibly creating carboxylate and oxalate groups. In addition to promoting charge of Li<sub>2</sub>O<sub>2</sub> in an efficient manner, it has been found that with the SEI coating, the discharge capacity significantly increased to > 3 mAh cm<sup>-2</sup> versus 1 mAh cm<sup>-2</sup> for only carbon paper.
- The ANL / University of Illinois, Chicago, (UIC) team reveals that the SnI<sub>2</sub> decomposition on the lithium surface results in LiI formation. The LiI is known to act as an effective redox mediator (RM) to reduce the charge potential for decomposing Li<sub>2</sub>O<sub>2</sub>. The SnI<sub>2</sub> additive can provide the LiI needed for the RM to assist in the catalysis of the charge reaction and results in a lower charge potential for the SnS-based cathode compared to when the SnI<sub>2</sub> is not included as an additive.
- The UIC team reports a Li-CO<sub>2</sub> battery based on new two-dimensional-based medium-entropy alloys as cathode catalysts comprised of sulfur and tellurium chalcogenides that work in synergy with an electrolyte blend of ionic liquid (IL). The best battery cycling results of 220 cycles at the current density of 1 mA/cm<sup>2</sup> are achieved with optimized IL of 40%; further, the best battery cycling results are achieved with a tellurium-based rather than sulfur-based alloy structure.

## Task 6.1 – Lithium-Air Batteries (Khalil Amine and Larry A. Curtiss; Argonne National Laboratory)

**Project Objective.** This project will develop new cathode materials and electrolytes for Li-air batteries for long cycle life, high capacity, and high efficiency. The goal is to obtain critical insight that will provide information on the charge and discharge processes in Li-air batteries to enable new advances to be made in their performance. This will be done using state-of-the-art characterization techniques combined with state-of-the-art computational methodologies to understand and design new materials and electrolytes for Li-air batteries.

**Project Impact.** The instability of current nonaqueous electrolytes and degradation of cathode materials limits performance of Li-air batteries. The project impact will be to develop new electrolytes and cathode materials that are stable and can increase energy density of electrical energy storage systems based on lithium.

**Approach.** The project is using a joint theoretical/experimental approach for design and discovery of new cathode and electrolyte materials that act synergistically to reduce charge overpotentials and increase cycle life. Synthesis methods, in combination with design principles developed from computations, are used to make new cathode architectures. Computational studies are used to help understand decomposition mechanisms of electrolytes and how to design electrolytes with improved stability. The new cathodes and electrolytes are tested in Li-O<sub>2</sub> cells. Characterization, along with theory, is used to understand the performance of materials used in the cell and to make improved materials.

**Out-Year Goals.** The out-year goals are to find catalysts that promote discharge product morphologies that reduce charge potentials and to find electrolytes for long cycle life through testing and design.

**Collaborations.** This project engages in collaboration with K. C. Lau (University of California, Norridge), Y. Wu (Ohio State University), and R. Shahbazian-Yassar (University of Illinois, Chicago).

### Milestones

1. Design functionalized cathodes to achieve high electrochemical performance of Li-O<sub>2</sub> batteries. (Q1, FY 2022; Completed)
2. Characterize cathode materials and investigate electrochemical behaviors. (Q2, FY 2022; Completed)
3. Gain understanding of the lithium superoxide discharge product resulting from use of new templating Ir<sub>3</sub>Li alloy. (Q3, FY 2022; Completed)
4. Engineer new catalysts with improved catalytic performance to suppress side reactions. (Q4, FY 2022; Completed)

## Progress Report

In previous reports this year, the team summarized their finding of a new metal-free catalyst platform for enabling low overpotential charge of Li-O<sub>2</sub> batteries across various current densities and types of carbon-based substrate materials. They determined that there are likely carboxyl groups formed after exposure to pure O<sub>2</sub>, possibly creating carboxylate and oxalate groups. After cycling, these same groups were found on the separator of the cell, indicating these functional groups exist on soluble species. Accordingly, the team suspects that these groups have a potential role in catalyzing the oxidation of lithium peroxide via a solution-phase mechanism.

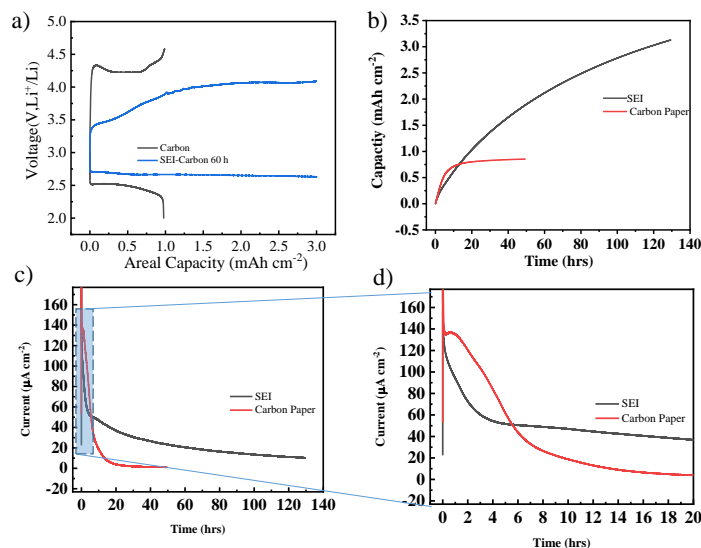


**Figure 138.** (a) Deep discharge of Li-O<sub>2</sub> using carbon paper and using SEI-coated carbon paper at 50 µA cm<sup>-2</sup> until 3 mAh cm<sup>-2</sup> or until voltage cutoff of 2 V versus Li<sup>+</sup>/Li is reached. Potentiostatic hold of Li-O<sub>2</sub> battery at 2.5 V versus Li<sup>+</sup>/Li. (b) The cumulative capacity by integrating the current response. (c) The current response of the carbon paper and the SEI-coated carbon paper. (d) Expanded view of the current response showing details of the current peak, indicating passivation.

Up to this point it is clear that the benefit of the solid electrolyte interphase (SEI) coating is at least in its ability to charge Li<sub>2</sub>O<sub>2</sub> in an efficient manner. However, the team did not discuss its advantage in regard to participation in discharge or Li<sub>2</sub>O<sub>2</sub> deposition. Figure 138a displays the deep discharge of their SEI-coated layer in comparison to a baseline carbon paper cell. It is apparent that with the SEI coating, the discharge capacity significantly increased (> 3 mAh cm<sup>-2</sup> versus 1 mAh cm<sup>-2</sup> of carbon paper). This is a somewhat odd finding, as the deposition of the SEI layer does not change, to any significant degree, the morphology of the carbon paper. To investigate the mechanism, they employed reduction-chronoamperometry. In alignment with their constant current discharges, the capacity of the SEI-coated carbon paper has a much higher capacity (Figure 138b). Figure 138c-d shows that the carbon paper possesses a very strong current peak, which according to the Avrami equation indicates a very fast kinetic growth constant. This appears to result in poor performance. The SEI does not have such a large sharp peak, but has a broad peak. To corroborate this result, the team performed scanning electron microscopy (Figure 139a-b) on the discharge product and found almost no large deposits of Li<sub>2</sub>O<sub>2</sub> in comparison to the pristine carbon paper samples (Figure 139c-d). Moreover, cryogenic transmission electron microscopy (Figure 139e) and select area electron diffraction (Figure 139f) further indicate that the location of the Li<sub>2</sub>O<sub>2</sub> growth is on top of the SEI and not within nor underneath the SEI. These results appear to have conflicting conclusions. Specifically, why does smaller size Li<sub>2</sub>O<sub>2</sub> passivate the surface of the carbon paper less quickly than the larger sized Li<sub>2</sub>O<sub>2</sub> (from the pristine carbon paper). The team is working on an explanation for this process and will present it in the next report, which could change how they understand the Li<sub>2</sub>O<sub>2</sub> deposition.

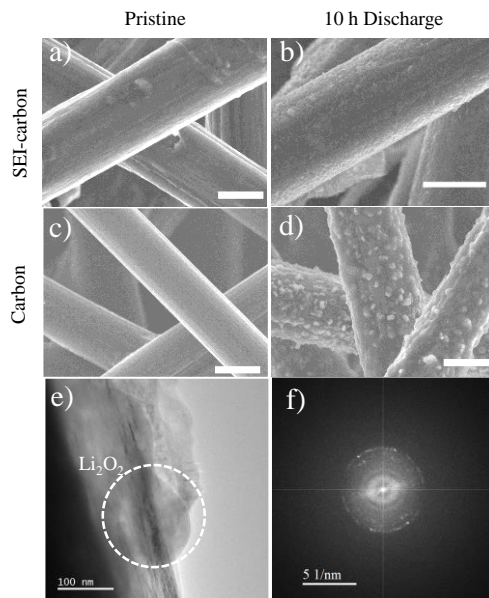


**Figure 139. Microscopy of discharge product.** Scanning electron microscopy (SEM) of SEI-carbon paper (a) before and (b) after discharge. SEM of carbon paper (c) before and (d) after discharge. (e) Cryogenic transmission electron microscopy of discharge product clearly indicating the  $\text{Li}_2\text{O}_2$  spatially sits over the SEI layer rather than inside. (f) Select area electron diffraction of the discharge product indicating it is mostly  $\text{Li}_2\text{O}_2$

## Patents/Publications/Presentations

### Publication

- Plunkett, S. T., A. Kondori, D. Y. Chung, J. Wen, M. Wolfman, S. H. Lapidus, Y. Ren, R. Amine, K. Amine, A. U. Mane, M. Asadi, S. Al-Hallaj, B. P. Chaplin, K. C. Lau, H-H. Wang, and L. A. Curtiss. “A New Cathode Material for a Li–O<sub>2</sub> Battery Based on Lithium Superoxide.” *American Chemical Society Energy Letters* 7, no. 8 (2022): 2619–2626.

## Task 6.2 – Lithium Oxygen Battery Design and Predictions

(Larry A. Curtiss / Anh Ngo, Argonne National Laboratory; Amin Salehi-Khojin, University of Illinois, Chicago)

**Project Objective.** The objective of this work is to develop new materials for Li-O<sub>2</sub> batteries that give longer cycle life and improved efficiencies in an air environment. New electrolyte blends and additives will be investigated that can reduce clogging and at the same time promote the cathode functionality needed to reduce charge overpotentials. New cathode and anode materials will be investigated that can work in conjunction with the electrolytes to improve cycle life in the presence of air components.

**Project Impact.** Li-air batteries are considered as a potential alternative to Li-ion batteries for transportation applications due to their high theoretical specific energy. The major issues with the existing Li-O<sub>2</sub> systems include degradation of the anode electrode, reactions with air components, clogging of the cathode, and electrolyte instability. Thus, this project is using a comprehensive approach to improve cycle life and efficiency through developing new materials for electrodes, anodes, and electrolytes that work in synergy.

**Approach.** The experimental strategy is to use cathode materials based on two-dimensional transition metal dichalcogenides (TMDs) that the team has found to be among the best oxygen reduction reaction (ORR) / oxygen evolution reaction (OER) catalysts. These cathode materials will be combined with new electrolyte blends and additives that work in synergy to reduce charge potentials and increase stability of the Li-air system. Density functional theory (DFT) and *ab initio* molecular dynamics (AIMD) simulations are used to gain insight at the electronic structure level of theory of the electrolyte structure, and function both in bulk and at interfaces with the cathode, anode, and discharge product. The team is using classical molecular dynamics to obtain understanding at longer length and time scales of processes occurring in the electrolyte and growth mechanisms of discharge products. They will also utilize a high-throughput (HT) screening strategy based on experiment and theory to develop a large database of properties and outcomes of electrolyte combinations that can be analyzed using machine learning to predict electrolytes and additives with the best performance.

**Out-Year Goals.** The out-year goals are to find electrolytes that give high capacities and long cycle life in an air atmosphere using HT screening.

**Collaborations.** This project engages in collaboration with R. Assary, J. G. Wen, and S. Tepavcevic of Argonne National Laboratory; B. Narayanan of University of Louisville; T. Li of Northern Illinois University; and F. Khalili-Araghi and R. Klie of University of Illinois, Chicago.

### Milestones

1. Investigation of a highly active tin sulfide (SnS)-based catalyst for high-rate Li-O<sub>2</sub> battery performance. (Q1, FY 2022; Completed)
2. Computational studies of the active sites and electronic structure of the SnS catalyst. (Q2, FY 2022; Completed)
3. Development of new electrolyte redox mediators (RMs) that work with the SnS catalyst to decrease charge potentials and provide anode protection. (Q3, FY 2022; Completed)
4. Computation investigation of a bifunctional additive for lowering charge potentials and anode protection. (Q4, FY 2022; Completed)

## Progress Report

Li-air batteries are considered as strong candidates for the next-generation energy storage systems designed for electrical transportation. However, low cyclability and low current rates are two major drawbacks that hinder these batteries from actual use as batteries. These issues necessitate discovery of novel electrocatalytic processes to significantly enhance the formation and decomposition of the products during battery cycling. The team is working on a system comprised of tin sulfide (SnS) nanoflakes (NF) / reduced graphene oxide (rGO) as a solid catalyst. The goal of this work is to develop a system that enables operating the battery at high current rates of up to 1 mA/cm<sup>2</sup>. It was previously reported that the catalytic activity of a SnS NFs/rGO catalyst for both ORRs and OERs occurring during the discharge and charge, respectively, far exceeds that of state-of-the-art catalysts from carbon, noble metal, and TMD families. This quarter the team used computational methods to study a new bifunctional additive, SnI<sub>2</sub>, for RM and lithium anode protection for insight into how it works in experiments reported previously.

AIMD DFT calculations were used to provide insight into several aspects of the new bifunctional additive for Li-air cells and how they work. First, the mechanism by which the new SnI<sub>2</sub> electrolyte additive can provide an anode protection layer and not affect the cathode was investigated using AIMD simulations. Second, the role of the SnI<sub>2</sub> additive in reducing the charge potential was explained.

The results from the team's DFT calculations on the SnI<sub>2</sub> additive are given in Figure 140. The calculations are based on AIMD simulations with a lithium bis(trifluoromethanesulfonyl)imide / dimethylsulfoxide / 1-ethyl-3-methylimidazolium tetrafluoroborate electrolyte and added SnI<sub>2</sub> molecules. The results for SnI<sub>2</sub> reacting on a Li-metal (100) surface in at the electrolyte interface (initial and final structures) are given in Figure 140a. It shows that the SnI<sub>2</sub> dissociates with the surface, and tin migrates into the lithium. This is the first step in the formation of the protective tin film on the lithium. The reaction of SnI<sub>2</sub> with a SnS surface was also used to investigate whether it would have any detrimental effect on the cathode surface. The result (initial and final structures) is given in Figure 140b, showing that the SnI<sub>2</sub> does not dissociate on the SnS surface, unlike on the lithium surface. The result for the anode surface provides an explanation for the formation of the tin film to protect the lithium anode, as found in experimental studies presented previously.

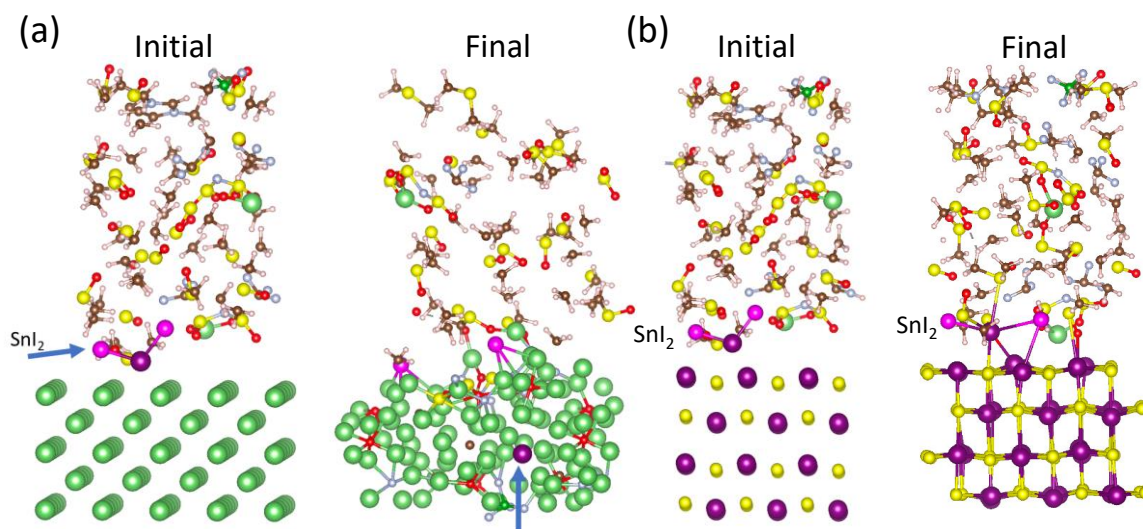


**Figure 140.** Density functional theory calculations for (a) initial and final structure of SnI<sub>2</sub> reacting on a Li-metal (100) surface and for (b) initial and final structure of SnI<sub>2</sub> reacting on a SnS surface.

The SnI<sub>2</sub> additive also has a role in reducing the charge potential. The AIMD calculations in Figure 140a reveal that the SnI<sub>2</sub> decomposition on the lithium surface results in LiI formation. The LiI is known to act as an effective RM to reduce the charge potential for decomposing Li<sub>2</sub>O<sub>2</sub>. In a previous study, the team has shown

by DFT calculations how when LiI is oxidized to form LiI<sub>3</sub> at ~ 3.5 V versus Li/Li<sup>+</sup>, the LiI<sub>3</sub> can act as a catalyst with a small barrier of ~ 0.5 eV to facilitate decomposition of the Li<sub>2</sub>O<sub>2</sub>. These DFT calculations explain how the SnI<sub>2</sub> additive can provide the LiI needed for the RM to assist in the catalysis of the charge reaction. This results in a lower charge potential for the SnS-based cathode compared to when the SnI<sub>2</sub> is not included as an additive. With inclusion of the additive, the charge potential is reduced from > 4 V to ~ 3.5 V, which is a significant improvement.

## Patents/Publications/Presentations

### Publication

- Zhang, C., A. Jaradat, S. K. Singh, T. Rojas, A. Ahmadiparidari, S. Rastegar, S. Wang, L. Majidi, P. Redfern, A. Subramanian, A. T. Ngo, L. A. Curtiss, and A. Salehi-Khojin. “Novel Co-Catalytic Activities of Solid and Liquid Phase Catalysts in High-Rate Li-Air Batteries.” *Advanced Energy Materials* (2022): 202201616. doi: <https://doi.org/10.1002/aenm.202201616>.

## Task 6.3 – Development of a High-Rate Lithium-Air Battery Using a Gaseous CO<sub>2</sub> Reactant (Amin Salehi-Khojin, University of Illinois, Chicago)

**Project Objective.** The main objective of this project is to develop a novel strategy to enable operation of Li-CO<sub>2</sub> batteries at high-capacity high-rate with a long-cycle-life. The experiments will be performed in both Swagelok and pouch cells. In the former case, the team will use: (1) a novel co-catalyst system comprised of inexpensive and earth-abundant transition metal dichalcogenide (TMD) materials that work in synergy with ionic liquid (IL) – based electrolytes to enhance efficiency of reactions during discharge and charge processes, (2) a solution-based catalyst (redox mediator) to reduce charge overpotential and increase energy efficiency of the battery, (3) high-porosity cathode electrodes to increase electrode surface area, gas permeability, stability, electrical conductivity, and lifetime of battery operation, and (4) solid electrolyte interphase layer to protect the anode against oxidation without affecting the ionic transport of Li<sup>+</sup> species in the system. At the pouch-cell level, the team will design and construct a stackable pouch cell to deliver a capacity of > 200 mAh.

**Impact.** Li-air batteries are considered as a potential alternative to Li-ion batteries for transportation applications due to their high theoretical specific energy. Most work in this area focuses on use of O<sub>2</sub> as the reactant. However, newer concepts for using gaseous reactants (such as CO<sub>2</sub>, which has a theoretical specific energy density of 1,876 Wh/kg) provide opportunities for further exploration. This project will produce a thorough understanding of key chemical and electronic parameters that govern the operation of Li-CO<sub>2</sub> batteries in realistic conditions. Achieving the project objectives will generate a library of fundamental properties of TMD- and IL-based electrolytes with the most promise for Li-CO<sub>2</sub> battery applications. The methodologies employed, and the insight generated, will also be valuable beyond advancing the field of Li-CO<sub>2</sub> batteries.

**Approach.** The above targets will be achieved through an integrated approach based on materials synthesis, testing, characterization, analysis, and computation. The team will synthesize catalysts and test them in cells along with developing new electrolytes and additives. These cathode materials with new electrolyte blends and additives will work in synergy to reduce charge potentials and increase battery stability. Density functional theory (DFT) and *ab initio* molecular dynamics simulations will be performed to understand battery operation and make predictions of new materials for the Li-CO<sub>2</sub> battery.

**Out-Year Goals.** The out-year goals are to find novel two-dimensional (2D) catalysts and IL-based electrolytes that give high capacities and long cycle life in a CO<sub>2</sub> atmosphere.

**Collaborations.** This project collaborates with L. A. Curtiss (Argonne National Laboratory), F. Khalili-Araghi (University of Illinois, Chicago, or UIC), A. Subramanian (UIC), and Z. Huang (Stockholm University).

### Milestones

1. Successful synthesis and characterization of bulk and 2D forms of six alloy TMDs for electrocatalysis and battery experiments. (Q1, FY 2022; Completed)
2. Successful exfoliation of TMD alloys with desired lateral sizes for battery experiments. (Q2, FY 2022; Completed)
3. Computation studies of surface stabilities of TMD alloy for batteries. (Q3, FY 2022; Completed)
4. Charge transfer properties of different TMD alloys. (Q4, FY 2022; Completed)

## Progress Report

In the first, second, and third quarters, the team reported on a novel combination of transition metal chalcogenide,  $(\text{NbTa})_{0.5}\text{BiS}_3$ , as a cathode catalyst and a  $\text{ZnI}_2$  additive that works in synergy with IL-based electrolyte to operate a Li- $\text{CO}_2$  battery at the high rate of up to  $0.5 \text{ mA/cm}^2$ . Their results indicate that at such a high current density, the battery can operate up to 125 cycles with the capacity of  $0.25 \text{ mAh/cm}^2$ . They performed computational studies of the catalyst used in this battery and the reason it can operate at high rates. DFT was used to investigate the  $\text{Li}_2\text{CO}_3/\text{C}$  formation on a  $(\text{NbTa})_{0.5}\text{BiS}_3$  catalyst as well as the stability of the catalyst. They identified a facet with lowest surface energy, and the reaction mechanism was elucidated for  $\text{C}/\text{Li}_2\text{CO}_3$  formation.

This quarter, the team reports a Li- $\text{CO}_2$  battery based on new 2D-based medium-entropy alloys as cathode catalysts comprised of sulfur and tellurium chalcogenides that work in synergy with an electrolyte blend of IL of 1-ethyl-3-methylimidazolium tetrafluoroborate (EMIM- $\text{BF}_4$ ) and dimethylsulfoxide (DMSO) with the volumetric ratio of 4:6,  $\text{ZnI}_2$ , lithium bis(trifluoromethanesulfonyl)imide. The catalysts will be disclosed in the next report due to a patenting process. Their results using new catalysts demonstrate that the battery can run at high current density of  $1 \text{ mA/cm}^2$  with capacities of  $0.2 \text{ mAh/cm}^2$  and  $0.4 \text{ mAh/cm}^2$ . As shown in Figure 141a, the battery with Te-based catalyst and 10% of IL performs for 150 cycles. However, the battery with S-based catalyst was only able to operate for 70 cycles. For comparison, they performed battery experiments with different catalyst such as  $\text{MoS}_2$ , gold, and platinum under identical conditions. As shown in Figure 141b, these batteries fail at an early stage with a high charge potential of  $> 4.5 \text{ V}$  at lower cycling of  $< 20$ .

To study the contribution of IL on battery performance, the team carried out optimization experiments with different IL ratios (that is, 10%, 40%, and 90%). They unraveled that the battery with IL of 40% runs for a longer life cycle of 220 cycles at cut off potentials of 2.5 V and 4.6 V (Figure 142). These results confirm that IL:DMSO (4:6) ratio has the best cycling results. From these results, they conclude the following: (1) the best battery cycling results of 220 cycles at the current density of  $1 \text{ mA/cm}^2$  are achieved with optimized IL of 40%, and (2) the best battery cycling results are achieved with a Te-based rather than a S-based alloy structure. The team is conducting further electrochemical and structural characterization of the catalysts before and after experiments, linear sweep voltammetry, and electrochemical impedance spectroscopy experiments, as well as computational studies to understand the reaction mechanisms.

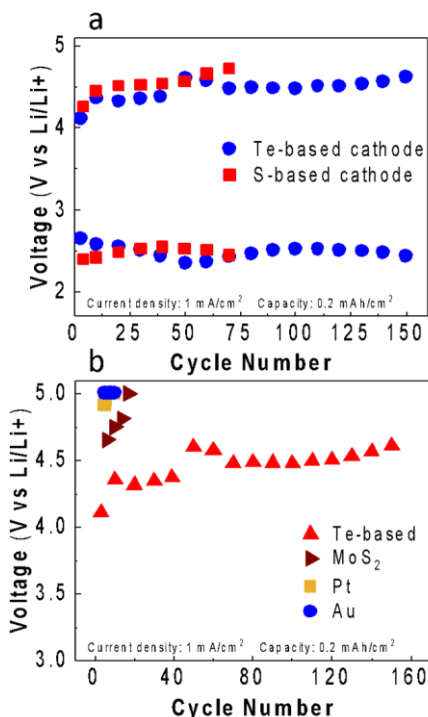


**Figure 141.** Cycling results of Li- $\text{CO}_2$  batteries with (a) Te-based and S-based cathode and (b)  $\text{MoS}_2$ , Au, Pt-, and Te-based cathodes under a current density and capacity of  $1 \text{ mA/cm}^2$  and  $0.2 \text{ mAh/cm}^2$ , respectively.

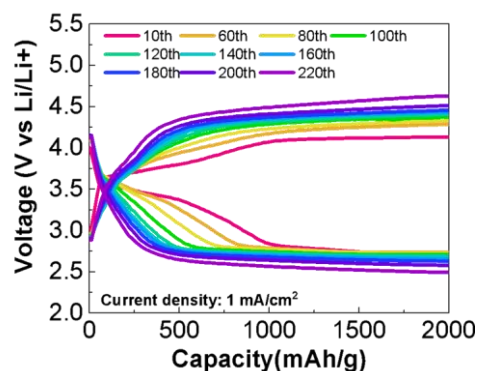


**Figure 142.** Cycling results of Li- $\text{CO}_2$  batteries with Te-based cathode under a current density of  $1 \text{ mA/cm}^2$  at a capacity of  $0.2 \text{ mAh/cm}^2$ .

## Patents/Publications/Presentations

The project has no patents, publications, or presentations to report this quarter.

## TASK 7 – SODIUM-ION BATTERIES

Team Lead: Xiao-Qing Yang, Brookhaven National Laboratory

### Summary

The Na-ion battery will require investigations to identify optimal electrode materials, electrolytes, separators, and binders to reach full potential. The BMR program will therefore have a limited effort directed toward identifying Na-ion battery materials that have potential value for vehicle applications. Progress on these projects this quarter is described in this report.

### Highlights

The highlights for this quarter are as follows:

- The Argonne National Laboratory team, using electrochemistry and *operando* X-ray diffraction, has found that Fe-based layered oxide cathodes with the O3 structure and greater than 50% mol iron have major layer gliding when charged to high voltages, which promotes movement of Fe<sup>4+</sup> into the sodium layer. During discharge, iron moves back to the transition-metal layer with partial reversibility. Dopants will be required to retard the movement of tetravalent iron and promote high-voltage operation with higher reversible capacities.
- The Brookhaven National Laboratory team completed *ex situ* soft x-ray absorption spectroscopy studies for P3-structured Na<sub>0.66</sub>[Cu<sub>0.33</sub>Mn<sub>0.67</sub>]O<sub>2</sub>. After being charged to 3.66 V, the white line peak of L3-edge of copper shifts towards higher energy, indicating the oxidation of Cu<sup>2+</sup> cation, while the new shoulder peak is likely related to hybridization with ligand oxygen and oxygen hole states formation. After charged to 4.10 V, the electronic features observed herein oxygen K-edge at 4.10 V fit the profile of Zhang-Rice singlet state that was first reported for high technetium superconducting cuprate materials, indicating the likelihood of lattice oxygen domination for the redox reaction at 4.10 V with a new correlated electronic state formed between the oxygen hole and Cu<sup>2+</sup> hole.
- The Lawrence Berkeley National Laboratory team carried out the gas evolution measurements from half cells containing sodium titanate anodes using differential electrochemical mass spectroscopy. The cell containing a material heat-treated at 500°C evolved much less hydrogen on charge than one containing a material that was heat treated at 60°C.
- The Pacific Northwest National Laboratory team completed the study of localized high concentration electrolyte (LHCE) for Na-ion batteries, which demonstrated lower Coulombic efficiency (CE) of sodium plating/stripping compared to tetraglyme electrolyte (99.3% versus 99.8%). They also studied Na-free-anode cell using copper current collector and Na<sub>3</sub>V<sub>2</sub>(PO<sub>4</sub>)<sub>3</sub> cathode in LHCE electrolytes, which showed better initial CE and capacity retention compared to the tetraglyme-based electrolyte.

## Task 7.1 – Exploratory Studies of Novel Sodium-Ion Battery Systems (Xiao-Qing Yang and Enyuan Hu, Brookhaven National Laboratory)

**Project Objective.** To meet the challenges of powering plug-in hybrid electric vehicles and battery electric vehicles, new rechargeable battery systems with high energy and power density, low cost, good abuse tolerance, and long calendar and cycle life need to be developed. The primary objective of this project is to develop new advanced synchrotron-based material characterization techniques and apply these techniques to study the new rechargeable battery systems beyond the Li-ion batteries, namely the Na-ion battery systems for electric vehicles (EVs).

**Project Impact.** The results of this project will be used for developing technologies that will significantly increase the energy density and cycle life and reduce the cost of beyond Li-ion battery systems. This will greatly accelerate deployment of EVs and reduce carbon emission associated with fossil fuel consumption and will help in the direction of building U. S.-based energy storage manufacture chains.

**Approach.** This project will use synchrotron-based *in situ* X-ray diagnostics such as *in situ* X-ray diffraction (XRD) and *in situ* X-ray absorption (XAS) tools, combined with transmission electron microscopy (TEM), scanning transmission electron microscopy, and transmission X-ray microscopy imaging techniques developed at Brookhaven National Laboratory (BNL) to evaluate the new materials and redox couples to obtain in-depth understanding of the reaction mechanisms of these materials, aiming to improve existing materials and to provide guidance for new materials and new technology development for Na-ion battery systems.

**Out-Year Goals.** The out-year goal is to complete the synchrotron-based XRD, XAS, and X-ray absorption near-edge structure (XANES) studies of new cathode materials of NaMnFeCoNiO<sub>2</sub> (NMFCN) and P2-Na<sub>0.66</sub>[Cu<sub>0.33</sub> Mn<sub>0.67</sub>]O<sub>2</sub> for Na-ion batteries.

**Collaborations.** The BNL team has been closely working with top scientists on new material synthesis at Argonne National Laboratory, Lawrence Berkeley National Laboratory, and Pacific Northwest National Laboratory, with U. S. industrial collaborators at General Motors and Johnson Controls, and with international collaborators.

### Milestones

1. Complete XRD and TEM studies on a high-capacity and high-C rate multicomponent sodium cathode materials NMFCN at pristine and after 1<sup>st</sup> charge state to study the structural changes of this material. (Q1, FY 2022; Completed)
2. Complete *in situ* XRD studies on a new P2-structured Na<sub>0.66</sub>[Cu<sub>0.33</sub> Mn<sub>0.67</sub>]O<sub>2</sub> cathode material for Na-ion batteries during charge-discharge cycling. (Q2, FY 2022; Completed)
3. Complete *in situ* copper and manganese K-edge XAS studies on P2-structured Na<sub>0.66</sub>[Cu<sub>0.33</sub> Mn<sub>0.67</sub>]O<sub>2</sub> materials during charge-discharge cycling to understand the redox contributions of copper and manganese of this material. (Q3, FY 2022; Completed)
4. Complete the soft XAS (sXAS) studies of Na<sub>0.66</sub>[Cu<sub>0.33</sub> Mn<sub>0.67</sub>]O<sub>2</sub> materials at pristine, charged to 3.6 V, and charged to 4.1 V states to understand the redox contribution of oxygen. (Q4, FY 2022; In progress)

## Progress Report

This quarter, *ex situ* sXAS studies have been completed for P3-structured  $\text{Na}_{0.66}[\text{Cu}_{0.33}\text{Mn}_{0.67}]\text{O}_2$ . At pristine state (Figure 143), the L3-edge of copper shows a nearly standard  $\text{Cu}^{2+}$  feature with only one sharp white line peak at  $\sim 930$  eV (Figure 143a, vertical dotted line), which corresponds to the transition from  $d^9$  ground electronic configuration to the  $\underline{c}d^{10}$  ( $\underline{c}$  denotes a core hole). After being charged to 3.66 V, the white line peak at  $\sim 930$  eV shifts towards higher energy, indicating the oxidation of  $\text{Cu}^{2+}$  cation. Meanwhile, a new shoulder peak emerges just above 932 eV (Figure 143a, upward arrows), which is likely related to hybridization with ligand oxygen and oxygen hole states formation. This interpretation is also supported by the oxygen K-edge XANES data measured at the same time (Figure 143b), where a shoulder peak ( $\sim 526.5$  eV; Figure 143b, upward arrows) clearly emerges at the end of 3.66 V plateau before the main pre-edge peak ( $< \sim 528$  eV; Figure 143b, vertical dotted line) that has nearly zero shift from pristine state. The changes of copper L3- and oxygen K-edge XANES together suggest that, during 3.66 V plateau,  $\text{Cu}^{2+}$  is oxidized and Cu-O hybridization becomes stronger. After being charged to 4.10 V (Figure 143a), the white line peak at  $\sim 930$  eV of copper L3-edge XANES surprisingly moves back to the original position of the pristine state. Though it seems that copper gets back to +2 valence state, the shoulder peak at  $\sim 932$  eV is preserved and becomes even stronger, with only slight shift toward lower energy relative to that of the end of 3.66 V plateau, implying a different electronic state from that of standard  $\text{Cu}^{2+}$  at pristine state. This new feature is closely related to ligand oxygen anions. As seen in Figure 143b, both the main pre-edge peak at  $\sim 528$  eV and the shoulder peak at  $\sim 526.5$  eV slightly shift toward higher energy end, and the shoulder peak becomes more prevalent compared to that at the end of 3.66 V plateau, which suggests more participation of oxygen in the active redox at 4.10 V. In fact, the electronic features observed here at 4.10 V fit the profile of the Zhang-Rice (ZR) singlet state that was first reported for high technetium superconducting cuprate materials. The ZR state refers to a special correlated electronic state formed between a center  $\text{Cu}^{2+}$  with one hole in its  $e_g$  orbital and a ligand oxygen also with one hole in its p orbital (that is,  $\text{Cu}^{2+}:3d^9\text{-O}:2p^5$ , or simplified as  $d^9\underline{L}$  where  $\underline{L}$  denotes a ligand hole). The 530 eV white line peak and a shoulder peak at  $\sim 531.5$  eV  $\sim 532$  eV of copper L3-edge XANES are a signature of ZR singlet state corresponding to the excitation from  $d^9\underline{L}$  to  $\underline{c}d^{10}\underline{L}$ . Therefore, it is very likely that lattice oxygen dominates the redox reaction at 4.10 V, with a new correlated electronic state formed between oxygen hole and  $\text{Cu}^{2+}$  hole.

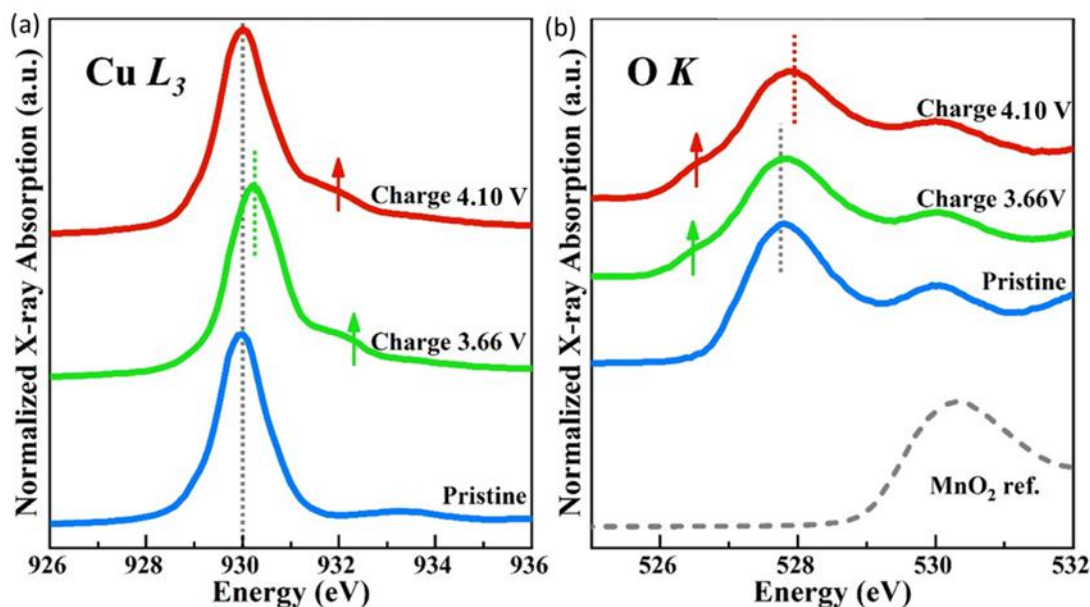


Figure 143. Copper L<sub>3</sub> edge (left panel) and oxygen K-edge (right panel) for P3-NaCuMnO at pristine state, charged to 3.66 V, and charged to 4.10 V. The vertical dotted lines indicate the position of main peak, and the upward arrows indicate the rising of shoulder peaks and their positions.

## Patents/Publications/Presentations

### Publication

- Yao, L., P. Zou, C. Wang, J. Jiang, L. Ma, S. Tan, K. A. Beyer, F. Xu, E. Hu,\* and H. L. Xin.\* “High-Entropy and Superstructure-Stabilized Layered Oxide Cathodes for Sodium-Ion Batteries.” *Advanced Energy Materials* 12, no. 41 (2022): 2201989. doi: <https://doi.org/10.1002/aenm.202201989>.

## Task 7.2 – Development of a High-Energy Sodium-Ion Battery with Long Life (Chris Johnson and Khalil Amine, Argonne National Laboratory)

**Project Objective.** The project objective is to develop a high-energy Na-ion battery with long life. Moreover, the battery chemistry should utilize low-cost materials. The energy density target is 200 Wh/kg and/or 500 Wh/L, wherein the anode and cathode capacity targets are 600 mAhg<sup>-1</sup> and 200 mAhg<sup>-1</sup>, respectively.

**Project Impact.** A Na-ion battery on par with the energy density of a Li-ion battery can have a high impact in the transportation sector with the assumption that the cost is significantly below \$85/kWh and that the battery pack provides a 300-mile range. The consumer is not concerned about the battery chemistry employed if these metrics can be met. Development of these battery chemistries will situate the United States in a strong position as relates to new low-cost energy storage systems beyond lithium ion.

**Approach.** In a team approach, the Na-ion battery group will create a versatile Na-ion battery chemistry with beneficial advantages such as low cost, safety, recycling, and sustainability of materials used. The team will work synergistically so that the final design is the culmination of advances in phosphorus carbon composites mated with optimized lead or other highly dense metalloids, such as tin and/or antimony and derivatives thereof, for the recyclable anode. Synthesis and optimization of such blended composite anodes will be conducted in parallel to diagnostic characterization of structures, phase formation, and cycling stability. Cathode work will begin at the end of the first year and will involve gradient cathodes consisting of Fe-Mn compositions, as well as intergrowths of layer stacking sequenced oxides. If resources allow, the team also will attempt to stabilize cathode surfaces using atomic layer deposition methods, particularly for the benefit of staving off dissolution of manganese and iron / electrolyte reactivity. Electrolytes will be partly procured from H. Li at Pacific Northwest National Laboratory (PNNL).

**Out-Year Goals.** The state-of-the-art Na-ion battery in the literature has now been surpassed by this team, but performance is still too low for commercialization. Thus, the goal is to move forward and continually invent the most superior Na-ion battery chemistry that can compete worldwide through work output from this project.

**Collaborations.** Researchers from PNNL who are developing electrolytes for Na-ion batteries will provide this project with formulations to test with the various electrode combinations investigated at Argonne National Laboratory (ANL).

### Milestones

1. Synchrotron X-ray understanding on the capacity fade of O3 sodium layered cathodes. (Q1, FY 2022; Completed)
2. Transmission electron microscopy characterization on the effect of native lattice strain. (Q2, FY 2022; Completed)
3. Develop engineered surface for better air-storage and high-voltage stability. (Q2, FY 2022; Completed)
4. Development of high-capacity single-crystal layered oxide cathodes with > 150 mAh/g and stable cycle life of > 100 cycles. (Q3, FY 2022; Completed)
5. Development of concentration gradient layered oxide cathode with 130 mAh/g and stable cycle life of > 200 cycles. (Q4, FY 2022; In progress)
6. Investigate novel local atomic structural features to stabilize the high oxidation state of iron active species. (Q4, FY 2022; In progress)

## Progress Report

Previous studies of layered sodium transition metal (TM) oxides have shown that iron substitution can improve the electrochemical performance and air-storage stability of the layered cathodes, not to mention its economic advantage. Regarding the optimum iron content, less than 50% substitution has been unequivocally suggested in the literature. The high-Fe composition tends to aggravate the cycle performance of the cathodes, even more so when a high cut-off voltage is used. Despite the growing number of works in Fe-containing layered cathodes, most of these works focus on cycling under moderate voltage ranges, such as below 4.0 V versus sodium, and the origin of the high-voltage cycling vulnerability of the Fe-rich compositions remains unclear. In previous reports, the team discussed the detailed mechanisms that govern the surface degradation of charged cathodes, which are mainly triggered by the highly reactive  $\text{Fe}^{4+}$  species.<sup>[1]</sup> As part of their continued efforts toward high-performance Fe-based cathodes, this quarter they report the effect of iron content on bulk structural stability and high-voltage cycling performance of layered oxide cathodes.

The  $\text{NaNi}_{1/3}\text{Mn}_{1/3}\text{Fe}_{1/3}\text{O}_2$  (NMF-111) and  $\text{NaNi}_{1/4}\text{Mn}_{1/4}\text{Fe}_{1/2}\text{O}_2$  (NMF-112) powder samples were synthesized by solid-state reaction of  $(\text{Ni}_{0.5}\text{Mn}_{0.5})_{1-x}\text{Fe}_x(\text{OH})_2$  and NaOH precursors. The TM hydroxide precursors were prepared by co-precipitation method using a continuous-stir-tank-reactor. The prepared oxide particles have spherical, secondary particle morphology (average particle size  $\sim 10 \mu\text{m}$ ). The Rietveld refinement analysis of the powder X-ray diffraction (XRD) data confirms a highly crystalline single-phase material with  $\alpha\text{-NaFeO}_2$  layered structure (Figure 144a-b). The calculated lattice parameters are  $a = 2.987 \text{ \AA}$  and  $c = 15.972 \text{ \AA}$  for NMF-111; and  $a = 2.997 \text{ \AA}$  and  $c = 16.009 \text{ \AA}$  for NMF-112. The lattice parameters and cell volume increase with higher iron content due to the larger ionic radii of high-spin  $\text{Fe}^{3+}$  than that of  $(\text{Ni}^{2+}_{0.5}\text{Mn}^{4+}_{0.5})$ .

In Figure 144c-f, both cathodes show similar reversible capacity and cycle stability when the low cut-off voltage of 3.8 V versus sodium is used. However, when a higher cut-off voltage (that is,  $> 4.0 \text{ V}$  versus sodium) is applied, NMF-112 exhibits more severe degradation in cycle performance than NMF-111 exhibits. According to the team's previous study on the charge compensation mechanism of NMF-111, nickel redox accounts for the majority of charge compensation below  $\sim 4.0 \text{ V}$ , and iron redox is only activated in the higher voltage range.<sup>[2]</sup> Interestingly, the threshold cut-off voltage above which the cycle stability significantly degrades corresponds well with the point where  $\text{Ni}^{2+}/\text{Ni}^{4+}$  redox is depleted and  $\text{Fe}^{3+}/\text{Fe}^{4+}$  redox kicks in. This observation suggests that the destabilization of NMF-111 and NMF-112 during high-voltage charging is closely associated with the activation of  $\text{Fe}^{3+}/\text{Fe}^{4+}$  redox.

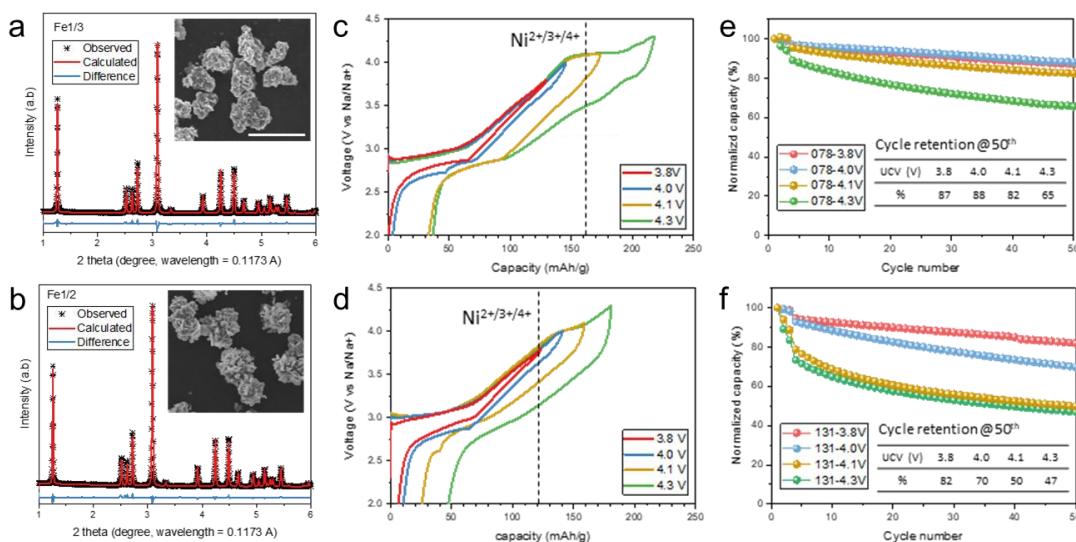


**Figure 144.** X-ray diffraction pattern (a-b), voltage profile (c-d), and cycle performance (e-f) of NMF-111 (a/c/e) and NMF-112 (b/d/f); ( $i = 10 \text{ mA/g}$  for the 1<sup>st</sup> three cycles and  $30 \text{ mA/g}$  for the next cycles).

Figure 145a-b shows the *operando* synchrotron XRD data of the NMF-111 and NMF-112 cells collected during the initial cycle between 2 V and 4.3 V versus sodium. Both cathode materials exhibit similar O3 to P3 and O'3 (monoclinically distorted O3 phase) type phase transitions overall. However, a more careful examination of the phase evolution reveals that NMF-112 has extended O3/P3 and P3/O'3 biphasic regions (Figure 145b). This trend is even more evident when compared with the phase evolution of the Fe-free,  $\text{NaNi}_{0.5}\text{Mn}_{0.5}\text{O}_2$  cathode (NM11), in which distinct single-phase regions develop sequentially, along with narrower biphasic regions in between, as the phase transition proceeds. Figure 145c-f shows the synchrotron XRD patterns selected at different states of charge (SOCs; 3.8, 4.0, and 4.3 V versus sodium) and after being discharged from those SOC. In Figure 145c-d, the NMF-112 shows severe peak broadening and a decrease in peak intensity when charged above 4.0 V versus sodium. This can be attributed to the increased structural disordering due to the migration of iron ions from the TM layers to sodium layers.<sup>[3-4]</sup> The much smaller c-axis parameter for the NMF-112 at the 4.3 V SOC further suggests significant c-axis contraction due to the high concentration of the migrated iron ions in the sodium layers. Figure 145e-f compares the structural reversibility after the initial cycle. NMF-111 recovers its pristine structure after one charge and discharge cycle up to 4.3 V. However, NMF-112 indicates incomplete phase recovery after 4.3 V cycling, whereas the phase transition is relatively reversible when cycled up to a lower cut-off voltages ( $\leq 4.0$  V versus sodium).

The electrochemical performance and *operando* XRD data shed light on the fundamental structural origin of the poorer cycle stability of the high-Fe NMF cathodes. First, the facile layer gliding and phase transition from the pristine O3 to P3 structure are hindered by a pinning effect from the migrated iron ions in the sodium layer. Second, the migrated iron provides a tighter inter-slab binding in the sodium layer, resulting in a higher energy barrier for the stabilization of single P3 phase, and an earlier transition to the O'3 phase at high SOC. Such an early transition to the high-SOC O'3 phase in NMF-112 results in premature contraction of the c-axis, making further sodium extraction difficult. Third, the iron migration is only partially reversible, and the high concentration of residual iron in sodium layers after a discharge increases the impedance for sodium extraction and insertion in the following cycles. In conclusion, the team's work clearly indicates that the bulk structural issues associated with iron migration, as well as the chemical instability at the particle surface, need to be addressed to enable the stable, high-capacity cycling of the high-Fe NMF cathodes. At ANL, multi-faceted surface/bulk modification strategies are being pursued to this end.

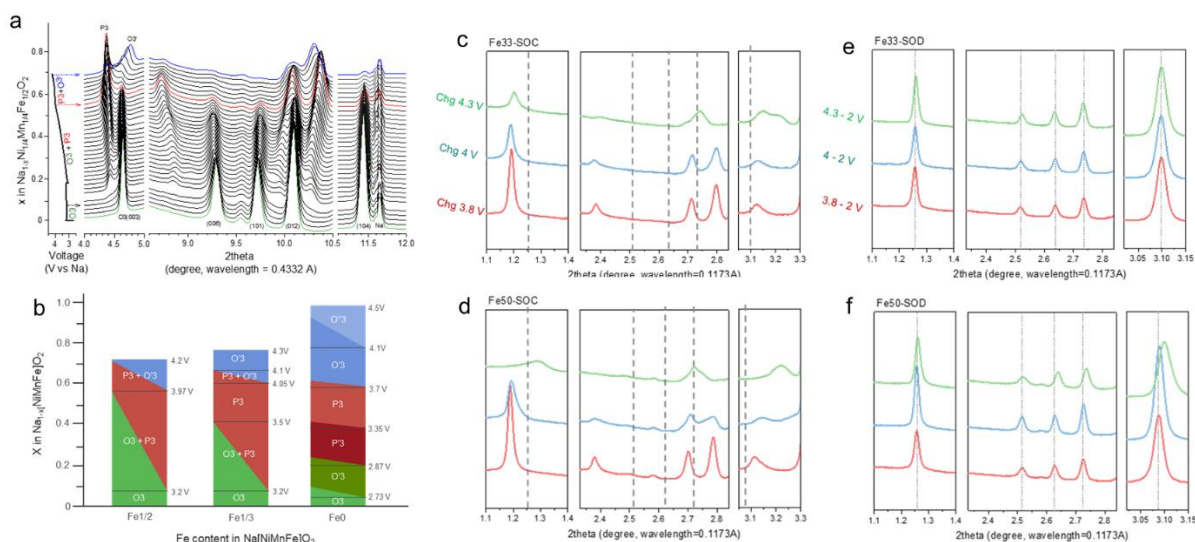


**Figure 145.** *Operando* synchrotron X-ray diffraction (XRD) analysis of NMF-111 and NMF-112. (a) *Operando* XRD of NMF-112 during the initial charge. (b) Comparison of the phase transition as a function of the sodium content. (c-d) Selected XRD patterns during the initial charge, and (e/f) after the 1<sup>st</sup> cycles up to different cut-off voltages: NMF-111 (c/e) and NMF-112 (d/f).

## References

- [1] Park, J., K. Ku, S-B. Son, J. Gim, Y. Kim, E. Lee, and C. Johnson. *Journal of the Electrochemical Society* 169 (2022): 30536.
- [2] Deng, C., E. Gabriel, P. Skinner, S. Lee, P. Barnes, C. Ma, J. Gim, M. L. Lau, E. Lee, and H. Xiong. American Chemical Society *Applied Materials & Interfaces* 12 (2020): 51397.
- [3] Lee, E., D. E. Brown, E. E. Alp, Y. Ren, J. Lu, J-J. Woo, and C. Johnson. *Chemistry of Materials* 27 (2015): 6755.
- [4] Talaie, E., V. Duffort, H. L. Smith, B. Fultz, and L. Nazar. *Energy & Environmental Science* 8 (2015): 2512–2523.

**Patents/Publications/Presentations**

## Patent

- Xu, G., C. Zhao, Y. Liu, and K. Amine. Coatings For Battery Cathode Materials. U. S. patent application; filed on September 28, 2022.

## Presentations

- 242<sup>nd</sup> Electrochemical Society (ECS) Meeting, Atlanta, Georgia (October 9–13, 2022); “Insights into the Na-Alloying Mechanism and Zintl Phase Transition of Lead-Based Anodes”; J. Park et al.
- 242<sup>nd</sup> ECS Meeting, Atlanta, Georgia (October 9–13, 2022); “The Air Stability of Sodium Layered Oxide Cathodes”; W. Zuo, G. Xu, and K. Amine.

## Task 7.3 – Tailoring High-Capacity, Reversible Anodes for Sodium-Ion Batteries (Marca M. Doeff, Lawrence Berkeley National Laboratory)

**Project Objective.** The project objective is to understand the role that vacancies, surface defects, and bulk structure play in determining electrochemical properties of high capacity, stepped layered titanate anodes.

**Project Impact.** Although several suitable cathode materials for Na-ion batteries exist, there are few suitable anode materials due to low potential instabilities. Sodium titanate anodes are a promising class of materials for this application. The electrochemical properties can be manipulated through structural and surface modifications.

**Approach.** The structure and surface properties of candidate stepped layered titanates will be modified through manipulation of synthetic parameters. Materials will then be characterized electrochemically and physically to understand the role that surface defects, vacancies, and bulk structure play in determining electrochemical behavior.

**Out-Year Goals.** The out-year goal is to achieve development of an electrode that can deliver 225 mAh/g at C/3 rate with good capacity retention (80% or better) for 100 cycles.

**Collaborations.** The team collaborates with beam line scientists at Stanford Synchrotron Radiation Lightsource and the Advanced Light Source at Lawrence Berkeley National Laboratory.

### Milestones

1. Conduct hot stage experiments on lepidocrocite titanates. (Q1, FY 2022; Completed)
2. Complete physical and electrochemical characterization of lepidocrocite titanates. (Q2, FY 2022; Completed)
3. Attempt surface modification of lepidocrocite titanates. (Q3, FY 2022; In progress)
4. *Go/No-Go Decision:* Surface modification methods; stop if performance is not improved. (Q4, FY 2022; In progress)

## Progress Report

This quarter, the team used differential electrochemical mass spectrometry to quantify the specific gases evolved from cells made of sodium titanate anodes ( $\text{Na}_{0.74}\text{Ti}_{1.815}\square_{0.185}\text{O}_4 \cdot 1.27\text{H}_2\text{O}$ , NTO) treated under different conditions: NTO heated at 60°C with and without air-exposure for 10 minutes and NTO heated at 500°C (Figure 146). No other gas (molar mass ratio 1-80) besides  $\text{H}_2$  was observed during the initial two cycles of all three cells.  $\text{H}_2$  generation in this system could have multiple origins: (1) reduction of physisorbed and/or interlayer water from NTO electrodes, (2) chemical reactivity of water with sodium metal, and (3) reduction of protons that result from degradation of the salt or diglyme solvent. The cell made of air-exposed NTO electrode exhibits much more  $\text{H}_2$  gassing than the cell made with NTO electrode dried at the same temperature (60°C) while avoiding exposure to air (Table 9), suggesting high hygroscopicity of NTO. The lowest amount of  $\text{H}_2$  is generated from the cell containing an NTO electrode heated at the highest temperature (500°C). The  $\text{H}_2$  evolution observed during charging in the cell made with the 60°C-heated NTO might be related to the formation of a fresh Na-metal surface caused by  $\text{Na}^+$  plating, which then further reacts with residual water in the cell. However,  $\text{H}_2$  evolution was not detectable during the charge process of 500°C-heated NTO cell because of its lower water content, suggesting that extraction of protons from the solvent was not a major contributor. This finding highlights the importance of proper dehydration in optimizing the electrochemical properties of NTO anodes. The team is also working on surface modifications of sodium titanates; results are expected to be reported next quarter.

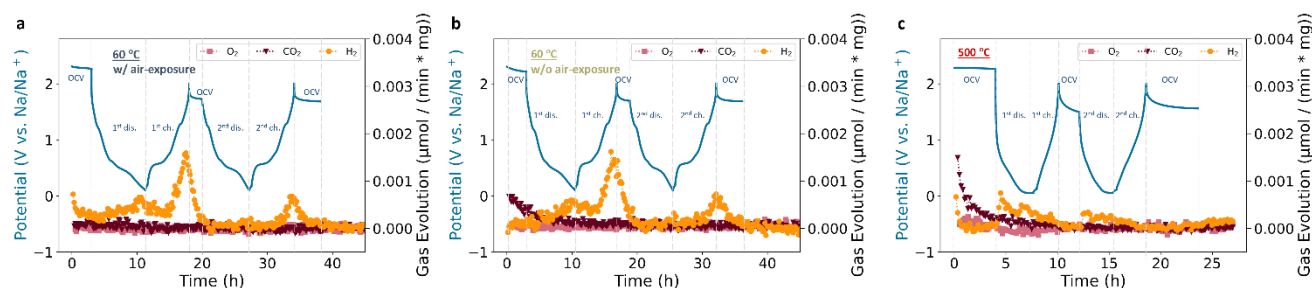


**Figure 146.** Gas evolution in the initial two cycles of sodium half cells made with 60°C-heated sodium titanate anodes, or NTOs, (a) with and (b) without 10 minutes of air-exposure, and (c) 500°C. The cells were cycled at a current rate of 32 mA g<sup>-1</sup> using 0.5 M NaBPh<sub>4</sub> in DEGDM as the electrolyte. The CO<sub>2</sub> signals observed during the open circuit voltage (OCV) period were from residual CO<sub>2</sub> in the instrument. The H<sub>2</sub> signals detected during the second OCV period are mostly from the residual H<sub>2</sub> generated during the previous charge.

**Table 9.** Normalized H<sub>2</sub> generation (μmols/mg<sub>active material mass</sub>) in the initial two cycles of sodium half cells made with sodium titanate anodes (NTOs).

Sample Name	1 <sup>st</sup> discharge	1 <sup>st</sup> charge	2 <sup>nd</sup> discharge	2 <sup>nd</sup> charge
60°C-heated NTO with air-exposure	0.257	0.288	n/a	0.151
60°C-heated NTO without air-exposure	0.125	0.191	n/a	0.097
500°C-heated NTO	0.091	n/a	0.049	n/a

## Patents/Publications/Presentations

### Publication

- Yin, W., G. Barim, X. Peng, E. A. Kedzie, M. C. Scott, B. D. McCloskey, and M. M. Doeff. “Tailoring the Structure and Electrochemical Performance of Sodium Titanate Anodes by Post-Synthesis Heating.” *Journal of Materials Chemistry A* 10 (2022): 25178–25187. doi: <https://doi.org/10.1039/D2TA07403F>.

### Presentation

242<sup>nd</sup> Electrochemical Society Meeting, Atlanta, Georgia (October 9–13, 2022): “Developing Titanate Anodes for Sodium Ion Batteries”; M. M. Doeff, W. Yin, and G. Barim.

## Task 7.4 – Electrolytes and Interfaces for Stable High-Energy Sodium-Ion Batteries (Phung M. L. Le, Pacific Northwest National Laboratory)

**Project Objective.** The Na-ion battery is a potential alternative energy source for electric vehicles (EVs) and grid applications due to the low cost and the natural abundance of sodium. The performance of Na-ion batteries largely depends on development of electrode materials and electrolytes. In recent years, a series of potential electrode materials has been developed. However, a fundamental understanding of the electrochemistry of Na-ion batteries, especially the stability of the electrode-electrolyte interface in these batteries, is still not well established. This project will develop innovative electrolytes to enable fundamental understanding on the interface between electrode and electrolyte for stable operation of high-energy Na-ion batteries. A high-capacity anode will also be developed. The proposed research will enhance the achievable capacities of both anode and cathode for Na-ion battery and improve the stability of electrodes/electrolyte interface, establish correlation (electrolyte design rule) between electrochemical performances of Na-ion batteries and the electrolyte/interface properties, and enable long cycle life and safe operation of high-energy Na-ion batteries.

**Project Impact.** This project will develop new electrolytes to enable long cycle life and safe operation of Na-ion batteries. If successful, the resulting improvements in energy, life, and safety will provide a solid contribution to the understanding of fundamental scientific questions and the development for Na-ion battery technology and promote its practical application as a competitive alternative to the current Li-ion batteries and greatly reduce the cost of energy storage systems for EVs.

**Approach.** This project will continuously optimize the electrolyte components and concentrations to develop innovative electrolytes and additives with improved electrochemical and physical properties. Ether-based electrolytes with different salts and additives will be optimized toward both anode [sodium metal and hard carbon (HC)] and cathode. Phosphate-based localized high-concentration electrolyte (LHCE) will be optimized to improve cycling performance of Na-ion batteries. Solid electrolyte interphase (SEI) / cathode electrolyte interphase (CEI) components of Na-ion battery in ether and phosphate electrolytes will be studied using X-ray photoelectron spectroscopy (XPS) and scanning electron microscopy / transmission electron microscopy (TEM) techniques to reveal the fundamental mechanism behind the improved stable performance of Na-ion batteries. Electrolyte additives in carbonate electrolyte will also be investigated to improve the electrochemical cathode performance. These approaches will unravel the origin of the SEI at the dynamic interface, providing guidance for the electrolyte and interface design and enabling high capacity and long life of Na-ion batteries.

**Out-Year Goals.** This project will select electrolyte compounds and identify formation of interfacial SEI layer on HC and CEI layer-on-layer oxide cathode and its effect on electrode materials. It will also guide electrolyte optimization and improving Coulombic efficiency (CE) of sodium deposition/stripping to be more than 99%.

**Collaborations.** This project will collaborate with leading scientists at Argonne National Laboratory, Lawrence Berkeley National Laboratory, and other organizations in the field of cathode and anode materials for Na-ion batteries. It will also collaborate with C. Wang and M. Engelhard of Pacific Northwest National Laboratory for TEM and XPS characterization.

### Milestones

1. Develop high-voltage electrolytes based on fluorinated solvent ( $\geq 4.2$  V) to be compatible with high-voltage cathode material. (Q1, FY 2021; Completed)
2. Characterize CEI/SEI interphase properties in optimized electrolyte to probe the mechanism of high-voltage cycling stability of Na-ion batteries. (Q2, FY 2022; Completed)

- Design new electrolytes to enable extremely high CE (> 99.5%) of sodium stripping/plating process on different current collectors. (Q3, FY 2022; Completed)
- Investigate feasibility of anode-free sodium batteries using new electrolytes and  $\text{Na}_3\text{V}_2(\text{PO}_4)_3$  cathode. (Q4, FY 2022; Completed)

## Progress Report

This quarter, ether-based electrolytes have been studied for sodium anode-free cells with  $\text{Na}_3\text{V}_2(\text{PO}_4)_3$  (NVP) cathode. Various current collectors (that is, aluminum, Cu/C, Al/C, and copper) were used as an anode to test for the feasibility of anode-less cells in baseline electrolyte 1 M  $\text{NaPF}_6$ /tetraethylene glycol dimethyl ether (TEGDME; tetraglyme) and LHCE using ether solvent. Figure 147 and Figure 148 show the compatibility test of electrolytes with sodium anode and NVP cathode using  $\text{Na}||\text{Cu}$  and  $\text{Na}||\text{NVP}$  half cell in test cycle. Both baseline and LHCE are well-compatible with anode and cathode, which is demonstrated by high CE of the sodium stripping/plating process (> 99.0 %) and high discharge capacity ( $115 \text{ mAh g}^{-1}$  and  $120 \text{ mAh g}^{-1}$  for baseline and LHCE, respectively).

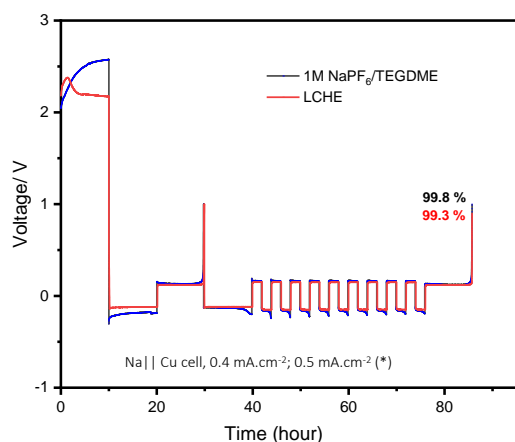


**Figure 147.** Sodium stripping/plating efficiency in two different electrolytes (testing condition: plating  $4 \text{ mAh cm}^{-2}$  and fully stripping to 1 V and cycling for 10 cycles at  $0.5 \text{ mA cm}^{-2}$ ).

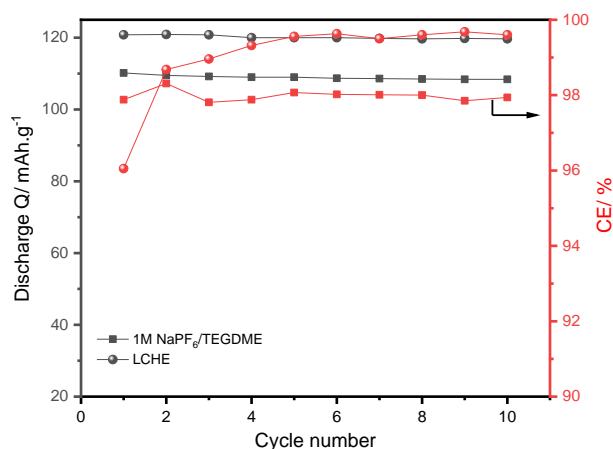


**Figure 148.** Cycling performance of half-cell  $\text{Na}||\text{NVP}$  cathode in 10 cycles at 0.2C.

The performance of sodium anode-free cells is displayed in Figure 149. To eliminate the loss of Na-ion inventory by unexpected factors, both anode and cathode sides were pre-cycled before making the full cell. As a result, the voltage profile of anode-free cells in both electrolytes looks similar to that of the  $\text{Na}||\text{NVP}$  half cell, indicating the regular operation of the cells. The initial discharge capacity and CE in baseline electrolyte are relatively lower than the values obtained for LHCE (Table 10), even though its sodium stripping/plating CE is much higher. In long-cycling performance, the capacity fading is quickly observed for the baseline electrolyte started in the third cycle, while LHCE shows capacity reduced promptly from the 30<sup>th</sup> cycle. Indeed, the capacity retention of LHCE-based electrolyte is about 65% after 50 cycles. Further work will continuously analyze the factors causing this fading and the strategies to extend the cycle life of anode-free cells.

Table 10. The values indicating the performance of sodium anode-free cells in two electrolytes.

Electrolyte	1 <sup>st</sup> Discharge Q / (mAh.g <sup>-1</sup> )	1 <sup>st</sup> CE / %	50 <sup>th</sup> Discharge Q / (mAh.g <sup>-1</sup> )	50 <sup>th</sup> CE / %	Capacity Retention after 50 Cycles
1M NaPF <sub>6</sub> /TEGDME	101.2	83.4	0.3	62.4	-
LHCE	107.5	94.2	64.6	89.5	60.1

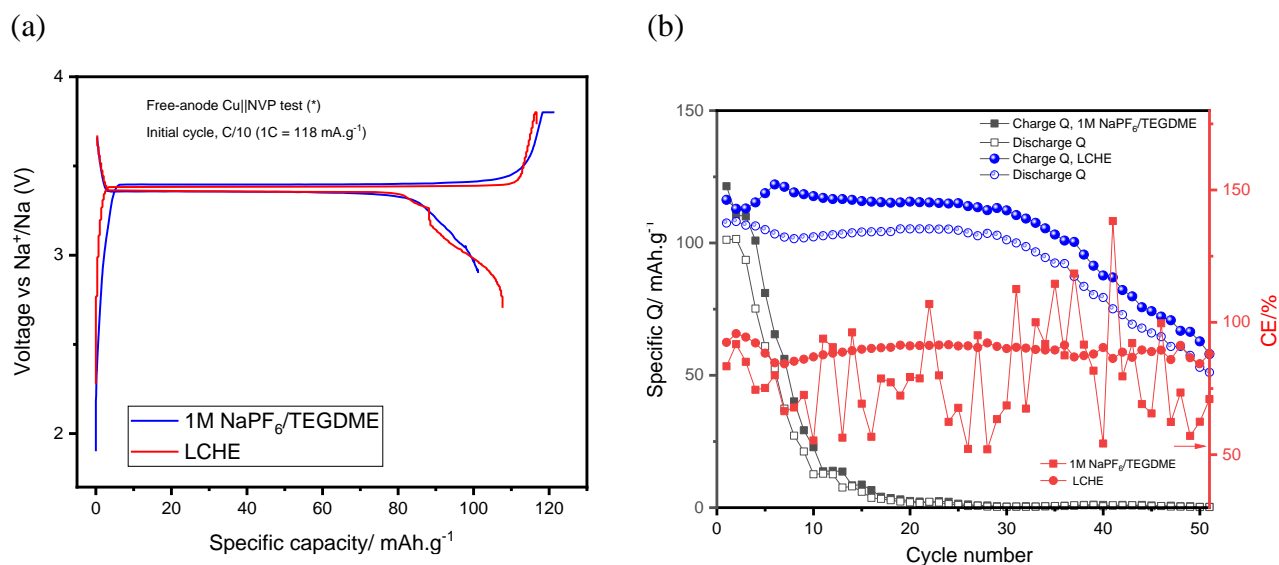


Figure 149. (a) Initial charge-discharge profile of Cu||NVP cell in two electrolytes. (b) Cycling performance of the anode-free cells for 50 cycles (formation cycle: 1<sup>st</sup> cycle: 0.1 C, charge cyclic voltammetry (CV), cycling: 2<sup>nd</sup> – 7<sup>th</sup> cycle: 0.2 C, charge CV, 8<sup>th</sup> cycle: 0.3 C, discharge 0.2 C, charge CV; NVP loading mass: 3-4 mg/cm<sup>2</sup>).

## Patents/Publications/Presentations

### Publication

- Jin, Y., Y. Xu, B. Xiao, M. H. Engelhard, R. Yi, T. D. Vo, B. E. Matthews, X. Li, C. Wang, P. M. L. Le,\* and J-G. Zhang. “Stabilizing Interfacial Reactions for Stable Cycling of High-Voltage Sodium Batteries.” *Advanced Functional Materials* 32, no. 40 (2022): 2204995. doi: <https://doi.org/10.1002/adfm.202204995>.

## Innovation Center for Battery500 (Jun Liu, Pacific Northwest National Laboratory; Yi Cui, Stanford University)

**Project Objective.** The overall goal of the consortium is to increase the energy density of advanced lithium batteries to beyond what can be achieved in today's state-of-the-art Li-ion batteries. The Battery500 Consortium aims to increase the specific energy (up to 500 Wh kg<sup>-1</sup>) and achieve 1,000 charge/discharge cycles, with cost reduction of the cells to significantly less than \$100 per kWh<sup>-1</sup>. This goal directly addresses the U. S. Department of Energy priority to achieve a carbon-free electricity sector by 2035 and to decarbonize the transportation sector by developing and manufacturing the next-generation, high-energy, low-cost batteries to enable a wide deployment of electric vehicles (EVs) in the marketplace.

**Project Impact.** Battery500 will develop next-generation lithium battery technologies that will significantly increase energy density, improve cycle life, and reduce cost. This will greatly accelerate deployment of EVs and reduce carbon emission associated with fossil fuel consumption. The consortium will utilize first-class expertise and capabilities in battery research in the United States and develop an integrated and multidisciplinary approach to accelerate development and deployment of advanced electrode and electrolyte materials in commercially viable high-energy batteries. The advances made in this consortium will also benefit improvement of current Li-ion battery technologies. This project will provide tremendous opportunities for students and scientists for battery-related training that will enhance the workforce for the United States to maintain global leadership in the battery research and development field.

**Approach.** This project focuses on the two most promising battery chemistries: Li-metal anode with high-voltage/high-capacity metal oxide cathodes like LiNi<sub>x</sub>Mn<sub>y</sub>Co<sub>1-x-y</sub>O<sub>2</sub> (NMC), and lithium metal with sulfur cathodes. The project focus is to design novel electrode and cell architectures to meet the 500 Wh/kg goal. The consortium will work closely with battery/material manufacturers, suppliers, and end users / original equipment manufacturers in the United States to ensure the technologies being developed by this project are well aligned with industry needs, poised for transitioning to real production, and helpful in securing the supply chain in the United States.

**Out-Year Goals.** The out-year goals are to improve cycle life of the Li||NMC pouch cell with 400 Wh/kg energy density and cycle life of > 200, and to fabricate and test the pouch cells with 450 Wh/kg energy density and cycle life of > 100.

**Collaborations.** Collaboration among consortium team members will be well coordinated by the leadership team, which also includes four keystone project leads and co-leads along with principal investigators at all member institutions. Collaboration with the community outside of this consortium and with industry will be facilitated by the executive committee and the advisory board.

### Milestones

1. Complete synchrotron-based transmission X-ray microscopy studies on cathode electrolyte interphase (CEI) protection for NMC cathode cycled at high-voltage limit. (Q1, FY 2022; Completed)
2. Complete electrochemical atomic force microscopy (AFM) imaging in glovebox to study the nucleation of Li-metal anode during lithium plating. (Q2, FY 2022; Completed)
3. Complete Li-metal anode morphology studies by cryogenic electron microscopy (cryo-EM) and modeling. (Q3, FY 2022; Completed)
4. Improve cycle life of Li||NMC pouch cell with 350 Wh/kg energy density with cycle life of > 800, and with 400 Wh/kg energy density with cycle life of > 200. Fabricate and test pouch cells with 450 Wh/kg energy density and cycle life > 100. (Q4, FY 2022; Completed)

## Progress Report

## Keystone Project 1: Materials and Interfaces

## Thermal Stability Studies of Electrolytes and Solid Electrolyte Interphase (SEI)

This quarter, the Binghamton University team studied the following: reactivity of cell components; stability of the new ether electrolytes in contact with lithium; and (3) the heat evolved during evolution of the SEI layer.

The stainless-steel components used in coin cells can react with the electrolyte even when they are covered with aluminum (coated or foil). It was found that the Hohsen cell contains molybdenum in the steel (Figure 150a), which is less reactive than the MTI cells. The more reactive MTI cell results in an additional 10% heat release beyond that due to the reactions of the active material (Figure 150b).

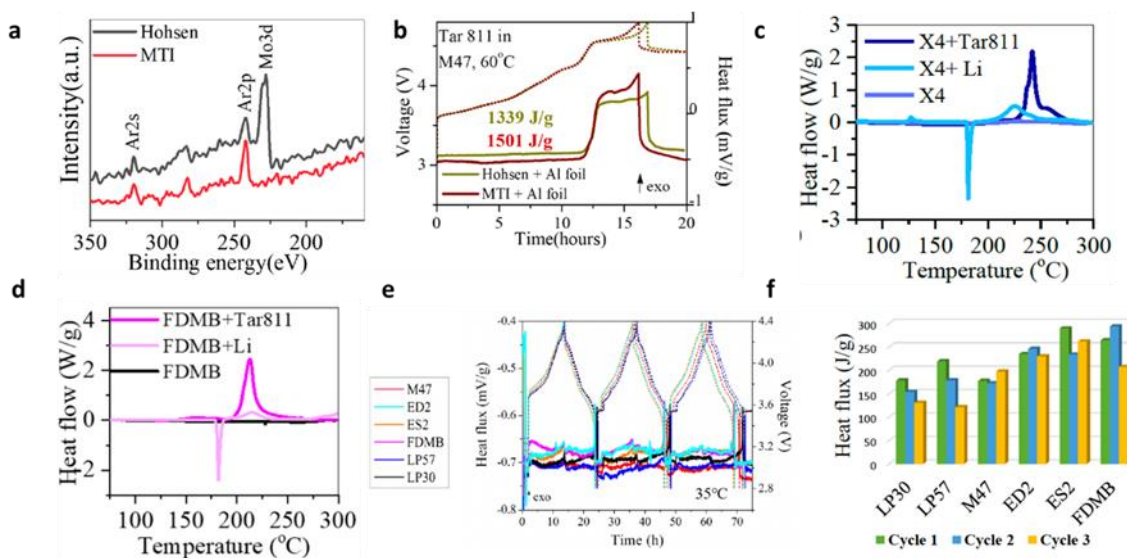


Figure 150. (a) X-ray photoelectron spectroscopy study of coin-cell components. (b) Heat evolved for NMC-811 with the M47 electrolyte using the aluminum protected Hohsen and MTI cells. (c-d) Studies of X4 (PNNL) and FDMB (Stanford) electrolytes. *Ex situ* differential scanning calorimetry profiles of electrolyte alone, electrolyte + Targray NMC-811 charged to 4.8 V, and electrolyte + Li-metal anode after charge. (e-f) Cycling and heat evolution of coin cells cycled between 4.4 V and 2.8 V at C/10 current rate.

The Li-bis(fluorosulfonyl)imide (LiFSI) – ether electrolytes were found to be stable to fresh lithium during the melting process (Figure 150c-d). The electrolytes alone showed no thermal events up to 300°C; all showed the expected endothermic melting peak of lithium and a subsequent exothermic reaction. In the presence of the  $\text{LiNi}_{0.8}\text{Mn}_{0.1}\text{Co}_{0.1}$  (NMC-811), the expected exothermic oxygen reaction was observed, but its peak temperature was found to be dependent on the electrolyte used and, in some cases, was higher than that of the NMC without electrolyte. This is being investigated.

Extra heat is expected to be evolved during formation of the SEI layer, and this should decrease after the formation of the SEI. Figure 150e shows the cycling of NMC-811 in several carbonate electrolytes and advanced ether electrolytes. The heat evolved for the first three cycles is shown in Figure 150f. The expected decrease in heat evolution was observed for the carbonate electrolytes, but this was not the case for the ether-based electrolytes, even with the heat increased in some cases. This is being followed up with more measurements after the 10<sup>th</sup> cycle.

## Electrolytes

### *Electrolyte Development for High-Ni Cathodes*

The University of Texas, Austin, (UT Austin) team continued development and analysis of localized saturated electrolyte (LSE) based on  $\text{LiPF}_6$  salt, which can stabilize high-Ni layered oxide cathodes. Figure 151a shows the schematics of the solvation structure of the developed  $\text{LiPF}_6$ -based LSE. By using different solvents and diluents, the  $\text{LiPF}_6$ -based LSEs showed different protection abilities against Co-free  $\text{LiNiO}_2$ . Figure 151b compares the cycling stability of  $\text{LiNiO}_2$  cathodes tested in LP57 electrolyte [1 M  $\text{LiPF}_6$  in 3:7 ethylene carbonate (EC) / ethyl methyl carbonate (EMC)] and the four types of LSEs using different solvents. The diluent was 1,1,2,2-tetrafluoroethyl-2,2,3,3-tetrafluoropropyl ether (TTE) for all four types of LSEs.  $\text{LiNiO}_2$  cathode with LP57 electrolyte shows an initial 1C-rate specific discharge capacity of  $206 \text{ mAh g}^{-1}$  and maintains 56.7% of its initial discharge capacity after 200 cycles. The LSE(EC/EMC) and LSE(fluoroethylene carbonate / EMC, or FEC/EMC) increased initial 1C-rate specific discharge capacities to  $208 \text{ mAh g}^{-1}$  and  $223 \text{ mAh g}^{-1}$ , respectively, and significantly improved capacity retentions after 200 cycles to 84.4% and 91.3%, respectively. By comparison, the LSE(1,2-dimethoxyethane, or DME) and LSE(triethyl phosphate, or TEP) reduced initial 1C-rate specific discharge capacities to  $202 \text{ mAh g}^{-1}$  and  $179 \text{ mAh g}^{-1}$ , respectively with low capacity retentions of 3.4% and 0.8% after 200 cycles. Figure 151c compares the cycling stability of LP57 electrolyte and LSE with using four different diluents. The solvent used was FEC/EMC for all four types of LSEs. All four LSEs increased the initial 1C specific discharge capacity from  $206 \text{ mAh g}^{-1}$  (LP57) to  $\sim 225 \text{ mAh g}^{-1}$  (LSEs). In addition, the 1C discharge capacity retentions after 200 cycles were increased from 56.7% (LP57) to 91.3% [LSE(TTE)], 87.3% [LSE(bis(2,2,2trifluoroethyl) ether, or BTFE)], and 83.2% [LSE(1,1,2,2-tetrafluoroethyl 2,2,2-trifluoroethyl ether, or TTFTE)]. However, the LSE(trimethylolethane, or TME) is not compatible with  $\text{LiNiO}_2$  cathode and/or the Li-metal anode, as indicated by a drastic capacity fade after less than 100 cycles (73.6%). The results suggest that TTE, BTFE, and TTFTE can be used as non-solvating diluents in  $\text{LiPF}_6$ -based LSEs while TME is not a good diluent for the  $\text{LiPF}_6$ -based LSE.

X-ray photoelectron spectroscopy (XPS) was conducted to investigate the composition of the interphase layers on both Li-metal anodes and  $\text{LiNiO}_2$  cathodes collected from cells using LP57 electrolyte and various LSEs (Figure 151d-g). Figure 151d shows that the concentration of the fluorine species in the SEI (mainly LiF) increases from 29.6% (LP57) to 46.4% [LSE(EC/EMC)], 56.7% [LSE(FEC/EMC)], 51.4% [LSE(DME)], and 61.7% [LSE(TEP)]. The quantitative analysis in Figure 151f suggests that the concentration of carbon atom is reduced from 37.0% (LP57) to 23.3% [LSE(EC/EMC)], 22.0% [LSE(FEC/EMC)], 19.2% [LSE(DME)], and 17.4% [LSE(TEP)]. As the organic species have carbon as their backbone, a reduced concentration of carbon in the SEI indicates fewer organic components and more inorganic components in the SEIs in the case of the LSEs. The XPS data suggest that LSEs help form inorganic-rich SEI with much more LiF species on the surface of Li-metal anode, which is believed to be beneficial to cell performance. Similarly, Figure 151e compares the fluorine 1s spectra in CEI on the cathode side. The peak at  $\sim 685.5 \text{ eV}$  can be attributed to LiF, and the peak at  $\sim 689 \text{ eV}$  can be assigned to C-F. Compared to LP57, the four LSEs have a stronger LiF peak at  $\sim 685.5 \text{ eV}$  with a fluorine atomic ratio (fluorine from the LiF) increased from 3.34% (LP57) to 6.77% [LSE(EC/EMC)], 5.86% LSE(FEC/EMC), 5.51% LSE(DME), and 4.18% LSE(TEP). The high LiF content in the CEI from LSE(EC/EMC) and LSE(FEC/EMC) may be one of the reasons for the improved cycling stability shown in Figure 151b. However, the LSE(DME) and LSE(TEP) show worse cycling stability than LP57, even though the CEIs formed with the two LSEs are also LiF-rich. Thus, the composition of CEI would only be one contributing factor to maintaining high cycling stability. There must be other more significant contributing factors that lead to poor performance of the cells tested with LSE(DME) and LSE(TEP).

Pair distribution function (PDF) and small angle X-ray scattering (SAXS) were applied to uncover the change of the solvation structure from low concentrations electrolyte (LCE) to the saturated electrolyte and LSE. Figure 152a shows the atom-atom bond lengths in these molecules taken from existing literature. In addition, the size of contact ion pair (CIP) and aggregate (AGG) clusters formed in localized high-concentration electrolytes (LHCEs) is in the range of  $5 \text{ \AA}$  to  $10 \text{ \AA}$  and depends on the type of salt, solvents, and salt concentration.

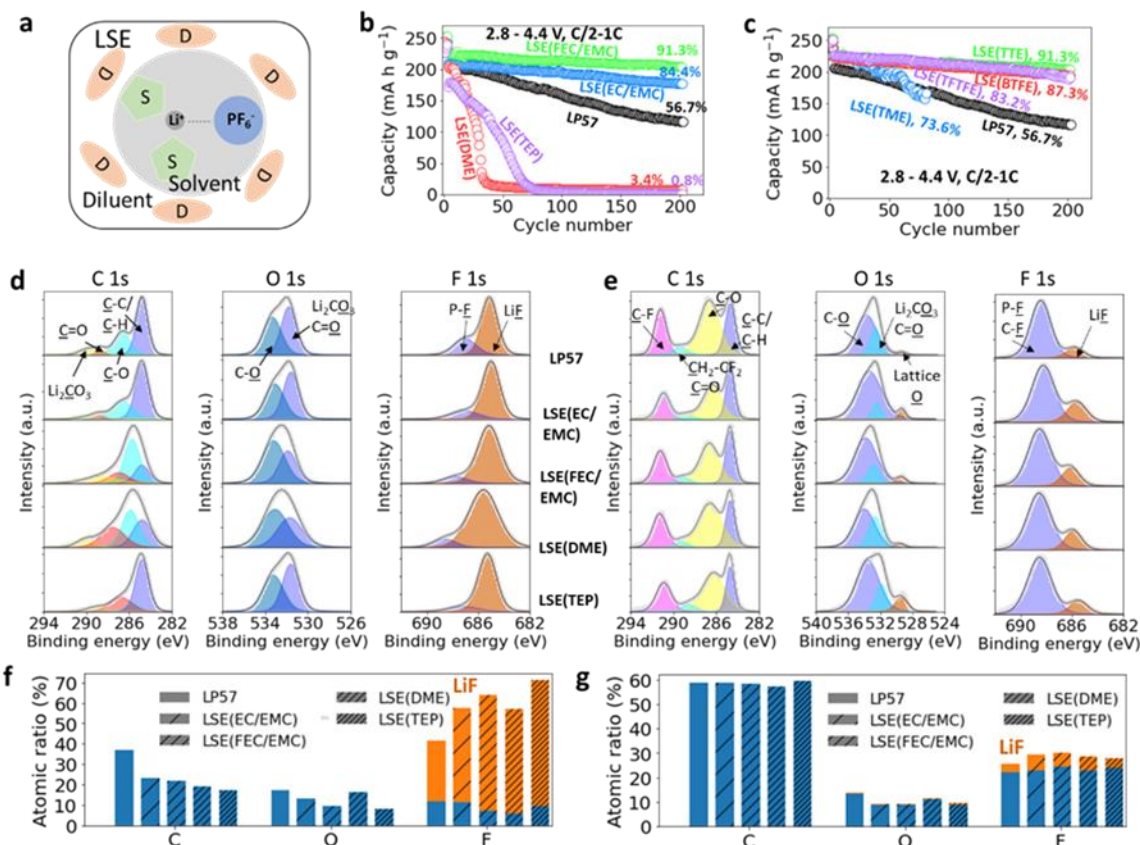
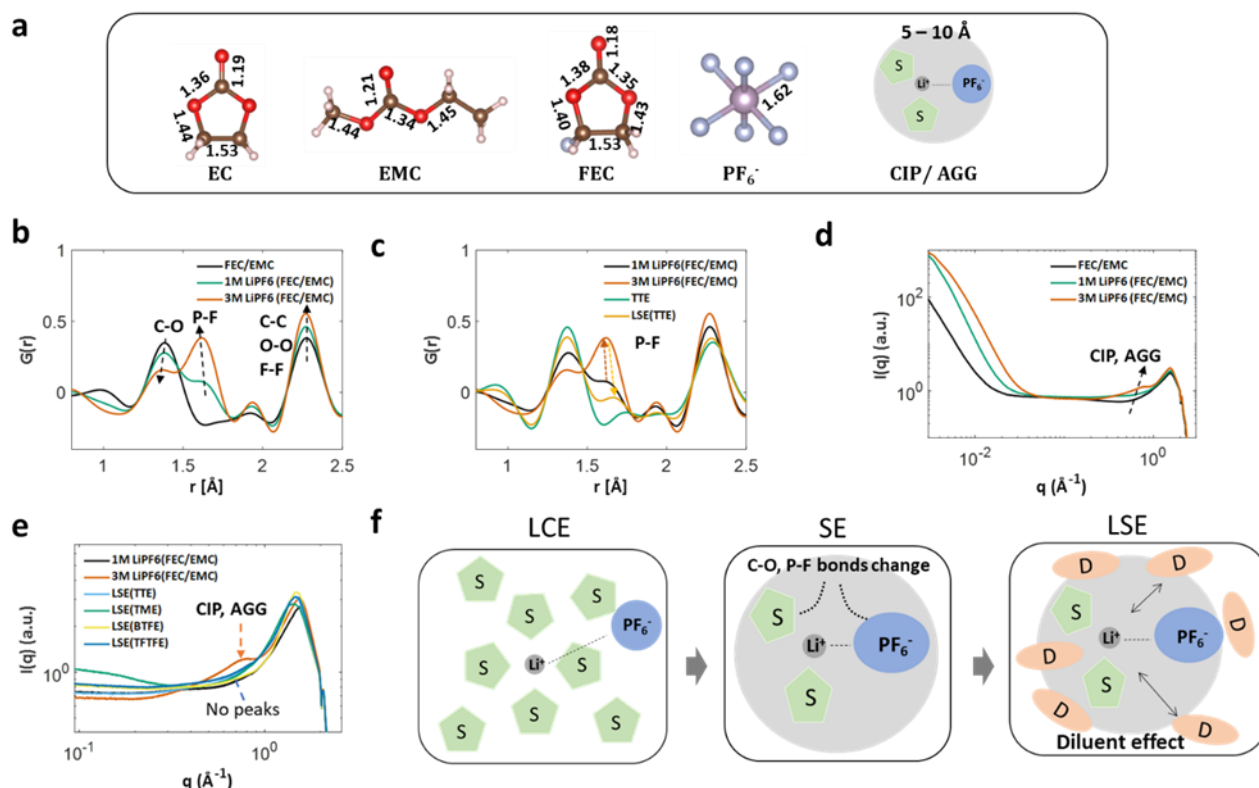


Figure 151. (a) Schematic illustrations of the localized saturated electrolyte (LSE). (b-c) Effect of solvents (b) and diluents (c) on the cycling stability of LiNiO<sub>2</sub>. The cycling was conducted at room temperature with 2 mA h cm<sup>-2</sup> loading of the cathode material. The charge rate was C/2 and the discharge rate was 1C in the voltage range of 2.8 V – 4.4 V. (d-e) X-ray photoelectron spectra for the SEI formed on Li-metal anode (d) and the CEI formed on LiNiO<sub>2</sub> cathode (e). (f-g) Quantitative analysis of different elemental components of the SEI (f) and the CEI (g).

Figure 152b labels C-O in EMC and P-F in PF<sub>6</sub><sup>-</sup>. The locations of the two peaks are at, respectively, ~1.38 Å and ~1.62 Å. The C-O peak in EMC is shifted from 1.38 Å to 1.37 Å after adding 1 M LiPF<sub>6</sub> salt, and the peak position is further reduced to 1.32 Å when adding 3 M LiPF<sub>6</sub> salt. The shift of the C-O peak to a smaller value indicates the shrinking of the C-O bond distance in EMC. Moreover, the intensity of the C-O peak also gradually decreases after adding the salt, which can be attributed to (1) the reduced number of solvent molecules in the detected volume because of the increased LiPF<sub>6</sub> salt concentration, and (2) the fluctuation of the C-O correlation induced by Li<sup>+</sup> and PF<sub>6</sub><sup>-</sup> ions. Similarly, the P-F bond in PF<sub>6</sub><sup>-</sup> is also affected by the LiPF<sub>6</sub> salt concentration. For example, the P-F peak position is decreased from 1.63 Å to 1.61 Å when the concentration of LiPF<sub>6</sub> is increased from 1 M to 3 M. The reduced bond length and change of chemical bond fluctuation may affect the lowest unoccupied molecular orbital (LUMO) and the highest occupied molecular orbital (HOMO) levels of these molecules, which is directly related to their reduction and oxidation stabilities. Figure 152c further shows the effect of adding the TTE diluent on the P-F peak. The effect of the other three diluents on the P-F peak is also shown by a similar trend (not included here). The results suggest that the P-F bond length in the PF<sub>6</sub><sup>-</sup> anion increases after adding a diluent. It was previously believed that a nonsolvating diluent should stay outside of the solvation structure. By shielding cations and anions in the inner solvation sheath from electrostatic attractions of ions in nearby solvation complexes, the diluent can further enhance cation-anion and ion-solvent interactions in the inner solvation sheath. However, the PDF result indicates the opposite effect of PF<sub>6</sub><sup>-</sup> anion after adding diluents, wherein the P-F peak position shifts back to a large *r* value. Thus, the diluent may affect the inner solvation structure and the interaction between Li<sup>+</sup> and PF<sub>6</sub><sup>-</sup>, at least for the electrolyte systems investigated herein.

SAXS has proven to be a powerful technique for uncovering electrolyte solvation structures, which has been further applied in this study to investigate the interaction between cations/anions and electrolyte solvents in different electrolytes. Figure 152d shows that a broad peak appears at the  $q$  range of  $0.5\text{-}0.8\text{ \AA}^{-1}$  in the 3 M LiPF<sub>6</sub> in FEC/EMC electrolyte, unlike FEC/EMC or 1 M LiPF<sub>6</sub> (FEC/EMC). The broad peak indicates the formation of CIP and/or AGG clusters with a physical dimension of  $7.9\text{-}12.6\text{ \AA}$  ( $d = 2\pi/q$ ). However, the broad peak at  $0.5\text{-}0.8\text{ \AA}^{-1}$  disappears after adding diluents (Figure 152e), suggesting that the diluent molecules affect the inner solvation structure and change the size distribution of the clusters in the saturated electrolytes. This phenomenon further supports the finding that the diluent may affect the inner solvation structure and change its size distribution in the electrolyte systems investigated herein.

The PDF and SAXS data provide a better understanding of the solvation structure of an electrolyte with the LiPF<sub>6</sub> salt on shifting from LCE to saturated electrolyte and further to LSE. Figure 152f schematically shows that increasing LiPF<sub>6</sub> salt concentration not only helps form unique Li<sup>+</sup> solvation structures (CIPs and AGGs), but also affects the bond lengths in solvents and the PF<sub>6</sub><sup>-</sup> anion. The change in the bond length affects the LUMO and HOMO levels in these molecules, leading to different reduction and oxidation stabilities compared to that in the corresponding LCE. In addition, the PDF data in Figure 152c and the SAXS data in Figure 152e indicate that a nonsolvating diluent could affect the inner solvation structure, which is different from the existing understanding of the role of the diluent. The schematic in Figure 152f proposes that diluent molecules can move in and out of the inner solvation structure easily due to their low dielectric constant. The movement of diluent molecules breaks the well-defined Li<sup>+</sup> solvation clusters and smears out the SAXS peak at  $0.5\text{-}0.8\text{ \AA}^{-1}$ .



**Figure 152.** (a) The molecular structures and estimated bond lengths (in Å) of EC, EMC, FEC, and PF<sub>6</sub><sup>-</sup> molecules. The size of a general contact ion pair (CIP) and aggregate (AGG) is also labeled. (b-c) Experimental pair distribution function (PDF) data in the range of  $0.8\text{-}2.5\text{ \AA}$  for different electrolytes. (d-e) Experimental small-angle X-ray scattering (SAXS) data of different electrolytes. (f) Proposed solvation structure evolution from a low concentration electrolyte (LCE) to a saturated electrolyte (SE) to a localized saturated electrolyte (LSE) based on the PDF and SAXS measurements.

The Pennsylvania State University (PSU) team introduced another new electrolyte formulation with all aspects of solvents, salts, and additives optimized to achieve the target Coulombic efficiency (CE) of 99.5%. The new highly wettable fluorinated electrolyte with a new solvating solvent system can stabilize the batteries under practical working conditions with retained solvation chemistry because they are high-concentration electrolytes (HCEs) with improved wettability on the separator and electrode surfaces. It consists of 1 M LiPF<sub>6</sub> dissolved in a mixture of carbonate-based solvating system and a fluorinated ether-based diluent, which is named as fluorinated saturated electrolyte (FSE). Here, the team marked E1 for conventional electrolyte 1M LiPF<sub>6</sub> in EC/EMC (1:1 v/v); AFSE stands for FSE with 0.1 wt% additive. The improved wettability between electrolyte/separator/electrode interfaces ensures homogeneous lithium transport, which lowers the risk of incomplete plating and stripping (that is, related to capacity loss) as well as local overcharge. In this approach, the Li<sub>2</sub>O–LiF-rich SEI nanostructure is completely different from the conventional SEI that displays a highly crystalline and Li<sub>2</sub>CO<sub>3</sub>-dominant structure.

The accurate CE of Li||Cu cell was determined by the Aurbach method using the simple plating and stripping process published by the Pacific Northwest National Laboratory (PNNL) team. In this method, an excessive amount of charge is used to deposit lithium onto the copper substrate first as a lithium reservoir, then a smaller portion of this charge is used to cycle lithium between working and counter electrodes for 10 cycles. After 10 cycles, a final exhaustive strip of the remaining lithium reservoir is performed to the cut-off voltage. The final stripping charge, corresponding to the quantity of lithium remaining after cycling, is measured as shown in Figure 153. Under a current density of 0.5 mA.cm<sup>-2</sup> and lithium deposition capacity of 1.0 mAh.cm<sup>-2</sup>, the baseline E1 only delivered a CE of 88%; in contrast, a substantially improved CE of 99.5% was achieved in AFSE with a new solvent system and additive (Figure 153a). The wettability of the FSE electrolyte is much improved on the separator compared to the conventional E1 electrolyte with poor wetting behavior (Figure 153d). After 10 hours of resting, the Li-metal anode after the 1<sup>st</sup> charge shows non-uniform lithium plating, especially at the center, while the lithium metal with FSE electrolyte shows homogeneous lithium deposition. In addition, for the cell using E1 electrolyte, it could not be charged after one hour of resting (black-dash line) and five hours of resting (red-dash line). In contrast, the cell using FSE shows normal charge curves for all cases (Figure 153b). This indicated that the resting periods of one hour and five hours are not enough for conventional electrolyte to wet out the surfaces of separator and electrodes to facilitate the charging process. However, with improved wettability, FSE can wet out the surfaces of separator and electrode even with only one hour of resting.

Figure 153c indicates that the FSE significantly improves the cycling stability of NMC-811 with a cutoff voltage of 4.3 V. All the cycling data were collected with CR-2016 type coin cells with a high loading cathode of 4 mAh cm<sup>-2</sup>, a 50-μm thin Li-metal anode, and lean electrolyte amount of 5.5 μL/mAh. As shown in Figure 153c, the NMC-811 cell with the FSE shows an initial discharge capacity of 2.78 mAh at 0.5C rate and retains 80% of its initial capacity after 265 cycles. Similarly, AFSE enabled significantly improved cycling stability, delivering an 80% capacity retention of 2.66 mAh after 280 cycles. In addition, the average CE is nearly 99.9% for the cells tested with FSE and AFSE. By comparison, using the baseline electrolyte of E1, the cell decays quickly and reaches 70% of its original capacity of 2.79 mAh only after 50 cycles. The average CE is only 99.0% in the first 50 cycles.

The lithium deposition morphology was probed on the Li-metal anode by using scanning electron microscopy (SEM). At a current density of 0.5 mA cm<sup>-2</sup>, the lithium seeds that formed in the E1 electrolyte have a needle-shaped morphology (Figure 154a) and are smaller than those formed in FSE and AFSE electrolytes. This finding implies that the growth of lithium dendrites is exaggerated in the conventional electrolyte without additives and at low Li<sup>+</sup> concentration. By contrast, lithium seeds formed in FSE and AFSE are uniform and show an island-shaped morphology. As shown in Figure 154d, the thickness of deposited lithium in the E1 electrolyte is 25 μm with loose and mossy structures, while the deposited lithium in the FSE and AFSE electrolytes is only 20 μm with dense and chunky structures (Figure 154e-f). The morphological difference indicates a significantly reduced surface area and thus restrained side reactions between Li-metal anode and electrolyte, resulting in limited SEI reformation and reduced electrolyte consumption.

In conclusion, the newly developed electrolyte AFSE can promote much more uniform lithium deposition and improved CE. More importantly, AFSE demonstrates improved cycling performance with the Li||NMC-811 full cells. Furthermore, SEM study reveals that the electrolyte greatly influences the SEI chemistry and compositions, generating a robust and non-dendritic lithium deposition on the anode surface.

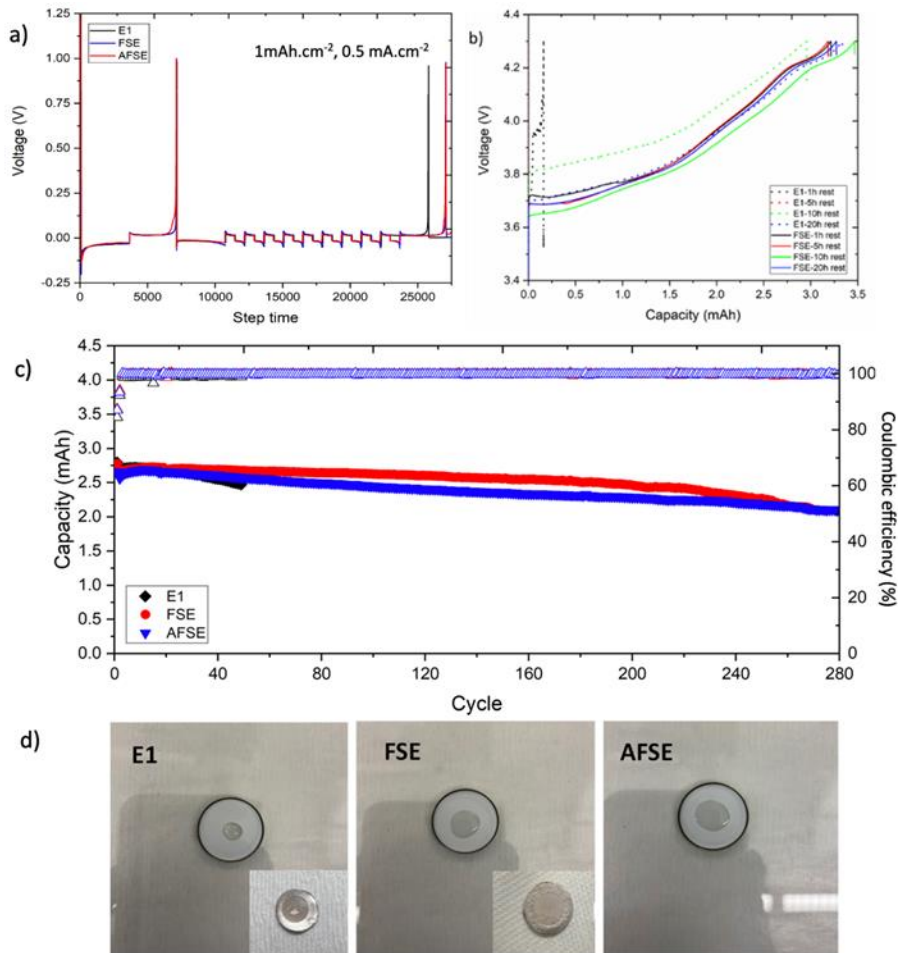


Figure 153. (a) Aurbach Coulombic efficiency of Li||Cu cell in different electrolytes. (b) Charge curves of different electrolytes with various resting time. (c) Electrochemical performance of the NMC-811||Li coin cells tested in different electrolytes. (d) Wettability of the electrolytes on Celgard separators and lithium metals after 1<sup>st</sup> charge.

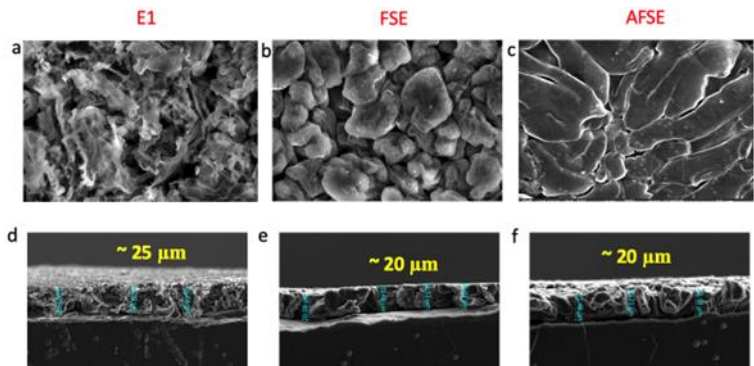


Figure 154. Morphology of Li-metal anode after 10 cycles: (a-c) top-view scanning electron microscopy images and (d-f) cross-view images of lithium anodes in different electrolytes.

## Electrolyte Development for Sulfurized Polyacrylonitrile (SPAN) Cathodes

The PNNL team has investigated several new electrolytes for Li||SPAN cells. Six solvating solvents were selected to prepare the HCEs first. Among these electrolytes, SS4-HCE shows the highest average lithium CE (~99.3%), as shown in Figure 155a. Since HCEs have a wettability issue to the polyolefin separators and the thick electrode laminates due to their high viscosities, LHCEs were developed by adding selected diluent in HCEs to reduce the viscosity and improve the wettability. These newly developed electrolytes are named SS4-based electrolytes. Two SS4-based LHCEs (SS4-LHCE-1 and SS4-LHCE-2) were prepared, and they demonstrate improved average lithium CEs (>99.5%) compared to SS4-HCE (97.9% to 99.1%, Figure 155b). The average lithium CEs are very similar to that of the Battery500 E-baseline electrolyte [LiFSI-DME-BTFE (0.901:1:2 by mol)] for SPAN cells. In general, the electrolyte with a higher efficiency could enhance the cycling performance of the Li||SPAN cells. To investigate the compatibility of the electrolytes with Li-metal anode, 1 mAh cm<sup>-2</sup> of lithium was deposited on the copper electrode at a current density of 0.5 mA cm<sup>-2</sup>. The lithium deposited with SS4-LHCEs exhibits larger particle size and denser morphologies than that deposited with E-baseline electrolyte (Figure 155c). This result indicates that SS4-LHCEs could be more compatible with Li-metal anode than E-baseline electrolyte.

For the cycle life test, the Li||SPAN cell consists of a SPAN cathode (4.5~5 mg cm<sup>-2</sup>, from University of California, San Diego, or UCSD), a polymer electrolyte separator (20- $\mu$ m thick), a lithium foil (250- $\mu$ m thick), and 30  $\mu$ L electrolyte. Before starting the cycle life test, all cells were conditioned by two formation cycles at a current density of C/20 (where 1C = 2.7-3.0 mA cm<sup>-2</sup>) under the voltage range of 1-3 V. In the initial charge/discharge profiles, the cells using three electrolytes show similar polarization (Figure 156a-c). The Li||SPAN cells with SS4-LHCE-1 and SS4-LHCE-2 have capacity retentions of 92.5% and 88.3%, respectively, after 150 cycles at a current density of C/5 (Figure 156d). The cells using SS4-LHCE-1 show a slightly higher capacity retention (92.5%) than those using E-baseline electrolyte (~89.6%). These cells are still being tested.

It is interesting to note that even though E-baseline electrolyte has a higher ionic conductivity (Figure 157a), SS4-LHCE-1 delivers a better charge-rate capability (Figure 157b). To understand the relationship between the ionic conductivity and the charge-rate capability, the compatibility of SS4-LHCEs with the SPAN cathode will be investigated. Furthermore, post-mortem analyses will be performed to reveal the interphase properties of SS4-LHCE and electrodes.

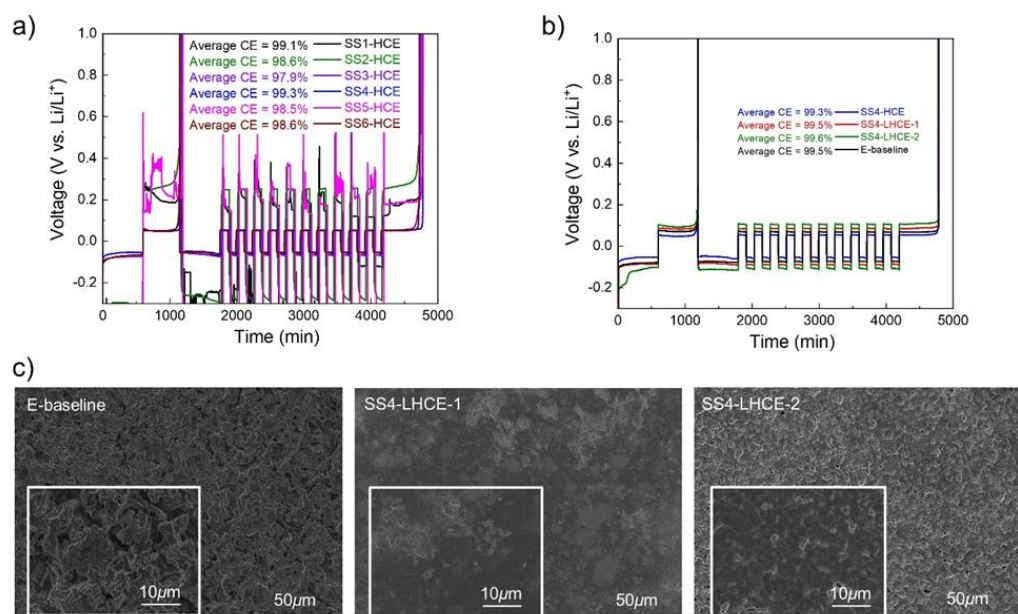


**Figure 155.** (a) Average Coulombic efficiency (CE) of Li||Cu cells with high-concentrated electrolytes with six solvating solvents. (b) Average CE of Li||Cu with SS4-based localized high-concentration electrolytes and E-baseline. (c) Lithium deposition morphologies on copper electrodes at a current density of 0.5 mA cm<sup>-2</sup> for a capacity of 1 mAh cm<sup>-2</sup>.

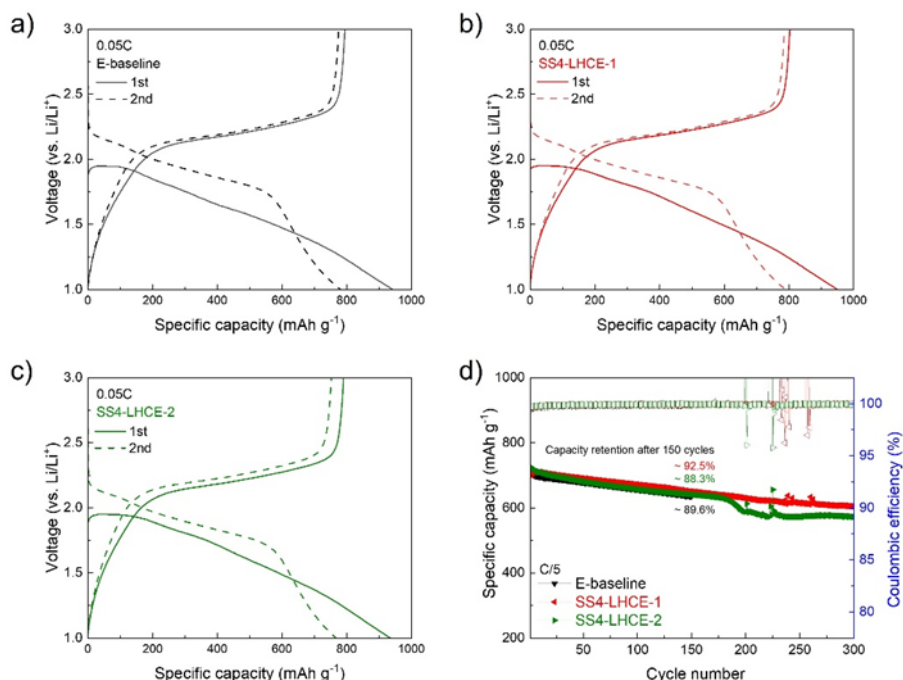


Figure 156. Charging/discharging profiles of Li||SPAN cells at a current density of C/20 with (a) E-baseline, (b) SS4-LHCE-1, and (c) SS4-LHCE-2. (d) Performances of Li||SPAN cells with studied electrolytes at a current density of C/5 in the voltage range of 1-3 V.

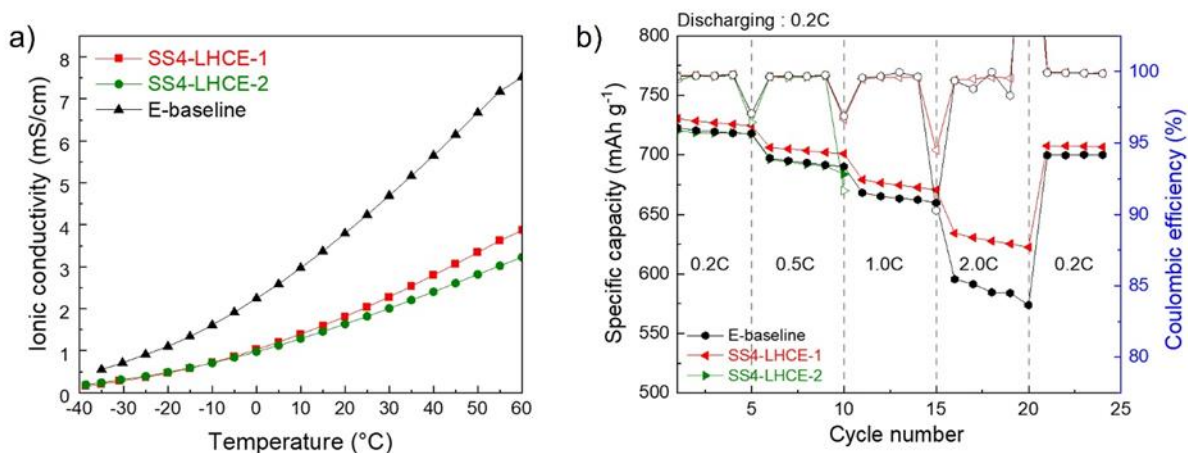
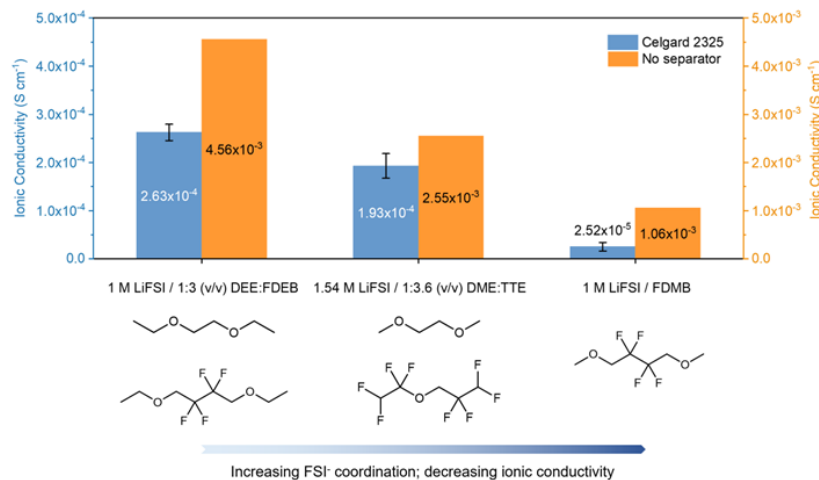


Figure 157. (a) Ionic conductivities at different temperatures. (b) Charge-rate capability of Li||SPAN cells with the studied electrolytes at a constant discharging current density of C/5 in the voltage range of 1-3 V.

### Electrolyte Development for Li-Metal Anode

The Stanford University team investigated the fast-charging stability of Li-metal batteries using different electrolytes. Rate performance (particularly charging rate) is an important metric to consider for Li-metal batteries. “Extreme fast charging” at 4C or above has been proposed as the target for Li-ion batteries for EV applications, and liquid electrolyte (LE) design is vital to achieving this goal. They investigated the fast-charging stability of three advanced electrolytes in Li-metal batteries: 1 M LiFSI in fluorinated 1,4-dimethoxybutane (FDMB), 1.54 M LiFSI in 1:3.6 (v/v) DME:TTE, and a new formulation of 1 M LiFSI in 1:3 (v/v) 1,2-diethoxyethane (DEE): fluorinated 1,4-diethoxybutane (FDEB), as shown in Figure 158. All three electrolytes feature > 99% CE (modified Aurbach method) with anion-derived SEI and good oxidation stability, whereas their ionic conductivities decrease in the order of DEE-FDEB, DME-TTE, and FDMB electrolytes.

To observe effects of charge rate on full-cell performance, the team constructed coin cells mimicking conditions in a practical high-energy-density battery. A high-loading NMC-811 cathode (ca. 4.5 mAh cm<sup>-2</sup>) was paired with a thin lithium foil (50- $\mu$ m thick, negative/positive capacity ratio N/P  $\sim$  2) and with non-flooded electrolyte condition (electrolyte/capacity ratio,  $\sim$  8.9 mL Ah<sup>-1</sup>). Previous studies on carbonate-based electrolytes found that Li-metal cycling stability was improved by setting the discharge rate higher than the charge rate. To avoid complication from these factors, the discharge rate was first set to 1C (1C = 4 mA cm<sup>2</sup>) for all cells, and slower or equal charge rates of up to 1C were selected. For the better-performing DEE-FDEB electrolyte, the 1.3C charge rate was further examined to find its limit. In addition, since the cycle life of Li-metal batteries is sensitive to cycling capacity, a constant-voltage charging step was applied at the upper cutoff voltage (4.4 V) with C/10 current cut-off to ensure similar initial cycling capacity regardless of charge rates.



**Figure 158. Chemical structures, compositions, and ionic conductivities of the three weakly solvating electrolytes under investigation. Notably, the ionic conductivities in Celgard 2325 separator (left blue axis) are lower by an order of magnitude than those without a separator (orange right axis).**

The discharge capacity and CE at various charge rates for each electrolyte are shown in Figure 159a-f. For all three electrolytes, full-cell cycle life decreased as the charging rate increased (Figure 159g). The only exception was DEE-FDEB cells at C/10, which showed worse performance than those at faster rates. This might be due to accumulated parasitic reactions at a longer cycling time due to the slower rate. At higher charge rates ( $\geq$  C/2), a casual correlation between cycle life and ionic conductivity was observed; at lower charge rates ( $\leq$  C/5), this correlation was lost (Figure 159g). These observations have three implications: (1) the cycling stability at low charge rates does not translate to high charge rates; (2) the design principles that lead to good cycle life at low charge rates are not necessarily applicable to high charge rates; and (3) there is a shift in the limiting factor for cycling stability going from low to high charge rates.

Notably, there is a threshold charge rate for each electrolyte above which cells consistently failed by soft shorting (that is, 1.3C for DEE-FDEB electrolyte, C/2 for DME-TTE electrolyte, and C/2 for FDMB electrolyte), as evidenced by a sharp decrease in CE (Figure 159b/d/f shaded region) and spiky voltage curves during charging (Figure 159h-i). The soft shorting was attributed to the formation of thin lithium filaments, which were found to be high in electrical resistance. As a result, the cells could still reach 4.4 V, although the total charge passed was much higher than the cathode capacity due to an internal short circuit. During the subsequent fast discharge, the large concentration gradient led to increased local current density at the tips of lithium protrusions, where lithium was preferentially stripped. These thin lithium filaments could then disconnect from the cathode and allow for a normal discharge voltage curve without any apparent short circuit (Figure 159h-i). However, if the cells were cycled continuously under soft shorting conditions, they would eventually become completely shorted.

In summary, by systematically varying charging current densities, short circuits were observed in all three electrolytes above certain current densities (that is,  $5.2 \text{ mA cm}^{-2}$  for DEE-FDEB electrolyte, and  $2 \text{ mA cm}^{-2}$  for DME-TTE and FDMB electrolytes) under the operating conditions. Extensive characterizations are in progress to investigate the mechanism leading to such poor cycling stability. The information gained through this project will guide future design of electrolytes to enable fast-charging Li-metal batteries.

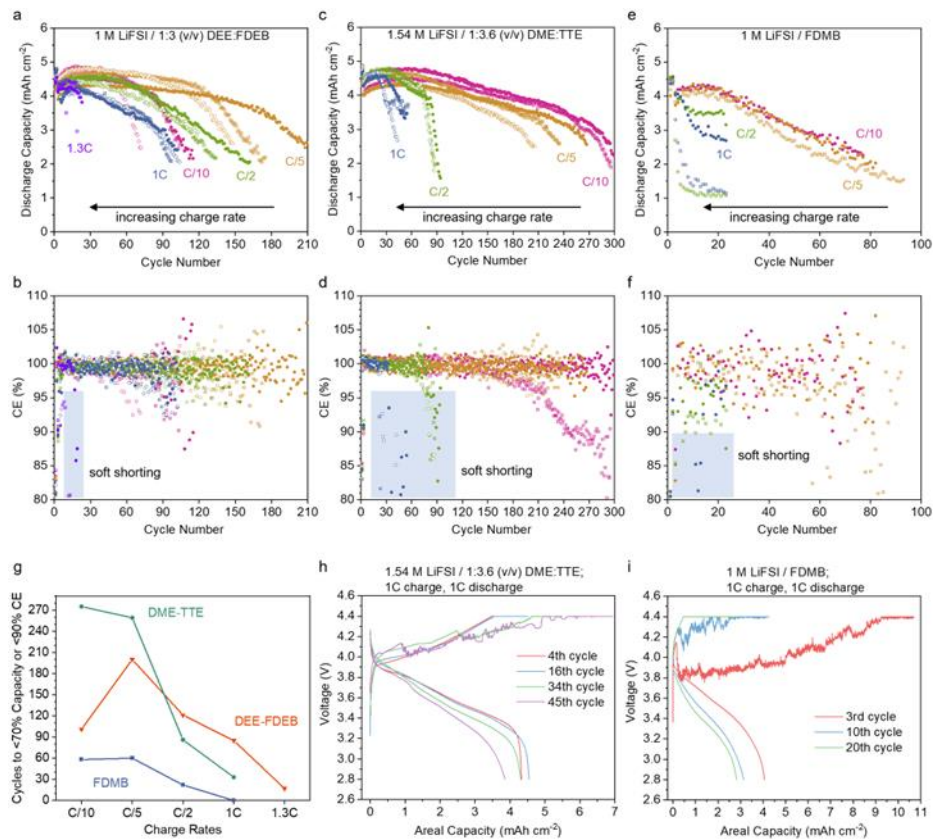


**Figure 159.** Full-cell performance at various charge rates and 1C discharge rate ( $1\text{C} = 4 \text{ mA cm}^{-2}$ ). Coin cells were assembled with NMC-811 (ca.  $4.5 \text{ mAh cm}^{-2}$ ),  $50\text{-}\mu\text{m}$  thick lithium foil ( $N/P \sim 2$ ), and relatively lean electrolyte amount ( $E/C \sim 8.9 \text{ mL Ah}^{-1}$ ). All cells were cycled between  $2.8 \text{ V}$  and  $4.4 \text{ V}$  versus  $\text{Li}^+/\text{Li}$ . Two formation cycles at C/10 charge and discharge rates were performed, followed by long-term cycling at various charge rates (labeled on the graph) and 1C discharge rate. A constant voltage step was applied at the end of charging until the current fell below C/10. (a-f) Discharge capacity and Coulombic efficiency (CE) over cycling for 1 M LiFSI in 1:3 (v/v) DEE:FDEB (a-b), 1.54 M LiFSI in 1:3.6 (v/v) DME:TTE (c-d), and 1 M LiFSI in FDMB (e-f). The replicated cells are shown in the same color and different symbols. (g) The dependence of cycle life on charge rates. Cycle numbers were calculated from the champion cell at each charge rate. The end of cycle life was defined as  $< 70\%$  discharge capacity of the 3<sup>rd</sup> cycle or  $< 90\%$  CE starting from the 4<sup>th</sup> cycle. (h-i) Voltage profiles showing soft shorting characteristics at 1C charge rate in 1.54 M LiFSI in 1:3.6 (v/v) DME:TTE (h) and 1 M LiFSI in FDMB (i).

### Refined XPS Characterization Protocol for SEI Studies

XPS is one of the most widely employed techniques for characterizing battery materials. Developing advanced electrolytes for high-energy Li-metal batteries will largely benefit from reliable XPS characterization to uncover formation and evolution of SEI between lithium metal and electrolyte. The Stanford team aimed to refine and innovate the existing protocols of XPS characterization to rationalize the electrolyte reactivity at the Li-metal anode while identifying potential experimental pitfalls.

First, by analyzing thin-film samples prepared from LEs, they have identified that three F-containing lithium salts [that is, LiFSI, lithium bis(trifluoro-methanesulfonyl)imide salt (or LiTFSI), and LiPF<sub>6</sub>] commonly used in battery research consistently degraded to generate LiF under Ar<sup>+</sup> sputtering during XPS measurements, potentially leading to artificial inflation of LiF content during SEI analysis (Figure 160a). Then, they found that an electrolyte system based on a specific salt-solvent combination produces distinct organic residues at the surface and in bulk which should be distinguished from the real organic SEI species in carbon 1s spectra. A systematic comparison of the elemental binding energies across these three lithium salts reveals sensitive shifts that reflect their distinct chemical environment, offering a useful reference for robust XPS peak assignment for the battery research community.

After establishing the above XPS benchmark, they proceeded to evaluate the effects of electrochemical FSI anion breakdown toward electrode surface passivation during electron transfer at the Cu/electrolyte interface. By adopting a non-washing XPS protocol, they managed to capture crucial reaction intermediates manifesting the details of SEI chemistry at the Cu/electrolyte interface. After cycling Li||Cu half cell at 0-1 V 100 times in ether-based electrolytes, the XPS results clearly revealed the SEI fingerprint species, such as Li<sub>2</sub>S, Li<sub>2</sub>O, and Li<sub>3</sub>N, despite the co-existence of LiFSI salt (Figure 160b). Importantly, the Li<sub>2</sub>O/Li<sub>2</sub>S stoichiometry ratio of ~ 2 suggested the cleavage of S = O double bonds via continuous reduction of the sulfur center, eventually leading to formation of Li<sub>2</sub>S + 2Li<sub>2</sub>O (Figure 160c). Further, deconvoluting the enriched nitrogen 1s spectra led to the identification of a N-SO<sub>x</sub> intermediate by 1<sup>st</sup> step of N-S cleavage prior to Li<sub>3</sub>N formation, whereas its relative population evolved as a function of reaction driving force. A systematic comparison of copper surface composition before and after solvent washing allowed the team to understand the relative dissolution trend of various inorganic compounds. Li<sub>2</sub>O/LiOH was found to be the dominating species in the compact SEI, whereas Li<sub>2</sub>S is the most soluble (least passivating) species present mostly in the liquid phase. Future efforts will focus on applying such a refined XPS protocol toward revealing SEI chemistry beyond LiFSI-based electrolytes.

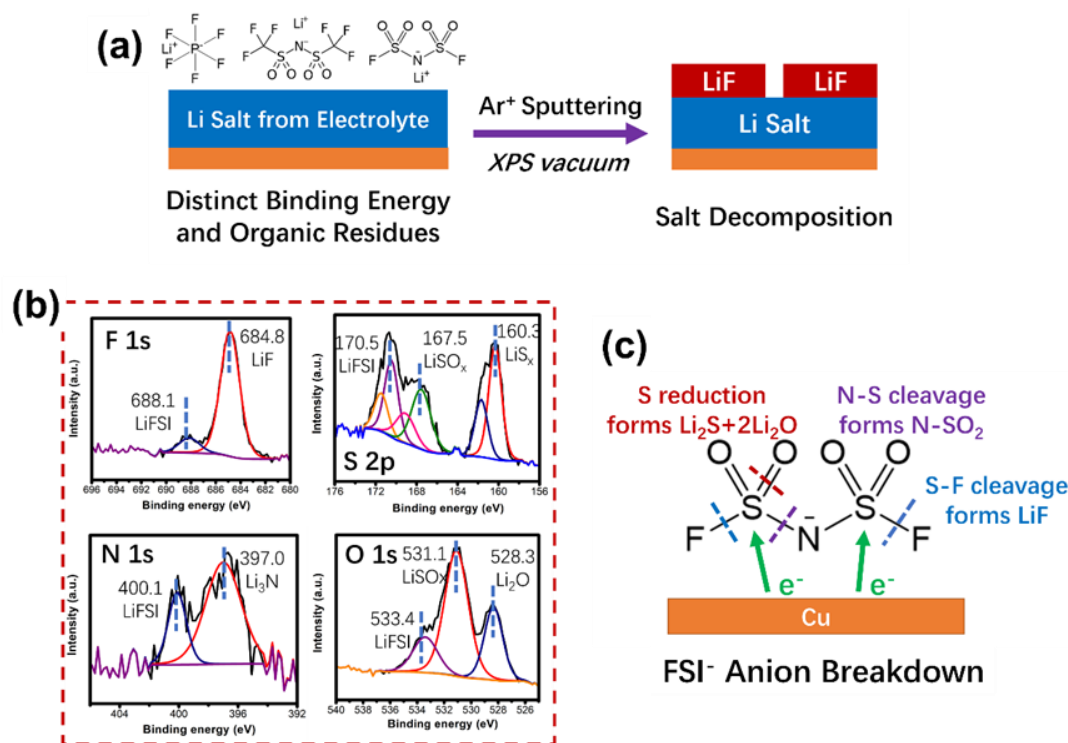


Figure 160. (a) Degradation of lithium salts into LiF under Ar<sup>+</sup> sputtering of X-ray photoelectron spectroscopy (XPS) measurements. (b) XPS analyses of unwashed copper electrode after cycling in a Li/Cu cell at 0-1 V for 100 times in DME / 1 M LiFSI electrolyte, revealing crucial fingerprint species of SEI chemistry. (c) Schematic of three basic steps of breaking down FSI<sup>-</sup> anion at Li<sup>0</sup>-metal potential based on XPS analyses.

## Highlights of Keystone Project 1

The highlights for this quarter are as follows:

- The Binghamton team found that FSI ether electrolytes are stable to fresh lithium during the melting process. Cycled NMC-811 became more thermally stable in carbonate electrolytes after the formation of the SEI, while no obvious trend was observed in ether-based electrolytes.
- The UT Austin team further investigated the effects of solvents and diluents used in their developed LSE on the protection ability against LiNiO<sub>2</sub> cathode. FEC/EMC and TTE are the best solvents and diluents, respectively, among those investigated. The investigation of Li<sup>+</sup> solvation structure in LSE by PDF and SAXS suggests that chemical bond lengths, such as C-O bonds in carbonates and P-F in PF<sub>6</sub><sup>-</sup>, are changed in LSE compared to the conventional LCE. Moreover, diluent molecules may interact with the Li<sup>+</sup> inner solvation structure, which alters the size distribution of Li<sup>+</sup> agglomerates.
- The PSU team developed a new electrolyte formulation, called AFSE, which enabled 99.5% lithium CE in Li||Cu cells and 80% capacity retention after 280 cycles in Li||NMC-811 coin cell with a high areal capacity (4.0 mAh cm<sup>-2</sup>) cathode, 50-μm thin Li-metal anode, and lean electrolyte (5.5 μL/mAh).
- The PNNL team developed new HCEs and LHCEs for Li||SPAN cells. Two types of LHCEs demonstrate lithium CE of ~ 99.5%. The lithium deposition morphologies in the two LHCEs show larger particle size and denser packing compared to the E-baseline electrolyte. The Li||SPAN cells exhibited capacity retentions of 92.5% (SS4-LHCE-1) and 88.3% (SS4-LHCE-2) after 150 cycles at a current density of C/5. Interestingly, despite the ionic conductivity of SS4-LHCE-1 being lower than that of the E-baseline, cells using the SS4-LHCE-1 deliver a better charge-rate capability.
- The Stanford team investigated the effect of charge rate on the cycling stability of Li-metal batteries and found that the cycling stability at low charge rates does not translate to high charge rates. There is a shift in the limiting factor for cycling stability going from low to high charge rates. The team also refined the existing XPS characterization protocol to rationalize the electrolyte reactivity at Li-metal anode while identifying potential experimental pitfalls.

## Keystone Project 2: Electrode Architecture

The goal of Keystone 2 is to design, model, fabricate, and characterize the effect of electrode architecture on the electrode and cell performance in support of reaching the project goal of 500 Wh kg<sup>-1</sup> cell specific energy. Research conducted includes the understanding and optimization of high loading electrodes; three-dimensional (3D) lithium anode architectures; synthesis and optimization of SPAN cathode; and development of high-capacity sulfur composites. Research highlighted this quarter includes the following: effect of oxide cathode thickness on rate capability (University of Washington, UW); reaction mechanisms in SPAN (UCSD); computational studies to identify catalysts for the Li-S reaction (University of Pittsburgh, U-Pitt); and the effect of 3D host on lithium metal plating (UW).

### Oxide Cathode Thickness Optimization (UW)

Thicker electrodes allow for a *de facto* increase in energy density since the weight percentage of electrochemically inactive current collectors is reduced in the stack. However, thicker cathodes can also run into diffusion limits at higher current densities, leading to underutilization of the active material. The optimization of an ideal cathode thickness is non-trivial and requires greater scientific understanding.

Coin cells were cycled with high-Ni NMC cathodes of thicknesses 50-200 μm, against Li-foil anodes, at a series of C-rates. The results showed a sharp capacity drop at high current densities, a hallmark of reaching the diffusion limit. However, the diffusion limit showed no thickness dependence (see Figure 161). This runs counter to the models in literature describing the diffusion limit, which predict a gravimetric capacity drop with increasing cathode thickness. This discrepancy appears in some published data as well, where the authors have

only looked at the capacity drop with C-rate, rather than looking at the capacity drop with current density and cathode thickness side-by-side. In the literature data, this discrepancy only appears for NMC cathodes, not for Li-Fe-P (LFP) cathodes.

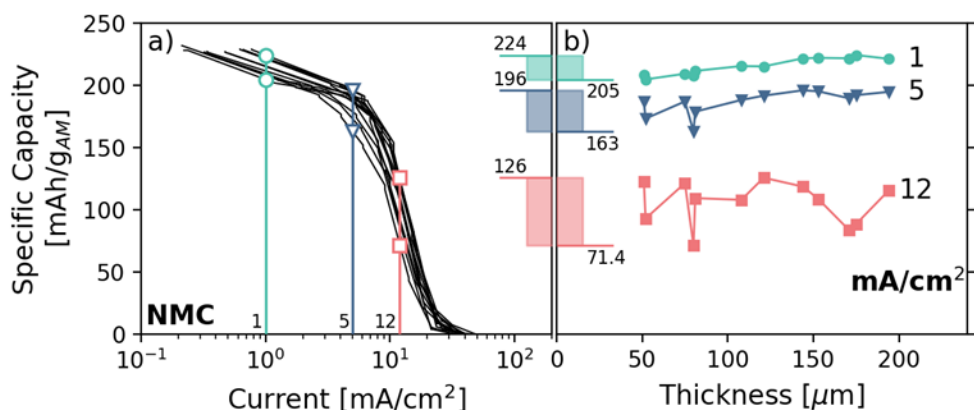


**Figure 161.** Initial data showing no significant impact to the specific capacity as a function of cathode thickness.

To study this discrepancy, further work is planned: a series of  $\text{LiNi}_{0.6}\text{Mn}_{0.2}\text{Co}_{0.2}$ ,  $\text{LiCoO}_2$ , and LFP cathodes with different thicknesses will be cycled at different current densities, to determine if there is a thickness dependence. For each cathode batch, electrochemical impedance spectroscopy will be used to measure the effective diffusion coefficient to verify the difference in morphology among different dried cathode strips. To test whether the lack of a thickness dependence in NMC cathodes is due to the absence of a diffusion limit, further tests will be conducted by varying the salt concentration in the electrolyte to reduce the ionic conductivity. Limiting the electrolyte concentration should, at some point, induce a diffusion limit if there is not one already.

### Reaction Mechanism of SPAN Cathode

Previously, the UCSD team has shown the reaction mechanism of the SPAN cathode and pinpointed the root cause for the 1<sup>st</sup> cycle irreversible capacity loss. According to the proposed reaction mechanism, after the 1<sup>st</sup> cycle, the aromaticity of the SPAN molecule will be increased. The enhanced conjugation structure of SPAN can in turn increase the electronic conductivity of the polymer molecule. To prove their hypothesis, a carbon-free and additive-free thin-film SPAN is made to study the electronic conductivity of SPAN before and after cycling.

To synthesize the thin-film SPAN, the polyacrylonitrile (PAN) – dimethylformamide (1M) solution is first spin-coated on a titanium substrate at 2000 rpm for 30 seconds. The films are later dried at 100°C for 1 hour and then sulfurized in an Ar-flowing tube furnace at 350°C for 6 hours. As shown in Figure 162, the thin-film SPAN deposited on the titanium substrate (Figure 162a) shows a thickness of only 200 nm (Figure 162b), a length scale similar to the particle size of SPAN. As shown in Figure 162c-d, there is no morphological change from precursor PAN to product SPAN. The thin-film SPAN is dense, pore-free, and smooth. In Figure 162e, the scanning transmission electron microscopy – energy dispersive X-Ray spectroscopy mapping shows that, like the regular SPAN powders, the nitrogen, sulfur, and carbon elements are uniformly distributed across the thin film. Fourier transform infrared (Figure 162f) shows that all functional groups of SPAN thin film are the same as those of SPAN powders. The thin-film SPAN on titanium is cycled in a coin-cell setup. Glass fiber is used as the separator, and 1 M LiTFSI in DME / 1,3-dioxolane (1:1) with 2 wt%  $\text{LiNO}_3$  is used as electrolyte. Galvanostatic charge/discharge is conducted in a fixed voltage range of 1–3 V versus  $\text{Li/Li}^+$  at room temperature with C/20 (1 C = 550 mAh/g) rate based on the SPAN loading. After cycling, the thin-film SPAN is recovered from the coin cell, and an 80-nm-thick copper is vapor deposited on the top of it in an argon glove box (Figure 162g). According to the team’s hypothesis, the loss/conversion of non-aromatic S/N during the 1<sup>st</sup> cycle is associated with an increase in the degree of conjugation. In principle, this should lead to an increase in the

electrical conductivity. This is indeed confirmed by measurement of the pristine and the 1<sup>st</sup> charged SPAN thin films (Figure 162h). After the 1<sup>st</sup> charge, SPAN conductivity increases by two orders of magnitude (from  $1.21 \times 10^{-7} \text{ S cm}^{-1}$  to  $4.43 \times 10^{-5} \text{ S cm}^{-1}$ ). This result further proves the proposed SPAN reaction mechanism: the unwanted non-aromatic S/N is lost after the 1<sup>st</sup> cycle, and the increased aromaticity can improve the cycling stability of the SPAN.

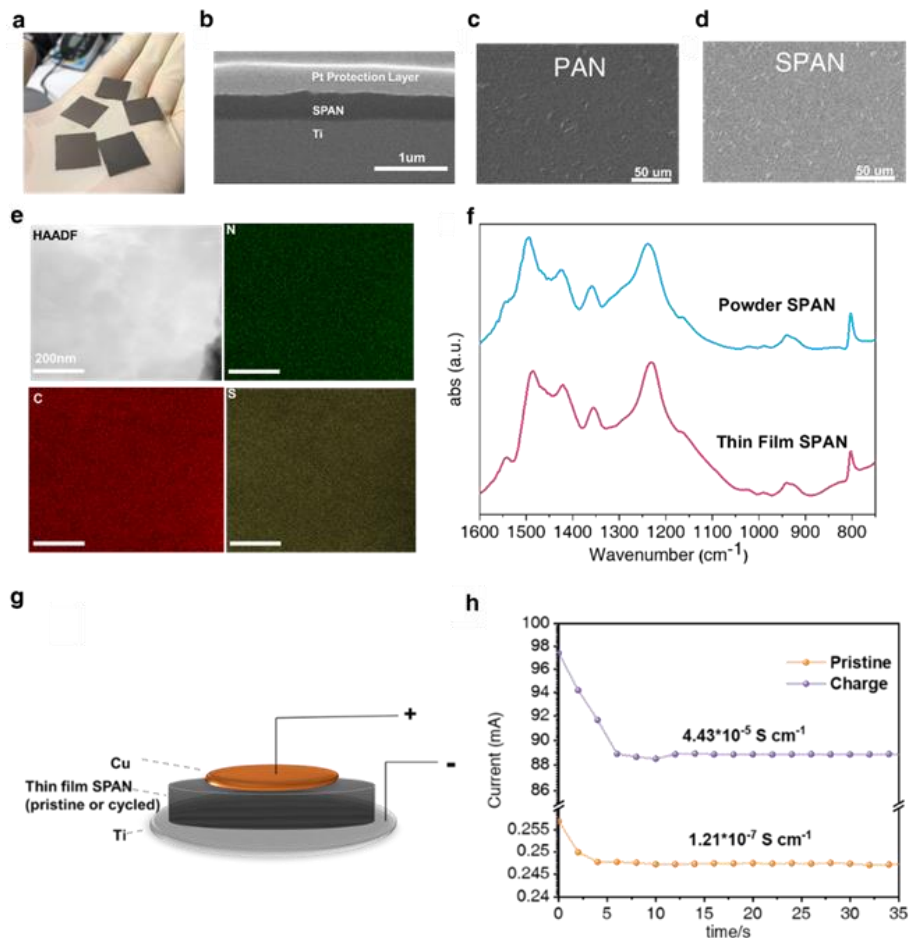


Figure 162. Characterizations of thin-film SPAN. (a) Photo of thin-film SPAN synthesized on top of titanium substrate. (b) Focused ion beam – scanning electron microscopy (FIB-SEM) image of the cross-section of thin-film SPAN on titanium substrate. Top-view SEM images for the (c) precursor (polyacrylonitrile) thin film and (d) SPAN thin film. (e) Scanning transmission electron microscopy – energy dispersive X-ray spectroscopy mapping of thin-film SPAN. (f) Fourier transform infrared spectra of the powder and thin-film SPAN. (g-h) Schematic and results of the electrical conductivity test for SPAN thin film before and after the 1<sup>st</sup> cycle.

### Computational Identification of Functional Electrocatalysts Enabling Conversion of $\text{Li}_2\text{S}_2$ to $\text{Li}_2\text{S}$

The U-Pitt team continued to conduct theoretical modeling to probe the conversion of  $\text{Li}_2\text{S}_2$ , the intermediate polysulfide phase, to  $\text{Li}_2\text{S}$ , the final phase. As discussed in previous reports, achieving the complete conversion of  $\text{Li}_2\text{S}_2$  to  $\text{Li}_2\text{S}$  is of prime importance for the discharge process since the very sluggish kinetics of this reaction prevent the full utilization of sulfur in the sulfur cathode. The typical end products of the discharge process are  $\text{Li}_2\text{S}$  and  $\text{Li}_2\text{S}_2$  mixtures giving significantly lower capacity of almost 50% and, consequently, the energy density as well commensurate with the lower sulfur utilization opposed to pure  $\text{Li}_2\text{S}$  due to the high activation barrier associated with the complete conversion of  $\text{Li}_2\text{S}_2$  to the desired, final state of  $\text{Li}_2\text{S}$ . Thus, calculation of this kinetic reaction barrier and identification of the appropriate electrocatalysts substantially decreasing or even leading to complete elimination of this activation barrier will result in efficient utilization of sulfur. Thus, the

main aim of the present computational study is to identify functional electrocatalysts that can decrease the activation barriers and promote rapid conversion of  $\text{Li}_2\text{S}_2$  to  $\text{Li}_2\text{S}$  during discharge and the corresponding backward reaction from  $\text{Li}_2\text{S}$  to  $\text{Li}_2\text{S}_2$  during the charge process.

The U-Pitt team previously demonstrated that there are two principal reactions steps where functional electrocatalyst can make a difference. Reaction 1,  $\text{Li}_2\text{S}^{(1)} \rightarrow \text{LiS} + \text{Li}$  in the discharge direction (from right to left) is almost spontaneous without registering any appreciable activation barrier, which indicates that the formation of  $\text{Li}_2\text{S}$  by seizing Li-ion during the discharge process does not hinder the overall kinetics of  $\text{Li}_2\text{S}_2 \rightarrow \text{Li}_2\text{S}$  conversion. Reaction 2,  $\text{Li}_2\text{S}_2 \rightarrow \text{Li}_2\text{S}^{(1)} + \text{S}$ , on the other hand, has a considerable barrier in both the charge and discharge directions, thus rendering this reaction as the rate determining step in the overall conversion of  $\text{Li}_2\text{S}_2$  to  $\text{Li}_2\text{S}$  and a focus of current study.

To obtain the thermodynamic properties, the density functional theory (DFT) approaches implemented in the Vienna *ab initio* simulation package (VASP) have been used, while a climbing image nudged elastic band (cNEB) method was utilized for determination of the activation energies and other pertinent kinetic parameters of the elementary reactions on the different prospective functional electrocatalytic surfaces. The model of the functional electrocatalyst considered consists of a surface slab with the most stable crystallographic orientation containing the attached  $\text{Li}_2\text{S}_2$  or  $\text{Li}_2\text{S}$  molecules. The slab with a thickness of  $\sim 5\text{-}7 \text{ \AA}$  is separated from its image perpendicular to the surface direction by  $\sim 20 \text{ \AA}$  to avoid their mutual interaction. The bottom two-to-three layers of the slab are then fixed with lattice parameters corresponding to the bulk state, while the remaining top layers along with the attached polysulfide molecule are allowed to completely relax. All the species are adsorbed on the functional electrocatalyst surface including the lithium and sulfur atoms.

The activation barriers for the elementary reactions were estimated using the cNEB method, where five intermediate points were chosen for calculations of the potential energy profile between the initial and final position of the Li-ion for the reaction 1 and sulfur atom for the reaction 2 at the functional electrocatalytic surface (totally 7 points). All computations have been executed within the projector-augmented wave method and the generalized gradient approximation as the exchange-correlation energy functionals in a form described by J. P. Perdew and Y. Wang implemented in the VASP software. To maintain the desired high precision for all the total energy and electronic structure calculations, a plane wave cutoff energy of 520 eV has been chosen. The relaxation procedure has been used to optimize the internal positions as well as the lattice parameters of the supercell. Additionally, the Monkhorst-Pack scheme has been used to sample the Brillouin zone and create the k-point grid for all the functional electrocatalytic surface slabs used in the current study. The selection of the appropriate numbers of k-points in the irreducible parts of the Brillouin zone were made on the grounds of the convergence of the total energy to 0.1 meV/atom.

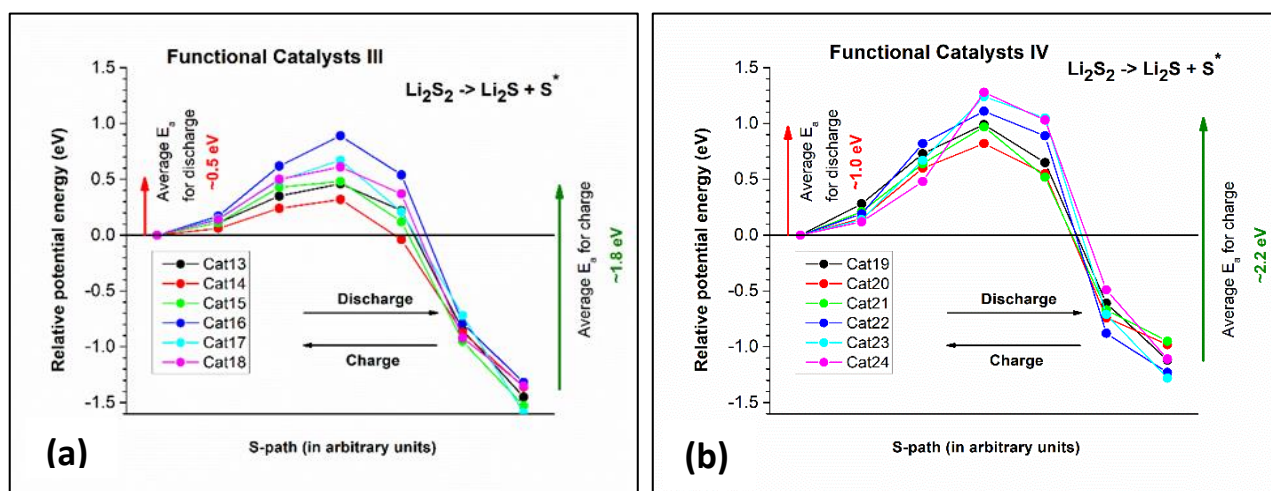


Figure 163. Potential energy profiles for Reaction 2 ( $\text{Li}_2\text{S}_2 \rightarrow \text{Li}_2\text{S} + \text{S}^*$ ) for the two types of functional electrocatalysts considered.

The potential energy profiles for Reaction 2 calculated for functional electrocatalysts comprising Functional Catalysts III, Type III, as well as Functional Catalysts IV, Type IV, are shown in Figure 163a-b, respectively. It can be observed that for all probed materials of both functional electrocatalysts of types III and IV, Reaction 2 in the discharge direction is exothermic, as expected, with the final product ( $\text{Li}_2\text{S}+\text{S}$ ) being more energetically favorable compared to  $\text{Li}_2\text{S}_2$ . However, in contrast to the spontaneous Reaction 1 discussed in previous reports, this reaction is not spontaneous with substantial activation barriers needed for the different electrocatalytic materials considered, and the average energy barrier is  $\sim 0.5$  eV for Type III and  $\sim 1.0$  eV for Type IV functional electrocatalysts. Type III functional electrocatalysts therefore demonstrate significantly lower average activation barriers than those observed and calculated for functional electrocatalyst of Type IV. For example, the electrocatalyst, Cat14 in Figure 163a, demonstrates the lowest activation barrier among all the prospective electrocatalytic materials considered so far ( $\sim 0.3$  eV). This is a very similar activation barrier value as calculated for Cat8 reported last quarter. However, there is still the need to further decrease the activation barriers for Reaction 2, which will then likely yield much higher specific capacity values for sulfur in the S-cathode. Studies to further identify better functional electrocatalysts continue. Results of the corresponding experimental work to validate findings of the theoretical calculations will also be reported in future quarters.

### 3D Anode Architecture

During this reporting period, the UW team has continued to explore the impact of 3D anode architectures on the CE of metallic lithium anodes. By implementing the Aurbach protocol for CE testing with the M47 electrolyte (PNNL LHCE) in half cells, no statistically significant advantages or disadvantages have been observed (see Figure 164). While their results do not demonstrate any clear CE benefits, the mass reduction of utilizing a porous current collector architecture can still provide significant gravimetric energy density benefits without negatively impacting CE.

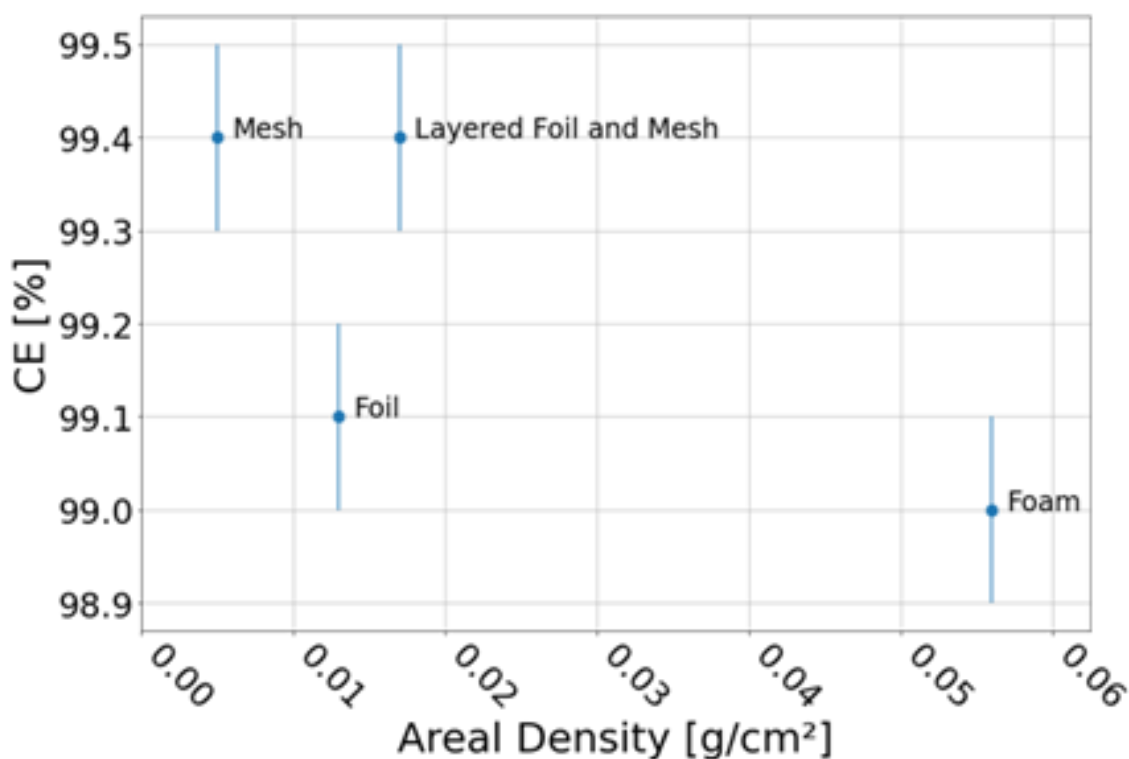
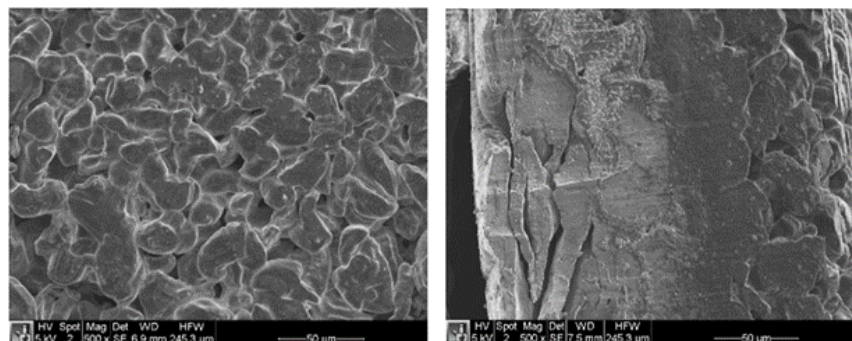


Figure 164. Coulombic efficiency versus areal density for four different current collector structures.



**Figure 165. Top-view (left) and cross-sectional view (right) of electrochemically deposited lithium metal on copper foam in LHCE.**

Additionally, the compatibility of commercial copper foil and foam as 3D host for Li-metal anode has been tested for compatibility with different electrolytes. The Aurbach protocol was used to test CE with a certain charge-discharge profile. 5 mAh/cm<sup>2</sup> of lithium metal was deposited on copper substitute first, 10 shallow cycles of 1 mAh/cm<sup>2</sup> follow, and all lithium metal was stripped with cut-off voltage of 1 V. The CE is calculated by the total stripped capacity divided by total deposited capacity. The results are listed in Table 11, showing that copper foam has lower CE than foil due to more lithium consumption for SEI formation at the higher surface area of foam.

**Table 11. Coulombic efficiency data for commercial foil and foam using four electrolytes.**

CE(%)	HCE	LHCE(M47)	F5	DOLDME
Cu Foil	99.4	99.5	99.5	98.7
Cu Foam	98.9	98.8	99.3	99.5

Li-metal deposition behavior on copper foam was studied by SEM after a capacity of 10 mAh/cm<sup>2</sup> of lithium metal was deposited (see Figure 165). The top view of copper foam shows porous structure of deposited lithium metal in LHCE-M47. The cross-sectional view shows the same porous deposited lithium metal on the right side, which is toward the separator. However, lithium metal was only deposited on the top surface of copper foam, instead of the bottom of it, due to the limitation of Li-ion diffusion in electrolyte and lithiophilicity of 3D host surface. The surface modification to enhance lithiophilicity needs to be studied further.

## Highlights of Keystone Project 2

The highlights for this quarter are as follows:

- The UW team discovered that the specific capacity is not closely related to the thickness of cathode at the same current density for high-Ni NMC cathodes.
- The UCSD group confirmed that the electronic conductivity of SPAN increases after the 1<sup>st</sup> cycle due to the increase in degree of conjugation resulting from the loss of non-aromatic S/N.
- The U-Pitt team identified additional candidates by computational studies to lower the reaction barrier and promote electrocatalysis of the rate limiting step for Li<sub>2</sub>S formation during the discharge process.
- The UW group clarified that porous copper leads to similar efficiency as copper foil, but at a reduced weight penalty.

### Keystone Project 3: Cell Fabrication, Testing, and Diagnosis

The General Motors (GM) team completed larger batch mixing process development with 500 mL mixer, which would provide up to 5-meter-long continuously single-side coating, or about 2-meter-long continuously double-side coating using current coater setup. The obtained “baseline” cathode from this process maintained  $\sim 4 \text{ mAh/cm}^2$  loading with 69.5 wt% sulfur content. During this quarter, the GM team sent a few batches of such “baseline” cathode to all Li-sulfur teams.

Aside from the coating parameter and formulation tuning, the GM team also initiated several engineering works on quality control. A complete process for basic quality check involving both chemical and physical characterizations has been initiated on material level including current collector, active materials, and additives to help identifying the uniformity and quality.

Aluminum current collector quality check was firstly finished by the thickness/unit weight ( $\text{mg/cm}^2$ ) uniformity examination. Two different commercial battery grade aluminum foils, which were used for baseline electrode fabrication, with thickness of 12  $\mu\text{m}$  and 20  $\mu\text{m}$ , respectively, were checked. To examine the unit weight variation throughout the width, samples were collected in different zones with adequate sample numbers. Figure 166a/c shows the illustration of sample picking zones of both aluminum foils. In Figure 166b/d, distribution curves of unit weight are plotted for comparison. The y axis shows the probability of the unit weight, which represents the variations of samples from the average unit weight. From the plots, it is very clear that the 12- $\mu\text{m}$  foil has much larger unit weight variation across the foil width, while the 20- $\mu\text{m}$  foil shows better uniformity in terms of unit weight. The standard deviations of these two foils are 0.060 and 0.033, respectively. The corresponding weight difference or variation of each foil is 8.39% and 2.88%, respectively. The statistical analysis results also confirm better uniformity of the 20- $\mu\text{m}$  foil than the 12- $\mu\text{m}$  foil.

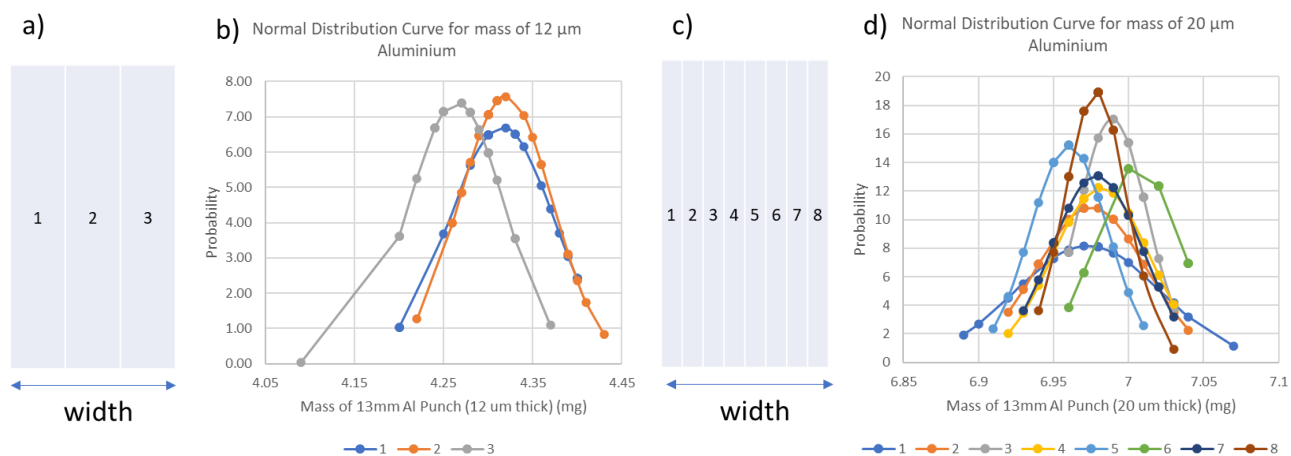


Figure 166. Normal distribution curve of unit weight of 12- $\mu\text{m}$  and 20- $\mu\text{m}$  thick aluminum foils.

This quarter, the GM team also helped in preparing several single-layer pouch cells using the baseline electrode with  $\sim 8 \mu\text{l/mgS}$  electrolyte amount for the Beamline test lead by the Brookhaven National Laboratory (BNL) team. The cathode was trimmed to  $4 \times 4 \text{ cm}^2$  to fit the cell fixture (Figure 167). In the test run, the single-layer pouch cell showed very stable performance (16 cycles so far) with no external pressure control (Figure 168).



Figure 167. Single-layer pouch cell using baseline electrode.

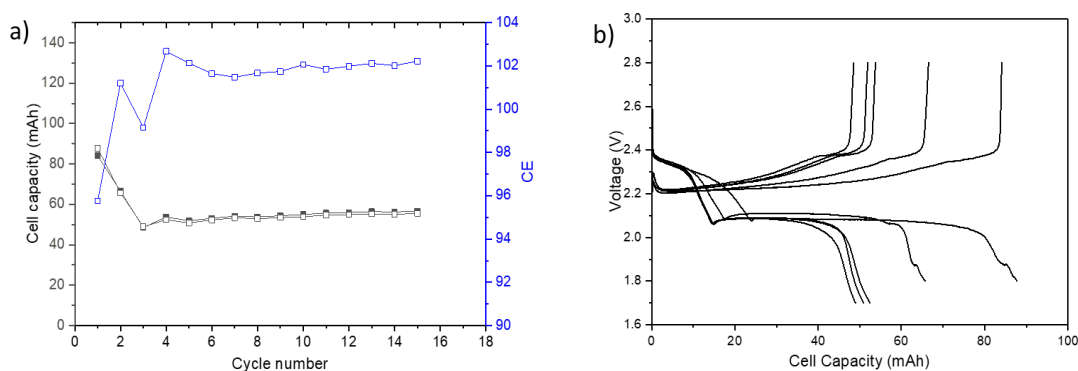


Figure 168. (a) Cycling stability of the single-layer pouch cell. (b) Voltage profiles for the first 5 cycles.

To accelerate development of new materials (for example, electrolytes) used in Li-SPAN batteries, the Idaho National Laboratory (INL) team is responsible for preparing reliable high-mass loading SPAN electrodes and providing them to Battery500 team members for coin-cell level study. The slurries for doctor-blade casting SPAN electrodes need to be optimized. The slurry recipe (Gen 1) results from UCSD (P. Liu's group; Figure 169a) had been used to prepare high-mass loading SPAN electrodes. However, the reproducibility when using this recipe is not good enough, and cracking on the edges of the electrodes after drying was frequently observed. Therefore, based on this recipe, the INL team optimized the slurry formula through the following aspects:

- (1) Carboxymethyl cellulose (CMC) binder is not very soluble in water. Therefore, 2 wt% of CMC aqueous solutions was added to slurries instead of the 5 wt% used in the original recipe to enable binders to be distributed uniformly in the slurries.
- (2) The total solid contents, including SPAN, super phosphorus, and CMC binders, were reduced from 25 wt% to 16.25 wt% to improve the uniformity of solids distribution in the slurries.
- (3) 10 wt% of isopropyl alcohol was added into slurries to further reduce the cracks or wrinkles.

Therefore, the INL team developed a reliable Gen 2 slurry recipe (Figure 169a) and reproduced at least 6 pieces of electrode without cracks and wrinkles. The areal mass loading of SPAN and electrode porosity are around  $6 \text{ mg/cm}^2$  and 60%, respectively. The electrochemical performances of the six batches of SPAN electrodes were evaluated with 4 M LiFSI in DME electrolytes in the coin cells. It can be seen from Figure 169b-c that the

reproducibility of the electrodes is very good in terms of electrochemical performance. Each SPAN electrode delivers the specific discharge capacity of over 650 mAh/g during aging cycles (at C/10). Those reliable and high-quality SPAN electrodes have been shipped to Battery500 team members (for example, GM, University of Michigan, PSU, SLAC National Accelerator Laboratory, and PNNL) for developing new materials.

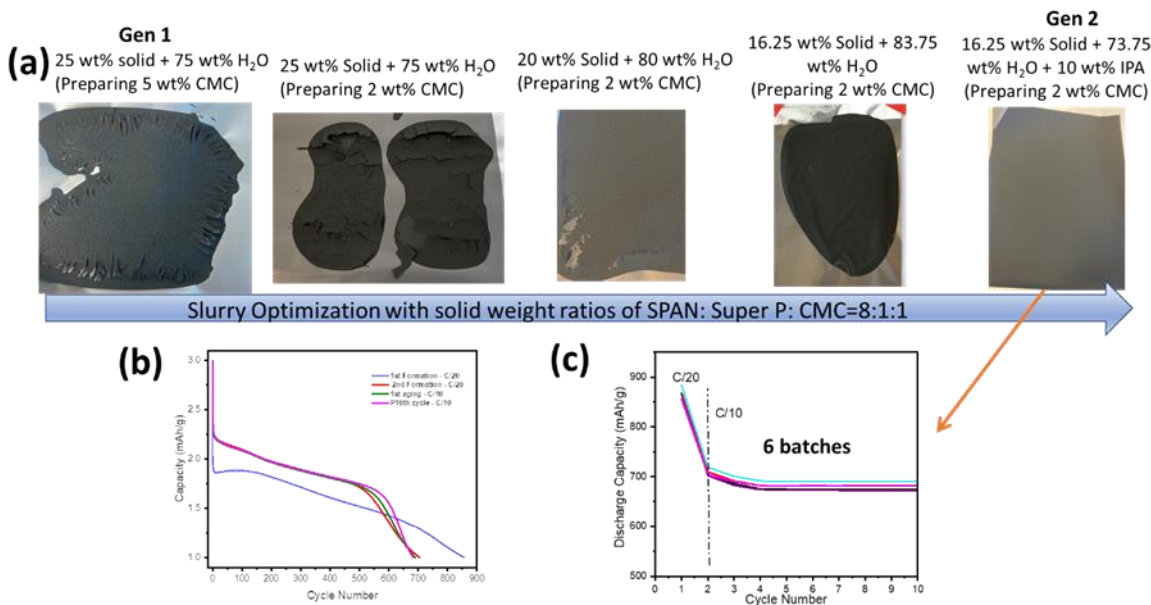


Figure 169. (a) Optimization of slurries for doctor-blade casting reproducible and high-quality SPAN electrodes. (b) Discharge curves of a typical SPAN electrode. (c) Discharge capacities versus cycling number for six batches of SPAN electrodes based on the Gen 2 recipe.

### Highlights of Keystone Project 3

The highlights for this quarter are as follows:

- The GM team completed the larger batch S/C cathode slurry mixing process development and initiated the quality check process for all components.
- The INL team successfully optimized the 2<sup>nd</sup> Gen SPAN slurry recipe and demonstrated SPAN cathode with reproducible 6 mg/cm<sup>2</sup> and 60% porosity using their optimized slurry recipe.

### Keystone Project 4: Cross-Cutting Efforts

The goal of the cross-cutting team is to develop and deploy advanced characterization tools in support of the three Keystone efforts, with a focus on probing specific materials and interfaces for Keystone 1, probing individual electrodes for Keystone 2, and probing the whole cell for Keystone 3. This quarter, the cross-cutting team completed its milestone of “Understand Li-SPAN mechanisms” (see details in the Keystone 2 section above). The BNL team investigated the origin of LiH in Li||NMC-811 cells. Their experimental and theoretical results suggest that LiOH present at the pristine surface of lithium metal is an important contributor to LiH formation in the SEI of Li||NMC-811 batteries. Complementing these speciation studies is characterization of SEI nanoscale heterogeneity at SLAC. Computational studies at Texas A&M University clarified the SEI and CEI formation pathways, including using larger-scale simulations. Finally, SLAC has established capabilities to map state-of-charge (SOC) nanoscale heterogeneity in cathodes, and the UCSD team has developed a systematic approach to quantify lithium and sulfur inventories in Li-S cells.

## Origin of LiH in the SEI of Li||NMC-811 Batteries

The BNL team led by E. Hu and X-Q. Yang, in collaboration with the PNNL Battery500 team and scientists at Army Research Laboratory revealed the origin of LiH in the SEI. This is a continuation of the previous work that revealed the prevalence of LiH in Li-metal SEI and has been documented in a previous Battery500 quarterly report (FY 2021, second quarter). To understand LiH formation mechanism, the team first devoted their efforts to differentiating hydrogen in the solvent from that in the electrolyte moisture. This was done by deuterating the DME solvent, thus replacing part or all of the hydrogen atoms in DME by deuterium ( $^2\text{D}$ ), while keeping all hydrogen atoms in the moisture in the form of hydrogen ( $^1\text{H}$ ). In limiting cases where the LiH is only contributed by solvent or moisture, the product should be either LiD or LiH, respectively. Otherwise, if both solvent and moisture make contributions, the product should be a solid solution of  $\text{LiD}_x\text{H}_{1-x}$ .

When preparing samples, the Li||NMC-811 cells were assembled and cycled with 1 M LiFSI in DME with various degrees of deuteration (that is, 0%, 50%, and 100%). The electrochemical performance was not affected by solvent deuteration. After 50 cycles, the electrodes were recovered from cells, and SEI samples were extracted for characterization using synchrotron X-ray diffraction (XRD).

The zoomed-in  $\text{LiD}_x\text{H}_{1-x}$  peaks in XRD patterns are shown in Figure 170a. When the solvent is not deuterated, the lattice parameter of  $\text{LiD}_x\text{H}_{1-x}$  matches exactly with that of lithium hydride standard, which is not only expected when  $x = 0$ , but, more importantly, serves as convincing evidence for the reliability of this method. As the deuteration amount increases, both the (111) and the (200) peaks shift to higher angles toward the position of LiD, indicating a decrease of lattice parameter and an increase of  $x$  value in the  $\text{LiD}_x\text{H}_{1-x}$  phase. This confirms the participation of solvents in  $\text{LiD}_x\text{H}_{1-x}$  formation. However, even when the solvent is completely deuterated (99% deuteration), the lattice parameter of  $\text{LiD}_x\text{H}_{1-x}$  is still far from that of the LiD standard, suggesting that the solvent contribution in  $\text{LiD}_x\text{H}_{1-x}$  formation has a limiting ceiling in this chemical process. This is quantitatively summarized in Figure 170b, in which the lattice parameter values obtained from Rietveld refinement are given. This seems to suggest that moisture is the main contributor to  $\text{LiD}_x\text{H}_{1-x}$  formation. However, an estimation using the assumption of 20 ppm moisture in electrolyte indicates that even when all the hydrogen in the electrolyte moisture is converted to  $\text{LiD}_x\text{H}_{1-x}$ , the amount of hydrogen is at least one order of magnitude lower than that observed experimentally.

Therefore, apart from the solvent and moisture, there must be an additional hydrogen source for  $\text{LiD}_x\text{H}_{1-x}$  formation. The team reexamined the pristine Li-metal surface to identify possible hydrogen sources. The XPS results in Figure 170c indicate there are considerable amounts of both  $\text{Li}_2\text{CO}_3$  and LiOH on the surface of pristine lithium metal. Of these two, LiOH is the only one that can potentially serve as an extra hydrogen source. To confirm this possibility, they characterized the Li-metal SEI both after the formation cycle and after 50 cycles using XRD; the results are shown in Figure 170d. The nascent SEI after the formation cycle has components of both LiOH and LiH. Surprisingly and intriguingly, LiOH completely disappeared in the aged SEI after 50 cycles, with the SEI exhibiting much more abundant LiH and a new component  $\text{Li}_2\text{O}$ . This shows that the SEI composition dynamic evolves during cycling, with the LiOH very likely being converted into  $\text{Li}_2\text{O}$  and LiH. To obtain a more quantitative thermodynamic understanding, DFT calculations were carried out for three possible reactions that can contribute to the experimentally observed transformations:



The Gibbs free energies were calculated to be -1.81 eV, -1.76 eV, and -1.70 eV for reactions (1), (2), and (3), respectively. These results suggest the conversion of LiOH to LiH is thermodynamically favored. The complementary experimental and theoretical results both support the overall conclusion that LiOH present at the pristine surface of lithium metal is an important contributor to LiH formation in the SEI of Li||NMC-811 batteries.

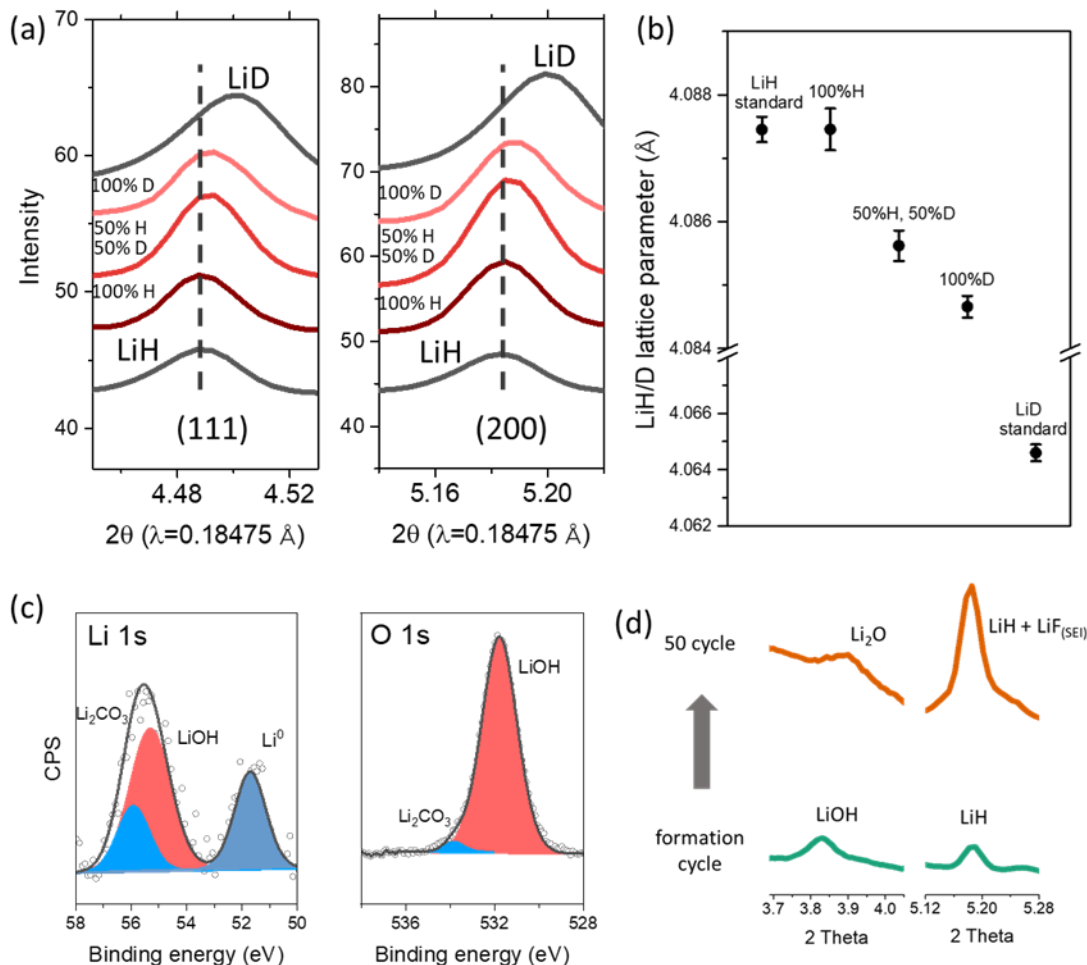


Figure 170. (a) (111) and (200) LiH/D X-ray diffraction (XRD) peaks from Li||NMC cell SEI using 100% H-DME, 50% H-DME + 50% D-DME, and 100% D-DME. (b) Lattice parameters obtained from the XRD fitting. (c) Lithium 1s and oxygen 1s X-ray photoelectron spectra of fresh lithium foil. (d) XRD results of SEI inside Li||NMC after formation cycle and after 50 cycles.

### Nanoscale SEI Heterogeneity

The SLAC team led by W. Chueh has developed *operando* electrochemical AFM (EC-AFM) to image lithium plating and SEI growth. Using this unique experimental capability, they probed the passivation behavior of lithium metal and assessed the SEI growth kinetics, a contributor to CE. This method complements other Battery500 SEI characterization capabilities such as cryo-EM as it measures the growth dynamics *in situ*, thereby removing the possibility of SEI damage and un-swelling during sample preparation. Collectively, these nanoscale characterizations provide validation data to the Texas A&M team on SEI simulation.

This quarter, as part of a larger multi-modal SEI characterization effort across the Battery500 Consortium, they developed secondary ion mass spectrometry (nanoSIMS) to map the local elemental composition of SEI. Previously, through EC-AFM, they observed the nucleation of nanoscale islands on the SEI on copper prior to lithium plating (at 30 mV versus  $\text{Li}^+/\text{Li}$ ). NanoSIMS complements the dynamic EC-AFM microstructure information by quantifying the elemental composition as a function of depth. As shown in Figure 171, nanoSIMS quantification of lithium, carbon, oxygen, and fluorine revealed that the islands formed during the formation step before lithium plating are rich in fluorine. Interestingly, depth-profiling performed as a function of SEI aging time showed that the initially-grown SEI (“inner” SEI) is richer in fluorine than the later-grown SEI (“outer” SEI). NanoSIMS, combined with EC-AFM and other characterization capabilities, provides a comprehensive microstructural and chemical picture of the SEI.

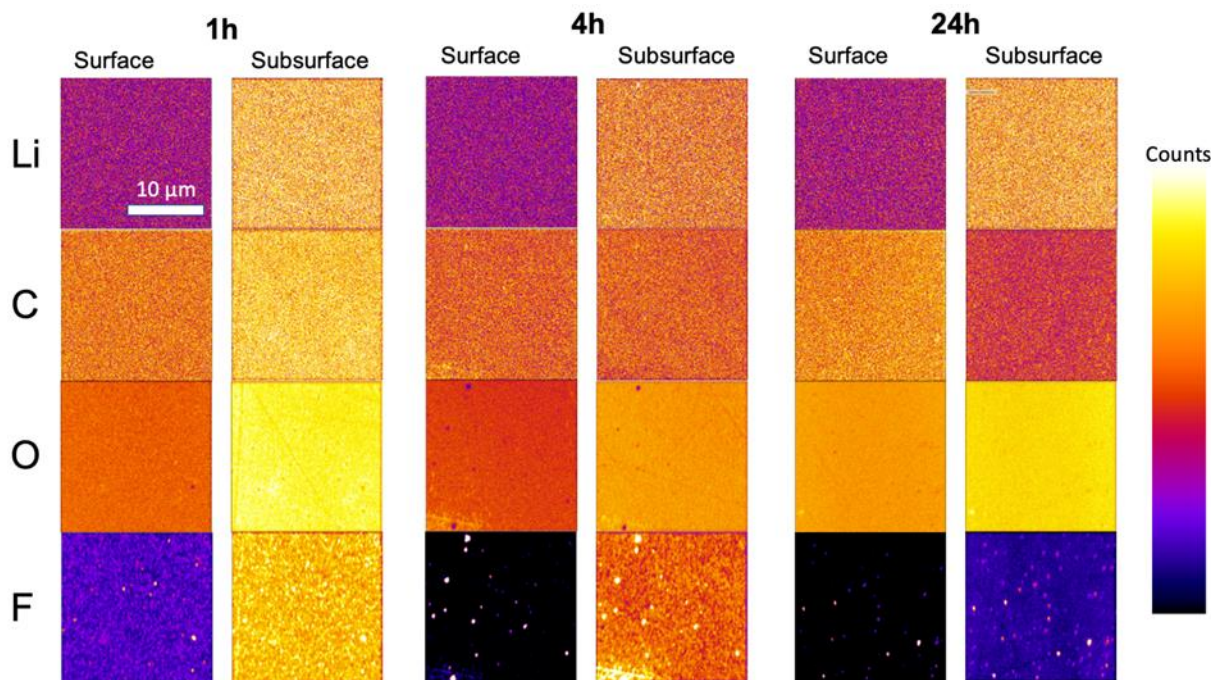


Figure 171. Nano secondary ion mass spectrometry elemental mapping of SEI formed on copper at 30 mV versus  $\text{Li}^+/\text{Li}$  as a function of hold time.

### DFT and *Ab Initio* Molecular Dynamics (AIMD) Studies of CEI and SEI Formation Mechanisms

The Texas A&M team has applied DFT and AIMD methods to study three aspects of CEI and SEI growth, as detailed below.

**Tracking LiF Formation on  $\text{LiNiO}_2$  Cathode CEI.** DFT and AIMD analysis performed on an LHCE mixture of LiFSI/DME/BTFE under electron-rich environments showed that the LiFSI salts are easily reduced and therefore very prone to defluorination. The decomposition of BTFE was also identified with formation of  $\text{F}^-$ ,  $\text{CH}_2\text{CF}^-$ , and other species. In contrast, DME showed good stability under these conditions. This decomposition behavior is different from the behavior of LHCE under electron-deficient environments, where DME and BTFE are more reactive and LiFSI salts remain stable. This indicates that the formation of LiF in the CEI is mainly derived from the decomposition of easily reduced LiFSI salts when the  $\text{LiNiO}_2$  cathode surface is discharged. These findings are relevant to passivation and degradation effects on the metal-oxide cathodes studied in Keystone 1.

**SEI Growth on Li-Metal during Cycling.** Multiscale modeling was applied to the interface of Li-metal anodes with an HCE to simulate SEI growth in extended cycling regimes with simultaneous lithium plating or stripping events. The team is studying a 4.4 M LiFSI/DME electrolyte; other formulations will be simulated later. The approach uses a newly developed 3D kinetic Monte Carlo algorithm. The Arrhenius equation is used to model rates of all reaction events with rate parameters evaluated from DFT and AIMD methods. The main descriptor for SEI growth is a bonding energy parameter specific to the species of interest (for example, lithium, oxygen, and fluorine) and its coordination environment. They hypothesize that this parameter is sufficiently versatile for modeling multiple microscopic events relevant to SEI formation and evolution: diffusion, dissolution, electrolyte adsorption, and decomposition. Full implementation is in progress. The first set of simulations is with SEI systems limited to inorganic phases such as lithium oxide and lithium fluoride. More complex systems (including heterogeneous inorganic and organic phases) will be investigated next. Understanding SEI and simultaneous plating/stripping during cycling is key to elucidating the origin of the degradation behavior in half-cell and full-cell performance, relevant to Keystone 3.

**SEI Growth at the Li-Metal Interface with an Ionic Liquid (IL) Electrolyte.** AIMD simulations were used to study the SEI initial formation and evolution at the interface between an IL (PYR14<sup>+</sup>FSI<sup>-</sup>) electrolyte with a TFSI<sup>-</sup> salt and lithium metal. As the SEI is formed, the decomposition pathways traversed by electrolyte components FSI<sup>-</sup>, PYR14<sup>+</sup>, and TFSI<sup>-</sup> both with and without a vinylene carbonate (VC) additive showed a variety of products. Three different dissociation mechanisms were identified for the salt anion TFSI<sup>-</sup>. The products formed through TFSI<sup>-</sup> Mechanism 1 and 2 are Li<sub>3</sub>C and LiF (inner layer) and Li<sub>2</sub>SO<sub>2</sub>, Li<sub>2</sub>NCF<sub>3</sub>SO<sub>2</sub> (outer layer). The products formed through TFSI<sup>-</sup> Mechanism 3 are Li<sub>2</sub>NCF<sub>3</sub>SO<sub>2</sub> and LiCF<sub>3</sub>SO<sub>2</sub> (outer layer). TFSI<sup>-</sup> Mechanisms 1 and 2 were found to be independent of the presence of VC. However, TFSI<sup>-</sup> Mechanism 3 is only observed when the VC is located at the interface, suggesting that the presence of VC helps to prevent further dissociation of TFSI<sup>-</sup>. For the IL anion FSI<sup>-</sup>, the team observed two different dissociation mechanisms. The products formed through FSI<sup>-</sup> Mechanism 1 are LiF (inner layer) and Li<sub>2</sub>SO<sub>2</sub> and Li<sub>3</sub>NSO<sub>2</sub> (outer layer). The products formed through FSI<sup>-</sup> Mechanism 2 are LiF (inner layer) and Li<sub>3</sub>NS<sub>2</sub>O<sub>4</sub> (outer layer). Even though the addition of VC does not affect FSI<sup>-</sup> products and dissociation mechanisms, it does slow down the degradation of FSI<sup>-</sup>. The new findings contribute to the Battery500 team effort to investigate the effect of alternative electrolytes on the SEI composition and morphology, as well as ion conduction and passivation properties.

### Quantification of Lithium and Sulfur Inventory Loss in Li-S Batteries

Previously many qualitative *ex situ* high-performance liquid chromatography (HPLC) studies of soluble polysulfide species have been done by derivatizing the polysulfides into stable methylated species. Those studies proved the applicability of these methods to the Li-S system and showed that identifying polysulfide species based on their chain lengths is possible. Last quarter, the UCSD team reported HPLC ultraviolet (UV) calibration data for quantifying dissolved elemental sulfur in the DME solution. This quarter, similar quantification was done by UCSD for Li<sub>2</sub>S<sub>2</sub> and Li<sub>2</sub>S<sub>3</sub> by preparing external standards from commercially available methylated shorter-chain polysulfides. The results are discussed in this report. Going forward, they will expand this methodology to quantify longer chain polysulfides. The ultimate long-term goal is to track the contribution of sulfur inventory loss to overall cell capacity losses.

A procedure was developed for using HPLC UV techniques to quantify Me<sub>2</sub>S<sub>2</sub> (CH<sub>3</sub>S<sub>2</sub>CH<sub>3</sub>) and Me<sub>2</sub>S<sub>3</sub> (CH<sub>3</sub>S<sub>3</sub>CH<sub>3</sub>). Specifically, 1  $\mu$ L of Me<sub>2</sub>S<sub>2</sub> (methylated Li<sub>2</sub>S<sub>2</sub>) and Me<sub>2</sub>S<sub>3</sub> each were diluted in 5 mL of DME in two individual volumetric flasks to make 2.22 mM of Me<sub>2</sub>S<sub>2</sub> and 1.904 mM of Me<sub>2</sub>S<sub>3</sub>, which was further diluted to concentrations of 1 mM, 0.5 mM, 0.1 mM, and 0.01 mM. Next, calibration curves for Me<sub>2</sub>S<sub>2</sub> and Me<sub>2</sub>S<sub>3</sub> quantification were derived by calculating the area under the intensity versus retention time data for different sample concentrations. The data used for calibration and the resulting calibration curves for Me<sub>2</sub>S<sub>2</sub> (left) and Me<sub>2</sub>S<sub>3</sub> (right) are shown in Figure 172. A linear relationship was observed with  $R^2 = 0.99429$  for Me<sub>2</sub>S<sub>2</sub> and  $R^2 = 0.99975$  for Me<sub>2</sub>S<sub>3</sub>. The HPLC-UV measurements were performed at 230-nm wavelength. Going forward, they will prepare and characterize additional Me<sub>2</sub>S<sub>x</sub> species, enabling the complete quantification of all polysulfide species found in Li-S batteries.

The SLAC team led by J. N. Weker is systematically investigating the calendar aging of single-layer Li-metal pouch cells with NMC-811 cathodes using the synchrotron measurement techniques of micro X-ray fluorescence ( $\mu$ -XRF) and micro X-ray absorption near-edge structure ( $\mu$ -XANES). Specifically,  $\mu$ -XRF provides elemental maps of the different transition metals (TMs) in the batteries, while  $\mu$ -XANES quantifies the oxidation states of the TMs and thus can be used to distinguish differences in SOC in regions of interest (ROIs) within the cathode. These studies are being carried out as part of a comprehensive Battery500 team effort starting with INL (fabrication and electrochemical testing of cells under different aging protocols) and BNL (non-destructive XRD mapping to identify ROIs), and finishing with SLAC (synchrotron  $\mu$ -XRF and  $\mu$ -XANES studies) and INL (laboratory characterization using XPS and other standard techniques). In preparation for these systematic long-term aging studies, preliminary proof-of-principle measurements were carried out on one single pouch cell to validate and optimize measurement and analysis procedures.

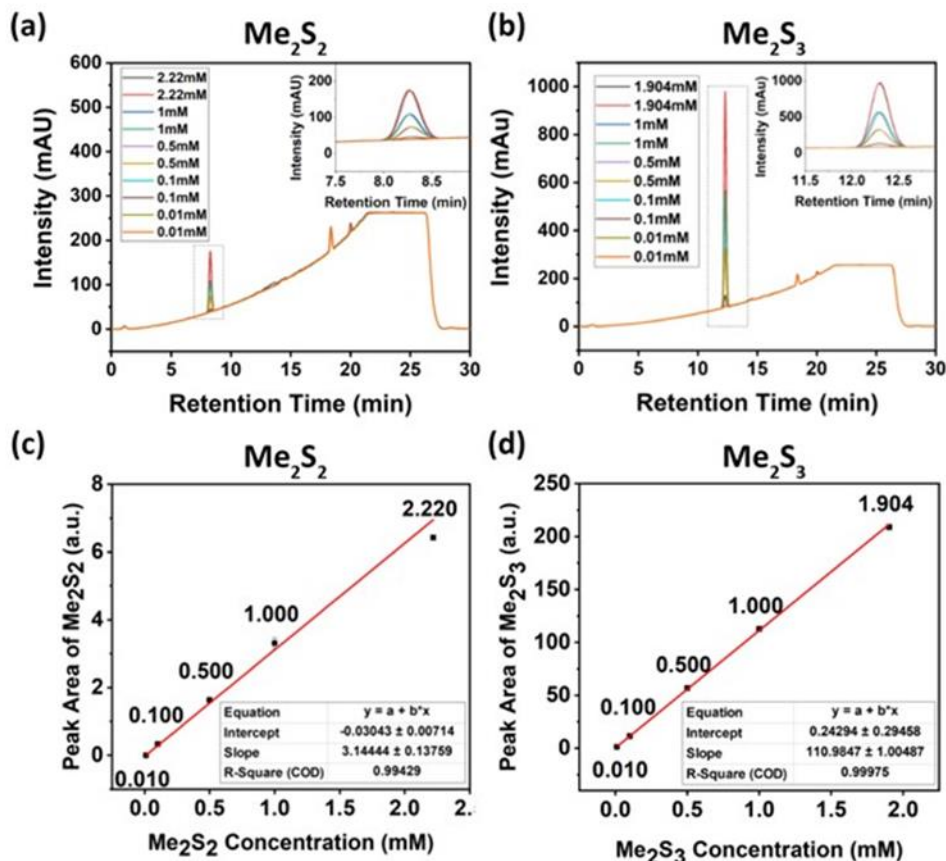


Figure 172. Chromatograms of samples of different concentrations of (a)  $\text{Me}_2\text{S}_2$ , (b)  $\text{Me}_2\text{S}_3$ , and the calibration curves for (c)  $\text{Me}_2\text{S}_2$  and (d)  $\text{Me}_2\text{S}_3$ .

### Spectroscopic Mapping of the Heterogenous SOC of NMC-811 Cathodes

Using Stanford Synchrotron Radiation Lightsource (SSRL) beamline 2-3, preliminary *in situ* and *ex situ* measurements were performed to collect data from both an aged pouch cell after 600 cycles and a pristine cathode sheet. The two samples were mapped using  $\mu$ -XRF on an instrument with an adjustable X-ray beam size of 1-5  $\mu\text{m}$ . Figure 173 shows elemental maps corresponding to the response of nickel, manganese, and cobalt taken simultaneously from the pristine NMC-811 electrode with 1  $\mu\text{m}$  focusing optics. From these maps, the distributions of each TM element in individual cathode particles of the NMC-811 cathode are clearly visible in a small ROI.

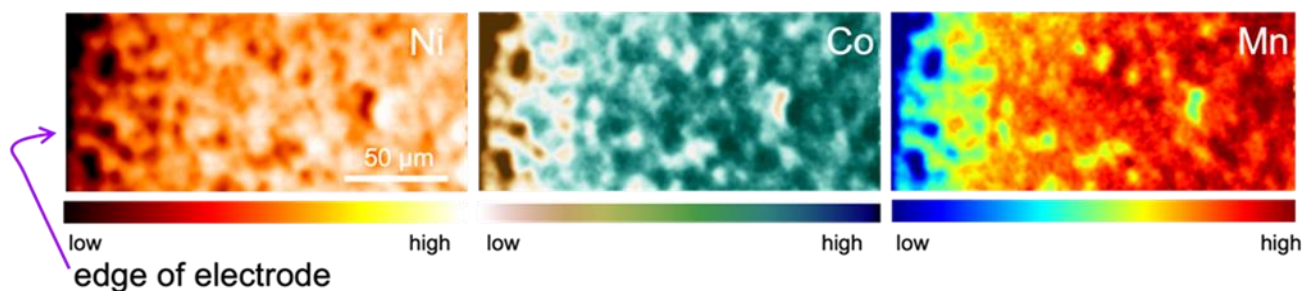


Figure 173. X-ray micro fluorescence maps for nickel, cobalt, and manganese of a pristine NMC-811 electrode using 1  $\mu\text{m}$  focusing optics.

As a baseline  $\mu$ -XANES measurement test, the team collected data along 32 points in a cycled pouch cell (Figure 174). There were no apparent differences between these spectra, suggesting that it is necessary to sample a larger portion of the electrode to see the heterogeneity expected based on the prior Battery500 characterization

of Li||NMC-811 cells. The preliminary data demonstrate the feasibility of using  $\mu$ -XANES to characterize the local NMC SOC, but also highlight the need for a larger X-ray beam and a larger imaging region. The remainder of the study will be conducted on beamline 7-2, a different  $\mu$ -XRF beamline that is better suited for larger samples. The focusing optics on beamline 7-2 allow for a larger spot size and therefore increased depth of focus, which will be important for *in situ* imaging of the electrode through the aluminized pouch material.

Moving forward, they will use  $\mu$ -XANES in concert with  $\mu$ -XRF to characterize heterogenous regions within the aged cells, especially on ROIs previously identified through non-destructive diffraction mapping measurements done by BNL at the NSLS-II synchrotron. They also plan to use *in situ* XANES radiography data collected with the micro-computed tomography capabilities of beamline 6-2 at SSRL for full-field, higher-resolution imaging on target ROIs.

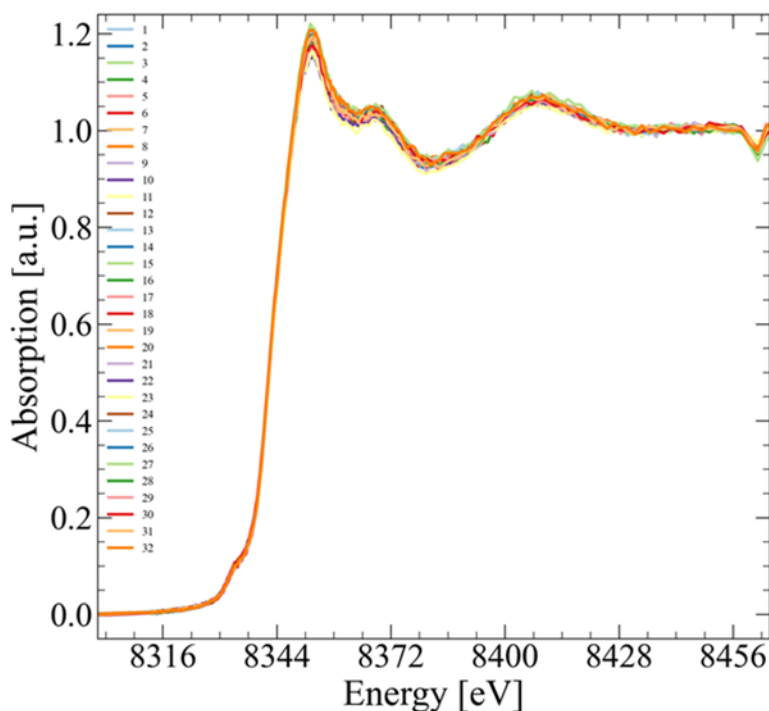


Figure 174. X-ray absorption near-edge spectra taken at 32 different points of a NMC cathode inside a pouch cell after 600 cycles.

#### Highlights of Keystone Project 4

The highlights for this quarter are as follows:

- The BNL team has identified LiOH on the surface of pristine Li-metal anode as an important contributor to the formation of LiH. LiOH converts into LiH and Li<sub>2</sub>O during cycling of the Li||NMC-811 cell.
- The SLAC team led by W. Chueh studied the depth-profiling as a function of SEI aging time showing that the initially-grown SEI (“inner” SEI) is richer in fluorine than the later-grown SEI (“outer” SEI) using nanoSIMS technique.
- Theoretical and computational analysis at Texas A&M provides new insights into electrolyte/electrode interactions in understanding the role of such rich chemistries in both CEI and SEI through developing a new theoretical approach that follows simultaneous interfacial film evolution with cation plating/stripping. Preliminary results provide the role of inorganic SEI phases (lithium oxide and lithium fluoride) on Li-metal surfaces.

- The UCSD team carried out quantification for  $\text{Li}_2\text{S}_2$  and  $\text{Li}_2\text{S}_3$  by preparing external standards from commercially available methylated shorter-chain polysulfides using HPLC-UV technique and the calibrations they have developed in the past.
- The SLAC team led by J. N. Weker has shown that  $\mu$ -XANES can be used to non-destructively image heterogeneity in the SOC of the NMC-811 cathode in a single-layer Li-metal pouch cell. This technique will be used to create higher-resolution images of ROIs identified through XRD maps performed by the BNL team on calendar-aged cells.

## Patents/Publications/Presentations

### Publications

- Kim, J., M. H. Engelhard, B. Lu, Y. Xu, S. Tan, B. E. Matthews, S. Tripathi, X. Cao, C. Niu, E. Hu, S-M. Bak, C. Wang, Y. S. Meng, J-G. Zhang,\* and W. Xu.\* “Fast-Charging Lithium Metal Batteries Enabled by Double-Layer Protected Lithium Metal Anode.” *Advanced Functional Materials* 32, no. 48 (2022): 2207172. doi: <https://doi.org/10.1002/adfm.202207172>.
- Xin, F., A. Goel, X. Chen, H. Zhou, J. Bai, S. Liu, F. Wang, G. Zhou, and M. S. Whittingham. “Electrochemical Characterization and Microstructure Evolution of Ni-Rich Layered Cathode Materials by Niobium Coating/Substitution.” *Chemistry of Materials* 34, no. 17 (2022): 7858–7866. doi: <https://doi.org/10.1021/acs.chemmater.2c01461>.
- Oyakhire, S. T., H. Gong, Y. Cui, Z. Bao, and S. F. Bent. “An X-ray Photoelectron Spectroscopy Primer for Solid Electrolyte Interphase Characterization in Lithium Metal Anodes.” *ACS Energy Letters* 7, no. 8 (2022): 2540–2546. doi: <https://doi.org/10.1021/acseenergylett.2c01227>.
- Yu, W., Z. Yu, Y. Cui, and Z. Bao. “Degradation and Speciation of Li Salts during XPS Analysis for Battery Research.” *ACS Energy Letters* 7, no. 10 (2022): 3270–3275. doi: <https://doi.org/10.1021/acseenergylett.2c01587>.
- Boyle, D. T., Y. Li, A. Pei, R. A. Vilá, Z. Zhang, P. Sayavong, M. S. Kim, W. Huang, H. Wang, Y. Liu, R. Xu, R. Sinclair, J. Qin, Z. Bao, and Y. Cui. “Resolving Current-dependent Regimes of Electroplating Mechanisms for Fast Charging Lithium Metal Anodes.” *Nano Letters* 22, no. 20 (2022): 8224–8232. doi: <https://doi.org/10.1021/acs.nanolett.2c02792>.
- Kim, S. C., J. Wang, R. Xu, P. Zhang, Y. Chen, Z. Huang, Y. Yang, Z. Yu, S. Oyakhire, W. Zhang, M. S. Kim, D. Boyle, P. Sayavong, J. Qin, Z. Bao, and Y. Cui. “High Entropy Electrolytes for Practical Lithium Metal Batteries.” *ChemRxiv* preprint (2022). doi: <https://doi.org/10.26434/chemrxiv-2022-j40p4>.
- Wu, Z., H. Liu, J. Holoubek, C. Anderson, L. Shi, H. Khemchandani, D. Lu, D. Liu, C. Niu, J. Xiao, and P. Liu. “The Role of Ion Transport in the Failure of High Areal Capacity Li Metal Batteries.” *ACS Energy Letters* 7, no. 8 (2022): 2701–2710. doi: <https://doi.org/10.1021/acseenergylett.2c01114>.
- Lu, B., W. Li, D. Cheng, M. Ceja, W. Bao, C. Fang, and Y. S. Meng. “Suppressing Chemical Corrosions of Lithium Metal Anodes.” *Advanced Energy Materials* (2022): 2202012. doi: <https://doi.org/10.1002/aenm.202202012>.
- Lu, B., W. Bao, W. Yao, J-M. Doux, C. Fang, and Y. S. Meng. “Methods—Pressure Control Apparatus for Lithium Metal Battery.” *Journal of the Electrochemical Society* 169, no. 7 (2022). doi: <https://doi.org/10.1149/1945-7111/ac834c>.

- Ren, Y., A. Bhargav, W. Shin, H. Sul, and A. Manthiram. “Anode-Free Lithium–Sulfur Cells Enabled by Rationally Tuning Lithium Polysulfide Molecules.” *Angewandte Chemie* 2022. doi: <https://doi.org/10.1002/anie.202207907>.
- Langdon, J., R. Sim, and A. Manthiram. “Gas Generation in Lithium Cells with High-Nickel Cathodes and Localized High-concentration Electrolytes.” *ACS Energy Letters* 2022. doi: <https://doi.org/10.1021/acseenergylett.2c01444>.
- Su, L., X. Zhao, M. Yi, H. Charalambous, H. Celio, Y. Liu, and A. Manthiram. “Uncovering the Solvation Structure of LiPF<sub>6</sub>-based Localized Saturated Electrolytes and Their Effect on LiNiO<sub>2</sub>-based Lithium-metal Batteries.” *Advanced Energy Materials* 2022. doi: <https://doi.org/10.1002/aenm.202201911>.
- Langdon, J., and A. Manthiram. “Crossover Effects in Lithium-metal Batteries with a Localized High Concentration Electrolyte and High-Nickel Cathodes.” *Advanced Materials* 2022. doi: <https://doi.org/10.1002/adma.202205188>.
- Su, L., and A. Manthiram. “Lithium-metal Batteries via Suppressing Li Dendrite Growth and Improving Coulombic Efficiency.” *Small Structures* (2022). doi: <https://doi.org/10.1002/ssstr.202200114>.
- Liu, J. X., W. Zhang, H. Wan, J. Zhang, J. Xu, J. Rao, T. Deng, S. Hou, B. Nan, and C. Wang. “Salt-in-Salt Reinforced Carbonate Electrolyte for Li Metal Batteries.” *Angewandte Chemie* 61, no. 35 (2022): e202207907. doi: <https://doi.org/10.1002/anie.202210522>.

#### Presentations (Invited)

- American Chemical Society (ACS) Fall Meeting, Chicago, Illinois (August 22, 2022): “Enabling Lithium Metal Anode by Advancing Electrolytes and Lithium Protection”; W. Xu, J. Kim, X. Cao, and J. Zhang.
- 1<sup>st</sup> Distinguished Engineering Lecture Series, University of New South Wales, Sydney, Australia (July 1, 2022): “Pushing the Limits of Li-Ion Batteries at their 50 Year Anniversary”; M. S. Whittingham.
- 23<sup>rd</sup> International Conference on Solid State Ionics, Boston, Massachusetts (July 19, 2022): “The Key Role of Solid State Ionics in the Development of Lithium-Ion Batteries”; M. S. Whittingham.
- John B. Goodenough 100<sup>th</sup> Birthday, Austin, Texas (July 22, 2022): “Lithium-Based Batteries: 1970 – Today”; M. S. Whittingham.
- International Society of Electrochemistry Meeting, Virtual (September 12, 2022): “Pushing the Limits of Lithium Batteries”; M. S. Whittingham, H. Zhou, F. Xin, B. Pei, I. Buyuker, K. Lee, J. Xiao, and the Battery500 team.
- International Conference on Niobium Based Batteries, Virtual (September 14, 2022): “Role of Nb in Nickel-Rich Layered Oxide Cathodes for Lithium-Ion Batteries”; M. S. Whittingham, F. Xin, and the Battery500 team.
- ACS Fall Meeting, Chicago, Illinois (August 21–25, 2022): “Solving a Metal Issue with Organic (Macro)Molecules”; Z. Huang, Y. Cui, and Z. Bao.
- ACS Fall Meeting, Chicago, Illinois (August 21–25, 2022): “Advanced Polymer Coatings for Li Metal Anodes”; Z. Huang, Y. Cui, and Z. Bao.
- ACS Fall Meeting, Chicago, Illinois (August 21–25, 2022): “Improving the Lithium Metal Battery Performance with a Polymer Layer”; Z. Huang, Y. Cui, and Z. Bao.
- ACS Fall Meeting, Chicago, Illinois (August 21–25, 2022): “Dynamic Enamine-One Bonds Enabled Sustainable Polymeric Materials”; Y. Lin and Z. Bao.
- ACS Fall Meeting, Chicago, Illinois (August 21, 2022): “Approaches to Mitigating Internal Shorting of Lithium Batteries”; P. Liu.

- International Conference on Materials for Humanity 2022, Singapore (September 21, 2022): “Designing Better Materials for Future Batteries”; Y. S. Meng.
- 242<sup>nd</sup> Electrochemical Society Meeting (ECS), Symposium A02: Research and Development of Primary and Secondary Batteries, Atlanta, Georgia (October 9–13, 2022): “From Lithiated Transition Metal Oxides to Silicon to Lithium-Sulfur: Evolution of Electrochemically Active Materials”; P. N. Kumta.
- 21<sup>st</sup> International Meeting on Lithium Batteries, Sydney, Australia (June 26 – July 1, 2022): “Delineating the Intricacies of High-Nickel Cathodes for Lithium-Ion Batteries”; A. Manthiram.
- Workshop on Electrochemical Energy Storage and Conversion Towards Carbon Neutrality, Hong Kong Polytechnic University, Hong Kong (July 4–5, 2022): “Battery Chemistries for a Sustainable Future”; A. Manthiram.
- PlugVolt Battery Seminar, Plymouth, Michigan (July 12–14, 2022): “Delineating the Intricacies of the Interfacial Chemistry of High-Nickel Cathodes in Lithium-Based Batteries”; A. Manthiram.
- 23<sup>rd</sup> International Conference on Solid State Ionics, Boston, Massachusetts (July 17–22, 2022): “Delineating the Intricacies of the Interfacial Chemistry of High-Nickel Cathodes in Lithium-Based Batteries”; A. Manthiram.
- John Goodenough Energy Storage Lecture Series, The University of Texas at Austin, Austin, Texas (September 8, 2022): “A Path Toward Sustainable Energy Storage”; A. Manthiram.
- University of Michigan, Ann Arbor, Michigan (September 16, 2022): “Sustainable Battery Chemistries for a Cleaner Planet”; A. Manthiram.
- University of Louisiana, Lafayette, Louisiana (September 23, 2022): “Electrical Energy Storage: Near-Term and Long-Term Perspectives”; A. Manthiram.
- 242<sup>nd</sup> ECS Meeting, Symposium A02: Research and Development of Primary and Secondary Batteries, Atlanta, Georgia (October 12, 2022): “PNNL R&D in Primary and Secondary Lithium Metal Batteries”; J. Xiao.
- ORCAS 2022: International Conference on Energy Conversion and Storage, San Juan, Washington (September 8, 2022): “An Integrated Science and Engineering Approach for Next-Generation Battery Materials and Technology”; J. Xiao.

## APPENDIX – ACRONYM GUIDE

Acronym	Full Description
1,4-DX	1,4-dioxane
1D	one-dimensional
2D	two-dimensional
3D	three-dimensional
3DOM	three-dimensional ordered microporous
3D-OMSH	three-dimensionally ordered microporous sulfur host
AB	acetylene black
ABL	active buffer layer
AC	alternating current
ACN	acetonitrile
ACPA	4,4'-azobis(4-cyanopentanoic acid
ACS	American Chemical Society
ADF	annular dark-field
AFLB	anode-free lithium battery
AFM	atomic force microscopy
AFSE	fluorinated saturated electrolyte with 0.1 wt% additive
AGG	aggregate
AIBN	azobisisobutyronitrile
AIMD	<i>ab initio</i> molecular dynamic
AIR	areal interfacial resistance
ALD	atomic layer deposition
ALS	Advanced Light Source
ANL	Argonne National Laboratory
ANN	artificial neural network
AOM	amphiphathic organic molecules
APS	Advanced Photon Source
APUP	Alliance Partner University Program
AQC	anthraquinone-2-carboxylic acid
AQT	1,5-bis(2-(2-(2-methoxyethoxy)ethoxy)ethoxy) anthra-9,10-quinone
ARC	accelerating rate calorimetry
ARL	U. S. Army Research Laboratory
ASR	area specific resistance
ASSB	all-solid-state battery
ASSLB	all-solid-state lithium battery
ASSLMB	all-solid-state Li-metal battery
ASSLSB	all-solid-state Li-S battery
ATR	attenuated total reflectance
$\beta$ -LPS	$\beta$ -phase $\text{Li}_3\text{PS}_4$
BBP	benzyl butyl phthalate
BCC	body-centered cubic
BE	baseline electrolyte
BEV	battery electric vehicle

Acronym	Full Description
BL	bottom layer
BMIM	1-butyl-3-methylimidazolium
BMR	Advanced Battery Materials Research Program
BNL	Brookhaven National Laboratory
BTFE	bis(2,2,2trifluoroethyl) ether
BV	Butler-Volmer
c-AIMD	constrained – <i>ab initio</i> molecular dynamics
CA	chronoamperometry
CAM	cathode active material
CC	constant current
CCCV	constant current / constant voltage
CCD	critical current density
CCD <sup>plating</sup>	plating critical current density
CCD <sup>stripping</sup>	stripping critical current density
CE	Coulombic efficiency
CEI	cathode electrolyte interface
CFM	carbon-based framework material
CIP	contact ion pair
CLP	cycle life projection
CM	co-melting
CMC	carboxymethyl cellulose
CMD	classical molecular dynamics
CN	coordination number
CNC	carbon nano-cage
cNEB	climbing image nudged elastic band
CNM	Center for Nanoscale Materials
CNT	carbon nanotube
COF	covalent organic frameworks
COP	critical overpotential
CP	cold pressed
CPE	composite polymer electrolyte
cryo	cryogenic
cryo-EM	cryogenic electron microscopy
cryo-FIB	cryogenic – focused ion beam
cryo-FIB-SEM	cryogenic – focused ion beam – scanning electron microscopy
cryo-STEM	cryogenic – scanning transmission electron spectroscopy
cryo-TEM	cryogenic – transmission electron microscopy
CS	corner-sharing
CSE	cluster-based solid electrolyte
CSF	corner-sharing frameworks
CSM	continuous symmetry measure
Csp	specific discharge capacity
CT	computed tomography
CV	cyclic voltammetry
DBE	dibutyl ether
DB-ML-FF	density-based machine-learning force field

Acronym	Full Description
DC	direct current
DCA	dicyanamide
DCT	diffraction contrast tomography (DCT)
DEB	double-end binding
DEC	diethyl carbonate
DEE	1,2-diethoxyethane
DEGDME	diethylene glycol dimethyl ether
DEMS	differential electrochemical mass spectrometry
DFE	defect formation energy
DFT	density functional theory
DiPE	diisopropyl ether
DIW	direct ink writing
DLR	Deutsches Zentrum für Luft- und Raumfahrt
DMC	dimethyl carbonate
DME	1,2-dimethoxyethane
DMF	dimethyl formamide
DMSO	dimethylsulfoxide
DOD	depth-of-discharge
DOE	U. S. Department of Energy
DOL	1,3-dioxolane
DOS	density of states
dP/dV	differential pressure
dPEO	dynamic bonds between polymer chains
dQ/dV	differential capacity
DRT	distribution of relaxation times
DSC	differential scanning calorimetry
DTL	dimethyl ether – trimethylolpropane – lithium nitrate
E/C	electrolyte/capacity
EC	ethylene carbonate
eCAD	electrochemical analytic diagnosis
EC-AFM	electrochemical atomic force microscopy
ECS	The Electrochemical Society
EDB	denotation for electrolyte of 1 M LiPF <sub>6</sub> in ethylene carbonate / diethyl carbonate (v/v = 1:1) with 1 wt% lithium difluoro(oxalate)borate
EDF	denotation for electrolyte of 1 M LiPF <sub>6</sub> in ethylene carbonate / diethyl carbonate (v/v = 1:1) with 15 wt% fluoroethylene carbonate
EDFB	denotation for electrolyte of 1 M LiPF <sub>6</sub> in ethylene carbonate / diethyl carbonate (v/v = 1:1) with 15 wt% fluoroethylene carbonate and 1 wt% lithium difluoro(oxalate)borate
EDL	electrical double layer
EDLi	electrochemically deposited lithium
EDS	energy-dispersive X-ray spectroscopy (also known as EDX)
EELS	electron energy loss spectroscopy
eGF	exfoliated graphene fluoride
EIS	electrochemical impedance spectroscopy
eLi	engineered lithium

Acronym	Full Description
EM	electron microscopy
EMC	ethyl methyl carbonate
EMIM-BF <sub>4</sub>	1-ethyl-3-methylimidazolium tetrafluoroborate
eNMR	electrophoretic nuclear magnetic resonance
EO	ethylene oxide
EPR	electron paramagnetic resonance
EQ-SANS	extended Q-range small-angle neutron scattering diffractometer
E/S	electrolyte/sulfur
EtOH	ethylene
EV	electric vehicle
EXAFS	extended X-ray absorption fine structure
F <sub>4</sub> EO <sub>2</sub>	1,1,1,2,2,3,3,4,4-nonafluoro-6-(2-methoxyethoxy)hexane
F5DEE	fluorinated-1,2-diethoxyethanes electrolyte
FAM	functional monomer additive molecule
FCC	face-centered cubic
FDEB	fluorinated 1,4-diethoxybutane
FDMB	fluorinated 1,4-dimethoxybutane
FDMH	fluorinated 1,6-dimethoxyhexane
FDMO	fluorinated 1,8-dimethoxyoctane
FDMP	fluorinated 1,5-dimethoxypentane
FEC	fluoroethylene carbonate
FEM	finite element method
FESEM	field emission scanning electron microscopy
FF	force field
FFT	fast Fourier transform
FIB	focused ion beam
fs	femtosecond
FSE	fluorinated saturated electrolyte
FSI	bis(fluorosulfonyl)imide
FTIR	Fourier transform infrared
FWHM	full width at half maximum
FZJ	Forschungszentrum Jülich
G3	triethylene glycol dimethyl ether
GB	grain boundary
<i>gc</i>	glass/ceramic
GCMA	glycerol carbonate methacrylate
GC-MS	gas chromatography – mass spectrometry
GCPL	galvanostatic cycling with potential limitation
GDL	gas diffusion layer
GE	gel electrolyte
GITT	galvanostatic intermittent titration technique
GM	General Motors
GOMD	Glass & Optical Materials Division
GP	Gaussian process
GPC	gel permeation chromatography
GPRA	Government Performance and Results Act

Acronym	Full Description
Gr	graphene
GRC	Gordon Research Conference
GSE	glassy solid electrolyte
GtO	graphite oxide
HAADF	high-angle annular dark-field
HATN	hexaazatrinaphthylene
HATN/CNT-S	hexaazatrinaphthylene / carbon nanotube polymer – sulfur composite
HATN-S	hexaazatrinaphthylene polymer – sulfur composite
HC	hard carbon
HCE	high-concentrated electrolyte
HCFM-S	sulfur-infiltrated high-surface-area carbon-based complex framework materials
HEV	hybrid electric vehicle
HEXRD	high-energy X-ray diffraction
HFB	hexafluorobenzene
HFE	hydrofluoroether
HFP	hexafluoropropylene
HG	hand grinding
H-NMR	hydrogen nuclear magnetic resonance
HOMO	highest occupied molecular orbital
HOPG	highly oriented pyrolytic graphite
HP	hot pressed
HPC	high-performance computing
HPLC	high-performance liquid chromatography
HRTEM	high-resolution transmission electron microscopy
HT	high throughput
IBA	International Battery Materials Association
IEEE	Institute of Electrical and Electronics Engineers
IL	ionic liquid
INL	Idaho National Laboratory
in-SEM	<i>in situ</i> scanning electron microscopy
IOFM	inorganic-organic framework material
IPA	isopropanol
IR	infrared
ISEL	Israel Electrochemical Society
ISU	Iowa State University
KAIST	Korea Advanced Institute of Science and Technology
KB	Ketjenblack
KMC	kinetic Monte Carlo
KPFM	Kelvin probe force microscopy
LAGP	Li-Al-Ge-P
LATP	Li-Al-Ti-P, such as $\text{Li}_{1+x}\text{Al}_x\text{Ti}_{2-x}(\text{PO}_4)_3$ or $\text{Li}_{1.3}\text{Al}_{0.3}\text{Ti}_{1.7}(\text{PO}_4)_3$
LBNL	Lawrence Berkeley National Laboratory
LBO	Li-B-O, such as $\text{Li}_3\text{BO}_3$
LBS	Li-B-S
LCE	low-concentration electrolyte
LCO	$\text{LiCoO}_2$

Acronym	Full Description
LCRC	Laboratory Computing Resource Center
LDBE	1.8 M LiFSI in dibutyl ether
LDEE	1.8 M LiFSI in diethyl ether / BTFE
LDiPE	1.8 M LiFSI in diisopropyl ether
LDME	1.8 M LiFSI in 1,2-dimethoxyethane
LE	liquid electrolyte
LFP	lithium iron phosphate
LGPS	Li-Ge-P-S, such as $\text{Li}_{10}\text{GeP}_2\text{S}_{12}$
LHCE	localized high-concentration electrolyte
LHS	left-hand side
LiBOB	lithium bis(oxalate)borate
LIC	Li-ion conductor
LiDFOB	lithium difluoro(oxalate) borate
LiDFP	lithium difluorophosphate
LiEDC	lithium ethylene decarbonate
LiFSI	Li-bis(fluorosulfonyl)imide
Li-MCA	lithium multicomponent alloy
Li-NMC	lithium – nickel manganese cobalt oxide
LIPS	lithium polysulfide
Li-SIA	Li-containing structurally isomorphous alloy
LiTFSI	lithium bis(trifluoromethanesulfonyl)imide
LLNL	Lawrence Livermore National Laboratory
LLTO	Li-La-Ti-O, such as $\text{Li}_{3x}\text{La}_{2/3-x}\text{TiO}_3$
LLZ	Li-La-Z
LLZO	Li-La-Z-O, such as $\text{Li}_7\text{La}_3\text{Zr}_2\text{O}_{12}$
LLZTO	Li-La-Zr-Ta-O, such as $\text{Li}_{6.75}\text{La}_3\text{Zr}_{1.75}\text{Ta}_{0.25}\text{O}_{12}$
LMR-NMC	Li- and Mn-rich Ni-Mn-Co
LNO	$\text{LiNiO}_2$
LOB	Li-O battery
LPC	large particle cathode
LPS	Li-P-S, such as $\text{Li}_3\text{PS}_4$
LPSB	Li-P-S-Br, such as $\text{Li}_3\text{PS}_4 + \frac{1}{2}\text{LiBr}$
LPSBI	Li-P-S-Br-I, such as $\text{Li}_7\text{P}_2\text{S}_8\text{Br}_{0.5}\text{I}_{0.5}$
LPSBr	Li-P-S-Br, such as $\text{Li}_6\text{PS}_5\text{Br}$
LPSCI	Li-P-S-Cl, such as $\text{Li}_6\text{PS}_5\text{Cl}$
LPSI	Li-P-S-I, such as $\text{Li}_3\text{PS}_4 + \frac{1}{2}\text{LiI}$
LPSIB	Li-P-S-I-Br, such as $\text{Li}_7\text{P}_2\text{S}_8\text{I}_{0.5}\text{Br}_{0.5}$
LSE	localized saturated electrolyte
LSiPCI	Li-Si-P-Cl, such as $\text{Li}_{9.54}\text{Si}_{1.74}\text{P}_{1.44}\text{S}_{11.7}\text{Cl}_{0.3}$
LSnS	Li-Sn-S, such as $\text{Li}_{3.85}\text{Sn}_{0.85}\text{Sb}_{0.15}\text{S}_4$
LSV	linear sweep voltammetry
LTO	$\text{Li}_4\text{Ti}_5\text{O}_{12}$
LUMO	lowest unoccupied molecular orbital
LYC / LYCI	Li-Y-Cl, such as $\text{Li}_3\text{YCl}_6$
MC	Monte Carlo; mechanochemical
MCA	multicomponent alloy

Acronym	Full Description
MD	molecular dynamics
METS	multiharmonic electrothermal spectroscopy
MGF	mixed glass former
MIC	molecular ionic composite
ML	machine learning
MLFF	machine learning force field
MLMD	molecular dynamics simulation with machine-learning potential
MOF	metal-organic framework
MOS	mixed oxy-sulfide
MOSN	mixed oxy-sulfide nitride
MPI	message-passing interface
MRS	Materials Research Society
MS	mass spectrometry
MSD	mean square displacement
MSE	mean squared error
MTU	Michigan Technological University
MWCNT	multiwalled carbon nanotube
MYEGA	Mauro–Yue–Ellison–Gupta–Allan model
NA	$\text{LiNi}_{0.95}\text{Al}_{0.05}\text{O}_2$
NaFSI	sodium bis(fluorosulfonyl)imide
NaNMC	Na-N-Mn-Co, such as $\text{NaNi}_{0.4}\text{Mn}_{0.4}\text{Co}_{0.2}\text{O}_2$ and $\text{NaNi}_{0.68}\text{Mn}_{0.22}\text{Co}_{0.1}\text{O}_2$
nano-CT	X-ray nano-computed tomography
nano-FTIR	Fourier transform infrared nano-spectroscopy
NASICON	sodium super ionic conductor
NaTFSI	sodium bis(trifluoromethylsulfonyl)imide
NATM	Ni-Al-Ti-Mg, such as $\text{LiNi}_{0.93}\text{Al}_{0.05}\text{Ti}_{0.01}\text{Mg}_{0.01}\text{O}_2$
NBO	nonbridging oxygen
NBR	nitrile butadiene rubber
NBS	nonbridging sulfur
NC	Ni-Co, such as $\text{LiNi}_{0.94}\text{Co}_{0.06}\text{O}_2$
NCEM	National Center for Electron Microscopy
NCM	Ni-Co-Mn
NCM-85105	$\text{LiNi}_{0.85}\text{Co}_{0.10}\text{Mn}_{0.05}\text{O}_2$
NCSE	non-calendered sulfur electrode
ND	di-coordinated nitrogen
NEB	nudged elastic band
NewEle	New Element
NF	nanoflake
NKB	nitrogen-doped integrated Ketjen Black
NLNMF	Na-Li-Ni-Mn-Fe, such as $\text{Na}_{0.85}\text{Li}_{0.1}\text{Ni}_{0.175}\text{Mn}_{0.525}\text{Fe}_{0.2}\text{O}_2$
NM	$\text{LiNi}_{0.95}\text{Mn}_{0.05}\text{O}_2$
NM11	$\text{NaNi}_{0.5}\text{Mn}_{0.5}\text{O}_2$
NMA	$\text{LiNi}_{0.9}\text{Mn}_{0.05}\text{Al}_{0.05}\text{O}_2$
NMC	Ni-Mn-Co
NMC-111	$\text{LiNi}_{1/3}\text{Mn}_{1/3}\text{Co}_{1/3}$
NMC-622	$\text{LiNi}_{0.6}\text{Mn}_{0.2}\text{Co}_{0.2}$

Acronym	Full Description
NMC-811	$\text{LiNi}_{0.8}\text{Mn}_{0.1}\text{Co}_{0.1}$
NMDC	Nanotechnology Materials and Devices Conference
NMF	nonnegative matrix factorization
NMF-111	$\text{NaNi}_{1/3}\text{Mn}_{1/3}\text{Fe}_{1/3}\text{O}_2$
NMF-112	$\text{NaNi}_{1/4}\text{Mn}_{1/4}\text{Fe}_{1/2}\text{O}_2$
NMFCN	Na-Mn-Fe-Co-Ni
NMP	N-methyl-pyrrolidone
NMR	nuclear magnetic resonance
NN	neural network
N/P ratio	capacity ratio between anode (negative electrode) and cathode (positive electrode)
NP	nanoparticle
NPCE	nonflammable polymer composite electrolyte
n-PDF	neutron diffraction and pair distribution function
NPT	constant number of atoms (N), pressure (P), and temperature (T)
NREL	National Renewable Energy Laboratory
ns	nanosecond
NSLS	National Synchrotron Light Source
NT	tri-coordinated nitrogen
NTO	sodium titanate
NVE	constant number (N), volume (V), and energy (E)
NVP	$\text{Na}_3\text{V}_2(\text{PO}_4)_3$
NVT	constant temperature, constant volume ensemble
OBd	Organic Battery Days Workshop
OCV	open circuit voltage
OER	oxygen evolution reaction
OMSH	ordered microporous sulfur host
ORNL	Oak Ridge National Laboratory
ORR	oxygen reduction reaction
OSU	Ohio State University
PAH	polycyclic aromatic hydrocarbon
PAN	polyacrylonitrile
PAQS	poly (anthraquinonyl sulfide)
PBDT	poly(2,2'-disulfonyl-4,4'-benzidine terephthalamide)
PC	propylene carbonate
PCA	principal component analysis
PCC	Pearson correlation coefficient
PC-LCHE	polymeric colloidal localized high-concentration electrolyte
PDF	pair distribution function
PDMS	polydimethylsiloxane
PE	polyelectrolyte, or polymer electrolyte
PEEK	polyether ether ketone
PEG	poly(ethylene glycol)
PEGDA	poly(ethylene glycol) diacrylate
PEGMA	poly(ethylene glycol) methacrylate
PEGMEA	poly(ethylene glycol) methyl ether acrylate

Acronym	Full Description
PEI	polyethylenimine
PEM	poly(ethylene malonate)
PEO	poly(ethylene oxide)
PES	photon emission spectroscopy
PETEA	pentaerythritol tetraacrylate
PFG	pulsed field gradient
PFIB	plasma focused ion beam
PFPE	perfluoropolyether
PFY	partial fluorescence yield
PGE	polymer gel electrolyte
PHEV	plug-in hybrid electric vehicle
PHM	poly(hexylene malonate)
PI	principal investigator
PICOFM	porous inorganic covalent-organic framework materials
PI-G	polyimide-graphene
PLiMTFSI	poly((trifluoromethanesulfon)imide lithium methacrylate)
PM	planetary mill
PMF	poly(melamine-co-formaldehyde) methylation
PMMA	polymethyl methacrylate
PMTH	dipentamethylenethiuram hexasulfide
PNNL	Pacific Northwest National Laboratory
POFM	porous organic framework materials
POSS	polyhedral oligomeric silsesquioxane
PP	polypropylene
ppm	parts per million
PPM	poly(pentylene malonate)
PPO	poly(phenylene oxide)
PS-SEI	polymer-supported solid electrolyte interphase
PST	partially sintered tape
PSTFSI	poly(4-styrenesulfonyl(trifluoromethanesulfonyl)imide)
PSU	Pennsylvania State University
PTFE	polytetrafluoroethylene
PTFSI	triflimide-based polyion
PTM	poly(trimethylene malonate)
PTO	pyrene-4,5,9,10-tetraone
PVB	polyvinyl butyral
PVDF	polyvinylidene (di)fluoride
PVP	polyvinylpyrrolidone
Pyr	pyrrolidinium
PyTFSI	pyrrolidinium (trifluoromethanesulfonyl)imide
RAFT	reversible addition–fragmentation chain-transfer
RDF	radial distribution function
RDS	rate determining step
RE	rare earth
ReaxFF	reactive force field
RF	random forest

Acronym	Full Description
rGO	reduced graphene oxide
RHS	right-hand side
RM	redox mediator
RMD	reactive molecular dynamics
RMSE	root mean square error
ROI	regions of interest
RP	red phosphorus
rpm	revolutions per minute
RPT	reference performance test
RR	reduced-repulsion
$R_{wp}$	weighted-profile R-factor
SAED	select area electron diffraction
SAEP	salt affinitive electrolyte phobic
SAM	scanning Auger microscopy
SANS	small angle neutron scattering
SASP	salt affinity solvent phobic
SAXS	small angle X-ray scattering
SBR	styrene-butadiene rubber
SC	single crystalline
SE	solid electrolyte
SEB	single-end binding
SEI	solid electrolyte interphase
SEM	scanning electron microscopy
SEO	polystyrene- <i>b</i> -poly(ethylene oxide) block copolymer
SERS	surface-enhanced Raman spectroscopy
SFSU	San Francisco State University
SHE	standard hydrogen electrode
SIA	structurally isomorphous alloy
SIC	single ion conductor
SIL	solvate ionic liquid
SIMS	secondary ion mass spectrometry
SLAC	Stanford Linear Accelerator Center
SLD	scattering length density
SNL	Sandia National Laboratory
SnS	tin sulfide
SOC	state of charge
SP <sup>2</sup>	salt-philic solvent-phobic
SPAN	sulfurized polyacrylonitrile
SPC	small particle cathode
SPC-1	sulfur polymerized composite – generation 1
SPC-2	sulfur polymerized composite – generation 2
SPE	solid polymer electrolyte
SPM	scanning probe microscopy
SPZ	sulfur polymerized composite
SQUID	superconducting quantum interference device
SRO	short-range order

Acronym	Full Description
SS	solid-state
SSB	solid-state battery
SSE	solid-state electrolyte
SSI	solid-state ion
SSLB	solid-state lithium battery
SSLMB	solid-state Li-metal battery
SS-NEB	solid-state nudged elastic band
SSPC	Solid-State Proton Conductors Conference
SSRL	Stanford Synchrotron Radiation Lightsource
S-SSE	sulfide-based solid-state electrolyte
STD	standard deviation
STEM	scanning transmission electron microscopy
SUS	stainless steel
SWCNT	single-walled carbon nanotube
sXAS	soft x-ray absorption spectroscopy
SXRD	synchrotron-based X-ray diffraction
T <sub>c</sub>	glass crystallization temperature
TCR	thermal contact resistance
TEGDME	tetraethylene glycol dimethyl ether
TEM	transmission electron microscopy
TEMPO	2,2,6,6-tetramethyl-1-piperidinyloxy
TEP	triethyl phosphate
TES	tender energy X-ray absorption spectroscopy
TEY	total electron yield
TFC	thin-film composite
TFP	tris(2,2,2-trifluoroethyl) phosphate
TFSI	(trifluoromethanesulfonyl)imide
TFTFE	1,1,2,2-tetrafluoroethyl 2,2,2-trifluoroethyl ether
T <sub>g</sub>	glass transition temperature
TGA	thermal gravimetric analysis
TGC	titration gas chromatography
THF	tetrahydrofuran
TL	top layer
TM	transition metal
TMA	trimethylaluminum
TMD	transition metal dichalcogenide
TME	trimethylolethane
TMP	trimethyl phosphate
TMPMA	acetone-protected trimethylolpropane methacrylate
TMS	tetramethylsilane
TOF-SIMS	time-of-flight secondary ion mass spectrometry
TRL	technology readiness level
TTE	1,1,2,2-tetrafluoroethyl-2,2,3,3-tetrafluoropropyl ether
TXM	transmission X-ray microscopy
UCB	University of California, Berkeley
UCSD	University of California, San Diego

Acronym	Full Description
UH	University of Houston
UHV	ultrahigh vacuum
UIC	University of Illinois, Chicago
UK	University of Kentucky
UM	University of Michigan
UMD	University of Maryland
UNLS	ultra-nanocrystalline lithium superoxide
U-Pitt	University of Pittsburgh
UT	University of Texas
UV	ultraviolet
UW	University of Washington
UWM	University of Wisconsin, Madison
VASP	Vienna <i>ab initio</i> simulation package
VBM	valence band maximum
VC	vinylene carbonate
VE	virtual electrode
VE-SAM	virtual electrode scanning Auger microscopy
VE-XPS	virtual-electrode X-ray photoelectron spectroscopy
VGCF	vapor-grown carbon fibers
VOC	volatile organic compound
VTO	Vehicle Technologies Office
WAXS	wide-angle X-ray scattering
WL	white light
XAFS	X-ray absorption fine structure
XANES	X-ray absorption near-edge structure
XAS	X-ray absorption spectroscopy
x-PDF	synchrotron X-ray diffraction and pair distribution function
xPEO	crosslinked poly(ethylene oxide)
XPS	X-ray photoelectron spectroscopy
XRD	X-ray diffraction
XRF	X-ray fluorescence
XRT	X-ray tomography
zPU	zwitterionic polyurethane
ZR	Zhang-Rice singlet